

UNIVERSIDADE DE SÃO PAULO
INSTITUTO DE QUÍMICA
Programa de Pós-Graduação em Química

Vagner Roberto Magri

**Development of Nanocomposites based on Layered
Double Hydroxides and Graphene-like Materials**

Versão corrigida da Tese conforme Resolução CoPGr 5890
O original se encontra disponível na Secretaria de Pós-Graduação do IQ-USP

São Paulo
Data do Depósito na SPG:
16/02/2023

Vagner Roberto Magri

**Desenvolvimento de Nanocompósitos à base de
Hidróxidos Duplos Lamelares e Materiais do tipo
Grafeno**

*Tese apresentada ao Instituto de
Química da Universidade de São
Paulo para obtenção do Título de
Doutor em Ciências (Química)*

Orientadora: Profa. Dra. Vera R. L. Constantino

São Paulo
Data do Depósito na SPG:
16/02/2023

Autorizo a reprodução e divulgação total ou parcial deste trabalho, por qualquer meio convencional ou eletrônico, para fins de estudo e pesquisa, desde que citada a fonte.

Ficha Catalográfica elaborada eletronicamente pelo autor, utilizando o programa desenvolvido pela Seção Técnica de Informática do ICMC/USP e adaptado para a Divisão de Biblioteca e Documentação do Conjunto das Químicas da USP

Bibliotecária responsável pela orientação de catalogação da publicação:
Marlene Aparecida Vieira - CRB - 8/5562

M212d Magri, Vagner Roberto
Development of Nanocomposites based on Layered
Double Hydroxides and graphene-like materials /
Vagner Roberto Magri. - São Paulo, 2023.
204 p.

Tese (doutorado) - Instituto de Química da
Universidade de São Paulo. Departamento de Química
Fundamental.

Orientador: Constantino, Vera Regina Leopoldo

1. Layered Double Hydroxides. 2. Layered Double
Oxides. 3. Folic Acid. 4. Graphene-like materials.
5. Carbon-based nanocomposites. I. T. II.
Constantino, Vera Regina Leopoldo , orientador.

Dedico essa tese ao meu companheiro Rodrigo Zieri e aos meus pais Maria Isabel Tognoli Magri e Mauro Roberto Magri pelo apoio e amor incondicional.

Agradecimentos (Acknowledgment)

Não cheguei aqui sozinho. Por isso, agradeço...

Aos meus pais, Maria Isabel Tognoli Magri e Mauro Roberto Magri, por todo apoio e pelo amor incondicional. Amo vocês!

Ao meu companheiro, Rodrigo Zieri, pois não teria conseguido sem você. Me lembro que no dia da prova de ingresso do doutorado você viajou comigo pra São Paulo pra me apoiar e, durante todos esses anos que estamos juntos, você sempre me incentivou a seguir em frente e nunca me limitou a nada, mesmo estando distantes fisicamente. Por isso, meu muito obrigado por tudo. Te amo! Agradeço também a Marie, nossa cachorrinha que foi adotada durante a pandemia. Ela fez toda a diferença em nossas vidas naquele período difícil, e continua fazendo...com seu companheirismo que é único dos cachorros.

À minhas avós, Gema e Maria José, à minha irmã Débora e ao meu sobrinho Luiz Gustavo, pelo amor e carinho.

Às minhas amigas e aos amigos da vida, Ferzinha, Mômô, Ferzona, Dan, Chica e Deroco, pela amizade sincera, pelas conversas e pelas cervejas. Amo vocês!

À minhas amigas e aos meus amigos do Laboratório de Sólidos Lamelares (LaSol Instituto de Química – USP), Carol, Mari, Vanessinha (*in memoriam*), Rafael, Victor, Denise, Vanessa Roberta, Alfredo e Michele. Muito obrigado por terem me recepcionado tão bem! Vocês são profissionais incríveis que me ensinaram muito durante o período do meu doutoramento. Faço um agradecimento especial a Carol (minha melhor amiga em São Paulo XD), por sempre segurar a minha mão (XD), pelas fofocas, pela amizade sincera, e por me fazer acreditar no meu potencial.

Aos amigos do IQ/USP, Lais Matos (Broto) e Ronaldo Amaral, por sua amizade sincera e por me ajudarem sempre que precisei.

À moradia estudantil, CRUSP, por garantir minha permanência estudantil nos últimos anos de doutoramento. Também aos amigos do CRUSP, Luana, Lua e Marcelo, por tornarem essa breve estada mais leve e divertida.

Ao grupo de pesquisa da Profa. Ana Maria Ferreira Costa, em especial a Cida e ao Ricardo. Vocês sempre foram muito solícitos em me ajudar nesse trabalho, sou muito grato por isso.

A equipe do Laboratório de Espectroscopia Molecular (LEM, Instituto de Química – USP), em nome das Profas. Dalva Lúcia e Márcia Temperini, pela amizade, pelos

ensinamentos e pelo apoio nas análises de espectroscopia vibracional. Agradeço também aos colegas, Otávio, Iza, Jair, Laura e Rafa pelas conversas e pelo auxílio nas análises.

Agradeço também ao Laboratório de Cristalografia (Instituto de Física - USP), em nome da Profa. Marcia Fantini e dos técnicos Tarsis e Antônio Carlos, por todo apoio com as análises de cristalografia de raios X.

Agradeço a equipe de *Matériaux Inorganiques* do Institut de *Chimie de Clermont-Ferrand*, em nome da Profa. Christine Taviot-Gueho. E também aos amigos e amigas que lá fiz, Nawal, Ali, Marwa, Cedric, Nour, Cristian, Henrique e Alexandra, pela amizade, pelas conversas e pelas cervejas.

A minha orientadora, Profa. Vera R. L. Constantino, por me receber em seu laboratório, pela orientação, pelos ensinamentos compartilhados e pela amizade construída ao longo desses anos. Serei eternamente grato! Aprendi e cresci muito em seu laboratório, profissionalmente e como pessoa humana. Te admiro! Muito obrigado por tudo!

A Universidade de São Paulo, ao Instituto de química (IQ/USP) e ao Departamento de Química Fundamental, pela infraestrutura e as condições necessárias para realização desse trabalho.

A Central Analítica do Instituto de Química da Universidade de São Paulo (CA-IQUSP), em nome da Michele, do Alfredo e da Rebeca, por toda ajuda técnica e pela estrutura disponibilizada para realização desse trabalho.

Por fim, agradeço as agências de fomento, porque sem financiamento não se faz pesquisa. A Coordenação de Aperfeiçoamento de Pessoal de Nível Superior – CAPES pela bolsa concedida (33002010191P0 – Química), ao CNPQ e à FAPESP pelo apoio financeiro de projetos do LaSol. Agradeço também ao *Centre National de la Recherche Scientifique (CNRS)* da França pela bolsa de estágio concedida por meio do projeto Pack Ambition International 2019 E LS 200788.

“Educação não transforma o mundo.

Educação muda as pessoas.

Pessoas transformam o mundo.”

Paulo Freire (1921-1997)

ABSTRACT

Magri, V.R. **Development of Nanocomposites based on Layered Double Hydroxides and graphene-like materials**. 2023. 200p. Tese de Doutorado - Programa de Pós-Graduação em Química. Instituto de Química, Universidade de São Paulo, São Paulo

Nanocomposites based on layered double hydroxides (LDH) and graphene-like materials (C), e.g., graphitic carbon and carbon quantum dots (C-dots), have been applied in sensing, catalysis, environmental protection, electronic devices, and as bioimaging and theragnostic agents, for instance. In this work, hybrid materials constituted of M_2Al -LDH ($M = Mg^{2+}$ or Zn^{2+}) intercalated with carboxymethylcellulose polymer (CMC) or folate anions from Folic Acid (FA) were synthesized and investigated as precursors of carbon-based materials. Their thermal behavior was evaluated by simultaneous thermogravimetric analysis (TGA) and differential scanning calorimetry (DSC), as well as evolved gas analysis (EGA) through TGA coupling to mass spectroscopy (MS) and/or infrared spectroscopy (IR). Based on the TGA/DSC results, the materials were pyrolyzed in a furnace, and resulting nanocomposites were structurally and spectroscopically characterized. The main findings of the work were: *(i)* M_2Al -FA and M_2Al -CMC were suitable sources of carbon-based nanocomposites composed of layered double oxides (LDO-C); *(ii)* from pyrolysis of FA itself, N-doped C-dots could be synthesized at 350 °C, whereas graphitic carbon was optimally obtained above 800 °C; *(iii)* the carbonization of folate anions was delayed after intercalation; *(iv)* vibrational spectroscopy characterization of FA and sodium folate salts (Na_2HFol and Na_3Fol), supported by density functional theory (DFT) calculations, were helpful in characterize related graphite-like materials and carbon-based nanocomposites; *(v)* the crystallization of metal oxides (*i.e.*; MgO and ZnO) and/or spinel-like structures (*i.e.*, $MgAl_2O_4$ e $ZnAl_2O_4$) were hindered for M_2Al -LDH hybrid materials when compared with their counterparts intercalated with simple anions, for instance, carbonate (CO_3^{2-}) and chloride (Cl^-). Such hindrance was attributed to the carbonized matter formed during pyrolysis; *(vi)* for Zn_2Al -LDH hybrids material, it was noticed a carbothermic reaction involving ZnO occurring above 800 °C, which led to the loss of zinc vapor; *(vii)* LDO-C obtained from M_2Al -FA pyrolysis could be successfully restored into the LDH-C structure through reaction in water (“memory effect”). Nanocomposites presenting intimately mixed components were obtained up to 600 and 800 °C from Zn_2Al -FA and Mg_2Al -FA precursors, respectively; *(viii)* LDH-FA were also potential precursors of nanocomposites based on LDH/C-dots and the proper temperature limit was determined to be around 400 °C. The exploration of nanocomposite precursors with different physicochemical properties allowed us to provide a wide-ranging knowledge of important features regarding the synthesis of nanocomposites based on LDH and graphene-like materials. Hence, this research can drive new strategies to synthesize LDH-C and LDO-C with assorted potential applications.

Keywords: Layered Double Hydroxides; Layered Double Oxides; Folic Acid; Graphene-like materials; Carbon-based nanocomposites.

RESUMO

Magri, V.R. **Desenvolvimento de Nanocompósitos à base de Hidróxidos Duplos Lamelares e Materiais do tipo Grafeno**. 2023. 200p. Tese de Doutorado - Programa de Pós-Graduação em Química. Instituto de Química, Universidade de São Paulo, São Paulo

Nanocompósitos à base de hidróxidos duplos lamelares (*LDH*) e materiais do tipo grafeno (*C*), *e.g.*, carbono grafítico e pontos quânticos de carbono (*C-dots*), têm sido aplicados em sensores, catálise, remediação ambiental, dispositivos eletrônicos, e como agentes teranósticos e de diagnóstico por imagem, por exemplo. Neste trabalho, materiais híbridos constituídos por $M_2Al-LDH$ ($M = Mg^{2+}$ ou Zn^{2+}) intercalados com o polímero carboximetilcelulose (*CMC*) ou ânions folato oriundos do ácido fólico (*FA*) foram sintetizados e investigados como precursores de materiais à base de carbono. O comportamento térmico dos materiais foi avaliado simultaneamente por análise termogravimétrica (*TGA*) e calorimetria diferencial exploratória (*DSC*), bem como análise de gases (*EGA*) por meio de *TGA* acoplada à espectrometria de massas (*MS*) e/ou espectroscopia no infravermelho (*IR*). Com base nos resultados de *TGA/DSC*, os materiais foram pirolisados em forno e os nanocompósitos obtidos foram caracterizados por análise de estrutura e por espectroscopia. Os principais resultados do trabalho foram: (i) os materiais M_2Al-FA e $M_2Al-CMC$ foram precursores adequados para a síntese de nanocompósitos à base de carbono constituídos por óxidos duplos lamelares (*LDO-C*); (ii) partindo-se da pirólise do *FA* puro, *C-dots* dopados com nitrogênio foram sintetizados a 350 °C, enquanto que a temperatura ideal para se obter carbono grafítico foi acima de 800 °C; (iii) a carbonização dos ânions folato foi retardada após a intercalação; (iv) a caracterização do *FA* e sais de folato de sódio (Na_2HFol e Na_3Fol) por espectroscopia vibracional, apoiada por cálculos da teoria do funcional da densidade (*DFT*), auxiliou na caracterização dos respectivos materiais do tipo grafeno e dos nanocompósitos à base de carbono; (v) a cristalização de estruturas de óxidos metálicos (isto é, MgO e ZnO) e/ou espinélio (*e.g.*, $MgAl_2O$ e $ZnAl_2O$) foi dificultada para os materiais híbridos de $M_2Al-LDH$ comparados com os respectivos materiais intercaladas com ânions simples, por exemplo, carbonato (CO_3^-) e cloreto (Cl^-). Esse efeito foi atribuído à matéria carbonizada formada durante a pirólise; (vi) para os híbridos de $Zn_2Al-LDH$, notou-se a reação carbotérmica envolvendo ZnO que ocorre acima de 800 °C, levando à perda de zinco metálico na forma de vapor; (vii) materiais do tipo *LDO-C*, obtidos da pirólise de M_2Al-FA , puderam ser reconstituídos a fase *LDH-C* por meio da reação em água (“efeito memória”). Nanocompósitos apresentando componentes intimamente misturados foram obtidos até 600 e 800 °C, a partir dos precursores Zn_2Al-FA e Mg_2Al-FA , respectivamente; (viii) *LDH-FA* também foram potenciais precursores de nanocompósitos à base de *LDH/C-dots* e o limite de temperatura adequado foi determinado para ser em torno de 400 °C. A investigação de precursores que apresentam diferentes propriedades físico-químicas permitiu fornecer um amplo conhecimento dos principais aspectos relacionados a síntese de nanocompósitos à base de *LDH* e materiais do tipo grafeno. Deste modo, este trabalho poderá auxiliar no desenvolvimento de novas estratégias para sintetizar *LDH-C* e *LDO-C* com diversas aplicações em potencial.

Palavras-chave: Hidróxidos duplos lamelares; Óxidos duplos lamelares; Ácido fólico; materiais do tipo grafeno; nanocompósitos à base de carbono.

CONTENTS

Chapter 1. Introduction	11
Chapter 2. Investigation of Thermal Behavior of Layered Double Hydroxides Intercalated with Carboxymethylcellulose Aiming Bio-Carbon Based Nanocomposites	43
Chapter 3. Folic acid and sodium folate salts: Thermal behavior and spectroscopic (IR, Raman, and solid-state ^{13}C NMR) characterization	61
Chapter 4. Pyrolysis mechanism of Folic Acid: identification of gaseous products and characterization of N-doped carbon materials	105
Chapter 5. Hybrid nanomaterials based on Folic Acid intercalated into $\text{M}^{2+}/\text{Al}^{3+}$ ($\text{M}^{2+} = \text{Mg}^{2+}$ and Zn^{2+}) Layered Double Hydroxides as precursors of Carbon-based Nanocomposites	149
Appendix I. Supporting Information material of Chapter 2	205
Appendix II. Supporting Information material of Chapter 3	214
Appendix III. Supporting Information material of Chapter 4	251
Appendix IV. Supporting Information material of Chapter 5	288
Súmula Curricular	332

Introduction

Human beings have been using nanomaterials since prehistoric times in rupestrian paintings made of carbon nanomaterials from smoke and soot [1]. The advent of nanoscience and nanotechnology in the modern age has been increasing life quality thanks to the contribution to developing several fields in society, such as medicine and healthcare, environment, energy, agriculture, industry, and technology, as well as education, among many others [1–4]. The implementation of nanomaterials by industries and in day-by-day human products is a reality and the market associated is currently valued in billions of dollars [1,5,6]. Examples include the use of nanomaterials in drug delivery systems, prostheses, cosmetics, fabrics, fertilizers, automobiles, and electronic devices [1–5], for instance.

The interest in nanomaterials is based on their unique physical-chemical properties (e.g., high surface area, outstanding electronic properties, etc.) compared to related bulk materials, owing mainly due to the reduced size of nanoparticles [1,5,7,8]. Nanomaterials can be defined as materials in which at least one of their dimensions is in the submicrometric size of approximately 1 to 100 nm [9]. According to their dimensionality, nanomaterials can be classified as follows (**Figure 1**):

(i) zero-dimensional (0D): materials that have all dimensions on the nanometric scale, such as, fullerenes, carbon quantum dots (C-dots), and gold nanoparticles.[1,5,7,8]

(ii) one-dimensional (1D): materials that present one dimension in the micrometric scale (e.g.; graphene nanotubes and nanoribbons) [1,5,7,8];

(iii) two-dimensional (2D): materials composed of layers in which one dimension is in the nanometric domain, for example, graphene, layered double hydroxides (LDH) and montmorillonite clay mineral [1,5,7,8]. The International Union for Pure and Applied Chemistry (IUPAC) defines layered materials as “*a crystalline material wherein the atoms in the layers are cross-linked by chemical bonds, while the atoms of adjacent layers interact by physical forces. A single layer is called a lamella, slab or sheet. A layered compound has a well-defined X-ray diffraction (XRD) pattern, which demonstrates its lamellar structure*” [10]. In addition, such materials can form intercalated compounds that IUPAC defines as “*compounds resulting from reversible inclusion, without covalent bonding, of one kind of molecule in a solid matrix of another compound, which has a laminar structure. The host compound, a solid, may be macromolecular, crystalline or amorphous*” [11].

(iv) three-dimensional (3D): all dimensions of this type of material are larger than 100 nm, but it is constituted by nanomaterials, for instance, bulk solids (*e.g.*, graphite) and some nanocomposites [1,5,7,8].

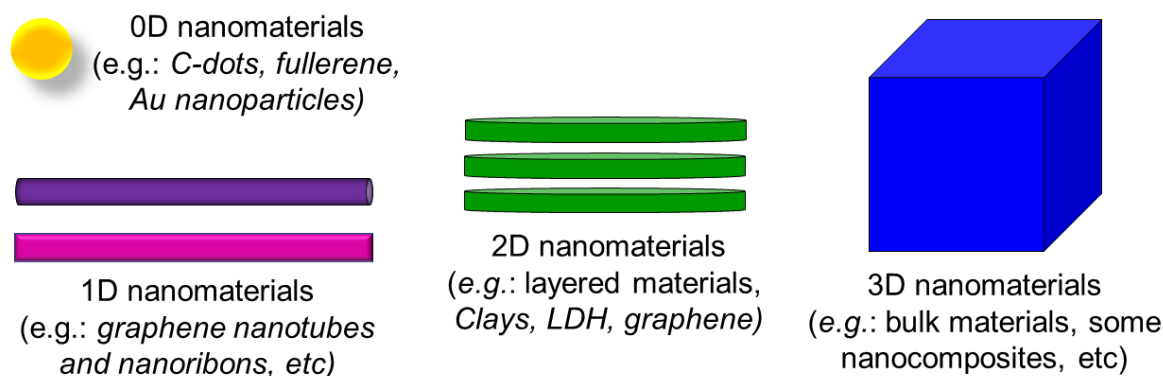


Figure 1. Schematic representation of the classification of nanomaterials according to their dimensionality.

The synthesis methods of nanomaterials can be divided into (i) bottom-up routes, in which bulk materials are segmented in nanostructured materials; and (ii) top-down routes, in which atoms and molecules are used as building blocks to form nanostructures [1,7]. Furthermore, nanomaterials can be combined with different compounds or other (nano)materials, forming nanocomposites or hybrid materials with synergistic properties [12–20]. A composite is defined by IUPAC as “*multicomponent material comprising multiple, different (non-gaseous) phase domains in which at least one type of phase domain is a continuous phase*” and a nanocomposite as “*Composite in which at least one of the phase domains has at least one dimension of the order of nanometres*” [21]. On the other hand, a hybrid material is defined as “*material composed of an intimate mixture of inorganic components, organic components, or both types of components. The components usually interpenetrate on scale of less than 1 μm* ” [21].

Nanocomposites constituted by LDH or layered double oxides (LDO) and graphene-like materials (*e.g.*, graphitic carbon and C-dots) are of great scientific, technological, and biomedical interest because of the synergistic properties that combine the chemical reactivity of LDH/LDO with the outstanding electrical/thermal conductivity, mechanical strength, and optical properties (*e.g.*, photoluminescence/phosphorescence) of nanocarbons [12–19]. Such carbon-based nanocomposites have been applied in catalysis, energy storage and conversion, sensors, environmental protection, and as theragnostic agents, for instance [12–20]. **Table 1** gives the review works published regarding the synthesis methods, properties, and applications of nanocomposites constituted of LDH (or LDO) and carbon-based materials.

Table 1. Reviews works regarding LDH/LDO and graphite-like carbon up to 2022.

Title	Year	Ref.
Hierarchical Nanocomposites Derived from Nanocarbons and Layered Double Hydroxides - Properties, Synthesis, and Applications	2012	[12]
Graphene/layered double hydroxides nanocomposites: A review of recent progress in synthesis and applications	2016	[13]
Graphene/layered double hydroxide nanocomposite: Properties, synthesis, and applications	2016	[14]
Layered double hydroxide- and graphene-based hierarchical nanocomposites: Synthetic strategies and promising applications in energy conversion and conservation	2016	[15]
Graphene-supported organic-inorganic layered double hydroxides and their environmental applications: A review	2020	[16]
A review of the synthesis methods, properties, and applications of layered double hydroxides/carbon nanocomposites	2022	[17]
A Comprehensive Review of Layered Double Hydroxide-Based Carbon Composites as an Environmental Multifunctional Material for Wastewater Treatment	2022	[18]
Layered Double Hydroxide/Nanocarbon Composites as Heterogeneous Catalysts: A Review	2022	[19]

LDH, known as hydrotalcite-like materials, is a class of solids with a structure similar to the $Mg(OH)_2$ brucite mineral [22,23], as represented in **Figure 2**. LDH layers are 2D nanostructures constituted by edge-sharing metal-coordinated hydroxyl octahedral, $M(OH)_6$ [20,23–26]. The bonds among the octahedrons extend along the crystallographic a and b axes, forming layers that stack face-to-face along the c axis [23,26,27]. The isomorphic substitution of a fraction of the bivalent cations by trivalent ones confers a positive residual charge to the layer.[22–28] The residual charge is equivalent to the isomorphic substitution degree, and it is compensated by the intercalation of hydrated anions between the layers [22–28]. LDH can be represented by the $[M^{2+(1-x)}M^{3+x}(OH)_2]^{x+}[(A^{n-})_{x/n} \cdot mH_2O]$ general formula, in which M^{2+} represents the divalent cations (Mg^{2+} , Zn^{2+} , Ni^{2+} , Co^{2+} , Ca^{2+} etc.), M^{3+} the trivalent cations (Al^{3+} , Ga^{3+} , Co^{3+} , Fe^{3+} etc.), and A^{n-} is the compensation anion with a n charge (CO_3^{2-} , Cl^- , NO_3^- , anionic organic species, etc.) [22–28]. The value of x indicates the $[M^{3+}]/[(M^{2+} + M^{3+})]$ molar fraction that usually vary between $0.2 \leq x \leq 0.33$ ($R = M^{2+}/M^{3+}$ corresponding to 4:1 and 2:1) and is related to the charge density of the layer [23,27].

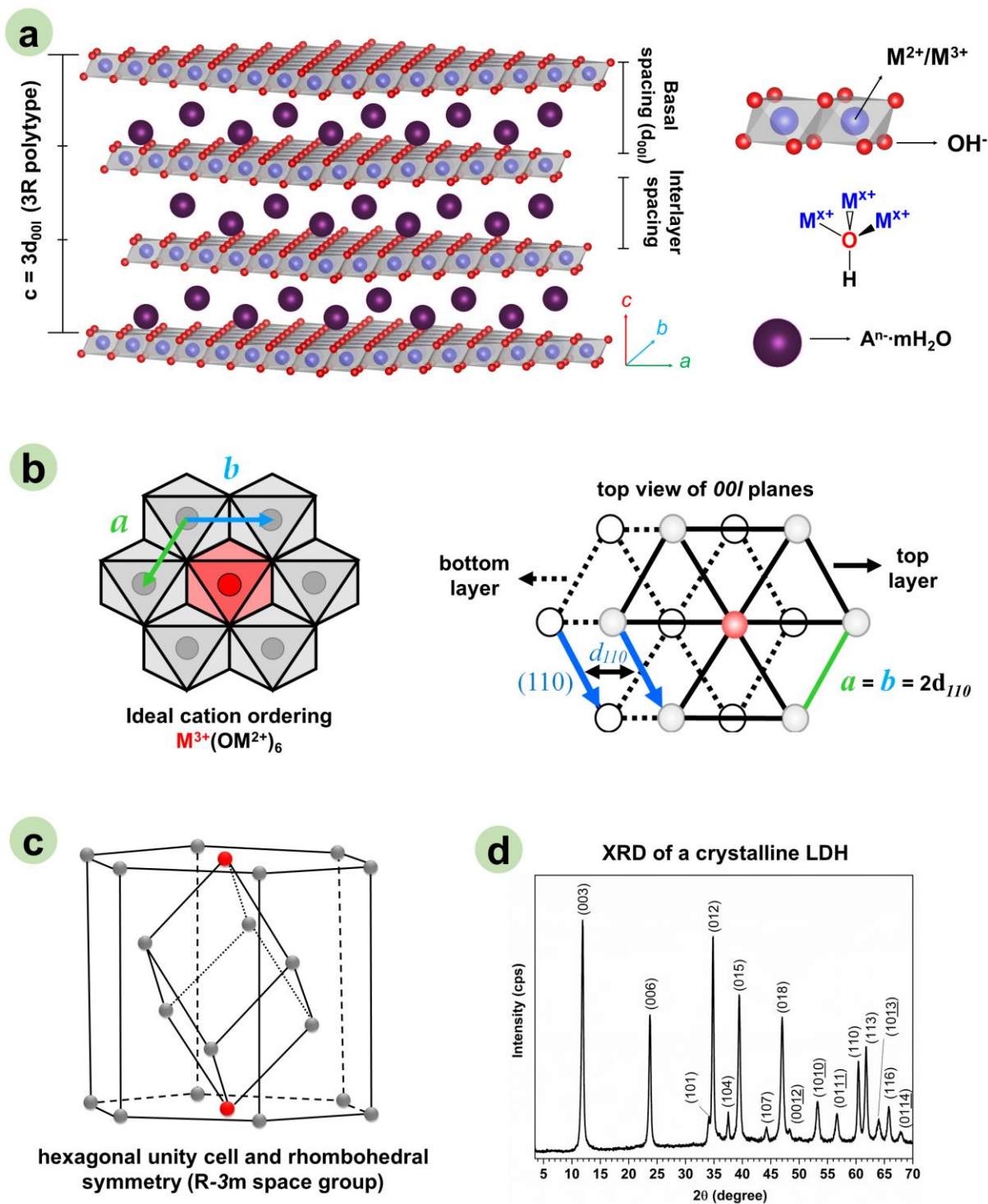


Figure 2. (a) Schematic representation of the crystalline structure and the (a, b) lattice parameters of a hypothetical LDH with (c) triple hexagonal unit cell in a primitive rhombohedral cell (3R polytype in R-3m space group). (d) The XRD (CuK α radiation) of an LDH with Zn₂Al(OH)₆(CO₃)_{0.50}·2H₂O formula.

LDH can present distinct polytypes with different layers stacking along c direction, such as two-layer stacking (2H polytype; hexagonal symmetry) or three-layer stacking (3R polytype; rhombohedral symmetry) sequence [23,26,27]. In general, synthetic LDH presents a hexagonal unit with rhombohedral symmetry (R-3m space group) [23,26,27,29,30], as shown in Figure 2a,c. [23,26,27,29,30], as represented in **Figure 2a,c**. X-ray diffractometry (XRD) is the primary technique to evaluate the LDH structure [23,26,27]. At the small angle region of the diffractogram (below $30^\circ/2\theta$ for CuK α radiation; **Figure 2d**), it is observed the peaks attributed to the family of (00 l) diffraction planes, which is related to the basal spacing ($d_{\text{basal}} = \{[d_{003}+(2d_{006})+\dots(nd_{00l})]/n\}$) and varies according to the dimension and packing of the intercalation anion [23,26,27]. The d_{basal} space corresponds to the sum of layer thickness (approximately 0.48 nm) and the interlayer space [23,26,27]. For materials with rhombohedral symmetry, the cell parameter c is equal to $3d_{\text{basal}}$ [23,26,27] (**Figure 2a**). The diffraction peak of (110) plane in the $60^\circ/2\theta$ corresponds to the distance between the metallic cations (d_{110}) in the layer [23,26,27] (**Figure 2b,d**). It varies according to the ionic radius (coordination number equal to 6) of metallic cations and M^{2+}/M^{3+} molar ratio, and it is related to the a and b cell parameters by the formula $a = b = 2d_{110}$ [23,26,27] (**Figure 2b**).

LDH can be easily synthesized in the laboratory, and one of the most widely used synthesis methods is co-precipitation [24,25,28] based on Miyata's work reported in the 70s [31]. In addition, such materials are versatile in terms of composition due to the wide availability of M^{2+} and M^{3+} cations and anions that can be used for the LDH synthesis, as well as the possibility to vary the M^{2+}/M^{3+} molar fraction [20,22–28,32]. Thus, it is possible to obtain a wide variety of inorganic materials or organic-inorganic hybrid materials with distinct physicochemical properties [20,22–28,32]. In general, LDH exhibits properties such as dissociation in an acidic solution and anion-exchange capacity [24,25,33,34]. Depending on its composition, LDH can exhibit catalytic[35–37], electrochemical[32], and photoluminescent/phosphorescent[20] properties, as well as low cytotoxicity and *in vivo* and *in vitro* biocompatibility [25,38–44]. For instance, LDH composed of Mg^{2+} , Zn^{2+} , Cu^{2+} , and Fe^{3+} are suitable for the development of drug delivery systems, tissue engineering, and as theragnostic materials due to their biocompatibility [25,38–44]. On the other hand, those consisting of Ni^{2+} , $Co^{2+/3+}$, and Fe^{3+} are electroactive and can be used in the development of electrochemical devices [32]. LDH can also act as a catalyst support[37] and can be used in the preparation of polymer-based nanocomposites [43–45]. In addition, LDH can be precursor of LDO or mixed metal oxides (MMO) and spinel-like materials [36,37,46–52] with acid-base

catalytic properties [53]. The advantage of obtaining LDO is the possibility of reconstitution into the hydroxylated phase by reaction with water, the so-called “memory effect” [52–54].

Figure 3 shows a schematic representation of the main methods used to obtain nanocomposites constituted by LDH or derivatives (*i.e.*, MMO and LDO) and carbon-based materials. The nanocomposites can be prepared from: (i) the co-assembly of LDH and carbonaceous materials nanoparticles previously synthesized separately [12–20] (**Figure 3a**); (ii) the *in situ* co-precipitation of LDH in the presence of carbonaceous materials nanoparticles [12–20] (**Figure 3b**); or (iii) by template-assisted approaches, in which the carbon source loaded in LDH is carbonized *in-situ* [12–20] (**Figure 3c**). The organic-inorganic hybrid materials constituted by organic anions intercalated into LDH are potential precursors of such carbon-based nanocomposites [55–59]. The organic species work as a carbon source in a bottom-up approach, and they can be carbonized *in-situ* in a confined space between the LDH layers [55–59]. The structural arrangement of LDH makes this material an excellent matrix for template-assisted synthesis [55–59]. LDH layers can act as a nanoreactor, making it possible to control the growth of carbon-based materials, and consequently, the size, structure, and composition of their nanoparticles owing to the confined space of the interlayer region [12,14,55–59]. Since the LDH are soluble in acidic solutions, carbonaceous materials can be easily isolated if necessary [55–59]. Furthermore, LDH can be converted to LDO, MMO, and/or metallic nanoparticles during the synthesis, which extends the range of multifunctional carbon-based nanocomposites that can be obtained [12,14,51,55–57,60].

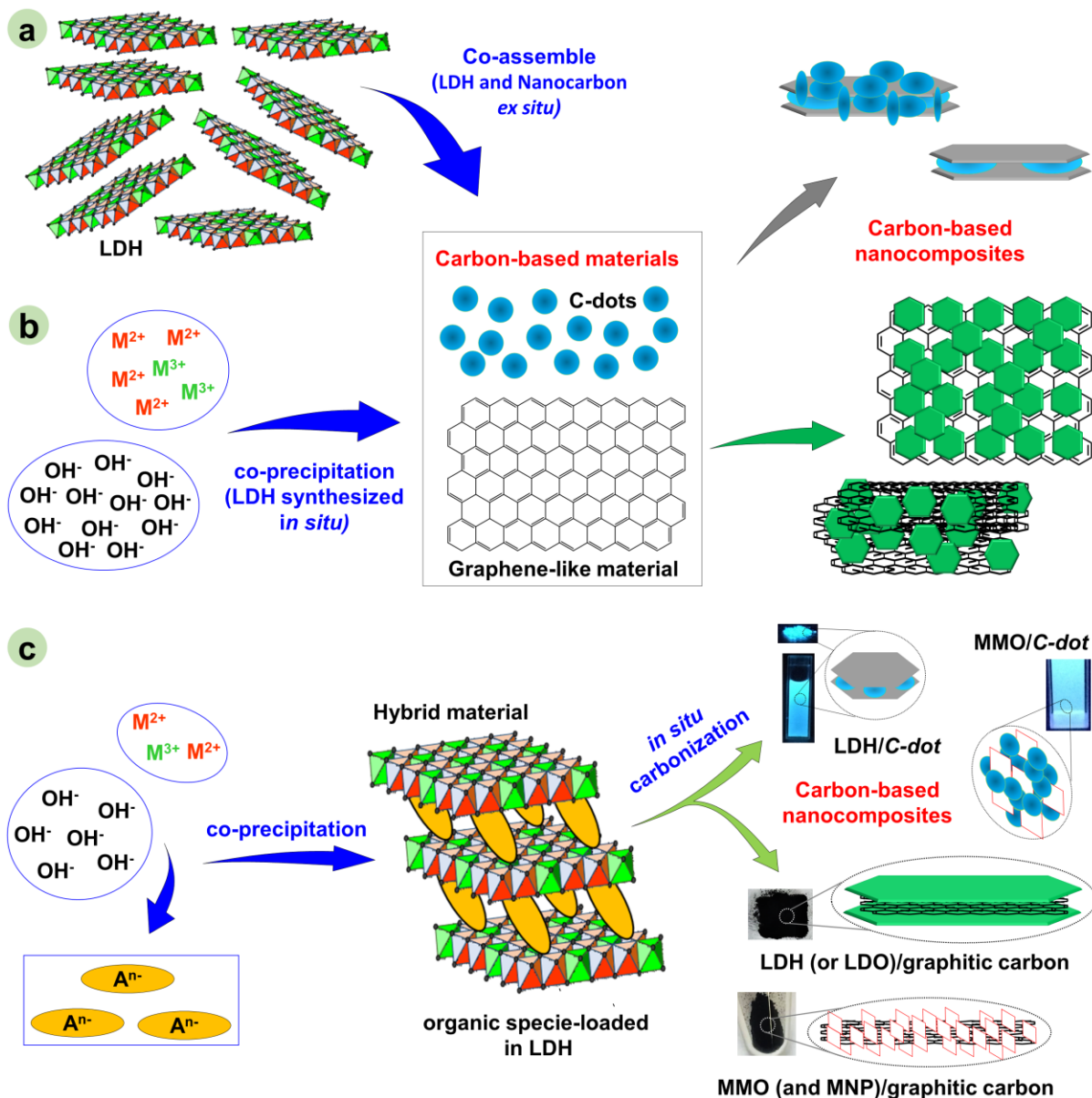


Figure 3. Simplified schematic representation of synthesis methods applied in the obtention of carbon-based nanocomposites constituted by LDH (or derivatives). M^{2+} and M^{3+} : divalent and trivalent metal cations; A^{n-} : organic anion of charge n ; *C-dot*: carbon dots; **LDH**: layered double hydroxides; **LDH**: layered double oxides; **MMO**: mixed metal oxides; **MNP**: metallic nanoparticles.

Graphene-like materials can be denoted as compounds with structures derived or similar to graphene (*e.g.*, graphene oxide, C-dots, fullerene, graphitic carbon, etc.) [8,15,61,62]. The 2D graphene structure is constituted of Csp^2 atoms arranged in a hexagonal lattice [61,63,64]. In the graphene layer, each C atom is linked to the other three atoms through σ -bonds (in the layer plane) formed by the overlapping of sp^2 orbitals, whereas the adjacent free p orbitals (perpendicular to layer plane) form π -bonds (**Figure 4**) [61,63,64]. The one-atom thick layers are formed by the extension of the bonds along the crystallographic axis a and b , yielding an

extensive and highly conjugated system of delocalized π -bonds [63–65]. Graphene is the building-block for other carbon allotropes such as graphite (bulk structure formed by the stacking of graphene layers), fullerenes, C-dots, and graphene nanotubes, for instance [8,62]. The interest in graphene is because of its outstanding properties. It is a zero band-gap semiconductor with electrical mobility of $\geq 200,000 \text{ cm}^2(\text{V}\cdot\text{s})^{-1}$ and thermal conductivity of $\approx 3,000\text{-}5,000 \text{ W}(\text{m}\cdot\text{K})^{-1}$ [66,67]. Besides, graphene presents a high mechanical strength (≈ 200 times higher than steel) and theoretical surface area of $2,630 \text{ m}^2 \text{ g}^{-1}$ as well as it is light (0.77 mg m^{-2}), flexible, transparent (2.3% of absorbance), impermeable, and can be functionalized [5,65–67]. The graphene-like materials can be applied in many fields, from the development of electro-electronic devices to nanomedicine, for instance [5,67,68].

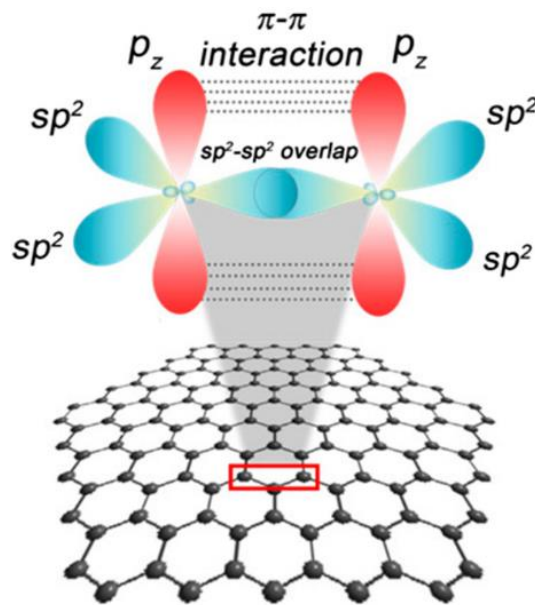


Figure 4. sp^2 -hybrid carbon arrangement in the graphene layer. Modified from Reference[61].

Among the graphene-like materials nanocomposites, the ones constituted of C-dots have been gaining significant attention. C-dots are 0D carbon with photoluminescent properties and particle size smaller than 10 nm. They were accidentally discovered in 2004 by Xu et al.[69] (top-down route) and between 2009-2013 new bottom-up synthesis protocols were established by microwave[70] and hydrothermal carbonization[71] as well as pyrolysis[72]. Since then, C-dots have attracted considerable attention due to their properties such as photoluminescence/phosphorescence, up-conversion, photostability, solubility in water, activity as electron donor-acceptors, low cytotoxicity and biocompatibility [73–93]. C-dots have been successfully applied as sensors, photocatalysts, reductant agents, theragnostic agents,

and in bioimaging as well as to produce optoelectronic, electrochemical, and energy conversion-storage devices [73–93] C-dots can be classified according to their structure and composition into three groups: Graphene Quantum Dots (GQDs), Carbon Nanodots (CNDs) and Polymer Dots (PD) [86,89]. The structure, composition, and consequently, the properties of C-dots are highly dependent on the synthesis method

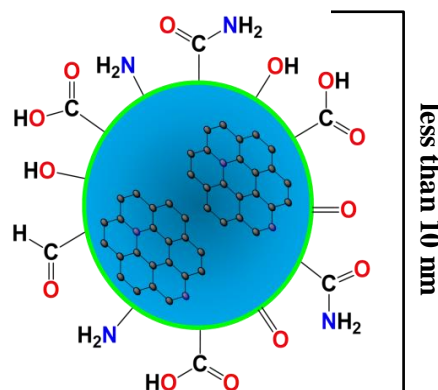


Figure 5. Schematic representation of a hypothetical *C-dot* structure.

and on the reagents used as a carbon source [78,86,89]. In general, C-dots are constituted by a nucleus of carbon with sp^2/sp^3 hybridization (doped or not with nitrogen atoms, for instance) surrounded by organic functional groups (*e.g.*, $-COOH$, $-OH$, $-NH_2$, $-CONH_2$) [86,89], as represented in **Figure 5**. The C-dots photoluminescent properties are dependent on their particle size, surface groups (surface chemistry), or fluorophore species/molecules formed during the synthesis that stay imbibed/absorbed in their structure [78,81,82,91]. Accordingly, a sample can display excitation radiation-dependent emission [91]. In addition, nitrogen doping can improve the electronic properties of materials, for instance, quantum luminescence yield and photoreduction properties [78,86,91]. C-dots can present fluorescence from blue/green (short-wavelength-emitting) to yellow/red (long-wavelength-emitting) and are an alternative to dyes and semiconductor quantum dots [73–93]. **Table 2** presents some review works focused on the synthesis method, structure, composition, properties, and applications of C-dots.

The C-dots can be synthesized through bottom-up methods from the carbonization of small organic molecules or polymers by hydrothermal routes, by pyrolysis or by microwave synthesis [78,79,85,87,89]. Although biomass can be used as carbon source in the C-dots synthesis, depending on the desired application, it is preferred using pure precursors to the obtention of materials with high purity and to ensure reproducibility [82]. Another approach is the template-assisted synthesis in a confined space inside a nanostructured reactor, like micelles [94], mesoporous silica [95] and LDH [56,57,59,96–103] (**Figure 3c**).

Table 2. Review works regarding C-dots synthesis methods, structure, properties and applications up to 2022.

Title	Year	Ref.
Luminescent Carbon Nanodots: Emergent Nanolights	2010	[73]
Graphene quantum dots: emergent nanolights for bioimaging, sensors, catalysis and photovoltaic devices	2012	[74]
Carbon Nanodots: Synthesis, Properties and Applications	2012	[85]
Carbon quantum dots: synthesis, properties and applications	2014	[87]
Carbon and Graphene Quantum Dots for Optoelectronic and Energy Devices: A Review	2015	[88]
The Photoluminescence Mechanism in Carbon Dots (Graphene Quantum Dots, Carbon Nanodots, and Polymer Dots): Current State and Future Perspective.	2015	[89]
Carbon dots: large-scale synthesis, sensing and bioimaging	2015	[90]
Mechanism for excitation-dependent photoluminescence from graphene quantum dots and other graphene oxide derivatives: consensus, debates and challenges	2016	[91]
Graphene and Carbon Quantum Dot-Based Materials in Photovoltaic Devices: From Synthesis to Applications	2016	[92]
The polymeric characteristics and photoluminescence mechanism in polymer carbon dots: A review	2017	[93]
Fluorescent carbon dots and their sensing applications	2017	[75]
Polymers in carbon dots: A review	2017	[76]
Carbon Dots: The next Generation Platform for Biomedical Applications	2019	[77]
Carbon Dots: Synthesis, Formation Mechanism, Fluorescence Origin and Sensing Applications.	2019	[78]
Design, Synthesis, and Functionalization Strategies of Tailored Carbon Nanodots	2019	[79]
Biocompatible nitrogen-doped carbon dots: synthesis, characterization, and application	2020	[80]
Surface states of carbon dots and their influences on luminescence	2020	[81]
Roles of Impurity and Sample Heterogeneity in Intriguing Photoluminescence Properties of Zero-Dimensional (0D) Carbonaceous Materials	2022	[82]
Carbon Dots as New Building Blocks for Electrochemical Energy Storage and Electrocatalysis	2022	[83]
Carbon Nanodots from an In Silico Perspective	2022	[84]
A multifunctional chemical toolbox to engineer carbon dots for biomedical and energy applications	2022	[86]

The use of inorganic matrices such as LDH presents some structural and synergic advantages. C-dots can be well dispersed in the LDH matrix, which avoids aggregation and self-quenching, promoting solid-state photoluminescence [57,58,102–104]. In addition, the confinement effect assisted by the rigid LDH structures and physicochemical interactions between C-dots and layers, inhibits non-radiative decay and improves the exciton lifetime of C-dots [98–101,104]. Such features can extend the fluorescence lifetime and enhance the

quantum yield in favor of the bioimaging [105] as well as facilitate the electron-transfer rate in photocatalysis [99] and promote phosphorescence phenomena [98,100,101]. The photo and thermal stability of C-dots are also improved when they are combined with LDH [57,104]. Additionally, LDH composed of electroactive metals can interact electronically with C-dot and facilitate the electron-transfer migration, favoring catalyzed redox reactions [106] and enhancing the electrochemical activity of LDH [107]. The physicochemical features of LDH (or derivatives) surface can be changed by the incorporation of C-dots, improving the interaction of nanocomposites with pollutants (H-bonds, π - π interaction, electrostatic interaction, etc.) [97,108–110] for the benefit of wastewater treatment. **Table 3** summarizes the main works regarding nanocomposites constituted by LDH (or derivatives) and C-dots, which points out the chemical composition, characterization techniques, and their applications.

Table 3. Published works related to nanocomposites based on LDH (or derivatives) and *C-dots* (until December 2022).

a) <i>Co-assemble: LDH and C-dots synthesized separately</i>					
LDH [#]	C and/or N sources	C-dots synthesis route	Characterization [†]	Application [‡]	Ref.
Mg ₃ Al-CO ₃	PEG and serine	Microwave	XRD, SEM, HRTEM, N ₂ adsorption-desorption (SAA-BET) and pore size distributions (BJH), Zeta potential, FTIR, and Fluorescence spectroscopy	Adsorbent for removal organic dyes from water	[108]
HRP@Co ₂ Fe-Cl	Sodium citrate and NH ₄ HCO ₃	Hydrothermal (180 °C/4h)	XRD, SEM, UV-vis, and Fluorescence spectroscopies; Electrochemical measurements	H ₂ O ₂ biosensor	[111]
Ni ₃ Al-CO ₃	Citric acid	Hydrothermal (200 °C/3h)	XRD, TEM, EDX, XPS, Zeta potential, FTIR, Fluorescent properties measurements; Electrochemical measurements	H ₂ O ₂ sensor	[112]
Mg ₂ Al-NO ₃ (exfoliated)	Citric acid and ethylenediamine	Hydrothermal (200 °C/5h)	XRD, SEM, HRTEM, AFM, Zeta potential, hydrodynamic size (DLS), FTIR and spectroscopies and fluorescent properties measurements; Electrochemical measurements; DFT calculations	Fundamental studies: ultrathin luminescent films for developing optical/optoelectronic sensing devices	[104]
Ni ₃ Al-LDH	Wood-based activated carbon	Mechanic (high-energy ball mill)	XRD, SEM, HRTEM, and FTIR; Electrochemical measurements	Acetylcholine Biosensor	[107]
Mg ₂ Al-NO ₃	Citric acid and urea	Microwave	XRD, TEM, EDX elemental mapping, Zeta potential, XPS, FTIR, and solid-state ¹³ C NMR	Radionuclides Sr ²⁺ and SeO ₄ ²⁻ water removal	[109, 113]
Ag@Mg ₃ (AlCe)-NO ₃	Citric acid and 1,10-phenanthroline	Hydrothermal (180 °C/2h)	XRD, SEM, TEM/HRTEM, HAADF, EDX, XPS, N ₂ adsorption-desorption (SAA-BET) and pore size distributions (BJH), elemental analysis, FTIR and Fluorescence spectroscopy; Electrochemical measurements	Heterogeneous catalyst for wastewater treatment	[106]
Ce6@Mg ₂ Al-LDH (exfoliated)	<i>p</i> -hydroxybenzoic acid and ethylenediamine	Hydrothermal (180 °C/6h)	TEM/HRTEM, AFM, XPS, Zeta potential, hydrodynamic size (DLS), FTIR, Raman, UV-Vis, and Fluorescence spectroscopies	Theragnostic material (<i>in vitro</i>)	[114]

ICG@Mg ₃ Al-LDH (exfoliated)	<i>p</i> -phenylenediamine and 3-(triethoxysilyl) propyl isocyanate	Solvothermal (180 °C/12h)	XRD, TEM/HRTEM, AFM, XPS, Zeta potential, hydrodynamic size (DLS), FTIR, UV-Vi and Fluorescent properties measurements	Theragnostic material (<i>in vitro</i> and <i>in vitro</i>)	[105]
Zn _{2.5} (AlGdDy)-LDH	Folic acid and L-lysine	Hydrothermal (180°C/30min)	XRD, TEM, SEM, EDS, FTIR, XPS, ¹ H-NMR, UV-Vis and MRI and Fluorescent properties measurements	Theragnostic material (<i>in vitro</i>)	[115]
PDA@PNIPAM@Pd @Mg ₃ Al-LDH	citric acid and tris-hydroxyaminomethane	Calcination (275 °C/20min)	XRD, SEM, EDX elemental maps, FTIR, XPS and TGA	Heterogeneous catalyst for organic reactions	[116]
Ni _R Co-LDH (R=1–4)	field bindweed	Hydrothermal (180°C/6h)	XRD, SEM, EDS, FTIR, UV-vis and Fluorescence spectroscopies; electrochemical properties measurements	Electrocatalyst for water oxidation	[117]
Ni _x Co-LDH (MOF-derived)	pyrene and HNO ₃	Calcination (80 °C/2d)	XRD, SEM, EDS, TEM, XPS and TGA; electrochemical measurements	Supercapacitor	[118]
Ni _x Co-LDH	Graphene oxide	Hummer's method	XRD, SEM, HAADF, TEM, AFM, N ₂ adsorption-desorption (SAA-BET) and pore size distributions (BJH), XPS, FTIR, Raman, UV-vis and Fluorescence spectroscopies and static contact angle; electrochemical properties measurements; DFT calculations	Supercapacitor	[119]
b) LDH synthesized in the presence of C-dots					
LDH [#]	C and/or N sources	C-dots synthesis route	Characterization [†]	Application [‡]	Ref.
Ni ₅ Fe-LDH	Graphite	Electrochemical	XRD, SEM, EDS, TEM/HRTEM, AFM, XPS, UV-vis, Fluorescence, FTIR, and Raman spectroscopies; Electrochemical measurements	Electrocatalyst for oxygen evolution reaction (OER)	[120]
Ni ₃ Al-LDH	Graphite	Electrochemical	XRD, SEM, TEM/HRTEM, XPS, FTIR, N ₂ adsorption-desorption (SAA-BET), and pore size distributions (BJH); Electrochemical measurements	Supercapacitor	[121]
Ni ₂ CoAl-LDH	Citric acid	Calcination (180 °C/30min)	XRD, SEM, TGA/DTA, FTIR, and Fluorescence spectroscopies; Electrochemical measurements	Glucose sensor	[122]

Zn ₂ Al-LDH	Ammonium citrate	Hydrothermal (170 °C/5h)	XRD, TEM, EDX, and FTIR spectroscopy	Cd ²⁺ water removal	[110]
Mg ₂ Al-LDH	Sodium citrate and L-cysteine	Hydrothermal (160 °C/10h)	XRD, SEM, TEM, AFM, EDS elemental mapping, FTIR, UV-vis, and Fluorescence spectroscopies	Adsorbent for Hg ²⁺ and Ag ⁺ uptake	[123]
Ni ₃ Mn-LDH	citric acid and ethanolamine or citric acid and ethylenediamine	Hydrothermal (200 °C/4h or 200 °C/5h)	XRD, SEM, EDS, HRTEM, N ₂ adsorption-desorption (SAA-BET), TGA, XPS, and FTIR; electrochemical measurements	Synthesis of NiMn-MMO/C-dots to be used as anode of lithium-ion batteries	[124]
Ni _x Co-LDH	fungus bran and L-lysine	Hydrothermal (180 °C/12h)	XRD, SEM, EDX elemental mapping, TEM, N ₂ adsorption-desorption (SAA-BET) and pore size distributions (BJH), Zeta potential, XPS, FTIR, and Raman spectroscopies; electrochemical measurements	Supercapacitors	[125]
Co ₃ Al-LDH	magnolia blossoms	Solvothermal (180 °C/5h)	XRD, SEM, EDS, HRTEM, HAAD, AFM, XPS, N ₂ adsorption-desorption (SAA-BET), FTIR, UV-Vis, and Fluorescence spectroscopies; electrochemical measurements	Photocatalyst for CO ₂ photoreduction into CO and CH ₄	[126]
Ni _x Fe-LDH (MOF-derived)	citric acid, citric acid and NH ₃ or glucose and H ₃ BO ₃	Hydrothermal (200 °C/3h or 160 °C/3h)	XRD, SEM, HRTEM, XPS, XAS, FTIR, Raman, UV-Vis, and Fluorescence spectroscopies; electrochemical measurements	electrocatalysts for oxygen evolution reaction (OER)	[127]
Ni _x Ga-LDH@NF (MOF-derived)	Citric acid and urea	Hydrothermal (180 °C/5h)	XRD, SEM, TEM/HRTEM, elemental mapping, N ₂ adsorption-desorption (SAA-BET) and pore size distributions (BJH), XPS, FTIR, Raman, and UV-Vis spectroscopies; static contact angle; electrochemical measurements	Supercapacitor	[128]
e) Template-assisted synthesis from LDH-organic anion hybrids					
LDH[#]	C and/or N sources	C-dots synthesis route	Characterization[†]	Application[‡]	Ref.
Mg ₃ Al-Citrate	NH ₃	Hydrothermal (180 °C/8h)	XRD, TEM/HRTEM, AFM, ¹³ C- and ¹ H-NMR, XPS, GPC chromatography, UV-vis, Raman and FTIR spectroscopies and fluorescent properties measurements; DFT calculations	Fundamental studies	[56]

Mg ₃ Al-Citrato	NH ₃	Hydrothermal (180 °C/8h)	XRD, TEM/HRTEM, AFM, XPS, UV-vis, Raman, and FTIR spectroscopies and fluorescent properties measurements;	Optic sensor for NO ₂	[58]
Mg ₃ Al-Citrate/SDS	NH ₃	Hydrothermal (180 °C/8h)	XRD, SEM, TEM/HRTEM, TGA, FTIR, UV-vis, and Fluorescence spectroscopies	Adsorbent of 2,4,6-triclorofenol	[97]
Mg _R Al-Citrate (R= 2–5)	ethylenediamine	Hydrothermal (150 °C/6h)	XRD, SEM, TEM/HRTEM, EDS elemental mapping, AFM, XPS, ¹³ C- and ¹ H-NMR, elemental analysis, Zeta potential, hydrodynamic size (DLS), FTIR, Raman, UV-vis and Fluorescence spectroscopies; Electrochemical measurements; molecular dynamics simulation	Fundamental studies: Thermosensor and blue LED production	[57]
Mg ₃ Al-EDTA Zn ₃ Al-EDTA Mg ₃ Al-SDS/EDTA	--	Pyrolysis (200-400 °C/4h)	XRD, TEM/HRTEM, EDS elemental mapping, XPS, TGA, FTIR, Raman and UV-vis spectroscopies, Fluorescent and Phosphorescent properties measurement	Fundamental studies	[98]
Mg ₃ Al-EDTA Mg ₃ Al-[Cu(EDTA)]	--	Pyrolysis (250 °C/4h)	XRD, SEM, TEM/HRTEM, AFM, ESR, TGA, XPS, FTIR, Raman and UV-vis spectroscopies, Fluorescent and Phosphorescent properties measurement; Electrochemical measurements; DFT calculations	Fundamental studies: photocatalysis	[99]
Mg ₂ Al-EDTA	--	Pyrolysis (300 °C/4h)	XRD, SEM, TEM/HRTEM, AFM, ¹ H- and ¹³ C-NMR, XPS, FTIR, Raman and UV-vis spectroscopies, fluorescent and phosphorescent properties measurement; cyclic voltammetry; DFT calculations	Fundamental studies: anti-counterfeiting marker	[59]
Mg ₂ Al-PDTA Mg ₂ Al-[Zn(PDTA)]	--	Pyrolysis (250 °C/4h)	XRD, SEM, TEM/HRTEM, AFM, TGA, XPS, FTIR, Raman and UV-vis spectroscopies, Fluorescent and Phosphorescent properties measurement; cyclic voltammetry	Fundamental studies: data security devices and sensors	[101]
Mg ₃ Al-EDTA Mg ₃ Al-[Zn(EDTA)]	--	Hydrothermal (250 °C/24h)	XRD, SEM, TEM/HRTEM, AFM, TGA, ¹ H- and ¹³ C-NMR, ESR, XPS, FTIR, Raman and UV-vis spectroscopies, Fluorescent and Phosphorescent properties measurements; cyclic voltammetry	Fundamental studies	[100]

CS@Mg ₄ Al-LDH	--	Pyrolysis (500 °C/6h)	XRD, SEM, EDX elemental mapping, TEM/HRTEM, EXAFS, N ₂ adsorption-desorption (SAA-BET) and pore size distributions (BJH), XPS, FTIR, and fluoresce spectroscopies	Synthesis of Mg ²⁺ /Al ³⁺ -MMO composite to U(IV) and ²⁴¹ Am(III) water removal	[129]
Mg ₃ Al-SDS/DABS ([SDS/DABS] from 1:9 to 9:1)	--	Hydrothermal (200 °C/4 h)	XRD, SEM, TEM, AFM, element analysis, XPS, FTIR, Raman, and UV-Vis spectroscopies and fluorescent properties measurements	Fundamental studies: solid-state luminescence and white LED production	[102]
HIS@Zn ₂ Al-LDH	--	Hydrothermal (170 °C/8h)	XRD, FTIR, SEM, HRTEM and ESR	Synthesis of C-dots/ZnO/ZnAl ₂ O ₄ composite to be used as antibacterial agent	[130]
Mg ₃ Al-AS	--	Hydrothermal (220 °C/10h)	XRD, SEM, HRTEM, AFM, FTIR, Raman, XPS, ¹ H-NMR, UV-Vis and fluorescent/phosphorescent properties measurements; cyclic voltammetry	Pressure sensor	[103]
Mg ₃ Al-[Zn(EDTA)]	--	Hydrothermal (250 °C/24h)	XRD, SEM, TEM/HRTEM, AFM, TGA, ESR, XPS, FTIR, Raman, and UV-vis spectroscopies and Fluorescent and Phosphorescent properties measurements;	O ₂ sensor	[96]
SDBS@Mg _{3.2} Al-LDH	--	Pyrolysis (350-650 °C/2h)	XRD, SEM, EDS elemental mapping, HRTEM, Zeta potential, N ₂ adsorption-desorption (SAA- BET), FTIR, XPS, and static contact angle	Synthesis of MgAl-MMO/C-dots to be used as adsorbent of organic dye pollutants	[131]

#nominal M²⁺/M³⁺ molar ratio, x: metal molar ratio not reported; M2+/M3+-LDH was used when the intercalation anion was not specified; **Ag**: silver nanoparticles; **AS**: Aminobenzene sulfonic acid; **Ce6**: chlorin e6; **CS**: chitosan; **DABS**: 2,5-Diaminobenzenesulfonate; **DBS**: dodecylbenzene sulfonate; **DOX**: doxorubicin; **EDTA**: ethylenediamine tetraacetate ([Cu(EDTA)] and [Zn(EDTA)] are the related organo-complex of Cu²⁺ or Zn²⁺, respectively); **HIS**: histidine; **HRP**: Horseradish peroxidase enzyme; **ICG**: indocyanine green; **MOF**: metal-organic frameworks; **NF**: Nickel foam; **Pd**: palladium nanoparticles; **PDA**: polydopamine polymer; **PDTA**: diethylenetriaminepentaacetate ([Zn(PDTA)] is the related organo-complex of Zn²⁺); **PEG**: poly(ethylene glycol) polymer; **PS**: polystyrene polymer; **PNIPAM**: poly(N-isopropylacrylamide); **S**: sulfide nanoparticles; **SDBS**: sodium dodecylbenzene sulfonate; **SDS**: sodium dodecyl sulphate;

†**AFM**: Atomic Force Microscopy; **BET**: Brunauer–Emmett–Teller; **BJH**: Barrett–Joyner–Halenda; **DFT**: Density Functional Theory; **DLS**: Dynamic Light Scattering; **DTA**: Differential Thermal Analysis; **EDS**: Energy Dispersive Spectroscopy; **EDX**: Energy Dispersive X-ray; **ESR**: Electron Spin Resonance; **ESI**: Electrochemical Impedance Spectroscopy; **EXAFS**: Extended X-ray Absorption Fine Structure; **FTIR**: Fourier Transform Infrared; **GPC**: Gel Permeation Chromatography; **HAADF**: High-angle Annular Dark-field Imaging; **HRTEM**: High-resolution Transmission Electron Microscopy; **MRI**: Magnetic Resonance Imaging; **NMR**: Nuclear Magnetic Resonance; **SAA**: Specific surface area; **SEM**: Scanning Electron Microscopy; **TEM**: Transmission Electron Microscopy; **TGA**: Thermogravimetry Analysis; **XAS**: X-ray Absorption Spectroscopy; **XPS**: X-ray Photoelectron Spectroscopy; **XRD**: X-ray Diffraction;

‡**LED**: Light Emitting Diode; **MMO**: Mixed Metal Oxides

The potential of such materials in terms of their properties and, consequently, their applications is reflected in the number of scientific articles published trying to the synthesis of nanocomposites composed of LDH (or derivatives) and C-dots (**Table 2** and **Figure 6**). Searching in the “Web of Science” platform, crossing the terms “carbon dots” and “layered double hydroxides”, 103 related works were found. However, after a detailed refinement, it was selected 55 works about such nanocomposites. Ten years after the C-dots discovering, in 2014, the first works were published reporting co-assembly methods [108,111] or synthesizing LDH in the presence of C-dots [120]. Since then, the number of publications has been increasing, with China being the biggest scientific producer in the field, corresponding to approximately 76% of the publications (**Figure 6**). The first work reporting the template-mediated synthesis of C-dot was reported by Song et al [56] in 2015. The method consisted of hydrothermal carbonization of citrate intercalated into Mg₃Al-LDH and using NH₃ as N-dopant source. Among the 55 works, 16 used organic-inorganic hybrid materials as precursor of nanocomposites, but in only 13 the organic anions were intercalated into LDH, *i.e.*, the real template-assisted synthesis (**Figure 6**). Almost all works reported exclusively the use of LDH composed by Mg²⁺/Al³⁺ cations intercalated with simple organic anions such as citrate, EDTA (or EDTA metal-complex), PDTA (or PDTA metal-complex) as well as SDS co-intercalated with DBS or citrate (**Table 4c**).

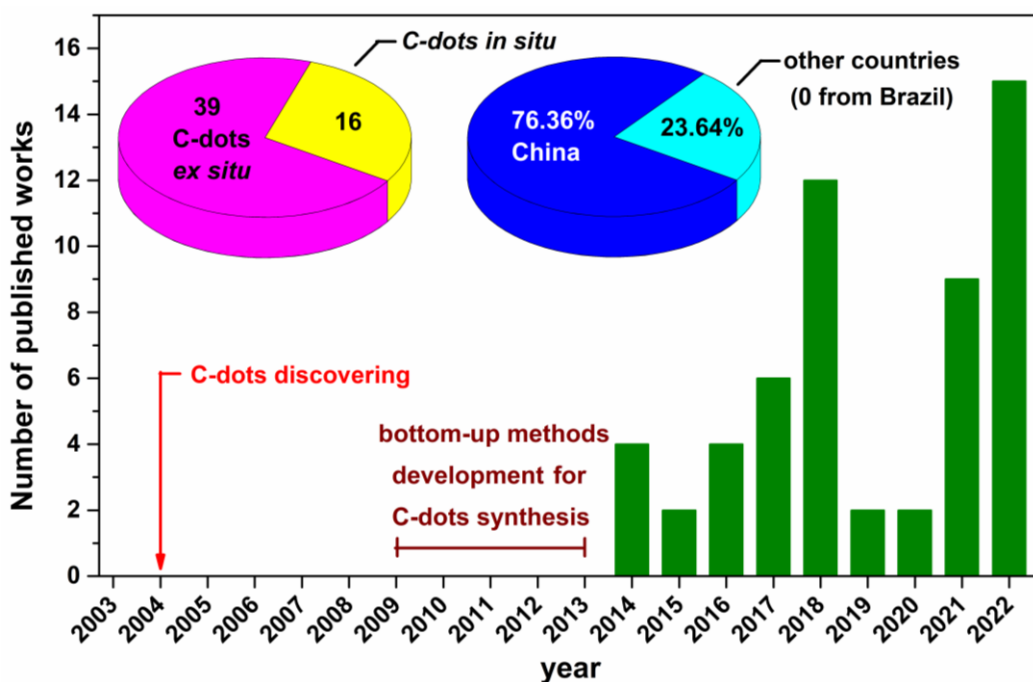


Figure 6. Scientific production data from 2004-2022 regarding nanocomposites based on LDH (or derivatives) and C-dots. The numbers were taken from Web of Science platform in January 2023.

Carbon-based nanocomposites have enormous economic potential considering their versatile properties and assorted applications. In the prospective study on nanotechnology published in 2010 by the *Agência Brasileira de Desenvolvimento Industrial (ABDI)* [2] themes like as nanomaterials, nanoelectronics, nanophotonic, nanobiotechnology, nanoenergy and nanoenvironment were identified as the most promising and strategic for Brazil. Nanocomposites are also included in the prospective study, and it was considered as desirable situation [2]. Although no LDH/graphitic-like carbon nanocomposite is in the market yet, the Merck company has already been commercializing blue luminescent graphene quantum dots ($1.0 \text{ mg}\cdot\text{mL}^{-1}$ in H_2O ; approximately US\$ 190.00) for research purposes. Furthermore, as a practical example of marketing products consisting of layered double hydroxide, the synthetic LDH with $[\text{Mg}_6\text{Al}_2(\text{OH})_{16}]\text{CO}_3\cdot 4\text{H}_2\text{O}$ formula, known as hydrotalcite-like compound, is commercialized by Bayer as the antacid Talcid™. Also, an Italian company started commercializing the Azelike™ cream to treat skin diseases (acne, inflammation, hyperpigmentation), in which the active principle is the anion from azelaic acid intercalated into LDH. Interestingly, the system was developed by a research group from the Department of Chemistry at the University of Perugia, which has been working for years in the field of layered materials.

Our group has been working with LDH for more than twenty years. However, studies with the intercalation of organic species began fifteen years ago, focusing on the physical-chemical characterization by structural, spectroscopic, and thermal techniques but also testing the buffering effect of LDH in acid medium. Subsequently, the characterization techniques were expanded to allow for greater structural detailing of the LDH materials, which include solid-state nuclear magnetic resonance (NMR) and high-resolution transmission electron microscopy (HRTEM). The adjustment of the synthesis parameters has made it possible to obtain hybrid systems LDH-organic species of high crystallinity, which allows for carrying out computational simulations with the generation of one-dimensional electronic density maps from the XRD results and the pair distribution function (PDF) calculations. The vibrational spectroscopic results (Raman and FTIR) of organic species have also been validated by density functional theory (DFT) calculations. In addition, studies have recently evaluate the potential of using hybrid materials constituted of LDH intercalated with anionic organic species as precursors of carbon-based nanocomposites [51,132,133].

In this work, hybrid materials constituted of $\text{M}_2\text{Al-LDH}$ ($\text{M} = \text{Mg}^{2+}$ or Zn^{2+}) intercalated with carboxymethyl cellulose polymer (CMC) or anions from Folic Acid (FA; vitamin B9) were evaluated as precursors of carbon-based nanocomposites by *in-situ* carbonization

(template-mediated methods) carried out mainly by pyrolysis, but also by hydrothermal carbonization. CMC (**Figure 7a**) was chosen because it is a good source of carbon-based materials, is derived from biomass, and can be intercalated into LDH. FA (**Figure 7b**) was chosen because it is widely investigated as precursor of graphite-like materials by bottom-up methods. In addition, it can work both as a carbon and nitrogen source, exempting the use of additional dopant sources, and has aromatic rings, which can help to form graphitic carbon nuclei. Mg₂Al-LDH and Zn₂Al-LDH matrices were chosen due to their biocompatibility, abundance, and low cost and because of their differences in terms of crystallite size, reactivity and physicochemical and thermal properties [30,54,134]. For instance, the thermal stability of Zn₂Al-LDH is much lower than Mg₂Al-LDH [30,41,135,136]. Mg(OH)₂ and Zn(OH)₂ have different solubility product constants of 5.61x10⁻¹² and 3.0x10⁻¹⁷, respectively [137]. Furthermore, such LDH compositions are not classified as catalysts of graphitization [12], which makes it possible to evaluate purely the potential use of these materials as nanoreactors in the template-assisted synthesis of carbon-based materials.

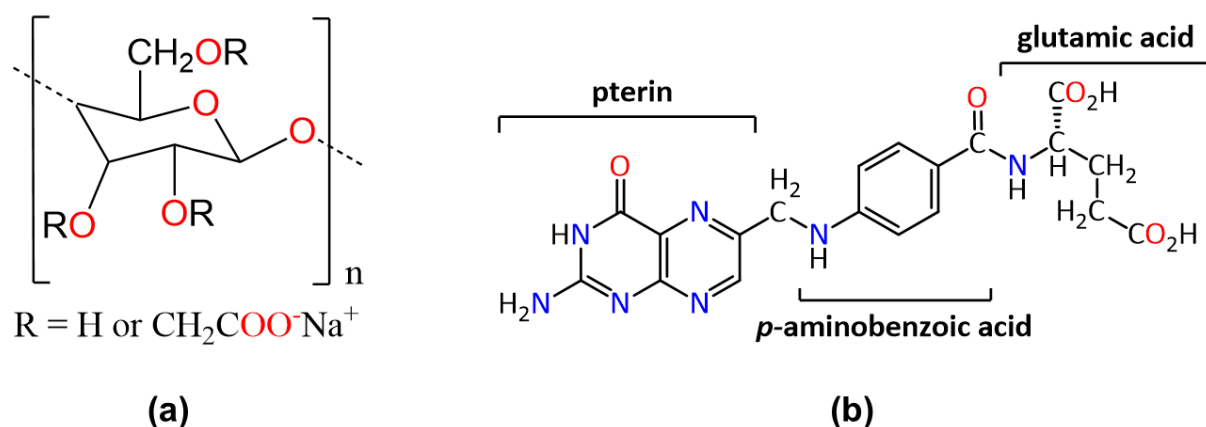


Figure 7. Structural formula of sodium carboxymethylcellulose (a) and folic acid (b).

One of the main goals of this work was to evaluate how much the composition of nanocomposite depends on the composition of the M₂Al-LDH hybrid precursor. Initially, the thermal behavior of the hybrid materials was evaluated by simultaneous thermogravimetric analysis (TGA), differential scanning calorimetry (DSC), and evolved gas analysis (EGA) by mass spectrometry (TGA-MS) and/or infrared spectroscopy (TGA-IR). Appropriately, the temperature values of pyrolysis were selected and the precursors were pyrolyzed in a furnace. Subsequently, the characterization of the obtained carbon-based materials was performed by standard techniques in laboratory, such as X-ray Diffraction (XRD), Fourier Transform Infrared

(FTIR) and Raman spectroscopy, and Scanning Electron Microscopy and Energy Dispersive Spectroscopy (SEM-EDS). Based on the results, the proper temperature range was pointed out for the obtention of carbon-base nanocomposites.

This thesis was organized into chapters in the format of scientific articles. **Chapter 2** presents the work published in *ChemEngineering* **2019** titled “*Investigation of Thermal Behavior of Layered Double Hydroxides Intercalated with Carboxymethylcellulose Aiming Bio-Carbon Based Nanocomposites*” [51]. In this work, the thermal behavior of M_2Al -CMC (M= Mg or Zn) hybrid materials was investigated by TGA/DSC and TGA-MS analysis. Accordingly, M_2Al -CMC were pyrolyzed between 500-1000 °C, and the carbon-based nanocomposites were further characterized by XRD, FTIR, Raman, and SEM-EDS. For comparison purposes, LDH intercalated with carbonate (M_2Al -CO₃) were pyrolyzed in the same temperature range. The formation of graphitic carbon was observed above 600 °C, as determined by Raman spectroscopy. XRD results showed that the Mg_2Al -CMC pyrolyzed between 600-1000 °C presented poorly crystallized MgO and the formation of spinel structures ($MgAl_2O_4$) was hindered in comparison with the LDH-CO₃ counterpart. On the other hand, for Zn_2Al -CMC, it was observed the formation of well-crystallized nanometric ZnO at 800 °C. As far as the temperature increased, it was indirectly noticed that the ZnO was converted to zinc vapor (TGA/DSC, XRD, SEM-EDS) by carbothermic reaction. The residual phase at 1000 °C presented indicative of $ZnAl_2O_4$ (spinel) and γ -Al₂O₃ phases, differently than was observed for Zn_2Al -CO₃ sample (ZnO and $ZnAl_2O_4$), confirming the effect of graphitic carbon in reducing ZnO. Accordingly, it was established that for obtaining nanocomposites constituted by MMO/LDO and graphitic carbon, the best temperature range is 600-1000 °C or 600-800 °C, when the precursors were Mg_2Al -LDH and Zn_2Al -LDH hybrid materials, respectively.

In **Chapter 3** is presented the work titled “*Folic acid and sodium folate salts: Thermal behavior and spectroscopic (IR, Raman, and solid-state ¹³C NMR) characterization,*” published in *Spectrochimica Acta Part A: Molecular and Biomolecular Spectroscopy* **2022** [138]. The spectroscopic investigation of FA and its synthesized sodium salts in the dianion (Na₂HFol) or trianion (Na₃Fol) form was scrutinized in their solid state. The interpretation of spectroscopic data was supported by theoretical calculations using DFT. The thermal behavior of such compounds was also evaluated by TGA/DSC coupled to TGA-MS in a synthetic air atmosphere. The goal was to identify the main thermal (TGA/DTG-DSC-MS; in air atmosphere) and spectroscopic (IR, Raman, and solid-state ¹³C NMR) signatures of each species as well as investigate the influence of the protonation level on the physicochemical properties of the compounds. The spectral differences among them were mainly based on

signals assigned to glutamic acid (glutamate) and pterin (neutral or anionic) moieties of FA. In addition, the oxidative thermal stability was improved for sodium salts, following the order: FA > Na₂HFol > Na₃Fol. This work contributed to the characterization of carbon-based materials obtained from the pyrolysis of FA and its sodium salts (**Chapter 4**). It was also useful to characterize the hybrid materials of LDH intercalated with folate anions and their related nanocomposites (**Chapter 5**).

The work titled “*Pyrolysis mechanism of Folic Acid: identification of gaseous products and characterization of N-doped carbon materials*” was submitted for *Carbon* in **2023** and is presented in **Chapter 4**. Initially, the thermal behavior of FA was investigated and compared with its sodium salts (Na₂HFol and Na₃Fol) by TGA/DSC under an N₂ atmosphere. The gaseous/volatile products released during the pyrolysis were evaluated by simultaneous TGA-FTIR and TGA-MS. Hence, FA was pyrolyzed in a set of temperature values up to 1000 °C, and the samples were further characterized by XRD, FTIR, Raman, and X-ray photoelectron spectroscopy (XPS). Subsequently, a pyrolysis mechanism was proposed for FA as follows: (i) decomposition of FA initiates at 200 °C; (ii) the formation of carbonaceous material through polymerization/condensation reaction (FTIR, Raman, and XPS) initiated from 200-350 °C and it was observed the release of 2-pyrrolidone and aniline (TGA-IR); (iii) between 350-1000 °C, the graphitization was enhanced (Raman), and N-graphite increased whereas the vanishing of amidic groups was observed (XPS). Furthermore, C-dots could be extracted from the sample pyrolyzed at 350 °C, as confirmed by transmission electron microscopy (TEM). The ideal temperature for synthesizing graphitic carbon containing N-graphite was determined to be above 800 °C. On the other hand, for the sodium folate salts, it was observed that the cracking reactions were favored, and graphitization was precluded. In addition to the unprecedented results, this work also contributed to understanding how the mechanism of pyrolysis was altered when intercalated folate anions were pyrolyzed in the confined space between the LDH layers.

Finally, in **Chapter 5** is presented the work entitled “*Hybrid nanomaterials based on Folic Acid intercalated into M²⁺/Al³⁺ (M²⁺ = Mg²⁺ and Zn²⁺) Layered Double Hydroxides as precursors of Carbon-based Nanocomposites*”, that will be submitted to *Applied Clay Science*. In this chapter, M₂Al-LDH intercalated with folate anions (HFol²⁻ or Fol³⁻) were evaluated as precursor of carbon-based nanocomposites by pyrolysis and hydrothermal carbonization routes. Initially, TGA/DSC and EGA (TGA-MS and TGA-IR) analysis of Mg₂Al-Fol (Fol³⁻), Zn₂Al-Fol (Fol³⁻), and Zn₂Al-HFol (HFol²⁻) were carried out to investigate the influence of layer composition as well as the valence of the anion in the carbonization process. Results indicated that both factors influenced the pyrolysis mechanism. However, the profile of the TGA/DSC

curves and the EGA analysis suggested that the layer composition was the main factor. Hence, Mg₂Al-Fol and Zn₂Al-HFol hybrid materials were pyrolyzed in a set of temperatures according to the thermal analysis results. The carbonization of folate anions was delayed after intercalation into LDH in comparison with FA and its sodium salts (**Chapter 4**), as it was indicated by FTIR and Raman analysis. Although, the carbonization was observed to advance faster in Zn₂Al-LDH than in Mg₂Al-LDH. From XRD analysis, it was observed that the carbonaceous material (C) formed during the pyrolysis prevented the crystallization of metal oxides and spinel-like structures, similarly with was also observed for M₂Al-CMC counterparts. Nanocomposites constituted of graphitic carbon and crystallized metal oxides (MgO and ZnO) were only obtained at 800 °C. Furthermore, LDO was successfully restored to LDH structure through a reaction in water (XRD, SEM and TEM). The obtained nanocomposites presented a carbonaceous phase intimately mixed with the restored LDH structure (SEM-EDS and TEM). Additionally, after the regeneration essay, it was observed a conversion from the inherited structure of LDH-FA to the LDH-CO₃ phase, as far as the folate anions were carbonized. Also, separation of phases occurred for Zn₂Al-LDH (ZnO, Al(OH)₃ and LDH) and Mg₂Al-LDH (Mg(OH)₂ and LDH) samples pyrolyzed at 800 and 1000 °C, respectively. Spectrofluorimetric analysis showed that LDH-FA are potential precursors for LDH/C-dots nanocomposites. Materials presented photoluminescent properties that decreased in intensity as far as oxygenated and nitrogenated functional groups (e.g., COO⁻, NH, C=O) of folate were decomposed. The proper temperature range for obtaining LDH/C-dots was stated to be below the peak temperature of the first decomposition step of folates (410-430 °C). Hydrothermal carbonization was not suitable to obtain LDH/C-dots from Mg₂Al-Fol because occurred an anion exchange between folate and generated carbonate during the process, making the carbonization take place outside the layers. However, photoluminescent ZnO-nanocomposites could be obtained from Zn₂Al-LDH hydrothermally treated at 180 °C.

Considering the potential economic value of nanocomposites based on LDH (or derivatives) and graphite-like materials as well as their potential applications in several areas of science and technology. This thesis may contribute to the development of protocols to obtain multifunctional carbon-based nanocomposites for diagnostic imaging, environmental protection, and electronic-optoelectronic devices production, for instance. Besides the relevant social impact that this research can provide, the synthesis protocols reported in this thesis will allow Brazil to be internationally competitive in the field of nanocomposites based on LDH and graphene-like materials.

References

- [1] A. Barhoum, M.L. García-Betancourt, J. Jeevanandam, E.A. Hussien, S.A. Mekkawy, M. Mostafa, M.M. Omran, M. S. Abdalla, M. Bechelany, Review on Natural, Incidental, Bioinspired, and Engineered Nanomaterials: History, Definitions, Classifications, Synthesis, Properties, Market, Toxicities, Risks, and Regulations, **Nanomaterials**. 12 (2022) 177.
- [2] Agência Brasileira de Desenvolvimento Industrial (ABDI), **Estudo Prospectivo Nanotecnologia**, Brasília-DF, 2010.
- [3] M. Camboni, J. Hanlon, R.P. García, P. Floyd, A State of Play Study of the market for so called “Next Generation” **Nanomaterials**, 2019.
- [4] R.P. Singh, R. Handa, G. Manchanda, Nanoparticles in sustainable agriculture: An emerging opportunity, *J. Control. Release*. 329 (2021) 1234–1248.
- [5] S.K. Tiwari, V. Kumar, A. Huczko, R. Oraon, A. De Adhikari, G.C. Nayak, Magical Allotropes of Carbon: Prospects and Applications, **Crit. Rev. Solid State Mater. Sci.** 41 (2016) 257–317.
- [6] E. Inshakova, O. Inshakov, World market for nanomaterials: structure and trends, **MATEC Web Conf.** 129 (2017) 02013.
- [7] N. Baig, I. Kammakakam, W. Falath, I. Kammakakam, Nanomaterials: A review of synthesis methods, properties, recent progress, and challenges, **Mater. Adv.** 2 (2021) 1821–1871.
- [8] V. Georgakilas, J.A. Perman, J. Tucek, R. Zboril, Broad Family of Carbon Nanoallotropes: Classification, Chemistry, and Applications of Fullerenes, Carbon Dots, Nanotubes, Graphene, Nanodiamonds, and Combined Superstructures, **Chem. Rev.** 115 (2015) 4744–4822.
- [9] E. COMMISSION, **Commission Recommendation of 10 June 2022 on the definition of nanomaterial**, Off. J. Eur. Union. (2022) 1–5. <https://doi.org/10.2788/36237>.
- [10] R.A. Schoonheydt, T. Pinnavaia, G. Lagaly, N. Gangas, Pillared Clays and Pillared Layered Solids, **Pure Appl. Chem.** 71 (1999) 2367–2371.
- [11] G.P. Moss, P.A.S. Smith, D. Tavernier, Glossary of class names of organic compounds and reactivity intermediates based on structure (IUPAC Recommendations 1995), **Pure Appl. Chem.** 67 (1995) 1307–1375.
- [12] M.Q. Zhao, Q. Zhang, J.Q. Huang, F. Wei, Hierarchical nanocomposites derived from nanocarbons and layered double hydroxides - Properties, synthesis, and applications, **Adv. Funct. Mater.** 22 (2012) 675–694.
- [13] M. Daud, M.S. Kamal, F. Shehzad, M.A. Al-Harhi, Graphene/layered double hydroxides nanocomposites: A review of recent progress in synthesis and applications, **Carbon N. Y.** 104 (2016) 241–252.
- [14] Y. Cao, G. Li, X. Li, Graphene/layered double hydroxide nanocomposite: Properties, synthesis, and applications, **Chem. Eng. J.** 292 (2016) 207–223.

- [15] G.B.B. Varadwaj, V.O. Nyamori, Layered double hydroxide- and graphene-based hierarchical nanocomposites: Synthetic strategies and promising applications in energy conversion and conservation, **Nano Res.** 9 (2016) 3598–3621.
- [16] A.A. Wani, A.M. Khan, Y.K. Manea, M. Shahadat, S.Z. Ahammad, S.W. Ali, Graphene-supported organic-inorganic layered double hydroxides and their environmental applications: A review, **J. Clean. Prod.** 273 (2020) 122980.
- [17] M. Khorshidi, S. Asadpour, N. Sarmast, M. Dinari, A review of the synthesis methods, properties, and applications of layered double hydroxides/carbon nanocomposites, **J. Mol. Liq.** 348 (2022) 118399.
- [18] Y. Huang, C. Liu, S. Rad, H. He, L. Qin, A Comprehensive Review of Layered Double Hydroxide-Based Carbon Composites as an Environmental Multifunctional Material for Wastewater Treatment, **Processes.** 10 (2022).
- [19] D. Tichit, M.G. Álvarez, Layered Double Hydroxide/Nanocarbon Composites as Heterogeneous Catalysts: A Review, **ChemEngineering.** 6 (2022) 45.
- [20] R. Gao, D. Yan, X. Duan, Layered double hydroxides-based smart luminescent materials and the tuning of their excited states, **Cell Reports Phys. Sci.** 2 (2021) 1–23.
- [21] J. V. Alemán, A. V. Chadwick, J. He, M. Hess, K. Horie, R.G. Jones, P. Kratochvíl, I. Meisel, I. Mita, G. Moad, S. Penczek, R.F.T. Stepto, Definitions of terms relating to the structure and processing of sols, gels, networks, and inorganic-organic hybrid materials (IUPAC Recommendations 2007), **Pure Appl. Chem.** 79 (2007) 1801–1829.
- [22] F. Cavani, F. Trifirò, A. Vaccari, Hydrotalcite-type anionic clays: preparation, properties and applications, **Catal. Today.** 11 (1991) 173–301.
- [23] C. Forano, U. Costantino, V. Prévot, C.T. Gueho, **Layered Double Hydroxides (LDH)**, in: F. Bergaya, G. Lagaly (Eds.), *Handb. Clay Sci. -Developments Clay Sci.*, 2nd ed., Elsevier, 2013: pp. 745–782.
- [24] C. Taviot-Guého, V. Prévot, C. Forano, G. Renaudin, C. Mousty, F. Leroux, Tailoring Hybrid Layered Double Hydroxides for the Development of Innovative Applications, **Adv. Funct. Mater.** 28 (2018) 1703868.
- [25] Z. Cao, B. Li, L. Sun, L. Li, Z.P. Xu, Z. Gu, 2D Layered Double Hydroxide Nanoparticles: Recent Progress toward Preclinical/Clinical Nanomedicine, *Small Methods.* 4 (2020)
- [26] V. Rives, **Layered Double Hydroxides: Present and Future**, Nova Science Publishers, Inc., New York, 2001.
- [27] D.G. Evans, R.C.T. Slade, **Structural Aspects of Layered Double Hydroxides**, in: *Struct. Bond.*, Springer-Verlag, Berlin/Heidelberg, 2006: pp. 1–87.
- [28] S. Saha, S. Ray, R. Acharya, T.K. Chatterjee, J. Chakraborty, Magnesium, zinc and calcium aluminium layered double hydroxide-drug nanohybrids: A comprehensive study, **Appl. Clay Sci.** 135 (2017) 493–509.
- [29] V.R.R. Cunha, P.A.D. Petersen, M.B. Gonçalves, H.M. Petrilli, C. Taviot-Gueho, F. Leroux, M.L.A. Temperini, V.R.L. Constantino, Structural, spectroscopic (NMR, IR, and

- Raman), and DFT investigation of the self-assembled nanostructure of pravastatin-LDH (layered double hydroxides) systems, **Chem. Mater.** 24 (2012) 1415–1425.
- [30] M.A. Rocha, P.A.D. Petersen, E. Teixeira-Neto, H.M. Petrilli, F. Leroux, C. Taviot-Gueho, V.R.L. Constantino, Layered double hydroxide and sulindac coiled and scrolled nanoassemblies for storage and drug release, **RSC Adv.** 6 (2016) 16419–16436.
- [31] S. Miyata, The syntheses of hydrotalcite-like compounds and their structures and physico-chemical properties: The systems $\text{Mg}^{2+}\text{-Al}^{3+}\text{-NO}_3^-$, $\text{Mg}^{2+}\text{-Al}^{3+}\text{-Cl}^-$, $\text{Mg}^{2+}\text{-Al}^{3+}\text{-ClO}_4^-$, $\text{Ni}^{2+}\text{-Al}^{3+}\text{-Cl}^-$ and $\text{Zn}^{2+}\text{-Al}^{3+}\text{-Cl}^-$, **Clays Clay Miner.** 23 (1975) 369–375.
- [32] M. Zhao, Q. Zhao, B. Li, H. Xue, H. Pang, C. Chen, Recent progress in layered double hydroxide based materials for electrochemical capacitors: design, synthesis and performance, **Nanoscale.** 9 (2017) 15206–15225.
- [33] M.L. Parello, R. Rojas, C.E. Giacomelli, Dissolution kinetics and mechanism of Mg–Al layered double hydroxides: A simple approach to describe drug release in acid media, **J. Colloid Interface Sci.** 351 (2010) 134–139.
- [34] S. Miyata, Anion-Exchange Properties of Hydrotalcite-Like Compounds, **Clays Clay Miner.** 31 (1983) 305–311.
- [35] C. Li, M. Wei, D.G. Evans, X. Duan, Layered Double Hydroxide-based Nanomaterials as Highly Efficient Catalysts and Adsorbents, **Small.** 10 (2014) 4469–4486.
- [36] V.R.L. Constantino, T.J. Pinnavaia, Basic Properties of $\text{Mg}^{2+}_{1-x}\text{Al}^{3+}_x$ Layered Double Hydroxides Intercalated by Carbonate, Hydroxide, Chloride, and Sulfate Anions, **Inorg. Chem.** 34 (1995) 883–892.
- [37] M. Xu, M. Wei, Layered Double Hydroxide-Based Catalysts: Recent Advances in Preparation, Structure, and Applications, **Adv. Funct. Mater.** 28 (2018) 1802943.
- [38] F. Barahuie, M. Hussein, S. Fakurazi, Z. Zainal, Development of Drug Delivery Systems Based on Layered Hydroxides for Nanomedicine, **Int. J. Mol. Sci.** 15 (2014) 7750–7786.
- [39] Y. Kuthati, R.K. Kankala, C.-H. Lee, Layered double hydroxide nanoparticles for biomedical applications: Current status and recent prospects, **Appl. Clay Sci.** 112–113 (2015) 100–116.
- [40] C. Forano, F. Bruna, C. Mousty, V. Prevot, Interactions Between Biological Cells and Layered Double Hydroxides: Towards Functional Materials, **Chem. Rec. In press** (2018) 1–18.
- [41] V.R.R. Cunha, R.B. de Souza, A.M.C.R.P. da Fonseca Martins, I.H.J. Koh, V.R.L. Constantino, Accessing the biocompatibility of layered double hydroxide by intramuscular implantation: histological and microcirculation evaluation, **Sci. Rep.** 6 (2016) 30547.
- [42] M.P. Figueiredo, V.R.R. Cunha, F. Leroux, C. Taviot-Gueho, M.N. Nakamae, Y.R. Kang, R.B. Souza, A.M.C.R.P.F. Martins, I.H.J. Koh, V.R.L. Constantino, Iron-Based Layered Double Hydroxide Implants: Potential Drug Delivery Carriers with Tissue Biointegration Promotion and Blood Microcirculation Preservation, **ACS Omega.** 3 (2018) 18263–18274.

- [43] B. Izbudak, B. Cecen, I. Anaya, A.K. Miri, A. Bal-Ozturk, E. Karaoz, Layered double hydroxide-based nanocomposite scaffolds in tissue engineering applications, **RSC Adv.** 11 (2021) 30237–30252.
- [44] V. Regina, L. Constantino, M.P. Figueiredo, V.R. Magri, D. Eulálio, V. Roberta, R. Cunha, A. Clecia, S. Alcântara, G.F. Perotti, Biomaterials Based on Organic Polymers and Layered Double Hydroxides Nanocomposites: Drug Delivery and Tissue Engineering, (2023) 1–56.
- [45] Y. Liu, Y. Gao, Q. Wang, W. Lin, The synergistic effect of layered double hydroxides with other flame retardant additives for polymer nanocomposites: a critical review, **Dalt. Trans.** 47 (2018) 14827–14840.
- [46] H.W.P. Carvalho, S.H. Pulcinelli, C. V. Santilli, F. Leroux, F. Meneau, V. Briois, XAS/WAXS time-resolved phase speciation of chlorine LDH thermal transformation: Emerging roles of isovalent metal substitution, **Chem. Mater.** 25 (2013) 2855–2867.
- [47] M. Bellotto, B. Rebours, O. Clause, J. Lynch, D. Bazin, E. Elkaïm, Hydrotalcite Decomposition Mechanism: A Clue to the Structure and Reactivity of Spinel-like Mixed Oxides, **J. Phys. Chem.** 100 (1996) 8535–8542.
- [48] X. Zhao, F. Zhang, S. Xu, D.G. Evans, X. Duan, From layered double hydroxides to ZnO-based mixed metal oxides by thermal decomposition: Transformation mechanism and UV-blocking properties of the product, **Chem. Mater.** 22 (2010) 3933–3942.
- [49] C. Hobbs, S. Jaskaniec, E.K. McCarthy, C. Downing, K. Opelt, K. Güth, A. Shmeliov, M.C.D. Mourad, K. Mandel, V. Nicolosi, Structural transformation of layered double hydroxides: an in situ TEM analysis, **Npj 2D Mater. Appl.** 2 (2018) 4.
- [50] Takehira, K., Recent development of layered double hydroxide-derived catalysts – Rehydration, reconstitution, and supporting, aiming at commercial application, **Appl. Clay Sci.** 136 (2017) 112–141.
- [51] V.R. Magri, A. Duarte, G.F. Perotti, V.R.L. Constantino, Investigation of Thermal Behavior of Layered Double Hydroxides Intercalated with Carboxymethylcellulose Aiming Bio-Carbon Based Nanocomposites, **ChemEngineering.** 3 (2019) 55.
- [52] H. Ye, S. Liu, D. Yu, X. Zhou, L. Qin, C. Lai, F. Qin, M. Zhang, W. Chen, W. Chen, L. Xiang, Regeneration mechanism, modification strategy, and environment application of layered double hydroxides: Insights based on memory effect, **Coord. Chem. Rev.** 450 (2022) 214253.
- [53] K. Takehira, Recent development of layered double hydroxide-derived catalysts – Rehydration, reconstitution, and supporting, aiming at commercial application, **Appl. Clay Sci.** 136 (2017) 112–141.
- [54] Z. Gao, K. Sasaki, X. Qiu, Structural Memory Effect of Mg–Al and Zn–Al layered Double Hydroxides in the Presence of Different Natural Humic Acids: Process and Mechanism, **Langmuir.** 34 (2018) 5386–5395.
- [55] J. Sun, H. Liu, X. Chen, D.G. Evans, W. Yang, X. Duan, Synthesis of graphene nanosheets with good control over the number of layers within the two-dimensional galleries of layered double hydroxides, **Chem. Commun.** 48 (2012) 8126.

- [56] L. Song, J. Shi, J. Lu, C. Lu, Structure observation of graphene quantum dots by single-layered formation in layered confinement space, **Chem. Sci.** 6 (2015) 4846–4850.
- [57] W. Liu, S. Xu, R. Liang, M. Wei, D.G. Evans, X. Duan, In situ synthesis of nitrogen-doped carbon dots in the interlayer region of a layered double hydroxide with tunable quantum yield, **J. Mater. Chem. C** 5 (2017) 3536–3541.
- [58] L. Song, W. Shi, C. Lu, Confinement Effect in Layered Double Hydroxide Nanoreactor: Improved Optical Sensing Selectivity, **Anal. Chem.** 88 (2016) 8188–8193.
- [59] L. Bai, N. Xue, Y. Zhao, X. Wang, C. Lu, W. Shi, Dual-mode emission of single-layered graphene quantum dots in confined nanospace: Anti-counterfeiting and sensor applications, **Nano Res.** 11 (2018) 2034–2045.
- [60] C.S. de Matos, C.M. Ghimbeu, J. Brendlé, L. Limousy, V.R.L. Constantino, Thermal decomposition of a layered double hydroxide as a bottom up approach for the synthesis of metallic nanoparticles embedded in carbon structures, **New J. Chem.** 44 (2020) 16721–16732.
- [61] P. Suvarnapaet, S. Pechprasarn, Graphene-Based Materials for Biosensors: A Review, **Sensors.** 17 (2017) 2161.
- [62] A.K. Geim, K.S. Novoselov, The rise of graphene, **Nat. Mater.** 6 (2007) 183–191.
- [63] D.D.L. Chung, Graphite, **J. Mater. Sci.** 37 (2002) 1475–1489.
- [64] M.J. Allen, V.C. Tung, R.B. Kaner, Honeycomb Carbon: A Review of Graphene, **Chem. Rev.** 110 (2010) 132–145.
- [65] S. Eigler, A. Hirsch, Chemistry with Graphene and Graphene Oxide—Challenges for Synthetic Chemists, **Angew. Chemie Int. Ed.** 53 (2014) 7720–7738.
- [66] Y. Zhu, S. Murali, W. Cai, X. Li, J.W. Suk, J.R. Potts, R.S. Ruoff, Graphene and graphene oxide: Synthesis, properties, and applications, **Adv. Mater.** 22 (2010) 3906–3924.
- [67] K.S. Novoselov, V.I. Fal’ko, L. Colombo, P.R. Gellert, M.G. Schwab, K. Kim, A roadmap for graphene, **Nature.** 490 (2012) 192–200.
- [68] D. Chen, C.A. Dougherty, K. Zhu, H. Hong, Theranostic applications of carbon nanomaterials in cancer: Focus on imaging and cargo delivery, **J. Control. Release.** 210 (2015) 230–245.
- [69] X. Xu, R. Ray, Y. Gu, H.J. Ploehn, L. Gearheart, K. Raker, W.A. Scrivens, Electrophoretic Analysis and Purification of Fluorescent Single-Walled Carbon Nanotube Fragments, **J. Am. Chem. Soc.** 126 (2004) 12736–12737.
- [70] H. Zhu, X. Wang, Y. Li, Z. Wang, F. Yang, X. Yang, Microwave synthesis of fluorescent carbon nanoparticles with electrochemiluminescence properties, **Chem. Commun.** (2009) 5118–20.
- [71] S. Zhu, Q. Meng, L. Wang, J. Zhang, Y. Song, H. Jin, K. Zhang, H. Sun, H. Wang, B. Yang, Highly Photoluminescent Carbon Dots for Multicolor Patterning, Sensors, and Bioimaging, **Angew. Chemie Int. Ed.** 52 (2013) 3953–3957.

- [72] R. Liu, D. Wu, X. Feng, K. Müllen, Bottom-Up Fabrication of Photoluminescent Graphene Quantum Dots with Uniform Morphology, **J. Am. Chem. Soc.** 133 (2011) 15221–15223.
- [73] S.N. Baker, G.A. Baker, Luminescent Carbon Nanodots: Emergent Nanolights, **Angew. Chemie Int. Ed.** 49 (2010) 6726–6744.
- [74] J. Shen, Y. Zhu, X. Yang, C. Li, Graphene quantum dots: emergent nanolights for bioimaging, sensors, catalysis and photovoltaic devices, **Chem. Commun.** 48 (2012) 3686.
- [75] X. Sun, Y. Lei, Fluorescent carbon dots and their sensing applications, *TrAC Trends Anal. Chem.* 89 (2017) 163–180.
- [76] Y. Zhou, S.K. Sharma, Z. Peng, R.M. Leblanc, Polymers in carbon dots: A review, **Polymers** 9 (2017) 67.
- [77] K. Ghosal, A. Ghosh, Carbon dots: The next generation platform for biomedical applications, **Mater. Sci. Eng. C.** 96 (2019) 887–903.
- [78] M.L. Liu, B. Bin Chen, C.M. Li, C.Z. Huang, Carbon dots: synthesis, formation mechanism, fluorescence origin and sensing applications, **Green Chem.** 21 (2019) 449–
- [79] F. Arcudi, L. Đorđević, M. Prato, Design, Synthesis, and Functionalization Strategies of Tailored Carbon Nanodots, **Acc. Chem. Res.** 52 (2019) 2070–2079.
- [80] Y. Park, Y. Kim, H. Chang, S. Won, H. Kim, W. Kwon, Biocompatible nitrogen-doped carbon dots: synthesis, characterization, and application, **J. Mater. Chem. B.** 8 (2020) 8935–8951.
- [81] H. Ding, X.-H. Li, X.-B. Chen, J.-S. Wei, X.-B. Li, H.-M. Xiong, Surface states of carbon dots and their influences on luminescence, **J. Appl. Phys.** 127 (2020) 231101.
- [82] K. Mishra, M. Barai, S. Ghosh, Roles of Impurity and Sample Heterogeneity in Intriguing Photoluminescence Properties of Zero-Dimensional (0D) Carbonaceous Materials, **J. Phys. Chem. C.** 126 (2022) 16905–16918.
- [83] Y. Zhai, B. Zhang, R. Shi, S. Zhang, Y. Liu, B. Wang, K. Zhang, G.I.N. Waterhouse, T. Zhang, S. Lu, Carbon Dots as New Building Blocks for Electrochemical Energy Storage and Electrocatalysis, **Adv. Energy Mater.** 12 (2022) 2103426.
- [84] F. Mocci, L. de Villiers Engelbrecht, C. Olla, A. Cappai, M.F. Casula, C. Melis, L. Stagi, A. Laaksonen, C.M. Carbonaro, Carbon Nanodots from an In Silico Perspective, **Chem. Rev.** 122 (2022) 13709–13799.
- [85] H. Li, Z. Kang, Y. Liu, S.-T. Lee, Carbon nanodots: synthesis, properties and applications, **J. Mater. Chem.** 22 (2012) 24230.
- [86] L. Đorđević, F. Arcudi, M. Cacioppo, M. Prato, A multifunctional chemical toolbox to engineer carbon dots for biomedical and energy applications, **Nat. Nanotechnol.** 17 (2022) 112–130.
- [87] Y. Wang, A. Hu, Carbon quantum dots: synthesis, properties and applications, **J. Mater. Chem. C.** 2 (2014) 6921.

- [88] X. Li, M. Rui, J. Song, Z. Shen, H. Zeng, Carbon and Graphene Quantum Dots for Optoelectronic and Energy Devices: A Review, **Adv. Funct. Mater.** 25 (2015) 4929–4947.
- [89] S. Zhu, Y. Song, X. Zhao, J. Shao, J. Zhang, B. Yang, The photoluminescence mechanism in carbon dots (graphene quantum dots, carbon nanodots, and polymer dots): current state and future perspective, **Nano Res.** 8 (2015) 355–381.
- [90] J. Zhang, S. Yu, Carbon dots: large-scale synthesis, sensing and bioimaging, **Biochem. Pharmacol.** 00 (2015).
- [91] Z. Gan, H. Xu, Y. Hao, Mechanism for excitation-dependent photoluminescence from graphene quantum dots and other graphene oxide derivatives: consensus, debates and challenges, **Nanoscale.** 8 (2016) 7794–7807.
- [92] S. Paulo, E. Palomares, E. Martinez-Ferrero, Graphene and Carbon Quantum Dot-Based Materials in Photovoltaic Devices: From Synthesis to Applications, **Nanomaterials.** 6 (2016) 157.
- [93] S. Tao, S. Zhu, T. Feng, C. Xia, Y. Song, B. Yang, The polymeric characteristics and photoluminescence mechanism in polymer carbon dots: A review, **Mater. Today Chem.** 6 (2017) 13–25.
- [94] W. Kwon, S.W. Rhee, Facile synthesis of graphitic carbon quantum dots with size tunability and uniformity using reverse micelles, **Chem. Commun.** 48 (2012) 5256–5258. <https://doi.org/10.1039/c2cc31687k>.
- [95] J. Li, B. Wang, H. Zhang, J. Yu, Carbon Dots-in-Matrix Boosting Intriguing Luminescence Properties and Applications, **Small.** 15 (2019) 1805504.
- [96] J. Yao, J. Kong, L. Kong, X. Wang, W. Shi, C. Lu, The phosphorescence nanocomposite thin film with rich oxygen vacancy: Towards sensitive oxygen sensor, **Chinese Chem. Lett.** 33 (2022) 3977–3980.
- [97] Q. Yao, S. Wang, W. Shi, C. Lu, G. Liu, Graphene Quantum Dots in Two-Dimensional Confined and Hydrophobic Space for Enhanced Adsorption of Nonionic Organic Adsorbates, **Ind. Eng. Chem. Res.** 56 (2017) 583–590.
- [98] W.Y. Shi, X.R. Wang, C. Lu, L.Q. Bai, N. Xue, Activating efficient room temperature phosphorescence of carbon dots by synergism of orderly non-noble metals and dual structural confinements, **Nanoscale.** 9 (2017) 6658–6664.
- [99] N. Xue, X. Kong, B. Song, L. Bai, Y. Zhao, C. Lu, W. Shi, Cu-Doped Carbon Dots with Highly Ordered Alignment in Anisotropic Nano-Space for Improving the Photocatalytic Performance, **Sol. RRL.** 1 (2017) 1700029.
- [100] W. Shi, J. Yao, L. Bai, C. Lu, Defect-Stabilized Triplet State Excitons: Toward Ultralong Organic Room-Temperature Phosphorescence, **Adv. Funct. Mater.** 28 (2018) 1–8.
- [101] X. Kong, Y. Zhao, X. Wang, W. Shi, H. Cheng, Activating room temperature phosphorescence by organic materials using synergistic effects, **J. Mater. Chem. C.** 7 (2019) 230–236.

- [102] W. Liu, R. Liang, Y. Lin, Confined synthesis of carbon dots with tunable long-wavelength emission in a 2-dimensional layered double hydroxide matrix, **Nanoscale**. 12 (2020) 7888–7894.
- [103] X. Cui, X. Xing, X. Wang, W. Shi, C. Lu, Dual emission of singlet and triplet states boost the sensitivity of pressure-sensing, **Chinese Chem. Lett.** 32 (2021) 2869–2872.
- [104] W. Liu, S. Xu, Z. Li, R. Liang, M. Wei, D.G. Evans, X. Duan, Layer-by-Layer Assembly of Carbon Dots-Based Ultrathin Films with Enhanced Quantum Yield and Temperature Sensing Performance, **Chem. Mater.** 28 (2016) 5426–5431.
- [105] Y. Weng, S. Guan, H. Lu, X. Meng, A.Y. Kaassis, X. Ren, X. Qu, C. Sun, Z. Xie, S. Zhou, Confinement of carbon dots localizing to the ultrathin layered double hydroxides toward simultaneous triple-mode bioimaging and photothermal therapy, **Talanta**. 184 (2018) 50–57.
- [106] A.M. Kirillov, C. Shan, Y. Tang, K. Iqbal, A. Iqbal, W. Liu, A new multicomponent CDs/Ag@Mg–Al–Ce-LDH nanocatalyst for highly efficient degradation of organic water pollutants, **J. Mater. Chem. A**. 6 (2018) 4515–4524.
- [107] L. Wang, X. Chen, C. Liu, W. Yang, Non-enzymatic acetylcholine electrochemical biosensor based on flower-like NiAl layered double hydroxides decorated with carbon dots, **Sensors Actuators, B Chem.** 233 (2016) 199–205.
- [108] M. Zhang, Q. Yao, C. Lu, Z. Li, W. Wang, Layered Double Hydroxide–Carbon Dot Composite: High-Performance Adsorbent for Removal of Anionic Organic Dye, **ACS Appl. Mater. Interfaces**. 6 (2014) 20225–20233.
- [109] P. Koilraj, Y. Kamura, K. Sasaki, Carbon-Dot-Decorated Layered Double Hydroxide Nanocomposites as a Multifunctional Environmental Material for Co-immobilization of SeO_4^{2-} and Sr^{2+} from Aqueous Solutions, **ACS Sustain. Chem. Eng.** 5 (2017) 9053–9064.
- [110] O. Rahmanian, M. Dinari, M.K. Abdolmaleki, Carbon quantum dots/layered double hydroxide hybrid for fast and efficient decontamination of Cd(II): The adsorption kinetics and isotherms, **Appl. Surf. Sci.** 428 (2018) 272–279.
- [111] Y. Wang, Z. Wang, Y. Rui, M. Li, Horseradish peroxidase immobilization on carbon nanodots/CoFe layered double hydroxides: Direct electrochemistry and hydrogen peroxide sensing, **Biosens. Bioelectron.** 64 (2014) 57–62.
- [112] Y. Guo, X. Liu, X. Wang, A. Iqbal, C. Yang, W. Liu, W. Qin, Carbon dot/NiAl-layered double hydroxide hybrid material: facile synthesis, intrinsic peroxidase-like catalytic activity and its application, **RSC Adv.** 5 (2015) 95495–95503.
- [113] P. Koilraj, Y. Kamura, K. Sasaki, Synergetic co-immobilization of SeO_4^{2-} and Sr^{2+} from aqueous solution onto multifunctional graphene oxide and carbon-dot based layered double hydroxide nanocomposites and their mechanistic investigation, **J. Mater. Chem. A**. 6 (2018)
- [114] T. Hu, J. He, S. Zhang, X. Mei, W. Zhang, R. Liang, M. Wei, D.G. Evans, X. Duan, An ultrathin photosensitizer for simultaneous fluorescence imaging and photodynamic therapy, **Chem. Commun.** 54 (2018) 5760–5763.

- [115] K. Nava Andrade, P. Knauth, Z. López, G.A. Hirata, S.J. Guevara Martinez, G.G. Carbajal Arízaga, Assembly of folate-carbon dots in GdDy-doped layered double hydroxides for targeted delivery of doxorubicin, **Appl. Clay Sci.** 192 (2020) 105661.
- [116] Y. Yang, W. Zhu, D. Cui, C. Lü, Mussel-inspired preparation of temperature-responsive polymer brushes modified layered double hydroxides@Pd/carbon dots hybrid for catalytic applications, **Appl. Clay Sci.** 200 (2021) 105958.
- [117] L. Jafari Foruzin, Z. Rezvani, The improved water oxidation at neutral pH using field bindweed and NiCo- layered double hydroxides, **Appl. Clay Sci.** 201 (2021) 105921.
- [118] C. Zhang, L. Zhang, Q. Liu, Y. Ding, L. Cheng, M. Wu, Z. Li, Enhanced interfacial electron transfer by constructing NiCo-LDH hollow nanocages decorated N-doped graphene quantum dots heterojunction for high-performance supercapacitors, **Appl. Surf. Sci.** 602 (2022) 154352.
- [119] T. Zhao, C. Liu, T. Meng, W. Deng, L. Zheng, F. Yi, A. Gao, D. Shu, Graphene Quantum Dots Pinned on Nanosheets-Assembled NiCo-LDH Hollow Micro-Tunnels: Toward High-Performance Pouch-Type Supercapacitor via the Regulated Electron Localization, **Small.** 18 (2022) 2201286.
- [120] D. Tang, J. Liu, X. Wu, R. Liu, X. Han, Y. Han, H. Huang, Y. Liu, Z. Kang, Carbon Quantum Dot/NiFe Layered Double-Hydroxide Composite as a Highly Efficient Electrocatalyst for Water Oxidation, **ACS Appl. Mater. Interfaces.** 6 (2014) 7918–7925.
- [121] Y. Wei, X. Zhang, X. Wu, D. Tang, K. Cai, Q. Zhang, Carbon quantum dots/Ni–Al layered double hydroxide composite for high-performance supercapacitors, **RSC Adv.** 6 (2016) 39317–39322.
- [122] S. Samuei, J. Fakkar, Z. Rezvani, A. Shomali, B. Habibi, Synthesis and characterization of graphene quantum dots/CoNiAl-layered double-hydroxide nanocomposite: Application as a glucose sensor, **Anal. Biochem.** 521 (2017) 31–39.
- [123] H. Asiabi, Y. Yamini, M. Shamsayei, K. Molaei, M. Shamsipur, Functionalized layered double hydroxide with nitrogen and sulfur co-decorated carbon dots for highly selective and efficient removal of soft Hg²⁺ and Ag⁺ ions, **J. Hazard. Mater.** 357 (2018) 217–225.
- [124] H. Li, Y. Xie, Y. Liu, Y. Xiao, H. Hu, Y. Liang, M. Zheng, Surface chemical functionality of carbon dots: influence on the structure and energy storage performance of the layered double hydroxide, **RSC Adv.** 11 (2021) 10785–10793.
- [125] K. Qu, M. Chen, W. Wang, S. Yang, S. Jing, S. Guo, J. Tian, H. Qi, Z. Huang, Biomass-derived carbon dots regulating nickel cobalt layered double hydroxide from 2D nanosheets to 3D flower-like spheres as electrodes for enhanced asymmetric supercapacitors, **J. Colloid Interface Sci.** 616 (2022) 584–594.
- [126] J. Li, G. Gao, Y. Liu, Y. Li, Z. Liu, Highly-interspersed biomass-derived carbon quantum dots onto floral CoAl-LDH for significantly enhanced CO₂ photoreduction into CO and CH₄, **J. CO₂ Util.** 65 (2022) 102257.
- [127] M. Rinawati, Y.-X. Wang, W.-H. Huang, Y.-T. Wu, Y.-S. Cheng, D. Kurniawan, S.-C. Haw, W.-H. Chiang, W.-N. Su, M.-H. Yeh, Unraveling the efficiency of heteroatom-doped graphene quantum dots incorporated MOF-derived bimetallic layered double hydroxide towards oxygen evolution reaction, **Carbon N. Y.** 200 (2022) 437–447.

- [128] C. Li, G. Zhang, X. Li, H. Wang, P. Huo, X. Wang, Construction of nitrogen-doped graphene quantum dot embedded NiGa layered double hydroxide for high-performance asymmetric supercapacitors, **J. Phys. Chem. Solids**. 163 (2022) 110591.
- [129] W. Yao, X. Wang, Y. Liang, S. Yu, P. Gu, Y. Sun, C. Xu, J. Chen, T. Hayat, A. Alsaedi, X. Wang, Synthesis of novel flower-like layered double oxides/carbon dots nanocomposites for U(VI) and $^{241}\text{Am(III)}$ efficient removal: Batch and EXAFS studies, **Chem. Eng. J.** 332 (2018) 775–786.
- [130] X. Gao, X. Ma, X. Han, X. Wang, S. Li, J. Yao, W. Shi, Synthesis of carbon dot-ZnO-based nanomaterials for antibacterial application, **New J. Chem.** 45 (2021) 4496–4505.
- [131] J. Ge, L. Lian, X. Wang, X. Cao, W. Gao, D. Lou, Coating layered double hydroxides with carbon dots for highly efficient removal of multiple dyes, **J. Hazard. Mater.** 424 (2021) 127613.
- [132] C.S. de Matos, M.M. Nóbrega, M.L.A. Temperini, V.R.L. Constantino, Hybrid Ni Al layered double hydroxide: Characterization and in situ synchrotron XRD and vibrational spectroscopic studies under high-pressure, **Appl. Clay Sci.** 174 (2019) 152–158.
- [133] R.D.S. Macedo, **Materiais à Base de Hidróxidos Duplos Lamelares de Cobalto e Alumínio: Intercalação, Reatividade e Formação de Compósitos por Pirólise.** (Tese de Doutorado) Institute of Chemistry - São Paulo University, 2017.
- [134] A.-L. Troutier-Thuilliez, C. Taviot-Guého, J. Cellier, H. Hintze-Bruening, F. Leroux, Layered particle-based polymer composites for coatings: Part I. Evaluation of layered double hydroxides, **Prog. Org. Coatings**. 64 (2009) 182–192.
- [135] S. Britto, A.V. Radha, N. Ravishankar, P.V. Kamath, Solution decomposition of the layered double hydroxide (LDH) of Zn with Al, **Solid State Sci.** 9 (2007) 279–286.
- [136] R.L. Frost, W. Martens, Z. Ding, J.T. Kloprogge, DSC and high-resolution TG of synthesized hydrotalcites Mg and Zn, **J. Therm. Anal. Calorim.** 71 (2003) 429–438.
- [137] J. Speight, **Lange's Handbook of Chemistry**, Sixteenth Edition, 2005.
- [138] V.R. Magri, M.A. Rocha, C.S. de Matos, P.A.D. Petersen, F. Leroux, H.M. Petrilli, V.R.L. Constantino, Folic acid and sodium folate salts: Thermal behavior and spectroscopic (IR, Raman, and solid-state ^{13}C NMR) characterization, **Spectrochim. Acta Part A Mol. Biomol. Spectrosc.** 273 (2022) 120981.

V.R. Magri, A. Duarte, G.F. Perotti, V.R.L. Constantino, Investigation of Thermal Behavior of Layered Double Hydroxides Intercalated with Carboxymethylcellulose Aiming Bio-Carbon Based Nanocomposites, **ChemEngineering**. 3 (2019) 55.
<https://doi.org/10.3390/chemengineering3020055>

15/02/2023, 12:36

E-mail de Universidade de São Paulo - Request to use article in thesis



Vagner Roberto Magri <vrmagri@usp.br>

Request to use article in thesis

Laura Gasser <publisher@mdpi.com>
Para: Vagner Roberto Magri <vrmagri@usp.br>

14 de fevereiro de 2023 às 03:51

Dear Dr. Vagner R Magri,

Thank you very much for your interest in said material.

All MDPI journals are Open Access and subject to the Creative Commons Attribution License (CC BY). The CC BY permits unrestricted use, distribution, and reproduction of the material in any medium, even commercially, ***provided the original work is properly cited***. You do not have to pay anything for permission.

For more information on the CC BY License, please see here: <https://creativecommons.org/licenses/by/4.0/legalcode>

Best regards,
Laura Gasser

Le 13/02/2023 à 17:12, Vagner Roberto Magri a écrit :

CAUTION - EXTERNAL: This email originated from outside of MDPI organisation. BE CAUTIOUS especially to click links or open attachments.

Dear publisher,

I am writing to request permission to use the article intitled "Investigation of Thermal Behavior of Layered Double Hydroxides Intercalated with Carboxymethylcellulose Aiming Bio-Carbon Based Nanocomposites", published in *ChemEngineering* 2019. <https://doi.org/10.3390/chemengineering3020055>

I am the first author of this work and intend to use the entire article as a chapter of my thesis. One copy will be available online on "The Digital Library of Theses and Dissertations of the University of São Paulo" as well as one printed and one digital (compact disc) copy will be handed to the Institute of Chemistry of the same university.

Thank you very much in advance.

Sincerely,

Vagner R Magri
Phd student at Institute of Chemistry - University of São Paulo (IQ/USP)
Department of Fundamental Chemistry

--

Kind regards,
Laura Gasser
Financial Assistant

MDPI
St. Alban-Anlage 66
4052 Basel, Switzerland
Tel. +41 61 683 77 34
Fax +41 61 302 89 18
E-mail Accounting: billing@mdpi.com
E-mail: laura.gasser@mdpi.com
<http://www.mdpi.com/>

Disclaimer: The information and/or files contained in this message are confidential and intended solely for the use of the individual or entity to whom they are addressed. If you have received this message in error, please notify me and delete this message from your system. You may not copy this message in its entirety or in part, or disclose its contents to anyone.

<https://mail.google.com/mail/u/2/?ik=ff8ee87300&view=pt&search=all&permmsgid=msg-f%3A1757788207330627490&dsqt=1&siml=msg-f%3A1...> 1/2

Article

Investigation of Thermal Behavior of Layered Double Hydroxides Intercalated with Carboxymethylcellulose Aiming Bio-Carbon Based Nanocomposites

Vagner R. Magri¹, Alfredo Duarte¹, Gustavo F. Perotti^{1,2} and Vera R.L. Constantino^{1,*}

¹ Departamento de Química Fundamental, Instituto de Química, Universidade de São Paulo (USP), Av. Prof. Lineu Prestes 748, CEP 05508-000, São Paulo, SP, Brazil; vrmagri@usp.br (V.R.M.); aduarte@iq.usp.br (A.D.); vrlconst@iq.usp.br (V.R.L.C)

² Instituto de Ciências Exatas e Tecnologia, Universidade Federal do Amazonas (UFAM), Rua Nossa Senhora do Rosário 3863, CEP 69103-128, Itacoatiara, AM, Brazil; gustavoperotti@ufam.edu.br (G.F.P.)

* Correspondence: vrlconst@iq.usp.br; Tel.: +55-11-3091-9152

Received: 31 March 2019; Accepted: 27 May 2019; Published: date

Abstract. Carboxymethylcellulose (CMC), a polymer derived from biomass, was intercalated into layered double hydroxides (LDH) composed by M^{2+}/Al^{3+} (M_2Al -CMC, $M = Mg$ or Zn) and evaluated as precursors for the preparation of biocarbon-based nanocomposites by pyrolysis. M_2Al -CMC hybrids were obtained by coprecipitation and characterized by X ray diffraction (XRD), vibrational spectroscopies, chemical analysis, and thermal analysis coupled to mass spectrometry. Following, pyrolyzed materials obtained between 500–1000 °C were characterized by XRD, Raman spectroscopy, scanning electron microscopy (SEM) and energy dispersive spectroscopy (EDS). Above 600 °C, Raman spectra of all samples showed the presence of graphitic carbon, which plays a role in the *degree* of crystallinity of produced inorganic phases (for comparison purposes, M_2Al -CO₃ materials were investigated after calcination in the same experimental conditions). XRD patterns of Mg_2Al -CMC pyrolyzed between 600–1000 °C showed poorly crystallized MgO and absence of spinel reflections, whereas for Zn_2Al -CMC, it was observed well crystallized nanometric ZnO at 800 °C, and $ZnAl_2O_4$ and γ - Al_2O_3 phases at 1000 °C. Above 800 °C, the carbothermic reaction was noticed, transforming ZnO to zinc vapour. This study opens perspectives for nanocomposites preparation based on carbon and inorganic (mixed) oxides through precursors having organic-inorganic interactions at the nanoscale domain.

Keywords: intercalation compounds; layered materials; layered double hydroxides; hydrotalcite; thermal analysis; carboxymethylcellulose; carbon-based nanocomposites.

1. Introduction

More than forty minerals have been identified as layered double hydroxide (LDH) phases which structures are analogous to brucite mineral, $Mg(OH)_2$ [1]. In nature, partial replacement of magnesium ions by Al^{3+} , Fe^{3+} , Cr^{3+} , Mn^{3+} or Co^{3+} produces an excess of positive charges in the structure that are neutralized by simple counter ions such as carbonate, hydroxide, sulphate or chloride. In some minerals, divalent cations like Zn^{2+} , Ni^{2+} , Fe^{2+} or Mn^{2+} are present instead of magnesium. These materials are also called as hydrotalcite-type compounds given that the first identified LDH phase was nominated hydrotalcite (due to its textural resemblance with talc) [2].

The chemical composition of LDH materials is usually represented by the general formula $[(M^{2+}_{(1-x)}M^{3+}_x)(OH)_2]^{x+}[A^{m-}_{x/m} \cdot nH_2O]^{x-}$ and denoted as $M^{2+}_R M^{3+}_A$, where M is the metal ion, R is the M^{2+}/M^{3+} molar ratio and A^{m-} is a hydrated anion [2,3]. The M^{2+}/M^{3+} molar ratio in the minerals is usually 3 or 2 as for example in hydrotalcite ($[Mg_6Al_2(OH)_{16}]CO_3 \cdot 4H_2O$) and quintinite ($[Mg_4Al_2(OH)_{12}]CO_3 \cdot 3H_2O$), respectively [1]. In LDH structure, hydroxide ions are in a hexagonal close-packed arrangement in two adjacent planes in such a way that octahedral sites are occupied by metal

cations (Figure 1a). The octahedra are *edge-sharing* along the crystallographic axes *a* and *b*, forming two-dimensional (2D) structures as shown in Figure 1b [3]. Positive layers are stacked along the *c*-axis and the anions are intercalated between them [3]. Different layers stacking of the same material can produce LDH structures with different dimensions along *c* direction, i.e., distinct polytypes: 3R (rhombohedral symmetry) or 2H (hexagonal symmetry) [3].

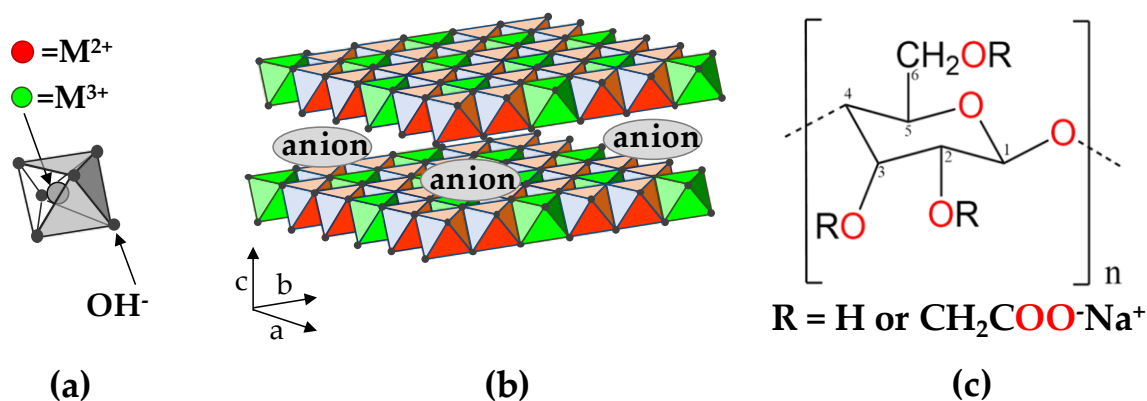


Figure 1. Schematic representation of (a) hydroxide ions coordinated to metal cation in an octahedral arrangement, (b) layered double hydroxide (LDH) structure comprising stacked positive layers intercalated by negative ions, (c) monomeric unit of carboxymethylcellulose (CMC).

From the 1970s, synthetic materials similar to LDH minerals have been prepared in a laboratory and characterized by increasingly advanced physicochemical techniques [4]. Such materials are very versatile in terms of the chemical composition of layers, as well as M²⁺/M³⁺ molar ratio, and a great number of combinations with different anions can be employed in LDH synthesis. Instead of simple anions, LDH hybrid materials can be synthesized by the intercalation of polyoxometalates [5], anionic metal complexes [6] and organic species like drugs, dyes, amino acids, synthetic polymers and biopolymers [4,7,8]. Owing to their compositional versatility, a variety of LDH with different physical-chemical properties can be obtained for diverse applications, ranging from heterogeneous catalysis [9], environmental remediation [10], energy production [11], drug carrier and diagnosis in medicine [12] up to nanoreactors for prebiotic life [13].

LDH organic-inorganic hybrid materials have significant potential as precursors for nanocomposites based on mixed metal oxides (MMO) and carbonaceous species (C). Through calcination, LDH can be converted into oxides (MO_x) and spinels (M₁M₂O₄) which display M²⁺-O²⁻ and M³⁺-O²⁻ acid-basic sites, high specific surface area, well dispersed metals and fine tuning interface of components species suitable for adsorption and/or heterogeneous catalysis in a wide range of reactions [14–16]. Some studies have reported the preparation of MMO/C composites by the bottom-up method where an organic source is carbonized within the confined space between LDH layers [17]. This approach reduces the number of synthetic steps compared to the physical mixture of pre-prepared LDH and nanocarbon form (e.g., carbon nanotubes or graphene oxide), allowing isolation of porous carbon and yielding more homogeneous materials at submicroscale, fostering synergistic effects. Metal oxides (or hydroxides) and carbonaceous materials show exciting adsorption and catalytic properties suitable for applications in environmental remediation or development of sensors [17].

In this study, LDH materials composed by zinc, magnesium and aluminum cations intercalated with carboxymethylcellulose (CMC) polymer were chosen to investigate the thermal preparation of MMO/C composites. CMC is a water-soluble anionic polymer obtained through chemical modification of cellulose polysaccharide, the most abundant natural polymer [18]. Such polymer is constituted by a chain of glucose rings connected by β-1,4 glycosidic linkages between C(1) and C(4) of adjacent units, with a carboxymethyl-substituted group mainly at C(6) position (Figure 1c). As a biomass derivative, CMC is a low-cost, abundant and sustainable source for biocarbon production and, as an anionic polyelectrolyte, can be intercalated into LDH structure. Small organic species intercalated into LDH can

be volatilized even under pyrolytic conditions precluding the carbon formation. The usage of polymeric organic species increases the possibility of carbon production in a non-oxidizing atmosphere.

Few studies were reported about systems comprising LDH and CMC but none of them focused on the preparation of MMO/C nanocomposites. $Mg_{1.15}Al$ -CMC material was prepared by exfoliation of nitrate-LDH in formamide and posterior restacking in a sodium CMC solution also in the organic solvent [19]. Later M_2Al -CMC ($M = Mg, Zn, Cu, Ni$) materials were isolated by coprecipitation method [20,21].

In this work, composite materials based on MMO/C were prepared at four temperature values (500, 600, 800 and 1000 °C) through pyrolysis of M_2Al -LDH ($M = Mg^{2+}$ or Zn^{2+}) intercalated with CMC, as represented in Figure 2. LDH materials constituted by Mg^{2+}/Al^{3+} and Zn^{2+}/Al^{3+} were chosen owing to dissimilar characteristics as thermal stability [22] and topological transformation from LDH to MMO [23,24]. Otherwise, for comparison purposes, LDH materials containing intercalated carbonate instead of CMC were also prepared to investigate the probable influence of CMC on the inorganic phases achieved in the pyrolysis process. Nanocomposites comprising of graphitic carbon, metal oxides and spinel phases were produced within the 600–1000 °C range. For the LDH hybrid material containing Zn^{2+} ions, ZnO nanocrystals were observed when pyrolysis was performed at 800 °C; zinc oxide underwent a carbothermic reaction at higher temperatures. Whereas, XRD pattern of Mg_2Al -CMC exhibited only MgO phase within the 600–1000 °C range, indicating that pyrolyzed CMC hindered the spinel phase crystallization.

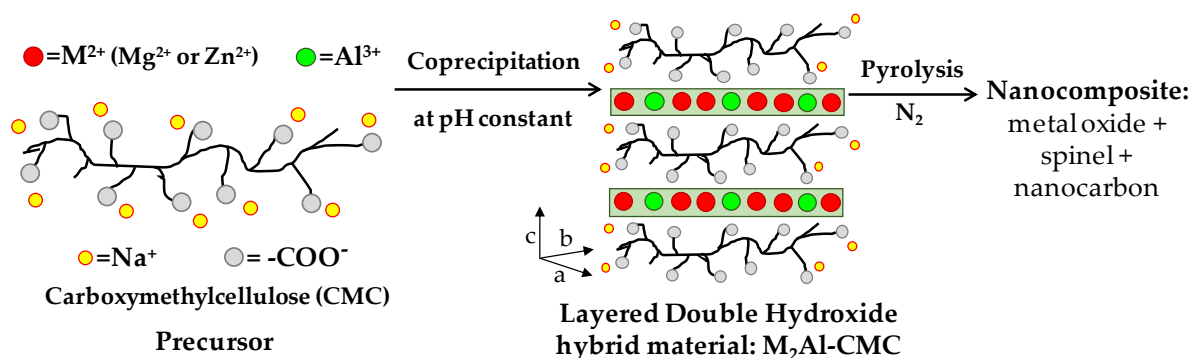


Figure 2. Schematic representation of the two-step synthetic approach used to produce MMO/carbon nanocomposites from layered double hydroxides.

2. Materials and Methods

2.1. Chemicals

Magnesium nitrate hexahydrate ($Mg(NO_3)_2 \cdot 6H_2O$, Merck), aluminum nitrate nonahydrate ($Al(NO_3)_3 \cdot 9H_2O$, Merck), zinc nitrate hexahydrate ($Zn(NO_3)_2 \cdot 6H_2O$, Merck), magnesium chloride hexahydrate ($MgCl_2 \cdot 6H_2O$, Sigma-Aldrich), aluminum chloride hexahydrate ($AlCl_3 \cdot 6H_2O$, Sigma-Aldrich), zinc chloride ($ZnCl_2$, Sigma-Aldrich), sodium hydroxide (NaOH, Sigma-Aldrich), sodium carbonate (Na_2CO_3 , Merck), sodium carboxymethylcellulose—CMC (90 kDa, Degree of substitution 0.7, Sigma-Aldrich) were used without further purification. Deionized water was used in all experimental procedures.

2.2. Preparation of LDH-CMC Hybrid Materials

The intercalation of CMC polymer into LDH was carried out by co-precipitation method and the best experimental conditions are described ahead. For the preparation of the Mg_2Al -CMC sample, 3.070 g of CMC was solubilized into 250 mL of deionized water and the pH value of the solution was adjusted to 9.5 by the addition of NaOH 0.2 mol·L⁻¹ solution. Afterwards, 250 mL of an aqueous solution containing 16.67 mmol of $MgCl_2 \cdot 6H_2O$ and 8.83 mmol of $AlCl_3 \cdot 6H_2O$ was added dropwise to CMC

solution under a nitrogen atmosphere and vigorous stirring. The pH value was maintained constant by the addition of NaOH 0.2 mol L⁻¹ solution. The co-precipitation reaction was carried at 60 °C and, after the complete addition of the metal cations solution, the suspension was maintained for 6 h at 60 °C. The white precipitate was centrifuged, washed four times with deionized water and dried at room temperature under reduced pressure.

For the preparation of the Zn₂Al-CMC sample, 20 g of CMC was solubilized into 850 mL of deionized water and the pH value of the solution was adjusted to 7.5 by the addition of NaOH 0.5 mol·L⁻¹ solution. Afterwards, 520 mL of an aqueous solution containing 41.20 mmol of ZnCl₂ and 21.41 mmol of AlCl₃·6H₂O was added dropwise to CMC solution under a nitrogen atmosphere, vigorous stirring and at room temperature. The pH value was maintained constant by the addition of NaOH 0.5 mol·L⁻¹ solution. After addition of the metal cations solution, the suspension was dialyzed for 3 days changing the water after each 12 h. The white precipitate was then freeze dried.

For comparison purpose, Mg²⁺/Al³⁺ and Zn²⁺/Al³⁺ LDH materials intercalated with carbonate anion (Mg₂Al-CO₃ and Zn₂Al-CO₃) were synthesized as described by Miyata [25] with modifications. Typically, the pH value of 250 mL of water was adjusted to 9.5 (for Mg₂Al-CO₃) or 9.0 (for Zn₂Al-CO₃) by the addition of Na₂CO₃ 0.2 mol·L⁻¹ solution. To this solution, 250 mL of a solution containing 16.67 mmol of Mg(NO₃)₂·6H₂O (or Zn(NO₃)₂·6H₂O) and 8.33 mmol of AlCl₃·6H₂O was added dropwise under stirring. The co-precipitation reaction was carried out at an ambient atmosphere and room temperature. The pH value was maintained constant by the addition of Na₂CO₃ 0.2 mol·L⁻¹ solution. After addition of the metal cations solutions, the suspension was maintained under stirring at ambient atmosphere and room temperature for 2 h. The white precipitate was centrifuged, washed five times with deionized water, one time with ethanol and dried at room temperature under reduced pressure.

2.3. Preparation of MMO/C Composites

Mg₂Al-CMC and Zn₂Al-CMC precursors were pyrolyzed on a Shimadzu TGA-50 furnace under a molecular nitrogen flow of 50 mL min⁻¹, using alumina crucibles and a heating rate of 10 °C min⁻¹, at temperatures of 500, 600, 800 and 1000 °C. For comparison purpose, Mg₂Al-CO₃ and Zn₂Al-CO₃ were calcined under nitrogen flow using the same parameters. Besides, Mg₂Al-CMC and Zn₂Al-CMC precursors were also calcined under synthetic air at 1000 °C, using the same conditions described to pyrolysis at N₂ environment. Afterwards, heated samples were stored in a desiccator containing silica gel under reduced pressure.

2.4. Physical Measurements

Elemental chemical analysis (carbon and hydrogen) were performed on a Perking Elmer model 2400 analyzer. Magnesium, zinc and aluminum contents were determined in triplicate by inductively coupled plasma optical emission spectroscopy (ICP OES) on a Spectro Arcos spectrometer. Both analyses were performed at the Central Analítica of Instituto de Química da Universidade de São Paulo (CA-IQUSP).

Mass spectrometry coupled to simultaneous thermogravimetric analysis and differential scanning calorimetry (TG-DSC-MS) were performed on a Netzsch thermoanalyzer model TGA/DSC 409 PC Luxx coupled to an Aëolos 403 C mass spectrometer under synthetic air or N₂ flow of 50 mL min⁻¹ employing alumina crucibles and a heating rate of 10 °C·min⁻¹.

X ray diffraction (XRD) patterns of powdered samples were recorded on a Bruker diffractometer model D8 DISCOVER equipped with Nickel-filtered CuK α radiation (0.15418 nm), operating at 40 kV, 30 mA, sample rotating at 20 rpm, from 1.5 to 70° (2 θ) at 0.05° intervals, 3 s per interval.

Fourier transform infrared (FTIR) spectra of powdered samples were recorded in the 4000–400 cm⁻¹ range on a Bruker Alpha spectrometer using a single bounce attenuated total diffuse reflectance (ATR) mode with a diamond crystal. Fourier transform Raman (FT-Raman) spectra were recorded on an FT-Raman Bruker FRS-100/S instrument using 1064 nm excitation radiation (Nd³⁺/YAG laser) and liquid nitrogen cooled Ge detector. Raman spectra of pyrolyzed samples were recorded in the 3500–100 cm⁻¹

range on a Renishaw inVia instrument coupled to a confocal Leica microscope and a CCD detector, using 532 nm excitation radiation (Nd³⁺/YAG laser).

Scanning Electron (SEM) micrographs were collected using a JEOL JSM7401F instrument, equipped with a field emission gun (FEG). Accelerating voltages (kV) are reported on each micrograph. Energy Dispersive X ray Spectra (EDS) were collected simultaneously on a Thermo Fischer Scientific detector, Pioneer model, 30 mm² Si Crystal, coupled to a Noran System Six signal processor (NSS). Powder samples were pulverized onto carbon conductive tapes prior to SEM imaging.

3. Results and Discussion

3.1. Characterization of LDH-CMC Hybrid Materials

XRD patterns of LDH-CO₃ and LDH-CMC synthesized samples showed profiles characteristic of layered double hydroxides (Figure 3). LDH-CO₃ samples are more crystalline than LDH-CMC, as evidenced by the high intensity and narrow diffraction peaks which can be indexed assuming a hexagonal cell with rhombohedral symmetry (3R polytype) and R-3m space group. The reflections observed at 2θ values below 30° are assigned to the (00l) planes that are related to interlayer distance (d_{basal}) and the cell parameter c (Figure 1b). The reflection observed in 2θ values in the region of 60° is attributed to the (110) plane related to the cell parameter a that gives the average distance between metal cations in the layer. The presence of broad XRD peaks associated with both (003) and (110) planes of LDH-CMC samples indicates that the crystal dimensions are both reduced in the crystallographic directions a and c in comparison to LDH-CO₃ materials [26]. Table S1 (Supplementary Materials) shows the 2θ values, the respective interplane distances (d_{hkl}) and the calculated unit cell parameters for LDH materials. For Zn₂Al-CO₃ and Mg₂Al-CO₃ samples, the d_{003} spacing values were respectively 0.754 nm and 0.765 nm. Samples Zn₂Al-CMC and Mg₂Al-CMC showed a shift of 003 diffraction peaks to 2.492 and 1.715 nm, respectively, indicating an expansion of the interlayer space in order to accommodate the macromolecules.

XRD pattern of Mg₂Al-CMC sample prepared by Yadollahi and Namazi [20] presented d_{003} spacing value equal to 1.73 nm while Zn₂Al-CMC sample reported by Yadollahi et al. [21] showed the d_{003} value of 1.58 nm. Considering that CMC is a polymer that may present different arrangements, the proposal of a conformation for the chains between the LDH layers is not straightforward. The basal spacing difference between Mg₂Al-CMC and Zn₂Al-CMC materials prepared in this work may be related to the higher water and CMC contents in the zinc matrix. The calculated d_{110} values for Zn₂Al-CO₃ and Zn₂Al-CMC were 0.153 nm, while for Mg₂Al-CO₃ and Mg₂Al-CMC were 0.152 nm and 0.151 nm, respectively, which means that the molar ratio between the metal cations is similar in the samples. These points will be discussed later when chemical elemental analysis will be presented.

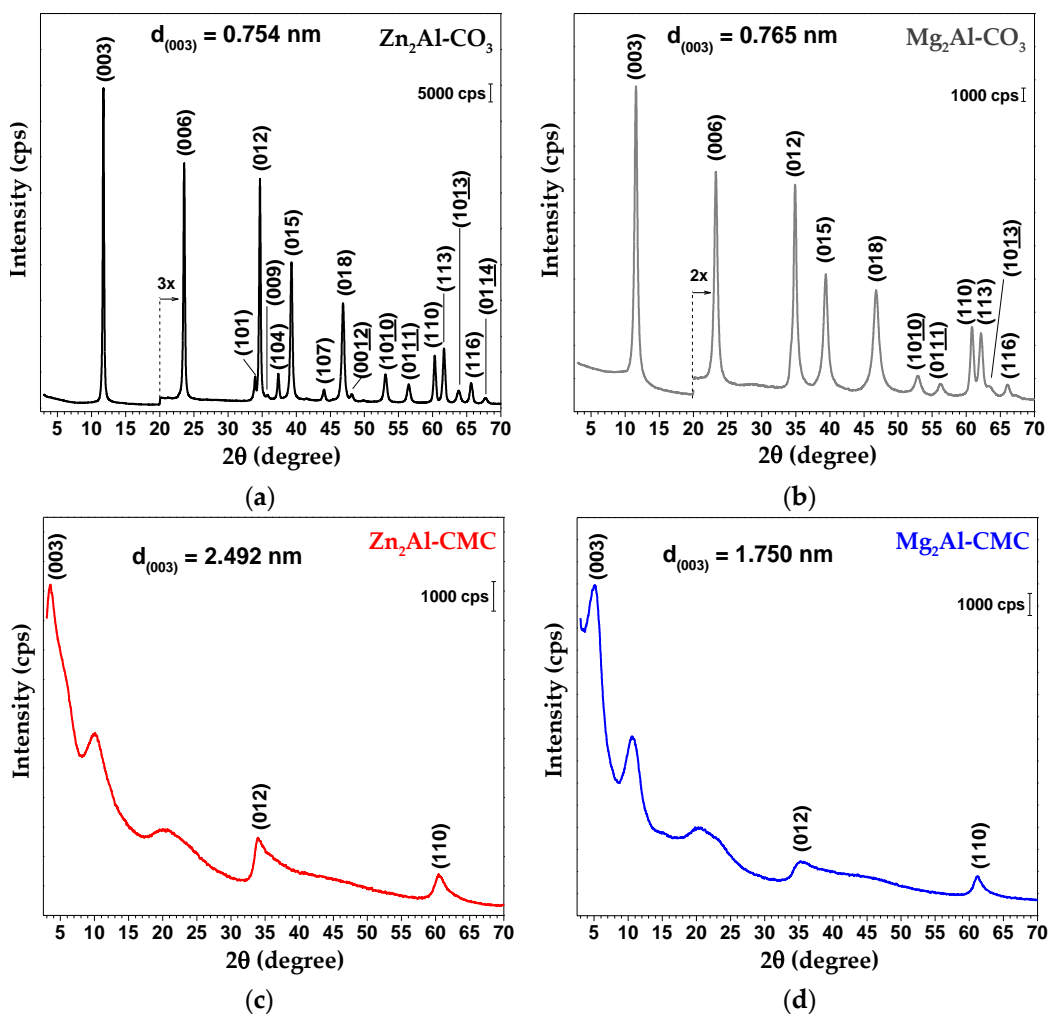


Figure 3. XRD patterns of $\text{Zn}_2\text{Al-CO}_3$ (a), $\text{Mg}_2\text{Al-CO}_3$ (b), $\text{Zn}_2\text{Al-CMC}$ (c) and $\text{Mg}_2\text{Al-CMC}$ (d) samples. The diffraction peaks in (a) and (b) were indexed according to ICSD 190041 and 86655, respectively.

XRD pattern of NaCMC exhibits mainly one broad peak around 2θ value of 20° (Figure S1, Supplementary Materials) which is associated with the low degree of organization of the macromolecules [27]. Considering the XRD patterns of LDH-CMC samples, it is observed a broad hump at $(2\theta) 20^\circ$ that could suggest that part of the polymer chains might not be confined within the interlayer space but rather adsorbed over LDH particles. XRD patterns of $\text{M}_2\text{Al-CMC}$ ($\text{M}^{2+} = \text{Mg}, \text{Zn}, \text{Ni}, \text{Cu}$) samples reported in the literature [21] also showed a broad peak in the same region.

The infrared and FT-Raman spectra of $\text{Zn}_2\text{Al-CO}_3$ and $\text{Mg}_2\text{Al-CO}_3$ are shown in Figure 4. The discussion about vibrational data is presented in Supplementary Materials, as well as a tentative attribution of the main vibrational bands (Table S2).

The spectroscopic characterization of sodium CMC and LDH-CMC samples was evaluated by FTIR-ATR and FT-Raman spectroscopies (Figure 4). Spectra of the polymer and hybrid materials are very similar, and the results clearly indicate the presence of CMC in the LDH structure. A tentative attribution regarding cellulose and carboxymethylcellulose spectroscopic data is presented in Table 1. The NaCMC bands attributed to antisymmetric and symmetric stretching of carboxylate groups are noticed at 1585 cm^{-1} ($\nu_{\text{as}}\text{COO}^-$) and 1412 cm^{-1} ($\nu_{\text{s}}\text{COO}^-$), respectively. In the LDH-CMC spectra, the $\nu_{\text{as}}\text{COO}^-$ band is shifted to 1577 cm^{-1} . The $\Delta\nu\text{COO}^-$ values calculated by the formula $\Delta\nu\text{COO}^- = \nu_{\text{as}} - \nu_{\text{s}}$ are very close to that one of NaCMC, indicating an electrostatic interaction of carboxylate groups with LDH layers. Bands in the $1100\text{--}980\text{ cm}^{-1}$ region are assigned to stretching and bending vibration of C–O bond from the glycosidic ring and hydroxyl groups. FT-Raman spectra of NaCMC and the hybrid

materials show very similar bands. The band at 2907 cm^{-1} is related to C–H stretching, at 1118 cm^{-1} is attributed to symmetric stretching of C(1)–O–C(4) group and ring breathing, and at 918 cm^{-1} is assigned to bending C(5)C(6)–H and HC(6)O.

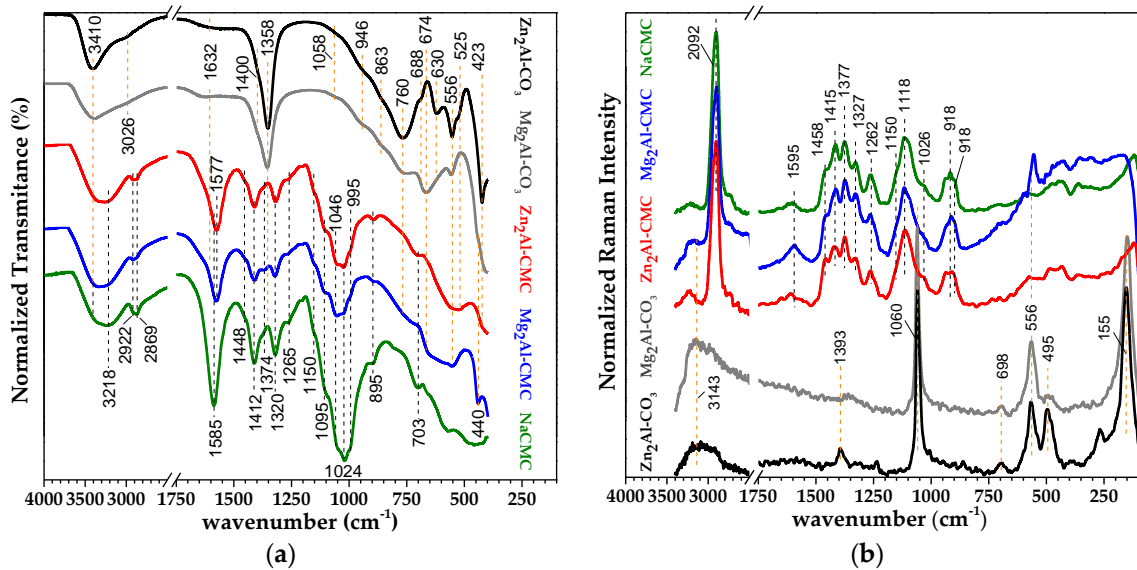


Figure 4. FTIR-ATR (a) and FT-Raman (b; $\lambda_{\text{exc}} = 1064 \text{ nm}$) spectra of $\text{Zn}_2\text{Al-CO}_3$ (black), $\text{Mg}_2\text{Al-CO}_3$ (grey), ZnAl-CMC (red), $\text{Mg}_2\text{Al-CMC}$ (blue) and sodium carboxymethylcellulose (NaCMC, green).

Table 1. Vibrational spectroscopic data of sodium carboxymethylcellulose.

Raman	IR	Tentative of Attribution	Reference
3400–3200	3600–3300 (bb)	vOH free or hydrogen bonded	[28–30]
2902	--	vCH	[28,30]
--	2922	vasC(6)H ₂	[28]
--	2869	vsC(6)H ₂	[28]
1595	1585	vasCOO-	[31]
1458(sh)	--	$\delta_{\text{sc}}\text{C}(6)\text{H}_2$	[30,32]
--	1448(sh)	$\delta_{\text{sc}}\text{CH}_2$ and $\delta_{\text{ip}}\text{COH}$	[29,32]
1415	--	δCH_2 and δCCH , δHCO , δCOH	[30,32]
--	1412	vsCOO-	[31]
1377	1374(sh)	δCH_2 and δCCH , δHCO , δCOH	[30,32]
1327	1320	$\delta_{\text{w}}\text{C}(6)\text{H}_2$ and δCCH , δHCO , δCOH	[30,32]
1262	1264	$\delta_{\text{tw}}\text{C}(6)\text{H}_2$ and δCCH , δHCO , δCOH	[30,32]
1150(sh)	1150(sh)	vasC–C and vasC–O (ring breathing)	[29,32]
1118	--	vsC(1)–O–C(4) and s ring breathing	[32]
--	1095(sh)	vC(2)–O	[29,33]
--	1046(sh)	$\delta\text{C}(6)\text{--O}$ and $\delta\text{C}(5)\text{--O}$	[33]
1026(sh)	1019	$\delta\text{C}(3)\text{--O}$	[33]
--	995 (sh)	vC(1)–O	[33]
918	--	$\delta\text{C}(5)\text{C}(6)\text{--H}$ and $\delta\text{HC}(6)\text{O}$	[30]
896	895	$\delta\text{C}(1)\text{--H}$	[32]
--	703	$\delta_{\text{rk}}\text{CH}_2$ and $\delta_{\text{oop}}\text{COH}$ (C6 and C3)	[29,34]

bb = broad band; sh = shoulder; v = stretching; as = antisymmetric; s = symmetric; δ = bending; w = wagging; tw = twisting; sc = scissoring; ip = in-plane; oop = out-of-plane; rk = rocking.

Thermal analysis technique indicated significant changes in the CMC thermal profile before and after the intercalation process. In the pristine form and under N₂ atmosphere, NaCMC exhibits four events of mass loss until 1000 °C (Figure S2, Supplementary Materials). The first event, endothermic, occurring from room temperature up to about 170 °C is attributed to the release of a total of 7.3 % of the initial mass as water molecules (release of fragment $m/z = 18$) presented initially in the hydrophilic polymer. According to TGA and DSC data, the polymer decomposition occurs in two exothermic steps [35,36]. The first step, steeper, in the 240–320 °C range, promotes release of water ($m/z = 18$), decarboxylation with CO₂ ($m/z = 44$) release and a low amount of C₃H₅ ($m/z = 41$); the second step, in the 320–530 °C range, yields a charred residue. The last event of mass loss, also endothermic, recorded above 800 °C can be related to the decomposition of carbonaceous matter to Na₂CO₃ [35]. CMC used in this study has 0.7 of the degree of substitution (*DS*) of carboxymethyl group and, as a result, the repeating unit (RU) can be represented by C₆H₁₀O₅(C₂H₂O₂Na)_{0.7}. Considering this composition, the expected percentage of Na₂CO₃ residue (13.7%) is very close to the experimental value (13.5%) obtained by TGA analysis (Figure S2).

The knowledge of the thermal behavior of carbonate LDH phases and the products produced in distinct temperatures is important to contrast with thermal properties of LDH-CMC precursors. According to TGA-MS results, for both carbonate-based layered structures, three main events of mass loss can be described (Figure 5). The first event, ranging from room temperature up to 220 °C is related to the release of interlayer and adsorbed water molecules [37], as indicated for MS curve (release of $m/z = 18$ fragment). The initial structure is proven to be modified even at temperatures above 100 °C owing to the detection of growing quantities of $m/z = 44$ (CO₂) fragment in MS analysis. In the second event of mass loss at temperatures above 200 °C, composition integrity of the layered structure is severely affected owing to the release of water molecules ($m/z = 18$) through a mechanism known as dehydroxylation [37]. For Zn₂Al-CO₃, the onset temperature for dehydroxylation was observed at a lower temperature (215 °C) in comparison to Mg₂Al-CO₃ (282 °C), and thus it can be inferred that the Mg₂Al-CO₃ structure is thermally more stable than the analogous phase of zinc.

Around the same temperature value and at higher temperatures, the release of $m/z = 44$ fragment (CO₂) is intensified for Mg₂Al-CO₃ as the third event of mass loss (decarbonation process) occurs. At around 480 °C, dehydroxylation is ended for Mg₂Al-CO₃ sample but carbonate decomposition (release of $m/z = 44$ fragment) is still observed at temperatures up to 700 °C (even though the majority of carbonate decomposes at around 440 °C). On the other hand, Zn₂Al-CO₃ material exhibits a distinct thermal behavior. Even though it dehydroxylates and is partially decarbonated (since the $m/z = 44$ fragment analysis reveals the increase of CO₂ detection above 200 °C), only a small fraction of carbonate ions is released. Just at temperature values higher than 520 °C, $m/z = 44$ fragment is detected in large quantities in an apparent two distinct mechanisms of mass loss up to 840 °C. Such differences in the decarbonation process for Zn₂Al-CO₃ compared to Mg₂Al-CO₃ can be a direct consequence of the occurrence of dehydroxylation of the Zn-based LDH at lower temperatures than the thermal decomposition of carbonate, which allows the coordination of CO₃²⁻ ion to metals present in the formed mixed oxide structure, increasing the anion thermal stability [22,23]. As the temperature of the analysis is increased, after dehydroxylation of the LDH is completed, it is formed an amorphous M²⁺(Al)O oxide phase, followed by the formation of crystalline oxide phases. Above temperature values of 500 and 800 °C, spinel phases are obtained respectively for Zn₂Al-CO₃ and Mg₂Al-CO₃ [23,38,39].

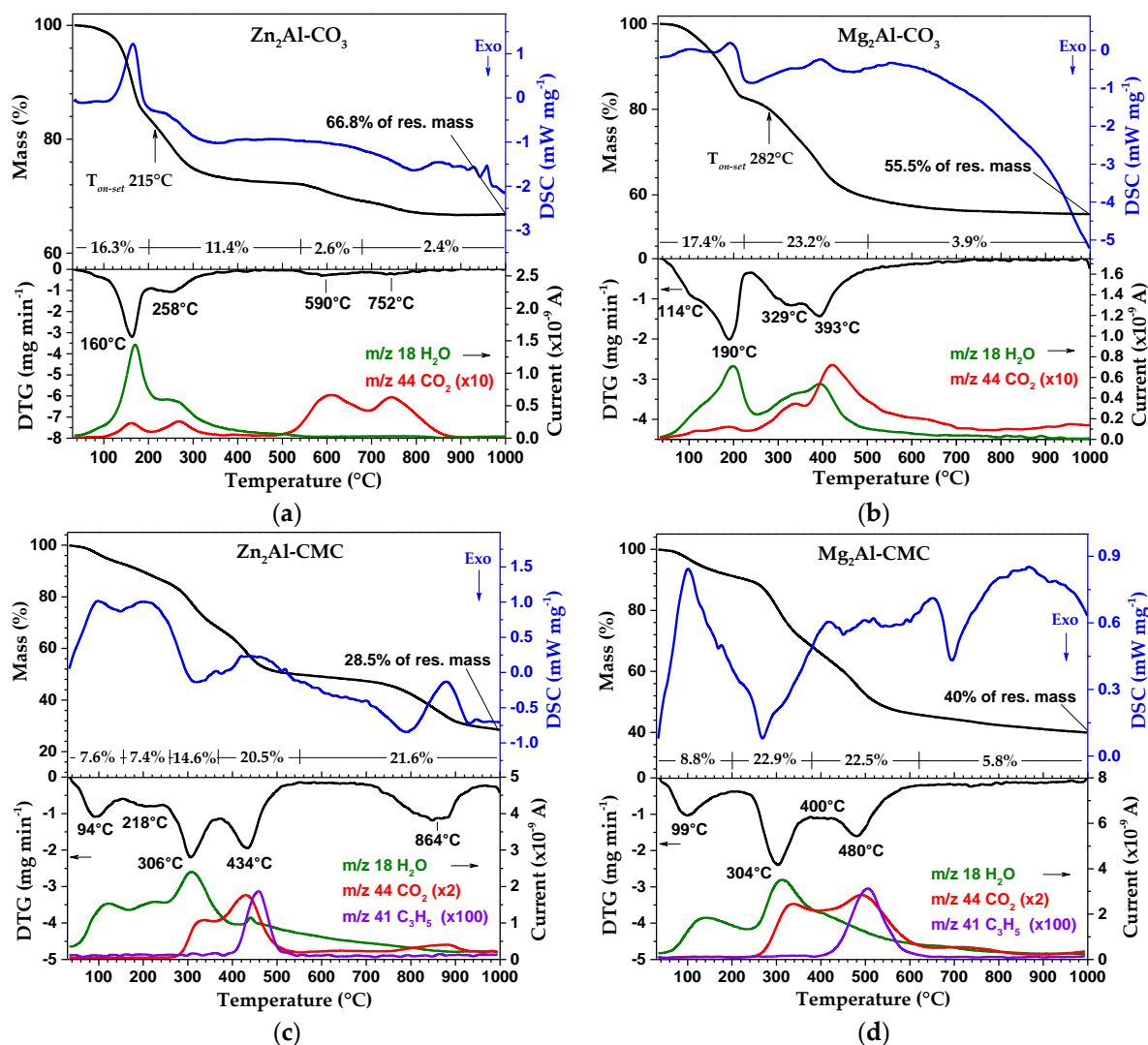


Figure 5. TG-DSC and DTG-MS curves of $\text{Zn}_2\text{Al-CO}_3$ (a), $\text{Mg}_2\text{Al-CO}_3$ (b), $\text{Zn}_2\text{Al-CMC}$ (c) and $\text{Mg}_2\text{Al-CMC}$ (d) samples under N_2 atmosphere.

For $\text{Zn}_2\text{Al-CMC}$, the dehydration step occurs within the 30–250 °C temperature range, closely followed by $\text{Mg}_2\text{Al-CMC}$ in the 30–225 °C range according to the increase in the amount of the $m/z = 18$ (H_2O) fragment detected (Figure 5). The second event of mass loss (from 250 to 380 °C) is related to the thermal decomposition of polymer chains through release of water molecules ($m/z = 18$) from hydroxyl groups in the polymer composition and decarboxylation of side groups ($m/z = 44$) for both layered systems, according to DTG data. Although the beginning of this decomposition event is not significantly shifted towards higher temperatures, when pristine NaCMC is compared to the intercalated polymer into LDH galleries, it is noticed that the polymer decomposition event exhibits larger thermal range after immobilization. Hence, the interaction between both inorganic and organic phases delays the start of polymer fragmentation.

Above 380 °C, MS curves of $\text{M}_2\text{Al-CMC}$ phases are altered substantially depending on the composition of the inorganic layers (Figure 5). At higher temperature values, glucose chains undergo fragmentation in both LDH samples yielding not only water and carbon dioxide molecules but also C_3H_5 fragments ($m/z = 41$). Even though the beginning of this event is around the same value for both Mg and Zn-based LDH, it is observed that this second decomposition step is extended to a wider temperature range for $\text{Mg}_2\text{Al-CMC}$ (380–605 °C) than for $\text{Zn}_2\text{Al-CMC}$ (380–520 °C). Mass changes are negligible above 605 °C for Mg-based hybrid material (Figure 5). On the other hand, the TGA curve of $\text{Zn}_2\text{Al-CMC}$ reveals one event of mass loss above 760 °C which is not observed in the same experiment

conducted at air atmosphere (data not shown). This observation is surprising considering that it is expected the release of less volatile compounds at N₂ atmosphere than at molecular oxygen environment. The ascription of this event will be clarified ahead in view of XRD and SEM data of pyrolyzed materials.

Based on the dehydration process observed by TGA and data from the chemical elementary analysis, a formula is proposed for LDH-CO₃ and LDH-CMC materials synthesized in this work (Table S3). Experimental M²⁺/Al³⁺ molar ratio is very close to the nominal value for carbonate or CMC intercalated LDH materials. Precursor hybrid materials present about 20–22% in mass of carbon element.

3.2. Characterization of MMO/C Composites

LDH-CMC samples pyrolyzed at 500, 600, 800 and 1000 °C (MMO/C nanocomposites) were evaluated by Raman spectroscopy to assess the type of carbonaceous material obtained (Figure 6). Raman spectra of both LDH-CMC pyrolyzed at 500 °C still show fluorescence that suppressed vibrational bands, as observed for NaCMC and LDH-CMC precursors (Figure S3).

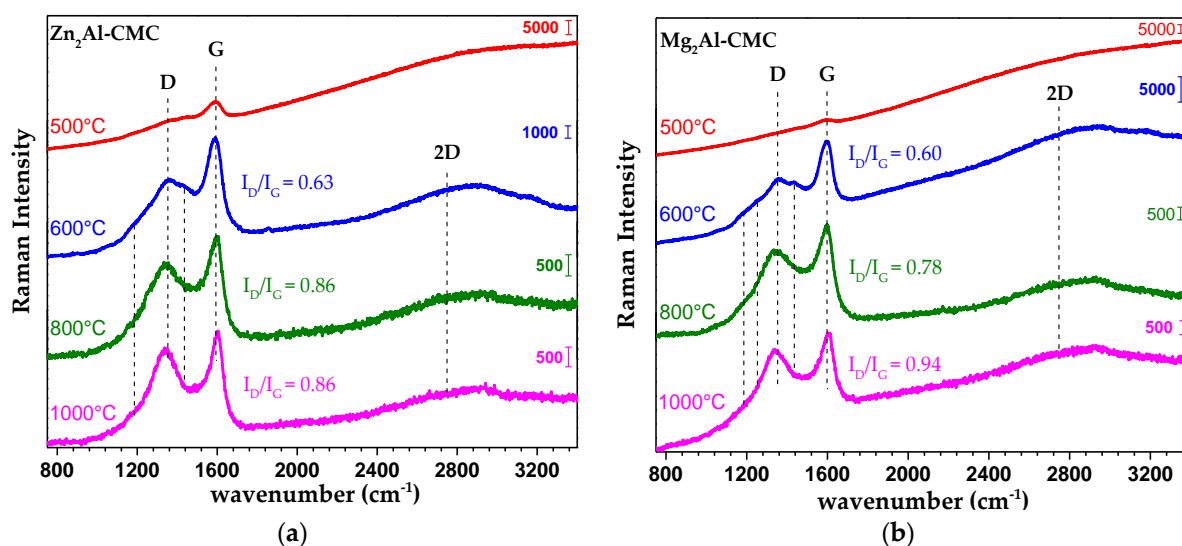


Figure 6. Raman spectra of Zn₂Al-CMC (a) and Mg₂Al-CMC (b) samples pyrolyzed at 500, 600, 800 and 1000 °C under N₂ atmosphere ($\lambda_{exc} = 532$ nm).

The characteristic spectral profile of graphitic materials is observed for samples obtained in the 600–1000 °C range (Figure 6): bands D (1340–1350 cm⁻¹), G (1590–1600 cm⁻¹) and 2D (2500–2800 cm⁻¹). Band G is assigned to the in plane stretching of the C=C bonds (Csp²) and is characteristic for all forms of sp² carbon. Band D is attributed to ring breathing and requires defects for its activation [40–42]. However, besides the graphitic bands, Raman spectra of pyrolyzed samples at 600 °C also exhibit shoulders attributed to amorphous hydrogenated carbonaceous material at 1180 cm⁻¹ (C–H in aromatic ring structure and correlated to a rich sp³ structure), 1430 cm⁻¹ (aromatic ring breathing for rings containing more than two fused aromatic rings), and 1250 cm⁻¹ (rich sp³ structure as an aryl-alkyl C–C (like polyacetylene) bonded to aromatic species) [42,43]. These bands disappear with temperature increasing up to 1000 °C. The intensity ratio between bands D and G (I_D/I_G) is also increased with temperature progression, pointing out dehydrogenation of carbonaceous material and intensification of aromatic rings [43]. Hence, amorphous carbon is produced between 500 and 600 °C, and yield a more organized structure as the temperature is further increased.

FTIR-ATR spectra of LDH-CMC pyrolyzed materials exhibit weak bands assigned to the organic polymer (Figure 7). A significant change is observed at 1150–990 cm⁻¹ region, attributed to C–O–C and C–O vibration modes of glycoside rings and to hydroxyl groups, indicating their conversion to other compounds as the temperature is increased. In general, bands observed below 900 cm⁻¹ are assigned to

vibrational modes of M–O bonds as already discussed in Supplementary Materials (Table S2). For comparison purpose, the FTIR-ATR spectra of LDH-CO₃ calcined samples (Figure S4) and the discussion about the results are presented in Supplementary Materials.

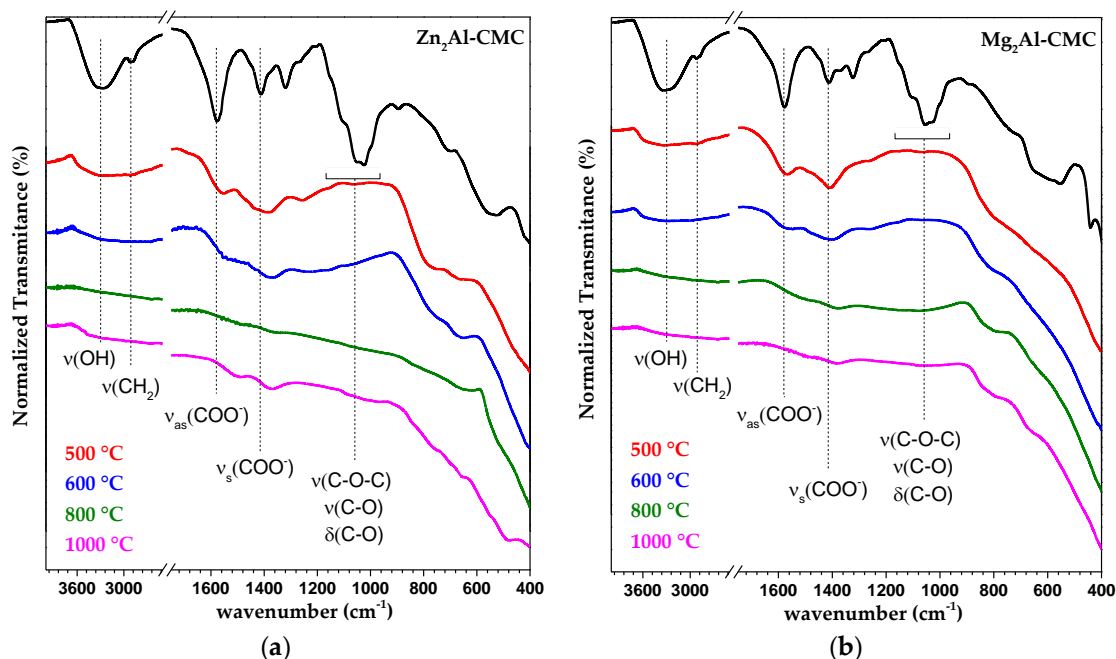


Figure 7. FTIR-ATR spectra of Zn₂Al-CMC (a) and Mg₂Al-CMC (b) samples pyrolyzed at 500, 600, 800 and 1000 °C under N₂ atmosphere.

To investigate the differences between the thermal transformations of Mg₂Al-LDH and Zn₂Al-LDH materials, XRD patterns of samples calcined between 500–1000 °C under N₂ flow were recorded (Figure 8). Zn₂Al-CMC pyrolyzed and Zn₂Al-CO₃ calcined at 500 and 600 °C are converted into a poor crystallized ZnO phase. However, at higher temperature values, the products from pyrolysis are very distinctive indicating an influence of the organic polymer in the structure and composition of the inorganic portion of the produced composite. ZnO phase produced from the hybrid LDH at 800 °C is significantly more crystalline than that one obtained from Zn₂Al-CO₃. On the other hand, Zn₂Al-CO₃ is transformed into a well crystallized ZnO and ZnAl₂O₄ (spinel) phases at 1000 °C, while XRD pattern of Zn₂Al-CMC presents peaks attributed to ZnAl₂O₄ and poor crystallized γ-Al₂O₃ phase. From 800 to 1000 °C, Zn₂Al-CMC material seems to lose the ZnO phase and this event should be correlated to that one noticed by thermal analysis in the same temperature range (Figure 5).

XRD patterns of Mg₂Al-CMC pyrolyzed between 500–1000 °C indicate the formation MgO phase which crystallinity is increased with the temperature evolution (Figure 8). Similarly, Mg₂Al-CO₃ sample calcined between 500–800 °C shows reflections of MgO. However, when calcined at 1000 °C, MgO and MgAl₂O₄ (spinel) phases are observed. The organic polymer intercalated into LDH modified the degree of organization of the inorganic portion of pyrolyzed products. If calcined under an air atmosphere at 1000 °C, both LDH-CMC materials produce metal oxide and spinel phases (Figure S5a) likewise LDH-CO₃ samples under nitrogen atmosphere (Figure 8). In addition, whereas the Mg₂Al-CMC sample calcined under synthetic air presented less residual mass than that calcined under N₂ at 1000 °C, as it is expected due to carbonized matter, curiously the opposite was observed for Zn₂Al-CMC sample (Figure S5b).

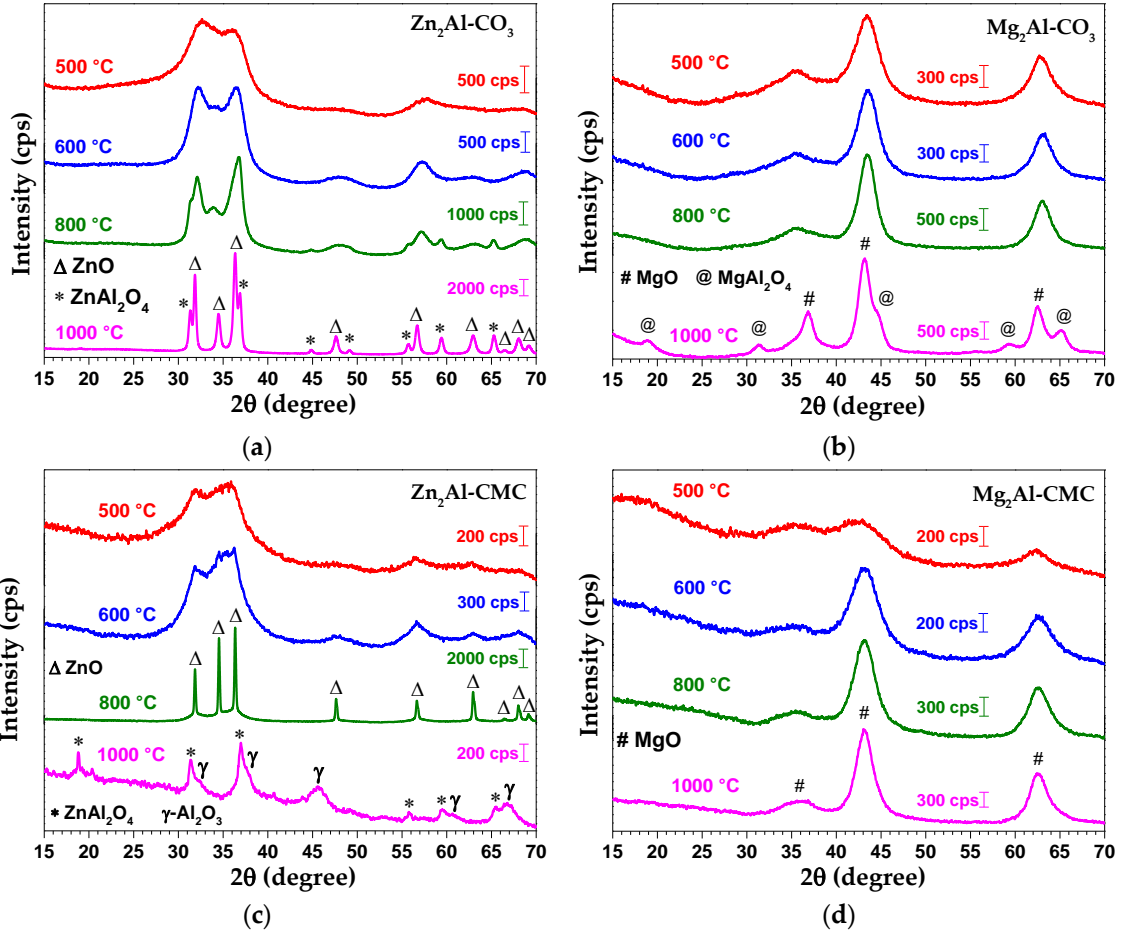
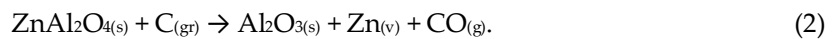


Figure 8. XRD patterns of $\text{Zn}_2\text{Al-CO}_3$ (a), $\text{Mg}_2\text{Al-CO}_3$ (b), $\text{Zn}_2\text{Al-CMC}$ (c) and $\text{Mg}_2\text{Al-CMC}$ (d) samples pyrolyzed at 500, 600, 800 and 1000 °C under N_2 atmosphere. The phases were indicated according to ZnO (wurtzita; ICSD 26170), ZnAl_2O_4 (ICSD 75091), MgO (periclase; ICSD 9863), MgAl_2O_4 (ICSD 31373) and $\gamma\text{-Al}_2\text{O}_3$ (ICSD 249140).

It can be proposed that graphitic carbonaceous material formed during the pyrolysis of hybrid LDH, and evidenced by Raman spectroscopy (Figure 6), hinders the formation of crystalline spinel phase in the obtained MMO/C nanocomposites, and allows the production of well crystallized ZnO particles at lower temperatures compared to $\text{Zn}_2\text{Al-CO}_3$. Besides that, comparing the results of thermal analysis (Figure 5), Raman spectroscopy (Figure 6) and XRD (Figure 8), it is proposed that a carbothermic reaction is occurring between 800–1000 °C, i.e., ZnO is reduced to metal form by carbon (from CMC pyrolysis) and released as vapour (zinc boiling point is 920 °C), as represented by the following chemical equation:



Metal zinc is produced by five industrial processes involving mainly the pyrometallurgical method. Carbon is mixed with ZnO and heated at about 1000–1300 °C to produce the metal in the vapour phase [44]. The presence of aluminum oxide at $\text{Zn}_2\text{Al-CMC}$ pyrolyzed at 1000 °C can indicate the partial reduction of spinel phase as observed for the mineral gahnite (a zinc aluminate of ZnAl_2O_4 composition) in the presence of carbon [45]. Hence, a spinel phase decomposition could be represented by the following chemical equation:



A discussion about thermodynamic aspects of reaction (1) can be found in Supplementary Materials (Table S4 and Table S5). The carbothermic reaction can explain the disappearance of ZnO

diffraction peaks (Figure 8) and the formation of γ - Al_2O_3 phase. As it is expected, under synthetic air this reaction is not observed because CMC is fully decomposed at 600 °C (data not shown). To the best of our knowledge, this is the first time that carbothermic reaction is reported for zinc-LDH intercalated with organic species.

SEM micrographs shown different morphological transition from LDH to oxides phases according to M^{2+} cation composition ($\text{M}^{2+} = \text{Mg}^{2+}$ or Zn^{2+}). The micrographs of LDH-CMC precursor samples (Figure 9a,b) exhibit a lack of surface distinction among particles, showing up as a continuous mass. This observation can be interpreted as a consequence of small particles formation as already suggested by XRD patterns (Figure 3); morphology of LDH-CMC samples are very distinct of $\text{M}_2\text{Al-CO}_3$ phases, which interparticle frontiers are usually easily distinguished (Figure S6). The presence of the polymer chains also on the external surfaces of LDH particles can contribute to the continuous mass aspect seen in the images. Through an agglomeration process, which occurs along with the sedimentation of particles from reactional media, high surface energies acting over a large number of very small particles can generate such aspect, and behave as a cohesive mass.

Morphological alterations are evident when the pyrolysis process is carried out at 800 °C, producing distinguishable particles at a nanoscale (Figure 9c–f). Thermal decomposition of $\text{Zn}_2\text{Al-CMC}$ agglomerates gives rise to denser and zinc/oxygen richer particles as shown respectively by brighter secondary electron contrast (Figure 9c) and EDS spectra (Figure S7). $\text{Zn}_2\text{Al-CMC}$ pyrolyzed at 800 °C is composed mainly by well-defined crystallites reaching up to hundreds of nanometers in size and connected through their grain boundaries (Figure 9e). These observations agree with its respective XRD pattern (Figure 6), which evidences the arising of a high crystalline ZnO phase. In comparison, the absence of prominent morphologies is noticed for $\text{Mg}_2\text{Al-CMC}$ pyrolyzed at 800 °C (Figure 9d), the sole new feature is the peeling appearance (Figure 9f). Possibly CMC thermal decomposition promotes the weakening and rupture of interfacial interactions among particles, previously acting as an interparticle connector; the subsequent gas evolution from polymer decomposition and matrix dehydroxylation (Figure 5) can also corroborate to the breakdown of the cohesive mass.

A new set of superficial transformations takes place when $\text{Zn}_2\text{Al-CMC}$ material is pyrolyzed at 1000 °C (Figure 9g). The zinc rich phase previously observed at 800 °C completely vanishes and a new one emerges, as can be visually depicted mostly as a collection of anisotropic acicular nanocrystals, assembled as branched particles onto the MMO/C composite surface. Besides, EDS spectra collected from this sample reveal considerable decrease in Zn signal (Figure S8). This observation is indicative of ZnO depletion owing to the carbothermic reduction, as suggested by thermal analysis (Figure 5), and XRD pattern recorded for $\text{Zn}_2\text{Al-CMC}$ pyrolyzed at 1000 °C (Figure 8). When comparing EDS spectra of acicular particles (Figure S8) to those observed at 800 °C, it is observed an inversion in the intensity between Zn and Al peaks. Branched particles produce EDS spectra with higher aluminum and oxygen intensities compared to those collected from their vicinity, indicating they are composed by Al_2O_3 (higher Al and O content) as observed by XRD for $\text{Zn}_2\text{Al-CMC}$ pyrolyzed at 1000 °C (Figure 8). The superficial features of $\text{Mg}_2\text{Al-CMC}$ pyrolyzed at 800 °C are preserved when heated up to 1000 °C (Figure 9h). Also, no significant changes are detected in Mg/Al/O composition by EDS spectroscopy (data not shown) for samples obtained at both high temperature values.

Nanocomposites prepared in this study from a carbon precursor derived from biomass intercalated between LDH based on magnesium and aluminum in the 600–1000 °C range can be explored as adsorbent or catalyst. For example, composite constituted by MgO and biochar obtained by the electrochemical method, which was used for phosphate removal from water [46]. Nanocomposites obtained by $\text{Zn}_2\text{Al-CMC}$ pyrolysis in the 600–800 °C range produce incrustated ZnO particles in a matrix of graphitic carbon and spinel phase. Zinc oxide is a semiconductor with potential to be employed in devices for energy production such as dye-sensitized solar cells [47].

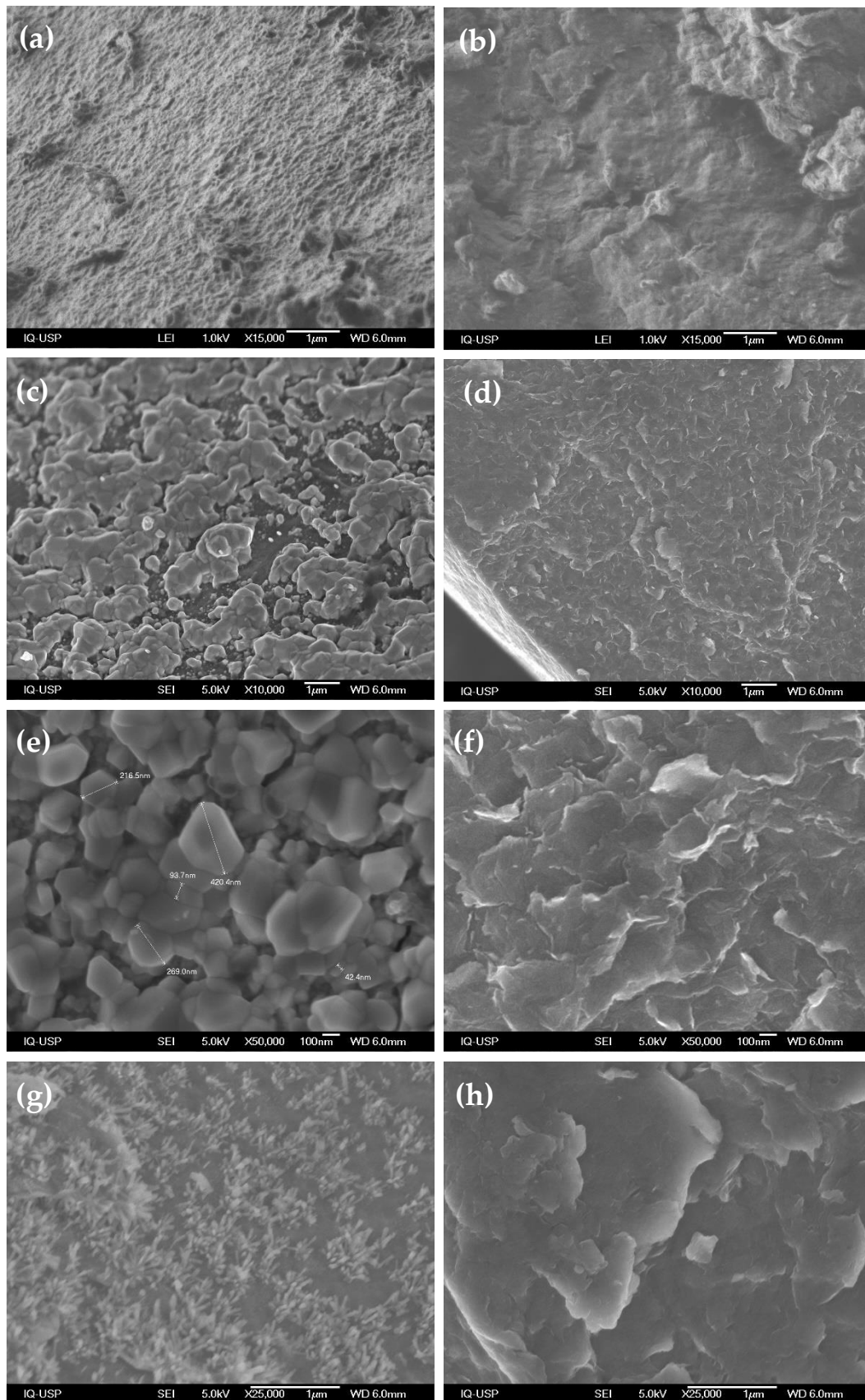


Figure 9. SEM micrographs of MMO/C samples obtained from Zn₂Al-CMC (left) and Mg₂Al-CMC (right) as synthesized (a, b) and pyrolyzed at 800 (c, d, e, f) and 1000 °C (g, h).

4. Conclusions

LDH materials intercalated with CMC polymer, a carbon source derived from biomass, were evaluated as a precursor for the preparation of MMO/C nanocomposites. Best experimental conditions were achieved to get carbon chains between the LDH layers to assure an organic-inorganic interaction at a nanoscale domain. Pyrolysis step conducted above 600 °C produced materials comprising graphitic carbon, which structural organization is increased at higher temperature values. In samples obtained from Mg₂Al-CMC, the biocarbon presence delays the crystallization of MgO when compared to Mg₂Al-CO₃ calcined at the same temperature, and also precludes the crystallization of MgAl₂O₄. On the other hand, biocarbon formed from Zn₂Al-CMC pyrolyzed at 800 °C promotes the generation of high crystalline ZnO particles if compared to Zn₂Al-CO₃ calcined at the same temperature, and also prevents crystallization of ZnAl₂O₄ phase. Above about 880 °C (endothermic peak in DSC curve), ZnO is reduced by graphitic carbon producing zinc vapour (carbothermic reaction); poor crystallized ZnAl₂O₄ spinel and γ -Al₂O₃ phases are noticed after pyrolysis at 1000 °C. Considering the results obtained in this study, to prepare nanocomposites constituted by graphitic carbonaceous material and metal oxides from CMC hybrid materials, the temperature range of pyrolysis process should be 600–800 °C for Zn₂Al-CMC and 600–1000 °C for Mg₂Al-CMC. Future studies should investigate the surface properties of these nanocomposites to explore application in adsorption processes, basic catalysis or photodevices.

Supplementary Materials: The following are available online at www.mdpi.com/xxx/s1, Figure S1: XRD pattern of sodium carboxymethylcellulose (NaCMC), Figure S2: TG-DSC and DTG-MS curves of sodium carboxymethylcellulose (NaCMC) under N₂ atmosphere, Figure S3: Raman spectra ($\lambda_{exc} = 532$ nm) of NaCMC and LDH-CMC samples, Figure S4: FTIR-ATR spectra of Zn₂Al-CO₃ and Mg₂Al-CO₃ samples calcined at 500, 600, 800 and 1000 °C under N₂ atmosphere, Figure S5: XRD patterns of M₂Al-CMC samples calcined at 1000 °C under synthetic air. Pictures of M₂Al-CMC samples calcined at 1000 °C under synthetic air or nitrogen atmosphere, indicating the percentage of residue after each heating process, Figure S6: SEM image of Mg₂Al-CO₃ sample, Figure S7: EDS spectra of Zn₂Al-CMC pyrolyzed at 800 °C, Figure S8: EDS spectra of Zn₂Al-CMC pyrolyzed at 1000 °C; Table S1: Interplanar distances d_{hkl} and 2θ (CuK α) values from X-ray diffraction data of LDH-CO₃ and LDH-CMC, Table S2: Vibrational data of Zn₂Al-CO₃ and Mg₂Al-CO₃, Table S3: Chemical analysis data and proposed formula for LDH-CO₃ and LDH-CMC, Table S4: Standard molar thermodynamic parameters of substances at 25 °C, Table S5: Standard molar thermodynamic values for the carbothermic reaction between graphitic carbon and zinc or magnesium oxides at 25 °C. Values are calculated using the data presented in Table S4.

Author Contributions: conceptualization, V.R.L.C., G.F.P. and V.R.M.; methodology, V.R.L.C., G.F.P. and V.R.M.; formal analysis, G.F.P., V.R.M. and A.D.; investigation, G.F.P. and V.R.M.; resources, V.R.L.C.; data curation, V.R.L.C.; writing—original draft preparation, V.R.L.C., G.F.P., V.R.M. and A.D.; writing—review and editing, V.R.L.C., G.F.P., V.R.M. and A.D.; visualization, V.R.L.C., G.F.P., V.R.M. and A.D.; supervision, V.R.L.C.; project administration, V.R.L.C.

Acknowledgments: This study was financed in part by the Coordenação de Aperfeiçoamento de Pessoal de Nível Superior—Brasil (CAPES)—Finance Code 33002010191P0—Química (scholarship to V.R.M.). V.R.L.C. is thankful to the Conselho Nacional de Desenvolvimento Científico e Tecnológico—Brasil for the research grant (CNPq 305446/2017-7). The authors are also grateful to the Fundação de Amparo à Pesquisa do Estado de São Paulo (FAPESP 2011/50318-1) for financial support and to the Laboratório de Espectroscopia Molecular (LEM-USP) for the Raman and FTIR spectra recording.

Conflicts of Interest: The authors declare no conflict of interest.

References

1. Mills, S.J.; Christy, A.G.; Génin, J.-M.R.; Kameda, T.; Colombo, F. Nomenclature of the hydrotalcite supergroup: Natural layered double hydroxides. *Miner. Mag.* **2012**, *76*, 1289–1336.
2. Cavani, F.; Trifirò, F.; Vaccari, A. Hydrotalcite-type anionic clays: Preparation, properties and applications. *Catal. Today* **1991**, *11*, 173–301.
3. Evans, D.G.; Slade, R.C.T. Structural Aspects of Layered Double Hydroxides. In *Structure & Bonding*; Springer: Berlin/Heidelberg, Germany, 2006; Volume 119; pp. 1–87, ISBN 3540282793.

4. Taviot-Guého, C.; Prévot, V.; Forano, C.; Renaudin, G.; Mousty, C.; Leroux, F. Tailoring Hybrid Layered Double Hydroxides for the Development of Innovative Applications. *Adv. Funct. Mater.* **2018**, *28*, 1703868.
5. Li, T.; Miras, H.; Song, Y.-F. Polyoxometalate (POM)-Layered Double Hydroxides (LDH) Composite Materials: Design and Catalytic Applications. *Catalysts* **2017**, *7*, 260.
6. Rives, V.; Angeles Ulbarri, M. Layered double hydroxides (LDH) intercalated with metal coordination compounds and oxometalates. *Coord. Chem. Rev.* **1999**, *181*, 61–120.
7. Leroux, F.; Taviot-Guého, C. Fine tuning between organic and inorganic host structure: New trends in layered double hydroxide hybrid assemblies. *J. Mater. Chem.* **2005**, *15*, 3628.
8. Rives, V.; del Arco, M.; Martín, C. Intercalation of drugs in layered double hydroxides and their controlled release: A review. *Appl. Clay Sci.* **2014**, *88–89*, 239–269.
9. Xu, M.; Wei, M. Layered Double Hydroxide-Based Catalysts: Recent Advances in Preparation, Structure, and Applications. *Adv. Funct. Mater.* **2018**, *28*, 1802943.
10. Zubair, M.; Daud, M.; McKay, G.; Shehzad, F.; Al-Harhi, M.A. Recent progress in layered double hydroxides (LDH)-containing hybrids as adsorbents for water remediation. *Appl. Clay Sci.* **2017**, *143*, 279–292.
11. Patel, R.; Park, J.T.; Patel, M.; Dash, J.K.; Gowd, E.B.; Karpoomath, R.; Mishra, A.; Kwak, J.; Kim, J.H. Transition-metal-based layered double hydroxides tailored for energy conversion and storage. *J. Mater. Chem. A* **2018**, *6*, 12–29.
12. Chimene, D.; Alge, D.L.; Gaharwar, A.K. Two-Dimensional Nanomaterials for Biomedical Applications: Emerging Trends and Future Prospects. *Adv. Mater.* **2015**, *27*, 7261–7284.
13. Erastova, V.; Degiacomi, M.T.G.; Fraser, D.; Greenwell, H.C. Mineral surface chemistry control for origin of prebiotic peptides. *Nat. Commun.* **2017**, *8*, 2033.
14. Debecker, D.P.; Gaigneaux, E.M.; Busca, G. Exploring, tuning, and exploiting the basicity of hydrotalcites for applications in heterogeneous catalysis. *Chem. A Eur. J.* **2009**, *15*, 3920–3935.
15. Yang, Z.; Wang, F.; Zhang, C.; Zeng, G.; Tan, X.; Yu, Z.; Zhong, Y.; Wang, H.; Cui, F. Utilization of LDH-based materials as potential adsorbents and photocatalysts for the decontamination of dyes wastewater: A review. *RSC Adv.* **2016**, *6*, 79415–79436.
16. Takehira, K. Recent development of layered double hydroxide-derived catalysts – Rehydration, reconstitution, and supporting, aiming at commercial application. *Appl. Clay Sci.* **2017**, *136*, 112–141.
17. Zhao, M.Q.; Zhang, Q.; Huang, J.Q.; Wei, F. Hierarchical nanocomposites derived from nanocarbons and layered double hydroxides—Properties, synthesis, and applications. *Adv. Funct. Mater.* **2012**, *22*, 675–694.
18. Kukrety, A.; Singh, R.K.; Singh, P.; Ray, S.S. Comprehension on the Synthesis of Carboxymethylcellulose (CMC) Utilizing Various Cellulose Rich Waste Biomass Resources. *Waste Biomass Valorization* **2018**, *9*, 1587–1595.
19. Kang, H.; Huang, G.; Ma, S.; Bai, Y.; Ma, H.; Li, Y.; Yang, X. Coassembly of Inorganic Macromolecule of Exfoliated LDH Nanosheets with Cellulose. *J. Phys. Chem. C* **2009**, *113*, 9157–9163.
20. Yadollahi, M.; Namazi, H. Synthesis and characterization of carboxymethyl cellulose/layered double hydroxide nanocomposites. *J. Nanopar. Res.* **2013**, *15*, 1563.
21. Yadollahi, M.; Namazi, H.; Aghazadeh, M. Antibacterial carboxymethyl cellulose/Ag nanocomposite hydrogels cross-linked with layered double hydroxides. *Int. J. Biol. Macromol.* **2015**, *79*, 269–277.
22. Rocha, M.A.; Petersen, P.A.D.; Teixeira-Neto, E.; Petrilli, H.M.; Leroux, F.; Taviot-Gueho, C.; Constantino, V.R.L. Layered double hydroxide and sulindac coiled and scrolled nanoassemblies for storage and drug release. *RSC Adv.* **2016**, *6*, 16419–16436.
23. Zhao, X.; Zhang, F.; Xu, S.; Evans, D.G.; Duan, X. From layered double hydroxides to ZnO-based mixed metal oxides by thermal decomposition: Transformation mechanism and UV-blocking properties of the product. *Chem. Mater.* **2010**, *22*, 3933–3942.
24. Hobbs, C.; Jaskaniec, S.; McCarthy, E.K.; Downing, C.; Opelt, K.; Güth, K.; Shmeliov, A.; Mourad, M.C.D.; Mandel, K.; Nicolosi, V. Structural transformation of layered double hydroxides: An in situ TEM analysis. *NPJ 2D Mater. Appl.* **2018**, *2*, 4.
25. Miyata, S. Physico-Chemical Properties of Synthetic Hydrotalcites in Relation to Composition. *Clays Clay Miner.* **1980**, *28*, 50–56.
26. Elmoubarki, R.; Mahjoubi, F.Z.; Elhalil, A.; Tounsadi, H.; Abdennouri, M.; Sadiq, M.; Qourzal, S.; Zouhri, A.; Barka, N. Ni/Fe and Mg/Fe layered double hydroxides and their calcined derivatives: Preparation, characterization and application on textile dyes removal. *J. Mater. Res. Technol.* **2017**, *6*, 271–283.

27. Shang, J.; Shao, Z.; Chen, X. Electrical Behavior of a Natural Polyelectrolyte Hydrogel: Chitosan/Carboxymethylcellulose Hydrogel. *Biomacromolecules* **2008**, *9*, 1208–1213.
28. Lee, C.M.; Mohamed, N.M.A.; Watts, H.D.; Kubicki, J.D.; Kim, S.H. Sum-frequency-generation vibration spectroscopy and density functional theory calculations with dispersion corrections (DFT-D2) for cellulose Ia and Ib. *J. Phys. Chem. B* **2013**, *117*, 6681–6692.
29. Maréchal, Y.; Chanzy, H. The hydrogen bond network in I(β) cellulose as observed by infrared spectrometry. *J. Mol. Struct.* **2000**, *523*, 183–196.
30. Wiley, J.H.; Atalla, R.H. Band assignments in the raman spectra of celluloses. *Carbohydr. Res.* **1987**, *160*, 113–129.
31. Cuba-Chiem, L.T.; Huynh, L.; Ralston, J.; Beattie, D.A. Beattie In Situ Particle Film ATR FTIR Spectroscopy of Carboxymethyl Cellulose Adsorption on Talc: Binding Mechanism, pH Effects, and Adsorption Kinetics. *Langmuir* **2008**, *24*, 8036–8044.
32. Schenzel, K.; Fischer, S. NIR FT Raman spectroscopy – A rapid analytical tool for detecting the transformation of cellulose polymorphs. *Cellulose* **2001**, *8*, 49–57.
33. Barsberg, S. Prediction of vibrational spectra of polysaccharides-simulated IR spectrum of cellulose based on density functional theory (DFT). *J. Phys. Chem. B* **2010**, *114*, 11703–11708.
34. Blackwell, J.; Vasko, P.D.; Koenig, J.L. Infrared and raman spectra of the cellulose from the cell wall of valonia ventricosa. *J. Appl. Phys.* **1970**, *41*, 4375–4379.
35. Basta, A.H.; El-Saied, H. Characterization of polymer complexes by thermal and ir spectral analyses. *Polym. Plast. Technol. Eng.* **2000**, *39*, 887–904.
36. El-Sayed, S.; Mahmoud, K.H.; Fatah, A.A.; Hassen, A. DSC, TGA and dielectric properties of carboxymethyl cellulose/polyvinyl alcohol blends. *Phys. B Condens. Matter* **2011**, *406*, 4068–4076.
37. Constantino, V.R.L.; Pinnavaia, T.J. Basic Properties of Mg^{2+1-x}Al^{3+x} Layered Double Hydroxides Intercalated by Carbonate, Hydroxide, Chloride, and Sulfate Anions. *Inorg. Chem.* **1995**, *34*, 883–892.
38. Bellotto Maurizio; Bernadette, R.; Olivier, C.; John, L.; Dominique, B.; Elkaim, E. Hydrotalcite Decomposition Mechanism: A Clue to the Structure and Reactivity of Spinel-like Mixed Oxides. *J. Phys. Chem.* **1996**, *100*, 8535–8542.
39. Warringham, R.; Mitchell, S.; Murty, R.; Schäublin, R.; Crivelli, P.; Kevin, J.; Pérez-Ramírez, J. Mapping the Birth and Evolution of Pores upon Thermal Activation of Layered Hydroxides. *Chem. Mater.* **2017**, *29*, 4052–4062.
40. Dresselhaus, M.S.; Jorio, A.; Hofmann, M.; Dresselhaus, G.; Saito, R. Perspectives on carbon nanotubes and graphene Raman spectroscopy. *Nano Lett.* **2010**, *10*, 751–758.
41. Ferrari, A.C.; Basko, D.M. Raman spectroscopy as a versatile tool for studying the properties of graphene. *Nat. Nanotechnol.* **2013**, *8*, 235–246.
42. Ferrari, A.C.; Robertson, J. Raman spectroscopy of amorphous, nanostructured, diamond-like carbon, and nanodiamond. *Philos. Trans. R. Soc. Lond. Ser. A Math. Phys. Eng. Sci.* **2004**, *362*, 2477–2512.
43. Kim, P.; Johnson, A.; Edmunds, C.W.; Radosevich, M.; Vogt, F.; Rials, T.G.; Labbé, N. Surface functionality and carbon structures in lignocellulosic-derived biochars produced by fast pyrolysis. *Energy Fuels* **2011**, *25*, 4693–4703.
44. Graf, G.G. Zinc. In *Ullmann's Encyclopedia of Industrial Chemistry*; Wiley-VCH Verlag GmbH & Co. KGaA: Weinheim, Germany, 2000; pp. 717–739.
45. Mardones, J.P. Processing of Spinel-Bearing Compounds for Zinc Extraction. Master' Thesis, Delft University of Technology, Faculty of Civil Engineering and Geosciences, Delft, The Netherlands, 2012.
46. Jung, K.-W.; Ahn, K.-H. Fabrication of porosity-enhanced MgO/biochar for removal of phosphate from aqueous solution: Application of a novel combined electrochemical modification method. *Bioresour. Technol.* **2016**, *200*, 1029–1032.
47. Vittal, R.; Ho, K.-C. Zinc oxide based dye-sensitized solar cells: A review. *Renew. Sustain. Energy Rev.* **2017**, *70*, 920–935.



© 2019 by the authors. Submitted for possible open access publication under the terms and conditions of the Creative Commons Attribution (CC BY) license (<http://creativecommons.org/licenses/by/4.0/>).

V.R. Magri, M.A. Rocha, C.S. de Matos, P.A.D. Petersen, F. Leroux, H.M. Petrilli, V.R.L. Constantino, Folic acid and sodium folate salts: Thermal behavior and spectroscopic (IR, Raman, and solid-state ^{13}C NMR) characterization, **Spectrochim. Acta Part A Mol. Biomol. Spectrosc.** 273 (2022) 120981. <https://doi.org/10.1016/j.saa.2022.120981>



Folic acid and sodium folate salts: Thermal behavior and spectroscopic (IR, Raman, and solid-state ^{13}C NMR) characterization

Author:
Vagner R. Magri, Michele A. Rocha, Caroline S. de Matos, Philippe A.D. Petersen, Fabrice Leroux, Helena M. Petrilli, Vera R.L. Constantino

Publication: Spectrochimica Acta Part A: Molecular and Biomolecular Spectroscopy

Publisher: Elsevier

Date: 15 May 2022

© 2022 Elsevier B.V. All rights reserved.

Journal Author Rights

Please note that, as the author of this Elsevier article, you retain the right to include it in a thesis or dissertation, provided it is not published commercially. Permission is not required, but please ensure that you reference the journal as the original source. For more information on this and on your other retained rights, please visit: <https://www.elsevier.com/about/our-business/policies/copyright#Author-rights>

BACK

CLOSE WINDOW

Folic Acid and Sodium Folate Salts: Thermal Behavior and Spectroscopic (IR, Raman, and Solid-state ^{13}C -NMR) Characterization

Vagner R. Magri,^a Michele A. Rocha,^a Caroline S. de Matos,^a Philippe A. D. Petersen,^b Fabrice Leroux,^{c,d} Helena M. Petrilli^b and Vera R. L. Constantino^{a*}

^aDepartamento de Química Fundamental, Instituto de Química, Universidade de São Paulo, Av. Prof. Lineu Prestes 748, CEP 05508-000, São Paulo, SP, Brazil

^bDepartamento de Física de Materiais e Mecânica, Instituto de Física, Universidade de São Paulo, Rua do Matão 1371, CEP 05508-090, São Paulo, SP, Brazil

^cUniversité Clermont Auvergne, Institut de Chimie de Clermont-Ferrand, BP 10448, F-63000 Clermont-Ferrand, France

^dCNRS, UMR 6296, ICCF, F-63178 Aubiere, France.

* Corresponding author.

E-mail address: yrlconst@iq.usp.br (V.R.L. Constantino)

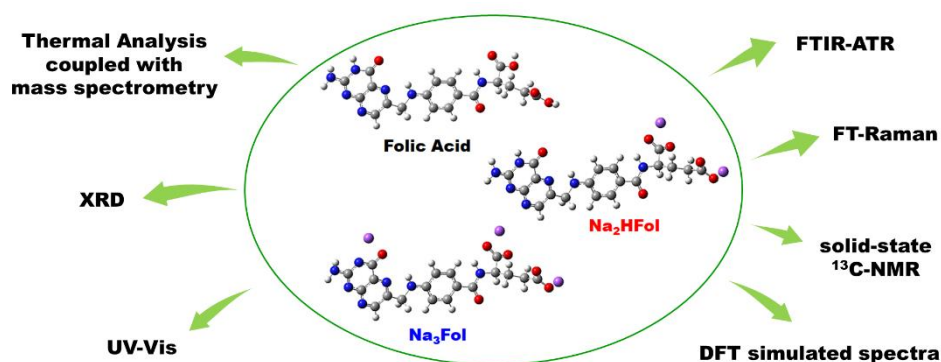
KEYWORDS

Folic Acid, Sodium Folate Salts, Pteroyl-L-glutamic acid, vitamin B9, DFT

HIGHLIGHTS

- The main spectroscopic signatures of Folic acid, Na₂Folate (dianionic) and Na₃Folate (trianionic) compounds were highlighted, as well as the influence of the protonation level in their physicochemical properties.
- Spectroscopic data interpretation was supported by theoretical calculations.
- The compounds were also characterized by UV-VIS diffuse-reflectance spectroscopy, thermal analysis (TG/DTG-DSC-MS), and X-ray diffractometry.

GRAPHICAL ABSTRACT



ABSTRACT

Folic acid (FA; vitamin B9) and its associated sodium salts, strongly relevant for many scientific and technological applications - from nutrition to pharmacology and nanomedicine, suffer from a lack of characterization combining experimental and theoretical. In this work, a spectroscopic investigation of FA and its synthesized sodium salts in the form of dianion (Na_2HFol) or trianion (Na_3Fol) was scrutinized in their solid state. The spectroscopic (infrared, Raman, and solid state ^{13}C -nuclear magnetic resonance) data interpretation was supported by theoretical calculations using the Density Functional Theory (DFT). Additionally, the compounds were characterized by UV-VIS diffuse-reflectance spectroscopy, combined thermal analyses (TG/DTG-DSC) coupled to mass spectrometry, and X-ray diffractometry. The main signatures of each species were identified, as well as the influence of the protonation level on their physicochemical properties. These distinct properties of the three compounds are mainly based on signals assigned to glutamic acid (glutamate) and pterin (neutral and anionic) moieties. This work should help develop new products based on FA or its anionic forms, such as theragnostic/drug delivery systems, supramolecular structures, nanocarbons, or metal complexes.

1. Introduction

Scientific, clinical, and public health interests concerning folic acid (FA; Pteroyl-L-glutamic acid) have long been established. The importance of FA and its anionic species in food engineering, pharmacology, nanotechnology, and nanomedicine, among other fields is undeniable. The global market of FA production has been estimated at around half a billion dollars per year, with an increasing prospect [1]. The list of uses for FA is extensive, mostly because its chemical composition and molecular structure. As illustrated in **Figure 1a**, the FA molecule is constituted by three distinct moieties: pterin (PT), *p*-aminobenzoic acid (*p*-ABA) and L-glutamic acid (Glu).

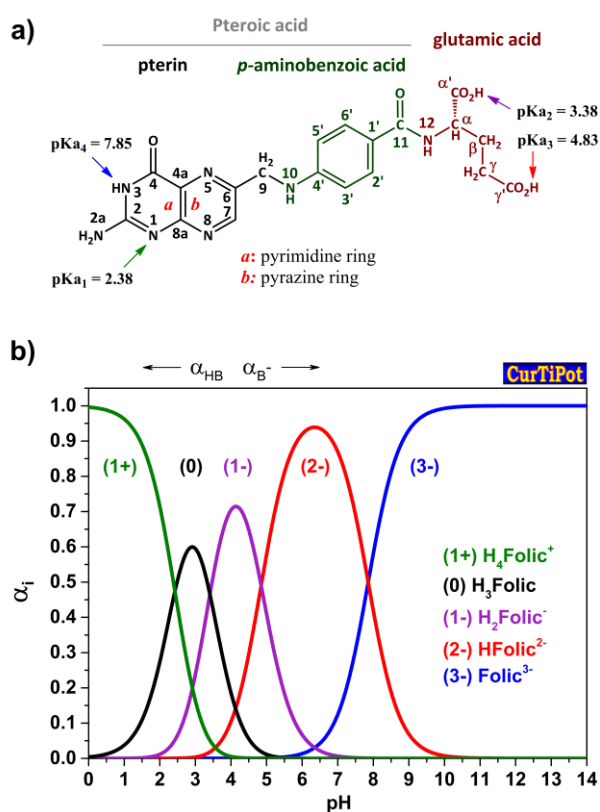


Figure 1. a) Molecular structure of FA and its apparent dissociation constants (pK_a 's values), as determined by Szakács and Noszál [2]; b) Chemical speciation of FA in the range of pH values from 0 to 14, obtained by CurTiPot software.

FA is the basic structural synthetic analogue and the most oxidized form of the essential micronutrients group commonly termed as folates and vitamin B₉ [3,4]. Folates act as enzymatic cofactors in a set of cellular biochemical reactions denominated as one-carbon (1C) metabolism

[5,6], and are necessary for the proliferation of cells, genic expression control and in the maintenance of the cellular redox balance [5,6]. Furthermore, FA presents antioxidant properties [7,8] and prevents inflammation, which can lead to endothelial dysfunction [8] and cognitive impairment/dementia [9]. FA consumption is encouraged in several countries to fight against malnutrition and strengthen the little ones, especially birth defects as FA-sensitive neural tube defects [10,11]. FA is taken orally using diverse drugs formulations [12], as well as some products containing FA and iron(II) complexes recommended as antianemia drugs by the United Nations Children's Fund (UNICEF), in line with the World Health Organization (WHO) [13].

The sustained release of FA is also reported in innovative formulations in cosmetics [7,14]. In nanomedicine field, studies focused on harnessing the power of FA as a targeting agent for imaging and/or therapy (theragnosis) of cancer and inflammatory diseases [15–18]. The nanoengineering of smart delivery systems includes plenty of organic and inorganic nanoparticles as well as FA-drug conjugates [16–18]. In addition, FA forms complexes with a series of metal cations by coordination with its Glu or PT moieties [19–24]. Such complexes can be used as antimicrobial agent [19,23], anticancer-drug [24] or in the treatment of diabetes [22]. In nanomaterial and nanotechnology science, FA has been used as precursor of supramolecular structures (liquid crystals and gels) [25–27] and nitrogen doped carbonaceous materials [27,28]. The development of photoelectric devices containing FA is envisaged because of its electronic properties [29].

Spectroscopic analyses combined with theoretical calculations using the Density Functional Theory (DFT) are powerful tools to characterize organic compounds and nanomaterials. Despite their very wide applicability, only a limited number of studies on FA following this approach are reported in the literature. Studies use crystalline FA as the standard, performing experimental infrared (IR) and/or Raman spectroscopies, and interpret the results

by combining with theoretical DFT calculations. Most works focus on the FA analysis by Surface-enhanced Raman scattering (SERS) spectroscopy because its promising use in analyses of biological samples. In general, the studies investigate the influence of the temperature and substrate (gold or silver) on the SERS spectral profile of FA [30] as well as the adsorption mechanism of FA onto different substrates [31–33]. Furthermore, the photodegradation (under UV) [34] and the hydrothermal decomposition [35] of FA is inspected by a spectroscopic approach combining experimental and theoretical data.

The solubility of neutral FA is low ($0.1069 \text{ mmol kg}^{-1}$ at $25 \text{ }^\circ\text{C}$, 1 bar and $\text{pH} = 4.28$) [36] and pH-dependent in water. It is significantly increased in pH values above 5 [37], for which the dianion (HFol^{2-}) and trianion (Fol^{3-}) are then dominant species [2] (**Figure 1b**). Therefore, folate anionic species which studies are often neglected must nevertheless be considered because of: (i) at physiological pH value for which HFol^{2-} is predominant [38–40]; (ii) the preparation of many materials and compounds (or the handle of FA in some studies) are performed at pH values above 5 [7,14,22–24,31–34]; and (iii) the supramolecules assembled by FA are pH-responsiveness [25–27]. Braga et al. [41] prepared dianionic folates salts (Li, Na and Ca) and showed their higher dissolution rate as well as higher thermal stability than FA. However, the experimental and theoretical spectroscopic analyses of folate salt are not accomplished yet. Gocheva et al. [38] studied the tautomerism of dianion folate (HFol^{2-}) in water by ^1H - and ^{13}C -NMR and interpreted the results based on DFT calculations with the Polarizable Continuum Model (PCM). Experimental and calculated IR spectra of palladium and platinum folate complexes were reported by He et al. [24], but the theoretical (DFT) values and the correlated attribution were not presented.

The knowledge of physical-chemical features of FA and its salts in the solid state by usual laboratory techniques is essential and useful because contribute to the development of new products, combined to a more assertive characterization of their properties. Our group has

performed the thermal and spectroscopic characterizations of bioactive molecules and their respective sodium salts [42–44]. In this study, the spectroscopy profile (IR, Raman, and solid state ^{13}C -NMR) of solid FA (commercial) is compared to its synthesized sodium salts used as a model of dianion (Na_2HFol) and trianion (Na_3Fol) forms of FA. The main signatures of each species are tracked as well as the influence of the protonation level in their physicochemical properties. The spectroscopic analyses are supported by theoretical calculations using DFT. The samples are also characterized by UV-VIS diffuse-reflectance spectroscopy, thermal analysis (TG/DTG-DSC-MS), and X-ray diffractometry. To the best of our knowledge, this is the first study comparing consistently the physical-chemical features of FA and its sodium salts in their solid-state. In addition, this work gives us the opportunity to compare data already published on FA.

2. Materials and Methods

2.1. Preparation of folate sodium salts

FA ($C_{19}H_{19}N_7O_6$, $\geq 97\%$), from Sigma-Aldrich, and standard aqueous sodium hydroxide $0.1 \text{ mol}\cdot\text{L}^{-1}$ solution, from Merck, were used as received. Na_2HFol and Na_3Fol samples were prepared by the stoichiometric reaction between 0.7 g of FA and the standard $0.1 \text{ mol}\cdot\text{L}^{-1}$ NaOH aqueous solution and further isolated by lyophilization process using Thermo Savant ModulyoD equipment (200 mPa and $-50 \text{ }^\circ\text{C}$).

2.2. Physical Measurements

X-ray diffraction (XRD) patterns of powdered samples were recorded on a Bruker diffractometer model D8 DISCOVER, equipped with Nickel-filtered $\text{CuK}\alpha$ radiation (0.15418 nm), operating at 40 kV and 30 mA, sample rotating at 30 rpm, and collected in the (2θ) 4–50 $^\circ$ range, with steps of $0.05 \text{ }^\circ/2\theta$ and scan speed of $0.05 \text{ }^\circ/3 \text{ s}$.

Diffuse reflectance spectra (Kubelka-Munk) of solid samples in the UV-VIS region were recorded in a Shimadzu model UV-2401PC spectrophotometer, equipped with an integration sphere. BaSO_4 (Waco Pure Chem.) was used to dilute the samples. FA titration was carried out in aqueous media ($0.024 \text{ mmol}\cdot\text{L}^{-1}$) using NaOH aqueous solution ($0.10 \text{ mol}\cdot\text{L}^{-1}$) and the UV-VIS electronic spectra of the resulting solutions were registered in a Shimadzu UV-1650PC spectrophotometer.

Thermal Analysis (TG/DTG-DSC-MS) were conducted on a Netzsch thermoanalyzer, model TGA/DSC 490 PC Luxx, coupled to Aeolos[®] 403 C Quadro mass spectrometer, from room temperature to $1000 \text{ }^\circ\text{C}$, under compressed air flow ($50 \text{ mL}\cdot\text{min}^{-1}$), using a heating rate of $10 \text{ }^\circ\text{C}\cdot\text{min}^{-1}$ and an alumina crucible. Differential Scanning Calorimetry (DSC) data under N_2 flow ($50 \text{ mL}\cdot\text{min}^{-1}$) were obtained from room temperature to $380 \text{ }^\circ\text{C}$, using a heating rate of

10 °C·min⁻¹. The sample modifications that occur during *heating* were also evaluated in a melting point apparatus from Microquimica, model MQAPF – 302, operating at a heating rate of 10 °C·min⁻¹; the powdered sample was sandwiched between cover glasses and placed on the heating block. During the analysis, the sample was illuminated by a lamp, and transformations could be visualized by magnifying lens.

The Fourier transform infrared (FTIR) spectra were recorded in a Bruker Alpha spectrophotometer (DTGS detector and KBr optics), using a single bounce Attenuated Total Reflectance (ATR) accessory equipped with a diamond crystal in the 4000–400 cm⁻¹ range with a spectral resolution of 4 cm⁻¹ and 512 scans. Data were collected on the absorbance mode and manually converted to transmittance. Raman spectra were recorded in a Bruker FT-Raman instrument, model MultiRam, equipped with Ge detector (cooled by liquid nitrogen) and Nd³⁺/YAG laser (1064 nm exciting radiation), in the range of 3500-100 cm⁻¹ with 4 cm⁻¹ of spectral resolution and 1024 scans, using 150 mW power on the samples.

¹³C (I = 1/2) solid state nuclear magnetic resonance (NMR) analysis was performed on Bruker Advance 300 MHz using magic angle spinning (MAS) at 10 kHz and a 4 mm diameter size zirconia rotor. ¹³C spectra were obtained by ¹H enhanced cross-polarization method (CP, contact time of 1 ms, recycling time of 5 s). Calibration was made using the carbonyl group of glycine as reference (176.03 ppm), and 2,000 to 10,000 scans were needed to obtain a proper signal for samples.

2.3. Theoretical Methods

Calculations in the Kohn-Sham (KS) scheme of the Density Functional Theory (DFT) were performed to obtain geometry optimizations, vibrational (IR and Raman) and NMR chemical shifts for FA and sodium folates (Na₂HFol and Na₃Fol). All geometries presented in this paper were obtained in a gas phase environment simulation, and the B3LYP hybrid

functional with the 6-311++G(d,p) Gaussian basis sets were employed [45,46]. The Gaussian09 software package was used for geometry optimizations, vibrational spectra acquisition, and NMR calculations [47]. Structural optimizations were performed considering the X-ray diffraction data of FA single crystal as a reference [48]. The theoretical infrared and Raman spectra (wavenumbers and intensities/activities) were acquired at the same level of theory as the geometry optimizations. The spectra were shown with a resolution of 1 cm^{-1} and applying a 0.975 scaling factor from 4000 to 1000 cm^{-1} to correct the anharmonicity effects on the vibrational spectra [49].

3. Results and Discussion

The neutral PT moiety exists in different tautomeric forms, while the anion form has different mesomers [38,50], as reviewed in Appendix A–Supplementary Material (SM). The neutral PT (as in FA and HFol^{2-} ion) exhibits a keto-enol (lactam-lactim) equilibrium between C4=O and N3-H groups (see **Figure A.1** in SM), and the keto form has two tautomers, comprising the hydrogen atom bonded to N3 or N1 atoms. Anionic PT (as in Folate³⁻) presents mesomer resonance structures as amidate (N3-C4=O) and enolate (N3=C4-O^-), as also shown in **Figure A.1**. In this work, the 3-lactam tautomer (**Figure 1a**) for FA and Na_2HFol samples, as well as the enolate mesomer form for Na_3Fol sample, were considered the main forms of PT based on stability data reviewed in **Section 1** of SM.

3.1. X-ray diffractometry and UV–VIS spectroscopy

The XRD patterns of powdered compounds are presented in **Figure 2**. Commercial FA presents XRD profile typical of a crystalline compound with some intense diffraction peaks observed at 2θ values of 5.51° , 10.97° and 13.18° . From Vesta software [51] and using the CIF from Ref. [52] (CCDC N 1489544), such peaks are assigned to the diffraction plans (002), (004) and (013), respectively. These results are in agreement with those reported for the dihydrate FA (primitive orthorhombic unit cell and space group $P2_12_12_1$) [41,48,52]. Kaduk, Crowder and Zhong [52] re-determined the structure of dihydrate FA using synchrotron X-ray diffraction analysis, Rietveld refinement techniques and DFT calculations. In the crystal (**Figure A.2**), the Glu chain exists in a bent conformation, while *p*-ABA and PT moieties are slightly tilted relative to each other. The molecules in the crystal are networking by intermolecular H-bonds, and the pyrimidine and benzene rings of adjacent molecules are stacked at around 0.34 nm (**Figure A.2**).

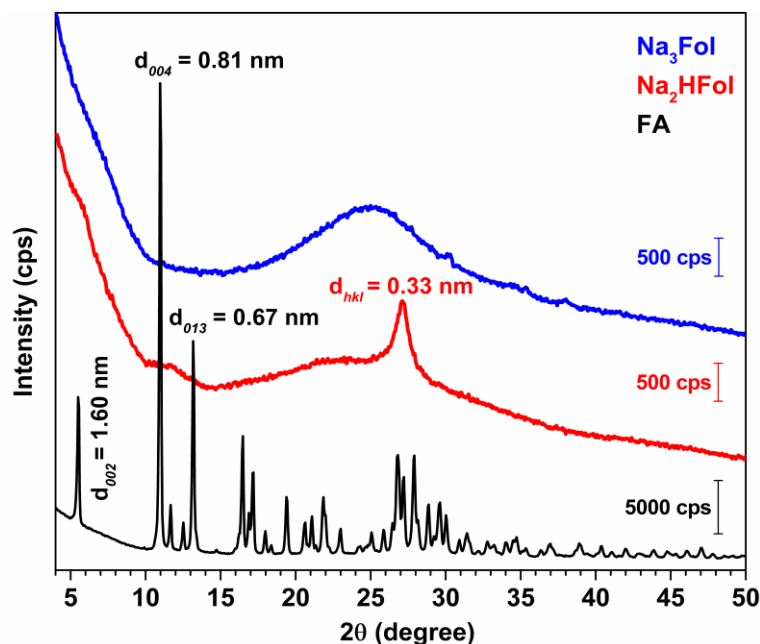


Figure 2. XRD patterns of dihydrate FA (commercial sample), and the Na₂HFol and Na₃Fol salts prepared in this work.

The XRD patterns of the powdered salts are characteristic of non-crystalline materials (**Figure 2**), possibly due to the isolation method used (see **Section 2.1**). Na₂HFol exhibits a diffraction peak at $2\theta = 27.10^\circ$ (*ca.* 0.33 nm) attributed to the distance among two disk-like structures π -stacked in a columnar array, formed by the self-assembly of HFol²⁻ anions in water [25,27,53], as discussed in **Section 3** of **SM**. Hence, the only coherence length detected by XRD is the ordered structure arising from the periodicity of π - π intermolecular stacking [53]. On the other hand, the XRD pattern of Na₃Folate presents only a broad peak centered around 2θ of 25° , indicating that the deprotonation of N(3)-H group precludes the formation of the disk-like tetramer arrays and their stacking, probably because of the repulsive forces between negatively-charged PT units.

Samples present distinct colors (not shown): while powdered commercial FA is yellow-orange, Na₂HFol is orange and Na₃Fol is yellow. The intermolecular interactions as H-bonds and π - π stacking modify the electronic and vibrational spectra of the molecular and anionic organic aggregates in comparison with their respective monomeric species [54,55]. The UV-VIS diffuse reflectance spectra of both FA and sodium salts were recorded to complement the XRD analysis. The electronic absorption spectra in the solid state (aggregated form) are compared with the spectra of compounds in aqueous solution (monomeric form), as displayed in **Figure 3**.

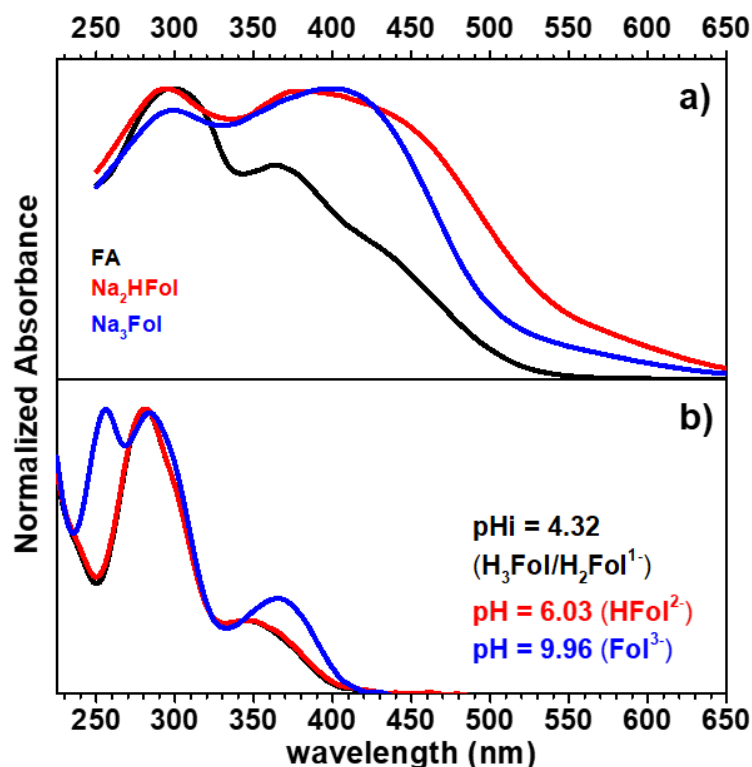


Figure 3. a) UV–VIS diffuse reflectance spectra of FA, Na₂HFol and Na₃Fol samples compared with b) electronic spectra of FA titrated in water; pHi is the initial pH value after FA dissolution in water.

Data on the electronic UV-VIS spectra of FA in solution are revisited and a discussion is reported in **Section 4** of **SM**. According to **Figure A.4**, only Fol³⁻ species can be distinguished in the solution. However, a solution-to-solid spectral shift is clearly observed, and the powdered samples present distinguishable electronic spectra, which could indicate the presence of different species and/or aggregated states.

UV-VIS electronic spectrum of commercial FA in solid state exhibits bands centered at 296 nm and 365 nm (**Figure 3**). The position of the higher-energy band is not affected by the deprotonation degree of the species as it is also observed for Na₂HFol and Na₃Fol. Considering that the band around 280 nm in water solution is attributed to the π – π^* transition of PT and *p*-ABA moieties in FA and Na₂HFol, and to the π – π^* transition of *p*-ABA [34,56] in Na₃Fol sample, the same assignment seems plausible for the solid state samples. The band at about 365

nm is tentatively correlated to the band at 346 nm present in the spectra recorded in the solution, which is attributed to the $\pi-\pi^*/n-\pi^*$ of PT ring [34,56]. The spectrum of FA in solid state presents additionally a shoulder in the 430 nm region that can be attributed to an intermolecular charge-transfer (CT) transition from the benzene to the pyrazine rings of aggregated molecules [29,57] because of their proximity in the crystal (**Figure A.2**).

The electronic spectrum of powdered Na_2HFol presents a very broad band in the region of 350-420 nm with an intense shoulder around 450-550 nm, which is not observed in water solution, as noticed to FA in solid state (**Figure 3**). As discussed previously, Na_2HFol assembles in a supramolecular structure, in which H-bonded folate tetramers are tightly packed in a π -stacking array (**Figure A.3**). Consequently, the spectral profile of the dianion salt in the 400-550 nm region could be attributed mainly to an CT transition favored by some intermolecular interactions, based on the study of a concentrated solution of FA [57] and nanoparticles of pyrazoline derivate [58]. On the other hand, Na_3Fol shows a distinct spectral profile, in which a broadband arising in the 400 nm region is more intense than the one at 296 nm. The hyperchromic shift should be attributed to the deprotonation of the PT ring, which changes the energy of $\pi-\pi^*/n-\pi^*$ transitions, as observed for Fol^{3-} in an aqueous solution. Besides, a tail extended up to about 500 nm is observed in the solid state Na_3Fol spectrum, also suggesting a charge transfer transition, but less intense than for Na_2HFol .

The UV-VIS diffuse reflectance results are in agreement with the XRD data interpretation regarding the structural arrangement of FA and folate species in the samples and their aggregation degree; these techniques can be used to differentiate disodium and trisodium folate compounds.

3.2. Thermal Analysis (TG/DTG-DSC) coupled to mass spectrometry (MS)

The DSC curves in N₂ atmosphere and the data from melting point analysis (**Figure A.5**) of FA, Na₂HFol and Na₃Fol pointed out that the samples decompose at about 210 °C, 280°C and 300°C, respectively, as discussed in **Section 5** in **SM**.

The results of thermal analysis in air atmosphere are displayed in **Figure 4**, summarized in **Table 1**, and detailed reported in **Table A.1** of the **SM**. The first thermal event for all samples is attributed to the dehydration step (endothermic processes), as indicated by the release of the fragment $m/z = 18$ (H₂O). Considering the beginning of the release of fragment attributed to CO₂ ($m/z = 44$ in MS curve; **Figure 4b**), the thermal stability of FA is significantly increased in salt forms: from 198 °C (FA) to 267 °C (Na₂HFol) and to 300 °C (Na₃Fol), in line with reported data for some folate metal complexes [19,21] and alkaline salts [41]. The decomposition temperature values of FA and its salts are practically the same in inert (N₂; **Section 5** of the **SM**) or oxidant (**Figure 4**) atmospheres, which indicates a process driven by thermolysis [59].

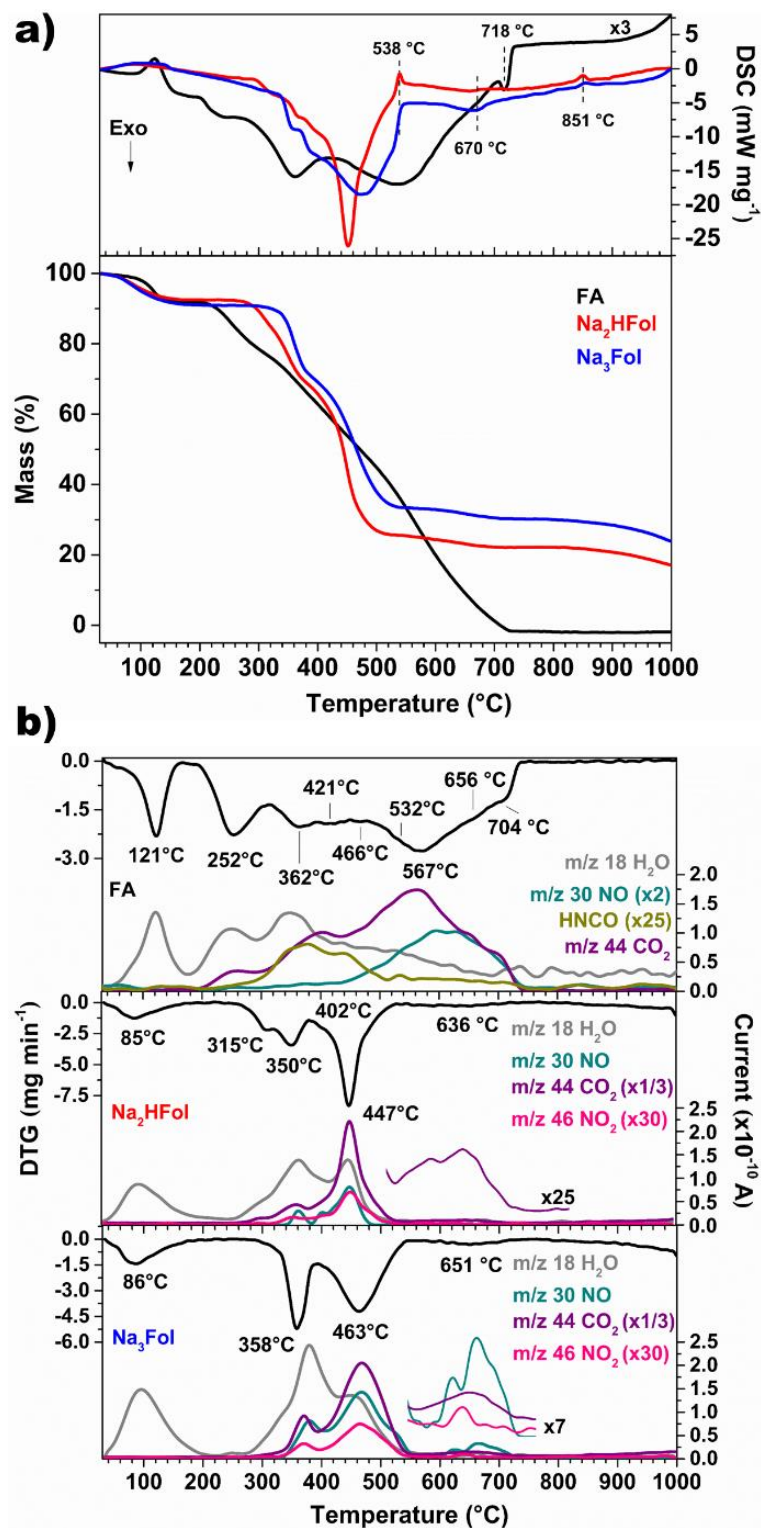


Figure 4. a) TG-DSC and b) DTG-MS curves of commercial FA, and synthesized Na₂HFol and Na₃Fol samples under air atmosphere.

Table 1Thermal analysis data of FA, Na₂HFol and Na₃Fol samples under air atmosphere.

Sample	H ₂ O (%) ^a	Organic matter (%)	Proposed Formula ^b
FA	7.9 (7.5)	93.8 (92.5)	C ₁₉ H ₁₉ N ₇ O ₆ ·2.0H ₂ O
Na ₂ HFol	7.6 (8.5)	81.5 (82.7)	Na ₂ C ₁₉ H ₁₇ N ₇ O ₆ ·2.5H ₂ O
Na ₃ Fol	9.0 (9.6)	76.7 (78.0)	Na ₃ C ₁₉ H ₁₆ N ₇ O ₆ ·3.0H ₂ O

^ahydration water; ^bfrom thermal analysis results; Values in parenthesis are the expected percentage considering the proposed formulas.

As previously recorded by Vora et al. [60], crystalline FA presents a complex thermal decomposition mechanism in N₂ atmosphere. Indeed, it was also observed in air atmosphere, as displayed in **Figure 4**, **Table A.1** and in **SM**. After dehydration, the TG curve of FA presents a slow weight loss profile. The oxidative decomposition of FA takes place in five consecutive events of mass loss, divided at least in nine overlapped steps (TG-DTG; **Table A.1**). The two overlapped events in 190-391 °C range may be mainly attributed to the Glu moiety decomposition (calc. 27.7%; exp. 27.5%). The former event is accompanied by the release of H₂O and CO₂ (190-391 °C), and by the release of a fragment with $m/z = 43$, assigned to HNCO (292-391 °C). In the region between 391-528 °C, the events can be mainly attributed to the oxidative decomposition of *p*-ABA group (calc. 25.4%; exp. 25.6%). The event is accompanied mainly by the release of H₂O, CO₂, and HNCO. Since the higher amounts of released $m/z = 30$ (NO) and $m/z = 44$ (CO₂) are observed between 528-707 °C, the event occurring in this temperature region is predominantly associated with the PT rings decomposition (calc. 39.4%; exp. 38.6%), which is the moiety with the highest nitrogen content.

A change in the thermal behavior of sodium folate salts is observed when compared with FA. The steps of the thermal oxidation of sodium salts are not easy to separate. Unlike FA, the TG curves of salts after dehydration present abrupt weight loss events (**Figure 4**). For Na₂HFol, the decomposition of the anhydrous sample occurs mainly in three events (six steps). In the range of 264-323 °C, the event is accompanied by the release of H₂O and CO₂. It can be related to the decomposition of the carbon chain (C₃H₄) of glutamate moiety (calc. 7.7%; exp. 7.8%). The following events are accompanied by the release of H₂O, CO₂, NO, and a fragment of m/z

=46 (NO₂) and are related to the decomposition of *p*-ABA (323-528°C; two steps) and PT (383-528 °C) groups. Dehydrated Na₃Fol presents only two overlapped events attributed to folate decomposition. In the region between 292-394 °C, the event is associated with the decomposition of glutamate and the initial decomposition of *p*-ABA. It is accompanied by the release of H₂O, CO₂, NO and NO₂. The next event (394-547 °C) is followed by the same gaseous product, and it may be mostly attributed to the final decomposition of *p*-ABA and PT.

The events of small weight loss for salts above 530 °C are associated with the release of different gaseous products (detected by MS, as detailed discussed in **Section 6** of **SM**). For Na₂HFol, the event is associated only with the release of CO₂, while for Na₃Fol, it is accompanied by the release of NO, NO₂ and CO₂. Residual mass at 800 °C is consistent with the formation of Na₂CO₃ residue: 22.6% (calc. 20.0%) for Na₂Hfol and 30.0% (calc. 28.3%) for Na₃Fol.

Regardless of the atmosphere (*i.e.*, air or N₂), the thermal stability ranks as Na₃Fol > Na₂HFol > FA. Sodium salts are an alternative to improve the thermal stability of FA, especially in the case of Na₃Fol salt with a gain of stability of about 100 °C. Additionally, the thermal analysis results indicate that the decomposition of Glu seems to be delayed in the salts, while the end of oxidative decomposition of the PT ring appears to be advanced.

3.3. Structural simulation of FA, Na₂Fol and Na₃Fol by DFT

The conformations calculated for FA, Na₂HFol and Na₃Fol, using the B3LYP/6-311++G(d,p) Gaussian basis sets in the DFT framework, are shown in **Figure 5**. The obtained structures (simulated in the gas phase) exhibit essentially the same extended conformation for the three species, independently of the protonation level: a planar pterioic acid unit (PT and *p*-ABA structures), a *trans* amide bond and a bent conformation of the Glu moiety.

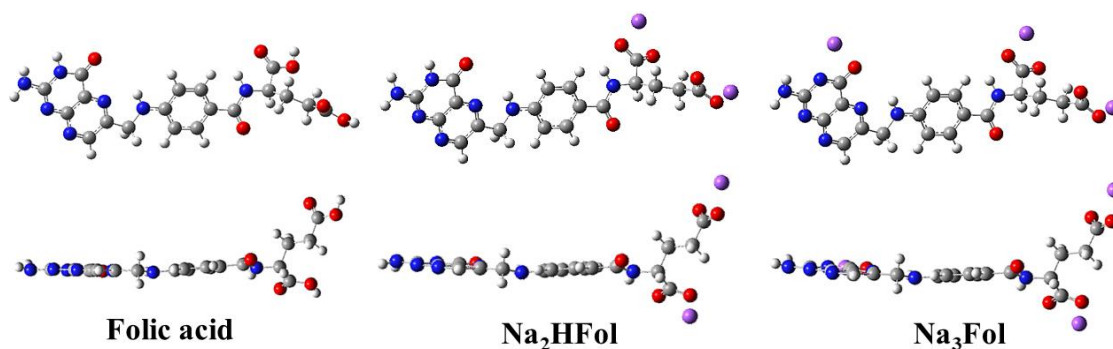


Figure 5. Theoretically (DFT) optimized structures (in vacuum) of FA, Na_2HFol and Na_3Fol . Color conventions: carbon (grey), hydrogen (white), oxygen (red), nitrogen (blue) and sodium (purple).

The DFT simulated FA structure achieved in this work was compared to the crystal structure of dihydrate FA resolved by the Rietveld refinement of powder X-ray diffraction data [52] (**Table A.2**). Kaduk et al. [52] performed geometry optimization *via* DFT (using the CRYSTAL09 software) and considering $\text{C}_{29}\text{H}_{29}\text{N}_2\text{O}_6(\text{H}_2\text{O})_2$ in the unit cell of FA. The main differences between experimental and simulated data are: (i) the PT and *p*-ABA acid units are not co-planar (**Figure 5**); and (ii) the bent of Glu moiety is not in the same three-dimensional conformation. In addition, such conformational structure significantly contrasts from that of FA and folate²⁻ predicted by molecular simulation in liquid solution [38,61], and of folate²⁻ complexed to enzymes, as the *dihydrofolate reductase* (DHFR) [40] or the folate receptor alpha ($\text{FR}\alpha$) [39].

A particularly good agreement between the calculated and experimental bond lengths and angles values is here obtained, although the simulations considered the isolated molecule, *i.e.*, intermolecular interactions are disregarded. It is worth noting that the calculated C4=O bond distance of 1.211 Å is close to the experimental value of 1.208 ± 0.004 Å [52], and it evidences the keto form PT moiety in FA. To the best of our knowledge, the crystal structure of dianion or trianion folate salts has not been reported so far, precluding any possible comparison.

Comparing the DFT results for FA with Na_2HFol (**Table A.2**), the main modifications are: (i) the length of C–O bonds of both carboxylic groups, indicating their deprotonation; (ii)

the elongation of $C\alpha-C\alpha'$ and $C\gamma-C\gamma'$ bonds; and (iii) the decreasing of $C\alpha-C\alpha'-O\alpha'$ and $C\gamma-C\gamma'-O\gamma$ angles. According to theoretical calculations (and as expected), deprotonation of FA into the dianion promotes changes in the glutamic unit, while the pteric acid moiety is insensitive. On the other hand, comparing the structural parameters calculated for Na_2HFol and Na_3Fol (**Table A.2**), the main differences are: (i) the $C4-O$ distance increases from 1.211 Å in the simulated FA and Na_2HFol to 1.258 Å in Na_3Fol , thus indicating that the bond order decreases and that the enolate turns to be the predominant mesomer form (**Figure A.1**).

In the pyrimidine ring, the $C4-N3$ and $C2-N3$ lengths decrease, respectively, from 1.408 Å to 1.367 Å and from 1.377 Å to 1.357 Å. The $N3-C4-C4a$ and $N1-C2-N3$ angles increase while the $O-C4-C4a$ and $C2-N3-C4$ angles are reduced. Although there are no experimental data to compare with the DFT in the case of Na_3Fol , the experimental crystallographic results obtained for PT anion coordinated to rhenium(I) [20] by $O4$ and $N5$ atoms show similar modifications (**Table A.2**). In the metal complex, the deprotonation of $N3$ promotes the shortening of $C4-N3$ (1.326(6) Å) and the elongation of the $C4-O$ (1.283(5) Å), characteristic of enolate mesomer form [20].

3.3. IR and Raman vibrational spectroscopies

The experimental IR and Raman spectra of FA and sodium folate salts in the 1800-800 cm^{-1} region are presented in **Figure 6**. Outside this spectral range, the information is limited; the bands in the region of 4000 and 2900 cm^{-1} are associated with the stretching modes of OH, NH, CH and CH_2 groups [62]. **Figures A.6-A.8** (full experimental spectra) show a strong band broadening in folate salts spectra, mainly due to intermolecular hydrogen bonds interactions between water molecules and/or folate anions groups such as $-NH$, $>C=O$ and $-COO^-$ [62]. The region below 800 cm^{-1} shows very weak bands similar to all samples.

As highlighted in gray in **Figure 6**, experimental IR and Raman spectra of FA, Na₂HFol and Na₃Fol show distinct profiles. The detailed assignment of FA and folates bands is not straightforward due to the structural complexity of the molecule/anions and because many vibrational modes are combined. Hence, a tentative attribution of vibration modes presented in **Table 2** is proposed considering the changes observed according to the protonation degree of the compound in the light of DFT calculations for the species in a vacuum, as well as from data in the literature [30,33,41–44, 62–74]. The comparison between experimental and theoretical spectra is shown in **Figures A.9-A.11**. As displayed in **Figure A.12**, a good linear correlation ($R^2 > 0.998$) is observed between the experimental and calculated energy (in wavenumber). In the following, the main distinct regions of vibrational spectra of FA, Na₂HFol and Na₃Fol are discussed, while some less relevant bands are considered in **SM (Figures A.9-A.11)**.

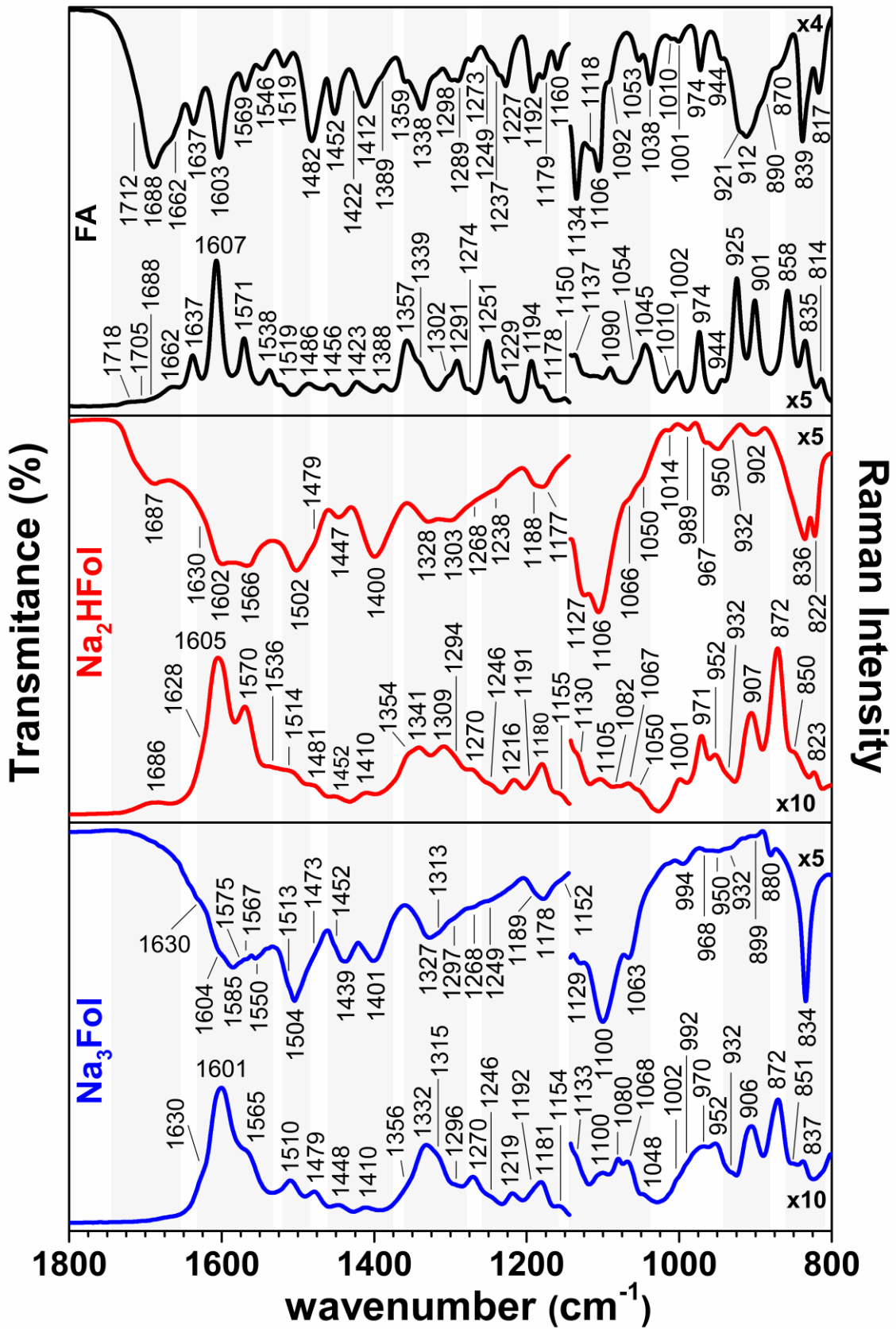


Figure 6. Experimental infrared (top) and Raman (down) spectra of FA, Na₂HFol and Na₃Fol samples.

Table 2. Experimental and calculated IR and Raman wavenumber values (cm⁻¹) for FA, Na₂HFol and Na₃Fol

Folic Acid			Na ₂ HFol			Na ₃ Fol			Tentative attribution of main groups involved in the vibration ^{b,c,d,e}
calc. ^a	exp.		calc. ^a	exp.		calc. ^a	exp.		
	IR	Raman			Raman		IR	Raman	
1766		1718 w							v(Cγ'=O)
1758	1712 sh	1705 w							v(Cα'=O)
1737	1688	1688 sh	1737	1687	1686				v(C4=O) + δ(N3H) + sc(NH ₂)
1656	1662 sh	1662	1654	1630 sh	1628 sh	1652	1630 sh	1630 sh	v(C11=O) + δ(N12H) + φ[8b]/D23
1634	1637	1637	1634						vas(N2C2N1) + sc(NH ₂) + δ(N3H)
1607	1603	1607	1608	1602	1605	1609	1604 sh	1601	φ[8a]/D3
						1598	1585	#	sc(NH ₂) + v(PT rings) + v(C4-O ⁻)
						1577	1575 sh	#	v(PT rings) + sc(NH ₂) + v(C4-O ⁻)
1563	1569	1571	1565	1566	1570				v(PT rings) + sc(NH ₂) + δ(N3H); φ[8b]/D23 + δ(N10H) + v(C11=O)
						1562	1567	1565 sh	φ[8b]/D23 + δ(N10H) + v(C11=O)
						1544			v(C4-O ⁻) + v(PT rings) + sc(NH ₂)
			1543	#	#	1541	1550 br	#	vas(Cα'OO ⁻) + v(C11N12)/δ(N12H)
1530	1546	1538	1528	#	1536 sh				v(PT rings) + δ(N3H) + v(C4=O);
									φ[19a]/D4 + v(N10-φ)/δ(N10H) + v(C11-φ) + δ(N12H)
1524	1519	1519 sh	1519	#	1514 sh				φ[19a]/D4 + v(N10-φ)/δ(N10H) + v(C11-φ) + v(C11N12)/δ(N12H);
									v(PT rings) + δ(N3H)
						1518	1513 sh	1510	v(PT rings) + sc(NH ₂) + v(C4-O ⁻);
									φ[19a]/D4 + v(N10-φ)/δ(N10H) + v(C11-φ) + v(C11N12)/δ(N12H);
			1515	1502 br		1514	1504 br		vas(Cγ'OO ⁻)
1480	1482		1475	1479 sh					v(C11N12)/δ(N12H); sc(CβH ₂); v(PT rings) + δ(N3H) + sc(C9H ₂); φ
						1468	1473 sh		v(C11N12)/δ(N12H); sc(CβH ₂); sc(C9H ₂) + v(PT rings); φ
1465	1452	1456	1460	1447	1452				sc(C9H ₂) + v(PT ring); sc(CβH ₂)/(CγH ₂); v(C11N12)/δ(N12H); φ
						1459	1452 sh	1448 br	sc(CβH ₂)/(CγH ₂); v(C11N12)/δ(N12H)
						1423	1439		v(PT rings) + v(C2N2)
1412	1412	#	1407	#	1410	1408	#	1410	φ[19b]/D4; ω(C9H ₂)
			1396			1396			vs(Cα'OO ⁻)/v(Cα-Cα') + ω(CβH ₂)/(CγH ₂);
			1386	1400 br		1386	1401 br		vs(Cγ'OO ⁻)/v(Cγ-Cγ') + ω(CγH ₂)
1385	1389 sh	1388							δ(OH) + ω(CβH ₂)/(CγH ₂)
1365	1359								δ(OH) + δ(CαH) + ω(CγH ₂)/τ(CβH ₂) + v(C11N12)/δ(N12H);
									ω(C9H ₂) + δ(N10H)/v(N10-φ) + φ; v(PT rings) + δ(N3H) + δ(C7H)
						1355			ω(C9H ₂) + δ(N10H)/v(N10-φ) + φ
						1346	#	1356 sh	v(PT rings) + v(C2N2) + δ(C7H)

Table 2. Continued...

Folic Acid			Na ₂ HFol			Na ₃ Fol			Tentative attribution of main groups involved in the vibration ^{b,c,d,e}
calc. ^a	experimental		calc. ^a	Experimental		calc. ^a	experimental		
	IR	Raman		IR	Raman		IR	Raman	
1346		1357	1344		1354 sh				v(PT rings) + τ(NH ₂) + δ(C7H) + ω(C9H ₂)
			1336	1328 br		1336	1327 br		ω(CβH ₂)/(CγH ₂) + δ(CαH) + vs(Cα'OO ⁻)
1333									δ(OH) + δ(CαH) + τ(CβH ₂)/ω(CγH ₂)
1326	1338	#							φ[14]/D25 + v(N10-φ) + ω(C9H ₂); τ(CβH ₂)/(CγH ₂) + δ(α'OH) + δ(CαH)
1323	#	1339	1323	#	1341				v(PT rings) + δ(N3H) + τ(NH ₂) + δ(C7H) + ω(C9H ₂) + v(N10-φ) + [14]/D25
			1318	1328 br	#				φ[14]/D25 + v(N10-φ) + ω(C9H ₂) + v(PT rings) + δ(N3H); ω(CβH ₂)/τ(CγH ₂) + δ(CαH)
						1320	1327 br	#	φ[14]/D25 + δ(N10H)/v(N10-φ); ω(CβH ₂)/(CγH ₂) + δ(CαH)
						1308	#	1332	v(PT rings) + τ(NH ₂) + δ(C7H) + ω(C9H ₂) + δ(N10H)/v(N10-φ) + φ
						1301	1313 sh	1315 sh	v(PT rings) + v(C2N2) + δ(C7H) + ω(C9H ₂);
1304	1298	1302 sh							δ(OH) + τ(CβH ₂)/(CγH ₂) + δ(CαH);
			1300	1303	1309				φ[3]/D26; v(PT rings) + δ(N3H) + v(C2N2);
						1299	1297 sh	1296 sh	φ[3]/D26 + v(C11N12)/δ(N12H) + δ(CαH) + τ(CβH ₂)/(CγH ₂);
1293									v(PT rings) + v(C2N2) + δ(N3H);
1286	1289	1291	1285	#	1294 sh				φ[3]/D26 + v(C11N12)/δ(N12H) + δ(CαH) + τ(CβH ₂)/(CγH ₂)
1114									δ(OH) + τ(CβH ₂)/(CγH ₂) + δ(CαH) + v(C11N12)/δ(N12H)
1104	1106	#	1104	1106	1105				v(PT rings) + δ(N3H) + v(C2N2) + δ(C7H) + ω(C9H ₂) + δ(N10H); φ
									v(C-O) _{OH} + ω(CβH ₂)/(CγH ₂)
						1101	1100	1100	φ[18b]/D24 + v(C9N10) + v(PT rings) + δ(N3H) + ρ(NH ₂)
									φ[18b]/D24 + v(C9N10) + v(PT rings)
			842*	836	#	841*	834	837	φ[17b]/D16 + δ _{oop} (C11N12H) + δ _{oop} (N10H);
838*	839	835							φ[17b]/D16 + δ _{oop} (C11N12H) + δ _{oop} (N10H);
									φ[18a]/D10 + v(Glu) _{ch} + δ _{oop} (COOH)
						832*	834	837	δ _{oop} (PT rings) + ρ(C9H ₂)
815*	817	814							δ _{oop} (PT rings) + ρ(C9H ₂); φ[10a]/D13
			816*	822	823				δ _{oop} (PT rings) + ρ(C9H ₂); φ[10a]/D13; τ(CγH ₂)/(CβH ₂) + δ _{oop} (COO ⁻)
652									δ _{oop} (γ'OH)
596	912(br)								δ _{oop} (α'OH)

(a) Selected values in wavenumbers (cm⁻¹) obtained using the functional/basis set B3LYP/6-311++G(d,p). Wavenumbers were multiplied by the 0.975 scaling factor (* indicates unscaled values); # are very weak and/or not resolved band; (b) Attributions were made in the light of DFT and works from the literature [30,33,41–44,62–74]; (c) vs = symmetric stretching, vas = antisymmetric stretching, δ = bending (in plane; ip); oop = out-of-plane, sc = scissoring (ip bending), ω = wagging (oop bending), ρ = rocking (ip bending), τ = twisting (oop bending), b = broad, sh = should, w = weak, (GLU)_{ch} = carbonic chain of Glu /glutamate; (d) The numbers and letters are related to the carbon indexation in FA structure shown in Figure 1a; (e) phenylene ring (φ) vibration modes were assigned using Wilson and Mulliken labelling [73];

1720-1630 cm^{-1} range. This region is assigned mainly to the bands related to the $\text{C}\alpha'=\text{O}$ and $\text{C}\gamma'=\text{O}$ stretching (ν) vibrational modes of Glu unit, $\text{C4}=\text{O}$ of PT ring and $\text{C11}=\text{O}$ of amide group. Compared to the FA vibrational spectra obtained by DFT (vacuum simulation), the experimental bands are not as well resolved and are shifted to a lower energy range (**Figure A.9**). It can be associated with the network of intermolecular hydrogen bonds in the solid (**Figure A.2**), which makes the $\text{C}=\text{O}$ bond weaker, leading to a red shift and a broadening of the related bands [62]. The three compounds possess hydration water, as observed in thermal analysis data, which bands observed around 1650-1620 cm^{-1} in the infrared spectra assigned to angular deformation [62].

The $\nu(\text{C}=\text{O})$ vibrational modes of Glu moiety, attributed to the carboxylic groups identified as α' and γ' in **Figure 1**, are predicted by DFT to be coupled. However, as noticed in **Figure A.13**, the energy of $\nu(\text{C}\gamma'=\text{O})$ vibration is higher than that of $\nu(\text{C}\alpha'=\text{O})$, as expected, considering that the first bonding is shorter than the second one (**Table A.2**). Experimentally, it is observed as a shoulder at around 1712 cm^{-1} in the infrared, and as weak bands in the FA Raman spectrum, in agreement with Braga et al. [41] These bands are not present in the spectra of the sodium salts, indicating the deprotonation of Glu moiety.

A band assigned to $\text{C4}=\text{O}$ stretching of PT ring is observed at around 1688 cm^{-1} , both in FA and Na_2HFol experimental infrared spectra, though less intense in the last compound. The band position agrees with the value for guanine (pyrimidine ring fused to imidazole) at 1697 cm^{-1} [69]. This band is absent in the Na_3Fol spectrum, indicating the deprotonation of N3 atom of PT and the formation of the enolate group (**Figure A.1**).

For the three species, the $\nu(\text{C11}=\text{O})$ of amide (Amide I) is predicted by DFT at 1650 cm^{-1} region. The experimental band is observed at 1662 cm^{-1} as a shoulder in infrared and a weak band in Raman spectra of FA, in line with results reported for peptides (peptide bonds) [65]. However, it is proposed here that this band is red-shifted to 1630 cm^{-1} due to intramolecular

hydrogen bonds between N12–H and γ 'COO⁻ groups, as suggested by Gocheva et al. [38] for Fol²⁻ in aqueous solution and by similar values observed for polypeptides [65].

According to DFT, in the FA spectrum, the band at 1637 cm⁻¹ (calc. 1634 cm⁻¹) can be attributed to antisymmetric stretching (vas) of guanidyl group (C2 bonded to N1, N2 and N3; C2N₃), coupled to NH₂ scissoring (sc) and N3–H bending (δ), as presented in **Figure A.14**.

1610-1520 cm⁻¹ range. Regardless of the sample, a strong band at about 1600 cm⁻¹ is observed in the infrared and Raman spectra (**Figure 6**), indicating a vibration from a group not involved in the deprotonation process. Based on DFT and in agreement with Kokaislová et al. [30] and Braga et al. [41], it is assigned to the C-C stretching of the phenylene ring of *p*-ABA group. For FA and Na₂HFol, the bands in the 1570 cm⁻¹ region of infrared and Raman spectra are attributed to vibrations from the pterioic acid unit (**Table 2**), consistent with experimental and theoretical results reported for guanine [64,69], *p*-ABA [71], PT [70], and FA [41]. A broadening of bands is observed from FA to Na₂HFol, possibly due to the H-bonds and π - π interactions, as discussed previously.

A comparison of the spectra of Na₂HFol and Na₃Fol shows remarkable changes in the spectral profile. According to DFT calculations, these changes are due to the deprotonation of N3–H group, which promotes a redshift ($\Delta\nu = 36$ cm⁻¹) of the band assigned to PT vibrational modes from 1634 cm⁻¹ (in FA; previously discussed) to 1598 cm⁻¹ in theoretical spectra (**Table 2** and **Figure A.14**). As theoretically predicted by Reibnegger [50] the N3–H deprotonation leads to the improvement of aromatic character of pyrimidine ring in anionic pterin. Considering that fused aromatic rings have almost the same vibrational energy as benzene derivatives [62], the shift of the band toward C-C stretching phenylene rings is in line with theoretical calculation [50] and with the statement of enolate mesomer form in Fol³⁻ (**Figure A.1**).

DFT calculations indicate a pronounced band redshift ($\Delta\nu = 193 \text{ cm}^{-1}$) from 1737 cm^{-1} to 1544 cm^{-1} of $\nu(\text{C4}=\text{O})$ due to the formation of $\text{C4}-\text{O}^-$ (enolate, Fol^{3-}), as noticed in **Table 2** and **Figure A.15**. Theoretical and experimental vibrational studies performed with uracil (pyrimidine-2,4(1H,3H)-dione) also indicated a similar band shift [72]. In addition, the band at around 1550 cm^{-1} for Na_3Fol also has the contribution of $\nu_{\text{as}}(\text{C}\alpha'\text{OO}^-)$ and $\nu(\text{C11N12})/\delta(\text{N12}-\text{H})$ vibrations.

1520-1460 cm^{-1} range. The infrared spectra of folate salts show a strong and broadband at about 1500 cm^{-1} attributed to the $\nu_{\text{as}}(\text{C}\gamma'\text{OO}^-)$. The broadening is probably due to some interactions by hydrogen bonds in the salts. DFT calculations indicate that the frequencies of the carboxylate groups band are distinct for both folates: around 1543 cm^{-1} for $\nu_{\text{as}}(\text{C}\alpha'\text{OO}^-)$ and 1515 cm^{-1} for $\nu_{\text{as}}(\text{C}\gamma'\text{OO}^-)$, as displayed in **Figure A.12**. Li et al. [67] observed the same result applying a DFT approach to the disodium salt of folinate (both folinic and folic acids have a Glu and *p*-ABA groups), and suggested that the proximity of $\text{C}\alpha'\text{OO}^-$ and $\text{N12}-\text{H}$ groups can be the main reason for this frequency to be higher compared to $\text{C}\gamma'\text{OO}^-$ group.

The band at 1504 cm^{-1} is the most intense in the experimental infrared spectra of Na_3Fol (**Figure A.8**), while for Na_2HFol , the intensity of the bands at 1502 cm^{-1} and 1600 cm^{-1} is similar. Hence, Fol^{2-} and Fol^{3-} species can be distinguished by infrared spectroscopy simply by analyzing the relative intensities of these bands. This change in the relative intensities can be attributed to the contribution of the band mainly assigned to $\nu(\text{PT rings})$ and $\nu(\text{C4}-\text{O}^-)$, as can be noticed by the shoulder at 1513 cm^{-1} in the Na_3Fol experimental spectra (**Figure 6** and **Table 2**). According to DFT calculations, such a band is redshifted from 1530 cm^{-1} in FA to 1518 cm^{-1} in Na_3Fol theoretical spectra (**Table 2**). As seen in **Figure A.15**, the deprotonation of N3 increases PT stretching vectors, thus as well increasing the aromaticity of PT ring in Na_3Fol .

1460-1380 cm^{-1} range. All samples present two main bands around 1450 cm^{-1} and 1410 cm^{-1} in experimental infrared spectra. As the profile and relative intensity of these two main

bands change according to the species (**Figure 6**), helpful to differentiate FA from folate salts. For FA and Na₂Hfol, the bands centered at around 1450 cm⁻¹ (calc. around 1460 cm⁻¹) can be assigned to CH₂ and NH bending modes with the contribution of PT rings stretching (**Table 2** and **Figure A.16**). The broad band around 1412 cm⁻¹ in experimental infrared spectra of FA is assigned to CH₂ vibrations with the contribution of in-plane δ(OH).

The broad and intense band observed at about 1400 cm⁻¹, in both infrared spectra of folate salts, can be mainly attributed to νs(COO⁻), as listed in **Table 2**. For Na₃Fol, the band around 1450 cm⁻¹ is observed as a shoulder in the experimental spectrum, and the contribution of PT vibration is no longer predicted by DFT (**Figure A.16**). Differently from Na₂HFol, a band centered at 1439 cm⁻¹ is observed in the experimental spectrum of Na₃Fol and with almost the same intensity as the above-mentioned band at 1400 cm⁻¹. Based on DFT calculations, it is correlated to the band at 1423 cm⁻¹, observed only in the simulated spectrum of Na₃Fol (**Figures A.9-A.11**) and attributed mainly to ν(PT rings), as displayed in **Table 2** and **Figure A.16**.

1360-1280 cm⁻¹ region. Infrared and Raman spectra of FA present mainly four bands in this spectral range: two overlapped at about 1360-1340 cm⁻¹ region and the other two at 1300-1290 cm⁻¹. As proposed in **Table 2**, based on DFT, such bands are mainly associated with OH, CH, and CH₂ bending of Glu moiety and CC/CN stretching of aromatic rings. Comparing FA and Na₂HFol spectra, modifications in the IR spectral profile are observed, while the position of the bands is not changed significantly in Raman.

Based on the DFT calculation and experimental results (**Figure 6** and **Table 2**), it is proposed that the bands at 1359 and 1338 cm⁻¹ in the IR spectra of FA are not from the same vibration of those respectively observed at 1357 and 1339 cm⁻¹ in Raman. The change observed in IR spectra from FA to folate salts, is mainly due to Glu deprotonation. Bands attributed to CH and CH₂ bending of Glu moiety are shifted from 1338 cm⁻¹ in FA to 1328/1327 cm⁻¹ in folate salts. On the other hand, from Na₂HFol to Na₃Fol, both Raman and infrared spectra

present significant modifications in this region. The infrared spectrum of Na₂HFol shows two bands centered at 1328 and 1303 cm⁻¹, while Na₃Fol shows only one broadband at 1327 cm⁻¹ (with a shoulder in 1313 cm⁻¹). In the Raman spectra, two resolved bands at 1341 cm⁻¹ and 1309 cm⁻¹ are observed for Na₂HFol, while for Na₃Fol such bands are overlapped and centered at 1332 cm⁻¹ (with a shoulder at 1315 cm⁻¹). The bands in this spectral region are related to the C-C/C-N stretching and N3-H deformation mode, the last being absent in the trisodium.

According to DFT, after deprotonation of the PT group, the C-C/C-N stretching is a redshift from 1523 to 1508 cm⁻¹, and a blue shift from 1286 to 1301 cm⁻¹, both with a $\Delta\nu$ value of about 15 cm⁻¹, as displayed in **Figure A.17**. The observations are consistent with theoretical and experimental results (but in a minor shift extension) reported to uracil, which presents such spectral features when its neutral pyrimidine ring is deprotonated in water [72]. The spectral profile in this region differentiates the dianionic from the trianionic folate. The resolution of the bands is higher in Raman than in infrared spectra. In addition, the shift observed for bands related to C-C/C-N stretching of PT unity after deprotonation occurs in a region around 1330 cm⁻¹ attributed to C-C stretching of the phenylene ring (**Table 2**). The results once again suggest an improvement in the aromaticity of PT ring and of the enolate mesomeric form (**Figure A.1**) in Na₃Fol.

The observed difference of 15-20 cm⁻¹ between theoretical and experimental results attribution of bands around 1360-1300 cm⁻¹ in the Raman spectra (**Table 2**) is related to π - π interaction of aromatic rings between species. As discussed in the UV-VIS spectra and XRD data analysis, such interactions change the vibronic band structure [55], which is not taken into account in the DFT calculations of a single molecule in vacuum. In fact, a set of broad bands and shoulder overlapped in this region is observed in the Raman spectrum of Na₂HFol.

1100 cm⁻¹ range. The band in the 1100 cm⁻¹ region of FA and folates can be attributed mainly to in-plane C-H bending of phenylene ring coupled to C9-N10, in agreement to studies

with tyrosine/tyrosinate [63] and as expected for amine linkage [62]. Vibrations attributed to $\nu(\text{C-OH})$ of carboxylic groups and $\nu(\text{PT rings})$ also have a contribution in this region (**Table 2** and **Section 8** of **SM**). The striking changes from FA to Na_2HFol are attributed to the deprotonation of Glu, and the spectral changes from Na_2HFol to Na_3Fol are attributed to the deprotonation of $\text{N}_3\text{-H}$. The band at 1100 cm^{-1} could be pointed as a marker of deprotonation degree since its relative intensity compared with other bands around 1130 cm^{-1} and 840 cm^{-1} regions change according to the species.

950-800 cm^{-1} region. Calculated DFT fits better with experimental spectra if the correction factor is not applied. This spectral range presents weak bands concerning out-of-plane $\delta(\text{COO}^-)$, and $\delta(\text{COOH})$ vibrations. The most remarkable change in infrared spectra from FA to folate salts is the disappearance of the band in the region of 912 cm^{-1} attributed to out-of-plane $\delta(\text{OH})$ group. DFT prediction for such vibration is not accurate if H-bonds are not considered [68]. For calculations of single molecule, the band is predicted to be located in the region of 600 cm^{-1} , while for dimers it is predicted and experimentally observed at $960\text{-}900\text{ cm}^{-1}$ region, as in the case of dimers of benzoic acid [68] and mefenamic acid [43]. In this work, the calculated values are 652 cm^{-1} ($\gamma'\text{OH}$) and 596 cm^{-1} ($\alpha'\text{OH}$), in agreement with the calculated values for benzoic acid [68]. The spectra of folate samples show bands at about 910 and 830 cm^{-1} assigned to the C-COO^- stretching, as observed for coumarate [42], pravastatin [44], or tyrosinate [74], for instance. As predicted by DFT calculations, the distance of $\text{C}\alpha\text{-C}\alpha'$ or $\text{C}\gamma\text{-C}\gamma'$ increases by about 0.016 \AA when FA is deprotonated (**Table A.1**), indicating that the chemical bond is weakened.

Another important change observed in the IR spectrum of FA and folates occurs in the region of $840\text{-}816\text{ cm}^{-1}$. FA and Na_2HFol present two bands in this region: (i) one at $839\text{-}836\text{ cm}^{-1}$ attributed mainly to out-of-plane C-H deformation of phenylene ring of *p*-ABA [63] and (ii) the other one at around $817\text{-}822\text{ cm}^{-1}$ attributed mainly to out-of-plane deformation of C-

C/C-N and out-of-plane C–H deformation [63] from PT and *p*-ABA moieties, respectively. Otherwise, only one band at 834 cm⁻¹ is observed for Na₃Fol. According to DFT calculations, the deprotonation of the PT unit leads to a blue shift ($\Delta\nu$ about 15 cm⁻¹) of C-C/C-N bending from 815 cm⁻¹ to 832 cm⁻¹ (**Figure A.18**).

3.5. Solid state ¹³C-NMR spectroscopy

To the best of our knowledge, the ¹³C-NMR data of di- and trianion folate species in solid state have not been reported in the literature. Solid state ¹³C and ¹⁵N CP-MAS NMR of FA were reported by Ghosh, Gayen, and Dey [75]. Experimental results reported for FA in deuterated DMSO by Bonechi et al. [61] indicated that the molecular conformation is different from that observed in the crystal because intermolecular interactions in solution are not as important as in the crystal due to the intramolecular interactions involving the Glu group. Experimental and simulated ¹³C-NMR results for Fol²⁻ in water and for FA in DMSO were reported by Gocheva et al.[38] The authors also noticed the distinct conformation of FA in solution, in relation to the crystal, and predict that the molecules shape in “U” or “V” conformation because of the bending of Glu with *p*-ABA as well as the *p*-ABA with PT moiety.

Solid state ¹³C-NMR spectra of AF, Na₂HFol and Na₃Fol samples are displayed in **Figure 7**. The peak assignments, based on DFT calculations and from data in the literature [38,61,75,76], are presented in **Table 3**. The attribution of ¹³C NMR spectra peaks does not fully agree with previous studies [38,61,75,76] when the chemical shifts are too close to each other (for instance, C2 and C8a). The experimental and calculated ¹³C-NMR spectra of samples are compared in **Figure A.19**. A good linear correlation ($R^2 > 0.994$) between experimental and the calculated ¹³C chemical shift can be noticed in **Figure A.20**.

The deprotonation of both carboxylic groups has a weak influence on the ¹³C chemical shifts of C α , C β , C γ , C α' and C γ' (**Figure 7; Table 3**), consistent with what was observed by

Gocheva et al. [38] in DMSO. In addition, based on the DFT calculations, after the deprotonation, the chemical shift of $C\gamma'$ is larger than for $C\alpha'$ (**Figure 7; Table 3**). Experimentally, both contributions merge at an average chemical shift value significantly smaller than that theoretically predicted but partially correlated (**Figure A.20**). Another important spectral change experimentally observed is the chemical shift of C11 (from 164.9 to around 168.5) and C1' (from 116.9 to around 120.0) related to the amide group after Glu deprotonation. Such chemical shifts are also in agreement with Gocheva et al.[38]. C11 is the carbonyl group that links *p*-ABA to Glu moiety and, like in C1', the chemical shift seems to be overestimated by calculation in the three organic forms. It can be related to hydrogen bonds between N12–H and $C\gamma'OO^-$ groups in anionic species [38], as discussed previously. For both salts, the C1' and C11 relative peak intensities of the sodic salts are weaker than for FA. In addition, after deprotonation, C6' and C4a+C2' peaks are overlapped in the spectra. DFT calculations are in close agreement with the experimental results for the two salts. However, the width of the contribution merging C6', C4a and C2' is more than 500 Hz (> 6 ppm), explained by the fact that the π – π interactions (**Figure A.3**) are not considered in the calculations.

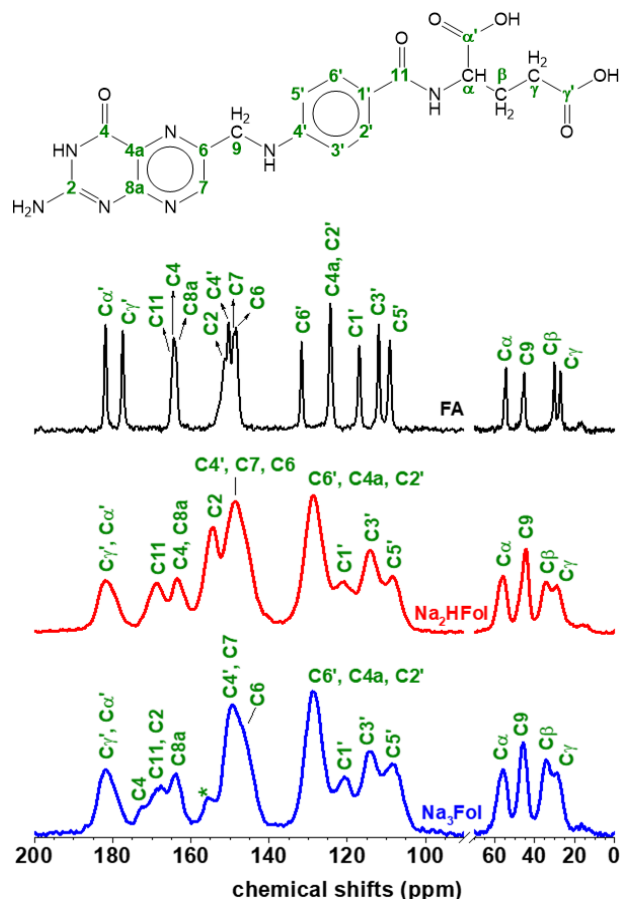


Figure 7. Experimental solid state ^{13}C -NMR spectra of commercial FA, and Na_2HFol and Na_3Fol samples prepared in this work. The peak marked with asterisk (*) indicates the possible presence of Na_2HFol .

The most remarkable chemical shift in the spectra of Na_3Fol compared with FA and Na_2HFol is associated with C4 and C2. Indeed, a pH superior to pK_{a4} induces a change from HN_3 to NaN_3 , strongly impacting the neighboring carbon atoms, C2 and C4, with a pronounced low-field shift. The results predicted by DFT are consistent with the experimental chemical shift reported by Cheung et al. [76] for folate in a water solution when the pH value is increased from 5.5 (Fol^{2-}) to 10 (Fol^{3-}). The same effect is predicted for DFT calculations but less pronounced for C4a and C8a (both engaged in the pyrazine resonant ring), but it is not experimentally observed because of the peaks broadening.

Table 3Experimental and calculated solid state ^{13}C -NMR chemical shifts (ppm) of FA, Na_2HFol and Na_3Fol samples.

Assignment	Folic Acid					Na_2HFol				Na_3Fol		
	calcd.	exp.	exp. ^{a)}	exp. ^{b)}	exp. ^{c)}	calcd.	exp.	exp. ^{d)}	exp. ^{e)}	calcd.	exp.	exp. ^{f)}
α' C	180.4	181.8	182.1	173.7	173.7	191.4	181.8	182.0		191.6	181.8	
γ' C	178.4	177.4	186.4	173.9	173.9	192.1	181.8	185.1		192.1	181.8	
C11	168.5	164.9 sh	168.9	166.4	166.3	167.0	168.6	172.2		167.3	167.7	
C4	162.5	164.4	157.1	161.2	160.8	163.2	163.5	169.3	165.8	181.1	172.3	174.2
8a	161.7	164.0 sh	152.8	153.8	153.6	162.6	163.5	156.5	154.8	164.1	163.9	156.7
C2	154.2	151.2 sh	155.9	156.2	156.5	154.1	154.4	159.4	155.6	166.2	167.7	165.1
C4'	154.8	150.3	155.2	150.8	150.7	153.7	148.6	153.5		154.5	149.3	
C7	153.5	148.9 sh	153.2	148.6	148.6	153.6	148.6	151.4	150.1	152.8	149.3	148.5
C6	151.1	148.4	154.0	148.6	148.4	153.2	148.6	151.7	151.3	148.5	147.1 sh	148.9
C6'	137.5	131.6	136.4			137.0	128.7			137.1	127.7	
4a	133.4	124.3	128.9	127.9	127.8	133.1	128.7	130.2	128.5	131.5	128.7	129.2
C2'	130.8	124.3	136.4			131.0	128.7			130.7	128.7	
C1'	126.6	116.9	121.1	121.3	121.1	131.3	121.2	124.5		130.0	120.5	
C3'	116.5	111.9	116.5	111.2		116.1	114.2			115.6	114.2	
C5'	111.2	109.1	113.3	111.2	111.1	111.0	108.4	115.1		111.0	108.4	
α C	54.3	54.2	58.1	51.8	51.6	57.7	55.8	58.8		57.8	55.8	
C9	46.2	45.1	49.2	45.9	45.7	47.0	44.4	48.5	47.0	46.7	45.7	47.2
β C	33.5	30.1	30.8	26.1	25.9	37.5	34.3	31.4		37.6	34.3	
γ C	31.6	27.1	33.9	30.4	30.3	37.3	29.1	37.1		37.2	28.9	

^{a)}solid state ^{13}C CP-MAS NMR from ref. [75]; ^{b)} FA in DMSO-d₆ solution from ref. [61]; ^{c)} FA in deuterated DMSO solution from ref. [38]; ^{d)}Fol²⁻ in water-d₆ solution (pH 7) from ref. [38]; ^{e)}Fol²⁻ in deuterated water (pH 5.5) from ref. [76]; ^{f)}Fol³⁻ in deuterated water (pH 10) from ref. [76].

4. Conclusion

In this work, di- (Na_2HFol) and trisodium (Na_3Fol) folates isolated in their solid state are compared to FA, commercially available, and applied in several fields. To highlight their respective characteristics, the three samples were characterized by spectroscopic (IR, Raman, and ^{13}C -NMR) and thermal techniques. The spectroscopic characterization, in combination with DFT theoretical calculations, allowed a complete spectral fingerprint of each compound. The main difference in the IR spectra between FA and Na_2HFol concerns the vibrational bands attributed to Glu /glutamate moiety, while the most significant change between Na_2HFol and Na_3Fol is the absence of bands in the region of C=O stretching ($1720\text{-}1660\text{ cm}^{-1}$) and the relative intensity of bands at 1500 cm^{-1} and 1600 cm^{-1} (C-C stretching of the phenylene ring). Prominent modifications in the $1360\text{-}1290\text{ cm}^{-1}$ region of Raman spectra are associated to the vibrational modes of PT rings.

Solid-state ^{13}C -NMR results show the successive deprotonation as a function of pH value. The carbon atoms of Glu moiety are not highly sensitive to the deprotonation, while pronounced changes are related to chemical shifts of C1' (benzene ring) and C11 (amidic), from FA to Na_2HFol , and of C2 and C4 (PT moiety), from Na_2HFol to Na_3Fol .

Singular thermal oxidative profiles are observed for FA, Na_2HFol and Na_3Fol . Thermal stabilities of the samples are independent of the atmosphere (*i.e.*, air or N_2) and follows the order: Na_3Fol ($300\text{ }^\circ\text{C}$) > Na_2HFol ($267\text{ }^\circ\text{C}$) > FA ($198\text{ }^\circ\text{C}$). XRD pattern of Na_2HFol exhibits a broad diffraction peak that is attributed to the distance between two disk-like structures π -stacked in a columnar array, as already identified in water, thus underlining such organization in solid state.

UV-VIS electronic spectra of the species in water solution compared to those ones of the powdered samples are clearly distinguishable. In solid state, the spectra of all the three compounds show a shoulder in the low energy region, that can be associated to intermolecular

charge-transfer (CT) transitions of packed FA molecules in the crystal, and in the case of sodium salts, be related to CT transitions in aggregated and/or supramolecular structures.

It is our belief that this work provides a comprehensive comparison between FA and its anionic folate species, helping to better understand and design new products based on them.

CRedit authorship contribution statement

V.R. Magri: Methodology, Investigation, Data curation, Writing - review & editing - original draft. **M.A. Rocha:** Methodology, Investigation, Data curation, Review. **C.S. de Matos:** Methodology, Investigation, Data curation, Review. **P.A.D. Petersen:** Theoretical calculations, Review. **F. Leroux:** NMR analysis, Review & editing. **H.M. Petrilli:** Theoretical calculations, Review & editing. **V.R.L. Constantino:** Conceptualization, Methodology, Visualization, Writing - review & editing, Supervision.

Declaration of Competing Interest

The authors declare that they have no known competing financial interests or personal relationships that could have appeared to influence the work reported in this paper.

Acknowledgments

V.R.M. is grateful to the Coordenação de Aperfeiçoamento de Pessoal de Nível Superior (CAPES, Finance Code 33002010191P0) for the PhD scholarship. C.S. de M. acknowledges the Fundação de Amparo à Pesquisa do Estado de São Paulo for research grant (FAPESP 2012/06291-4). V.R.L.C. and H.M.P. are thankful to the Conselho Nacional de Desenvolvimento Científico e Tecnológico (CNPq) for the research grants (305446/2017-7 and 311373/2018-6, respectively). This work is part of the Research Academic Cooperation

Agreement PRC-CNRS-FAPESP (PRC-Projets de recherché conjoints 1688 and SPRINT-São Paulo Researchers in International Collaboration 2016/50317-9). The authors also acknowledge the Laboratório de Cristalografia (Instituto de Física - USP) for the XRD *diffractograms* registration and the Laboratório de Espectroscopia Molecular (LEM, Instituto de Química – USP) for the FTIR and Raman spectra recording.

Appendix A. Supplementary material

Supplementary data to this article can be found online at <https://doi.org/XXX>.

References

- [1] R. Strouse, Folic Acid Market Size, Share & Trends Analysis Report by Application (Food & Beverages, Pharmaceuticals, Nutraceuticals), By Region, And Segment Forecasts, 2018 - 2025, Online. (n.d.) 135. <https://www.grandviewresearch.com/industry-analysis/folic-acid-market>.
- [2] Z. Szakács, B. Noszál, Determination of dissociation constants of folic acid, methotrexate, and other photolabile pteridines by pressure-assisted capillary electrophoresis, *Electrophoresis*. 27 (2006) 3399–3409. <https://doi.org/10.1002/elps.200600128>.
- [3] R.K. Saini, S.H. Nile, Y. Keum, Folates: Chemistry, analysis, occurrence, biofortification and bioavailability, *Food Res. Int.* 89 (2016) 1–13. <https://doi.org/10.1016/j.foodres.2016.07.013>.
- [4] R.L. Blakley, IUPAC-IUB Joint Commission on Biochemical Nomenclature (JCBN). Nomenclature and symbols for folic acid and related compounds. Recommendations 1986, *Eur. J. Biochem.* 168 (1987) 251–253. <https://doi.org/10.1111/j.1432-1033.1987.tb13413.x>.
- [5] J.L. Guéant, F. Namour, R.M. Guéant-Rodriguez, J.L. Daval, Folate and fetal programming: A play in epigenomics?, *Trends Endocrinol. Metab.* 24 (2013) 279–289. <https://doi.org/10.1016/j.tem.2013.01.010>.
- [6] G.S. Ducker, J.D. Rabinowitz, One-Carbon Metabolism in Health and Disease, *Cell Metab.* 25 (2017) 27–42. <https://doi.org/10.1016/j.cmet.2016.08.009>.
- [7] L. Qin, W. Wang, S. You, J. Dong, Y. Zhou, J. Wang, In vitro antioxidant activity and in vivo antifatigue effect of layered double hydroxide nanoparticles as delivery vehicles for folic acid, *Int. J. Nanomedicine*. 9 (2014) 5701. <https://doi.org/10.2147/IJN.S74306>.
- [8] P. Jones, M. Lucock, C.J. Scarlett, M. Veysey, E.L. Beckett, Folate and Inflammation – links between folate and features of inflammatory conditions, *J. Nutr. Intermed. Metab.* 18 (2019) 100104. <https://doi.org/10.1016/j.jnim.2019.100104>.
- [9] F. Ma, T. Wu, J. Zhao, A. Song, H. Liu, W. Xu, G. Huang, Folic acid supplementation improves cognitive function by reducing the levels of peripheral inflammatory cytokines in elderly Chinese subjects with MCI, *Sci. Rep.* 6 (2016) 1–11. <https://doi.org/10.1038/srep37486>.

- [10] J.B. Wallingford, L.A. Niswander, G.M. Shaw, R.H. Finnell, The Continuing Challenge of Understanding, Preventing, and Treating Neural Tube Defects, *Science* (80). 339 (2013) 1222002–1222002. <https://doi.org/10.1126/science.1222002>.
- [11] V. Kancherla, K. Wagh, Q. Johnson, G.P. Oakley, A 2017 global update on folic acid-preventable spina bifida and anencephaly, *Birth Defects Res.* 110 (2018) 1139–1147. <https://doi.org/10.1002/bdr2.1366>.
- [12] M.A. Hofsäss, J. de Souza, N.M. Silva-Barcellos, K.R. Bellavinha, B. Abrahamsson, R. Cristofolletti, D.W. Groot, A. Parr, P. Langguth, J.E. Polli, V.P. Shah, T. Tajiri, M.U. Mehta, J.B. Dressman, *Biowaiver Monographs for Immediate-Release Solid Oral Dosage Forms: Folic Acid*, *J. Pharm. Sci.* 106 (2017) 3421–3430. <https://doi.org/10.1016/j.xphs.2017.08.007>.
- [13] UNICEF Supply Division, Iron, folic acid and combined iron and folic acid tablets – technical bulletin, 2018. <https://www.unicef.org/supply/documents/iron-folic-acid-and-combined-iron-and-folic-acid-tablets-technical-bulletin>.
- [14] C. Pagano, L. Perioli, L. Latterini, M. Nocchetti, M.R. Ceccarini, M. Marani, D. Ramella, M. Ricci, Folic acid-layered double hydroxides hybrids in skin formulations: Technological, photochemical and in vitro cytotoxicity on human keratinocytes and fibroblasts, *Appl. Clay Sci.* 168 (2019) 382–395. <https://doi.org/10.1016/j.clay.2018.12.009>.
- [15] M. Scaranti, E. Cojocaru, S. Banerjee, U. Banerji, Exploiting the folate receptor α in oncology, *Nat. Rev. Clin. Oncol.* 17 (2020) 349–359. <https://doi.org/10.1038/s41571-020-0339-5>.
- [16] B. Farran, R.C. Montenegro, P. Kasa, E. Pavitra, Y.S. Huh, Y.-K. Han, M.A. Kamal, G.P. Nagaraju, G.S. Rama Raju, Folate-conjugated nanovehicles: Strategies for cancer therapy, *Mater. Sci. Eng. C.* 107 (2020) 110341. <https://doi.org/10.1016/j.msec.2019.110341>.
- [17] E. Nogueira, A.C. Gomes, A. Preto, A. Cavaco-Paulo, Folate-targeted nanoparticles for rheumatoid arthritis therapy, *Nanomedicine Nanotechnology, Biol. Med.* 12 (2016) 1113–1126. <https://doi.org/10.1016/j.nano.2015.12.365>.
- [18] P.S. Kharkar, G. Soni, V. Rathod, S. Shetty, M.K. Gupta, K.S. Yadav, An outlook on procedures of conjugating folate to (co)polymers and drugs for effective cancer targeting, *Drug Dev. Res.* 81 (2020) 823–836. <https://doi.org/10.1002/ddr.21698>.
- [19] M.G.A. El-Wahed, M.S. Refat, S.M. El-Megharbel, Synthesis, spectroscopic and thermal characterization of some transition metal complexes of folic acid, *Spectrochim. Acta - Part A Mol. Biomol. Spectrosc.* 70 (2008) 916–922. <https://doi.org/10.1016/j.saa.2007.10.008>.
- [20] F. Ragone, G.T. Ruiz, O.E. Piro, G.A. Echeverría, F.M. Cabrerizo, G. Petroselli, R. Erra-Balsells, K. Hiraoka, F.S. García Einschlag, E. Wolcan, Water-Soluble (Pterin)rhenium(I) Complex: Synthesis, Structural Characterization, and Two Reversible Protonation-Deprotonation Behavior in Aqueous Solutions, *Eur. J. Inorg. Chem.* 2012 (2012) 4801–4810. <https://doi.org/10.1002/ejic.201200681>.
- [21] P.R. Dametto, B. Ambrozini, F.J. Caires, V.P. Franzini, M. Ionashiro, Synthesis, characterization and thermal behaviour of solid-state compounds of folates with some bivalent transition metals ions, *J. Therm. Anal. Calorim.* 115 (2014) 161–166. <https://doi.org/10.1007/s10973-013-3276-z>.

- [22] A.M. Naglah, M.S. Refat, M.A. Al-Omar, M.A. Bhat, H.M. Alkahtani, A.S. Al-Wasidi, Synthesis of a vanadyl (IV) folate complex for the treatment of diabetes: Spectroscopic, structural, and biological characterization, *Drug Des. Devel. Ther.* 13 (2019) 1409–1420. <https://doi.org/10.2147/DDDT.S190310>.
- [23] A.A. El-Habeeb, Novel Gallium(III), Germanium(IV), and Hafnium(IV) Folate Complexes and Their Spectroscopic, Thermal Decomposition, Morphological, and Biological Characteristics, *Bioinorg. Chem. Appl.* 2020 (2020) 1–12. <https://doi.org/10.1155/2020/6678688>.
- [24] C. He, M. Heidari Majd, F. Shiri, S. Shahraki, Palladium and platinum complexes of folic acid as new drug delivery systems for treatment of breast cancer cells, *J. Mol. Struct.* 1229 (2021) 129806. <https://doi.org/10.1016/j.molstruc.2020.129806>.
- [25] S. Bonazzi, M.M. DeMoraes, G. Gottarelli, P. Mariani, G.P. Spada, Self-Assembly and Liquid Crystal Formation of Folic Acid Salts, *Angew. Chemie Int. Ed. English.* 32 (1993) 248–250. <https://doi.org/10.1002/anie.199302481>.
- [26] P. Xing, X. Chu, M. Ma, S. Li, A. Hao, Supramolecular gel from folic acid with multiple responsiveness, rapid self-recovery and orthogonal self-Assemblies, *Phys. Chem. Chem. Phys.* 16 (2014) 8346–8359. <https://doi.org/10.1039/c4cp00367e>.
- [27] X. Wang, J. Sun, T. Li, Z. Song, D. Wu, B. Zhao, K. Xiang, W. Ai, X.Z. Fu, J.L. Luo, Folic acid self-assembly synthesis of ultrathin N-doped carbon nanosheets with single-atom metal catalysts, *Energy Storage Mater.* 36 (2021) 409–416. <https://doi.org/10.1016/j.ensm.2021.01.024>.
- [28] H. Liu, Z. Li, Y. Sun, X. Geng, Y. Hu, H. Meng, J. Ge, L. Qu, Synthesis of Luminescent Carbon Dots with Ultrahigh Quantum Yield and Inherent Folate Receptor-Positive Cancer Cell Targetability, *Sci. Rep.* 8 (2018) 1086. <https://doi.org/10.1038/s41598-018-19373-3>.
- [29] S. Gawęda, G. Stochel, K. Szaciłowski, Bioinspired nanodevice based on the folic acid/titanium dioxide system, *Chem. - An Asian J.* 2 (2007) 580–590. <https://doi.org/10.1002/asia.200700025>.
- [30] A. Kokaislová, T. Helešicová, M. Ončák, P. Matějka, Spectroscopic studies of folic acid adsorbed on various metal substrates: does the type of substrate play an essential role in temperature dependence of spectral features?, *J. Raman Spectrosc.* 45 (2014) 750–757. <https://doi.org/10.1002/jrs.4557>.
- [31] J.J. Castillo, T. Rindzevicius, K. Wu, C.E. Rozo, M.S. Schmidt, A. Boisen, Silver-capped silicon nanopillar platforms for adsorption studies of folic acid using surface enhanced Raman spectroscopy and density functional theory, *J. Raman Spectrosc.* 46 (2015) 1087–1094. <https://doi.org/10.1002/jrs.4734>.
- [32] J.J. Castillo, T. Rindzevicius, C.E. Rozo, A. Boisen, Adsorption and Vibrational Study of Folic Acid on Gold Nanopillar Structures Using Surface-Enhanced Raman Scattering Spectroscopy, *Nanomater. Nanotechnol.* 5 (2015) 29. <https://doi.org/10.5772/61606>.
- [33] R.A.R. Teixeira, F.R.A. Lima, P.C. Silva, L.A.S. Costa, A.C. Sant’Ana, Tracking chemical interactions of folic acid on gold surface by SERS spectroscopy, *Spectrochim. Acta Part A Mol. Biomol. Spectrosc.* 223 (2019) 117305. <https://doi.org/10.1016/j.saa.2019.117305>.

- [34] M. Baibarac, I. Smaranda, A. Nila, C. Serbschi, Optical properties of folic acid in phosphate buffer solutions: the influence of pH and UV irradiation on the UV-VIS absorption spectra and photoluminescence, *Sci. Rep.* 9 (2019) 14278. <https://doi.org/10.1038/s41598-019-50721-z>.
- [35] A.M. Abramova, A.A. Kokorina, O.A. Sindeeva, F. Jolibois, P. Puech, G.B. Sukhorukov, I.Y. Goryacheva, A. V. Sapelkin, Molecular nature of breakdown of the folic acid under hydrothermal treatment: a combined experimental and DFT study, *Sci. Rep.* 10 (2020) 1–6. <https://doi.org/10.1038/s41598-020-76311-y>.
- [36] K. Wysoczanska, G. Sadowski, E.A. Macedo, C. Held, Toward Thermodynamic Predictions of Aqueous Vitamin Solubility: An Activity Coefficient-Based Approach, *Ind. Eng. Chem. Res.* 58 (2019) 7362–7369. <https://doi.org/10.1021/acs.iecr.9b00742>.
- [37] I.R. Younis, M.K. Stamatakis, P.S. Callery, P.J. Meyer-Stout, Influence of pH on the dissolution of folic acid supplements, *Int. J. Pharm.* 367 (2009) 97–102. <https://doi.org/10.1016/j.ijpharm.2008.09.028>.
- [38] G. Gocheva, N. Petkov, A. Garcia Luri, S. Iliev, N. Ivanova, J. Petrova, Y. Mitrev, G. Madjarova, A. Ivanova, Tautomerism in folic acid: Combined molecular modelling and NMR study, *J. Mol. Liq.* 292 (2019) 111392. <https://doi.org/10.1016/j.molliq.2019.111392>.
- [39] C. Chen, J. Ke, X.E. Zhou, W. Yi, J.S. Brunzelle, J. Li, E.-L. Yong, H.E. Xu, K. Melcher, Structural basis for molecular recognition of folic acid by folate receptors, *Nature.* 500 (2013) 486–489. <https://doi.org/10.1038/nature12327>.
- [40] A. Singh, N. Deshpande, N. Pramanik, S. Jhunjhunwala, A. Rangarajan, H.S. Atreya, Optimized peptide based inhibitors targeting the dihydrofolate reductase pathway in cancer, *Sci. Rep.* 8 (2018) 3190. <https://doi.org/10.1038/s41598-018-21435-5>.
- [41] D. Braga, L. Chelazzi, F. Grepioni, L. Maschio, S. Nanna, P. Taddei, Folic Acid in the Solid State: A Synergistic Computational, Spectroscopic, and Structural Approach, *Cryst. Growth Des.* 16 (2016) 2218–2224. <https://doi.org/10.1021/acs.cgd.6b00043>.
- [42] V.R.R. Cunha, V.R.L. Constantino, R.A. Ando, Raman spectroscopy and DFT calculations of para-coumaric acid and its deprotonated species, *Vib. Spectrosc.* 58 (2012) 139–145. <https://doi.org/10.1016/j.vibspec.2011.12.007>.
- [43] V.R.R. Cunha, C.M.S. Izumi, P.A.D. Petersen, A. Magalhães, M.L.A. Temperini, H.M. Petrilli, V.R.L. Constantino, Mefenamic acid anti-inflammatory drug: Probing its polymorphs by vibrational (IR and Raman) and solid-state NMR spectroscopies, *J. Phys. Chem. B.* 118 (2014) 4333–4344. <https://doi.org/10.1021/jp500988k>.
- [44] V.R.R. Cunha, P.A.D. Petersen, M.B. Gonçalves, H.M. Petrilli, C. Taviot-Gueho, F. Leroux, M.L.A. Temperini, V.R.L. Constantino, Structural, spectroscopic (NMR, IR, and Raman), and DFT investigation of the self-assembled nanostructure of pravastatin-LDH (layered double hydroxides) systems, *Chem. Mater.* 24 (2012) 1415–1425. <https://doi.org/10.1021/cm202953y>.
- [45] A.D. Becke, Density-functional thermochemistry. III. The role of exact exchange, *J. Chem. Phys.* 98 (1993) 5648–5652. <https://doi.org/10.1063/1.464913>.

- [46] A.D. Becke, Density-functional thermochemistry. IV. A new dynamical correlation functional and implications for exact-exchange mixing, *J. Chem. Phys.* 104 (1996) 1040–1046. <https://doi.org/10.1063/1.470829>.
- [47] M.J. Frisch, G.W. Trucks, H.B. Schlegel, G.E. Scuseria, E. Al, Gaussian 16, Revision B.01, (2009).
- [48] D. Mastropaolo, A. Camerman, N. Camerman, Folic acid: crystal structure and implications for enzyme binding, *Science* (80). 210 (1980) 334–336. <https://doi.org/10.1126/science.7423195>.
- [49] M.P. Andersson, P. Uvdal, New Scale Factors for Harmonic Vibrational Frequencies Using the B3LYP Density Functional Method with the Triple- ζ Basis Set 6-311+G(d,p), *J. Phys. Chem. A.* 109 (2005) 2937–2941. <https://doi.org/10.1021/jp045733a>.
- [50] G. Reibnegger, QT-AIM analysis of neutral pterin and its anionic and cationic forms, *Pteridines.* 25 (2014) 41–48. <https://doi.org/10.1515/pteridines-2014-0005>.
- [51] K. Momma, F. Izumi, VESTA 3 for three-dimensional visualization of crystal, volumetric and morphology data, *J. Appl. Crystallogr.* 44 (2011) 1272–1276. <https://doi.org/10.1107/S0021889811038970>.
- [52] J.A. Kaduk, C.E. Crowder, K. Zhong, Crystal structure of folic acid dihydrate, $C_{29}H_{29}N_2O_6(H_2O)_2$, *Powder Diffr.* 30 (2015) 52–56. <https://doi.org/10.1017/S0885715614000815>.
- [53] R. Atluri, M.N. Iqbal, Z. Bacsik, N. Hedin, L.A. Villaescusa, A.E. Garcia-Bennett, Self-Assembly Mechanism of Folate-Templated Mesoporous Silica, *Langmuir.* 29 (2013) 12003–12012. <https://doi.org/10.1021/la401532j>.
- [54] O. Ostroverkhova, Organic Optoelectronic Materials: Mechanisms and Applications, *Chem. Rev.* 116 (2016) 13279–13412. <https://doi.org/10.1021/acs.chemrev.6b00127>.
- [55] N.J. Hestand, F.C. Spano, Expanded Theory of H- and J-Molecular Aggregates: The Effects of Vibronic Coupling and Intermolecular Charge Transfer, *Chem. Rev.* 118 (2018) 7069–7163. <https://doi.org/10.1021/acs.chemrev.7b00581>.
- [56] G. Li, D. Magana, R.B. Dyer, Photoinduced electron transfer in folic acid investigated by ultrafast infrared spectroscopy, *J. Phys. Chem. B.* 116 (2012) 3467–3475. <https://doi.org/10.1021/jp300392a>.
- [57] A. Tyagi, A. Penzkofer, Fluorescence spectroscopic behaviour of folic acid, *Chem. Phys.* 367 (2010) 83–92. <https://doi.org/10.1016/j.chemphys.2009.10.026>.
- [58] H.B. Fu, J.N. Yao, Size effects on the optical properties of organic nanoparticles, *J. Am. Chem. Soc.* 123 (2001) 1434–1439. <https://doi.org/10.1021/ja0026298>.
- [59] A. Tiwari, B. Raj, *Reactions and Mechanisms in Thermal Analysis of Advanced Materials*, 1st ed., Wiley-Scrivener, 2015. <https://doi.org/10.1002/9781119117711>
- [60] A. Vora, A. Riga, K. Alexander, Processes to Identify the Degradation Mechanism of a Solid which Appears to Undergo a Complex Reaction: Folic Acid, *Instrum. Sci. Technol.* 30 (2002) 193–203. <https://doi.org/10.1081/CI-120003899>.

- [61] C. Bonechi, A. Donati, R. Lampariello, S. Martini, M.P. Picchi, M. Ricci, C. Rossi, Solution structure of folic acid: Molecular mechanics and NMR investigation, *Spectrochim. Acta - Part A Mol. Biomol. Spectrosc.* 60 (2004) 1411–1419. <https://doi.org/10.1016/j.saa.2003.08.007>.
- [62] N.B. Colthup, L.H. Daly, S.E. Wiberley, *Introduction to Infrared and Raman Spectroscopy*, 3rd ed., Academic Press, 1990.
- [63] B. Profantová, V. Profant, V. Zíma, V. Kopecký, L. Bednářová, C. Zentz, V. Baumruk, P.Y. Turpin, J. Štěpánek, Protonation effect of tyrosine in a segment of the SRF transcription factor: A combined optical spectroscopy, molecular dynamics, and density functional theory calculation study, *J. Phys. Chem. B.* 117 (2013) 16086–16095. <https://doi.org/10.1021/jp4099864>.
- [64] K.B. Beć, J. Grabska, M.A. Czarniecki, C.W. Huck, M.J. Wójcik, T. Nakajima, Y. Ozaki, IR Spectra of Crystalline Nucleobases: Combination of Periodic Harmonic Calculations with Anharmonic Corrections Based on Finite Models, *J. Phys. Chem. B.* 123 (2019) 10001–10013. <https://doi.org/10.1021/acs.jpcc.9b06285>.
- [65] A. Barth, Infrared spectroscopy of proteins, *Biochim. Biophys. Acta - Bioenerg.* 1767 (2007) 1073–1101. <https://doi.org/10.1016/j.bbabi.2007.06.004>.
- [66] B. Sjöberg, S. Foley, B. Cardey, M. Enescu, An experimental and theoretical study of the amino acid side chain Raman bands in proteins, *Spectrochim. Acta - Part A Mol. Biomol. Spectrosc.* 128 (2014) 300–311. <https://doi.org/10.1016/j.saa.2014.02.080>.
- [67] L. Li, T. Cai, Z. Wang, Z. Zhou, Y. Geng, T. Sun, Study on molecular structure, spectroscopic investigation (IR, Raman and NMR), vibrational assignments and HOMO–LUMO analysis of L-sodium folinate using DFT: A combined experimental and quantum chemical approach, *Spectrochim. Acta Part A Mol. Biomol. Spectrosc.* 120 (2014) 106–118. <https://doi.org/10.1016/j.saa.2013.10.011>.
- [68] C.K. Nandi, M.K. Hazra, T. Chakraborty, Vibrational coupling in carboxylic acid dimers, *J. Chem. Phys.* 123 (2005) 124310. <https://doi.org/10.1063/1.2039084>.
- [69] R.P. Lopes, M.P.M. Marques, R. Valero, J. Tomkinson, L.A.E.B. de Carvalho, Guanine: A Combined Study Using Vibrational Spectroscopy and Theoretical Methods, *Spectrosc. An Int. J.* 27 (2012) 273–292. <https://doi.org/10.1155/2012/168286>.
- [70] J.J. Castillo, C.E. Roza, L. Bertel, T. Rindzevicius, S.C. Mendez-Sanchez, F.M. Ortega, A. Boisen, Orientation of Pterin-6-Carboxylic Acid on Gold Capped Silicon Nanopillars Platforms: Surface Enhanced Raman Spectroscopy and Density Functional Theory Studies, *J. Braz. Chem. Soc.* 2 (2015) 123–125. <https://doi.org/10.5935/0103-5053.20150352>.
- [71] R. Świsłocka, M. Samsonowicz, E. Regulska, W. Lewandowski, Molecular structure of 4-aminobenzoic acid salts with alkali metals, *J. Mol. Struct.* 792–793 (2006) 227–238. <https://doi.org/10.1016/j.molstruc.2005.10.060>.
- [72] P. Ilich, C.F. Hemann, R. Hille, Molecular Vibrations of Solvated Uracil. Ab Initio Reaction Field Calculations and Experiment, *J. Phys. Chem. B.* 101 (1997) 10923–10938. <https://doi.org/10.1021/jp9706285>.

- [73] A. Andrejeva, A.M. Gardner, W.D. Tuttle, T.G. Wright, Consistent assignment of the vibrations of symmetric and asymmetric para-disubstituted benzene molecules, *J. Mol. Spectrosc.* 321 (2016) 28–49. <https://doi.org/10.1016/j.jms.2016.02.004>.
- [74] B. Hernández, Y.-M. Coïc, F. Pflüger, S.G. Kruglik, M. Ghomi, All characteristic Raman markers of tyrosine and tyrosinate originate from phenol ring fundamental vibrations, *J. Raman Spectrosc.* 47 (2016) 210–220. <https://doi.org/10.1002/jrs.4776>.
- [75] M. Ghosh, S. Gayen, K.K. Dey, An atomic resolution description of folic acid using solid state NMR measurements, *RSC Adv.* 10 (2020) 24973–24984. <https://doi.org/10.1039/D0RA03772A>.
- [76] H.T.A. Cheung, B. Birdsall, T.A. Frenkiel, D.D. Chau, J. Feeney, Carbon-13 NMR determination of the tautomeric and ionization states of folate in its complexes with *Lactobacillus casei* dihydrofolate reductase, *Biochemistry.* 32 (1993) 6846–6854. <https://doi.org/10.1021/bi00078a007>.

16/02/2023, 13:32 E-mail de Universidade de São Paulo - Fwd: CARBON-D-23-00460 - Confirming your submission to Carbon - [EMID:dd6d4...



Vagner Roberto Magri <vrmagri@usp.br>

Fwd: CARBON-D-23-00460 - Confirming your submission to Carbon - [EMID:dd6d400815cb523c]

Vera Regina Leopoldo Constantino <vrconst@iq.usp.br>
Para: Vagner Magri <vrmagri@usp.br>

16 de fevereiro de 2023 às 13:31

----- Forwarded message -----

De: **CARBON an International journal** <em@editorialmanager.com>
Date: qui., 16 de fev. de 2023 às 13:29
Subject: CARBON-D-23-00460 - Confirming your submission to Carbon - [EMID:dd6d400815cb523c]
To: Vera Regina Leopoldo Constantino <vrconst@iq.usp.br>



Pyrolysis mechanism of Folic Acid: identification of gaseous products and characterization of N-doped carbon materials
Research Paper

Dear Vera,

Your submission entitled "Pyrolysis mechanism of Folic Acid: identification of gaseous products and characterization of N-doped carbon materials" has been received by Carbon. It has been assigned the following manuscript number: CARBON-D-23-00460.

You may check on the progress of your paper by logging on to the Editorial Manager as an author. The URL is <https://www.editorialmanager.com/carbon/>.

Your manuscript will be given a reference number once an Editor has been assigned.

Thank you for submitting your work to this journal.

Kind regards,

Editorial Manager
Carbon
Impact Factor: 11.307

This journal uses the Elsevier Article Transfer Service. This means that if an editor feels your manuscript is more suitable for an alternative journal, then you might be asked to consider transferring the manuscript to such a journal. The recommendation might be provided by a Journal Editor, a dedicated Scientific Managing Editor, a tool assisted recommendation, or a combination. For more details see the journal guide for authors.

#AU_CARBON#

To ensure this email reaches the intended recipient, please do not delete the above code



<https://mail.google.com/mail/u/2/?ik=ff8ee87300&view=pt&search=all&permmsgid=msg-f%3A1758005942903470972&simpl=msg-f%3A1758005...> 1/2

Pyrolysis mechanism of Folic Acid: identification of gaseous products and characterization of N-doped carbon materials

Vagner R. Magri^a, Caroline S. de Matos^a, Michele A. Rocha^a, Christine Taviot-Gueho^{bc} and Vera R.L. Constantino^{*a}

^a*Departamento de Química Fundamental, Instituto de Química, Universidade de São Paulo, Av. Lineu Prestes 748, CEP 05508-000, São Paulo, SP, Brazil.*

^b*Université Clermont Auvergne, Université Blaise Pascal, Institut de Chimie de Clermont-Ferrand, BP 10448, F-63000 Clermont-Ferrand, France*

^c*CNRS, UMR 6296, ICCF, F-63178 Aubiere, France*

** Corresponding author.*

E-mail address: vrlconst@iq.usp.br (V.R.L.C.)

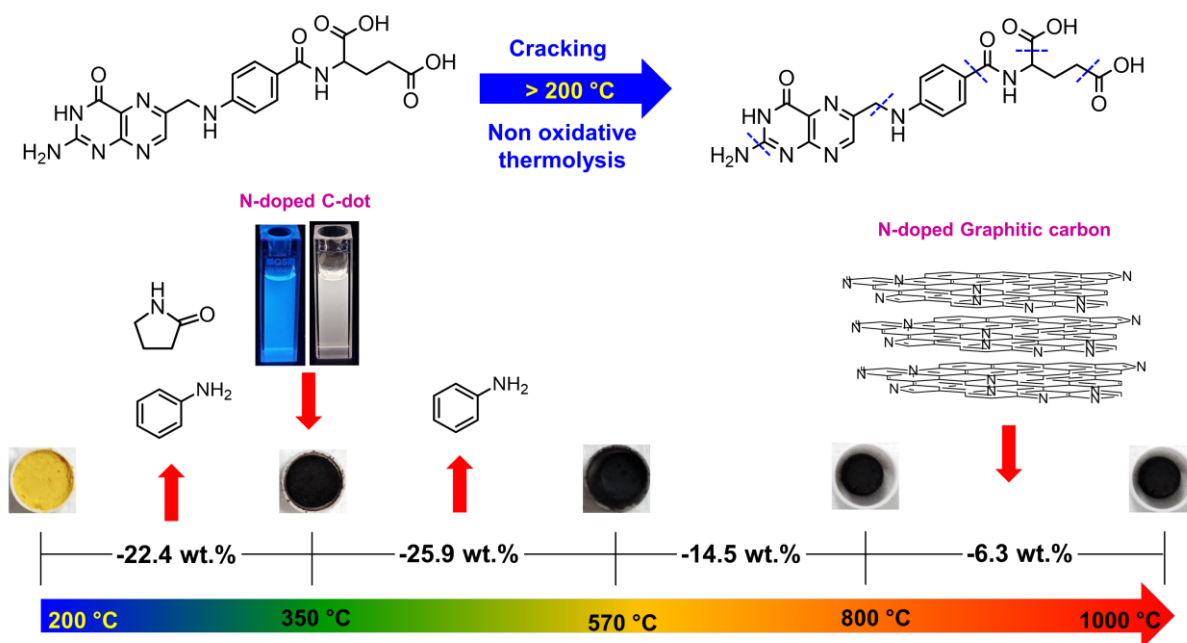
KEYWORDS

Folic Acid; vitamin B9; sodium folate salts; thermal analysis; pyrolysis; TG-FTIR; TG-MS; N-doped carbon materials. carbon dots; graphitic carbon.

HIGHLIGHTS

1. Elucidation of pyrolytic pathways of Folic Acid
2. Simultaneous Evolved Gas Analysis during the pyrolysis process of Folic Acid
3. Synthesis of N-doped graphene-like materials from Folic Acid pyrolysis

GRAPHICAL ABSTRACT



Abstract: Folic acid (FA) is a suitable source for producing different types of N-doped carbon materials by pyrolyzes, such as Carbon dots (C-dots) and graphitic carbon. However, the pyrolysis mechanism of FA is still unknown, especially above 350 °C, which hampers the smart design of tailor-made carbon materials by a one-pot route. In this work, the FA decomposition mechanism under nitrogen gas was investigated by simultaneous thermogravimetric analysis and differential scanning calorimetry (TGA/DSC) and by the analysis of the released gaseous/volatile products by TGA coupled with infrared spectroscopy and mass spectrometry. Based on thermal analysis data, FA was pyrolyzed in a furnace at 350, 430, 570, 800, and 1000 °C and the products were analysed by X-ray diffraction (XRD), vibrational spectroscopy (infrared and Raman), and X-ray photoelectron spectroscopy; *in-situ* high temperature XRD experiments were also performed. The formation of carbonaceous material was initiated between 200-350 °C through polymerization/condensation reactions, and it was marked by the release of 2-pyrrolidone and aniline. The carbonization was enhanced above 350 °C through denitrogenation (*e.g.*, NH₃, HNCO, and HCN release) and deoxygenation (*i.e.*, CO and CO₂ loss) reactions, providing N-graphite structures. The ideal temperature range for C-dots synthesis was between 200-350 °C, whereas N-doped graphitic carbon was obtained above 800 °C. The unprecedented data about the thermal decomposition of the low-cost FA allow optimizing the synthesis of new N-doped carbon materials suitable for applications in adsorption, sensing, catalysis, and energy storage.

1. Introduction

N-doped carbon materials present plenty of potential applications that cover the development of electronic devices and catalysts (or catalyst supports), adsorbents, sensors, and biocompatible materials [1–3]. Due to the electronic configuration of the nitrogen atom and its higher electronegativity compared to the carbon atom, the N-doping of the carbonaceous framework can either change or improve the reactivity and electronic properties of referred materials [1–3]. These effects occur because the doping changes the electronic band structure of carbonaceous material, which can increase its charge transfer efficiency (n-type conductivity), confer acid-base character, create sites of coordination/adsorption, and enhance its wettability, catalytic activity or luminescence quantum yield [1–3].

Bottom-up methods involving pyrolysis of small molecules, polymers, and biomass are extensively applied for the synthesis of N-doped carbon nanomaterials [1–3]. Pyrolysis is a cheap and scalable method that can be used to synthesize different forms or shapes of carbon particles, such as C-dots (zero-dimensional form, 0D) [3], carbon nanotubes (one-dimensional form, 1D) [4], graphitic carbon (two-dimensional form, 2D) and hierarchical nanostructures with three-dimensional (3D) shapes [5–8]. The structure, composition and properties of produced materials are strongly dependent on the temperature value of the synthesis and the nature of precursors (source of carbon) [1–3,5,9,10].

Folic acid (FA, vitamin B9), an inexpensive and multifunctional molecule, is a profitable precursor of different N-doped carbon-based nanomaterials with different shapes [4–9,11–14]. Composed of three moieties (**Fig. 1**), FA molecule works as an “all in one” precursor for N-doped carbon materials because it serves as Csp^2 building block (aromatic rings) and N source (22.2 wt.% per chemical formula), ruling out the demand of an additional N-containing molecule, and presents coordination/chelation sites for metal ions binding [6–8]. In addition, FA molecules can form supramolecular structures (*e.g.*, ribbons, tubes and layers), throughout

H-bonds and π - π stacking, contributing to the formation of nanostructured carbon materials during the carbonization process [4,6,8].

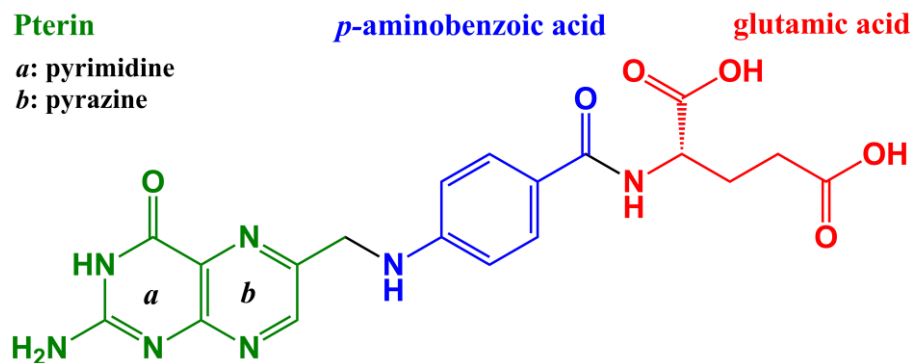


Figure 1. Molecular structure of Folic Acid (C₁₉H₁₉N₇O₆).

N-doped carbonaceous materials with high surface area and electrochemical properties have been obtained by the direct or template-assisted carbonization of FA associated or not to transition metals (*e.g.*, Ni²⁺ and Co²⁺) [4–9]. The potential applications of such materials have been explored in the development of supercapacitors [9], lithium–sulphur batteries [8], and electrocatalysts for O₂ reduction [5–7] or CO₂ reduction [4] reactions. The temperature value of pyrolysis strongly influences the composition (*e.g.*, nitrogen content and positioning: N-pyridine, N-pyrrole and N-graphite, etc) and properties (*i.e.*, specific surface area, porosity and capacitive performance) of such N-doped carbon materials [4,5,9]. FA is also applied as a precursor of C-dots, the luminescent allotropes of carbon with particle size less than 10 nm [3,12–14]. C-dots prepared by hydrothermal carbonization of FA presented higher luminescent quantum yield, solubility in water, thermal and photostability than the pristine precursor, and can act as cancer targeting and bioimaging agents [12–14]. So far, no work has been reported using pyrolysis of FA to produce C-dots, despite the feasibility and scalability of the method.

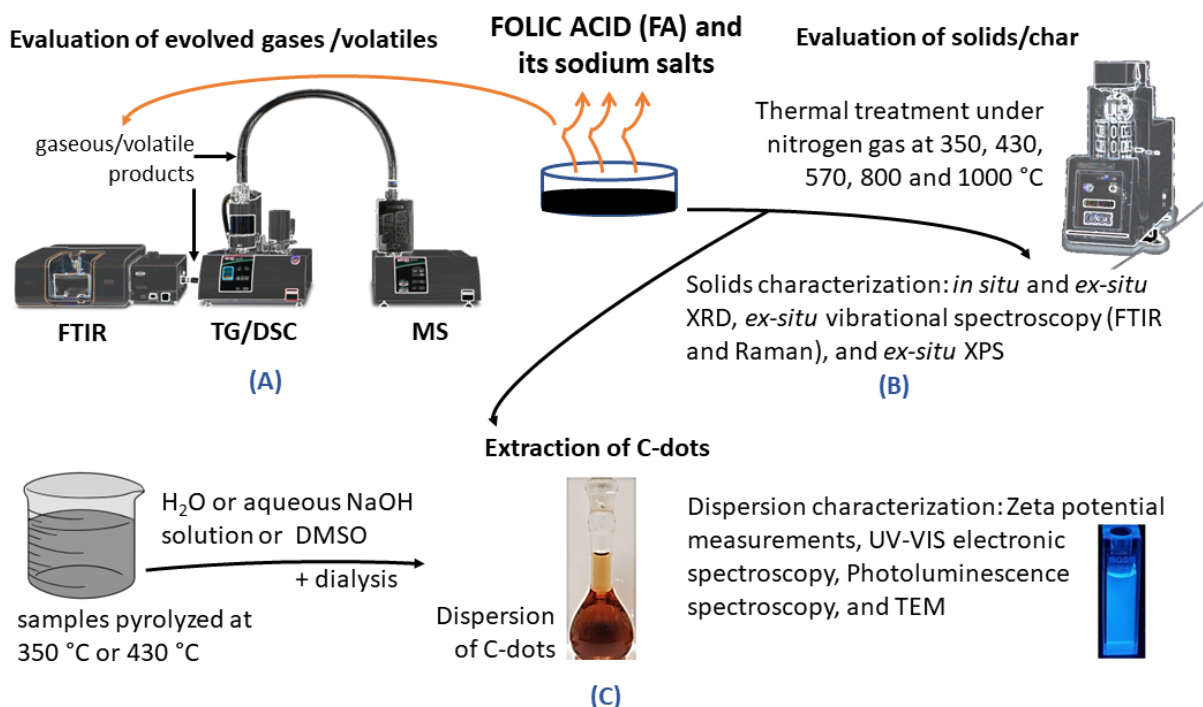
The knowledge about pyrolysis pathways of FA could be helpful in understanding the formation of carbonaceous structure and establish strategies to achieve a smart design of related N-doped carbon materials. Although the thermal oxidative stability of FA [15], folate salts [15–

17], or its metal complexes [16,18] has been well discussed in the literature, the mechanism of FA pyrolysis has been neglected. To the best of our knowledge, only Vora et al. [19] suggested an initial mechanism of FA decomposition by alloying thermal analysis under N₂ atmosphere as well as *ex-situ* X-ray diffractometry and infrared spectroscopic characterization of the solid products. However, the heating rate used in thermal analysis (10 °C min⁻¹) was not the same as used in the preparation of FA pyrolyzed samples (2 °C min⁻¹) [19], and the evaluated temperature range between 140 and 349°C is low in comparison of the common values used to produce graphitic carbon [4–9].

In this work, the FA pyrolysis process was detailed and evaluated up to 1000 °C by simultaneous thermogravimetric analysis and differential scanning calorimetry (TG/DSC), under N₂ atmosphere and heating rate of 10 °C min⁻¹, combined with evolved gas analysis (EGA) performed by coupled mass spectrometry (TG-MS) and Fourier transform infrared spectroscopy (TG-FTIR), as well as *in-situ* high-temperature X-ray diffraction (XRD) experiments. The structure and composition of solid products obtained by pyrolysis (referred as *char* in this text) were further characterized *ex-situ* by XRD, X-ray photoelectron spectroscopy (XPS), FTIR and Raman spectroscopies. The results obtained for pyrolyzed FA were also compared with those ones from di- (Na₂HFol) and trisodium folate (Na₃Fol) salts to evaluate precursors for the production of N-doped carbon materials. The preparation of N-doped C-dots from the pyrolysis of FA, Na₂HFol and Na₃Fol was also evaluated. Consequently, insights about the decomposition mechanism of FA and the structural evolution of the carbonaceous product were discussed. Furthermore, appropriate temperature ranges were identified to produce N-doped carbon materials with different structures and compositions. This work can be helpful to speed up the development of new N-doped carbon-based materials produced from the pyrolysis of FA, aiming at applications in adsorption, sensing, catalysis, and energy storage devices, for instance.

2. Experimental

Information about the chemicals used in this work are described in Supplementary Material (SM) file. **Scheme 1** shows the main experimental procedures performed in this work, which details will be mentioned ahead.



Scheme 1. Experiments related to the pyrolysis process of FA and its sodium salts are divided in three main procedures: (A) identification of main gases/volatiles by TGA-FTIR and TGA-MS data; (B) recovery of solid samples after pyrolysis at five temperature values and their physicochemical characterization; and (C) extraction of N-doped carbon materials named C-dots and characterization of its dispersions.

2.1. Thermal behaviour of Folic Acid

TGA/DSC analysis and the EGA by coupled infrared spectroscopy (TGA-FTIR) and mass spectrometry (TGA-MS) were conducted on a Netzsch thermoanalyzer, model STA 409 PC Luxx. The thermoanalyzer was coupled to a FTIR spectrometer Bruker, Tensor 27 model (MCT detector cooled with liquid N₂; 4400-650 cm⁻¹ region and 4 cm⁻¹ of resolution), and to a QMS 403C Aëolos quadrupole mass spectrometer. The evolved gases enter in the mass

spectrometer and FTIR spectrometer at 300 °C. The thermal data were recorded up to 1000 °C, under dynamic N₂ atmosphere with a flow rate of 50 mL·min⁻¹, heating rate of 10 °C·min⁻¹ and employing an alumina crucible. The FTIR spectra of gaseous/volatile products generated during pyrolysis were compared with their reference molecular gaseous spectra (**Fig. S1**) available online by National Institute of Standards and Technology (NIST;[20]) and HITRAN ([21]) databases.

2.2. Precursors pyrolysis

Based on TGA/DSC and EGA results, the FA precursor were pyrolyzed in a set of temperatures values: 350, 430, 570, 800, and 1000 °C. For comparison purposes, Na₂HFol and Na₃Fol were pyrolyzed at 430 and 570 °C. Pyrolysis was conducted on a Shimadzu TGA-50 furnace under a N₂ flow of 50 mL·min⁻¹ and a heating rate of 10 °C·min⁻¹, using alumina crucibles. The furnace presents an updraft design, in which the gas flows from up to down, and it is coupled to a cooler system turned on at the end of the process. The obtained products were stored in a desiccator containing silica gel under reduced pressure until the characterization step.

2.3. C-dots extraction

The extraction of C-dots from samples pyrolyzed at 350 °C or 430 °C was performed with the following media: deionized water, aqueous NaOH solution (0.1 mol L⁻¹), and DMSO. Initially, 0.25 g L⁻¹ suspensions were prepared, and the systems were kept under ultrasonication (Limp Sonic LS-3D ultrasonic equipment; 70 W and 40 kHz) for 30 minutes. Then, the systems were left standing for 24 h and submitted for more 30 minutes of ultrasonication. After that, the supernatant was passed through 0.02 µm membrane pores filter (Whatman[®] Anotop[®] 10 syringe filter) to isolate the C-dots. Samples extracted with NaOH solution were further

dialyzed using a cellulose tubing (cut off 2 kDa; Sigma-Aldrich) for 4 h changing the water every 30 minutes until the base excess was removed, monitored with phenolphthalein as shown in **Fig. S2**. The samples obtained from heated Na₂HFol and Na₃Fol under a nitrogen atmosphere were also dialyzed using the same procedure.

2.4. Apparatus

X-ray diffraction (XRD) patterns of char samples were recorded on a Bruker diffractometer model D8 DISCOVER, equipped with Nickel-filtered CuK α radiation (0.15418 nm), operating at 40 kV and 30 mA, sample rotating at 15 rpm, and with scan step of 0.05°, scan speed of 0.05° s⁻¹ in the 4-60° range. For the *in-situ* monitoring of structural changes of FA and its sodium salts upon pyrolysis, a high-temperature chamber (Anton Paar HTK-16) was installed on the X'Pert-pro diffractometer, enabling *in-situ* high-temperature XRD measurements under a controlled atmosphere. Measurements were carried out in a dynamic nitrogen atmosphere (24 mL min⁻¹) in the temperature range 25-800 °C; the heating rate was 10 °C min⁻¹, after an equilibration atmosphere time of 2 h. The diffracted beam was recorded over a range of 2-70° (2 θ) with a step size of 0.0167° (2 θ) and counting time 100 s/step.

Fourier transform infrared (FTIR) spectra were recorded on an Agilent spectrometer, model Cary 630 FTIR, in the 4000–650 cm⁻¹ range with a resolution of 4 cm⁻¹, using a ZnSe multibounce attenuated total diffuse reflectance (ATR) in transmittance mode. Raman spectra were recorded in a Renishaw inVia instrument coupled to a confocal Leica microscope and a CCD detector, using Nd³⁺/YAG laser with excitation radiation of 532 nm and in the 3200–500 cm⁻¹ range. The Raman spectra were baseline corrected and deconvoluted by Gaussian fitting [22].

Scanning electron microscopy (SEM) images were acquired in a Quanta 650 FEG microscope operating at 5 kV and using an EDT detector. Previously, the samples were

suspended in isopropyl alcohol, dropped onto a silicon wafer, dried at room atmosphere, and covered with a Pt nanolayer. Transmission electron microscopy (TEM) images were recorded using a JEOL JEM2100 microscope operating at 200 kV of accelerating voltage, equipped with a LaB₆ filament and a Gatan CCD camera (ORIOUS 832 SC1000B model). Previously, the samples were dropped on a 400-mesh copper grid covered with an ultrathin carbon film.

XPS spectra were acquired on a SPECS Flex PS X-ray photoelectron spectrometer operating at 50 W, at pass energies of 30 eV, and using monochromatic Al K α (1486.71 eV) as X-ray source. The calibration was made by using carbon as standard (C1s at 284.8 eV). The analysis and quantification of data were performed on Origin lab 9.0 software. A linear background subtraction was used for quantification, and a Gaussian line shape was applied in the deconvolution analysis. The sensitivity factors utilized were those ones reported by Ayiania et al. [10] as follows: 0.278, 0.78 and 0.477 for C1s, O1s and N1s, respectively.

Zeta potential measurements were performed on a Malvern Zeta NanoSizer ZS equipment. Ultraviolet and visible (UV-VIS) electronic spectra of C-dots dispersions were recorded in Shimadzu spectrophotometer, UV-2401PC model, equipped with an integration sphere. UV-VIS electronic absorption spectrum of FA in aqueous saturated solution were recorded in an Agilent HP8453 UV-VIS spectrophotometer. Photoluminescence spectra of C-dots dispersions were recorded in a Shimadzu spectrofluorophotometer, RF-5301PC model. Electronic UV-VIS absorption and photoluminescence spectra were carried out using quartz cuvettes with a path length of 1 cm.

3. Results and Discussion

3.1. Thermal Analysis (TGA/DSC)

To evaluate the thermal stability and the pyrolytic paths of FA, Na₂HFol and Na₃Fol, the simultaneous TGA/DTG-DSC curves of each compound was performed in N₂ atmosphere (**Fig.**

2). The samples presented overlapped steps of mass losses that can be divided in five (FA and Na₃Fol) and six (Na₂HFol) events, as summarized in **Table S1**. The profile of TG/DTG curve of FA is in line with that one reported by Vora et al. [19]. The first endothermic event around 30 and 200 °C observed for the three samples is attributed to their dehydration, while the subsequent events are assigned to their thermal decomposition. Folate sodium salts present higher thermal stability than FA, following the order: FA (200 °C) < Na₂HFol (270 °C) < Na₃Fol (300 °C), determined by the beginning of CO₂ release (data from TGA-MS and TGA-FTIR curves summarized in **Table S1**).

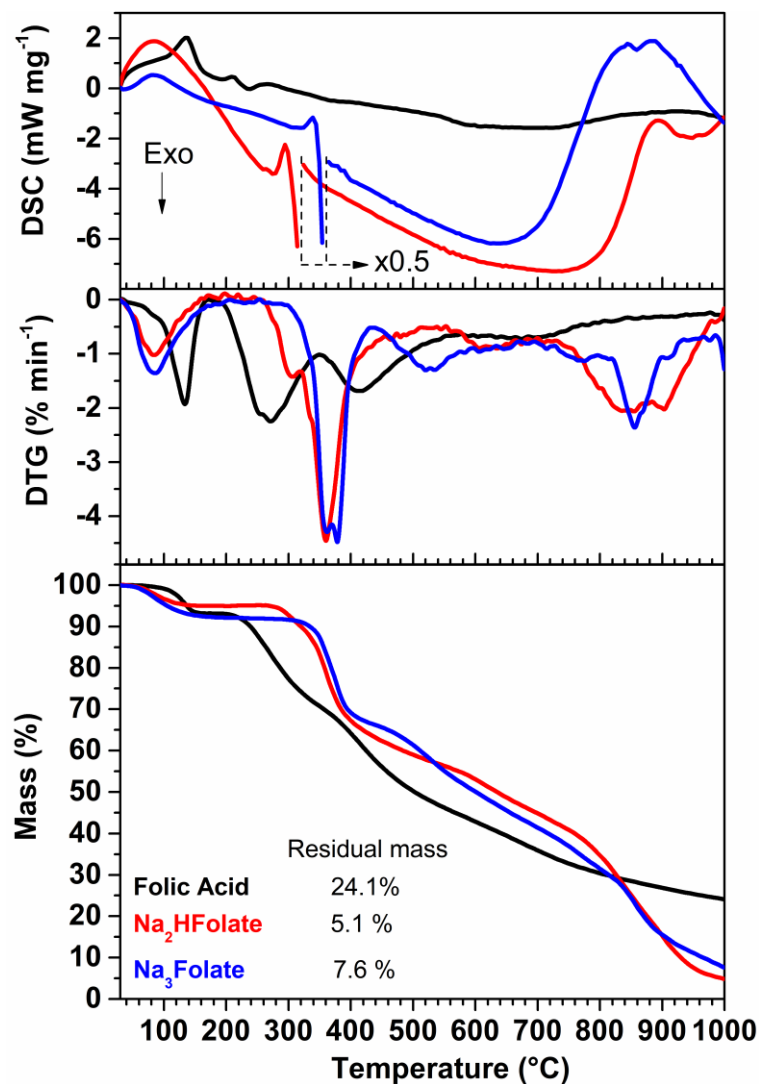


Figure 2. TGA/DTG-DSC curves from pyrolysis of FA, Na₂HFol and Na₃Fol.

As reported in previous work [15], the initial temperature values of the thermal decomposition of FA and folate sodium salts do not depend on the atmosphere (air or N₂), indicating that the process occurs through a non-oxidative mechanism of thermolysis that can involve radical formation. On the other hand, the progress of thermal decomposition under N₂ is completely different from the previous results observed in the oxidative atmosphere [15,17]. Indeed, TGA/DTG-DSC profiles under air indicated complete combustion of FA at 1000 °C, whilst sodium salts presented residual masses around 20% and 30% for Na₂HFol and Na₃Fol, respectively, tentatively attributed to the formation of the inorganic compounds Na₂CO₃ and Na₂O [15]. However, under N₂ atmosphere, the residual mass measured at 1000°C decreased to 24.1% for FA and to around 5-8% for sodium salts, as indicated in **Fig. 2**. Hence, sodium compounds formed during the pyrolysis seem to strongly affect the global pyrolysis mechanism of the folate ions. An interpretation of these observations will be given after the presentation of all characterization data.

3.2. Analysis of evolved gases/volatiles from pyrolysis by TGA-FTIR and TGA-MS

The gaseous/volatile products released during pyrolysis of FA were evaluated by TGA-FTIR (**Fig. 3**), while the respective results obtained for folate salts can be seen in **Fig. S3**.

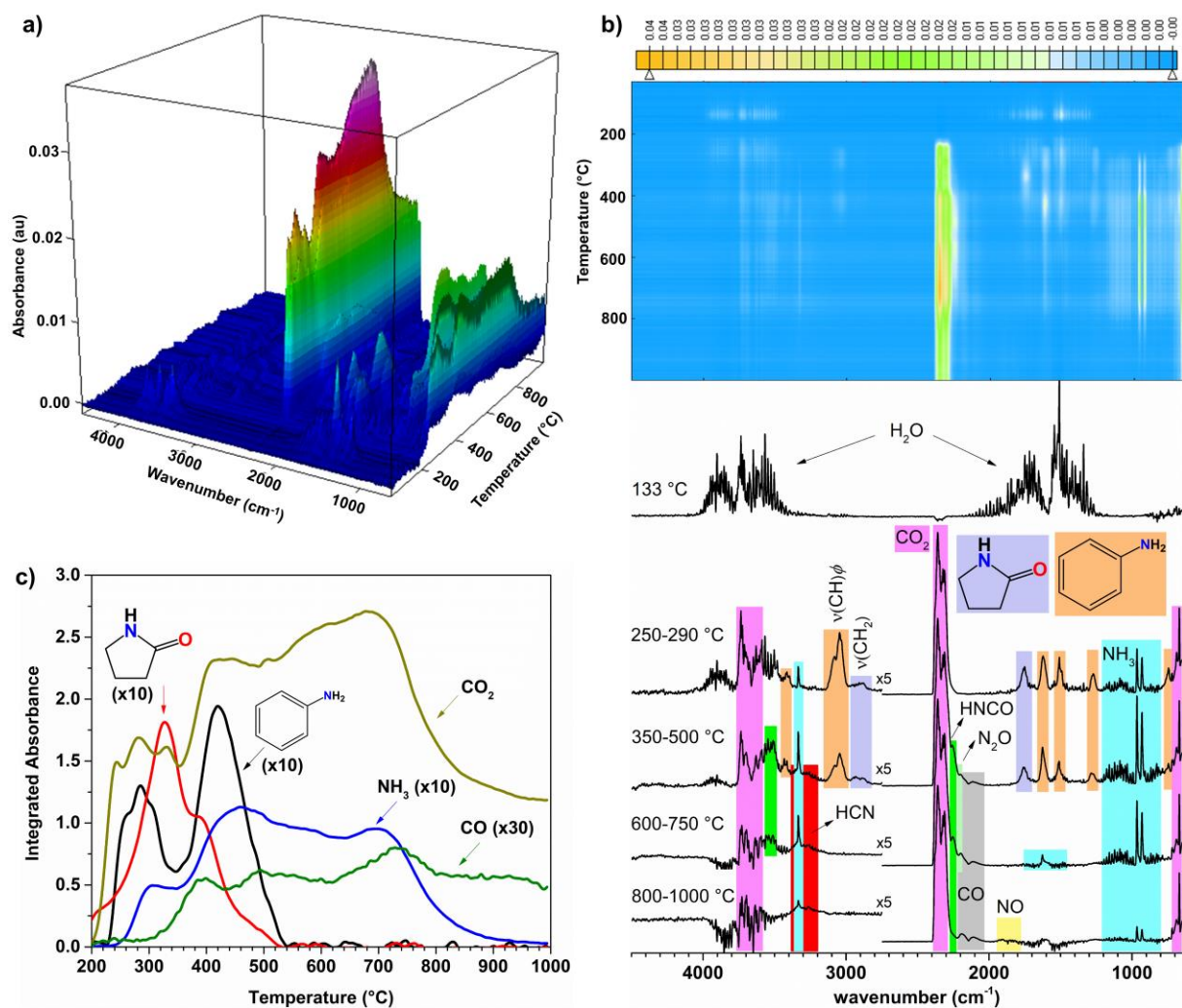


Figure 3. TGA-FTIR data for FA: (a) 3D plot; (b) contour map (superior; yellow and blue colours are defined as intensity increasing and decreasing, respectively) and FTIR spectra of gases/volatiles identified (inferior; at selected temperature ranges); and (c) integrated absorbance of TGA-FTIR curves of main released compounds: CO₂ (2360 cm⁻¹), CO (2114 cm⁻¹), 2-pyrrolidone (1760 cm⁻¹), aniline (1622 cm⁻¹), and NH₃ (966 cm⁻¹).

The 3D plot of TGA-FTIR data of FA permitted to visualize the main spectral regions related to the released products under an increased heating process (**Fig. 3a**). The release of H₂O observed by TG-FTIR (**Fig. 3b**) confirms that the first step of mass loss around 30-200 °C (**Fig. 2**) is due to FA dehydration. In the first pyrolysis step of FA (200-350 °C), beyond the release of CO₂, H₂O and NH₃, occurred the release of 2-pyrrolidone and aniline (**Fig. 3b-c**), which are characteristic of Glu [23,24] and *p*-ABA [25] moieties degradation, respectively. The second step of FA thermal decomposition (350-570 °C) involved the release of HNCO, HCN,

NH₃, N₂O and CO; the release of 2-pyrrolidone and aniline was still observed (**Fig. 3b-c**). At higher temperature range (570-1000°C), only the release of small-weight molecules, such as CO₂, CO, NH₃, NO, HCN and HNCO, was observed.

The comparative EGA results against the temperature of FA and its salts are depicted in **Figs. S4-S5** (TGA-FTIR and TGA-MS curves, respectively). The three compounds do not present a melting point [15,19]. The endothermic events observed in DSC curves (**Fig. 2**) at the beginning of the decomposition process of FA (211 °C and 266 °C), Na₂HFol (295 °C) and Na₃Fol (340 °C) can be assigned mainly to the volatilization of aniline and 2-pyrrolidone, which boiling points are 184 °C and 251 °C [26], respectively. In line with thermal analysis, EGA results showed that using sodium salts instead of FA changed the pyrolytic decomposition mechanism significantly. The initial pyrolysis stage of Na₂HFol (260-430 °C) and Na₃Fol (300-430 °C) were marked by the increase of CO₂, NH₃, H₂O and aniline releasing (**Figs. S4-S5**). Furthermore, the conversion of -COOH group into -COO⁻Na⁺ seems to change the decomposition mechanism of glutamic moiety. The release of 2-pyrrolidone occurred in a single step (**Fig. S5d**), and it decreased against the rise of allyl radical (C₃H₅), as can be evidenced by *m/z* 41 fragment in TGA-MS curve (**Fig. S5c**) and the vibrational bands of aliphatic C-H groups at 2800-3000 cm⁻¹ region (**Fig. S3c,f**). The water release was observed to increase above 300 °C for the folate salts (**Fig. S5**), which can be attributed to a catalytic effect of Na⁺ ion on the dehydration reaction during pyrolysis [27]. Additionally, the major gaseous products for Na₂HFol, above 600 °C, are CO₂, CO and NH₃ (**Fig. S4a-c**). On the other hand, the deprotonation of PT moiety in the Na₃Fol salt led to a substantial release of NO (**Figs. S3f and S5b**) over the whole temperature range (300-1000 °C), while NH₃ (**Fig. S4b**) and HCNO formation decreased (**Fig. S5b**), especially above 450 °C. The formation of NO⁺ species near 1000 °C was also observed as well as an unidentified product above 800°C, that present bands at 1465 cm⁻¹ and 882 cm⁻¹, marked in dark yellow in TGA-FTIR spectra (**Fig. S3f**).

The formation of N₂O (by-product of NH₃, HNCO and HCN [28]) and NO (**Fig. 3b** and **Figs. S3-S5**) was observed for all compounds above 340 °C, but the bands were still observed above 900 °C for Na₃Fol.

Based on the results presented above, the three compounds were pyrolyzed at selected temperature values according to their decomposition steps (**Table S1**). Owing to the better results obtained from FA pyrolysis than its sodium salts intending the production of N-doped carbon materials, the following sections was focused on the characterization of carbonaceous materials obtained from FA. A summary of the results obtained from sodium folate pyrolysis will be presented at the end of this text.

3.3. Analysis of pyrolyzed FA solids

3.3.1. XRD characterization

The *ex-situ* XRD patterns of pristine FA and carbon materials prepared from its pyrolysis over different temperature values are compared in **Fig. 4**. The sample heated above the dehydration temperature (175 °C) presented a diffraction pattern similar to that of pristine dihydrate FA (orthorhombic crystal system and P2₁2₁2₁ space group) [15,17] and no change in the sample colour was visualized (inset in **Fig. 4**). Braga et al. [17] reported that dehydrated FA presents a monoclinic unit cell and P2₁ space group, that could only be accessed by *in-situ* XRD because of its fast rehydration. In fact, *in-situ* XRD experiments performed in this work (**Figs. S6-S7**) confirm their observations. It was also noticed that the rehydration process is highly dependent on the heating time (**Fig. S6**): increasing the time of analysis from 5 to 60 minutes, the rehydration is not observed anymore, possibly because a partial decomposition of FA, as indirectly indicated by the yellow-grey colour of the residue. Then, the FA heating in an isothermal condition or lower heating rate [19] must be considered because such parameters affect the structure and composition of materials obtained from FA pyrolysis.

The materials obtained in a furnace over 350°C (**Fig. 4**, inset) were black, indirectly evidencing that FA carbonization occurred, at least partially. *Ex-situ* XRD data (**Fig. 4**) indicates the formation of an amorphous material at 350 °C, as noticed by broad peaks at low angle region, below 30° (2θ) value. The crystallinity slightly increased as the temperature increased to 1000°C, leading to two peaks noticed at 25.2° and 43.7°, related to the (002) and (101/100) crystallographic planes of graphitic carbon [8,29]. The broad aspect of the peaks indicated a small size of the coherent domain attributed either to small particle size and the presence of defects [9,29]. These results are consistent with those ones obtained by *in-situ* XRD (**Fig. S8**) and with data reported elsewhere for N-doped carbon materials obtained from FA [5–9].

To complement the microstructural characterization of char samples, their particle morphologies were analysed by SEM (**Fig. S9**). Materials presented carbon particles with varied size, differently of the porous texture previously observed for FA pyrolyzed in the presence of transition metals [5–7]. Particles obtained at 350 °C presented mainly small platelet-like morphology, while they changed to slab-like when heated at 570 °C. At 800 °C, materials were constituted by a mixture of small particles without a defined morphology and large aggregates with a conchoidal fracture pattern. The increase of temperature up to 1000°C did not change the morphology significantly, confirming the disorganized nature of the sample structure.

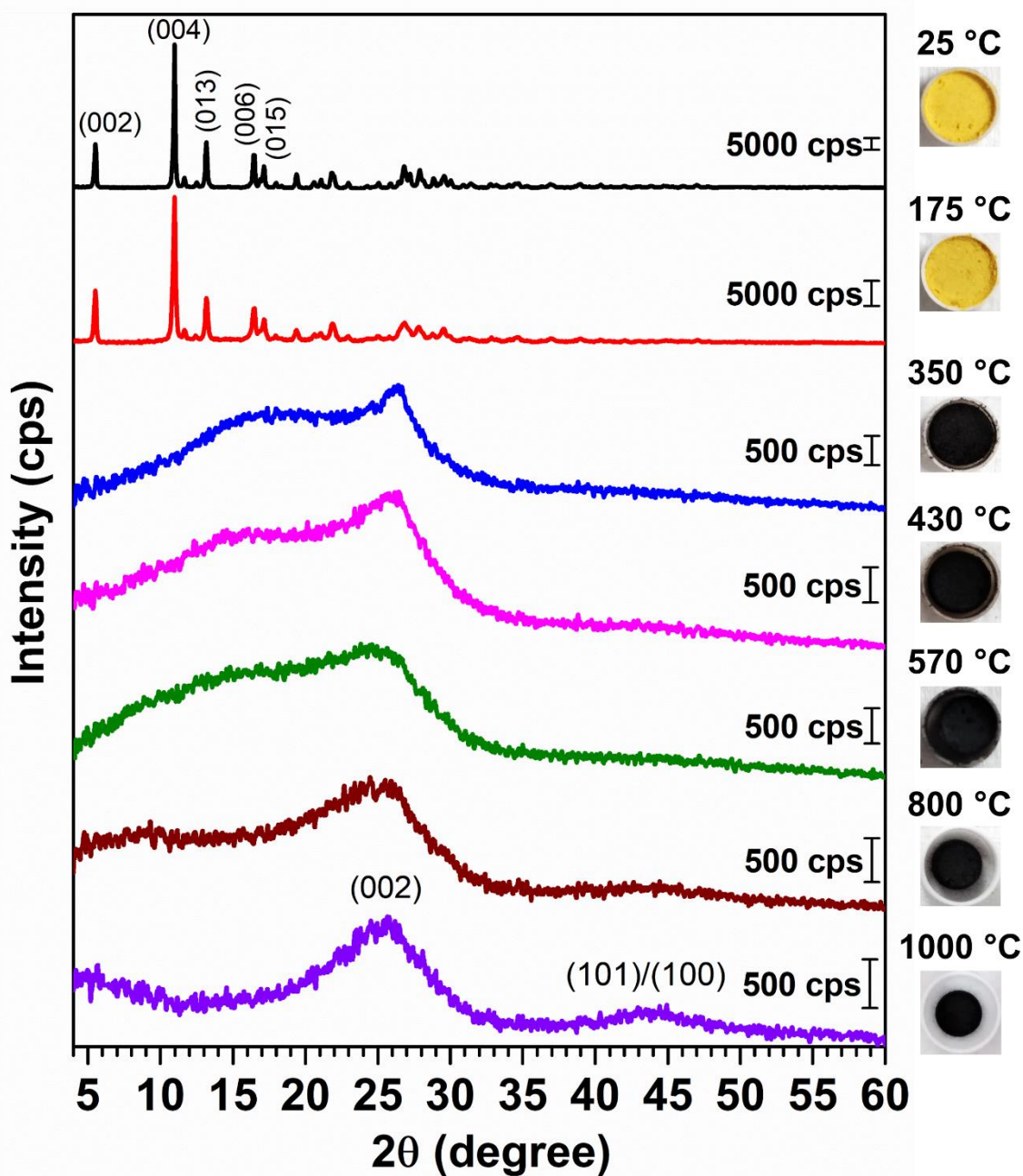


Figure 4. *Ex-situ* XRD patterns of FA and respective pyrolyzed samples. Insets show the colour change of samples upon heating.

Ex-situ XRD results of samples obtained from pyrolysis of folate salts are depicted in **Fig. S10**. The samples changed from yellow-orange powder to a black solid with a foam-like appearance at 430 and 570 °C, indirectly indicating their carbonization (insets in **Fig. S10**). The materials presented a broad (002) diffraction peak of graphitized carbon near 26.0° (2θ). Furthermore, XRD pattern of Na₂HFol pyrolyzed at 430 °C presented peaks indicative of

Na₂CO₃ formation, and its further conversion to NaO₂ and NaNCO at 570 °C. XRD profile of Na₃FoI showed peaks attributed to Na₂CO₃ and NaO₂ at 430 °C. The increase of temperature up to 570 °C led to the formation of NaNCO, although Na₂CO₃ and NaO₂ still remain. It is worth to note that the crystallization of inorganic compounds and even the formation of a foam-like material were not observed in *in-situ* analysis (**Figs S11-S12**). Initially, it was considered that a post-reaction with room atmosphere had occurred for *ex-situ* analysis, but this hypothesis does not explain the difference between the appearance of samples pyrolyzed in the distinct analysis setup. A such variance in results can be related to the different design of the heating cell of *in-situ* XRD equipment and the furnace used for pyrolysis. The distinct direction of gas flow can influence the reaction by favouring or not the reaction between char and released gases [30]. Therefore, results suggest that the composition and structure of char products can be influenced not only by the pyrolysis parameters, such as temperature and precursor but also by the pyrolysis furnace setup.

3.3.2. FTIR-ATR characterization

The FTIR-ATR spectra of FA and its pyrolyzed samples are depicted in **Fig. 5**. No detectable chemical change was observed in FTIR spectra when FA was heated up to 175 °C (**Fig. 5**), in agreement with XRD results. However, the results differ significantly from the ones reported by Vora et al. [19], who observed structural changes heating FA at 140 °C, probably due to the lower heating rate of 2 °C min⁻¹ used in pyrolysis. Fig. 2 shows that the water release of FA sample was gradual and observed since 100 °C. Hence, a low heating rate can favour the structural modification promoted by the dehydration reaction.

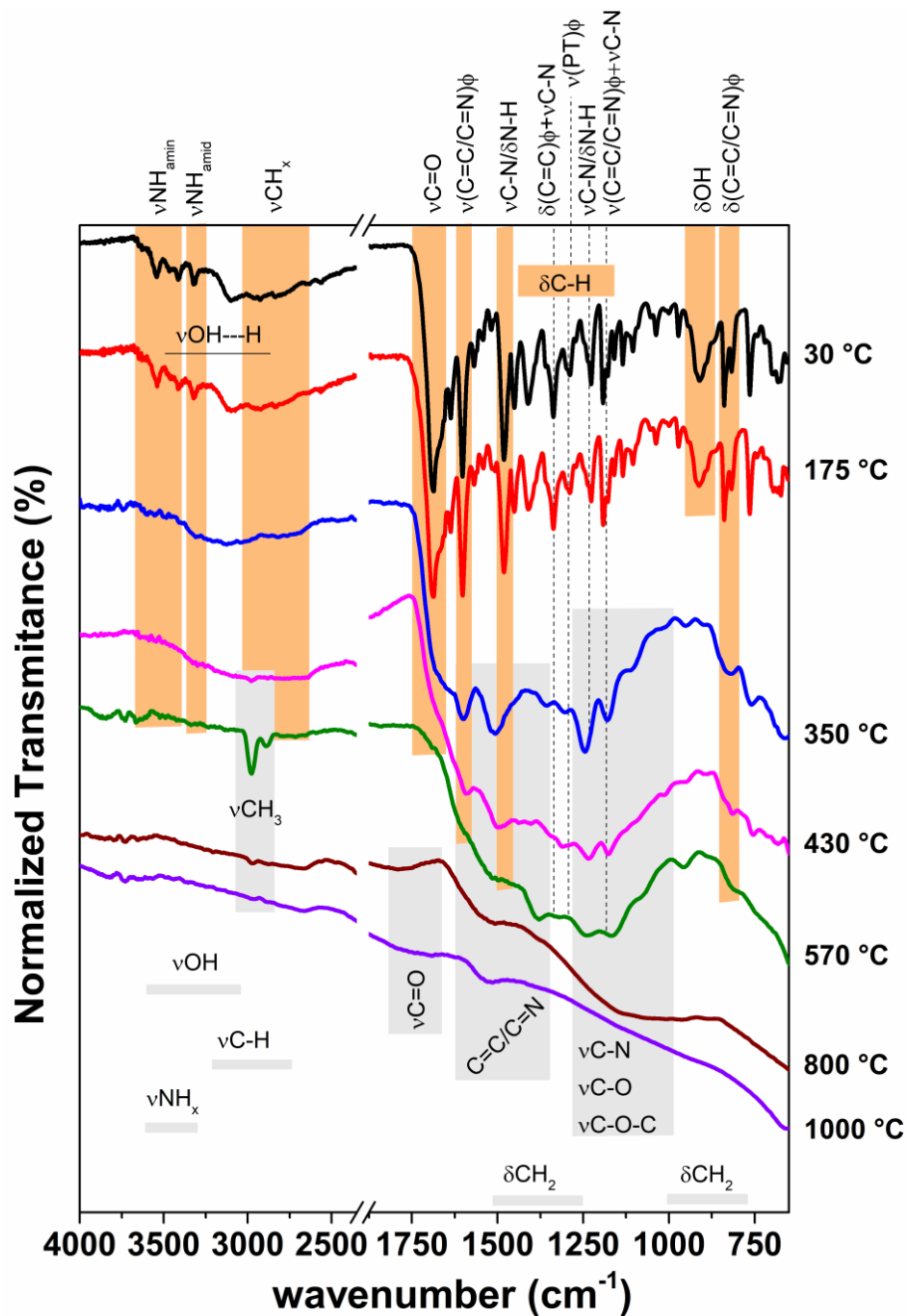


Figure 5. FTIR-ATR of FA and its pyrolyzed samples. ν = stretching, δ = bending, ϕ = aromatic ring, PT = pterin ring.

Noteworthy changes were observed when FA was pyrolyzed at 350 °C, although vibrational bands of functional groups from pristine FA were still observed, such as amine ($\nu\text{N-H}$ 3600-3400 cm^{-1}) [31,32], amide ($\nu\text{N-H}$ at 3310 cm^{-1} and at C=O 1680 cm^{-1}) [31,32], aromatic/aliphatic C-H ($\nu\text{C-H}$; 3100-2700 cm^{-1}) [31,32] and benzene and N-heteroaromatic

rings from *p*-ABA and PT moieties ($1600\text{-}1580\text{ cm}^{-1}$) [15]. The intensity of band attributed to $\nu\text{C}=\text{O}$ around 1680 cm^{-1} [15] slight decreased, and the bands of $\nu\text{N-H}$ in $3550\text{-}3450\text{ cm}^{-1}$ [31,32] region decreased significantly. The vibrational band related to δOH of carboxylic acid (912 cm^{-1}) [15] vanished completely. The results indicated that carboxylic acid (GLU moiety) and primary amine (PT moiety) were consumed in the first decomposition stage ($200\text{-}350\text{ }^\circ\text{C}$), in consonance with the release of NH_3 and 2-pyrrolidone detected by TGA-FTIR (**Fig. 3**). The broadening of the bands between $1600\text{-}1300\text{ cm}^{-1}$ can be attributed to the vibrations from $\text{C}=\text{C}/\text{C}=\text{N}$ sp^2 clusters in the carbonaceous structure [33,34].

For the materials obtained in the temperature range from $350\text{-}570\text{ }^\circ\text{C}$, the bands attributed to amine/amide and benzene decreased or were broadened, suggesting a chemical or structural change of such groups during the carbonization. FTIR spectrum of the sample prepared at $570\text{ }^\circ\text{C}$ presented bands attributed to C-H vibrations of aliphatic (methyl/methylene) and aromatic groups, as observed at regions of $2700\text{-}3100\text{ cm}^{-1}$ ($\nu\text{C-H}$), 1500 cm^{-1} (in-plane $\delta\text{C-H}$ coupled to $\nu\text{C}=\text{C}$), $1460\text{-}1275\text{ cm}^{-1}$ (in-plane and out-of-plane $\delta\text{C-H}_x$; aliphatic), $1150\text{-}1000\text{ cm}^{-1}$ (in-plane $\delta\text{C-H}$; aromatic) and $900\text{-}800\text{ cm}^{-1}$ (out-of-plane $\delta\text{C-H}$; aromatic) [31,35,36]. The signal in the region of $3500\text{-}3000\text{ cm}^{-1}$ can be attributed to νOH [32,36–38]. Also, physisorbed H_2O (due to the hydrophilicity character of the samples conferred by the presence of nitrogen [33]) presents a band in 3220 cm^{-1} region [39].

At $800\text{ }^\circ\text{C}$, the spectrum indicated the presence of broad bands related to ketone/lactone $\text{C}=\text{O}$ ($1800\text{-}1620\text{ cm}^{-1}$) [31,37,38], $\text{C}=\text{C}/\text{C}=\text{N}$ ($1600\text{-}1300$), C-N ($1300\text{-}1000\text{ cm}^{-1}$) [33,34] and C-O/C-O-C ($1200\text{-}1000\text{ cm}^{-1}$) groups [31,37,38]. Additionally, the vanishing of bands attributed to C-H, N-H, and amidic $\text{C}=\text{O}$ vibrations was observed. At $1000\text{ }^\circ\text{C}$, the C-N and C-O/C-O-C bands declined, and the spectral profile became more similar to that one reported for graphite [40]. Therefore, a substantial chemical transformation occurred above $570\text{ }^\circ\text{C}$,

evidencing the consumption of functional groups at the expense of carbonaceous structure formation.

The FTIR-ATR results of samples prepared from the pyrolysis of sodium folate salts are discussed in detail in the SM (**Fig. S13**). The data suggest that functional groups such as the benzene ring of *p*-ABA, amide groups, and carboxylate of glutamate were completely (or partially) consumed after the first pyrolysis stage of compounds at 430 °C. The formation of N-heteroaromatic rings derived from PT groups was also suggested. At 570 °C, the band in the region of C-N and C-O/C-O-C stretching modes increased, but in a minor extension for Na₃Fol. The results indicated the formation of carbonaceous materials with distinct structure compared to FA pyrolyzed samples. In addition, the presence of bands attributed to Na₂CO₃ and NaNCO (inorganic compounds; **Fig. S14**) were noticed for both salts, in line with the XRD results.

3.3.3. Raman spectroscopic characterization

Raman spectra (λ_{ex} 532 nm) of FA and its pyrolyzed samples are shown in **Fig. 6**. The vibrational bands of FA are hindered by fluorescence phenomena [31]. The spectrum of sample pyrolyzed at 350 °C still presented a fluorescence background. However, the indicative of G (1560-1600 cm⁻¹) and D (1340-1380 cm⁻¹) bands, which are characteristic of graphite-like structures [22,31,34,41–44], implied the presence of graphitic clusters into an amorphous matrix. Such spectral profile is similar to the polymeric hydrogenated amorphous carbon (C sp²/sp³ network with high H content) reported in the literature [41]. At 430 °C, the overlapped G and D bands were intensified and the luminescence background decreased, what can suggest an increase in the graphitization with depletion of hydrogenated groups content [22], in agreement with FTIR-ATR data. The signal around 2700 cm⁻¹ is attributed to the 2D band (overtone of peak D) and the low band resolution is an indicative of disordered carbon structure

[31,42], in agreement with XRD data. In addition, the weak signal observed in the region of 2200 cm^{-1} is attributed to $\text{-C}\equiv\text{N}$ groups (C sp^1) [34].

Amorphous carbon (Csp^2 clusters embedded into sp^3 matrix) containing heteroatoms (N and O) also presents secondary bands contributing to the Raman signal in the region of $1000\text{-}1800\text{ cm}^{-1}$ [31,43,44]. Kato et al. [31] and Garcia-Perez et al. [43,44] carried out theoretical calculations to interpret the experimental Raman results of (N,O)-doped carbon obtained by the pyrolysis of organic precursors. The disorder, the presence of (N,O)-functional groups and the vacancies in the structure of graphite can promote the breakdown of the symmetry and activate new vibrational modes besides the fundamental G and D bands in Raman spectra [43,44]. In this work, one of the main differences in Raman spectra as the temperature increased up to $1000\text{ }^\circ\text{C}$ was the lowering of the signal in the region of $1460\text{-}1550\text{ cm}^{-1}$ (**Fig. S15**). According to the literature [31,43,44], such spectral region can be related to (N,O)-functional groups in vacancies of carbon structure, small polyaromatic hydrocarbons (PAHs) and/or 7- and 5-membered ring groups. In fact, with the evolution of the temperature, the disappearing of bands related to nitrogenated and oxygenated functional groups was observed in FTIR-ATR spectra (**Fig. 5**).

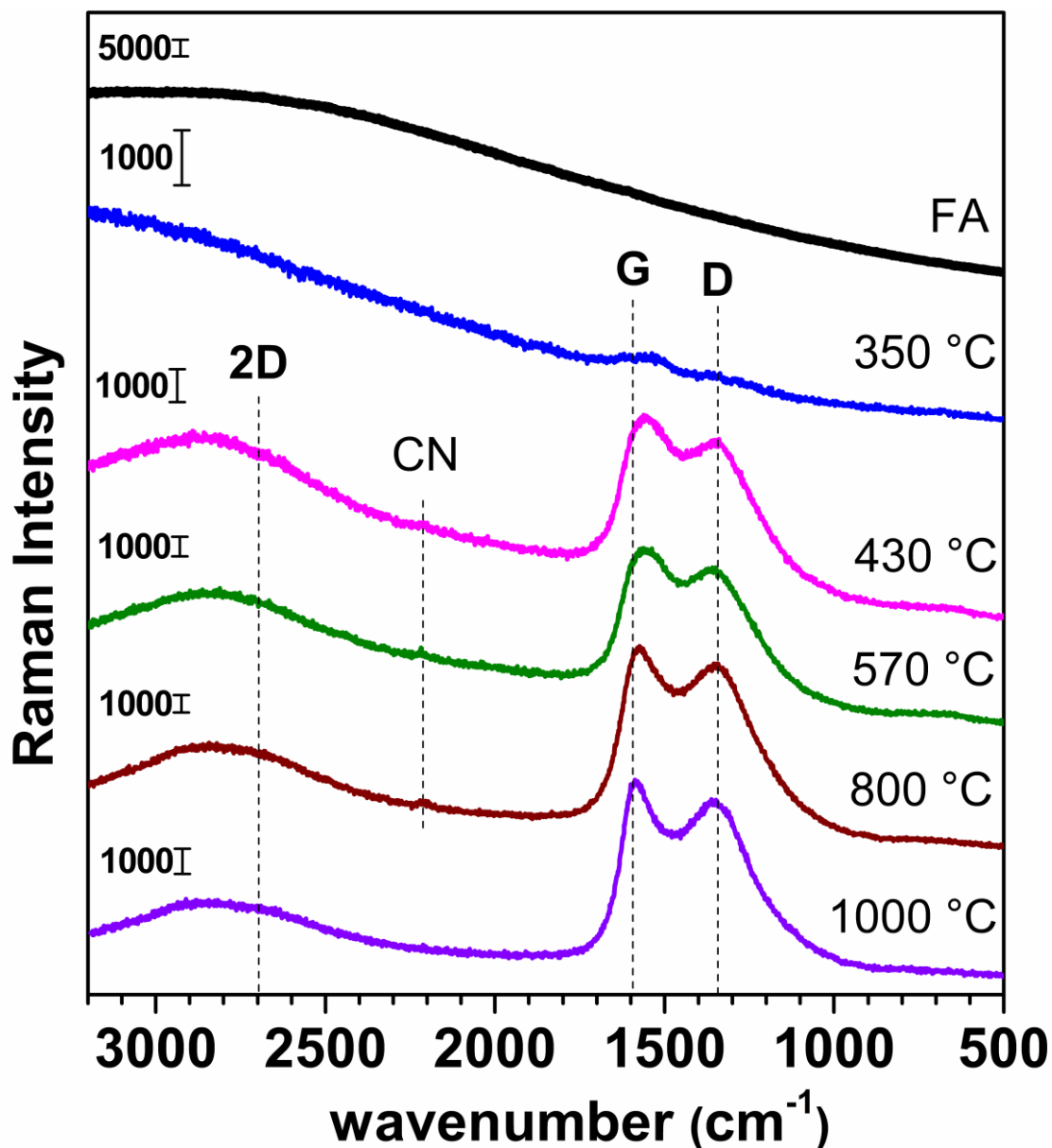


Figure 6. Raman spectra of FA pyrolysis products (λ_{ex} 532 nm).

The ratio between the intensity (I) of bands D and G, $I(\text{D})/I(\text{G})$, and G band position are parameters extensively used to determine the degree of structural organization of graphite-like carbon [22,31,34,41–44]. However, for amorphous/disordered material containing functional groups and vacancies, it is difficult to analyze such parameters. Simplifying, the results are presented in **Table S2** and in **Fig. S16**. The trend of G band to blue shift indicated that the pyrolysis temperature increase promotes the decrease of C sp^3 content in the materials [22,34].

The increase of I(D)/I(G) from 350-800 °C suggests the conversion of a polymeric/amorphous carbon to a nanographite-like structure [22,34]. Further, from 800 to 1000 °C, the spectral data indicated a tendency of conversion from nano to micrographite-like structure [22,34]. The inverse relation of bands area (A), A(D)/A(G), and FWHM of G band (**Fig. S16**) strengthen the hypothesis of polymer-like carbon structure conversion to graphite-like structure as the temperature increases [22].

The overlapped D and G bands of pyrolyzed folate salts were more asymmetric and presented shoulders compared to pyrolyzed samples from FA (**Figs. S15-S16**). These results indicated that such materials presented a more disorganized structure than pyrolyzed FA and defected structure constituted by non-hexagonal rings and small PAHs of different sizes [43,44]. The analysis of G band position, I(D)/I(G) and FWHM(G) against A(D)/A(G) (**Table S2** and **Fig. S16**) suggested that the formation of a more extensive graphite-like network was precluded starting from folate salts in comparison with respective samples prepared from FA pyrolysis. Raman spectrum of Na₃Fol pyrolyzed at 570 °C showed an active band at about 1060 cm⁻¹ assigned to the symmetric stretching of carbonate ion [45].

3.3.4. XPS characterization

Going further in the structural characterization of carbon materials, the FA pyrolyzed samples were characterized by XPS analysis. The full XPS survey scan and the relative percentage content of carbon, nitrogen, and oxygen atoms on the surface of materials are depicted in **Fig. 7**. The relative content of carbon was observed to increase as the temperature evolved from 350 °C to 1000 °C. On the other hand, the nitrogen and oxygen content decreased and increased according to the temperature range. After the first pyrolysis step (350 °C), the oxygen content stayed virtually constant while the amount of nitrogen decreased. As far as the temperature progressed up to 1000 °C, the oxygen content decreased to around 10 wt.%. In the

range from 350 to 800 °C, the nitrogen content raised to around 20 wt.% and decreased again to around 7 wt.%. Although a variation of the mass balance occurred during the carbonization process as a result of the release of N,O-groups, the results suggested that the volatiles gaseous products (*e.g.*, NH₃, H₂O and CO₂) were reacting over the char surface (reforming process) [46].

The N-enrichment can be reached by the thermal treatment of carbonaceous material in NH₃ atmosphere (or in the presence of NH₃ precursor; *i.e.*, urea) [10,47,48]. Ayiania et al. [10] reported that the N-enrichment of char produced by pyrolysis of cellulose and thermally treated in NH₃ atmosphere occurred between 500-700 °C. Bimmer et al.[48] and Pietrzak et al. [47] observed that the amount of nitrogen incorporated depends on the amount of O-containing group in carbonaceous structure. It is proposed in this work that the reforming of O-gaseous products can occur mainly in the 200-350°C range, considering data from Fig. 7b. On the other hand, the N-enrichment of carbonaceous material occurred by the NH₃ (mainly released between 350-800 °C; **Fig. 3c**) reforming in the expense of O-containing group. Once again, it is worth noting that the design of the furnace (*e.g.*, downdraft: carrier gas flow from top to bottom; updraft: gas flow from top to bottom) may affect the structure and composition of carbonaceous material [30,46]. The downdraft configuration can increase the contact time between the gaseous product and char [30], which favours such reforming reactions. Furthermore, it can be an approach applied to tune the surface chemistry of materials obtained from the pyrolysis of FA.

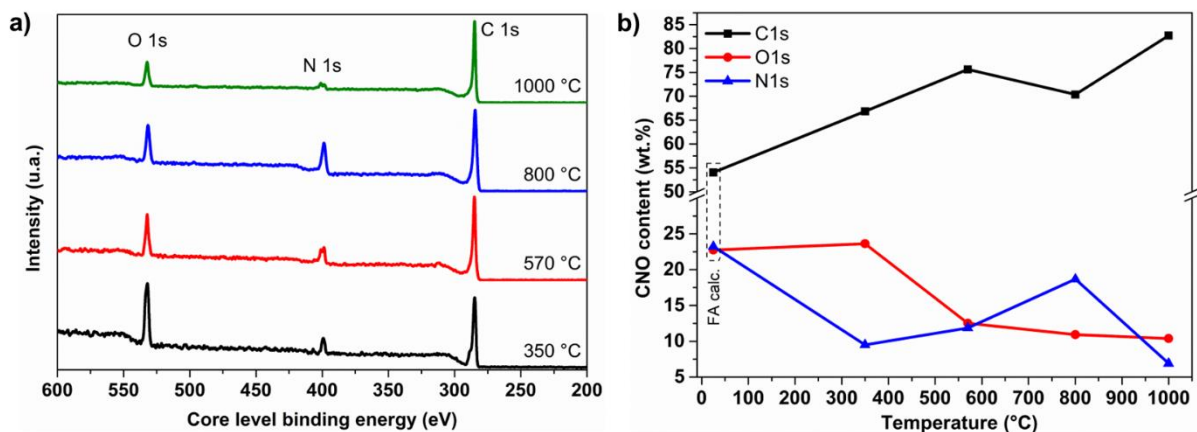


Figure 7. (a) Full XPS survey scan and (b) relative carbon, nitrogen, and oxygen (CNO) atoms content of FA pyrolyzed samples according to the pyrolysis temperature.

Fig. 8 shows the deconvoluted high resolution XPS spectra of C1s, N1s and O1s for FA pyrolyzed in 350-1000°C range; the results are summarized in **Table S3**. The peak position used in the spectra deconvolution as well as the peak assignments were made based on theoretical calculations from the literature [10,31,49], as detailed discussed in the SM.

The variation of C,N,O-functional groups on the surface of samples according to the temperature are depicted in **Fig. S17**. The content of graphitic C=C (and also the satellite π - π^* signal) increased from 350 to 1000°C, indicating the graphitization improvement, corroborating with Raman results. The C–C bond in 7 membered rings presented a decrease tendency with the progress of heating whereas C–C bond in 5 membered rings increased from 570-800°C and decreased again up to 1000 °C. The other C groups (*e.g.*, C=O, COO, C-O and Csp³-N) varied slightly, up and down, in the work temperature range. The N-amide group decreased in 350-570 °C range while the N-graphitic one increased. According to FTIR-ATR results, such amide groups were mainly from pyrimidine ring of PT moiety (**Figs. 1 and 5**). Hence, the disappearing of amide group in the second step (350-570 °C) allowed the polycondensation of the pyrazine ring, suggesting that the formation of graphite-like structure doped with N-graphite passed through the PT moiety decomposition. In the 570-800 °C range, the presence of N-pyridine, N-pyrrolic and nitrile groups intensified significantly possibly because the NH₃ reforming,

coherent with literature data about carbonaceous materials heated in NH_3 atmosphere [1,50]. However, the content of such groups further decreased up to 1000°C whereas the N-graphitic remained almost constant from 570°C to 1000°C , suggesting a higher stability of it in comparison with other N-containing groups at the temperature range used in this work. At 350°C , the most significant O-containing groups were C=O and C-O. Such groups decreased significantly in amount from 350°C to 570°C whereas the N-oxide ones intensified. Progressing the temperature up to 1000°C , the C=O and N-oxide groups remained virtually constant, but from 800 to 1000°C , the content of C-O bonded to aliphatic groups slightly decreased and C-O linked to aromatic groups fostered.

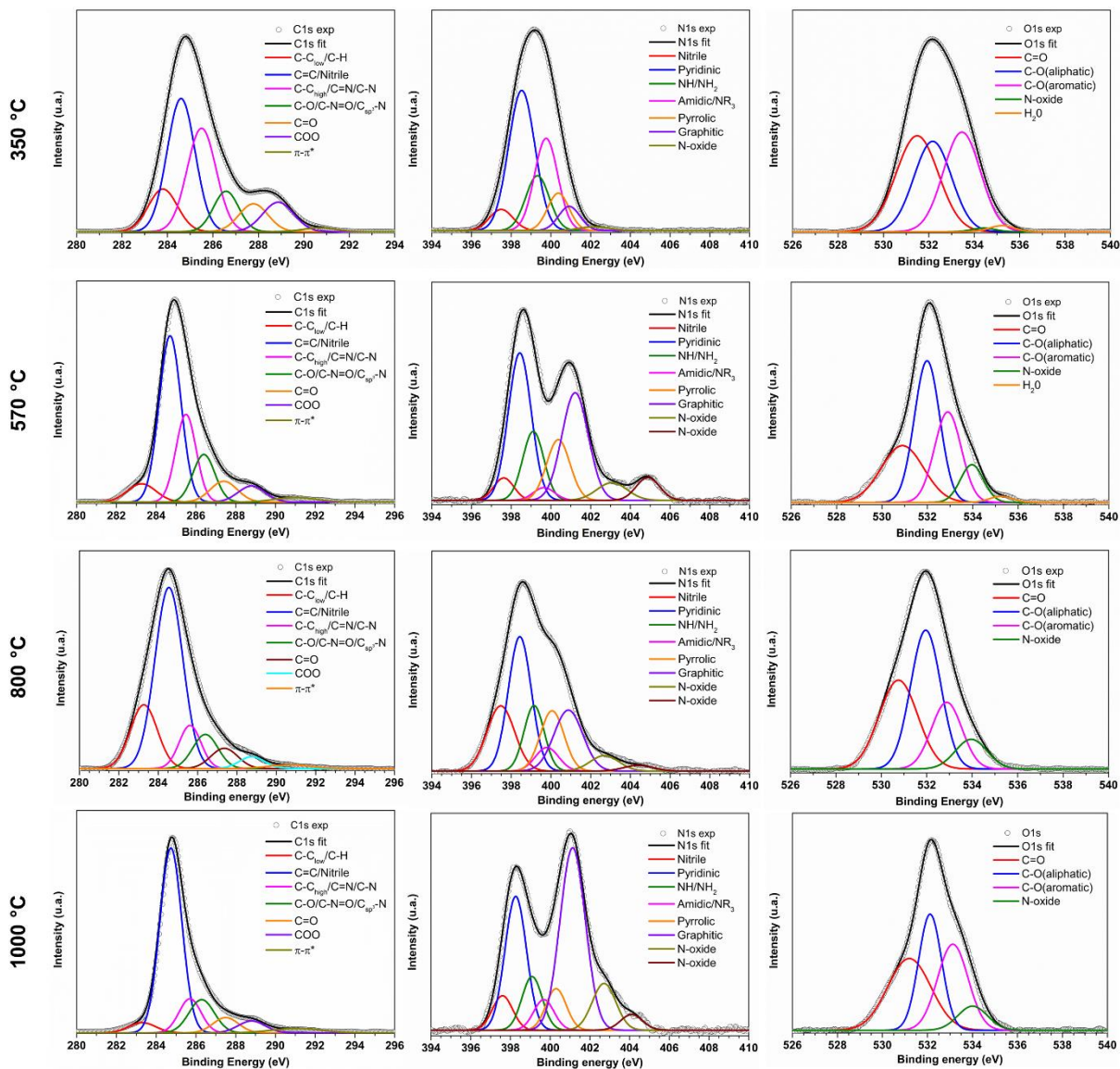


Figure 8. Deconvoluted C1s, N1s and O1s high resolution XPS spectra of FA pyrolyzed from 350 °C to 1000 °C.

3.4. Pyrolysis Mechanism

3.4.1. FA pyrolysis mechanism

The pyrolysis process comprises a set of complex and concurrent reactions, such as cracking, reforming, aromatization, polymerization/condensation and polycondensation [51–53]. In this section are discussed insights regarding the pyrolytic mechanism of FA based on the above-interpreted data from TGA/DSC coupled to EGA and char analysis (XRD, FTIR-ATR, Raman and XPS). **Table S4** brings a correlation between functional groups and released

gas detected during FA pyrolysis. A schematic representation of FA pyrolysis mechanism is depicted in **Figure 9**.

The first pyrolytic stage (200-350 °C) is marked by the cracking of FA followed by molecular polymerization and the beginning of graphitization (aromatization/condensation). The cracking occurs mainly by: (i) the breaking of C–NH₂ bond in PT moiety leading to the release of NH₃; (ii) the vanishing of GLU carboxylate groups releasing CO₂ and H₂O; (iii) the breaking of C–N bond linking PT and *p*-ABA as well as (iv) C–C=O bond linking *p*-ABA and GLU moieties; both marked by the release of aniline and 2-pyrrolidone/allyl radical (C₃H₅). The loss of nitrogen occurs in a major extension in this step against the reforming of O-containing species into groups C=O/C–O–C/C–OH, as indicated by XPS data. However, pyridine and amidic groups from PT moiety seem to be the most stable N-containing groups and pyrrole can be formed from the conversion of 2-pyrrolidone (**Scheme S1**) [23,24].

According to char analysis, the carbonaceous material generated at 350 °C is expected to present a polymeric network-like structure containing C-dots nanoparticles imbibed on in (formation of this type of carbon species will be discussed ahead). The whole material is constituted mainly by groups from FA precursor such as, amidic groups (and 2-pyrrolidone), aminobenzene and N-heteroaromatic rings (N-pyrrole; N-pyridine) linked to C sp²/sp³ network.

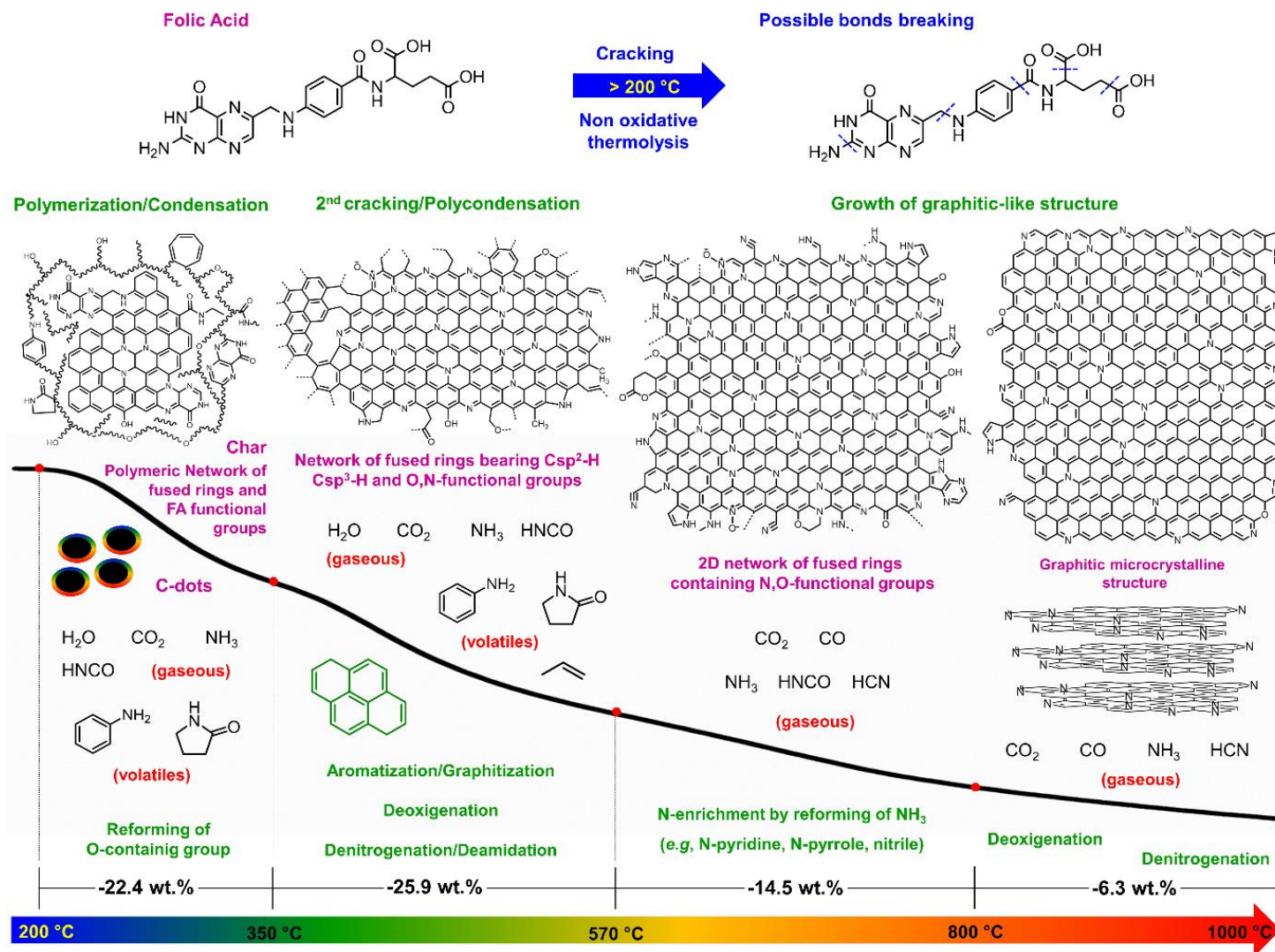


Figure 9. Schematic representation of FA pyrolytic mechanism.

In the second step (350-570 °C), secondary cracking of the char occurs and graphitization is enhanced, as evidenced by EGA analysis (aniline and 2-pyrrolidone release) and Raman spectroscopic results. As indicated by XPS and FTIR data, the N-graphitic content increased, whereas amidic groups from PT were consumed (HCNO and NH₃ release). The graphitization occurs through polycondensation reactions involving the pyrimidine ring of PT moieties and the decline of N,O-functional group by deoxygenation (CO and CO₂ release) and denitrogenation (NH₃, HCN, HCNO and NO) reactions.

The growth and organization of the structure occur with the temperature increasing up to 800 °C. Furthermore, in the third step (570-800 °C), the reforming of NH₃ was boosted by enriching char of amine, pyrrole, nitrile and pyridinic groups (indicated by XPS spectra). **Scheme S2** presents a possible mechanism for the reactions involved during the process. The low increase of amide in relation to other N-containing groups can indicate a higher amount of -OH groups on the surface of carbonaceous material [54]. The conversion of char to a carbon-rich product constituted by microcrystalline graphitic structure is favoured by the increase of temperature up to 1000 °C. The step is also marked by denitrogenation leaving N-graphitic and N-pyridinic as the main form of nitrogen doping of carbon-framework.

3.4.2. Sodium folate salts pyrolysis mechanism

Insights into the mechanism of pyrolysis of sodium folate salts are discussed in the SM file. Briefly, the sodium folate salts seem not to be a profitable precursor to produce graphitic carbon, probably because of the deleterious effect of Na⁺ in favour of carbonaceous structure cracking, which foster the graphitization, especially above 700 °C. According to the literature [4–9], such effect is not observed for folic acid associated with transition metals cations that present catalytic properties for graphitization reactions, such as Ni²⁺, Co²⁺, and Fe³⁺, for instance. Nevertheless, the effect of alkaline and earth-alkaline metals in the mechanism of

folate pyrolysis must be further evaluated as well as the viability of produce C-dots from the related salts.

3.5. Carbon dots extraction and characterization

The C-dots isolation was performed from the chars produced by the pyrolysis of FA under mild temperature values (350 and 430 °C). The temperature of pyrolysis and the extractor media (water, aqueous NaOH or DMSO) influenced the amount of nanoparticles isolated. The intensity of brown colour of the liquid dispersions indicated that the better conditions to isolate the nanoparticles were achieved from FA pyrolyzed at 350 °C and extracted with NaOH solution and DMSO. C-dots were also isolated from Na₂HFol or Na₃Fol pyrolyzed at 430 °C and extracted with water (**Fig. S18**).

Figures 10 and **S19** presented the TEM analysis of C-dots produced from FA (350 °C) and extracted with DMSO. The size (less than 10 nm) and shape of nanoparticles varied greatly (**Figs. 10** and **S19**). The graphite-like structure is confirmed by lattice spacing distances of 0.31 nm and 0.24 nm attributed to (002) and (100) crystal planes of sp² graphitic carbon, respectively [55]. The presence of surface deprotonated groups (*e.g.*, -COOH, -OH and -CONH) was indicated by the negative Zeta potential value of C-dots extracted with water, varying approximately from -15 to -30 mV (**Table S5**).

Fig. 11 presents the electronic UV-VIS, photoluminescence (PL) and excitation photoluminescence (PLE) spectra of sample obtained from FA heated at 350°C and extracted with DMSO. The spectra of other samples are compared in **Figs. S20-22**. Electronic UV-VIS spectra of C-dots presented bands bellow 300 nm that are generally attributed to π - π^* transition of C=C/C=N groups (sp² domain in carbon core) [56–58]. Around 300-400 nm, the bands are usually assigned to n- π^* transition from C=O surface groups [58,59]. The tale observed in some spectra above 400 nm (**Fig. S20b,c**) is attributed to surface states (*i.e.*, surface defects and N,O-

functional groups) [60,61]. The sample prepared from FA pyrolyzed at 450°C and extracted with DMSO or NaOH solution did not present bands in the region of surface states, while the sample prepared by extraction with H₂O did not produce detectable absorption bands in the 210-800 nm region as well (**Fig. 20a**), *i.e.*, C-dot particles were not extracted. These results suggested that the increase of temperature promoted the decomposition of N,O-groups, specially PT amidic group, over the growth of graphite-like framework structure, in consonance with FTIR, Raman and XPS results. Such behaviour was not observed for samples obtained from folate sodium salts pyrolyzed at 430 °C and extracted with water, suggesting the increase in the stability of surface groups.

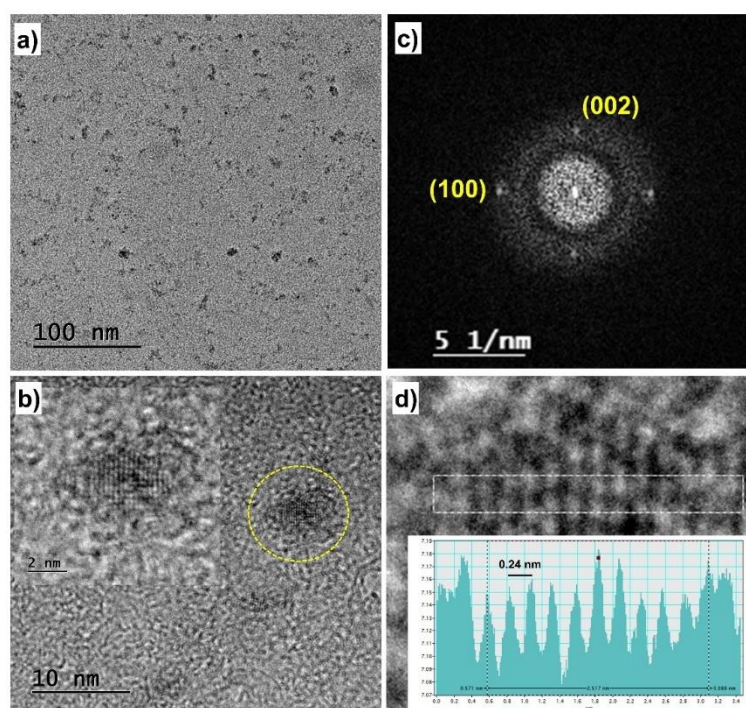


Figure 10. (a) Low and (b) high magnification TEM images of C-dots obtained from FA (350 °C) and extracted with DMSO; (c) fast-Fourier-transform (FFT) pattern of corresponding C-dot depicted in figure (b) showing the spots related to (002) and (100) planes of carbon framework; (d) *d*-spacing measurement between adjacent lattice planes of 0.24 nm corresponds to the (100) planes merged to the zoom in (b).

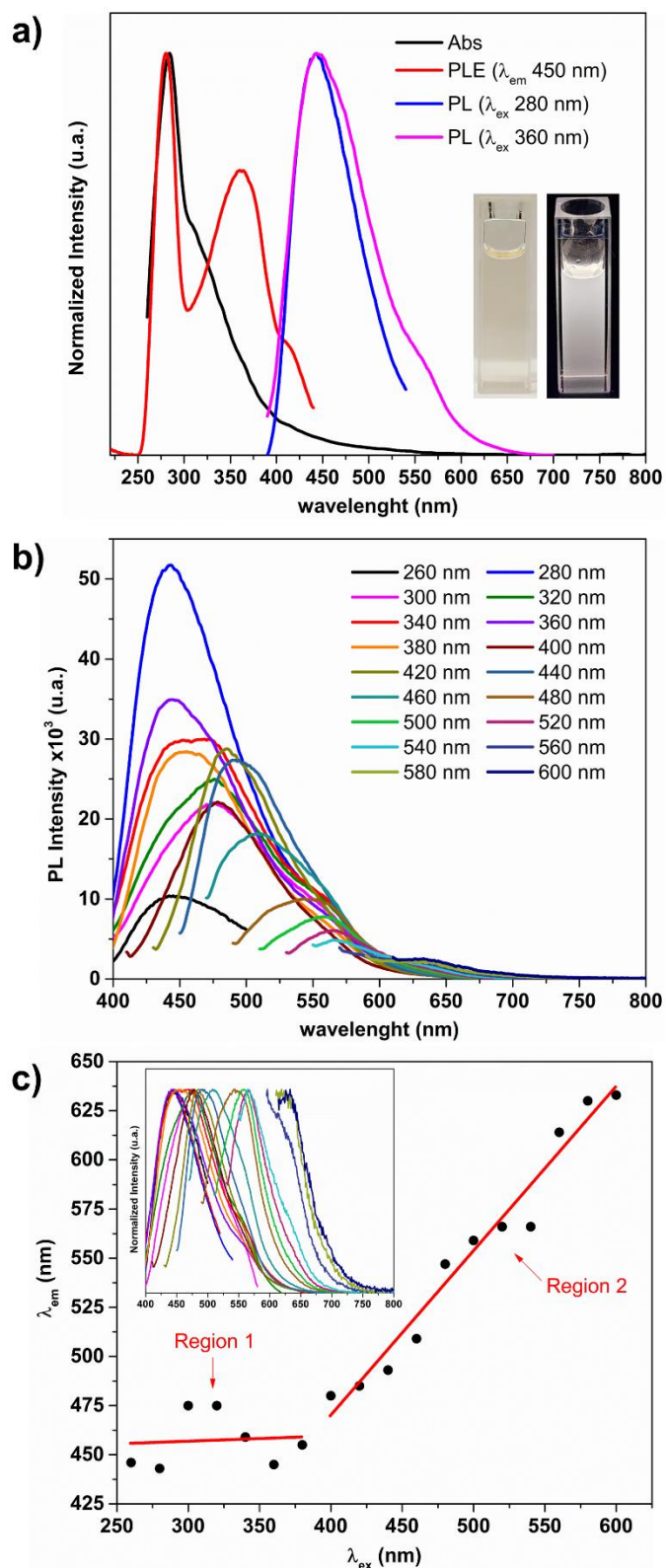


Figure 11. (a) Electronic UV-VIS, PL excitation (λ_{em} 450 nm) and PL emission spectra (λ_{ex} 280 and 360 nm) of C-dots from FA (350 °C) extracted with DMSO, inset: photographs of suspension under daylight (left) and UV lamp (right); (b) PL emission spectra of C-dots varying the excitation wavelength; (c) wavelength dependence of the maximum of PL emission as a function of excitation wavelength.

Except for FA (450 °C) extracted with water and DMSO, all other systems presented emission visually observed under UV lamp of 365 nm (**Fig. S18b**). Material extracted with DMSO presented white emission while the other materials emitted blue radiation. It can be related with solvent effect in separate C-dots with different physicochemical properties [62] or due to solvent-dependent PL [63].

The samples presented excitation-dependent PL (**Figs. 11** and **S21-S22**). For instance, sample from FA (350°C)/DMSO condition presented emission in a broad spectral range, from 440 to 625 nm (**Fig. 11b**). Two regions of maximum emission were observed when excitation was performed at 260-380 nm range and above 400 nm (**Figs. 11c** and **S22**). The PL mechanism is not the focus of this work, but in general it is related to the molecular species generated during pyrolysis (covalently linked to the core or imbibed in it), quantum effect (size of carbon core) and surface states (electron trap and defects promoted by surface groups) [64]. The PLE spectra of materials from emission in 450 nm (Region 1) presented similar profile of FA (**Figs. 11c**, **S21** and **S23**). The optical properties (absorption, PL and PLE spectra) of FA are highly dependent on its PT moiety [65], as can be noticed in **Fig. S23**. The results suggested that PT moiety is one of the mainly building block for C-dots and it can be imbibed or covalently bonded to carbon structure promoting a molecular PL behaviour in materials [64]. However, a more detailed PL characterization of C-dots from the method reported in this work is demanded to determine the PL mechanism and optical features of C-dots (*e.g.*, quantum yield, photostability etc.). Furthermore, considering the white emission of sample extracted with DMSO (inset of **Fig. 11a**), it opens the possibility to separate the particles by chromatography to obtain C-dots fraction that emit distinct colours, from blue to red, for instance [56].

4. Conclusion

This work presented a rational strategy to establish the proper temperature ranges to produce a set of N-doped carbon materials from the pyrolysis of FA, such as C-dots and ordered graphitic carbon. FA by itself is a suitable carbon source for producing N-doped carbon materials: C-dots can be synthesized using relatively low temperatures from 200-350 °C, while graphitic carbon is optimally obtained above 800 °C. EGA analysis shown the release of oxygenated and nitrogenated species, helping to elucidate the pyrolysis mechanism of FA. A comparison with the results of pyrolysis of di- and trisodium folate showed that salts decomposition favoured cracking reactions and precluded graphitization. The knowledge about the mechanisms involved during the FA pyrolysis must be profitable to tune the structure and composition of desired carbonaceous material and, consequently, it can be related to their properties. Also, parameters such as furnace design, heating rate/isothermal set up and heating time must be considered and better evaluated in future studies to produce N-doped carbon obtained from the pyrolysis of FA. This work can help to speed up the synthesis of new N-doped carbon material obtained from FA pyrolysis with the potential to be applied in the development of electronic/optoelectronic devices, in catalysis, as bioimaging agent, in CO₂ capture/conversion and so on.

CRedit authorship contribution statement

Vagner R. Magri: Conceptualization, Visualization, Methodology, Investigation, Data curation, Formal analysis, Writing – original draft, Writing - review & editing. **Caroline S. de Matos:** Methodology and Writing – review & editing. **Michele A. Rocha:** Methodology and Writing – review & editing. **Christine Taviot-Gueho:** Formal analysis and Writing – review & editing. **Vera R. L. Constantino:** Conceptualization, Methodology, Visualization, Formal analysis, Project administration, Funding acquisition, Writing – review & editing, Supervision.

Declaration of Competing Interest

The authors declare that they have no known competing financial interests or personal relationships that could have appeared to influence the work reported in this paper.

Acknowledgments

V.R.M. is grateful to the Coordenação de Aperfeiçoamento de Pessoal de Nível Superior (CAPES, Brazil, Finance Code 33002010191P0) for the PhD scholarship. C.S. de M. acknowledges the Fundação de Amparo à Pesquisa do Estado de São Paulo for research grant (FAPESP 12/06291-4). V.R.L.C. is thankful to the Conselho Nacional de Desenvolvimento Científico e Tecnológico (CNPq, 314034/2021-8) and Sao Paulo Research Foundation (FAPESP, INCT-INEO 2014/50869-6) for the research grants. This work was partially supported by region Auvergne- Rhone Alpes (Pack Ambition International AURA program). The authors also acknowledge MSc Alfredo Duarte and MSc Rebeca Yatsuzuka (Central Analítica do Instituto de Química da Universidade de São Paulo – CA-IQUSP) for helping with TEM and XPS analysis, respectively. The authors are thankful to the Laboratório de Cristalografia (Instituto de Física - USP) for the XRD diffractograms registration, the Laboratório de Espectroscopia Molecular (LEM, Instituto de Química – USP) for the Raman spectra recording, and the Laboratório de Caracterização Tecnológica (LCT – USP) for SEM analysis.

Appendix A. Supplementary material

Supplementary material of this article can be found online at <https://doi.org/>

References

- [1] M. Inagaki, M. Toyoda, Y. Soneda, T. Morishita, Nitrogen-doped carbon materials, *Carbon N. Y.* 132 (2018) 104–140. <https://doi.org/10.1016/j.carbon.2018.02.024>.
- [2] I. Jeon, H. Noh, J. Baek, Nitrogen-Doped Carbon Nanomaterials: Synthesis, Characteristics and Applications, *Chem. – An Asian J.* 15 (2020) 2282–2293. <https://doi.org/10.1002/asia.201901318>.
- [3] Y. Park, Y. Kim, H. Chang, S. Won, H. Kim, W. Kwon, Biocompatible nitrogen-doped carbon dots: synthesis, characterization, and application, *J. Mater. Chem. B.* 8 (2020) 8935–8951. <https://doi.org/10.1039/D0TB01334J>.
- [4] X. Wang, D. Wu, C. Dai, C. Xu, P. Sui, R. Feng, Y. Wei, X.-Z. Fu, J.-L. Luo, Novel folic acid complex derived nitrogen and nickel co-doped carbon nanotubes with embedded Ni nanoparticles as efficient electrocatalysts for CO₂ reduction, *J. Mater. Chem. A.* 8 (2020) 5105–5114. <https://doi.org/10.1039/C9TA12238A>.
- [5] X. Liu, S. Li, L. Liu, Z. Wang, Facile pyrolysis approach of folic acid-derived highgraphite N-doped porous carbon materials for the oxygen reduction reaction, *New J. Chem.* 45 (2021) 5949–5957. <https://doi.org/10.1039/D0NJ06174C>.
- [6] S. Zhao, J. Yang, M. Han, X. Wang, Y. Lin, R. Yang, D. Xu, N. Shi, Q. Wang, M. Yang, Z. Dai, J. Bao, Synergistically enhanced oxygen reduction electrocatalysis by atomically dispersed and nanoscaled Co species in three-dimensional mesoporous Co, N-codoped carbon nanosheets network, *Appl. Catal. B Environ.* 260 (2020) 118207. <https://doi.org/10.1016/j.apcatb.2019.118207>.
- [7] S. Xie, L. Li, Y. Chen, J. Fan, Q. Li, Y. Min, Q. Xu, Folic Acid Coordinated Cu-Co Site N-Doped Carbon Nanosheets for Oxygen Reduction Reaction, *ACS Appl. Mater. Interfaces.* 13 (2021) 3949–3958. <https://doi.org/10.1021/acsami.0c19124>.
- [8] X. Wang, J. Sun, T. Li, Z. Song, D. Wu, B. Zhao, K. Xiang, W. Ai, X.Z. Fu, J.L. Luo, Folic acid self-assembly synthesis of ultrathin N-doped carbon nanosheets with single-atom metal catalysts, *Energy Storage Mater.* 36 (2021) 409–416. <https://doi.org/10.1016/j.ensm.2021.01.024>.
- [9] Z.J. Zhang, X.Y. Chen, Nitrogen-doped nanoporous carbon materials derived from folic acid: Simply introducing redox additive of p-phenylenediamine into KOH electrolyte for greatly improving the supercapacitor performance, *J. Electroanal. Chem.* 764 (2016) 45–55. <https://doi.org/10.1016/j.jelechem.2016.01.017>.
- [10] M. Ayiania, M. Smith, A.J.R. Hensley, L. Scudiero, J.-S. McEwen, M. Garcia-Perez, Deconvoluting the XPS spectra for nitrogen-doped chars: An analysis from first principles, *Carbon N. Y.* 162 (2020) 528–544. <https://doi.org/10.1016/j.carbon.2020.02.065>.
- [11] Y. Wu, M. Lu, Y. Li, P. He, S.B. Maddine, J. Gao, J. Yao, Folic Acid Derived Bimetallic-Doped Hollow Carbon Nanostructures for Efficient Electrocatalytic Oxygen Evolution, *Chem. - An Asian J.* 13 (2018) 3274–3280. <https://doi.org/10.1002/asia.201801121>.
- [12] H. Liu, Z. Li, Y. Sun, X. Geng, Y. Hu, H. Meng, J. Ge, L. Qu, Synthesis of Luminescent Carbon Dots with Ultrahigh Quantum Yield and Inherent Folate Receptor-Positive

- Cancer Cell Targetability, *Sci. Rep.* 8 (2018) 1086. <https://doi.org/10.1038/s41598-018-19373-3>.
- [13] Q. Zhang, S. Deng, J. Liu, X. Zhong, J. He, X. Chen, B. Feng, Y. Chen, K. (Ken) Ostrikov, Cancer-Targeting Graphene Quantum Dots: Fluorescence Quantum Yields, Stability, and Cell Selectivity, *Adv. Funct. Mater.* 29 (2019) 1–11. <https://doi.org/10.1002/adfm.201805860>.
- [14] L. Wang, Y. Yin, A. Jain, H. Susan Zhou, Aqueous phase synthesis of highly luminescent, nitrogen-doped carbon dots and their application as bioimaging agents, *Langmuir*. 30 (2014) 14270–14275. <https://doi.org/10.1021/la5031813>.
- [15] V.R. Magri, M.A. Rocha, C.S. de Matos, P.A.D. Petersen, F. Leroux, H.M. Petrilli, V.R.L. Constantino, Folic acid and sodium folate salts: Thermal behavior and spectroscopic (IR, Raman, and solid-state ¹³C NMR) characterization, *Spectrochim. Acta Part A Mol. Biomol. Spectrosc.* 273 (2022) 120981. <https://doi.org/10.1016/j.saa.2022.120981>.
- [16] P.R. Dametto, F.J. Caires, B. Ambrozini, M. Ionashiro, Synthesis, characterization and thermal behaviour of light trivalent lanthanides folates on solid state, *J. Therm. Anal. Calorim.* 105 (2011) 831–836. <https://doi.org/10.1007/s10973-010-1233-7>.
- [17] D. Braga, L. Chelazzi, F. Grepioni, L. Maschio, S. Nanna, P. Taddei, Folic Acid in the Solid State: A Synergistic Computational, Spectroscopic, and Structural Approach, *Cryst. Growth Des.* 16 (2016) 2218–2224. <https://doi.org/10.1021/acs.cgd.6b00043>.
- [18] P.R. Dametto, B. Ambrozini, F.J. Caires, V.P. Franzini, M. Ionashiro, Synthesis, characterization and thermal behaviour of solid-state compounds of folates with some bivalent transition metals ions, *J. Therm. Anal. Calorim.* 115 (2014) 161–166. <https://doi.org/10.1007/s10973-013-3276-z>.
- [19] A. Vora, A. Riga, D. Dollimore, K.S. Alexander, Thermal stability of folic acid, *Thermochim. Acta.* 392–393 (2002) 209–220. [https://doi.org/10.1016/S0040-6031\(02\)00103-X](https://doi.org/10.1016/S0040-6031(02)00103-X).
- [20] P.J. Linstrom and W.G. Mallard, Eds., NIST Chemistry WebBook, NIST Standard Reference Database Number 69, National Institute of Standards and Technology, Gaithersburg MD, 20899, <https://doi.org/10.18434/T4D303>
- [21] I.E. Gordon, L.S. Rothman, R.J. Hargreaves, R. Hashemi, et al., The HITRAN2020 molecular spectroscopic database, *J. Quant. Spectrosc. Radiat. Transf.* 277 (2022) 107949. <https://doi.org/10.1016/j.jqsrt.2021.107949>.
- [22] C. Casiraghi, A.C. Ferrari, J. Robertson, Raman spectroscopy of hydrogenated amorphous carbons, *Phys. Rev. B.* 72 (2005) 085401. <https://doi.org/10.1103/PhysRevB.72.085401>.
- [23] J.K. Kibet, L. Khachatryan, B. Dellinger, Molecular products from the thermal degradation of glutamic acid, *J. Agric. Food Chem.* 61 (2013) 7696–7704. <https://doi.org/10.1021/jf401846t>.
- [24] H. Chen, Y. Xie, W. Chen, M. Xia, K. Li, Z. Chen, Y. Chen, H. Yang, Investigation on co-pyrolysis of lignocellulosic biomass and amino acids using TG-FTIR and Py-GC/MS, *Energy Convers. Manag.* 196 (2019) 320–329.

<https://doi.org/10.1016/j.enconman.2019.06.010>.

- [25] J.A. Teixeira, W.D.G. Nunes, A.L.C.S. do Nascimento, T.A.D. Colman, F.J. Cairés, D.A. Gálico, M. Ionashiro, Synthesis, thermoanalytical, spectroscopic study and pyrolysis of solid rare earth complexes (Eu, Gd, Tb and Dy) with p-aminobenzoic acid, *J. Anal. Appl. Pyrolysis*. 121 (2016) 267–274. <https://doi.org/10.1016/j.jaap.2016.08.006>.
- [26] D.R. Lide, *CRC Handbook of Chemistry and Physics*, 90th ed., CRC Press (an imprint of Taylor & Francis Group), Boca Raton, FL, 2009.
- [27] X. Zhou, H.B. Mayes, L.J. Broadbelt, M.W. Nolte, B.H. Shanks, Fast pyrolysis of glucose-based carbohydrates with added NaCl part 1: Experiments and development of a mechanistic model, *AIChE J.* 62 (2016) 766–777. <https://doi.org/10.1002/aic.15106>.
- [28] X. Liu, Z. Luo, C. Yu, B. Jin, H. Tu, Release mechanism of fuel-N into NO_x and N₂O precursors during pyrolysis of rice straw, *Energies*. 11 (2018). <https://doi.org/10.3390/en11030520>.
- [29] Z.Q. Li, C.J. Lu, Z.P. Xia, Y. Zhou, Z. Luo, X-ray diffraction patterns of graphite and turbostratic carbon, *Carbon N. Y.* 45 (2007) 1686–1695. <https://doi.org/10.1016/j.carbon.2007.03.038>.
- [30] R.D.S. Macedo, *Materiais à Base de Hidróxidos Duplos Lamelares de Cobalto e Alumínio: Intercalação, Reatividade e Formação de Compósitos por Pirólise.*, Institute of Chemistry - São Paulo University, 2017.
- [31] T. Kato, Y. Yamada, Y. Nishikawa, H. Ishikawa, S. Sato, Carbonization mechanisms of polyimide: Methodology to analyze carbon materials with nitrogen, oxygen, pentagons, and heptagons, *Carbon N. Y.* 178 (2021) 58–80. <https://doi.org/10.1016/j.carbon.2021.02.090>.
- [32] N.B. Colthup, L.H. Daly, S.E. Wiberley, *Introduction to Infrared and Raman Spectroscopy*, 3rd ed., Academic Press, 1990. <https://doi.org/10.1016/C2009-0-21628-X>.
- [33] S.E. Rodil, Infrared spectra of amorphous carbon based materials, *Diam. Relat. Mater.* 14 (2005) 1262–1269. <https://doi.org/10.1016/j.diamond.2005.01.044>.
- [34] A.C. Ferrari, S.E. Rodil, J. Robertson, Interpretation of infrared and Raman spectra of amorphous carbon nitrides, *Phys. Rev. B.* 67 (2003) 155306. <https://doi.org/10.1103/PhysRevB.67.155306>.
- [35] S. Kanazawa, Y. Yamada, S. Sato, Infrared spectroscopy of graphene nanoribbons and aromatic compounds with sp³C–H (methyl or methylene groups), *J. Mater. Sci.* 56 (2021) 12285–12314. <https://doi.org/10.1007/s10853-021-06001-1>.
- [36] X. Cui, H. Yan, P. Zhao, Y. Yang, Y. Xie, Modeling of molecular and properties of anthracite base on structural accuracy identification methods, *J. Mol. Struct.* 1183 (2019) 313–323. <https://doi.org/10.1016/j.molstruc.2019.01.092>.
- [37] M. Acik, G. Lee, C. Mattevi, M. Chhowalla, K. Cho, Y.J. Chabal, Unusual infrared-absorption mechanism in thermally reduced graphene oxide, *Nat. Mater.* 9 (2010) 840–845. <https://doi.org/10.1038/nmat2858>.

- [38] E. Fuente, J.A. Menéndez, M.A. Díez, D. Suárez, M.A. Montes-Morán, Infrared spectroscopy of carbon materials: A quantum chemical study of model compounds, *J. Phys. Chem. B.* 107 (2003) 6350–6359. <https://doi.org/10.1021/jp027482g>.
- [39] S. Gohda, M. Saito, Y. Yamada, S. Kanazawa, H. Ono, S. Sato, Carbonization of phloroglucinol promoted by heteropoly acids, *J. Mater. Sci.* 56 (2021) 2944–2960. <https://doi.org/10.1007/s10853-020-05393-w>.
- [40] K. Mochidzuki, F. Soutric, K. Tadokoro, M.J. Antal, M. Tóth, B. Zelei, G. Várhegyi, Electrical and Physical Properties of Carbonized Charcoals, *Ind. Eng. Chem. Res.* 42 (2003) 5140–5151. <https://doi.org/10.1021/ie030358e>.
- [41] P.K. Chu, L. Li, Characterization of amorphous and nanocrystalline carbon films, *Mater. Chem. Phys.* 96 (2006) 253–277. <https://doi.org/10.1016/j.matchemphys.2005.07.048>.
- [42] A.C. Ferrari, D.M. Basko, Raman spectroscopy as a versatile tool for studying the properties of graphene, *Nat. Nanotechnol.* 8 (2013) 235–246. <https://doi.org/10.1038/nnano.2013.46>.
- [43] M.W. Smith, I. Dallmeyer, T.J. Johnson, C.S. Brauer, J.-S. McEwen, J.F. Espinal, M. Garcia-Perez, Structural analysis of char by Raman spectroscopy: Improving band assignments through computational calculations from first principles, *Carbon N. Y.* 100 (2016) 678–692. <https://doi.org/10.1016/j.carbon.2016.01.031>.
- [44] M. Ayiania, E. Weiss-Hortala, M. Smith, J.S. McEwen, M. Garcia-Perez, Microstructural analysis of nitrogen-doped char by Raman spectroscopy: Raman shift analysis from first principles, *Carbon N. Y.* 167 (2020) 559–574. <https://doi.org/10.1016/j.carbon.2020.05.055>.
- [45] J.T. Klopogge, D. Wharton, L. Hickey, R.L. Frost, Infrared and Raman study of interlayer anions CO_3^{2-} , NO_3^- , SO_4^{2-} and ClO_4^- in Mg/Al-hydrotalcite, *Am. Mineral.* 87 (2002) 623–629. <https://doi.org/10.2138/am-2002-5-604>.
- [46] D. Xu, L. Yang, K. Ding, Y. Zhang, W. Gao, Y. Huang, H. Sun, X. Hu, S.S.A. Syed-Hassan, S. Zhang, H. Zhang, Mini-Review on Char Catalysts for Tar Reforming during Biomass Gasification: The Importance of Char Structure, *Energy & Fuels.* 34 (2020) 1219–1229. <https://doi.org/10.1021/acs.energyfuels.9b03725>.
- [47] R. Pietrzak, H. Wachowska, P. Nowicki, Preparation of nitrogen-enriched activated carbons from brown coal, *Energy and Fuels.* 20 (2006) 1275–1280. <https://doi.org/10.1021/ef0504164>.
- [48] J. Bimer, P.D. Sałbut, S. Bertozecki, J.P. Boudou, E. Broniek, T. Siemieniowska, Modified active carbons from precursors enriched with nitrogen functions: Sulfur removal capabilities, *Fuel.* 77 (1998) 519–525. [https://doi.org/10.1016/S0016-2361\(97\)00250-0](https://doi.org/10.1016/S0016-2361(97)00250-0).
- [49] M. Smith, L. Scudiero, J. Espinal, J.-S. McEwen, M. Garcia-Perez, Improving the deconvolution and interpretation of XPS spectra from chars by ab initio calculations, *Carbon N. Y.* 110 (2016) 155–171. <https://doi.org/10.1016/j.carbon.2016.09.012>.
- [50] W. Chen, H. Yang, Y. Chen, X. Chen, Y. Fang, H. Chen, Biomass pyrolysis for nitrogen-containing liquid chemicals and nitrogen-doped carbon materials, *J. Anal. Appl. Pyrolysis.* 120 (2016) 186–193. <https://doi.org/10.1016/j.jaap.2016.05.004>.

- [51] H. Yang, B. Huan, Y. Chen, Y. Gao, J. Li, H. Chen, Biomass-Based Pyrolytic Polygeneration System for Bamboo Industry Waste: Evolution of the Char Structure and the Pyrolysis Mechanism, *Energy and Fuels*. 30 (2016) 6430–6439. <https://doi.org/10.1021/acs.energyfuels.6b00732>.
- [52] H. Yang, M. Gong, J. Hu, B. Liu, Y. Chen, J. Xiao, S. Li, Z. Dong, H. Chen, Cellulose Pyrolysis Mechanism Based on Functional Group Evolutions by Two-Dimensional Perturbation Correlation Infrared Spectroscopy, *Energy & Fuels*. 34 (2020) 3412–3421. <https://doi.org/10.1021/acs.energyfuels.0c00134>.
- [53] G.S. Ghodake, S.K. Shinde, A.A. Kadam, R.G. Saratale, G.D. Saratale, M. Kumar, R.R. Palem, H.A. AL-Shwaiman, A.M. Elgorban, A. Syed, D.-Y. Kim, Review on biomass feedstocks, pyrolysis mechanism and physicochemical properties of biochar: State-of-the-art framework to speed up vision of circular bioeconomy, *J. Clean. Prod.* 297 (2021) 126645. <https://doi.org/10.1016/j.jclepro.2021.126645>.
- [54] W. Chen, K. Li, M. Xia, Y. Chen, H. Yang, Z. Chen, X. Chen, H. Chen, Influence of NH₃ concentration on biomass nitrogen-enriched pyrolysis, *Bioresour. Technol.* 263 (2018) 350–357. <https://doi.org/10.1016/j.biortech.2018.05.025>.
- [55] S.N. Baker, G.A. Baker, Luminescent Carbon Nanodots: Emergent Nanolights, *Angew. Chemie Int. Ed.* 49 (2010) 6726–6744. <https://doi.org/10.1002/anie.200906623>.
- [56] H. Ding, S.-B. Yu, J.-S. Wei, H.-M. Xiong, Full-Color Light-Emitting Carbon Dots with a Surface-State-Controlled Luminescence Mechanism, *ACS Nano*. 10 (2016) 484–491. <https://doi.org/10.1021/acsnano.5b05406>.
- [57] H. Ding, J.-S. Wei, H.-M. Xiong, Nitrogen and sulfur co-doped carbon dots with strong blue luminescence, *Nanoscale*. 6 (2014) 13817–13823. <https://doi.org/10.1039/c4nr04267k>.
- [58] Y. Deng, X. Chen, F. Wang, X. Zhang, D. Zhao, D. Shen, Environment-dependent photon emission from solid state carbon dots and its mechanism, *Nanoscale*. 6 (2014) 10388–10393. <https://doi.org/10.1039/C4NR02544J>.
- [59] S. Hu, A. Trinchi, P. Atkin, I. Cole, Tunable Photoluminescence Across the Entire Visible Spectrum from Carbon Dots Excited by White Light, *Angew. Chemie Int. Ed.* 54 (2015) 2970–2974. <https://doi.org/10.1002/anie.201411004>.
- [60] H. Ding, X.-H. Li, X.-B. Chen, J.-S. Wei, X.-B. Li, H.-M. Xiong, Surface states of carbon dots and their influences on luminescence, *J. Appl. Phys.* 127 (2020) 231101. <https://doi.org/10.1063/1.5143819>.
- [61] Y. Wang, S. Kalytchuk, Y. Zhang, H. Shi, S. V. Kershaw, A.L. Rogach, Thickness-Dependent Full-Color Emission Tunability in a Flexible Carbon Dot Ionogel, *J. Phys. Chem. Lett.* 5 (2014) 1412–1420. <https://doi.org/10.1021/jz5005335>.
- [62] Z. Huang, Y. Shen, Y. Li, W. Zheng, Y. Xue, C. Qin, B. Zhang, J. Hao, W. Feng, Facile synthesis of analogous graphene quantum dots with sp²hybridized carbon atom dominant structures and their photovoltaic application, *Nanoscale*. 6 (2014) 13043–13052. <https://doi.org/10.1039/c4nr03658a>.
- [63] D. Pan, J. Zhang, Z. Li, C. Wu, X. Yan, M. Wu, Observation of pH-, solvent-, spin-, and excitation-dependent blue photoluminescence from carbon nanoparticles, *Chem.*

Commun. 46 (2010) 3681. <https://doi.org/10.1039/c000114g>.

- [64] S. Tao, S. Zhu, T. Feng, C. Xia, Y. Song, B. Yang, The polymeric characteristics and photoluminescence mechanism in polymer carbon dots: A review, *Mater. Today Chem.* 6 (2017) 13–25. <https://doi.org/10.1016/j.mtchem.2017.09.001>.
- [65] A.M. Abramova, A.A. Kokorina, O.A. Sindeeva, F. Jolibois, P. Puech, G.B. Sukhorukov, I.Y. Goryacheva, A. V. Sapelkin, Molecular nature of breakdown of the folic acid under hydrothermal treatment: a combined experimental and DFT study, *Sci. Rep.* 10 (2020) 1–6. <https://doi.org/10.1038/s41598-020-76311-y>.

Hybrid nanomaterials based on Folic Acid intercalated into M^{2+}/Al^{3+} ($M^{2+} = Mg^{2+}$ and Zn^{2+}) Layered Double Hydroxides as precursors of Carbon-based Nanocomposites

Vagner R. Magri,^a Caroline S. de Matos^a, Michele A. Rocha^a, Rafael Macedo^b, Christine Taviot-Gueho^{cd} and Vera R.L. Constantino^{*a}

^aDepartamento de Química Fundamental, Instituto de Química, Universidade de São Paulo, Av. Prof. Lineu Prestes 748, CEP 05508-000, São Paulo, SP, Brazil.

E-mail: vrlconst@iq.usp.br

^b Escola Politécnica da Universidade de São Paulo - Departamento de Engenharia de Minas e de Petróleo, Laboratório de Caracterização Tecnológica, CEP 05508-030, São Paulo, SP, Brazil

^cUniversité Clermont Auvergne, Université Blaise Pascal, Institut de Chimie de Clermont-Ferrand, BP 10448, F-63000 Clermont-Ferrand, France

^dCNRS, UMR 6296, ICCF, F-63178 Aubiere, France

Keywords: Layered double hydroxide (LDH); Folic Acid; Thermal Analysis; Evolved Gas Analysis (EGA); Pyrolysis; Hydrothermal Carbonization; Memory Effect; graphene-like materials; Carbon-based nanocomposites.

Highlights

- Carbon-based nanocomposites were obtained from the pyrolysis of LDH intercalated with folate anions;
- Influence of LDH composition in the synthesis of carbon-based nanocomposites
- LDO-C structural reconstitution into LDH-C
- Synthesis of photoluminescent materials

Abstract: Layered double Hydroxides (LDH) of Mg^{2+}/Al^{3+} or Zn^{2+}/Al^{3+} compositions and intercalated with Folic Acid (FA) anions were evaluated as precursors of carbon-based nanocomposites through one-pot bottom-up methods. The thermal behaviour of the LDH-FA hybrid materials was evaluated under N_2 atmosphere by the simultaneous thermogravimetric analysis (TGA) and differential scanning calorimetry (DSC) and the evolved gas analysis (EGA) through TGA coupled to mass spectrometry (TGA-MS) and infrared spectroscopy (TGA-IR). LDH-FA materials were pyrolyzed in a set of temperatures to obtain nanocomposites based on carbonaceous material (C) and layered double oxide (LDO). Crystallization of metal oxides and spinel phases ($MgAl_2O_4$ or $ZnAl_2O_4$) was hindered by carbonized material formed between the layers during the pyrolysis and LDO-C composites constituted of graphitic carbon and crystalline metal oxides (MgO and ZnO) were only obtained in temperatures above $800\text{ }^\circ\text{C}$. The carbonization degree was more intense for Zn-LDH than for Mg-LDH. Furthermore, LDO-C was successfully converted to LDH-C through a reconstitution reaction in water, but phase separation occurred for Zn-LDH and Mg-LDH samples pyrolyzed at 800 and $1000\text{ }^\circ\text{C}$, respectively. LDH-C presented photoluminescent properties that decreased in intensity as far as the pyrolysis temperature increased up to $600\text{ }^\circ\text{C}$. For comparison, nanocomposites were also prepared by hydrothermal carbonization approach varying the temperature (150 and $180\text{ }^\circ\text{C}$) and the time (1 - 10 h). For Mg-LDH, the anion exchange between folate and carbonate generated during the process promoted carbonization outside the layers. Although, the Mg-LDH structure was maintained independent of the hydrothermal parameters, being progressively converted to LDH- CO_3 phase. Differently, ZnO-nanocomposites were obtained from Zn-LDH, increasing temperature and time. This work contributes to the development of new carbon-based nanocomposites from LDH hybrid materials, with the potential to be applied in sensing, catalysis, environmental protection as well as nanomedicine, among other fields.

1. Introduction

Nanocomposites constituted by graphene-like materials and layered double hydroxides (LDH) present potentiality to be applied in sensing, catalysis, energy storage devices, environmental remediation and in nanomedicine (drug delivery system and theragnostic agent), for instance (Zhao et al., 2012; Cao et al., 2016; Khorshidi et al., 2022). Assorted applications are allowed thanks to the synergism between the outstanding properties of graphene-like materials (*e.g.*, electronic conductivity, mechanical strength, photoluminescence) with the reactivity of LDH (Zhao et al., 2012; Cao et al., 2016; Khorshidi et al., 2022).

LDH are a class of layered material with brucite $\text{Mg}(\text{OH})_2$ -like structure (**Figure 1a**). The layers are formed by edge-sharing of octahedrons of metal cations coordinated to hydroxide ions in the vertices ($\text{M}(\text{OH})_6$) (Cavani et al., 1991; Taviot-Guého et al., 2018). Isomorphic substitution of bivalent by trivalent metal cations in the layers confers an equivalent positive residual charge ($[\text{M}^{3+}] = [q^+]$) to the material. The electroneutrality is reached by the intercalation of hydrated-exchangeable anions into the LDH interlayer spaces. LDH are versatile in terms of composition as represented by the general formula $[\text{M}^{2+}_{(1-x)}\text{M}^{3+}_x(\text{OH})_2]^{x+}[(\text{A}^{n-})_{x/n} \cdot m\text{H}_2\text{O}]$, where M^{2+} is a divalent metal cation (Mg^{2+} , Zn^{2+} , Ni^{2+} , Co^{2+} , Cu^{2+} , Fe^{2+} , *etc.*) and M^{3+} is a trivalent cation (Al^{3+} , Ga^{3+} , Co^{3+} , Fe^{3+} , *etc.*); A^{n-} is the compensation anion that can be inorganic (CO_3^{2-} , Cl^- , NO_3^- , *etc.*), organic, polymeric or a coordination compound (Cavani et al., 1991; Taviot-Guého et al., 2018). The x value represents the $[\text{M}^{3+}]/([\text{M}^{2+}]+[\text{M}^{3+}])$ molar fraction that generally varies between $0.2 \leq x \leq 0.33$ (or $[\text{M}^{2+}]/[\text{M}^{3+}]$ molar ratio between 4:1 and 2:1). The physicochemical properties of LDH are intrinsically dependent on their layer composition, but in general, such materials are soluble in acidic media and present anion-exchange properties (Cavani et al., 1991; Taviot-Guého et al., 2018; Ye et al., 2022). Besides, upon heating, LDH can be converted into reactive layered double oxides (LDO) or mixed-metal oxides (Takehira, 2017; Ye et al., 2022). Such LDH

derivatives present catalytic properties due to the acid-base pairs ($M^{2+}-O^{2-}$ and $Al^{3+}-O^{2-}$) generated during the layer dehydroxylation. The original LDH structure can be restored by reaction with water or moisture, the so-called “memory effect” (Takehira, 2017; Ye et al., 2022).

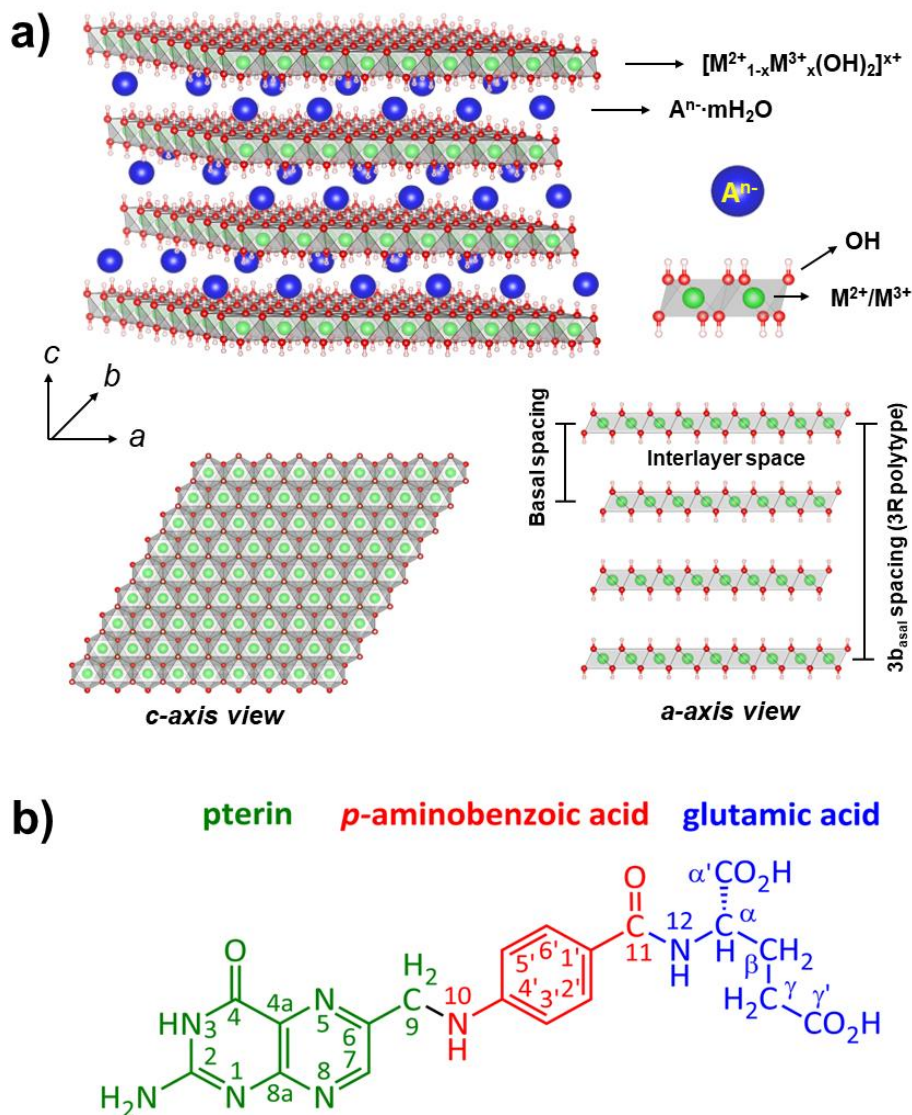


Figure 1. Schematic representation of the LDH structure with rhombohedral symmetry (3R1 three-layer polytype) in R-3m space group (a) and molecular structure of FA (b).

Hybrid materials constituted of LDH intercalated with anionic organic species are suitable precursors of carbon-based nanocomposites obtained by bottom-up methods through pyrolysis or hydrothermal carbonization (Sun et al., 2012; Song et al., 2015, 2016; Liu et al., 2017; Bai et al., 2018; Magri et al., 2019; de Matos et al., 2020). The use of hybrid materials as

a precursor of nanocomposites is advantageous because: (i) the synthesis can be carried out by one-pot methods, carbonizing the organic anion *in-situ* in the confined space of interlayer region; (ii) LDH structure works as a nanoreactor, controlling the reaction rate and contributing to the formation of graphene-like materials with homogeneous structure and composition, such as carbon dots (C-dots) (Song et al., 2015, 2016; Liu et al., 2017; Bai et al., 2018) and graphene single layers (Sun et al., 2012); (iii) concomitantly to the carbonization of the organic anion, LDH can be converted into magnetic metallic nanoparticles (de Matos et al., 2020) or LDO/mixed metal oxides (Magri et al., 2019), which opens an avenue of possibilities to prepare nanocomposites based on carbonaceous materials with different structures as nano-onions (de Matos et al., 2020) and graphitic carbon (Magri et al., 2019),.

Anionic organic species, such as citrate (Song et al., 2015, 2016; Liu et al., 2017), ethylene diamine tetraacetate (EDTA) (Bai et al., 2018), dodecyl sulfonate (DSO) (Sun et al., 2012) and carboxymethyl cellulose polymer (CMC) (Magri et al., 2019; de Matos et al., 2020), have been intercalated into LDH structure and used as a carbon precursor by *in-situ* carbonization approaches. Besides, nitrogenated species can be used for N-doping the carbon array (Song et al., 2015, 2016; Liu et al., 2017), improving the electronic and optical properties of materials (Inagaki et al., 2018; Liu et al., 2019). Since hundreds of organic anions can be intercalated into LDH structure (Taviot-Guého et al., 2018), the carbon source is not limited to a few organic molecules. For instance, hybrid materials intercalated with anions from folic acid (FA; vitamin B9) have a huge potential to be used as a precursor of carbon-based nanocomposites. FA presents a proper structure for the synthesis of N-doped carbon materials. As shown in **Figure 1b**, FA is formed by pterin (PT), p-aminobenzoic acid (*p*-ABA) and L-glutamic acid (Glu) moieties (**Figure 1b**), making it a source of carbon and nitrogen as well as building blocks of aromatic rings for graphene-like materials, such as C-dots (Zhang et al., 2019) and graphitic carbon (Liu et al., 2021). Although the intercalation of folate anions into

LDH has already been reported, to the best of our knowledge, the use of LDH-FA hybrid materials was not explored yet for such purposes.

In the perspective of LDH layer composition, there is a limitation in the literature regarding the influence of layer chemical composition in the carbonization process, even though one of the main factors influencing the thermal stability and the structural transformation of LDH upon heating is the layer composition (Zhao et al., 2010; Hobbs et al., 2018; Magri et al., 2019). The reconstitution of LDH structure after pyrolysis of hybrid materials is also poorly explored (Conterposito et al., 2018). Despite that, the reconstitution mechanism for calcined materials is well reported because of the role of memory effect in environmental remediation (Ye et al., 2022). Furthermore, no work was reported in the literature concerning the influence of the carbonization method in the synthesis of nanocomposites.

In this work, hybrid nanomaterials formed by folate anions (HFol^{2-} and Fol^{3-}) intercalated into the $\text{M}_2\text{Al-LDH}$ (M : Mg^{2+} or Zn^{2+}) were synthesized by the co-precipitation method. Aiming at the synthesis of carbon-based nanocomposites, the work was focused in four lines: (i) evaluation of thermal behaviour of hybrid materials by TGA/DSC and EGA analysis to address the adequate temperature range for the synthesis of carbon-based nanocomposites; (ii) pyrolysis of precursors to obtain nanocomposites constituted of LDO and graphite-like materials (LDO-C); (iii) reconstitution reaction of LDO-C into LDH-C and evaluation of the potential to obtain LDH/C-dots nanocomposites; and (iv) for comparison, the preparation of LDH/C-dots by hydrothermal carbonization approach. This work will contribute to a more assertive synthesis of new carbon-based nanomaterials constituted by LDO and LDH.

2. Experimental

2.1. Chemicals

All chemicals used in this work were reported in *Section SI.1* of supplementary information (SI).

2.2. Methods

The synthesis (*section SI.2*) and characterization (*section SI.3*) procedure of LDH were given in the SI. The materials were undermentioned as LDH-FA (intercalated with folate anions, $\text{H}_2\text{Fol}^{2-}$ or Fol^{3-}), LDH-Cl (intercalated with chloride anions) or $\text{M}_R^{2+}\text{Al-A}$, where M^{2+} is the divalent metal cation (Mg or Zn), R means the nominal $\text{M}^{2+}/\text{Al}^{3+}$ molar ratio equal two and A is the anion.

2.3. Thermal Behaviour

The thermal behaviour of materials was evaluated by thermogravimetry analysis (TGA) and differential scanning calorimetry (DSC) coupled to evolved gas analyses (EGA). TGA/DSC were conducted on a Netzsch thermoanalyzer, model STA 409 PC Luxx. The equipment was coupled to FTIR spectrophotometer Bruker, Tensor 27 model (MCT detector cooled with liquid N_2 ; 4400-650 cm^{-1} region and 4 cm^{-1} of resolution), and to a QMS 403C Aëolos MSD mass spectrometer to conduct the EGA by infrared spectroscopy (TGA-IR) and mass spectrometry (TGA-MS), respectively. The experiment was performed up to 1000 °C, under dynamic N_2 atmosphere with a flow rate of 50 $\text{mL}\cdot\text{min}^{-1}$, heating rate of 10 $^\circ\text{C}\cdot\text{min}^{-1}$ and using alumina crucible. The vibrational bands of TGA-IR spectra were attributed from comparing the results with spectra of reference gaseous molecules available online by National

Institute of Standards and Technology NIST (Linstrom and Mallard, 2023) and HITRAN (Gordon et al., 2022) databases.

2.2. Synthesis of LDO-C nanocomposites

The synthesis of LDO-C was evaluated by pyrolyzing the $Mg_2Al-Fol$ and $Zn_2Al-HFol$ hybrid precursors on a Shimadzu TGA-50 furnace under N_2 flow ($50\text{ mL}\cdot\text{min}^{-1}$), using a heating rate of $10\text{ }^\circ\text{C}\cdot\text{min}^{-1}$ and alumina crucibles. The temperature values of pyrolysis were selected based on TGA/DSC results, as follow: (i) $Mg_2Al-Fol$: at $360\text{ }^\circ\text{C}$, $410\text{ }^\circ\text{C}$, $450\text{ }^\circ\text{C}$, $600\text{ }^\circ\text{C}$, $800\text{ }^\circ\text{C}$ and $1000\text{ }^\circ\text{C}$; and (ii) $Zn_2Al-Fol$: at $360\text{ }^\circ\text{C}$, $430\text{ }^\circ\text{C}$, $500\text{ }^\circ\text{C}$, $600\text{ }^\circ\text{C}$ and $800\text{ }^\circ\text{C}$. To evaluate the influence of isothermal condition in the synthesis of LDO-C from the pyrolysis of LDH-FA, additional samples were pyrolyzed at $360\text{ }^\circ\text{C}$ with aneling time of 0.5 h. The nanocomposites obtained were stored in a desiccator containing silica gel under reduced pressure. The LDO-C materials were encoded as $M_R^{2+}Al-A-X$, where X indicates the temperature of pyrolysis (in $^\circ\text{C}$). The $M_R^{2+}Al-A-360/0.5$ denomination was given to the sample annealed at $360\text{ }^\circ\text{C}$ for 0.5 h.

2.3. Synthesis of LDH-C nanocomposites

The viability of obtaining LDH-C from LDO-C nanocomposites were evaluated by reconstruction essay in water. LDO-C were suspending in deionized water (LDO-C: H_2O mass ratio of $\approx 1:1000$) in sealed vials followed by stirring in a vortex equipment for 10 s. Then, the samples were taken under a low-power ultrasonic bath (Limp Sonic LS-3D ultrasonic equipment; 70 W and 40 kHz) for 5 min and stirred once again for more 5 min. Next, the samples were kept standing for 7 days in a room atmosphere and temperature. After that, the solid phases were isolated by centrifugation, and washed once with water and once with ethanol. Finally, the materials were dried under reduced pressure in a desiccator containing silica gel for

3 days and kept inside that until characterization. The LDH-C materials were encoded as $M_R^{2+}Al-A-Xr$, where “r” indicates that the materials were submitted to the reconstruction essay.

2.4. Hydrothermal Carbonization

The hydrothermal carbonization procedure, aiming to obtain of LDH/C-dots nanocomposites from LDH-FA, was performed based on works previously reported in the literature (Song et al., 2015; Liu et al., 2017) with some modifications. Initially, 0.136 g of LDH was suspended in 4 mL of water, inside a Teflon cup (25 mL volume) and under ultrasound for 5 min. The cup was transferred to stainless steel reactor, placed inside an oven, and heated at *ca.* $4\text{ }^\circ\text{C}\cdot\text{min}^{-1}$ (**Figure S1**). The experimental time (1-10 h) were considered after the oven reached the desired temperature (150 $^\circ\text{C}$ or 180 $^\circ\text{C}$). After that, the systems were cooled naturally to room temperature. The samples were isolated and washed with water twice by centrifugation (20 000 rpm for 10 min at 25 $^\circ\text{C}$) and dried by lyophilization. The materials were named as $M_R^{2+}Al-A-HTX/h$, where HT indicates hydrothermal carbonization, X is the temperature value, and h is the time in hours.

2.5. Characterization of materials

X-ray diffraction (XRD) patterns of powdered samples were recorded *ex-situ* in a Bruker D8 DISCOVER diffractometer equipped with Nickel filtered $\text{CuK}\alpha$ radiation ($\lambda = 0.15418\text{ nm}$) source and operating at 40 kV and 30 mA. The diffractograms were collected in the 3–70 $^\circ$ (2θ) range, with steps of $0.05^\circ/2\theta$ and a scan speed of $0.05^\circ/0.5\text{ s}$. *In-situ* XRD obtained under heating (HT-XRD) were acquired on the X’Pert-pro diffractometer equipped with the high-temperature chamber (Anton Paar HTK-16). The measurements were conducted after purging the furnace with N_2 for 2 h and heating in the 25-800 $^\circ\text{C}$ range, under the heating rate of $10\text{ }^\circ\text{C min}^{-1}$ and

dynamic nitrogen atmosphere (24 mL min^{-1}). The diffractograms were recorded in a range using a step size of 0.0167° (2θ) and a counting time of 100 s/step.

Fourier transform infrared (FTIR) spectra of powdered samples were recorded on a Bruker Alpha spectrometer (DTGS detector and KBr optics) in the attenuated total diffuse reflectance (ATR) mode with a diamond crystal, in the $4000\text{--}400 \text{ cm}^{-1}$ spectral range, 4 cm^{-1} of resolution and accumulating 512 scans. Raman spectra of nanocomposites were recorded in a Renishaw inVia Reflex instrument coupled to a confocal Leica microscope (50x lenses) and a CCD detector (600×400 pixels), using excitation radiation of 532 nm (Nd:YAG laser; power $\leq 3 \text{ mW}$) or 633 nm (HeNe laser; power of 8 mW), in the $3200\text{--}400 \text{ cm}^{-1}$ range.

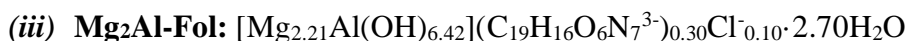
Electronic UV-VIS spectra were registered in Shimadzu spectrophotometer, UV-2401PC model, equipped with an integration sphere. For analysis, dispersions of $0.2 \text{ g}\cdot\text{L}^{-1}$ of carbon-based nanocomposites obtained by pyrolysis/reconstruction or hydrothermal carbonization were prepared under ultrasonication until obtaining visually a well-dispersed sample. Photoluminescence analyses were conducted in Shimadzu spectrofluorophotometer, RF-5301PC model, after diluting $50 \mu\text{L}$ of the suspensions in 2 mL of water. Both optical measurements were carried out using a quartz cuvette with a path length of 1 cm and shaking the cuvette manually before each measurement to overcome the aggregation.

Scanning electron microscopy (SEM) images were registered in a Quanta 650 FEG microscope equipped with an EDT detector. Samples were suspended in isopropyl alcohol, dropped onto a silicon wafer, dried at room atmosphere, and covered with a Pt nanolayer. Energy Dispersive Spectroscopy (EDS) analysis were conducted in the same equipment. Transmission Electron Microscopy (TEM) image was acquired on a Hitachi H-7650 microscope operating with an accelerating voltage of 80 kV. The sample was prepared by suspending the material in ethanol (1 mg mL^{-1}) under ultrasound for 0.5 h. Then, the suspension was dropped onto a copper grid (150 mesh) coated with Formvar/carbon film.

3. Results and Discussion

3.1. Characterization of LDH-FA precursors

The detailed characterization of LDH-FA precursors is presented in *Section 2* (SI). The displacement of peaks attributed to 00*l* family planes to lower 2θ angles, compared to the XRD results of the LDH-Cl counterparts (**Figure S3**), confirmed the successful intercalation of folate anions into the LDH structure. The d_{00l} values increased from around 0.77 nm (LDH-Cl) to 2.56 nm, 1.66 nm and 1.61 nm for Zn₂Al-HFol, Zn₂Al-Fol and Mg₂Al-Fol materials (**Table S1-2**), respectively. The level of protonation of the anionic species intercalated was dependent on pH value used in the synthesis (**Figure S2** and *section 1.2*), as confirmed by FTIR-ATR and FT-Raman spectroscopies (**Figure S6** and **Table S2**) as well as chemical elemental analysis (**Table S4-5**). Accordingly, the proposed chemical formulas for the materials were:



3.2. Thermal Behaviour of LDH-FA

The thermal behaviour of LDH-FA precursors was initially investigated to determine the best temperature range for obtaining carbon-based nanocomposites, to evaluate the influence of the layer composition (Mg²⁺/Al³⁺ or Zn²⁺/Al³⁺), and the valence of the organic anion (HFol²⁻ or Fol³⁻) in the pyrolysis mechanism of the hybrid materials. The TGA/DSC curves of Zn₂Al-HFol, Zn₂Al-Fol and Mg₂Al-Fol were depicted in **Figure 2a**. **Figure 2b** presented DTG-MS curves and the derivative curves extract from coupled IR analysis (3D FTIR and counter map in **Figure 3** and **Figure S5**). The percentage of mass loss, the temperature range, the peak temperature (Tp) of the event in DTG covers and the gaseous/volatile species released during the analysis were summarized in **Table S6**.

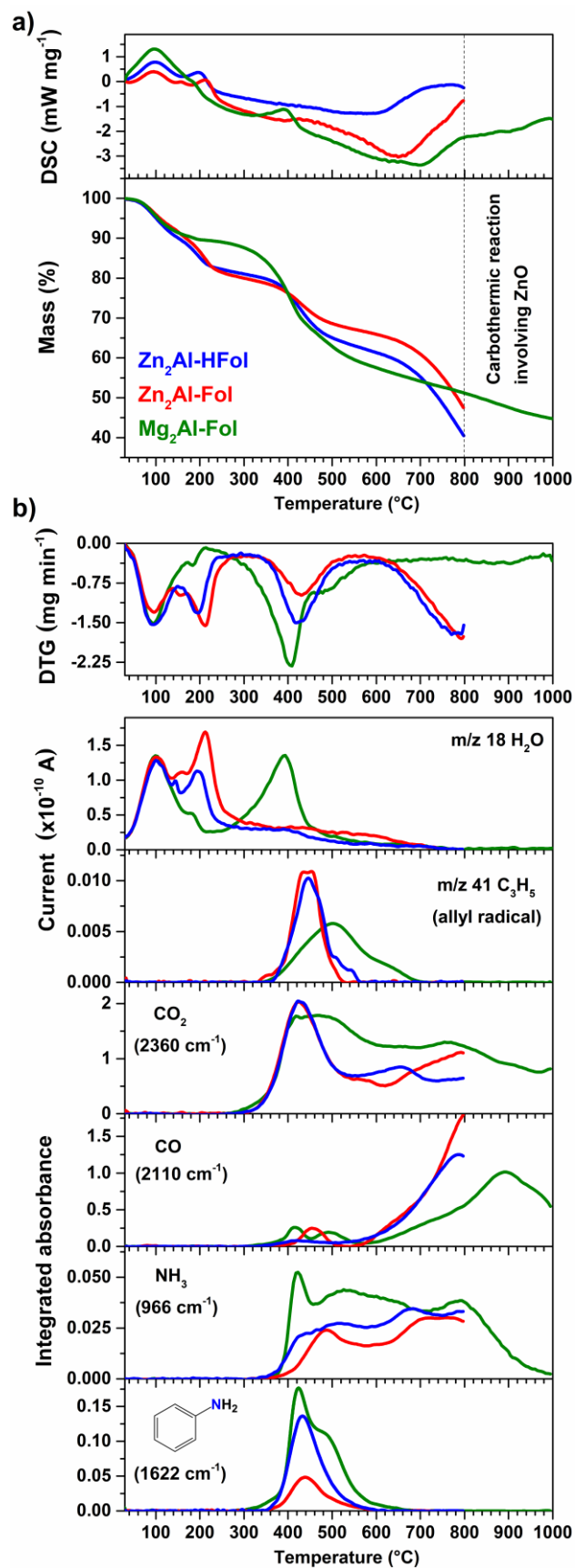


Figure 2. TGA/DSC (a) and DTG-MS-IR (b) curves for Zn₂Al-HFol (blue), Zn₂Al-Fol (red) and Mg₂Al-Fol (green).

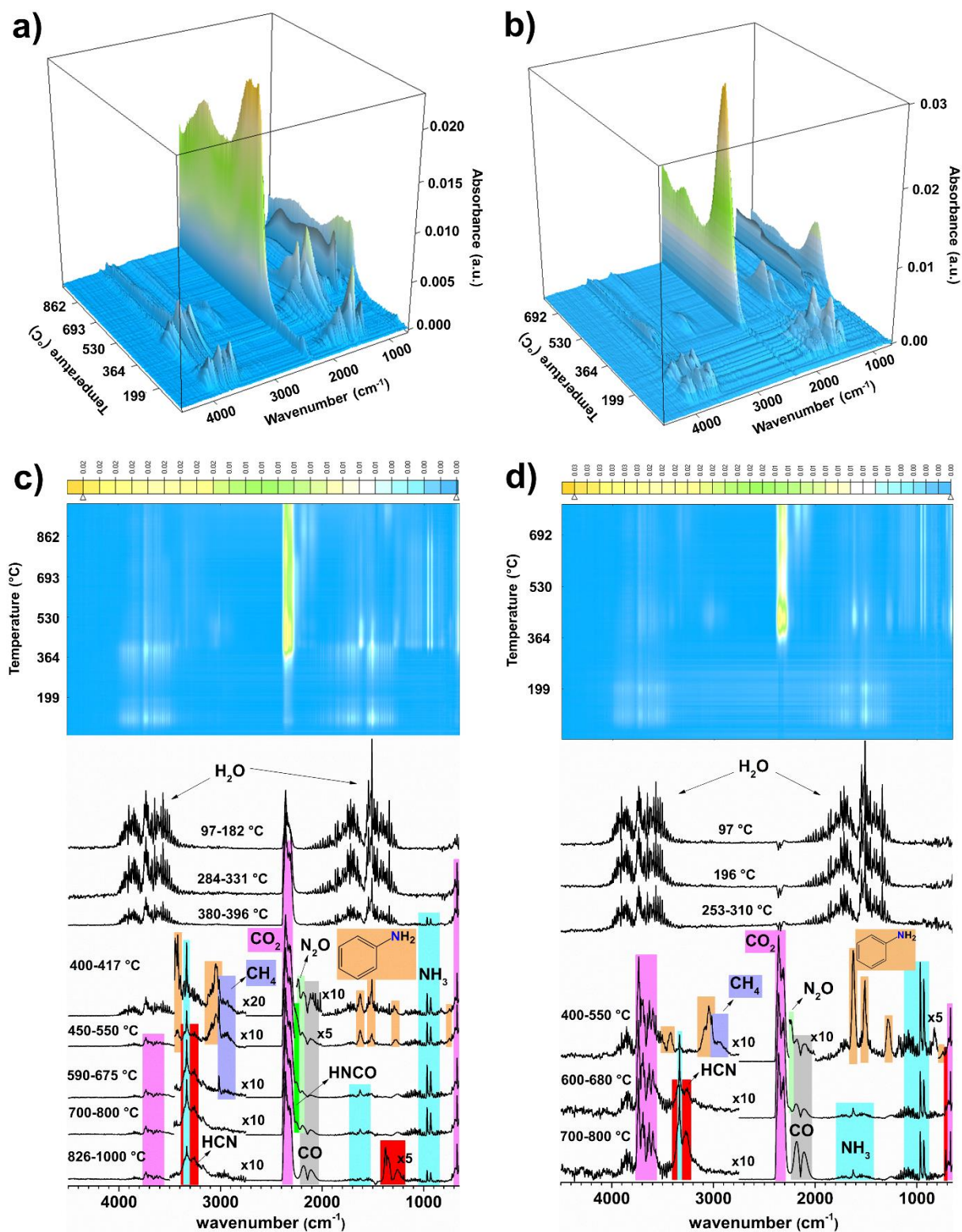


Figure 3. 3D plot of TGA-FTIR data (a,b) and contour map (superior; yellow and blue colours are defined as intensity increasing and decreasing, respectively) and FTIR spectra (inferior; at selected temperature ranges) (c,d) for Mg₂Al-Fol (a,c) and Zn₂Al-HFol (b,d).

The first endothermic event of mass loss around 30-200 °C (**Figure 2b**), marked by the release of m/z 18 fragment (H₂O), was typically assigned to the dehydration of materials (Magri et al., 2019). One of the main differences between the thermal behaviour of LDH materials composed by Mg²⁺/Al³⁺ and Zn²⁺/Al³⁺ consist in the higher thermal stability of the former against the dehydroxylation reaction (Rocha et al., 2016; Magri et al., 2019). For Mg₂Al-Fol, the dehydroxylation was observed at 250-450 °C, whereas for Zn₂Al-HFol and Zn₂Al-Fol, it occurred at around 160-270 °C, as can be verified from the release of water (m/z 18 fragment; **Figure 2b**). Such features are intrinsic of layer chemical composition (Rocha et al., 2016; Hobbs et al., 2018; Magri et al., 2019) and were independent of the intercalated anion (**Figure S6** and **Scheme S1**) or the atmosphere (**Figure S7**). Additionally, the Zn₂Al-LDH materials intercalated with organic anions can undergo to carbothermic reaction under an inert atmosphere above 800 °C (Magri et al., 2019). For this reason, the thermal analyses of Zn₂Al-LDH hybrid materials were not carried out up to 1000 °C. As shown in **Figure S8** (*section S2.1.5*), above 800 °C, the ZnO derived from LDH decomposition reacts with graphitic carbon formed by the carbonization of organic species, leading to the loss of Zn⁰ vapor and generates γ-Al₂O₃ at 1000 °C.

Considering the beginning of CO₂ release (**Figure 2b**), the decomposition of folate anions initiated at 270 °C for Mg₂Al-Fol, a temperature value slightly lower than the 300 °C observed for Zn₂Al-Fol and Zn₂Al-HFol. It can be explained by the grafting of the carboxylate groups to the inorganic phase after the dehydroxylation of Zn₂Al-LDH materials (Rocha et al., 2016), which can initially improve the stability of the organic anion. The pyrolysis of folate anions progressed in a set of overlapped events through deoxygenation (CO₂ and CO release) and denitrogenation reactions (formation of NH₃ and HCN), as summarized in **Table S6** and noticed in **Figures 2, 3** and **S5**. It was also observed the release of aniline (**Figures 2b** and **3**) and C₃H₅

allyl radical (m/z 41 fragment; **Figures 2b**) that are characteristic of FA and folate anions decomposition (*Chapter 4*).

Although it was not observed significant differences in terms of the nature of released species detected by EGA, comparing the LDH-FA materials, it could be stated that: (i) the release of aniline and NH_3 decreased overall and H_2O increased above $500\text{ }^\circ\text{C}$ for $\text{Zn}_2\text{Al-Fol}$ (**Figures 2b** and **S5**); (ii) the production of CO_2 , NH_3 and aniline were increased for $\text{Mg}_2\text{Al-Fol}$ and the release of the allyl radical were delayed (**Figure 2b**); and (iii) the CO production was higher and the formation of HNCO was not detected for both $\text{Zn}_2\text{Al-LDH}$ (**Figure 2b, 3** and **S5**). Thermal analysis and EGA results indicated that both charges of anion and LDH composition influence the pyrolysis mechanism of intercalated folate anions. Nonetheless, $\text{Zn}_2\text{Al-LDH}$ materials presented very similar profile of TGA/DSC, TGA-FTIR and TGA-MS curves (**Figure 2**), indicating that the pyrolysis mechanism of folate anions was more influenced by the layer composition than the electric charge of anionic species.

On the other hand, comparing with data reported in our previous work (*Chapter 4*) regarding the pyrolysis of sodium folate salts (Na_2HFol and Na_3Fol), it was observed that the pyrolysis mechanisms of HFol^{2-} and Fol^{3-} were altered by their intercalation into the LDH structure. The formation of 2-pyrrolidone and NO was wholly suppressed and the HNCO formation decreased significantly after intercalation. The release of CO_2 decreased as well, mainly when compared with respective sodium salts. Additionally, the release of aniline and NH_3 was delayed, and the allyl radical (m/z 41) formation increased. The difference marker from folate salts was the formation of CH_4 , which was observed mainly for $\text{Mg}_2\text{Al-Fol}$ and $\text{Zn}_2\text{Al-HFol}$ (**Figure 3**) and can indicate the hydrodealkylation of alkylated benzenes formed in the pyrolysis (Zheng et al., 2017). Compared to FA and related sodium salts (*Chapter 4*), the thermal stability follows the order: $\text{Zn}_2\text{Al-Fol}$ ($300\text{ }^\circ\text{C}$) = $\text{Zn}_2\text{Al-HFol}$ ($300\text{ }^\circ\text{C}$) = Na_3Fol ($300\text{ }^\circ\text{C}$) > $\text{Mg}_2\text{Al-Fol}$ ($270\text{ }^\circ\text{C}$) = Na_2HFol ($270\text{ }^\circ\text{C}$) > FA ($200\text{ }^\circ\text{C}$).

3.3. Synthesis of LDO-C nanocomposites

Based on TGA/DTG-DSC and EGA results, the $\text{Mg}_2\text{Al-Fol}$ and $\text{Zn}_2\text{Al-HFol}$ materials were selected for obtaining LDO-C by pyrolysis in the furnace because of the singularities of their thermal behaviour. Accordingly, the heating temperatures were chosen as follows (**Table S6**): (i) at 360 °C, slightly above the beginning of folate anions decomposition but below the T_p of the first decomposition step. The influence of annealing time was also evaluated pyrolyzing the samples in isothermal conditions for 0.5 h; (ii) at 410 °C and 430 °C, near the T_p of the first decomposition step of folate anions in $\text{Mg}_2\text{Al-Fol}$ and $\text{Zn}_2\text{Al-HFol}$ samples, respectively; (iii) temperature values near the end of second decomposition step, at 450 ° and 500 °C, respectively; (iv) and at 600 and 800 °C for both materials and additionally at 1000 °C for $\text{Mg}_2\text{Al-Fol}$. The materials were characterized by FTIR and Raman spectroscopies as well as XRD analysis.

Figure 4a presents the images of as prepared LDO-C nanocomposites obtained from the pyrolysis of $\text{Mg}_2\text{Al-Fol}$ and $\text{Zn}_2\text{Al-HFol}$. The colour change, initially from yellow to brown and, posteriorly, to black, indirectly indicated the carbonization of folate anions as far as the temperature increases. FTIR spectra of LDO-C composites are presented in **Figures 4b,c**. Vibrational bands attributed to hydroxyl stretching (νOH) of H_2O and $\text{M}^{\text{x}+}\text{-OH}$ in the layers (Kloprogge et al., 2004) in the 3346 cm^{-1} region, decreased with the increase of temperature, which was attributed to the dehydroxylation of LDH layers. Such decrease was more accentuated for $\text{Zn}_2\text{Al-Fol-360}$ than $\text{Mg}_2\text{Al-Fol-360}$ sample, in line with the lower thermal stability of the former against the dehydroxylation reaction, as observed by TGA/DSC and DTG-MS curves (**Figure 2**). The broadband that was still observed in 3600-3200 cm^{-1} region for LDO-C nanocomposites could be attributed to νOH from C-OH groups and/or physisorbed H_2O (Hammer et al., 2000; Acik et al., 2011; Kato et al., 2021).

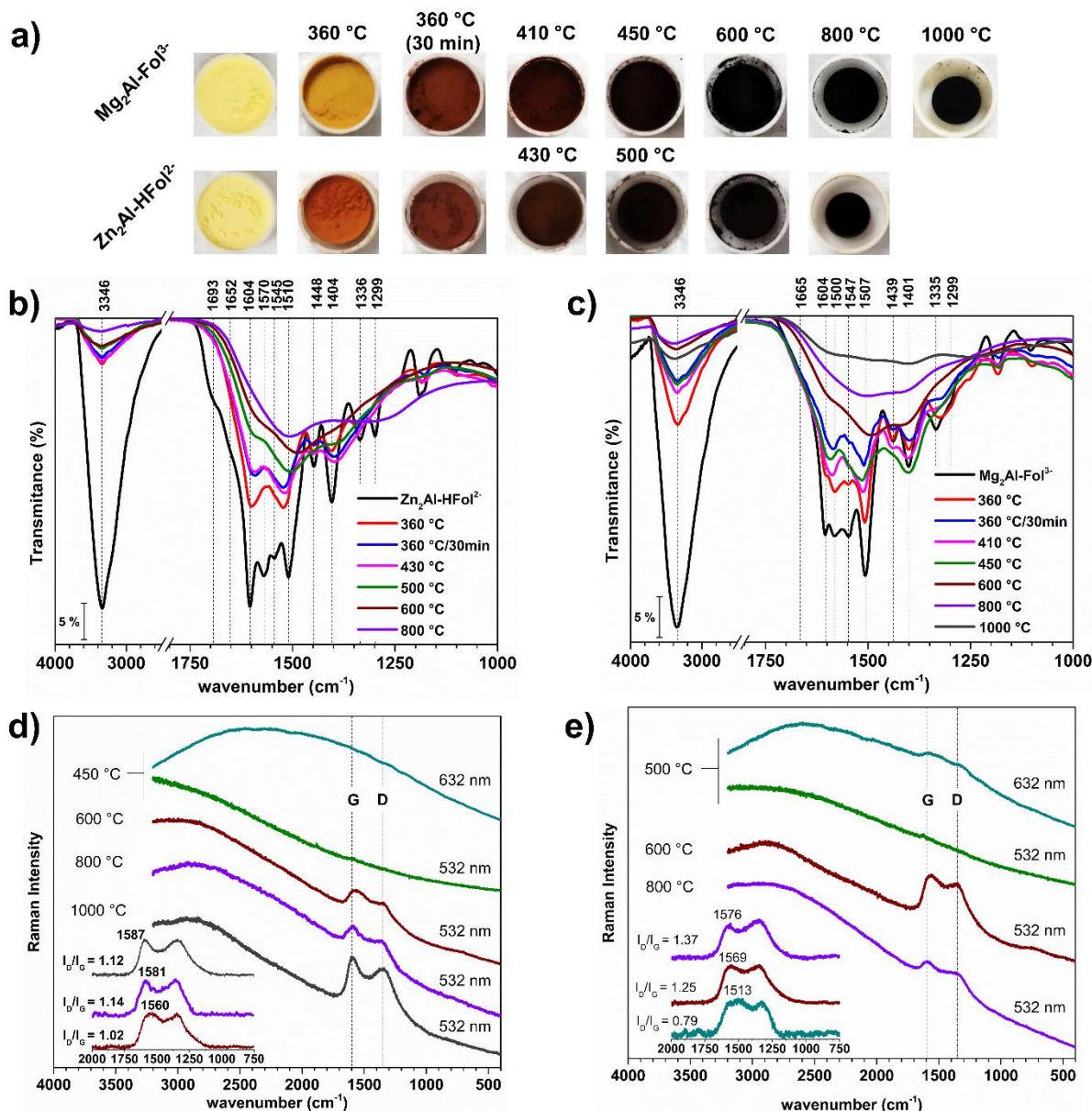


Figure 4. Images (a), FTIR-ATR (b,c) and Raman (d,e) spectra of as prepared LDO-C nanocomposites from pyrolysis of Zn₂Al-HFol (b,d) and Mg₂Al-Fol (c,e) materials.

The increase in the temperature led to the vanishing of vibrational bands (**Figure 4b,c**) attributed to folate anions (a tentative attribution was given in **Table S3**). The temperature effect was more perceptible for Zn₂Al-HFol-X than for Mg₂Al-Fol-X series and one of the main differences was related to vibrations attributed to the GLU moiety. For instance, the bands at 1640 (νC11=O), 1545 (νC11–N12/δN12–H), 1330 (δC–H of alkyl chain) and 1300 cm⁻¹ (νC11–N12/δN12–H + δC–H of alkyl chain) decreased in the spectra of Zn₂Al-HFol-360 in

relation to pristine Zn₂Al-HFol. In contrast, indications of such bands were still observed in the Mg₂Al-Fol-450 sample (**Figure 4c**). These results suggested the higher stability of GLU moiety in Mg₂Al-Fol samples, in line with EGA (**Figures 2b** and **3**) that showed the delay of allyl radical (m/z 41) formation as well as the release of HNCO (from the amide group) above 450 °C. Additionally, the disappearance of νC=O vibrational band (1693 cm⁻¹) was readily observed for Zn₂Al-HFol-360 when compared with its precursor. The bands attributed to stretching vibrations of carboxylate groups 1500 cm⁻¹ (ν_{as}COO⁻; and C4–O⁻ from PT for Mg₂Al-Fol) and 1400 cm⁻¹ (ν_sCOO⁻) regions were observed to decrease for both LDH-FA series, in line with the high CO₂ release in the 300-500 °C range (**Figure 2b**). For Zn₂Al-HFol-360 specifically, the band shifted from 1510 to 1520 cm⁻¹ (in relation to the precursor), endorsing the grafting of COO⁻ groups in Zn-LDO phase after the dehydroxylation of layers. It enhanced the initial stability of carboxylate but seemed to favour the degradation of GLU moiety, as noticed by the high alkyl radical (m/z 41) release at 430 °C (**Figure 2b**).

The decrease of bands attributed to *p*-ABA moiety (νC=C; 1604 cm⁻¹) and amine group vibration (νNH₂ from PT at 1547 cm⁻¹) was observed in the temperature range of 360-500 °C for both precursors. However, it was more accentuated for Mg₂Al-Fol series, in agreement with its highest release of aniline and NH₃ compared to the Zn₂Al-HFol (**Figures 2b**). On the other hand, the higher stability of PT group in relation to *p*-ABA group was evidenced for both LDH-FA series, as can be noticed by the presence of bands attributed to PT rings (νC=C/C=N at 1580, 1510 and 1440 cm⁻¹ regions) in the spectra of Zn₂Al-HFol-500 and Mg₂Al-Fol-450 samples. These data are consistent with those previously observed for FA and its sodium salts (*Chapter 4*), indicating that PT was the main building block of carbonaceous material.

The spectral profile of Zn₂Al-HFol-430/0.5 and Mg₂Al-Fol-360/0.5 samples (360 °C for 0.5 h) indicated that the pyrolysis in isothermal conditions was also an important parameter for the synthesis of LDO-C nanocomposites because the tendency of their spectral profile

progressed closer to the ones observed for Zn₂Al-HFol-430 and Mg₂Al-Fol-410 (**Figure 4b,c**). It is consistent with the darker colouring of samples compared to their Zn₂Al-HFol-360 and Mg₂Al-Fol-360 counterparts (**Figure 4a**).

Above 500-600 °C, the bands attributed to functional groups from folate anion (*e.g.*, COO⁻, NH, C=O) significantly decrease. Additionally, the broad bands observed in the region of 1600-1000 cm⁻¹ could be attributed to νC=C/C=N (1250-1600 cm⁻¹) of carbonaceous material presenting sp²-hybridized structure (Hammer et al., 2000; Ferrari et al., 2003), with contributions of C–N (Hammer et al., 2000) and C–O/C–O–C vibrations (Acik et al., 2011) in the range of 1300-1000 cm⁻¹. It was an essential information because oxygenated and nitrogenated functional groups could play a role in the optical properties of C-dots (Gan et al., 2016; Liu et al., 2019).

Raman spectra (excitation radiation in the visible region) of samples pyrolyzed above 450-500 °C are depicted in **Figure 4d,e**. The characteristic D (A_{1g} breathing mode; near 1360 cm⁻¹) and G (E_{2g} stretching mode; near 1580 cm⁻¹) bands of graphitic carbon (Ferrari and Robertson, 2000; Ayiania et al., 2020) were detected for Zn₂Al-Fol-500, Mg₂Al-Fol-600 and nanocomposites prepared in higher temperatures. However, the D and G bands could not be accessed for LDO-C materials prepared in lower temperatures because the laser excitation wavelengths triggering the fluorescence of the sample and C-dots (Mocci et al., 2022), as noticed for Mg₂Al-Fol-450 and Zn₂Al-Fol-500 samples. The blue shift of G band and the increase in the intensity ratio of D/G bands (I_D/I_G; **Figure 4d,e**) indicated the tendency to form nanocrystalline domains of graphitic carbon as far as the temperature increases (Ferrari and Robertson, 2000).

Nonetheless, the formation of graphitic carbon structure occurred in temperatures much higher than what was previously reported for FA and its sodium salts (*Chapter 4*), for instance: at 350 °C (FA) and 430 °C (sodium folate salts), readily after the first step of thermal

decomposition. The hindrance of graphitization of organic species after intercalation can be attributed to: (i) the ordered distribution of organic anions between the layer hindered their collision under heating, controlling the rate of condensation and graphitization reactions (confinement effect) (Song et al., 2016; Liu et al., 2017); and/or (ii) LDH phase could be absorbing the heat in the expense of dehydration and dehydroxylation of the layered structure, reducing the thermic energy available for the carbonization (Liu et al., 2018). In fact, the darker colouring of Zn₂Al-HFol-360 sample in comparison with Mg₂Al-HFol-360 indirectly evidence such effect (**Figure 4a**). Besides, for Zn₂Al-HFol series, the FTIR and Raman indicated that folate functional groups were almost totally decomposed, and graphitization was observed to be initiated at 500 °C (near the end of the second decomposition step). However, it cannot be neglected that the amount of folate anions in Mg₂Al-Fol was lower than in Zn₂Al-HFol (**Table S4**) because a lower amount of Fol³⁻ was necessary to neutralize the charges of the LDH layers. Consequently, the intercalated Fol³⁻ anions were more distant of each other inside the interlayer space of Mg₂Al-Fol, which would contribute to hinder the collision of Fol³⁻ under heating (*steric blockage*) when compared with HFol²⁻ inside the Zn₂Al-HFol (de Matos et al., 2019).

The *ex-situ* XRD and *in-situ* HT-XRD results are depicted in **Figures 5** and **S9-S10**, respectively. The shift of (003) peak from 5.46°/2θ ($d_{00l} = 1.62$ nm) to 6.87°/2θ ($d_{00l} = 1.29$ nm) and the shift of (006) from 7.77°/2θ ($d_{00l} = 2.27$ nm) to 8.84°/2θ ($d_{00l} = 2.00$ nm), observed in HT-XRD analysis for Mg₂Al-Fol (**Figure S9**) and Zn₂Al-HFol (**Figure S10d**), respectively, could indicate a reorientation (Prevot et al., 1998) or a close packing (Santos et al., 2017) of folate anions after dehydration step. Besides, XRD data showed the complete loss of LDH structure of Zn₂Al-HFol-360, whereas the diffraction peak of the (003) plane was still observed for Mg₂Al-Fol-410 (**Figure 5**). These observations are in line with the higher thermal stability of Mg₂Al-LDH when compared to Zn₂Al-LDH materials.

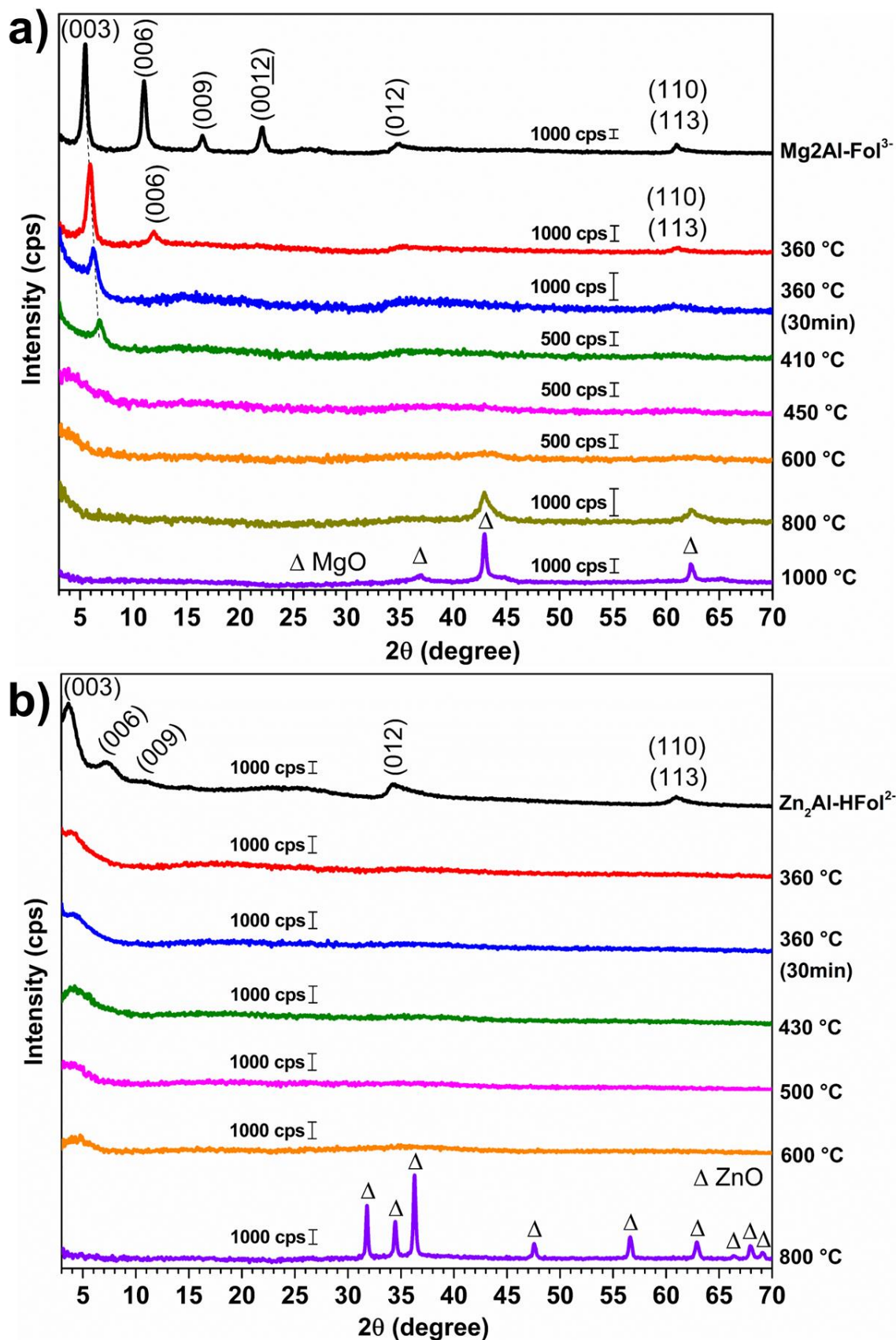


Figure 5. *Ex-situ* XRD of LDO-C nanocomposites materials obtained from $\text{Mg}_2\text{Al-Fol}^{3-}$ (a) and $\text{Zn}_2\text{Al-HFol}^{2-}$ (b).

Above the temperatures of dehydroxylation (*i.e.*, 272 °C for Zn₂Al-HFol and 450 °C for Mg₂Al-Fol), the formation of an amorphous phase was verified by the absence of diffraction peaks (**Figures 5** and **S9-S10**). As the temperature increased to 800 °C, the formation of crystalline ZnO (wurtzite; ICSD 26170) and MgO (periclase; ICSD 9863) was observed. No separated phases of Al₂O₃ and spinel spinel-like phase (MgAl₂O₄ or ZnAl₂O₄) were observed, which could indirectly indicate that Al³⁺ cations were inserted in the lattice of oxide phases as M(Al)O (Millange et al., 2000). Furthermore, the formation of crystalline spinel was completely hindered up to 1000 °C, in agreement with our previous findings for LDH counterparts intercalated with CMC (Magri et al., 2019). Additionally, the *in-situ* HT-XRD patterns (**Figure S10**) showed that the formation of crystalline oxides was hindered in LDH-Fol materials compared with LDH-Cl counterparts. For instance, Zn₂Al-Cl and Mg₂Al-Cl presented indications of oxides formation at 360 °C and 410 °C in HT-XRD analysis, respectively.

According to the literature (Zhao et al., 2010; Warringham et al., 2017; Hobbs et al., 2018), the structural transformation of Mg/Al-LDH upon heating is topotactic: the formation of oxide and spinel phases occur in the 00 l plane of LDH and the platelet morphology of particles is preserved up to 850 °C. On the other hand, the non-topotactic transformation was observed for Zn/Al-LDH materials (Zhao et al., 2010). The nucleation of ZnO(wurtzite)/ZnAl₂O₄ spheres occurs concurrently with dehydroxylation of the layers, and the loss of layered structure takes place in the 500-800 °C range (Zhao et al., 2010).

The whole process is accompanied by the migration of cations from the octahedral layered-structure to the interlayer region in tetrahedral coordination sites (Bellotto et al., 1996; Bokhoven et al., 2001; Radha et al., 2010; Carvalho et al., 2013; Takehira, 2017). The cation migration (mainly Al³⁺) initiates after sample dehydration and the formation of intermediate nanostructures of oxides and spinel can occur concomitantly (Bellotto et al., 1996; Bokhoven et al., 2001; Radha et al., 2010; Zhao et al., 2010; Carvalho et al., 2013; Santos et al., 2017).

The disruption of the layered structure and the crystallization of mixed metal oxide were observed above temperature values of dehydroxylation and interlayer anion decomposition (Bellotto et al., 1996; Bokhoven et al., 2001; Radha et al., 2010; Zhao et al., 2010; Carvalho et al., 2013; Santos et al., 2017). The segregation of the oxide (MgO or ZnO) and spinel (MgAl₂O₄ or ZnAl₂O₄) phases occurs at temperatures above 800 °C and 900°C for Zn₂Al-LDH and Mg₂Al-LDH, respectively (Zhao et al., 2010; Warringham et al., 2017).

Since the formation of crystalline oxide and spinel phases is in some way dependent on the decomposition of the intercalated anion (Bellotto et al., 1996; Bokhoven et al., 2001; Radha et al., 2010; Zhao et al., 2010; Carvalho et al., 2013; Santos et al., 2017), it is assumed in this work that the material carbonized mainly between the LDH layers could hinder the migration of cations to the interlayer space, precluding the growth of oxide nanoparticles. Hence, the intercalated anion has an important role in the thermal conversion of LDH into crystalline oxide and spinel phases. For instance, in our previous work (Magri et al., 2019), the crystallization of the spinel phase was precluded by the presence of graphitic carbon formed during the pyrolysis of LDH-CMC materials. The same effect was not observed for Zn₂Al-CO₃ and Mg₂Al-CO₃ counterparts because the complete decomposition of carbonate ion occurred below 800 °C and the formation of spinel was observed at 800 and 1000 °C, respectively. However, the presence of metal oxides was observed in the XRD patterns of nanocomposites obtained by the pyrolysis of LDH-CMC at 500 °C, while the temperature needed to reach 800 °C when using LDH-Fol as the precursor. (**Figure 5**). In the case of LDH-CMC materials, the mass loss related to polymer decomposition was higher than for folate anions presented in this work. Taking the Zn₂Al-LDH as an example (both Zn₂Al-CMC and Zn₂Al-HFol samples contained around 20wt.% of carbon), the mass loss between 260-700 °C was around 35% and 22%, respectively. Therefore, the hindrance of oxide and spinel crystallization seemed to be dependent on (i) the

thermal stability of intercalated anion; and (ii) the mechanism of decomposition that influence amount of carbon formed during the process.

Considering the XRD and Raman data discussed above, it can be stated that LDH-FA precursors are suitable sources of carbon-based nanocomposites formed of zinc or magnesium metal oxides and graphitic carbon, and with the capacity to be applied as adsorbent, heterogenous catalyst, and so on (Takehira, 2017; Wani et al., 2020; Ye et al., 2022). The best temperature range to obtain nanocomposites of crystalline metal oxides and ordered graphitic carbon was 500-800 °C and 600-1000 °C for Zn₂Al-HFol and Mg₂Al-Fol, respectively.

3.4. LDH-C nanocomposites

The hindrance of oxides and spinel crystallization can be profitable to recover the pristine LDH structure by reaction with water (Takehira, 2017; Ye et al., 2022) for producing LDH-C nanocomposites. To evaluate this aspect, reconstruction experiments with LDO-C were carried out in the water. The images of obtained materials are presented in **Figure 6a**. The colour of powders was maintained in comparison with the original LDO-C samples (**Figure 4a**), indirectly suggesting that the carbonaceous material remained in the samples after the hydration/reconstruction process. Also, the supernatant of aqueous systems was clean after the isolation of LDH-C materials, endorsing that the carbonaceous phase stayed in the sample after the reconstruction process.

The XRD data (**Figure 6b,c**) showed the successful obtention of LDH-C nanocomposites through the restoration of LDH structure, at least partially. Even though, the materials presented lower crystallinity compared to the original LDH-FA (**Figure 5**), no peaks attributed to M²⁺ and Al³⁺-oxide/hydroxide phases were observed below 800 °C and 600 °C for Mg₂Al-Fol and Zn₂Al-HFol, respectively. In addition, despite the absence of the (003) peak in XRD patterns of Zn₂Al-HFol-360r and Zn₂Al-HFol-430r (where “r” means reconstruction), the appearance of

peaks attributed to (012) and (110)/(113) planes indicated the restoration of LDH layers. According to Santos et al. (2017), the low intensity of the XRD peaks could indicate that the LDH structure was not fully recovered or that reconstructed materials are less organized than the original (mainly in the layers stacking direction).

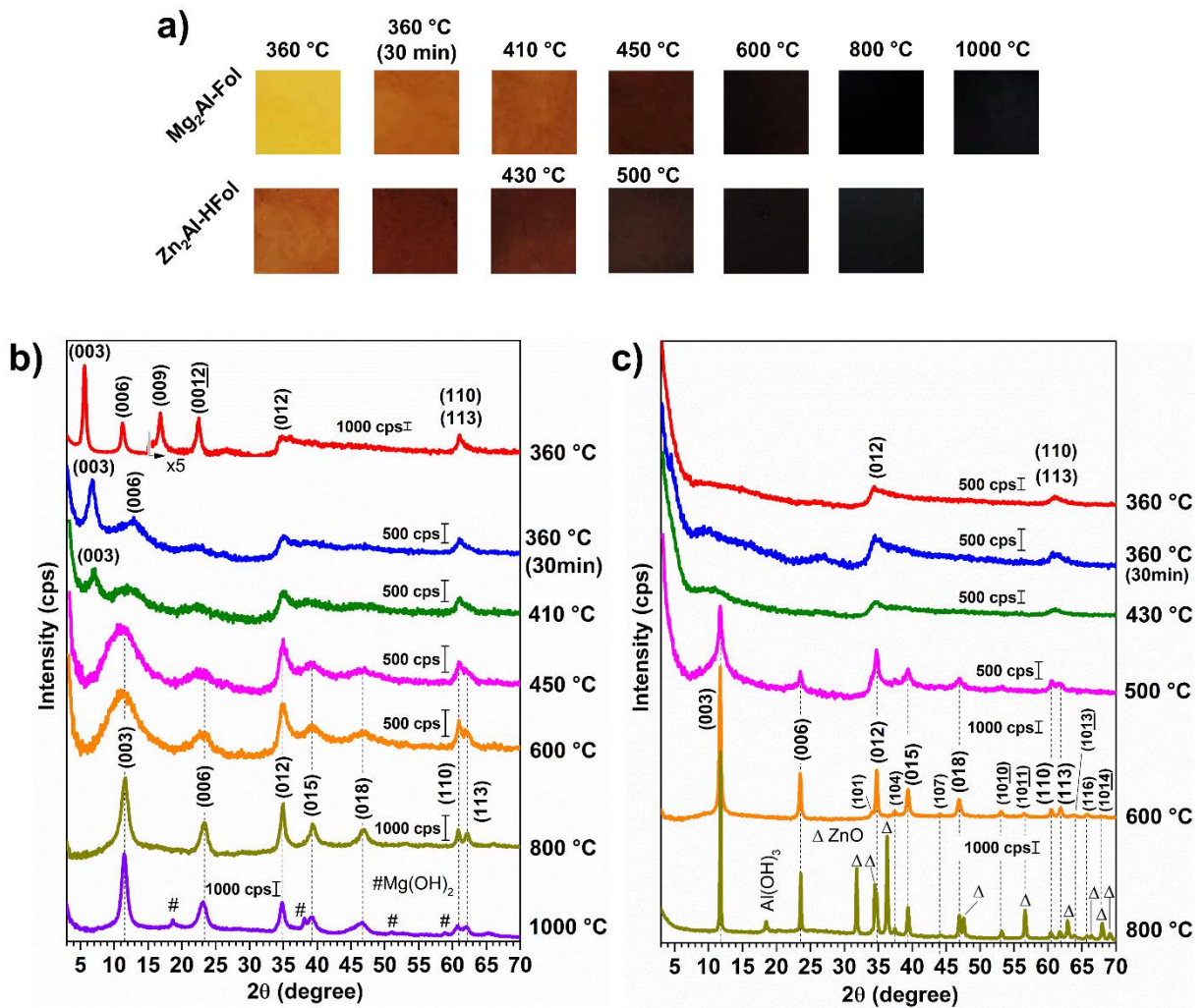


Figure 6. Representative images of LDH-C samples prepared by reconstruction of LDO-C (a) and results concerning XRD patterns (b, c) of materials related to Mg₂Al-Fol (b) and Zn₂Al-HFol (c) precursors.

A change from the original LDH-FA to LDH-CO₃ phase (dashed lines in XRD; **Figure 6b,c**) was initiated for samples prepared above 410 °C and 430 °C (Tp of first step of folate anions decomposition, **Figure 2**) for Zn₂Al-HFol and Mg₂Al-Fol, respectively. The LDH-CO₃

phase was identified in the XRD patterns of Zn₂Al-HFol-600r and Mg₂Al-Fol-800r. The synthesis of LDH-CO₃ from the reconstruction method was predicted to be spontaneous according to the Gibbs free energy of formation of Mg₂Al-CO₃ ($\Delta G_m^\circ = -18.3 \text{ kJ mol}^{-1}$) and Zn₂Al-CO₃ ($\Delta G_m^\circ = -0.6 \text{ kJ mol}^{-1}$) (Bravo-Suárez et al., 2004). It is worth noting that deionized water was used in the reaction, and so the carbonate anions came from atmospheric CO₂, as also reported elsewhere (Conterosito et al., 2018).

The formation of Al(OH)₃ (gibbsite-like structure; ICSD 6162) was verified for Zn₂Al-HFol-800r, while ZnO was still observed. The XRD of Mg₂Al-Fol-1000r presented both diffraction peaks attributed to LDH-CO₃ and Mg(OH)₂ (brucite-like structure; ICSD 34401), which can indicate segregation of phase during the pyrolysis (Takehira, 2017).

FTIR-ATR spectra of LDH-C samples are presented in **Figure 7**. One of the main differences in relation to LDO-C results was associated with the intensity increase of broad bands attributed to ν OH mode (3650-3000 cm⁻¹) of M^{x+}-OH and H₂O (Kloprogge et al., 2004), which endorses the restoration of hydroxylated structure of LDH. For Mg₂Al-Fol-1000r sample, the band at 3693 cm⁻¹ was attributed to ν OH of brucite (Schroeder, 2002), in agreement with XRD analysis. Results also confirm that the restoration procedure applied in this work was conducted to LDH-CO₃. The bands attributed to intercalated CO₃²⁻ were observed at 3000 cm⁻¹ (shoulder; H₂O---CO₃²⁻ bridge) and 1357 cm⁻¹ (ν_3 CO₃²⁻) regions (Kloprogge et al., 2004). The ratio between the intensity of bands attributed to CO₃²⁻ (1357 cm⁻¹) and carboxylate groups (ν_{as} COO⁻ at 1505 cm⁻¹ region) of folate anions showed that the formation of LDH-CO₃ increased as far as the COO⁻ (and C4-O⁻ for Mg₂Al-Fol) group were decomposed (**Figure 7c**). The results fitted well to sigmoidal-Boltzmann equation, in which the inflection point was the T_p temperature of first step of folate anions decomposition (*i.e.*, 410 °C and 430 °C for Zn₂Al-HFol and Mg₂Al-Fol, respectively). It is in line with the transition from LDH-FA to LDH-CO₃ phase observed by XRD analysis (**Figure 6b,c**).

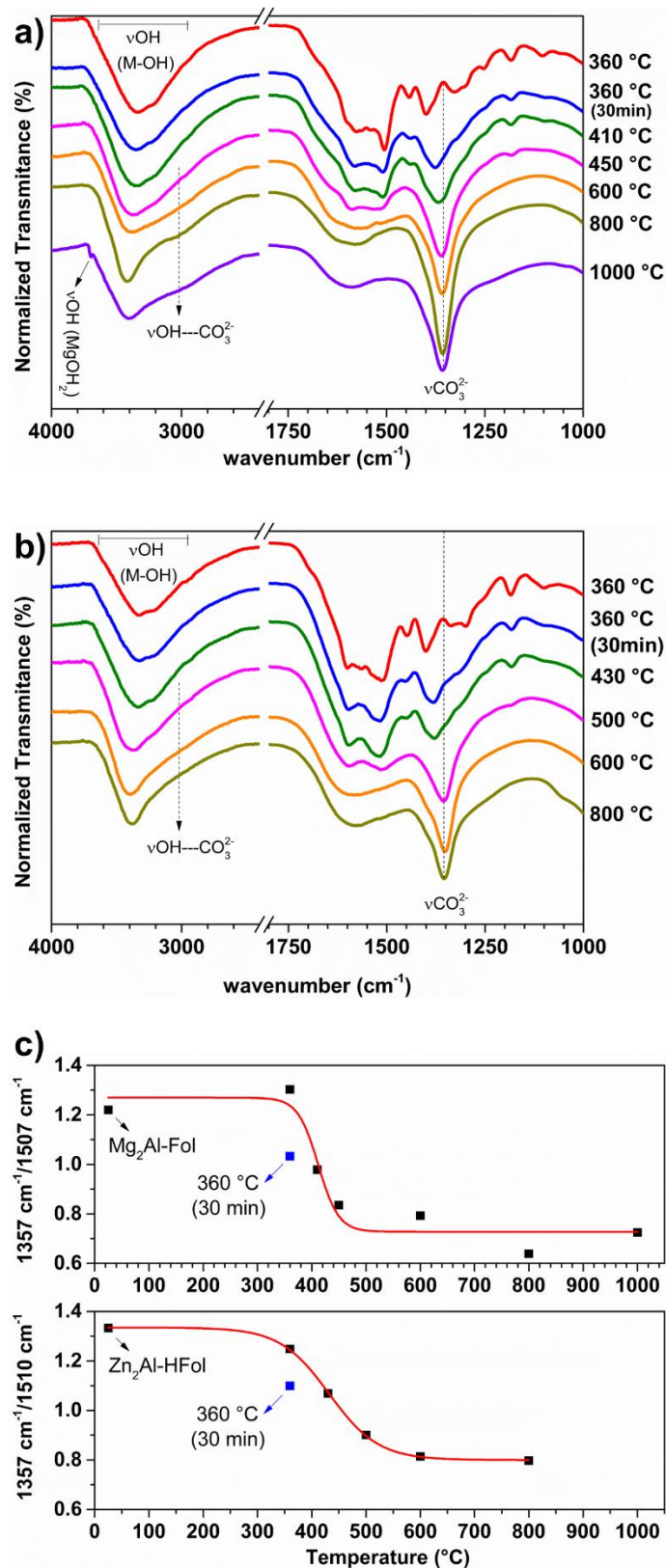


Figure 7. FTIR-ATR spectra from LDH-C samples prepared from $\text{Mg}_2\text{Al-Fol}$ (a) and $\text{Zn}_2\text{Al-HFol}$ (b) from LDO-C. Transmittance ratio of $\nu_3\text{CO}_3^{2-}$ (1357 cm^{-1}) and $\nu_{\text{as}}\text{COO}^-$ (folate anions; 1505 cm^{-1} region) bands fitted with sigmoidal-Boltzmann equation (c). For achieve a better fitting, the results of LDH-C from samples prepared by 30 min of annealing (squares in blue) were disregarded.

SEM-EDS analyses were performed to characterize the habit of Mg₂Al-Folate and Zn₂Al-HFolate after pyrolysis and reconstitution experiments. The SEM images showed that Mg₂Al-Fol (**Figure 8a**) and Zn₂Al-HFol (**Figure 9a**) precursors presented flower-like structure formed by the interconnection of layered platelets. The morphology of materials was influenced by the intercalated anion. The intercalation of Fol³⁻ led to the formation of larger platelets (around 1 μm) and disordered agglomerates, as also noticed for Zn₂Al-Fol (**Figure S11a**). On the other hand, Zn₂Al-HFol presented small platelets (around 20 nm) and aggregates more ordered. Additionally, The LDH-FA materials had a distinct morphology compared to the LDH-Cl counterparts, which presented disforme-stacked platelets with irregular edges, as noticed in **Figure S11b,c**.

At 360 °C, both LDH-C nanocomposites conserved the habit of the original material (**Figures 8b** and **9b**). Increasing the temperature value to 410 °C and 430 °C for Mg₂Al-Fol and Zn₂Al-HFol, respectively, was observed significant changes. A complex texture of nanometric particles growing above the large platelets inherited from the precursor was observed for Mg₂Al-Fol-410r (increment in **Figure 8d**), in contrast with Zn₂Al-HFol-430r image (**Figure 9d**). The ordered structure observed for pristine Zn₂Al-HFol (**Figure 9a**) disappeared and shapeless particles were observed (**Figure 9d**). Same feature was observed for Zn₂Al-HFol-360/0.5r sample (**Figures 9c**), but not for Mg₂Al-Fol-360/0.5r (**Figures 9c**).

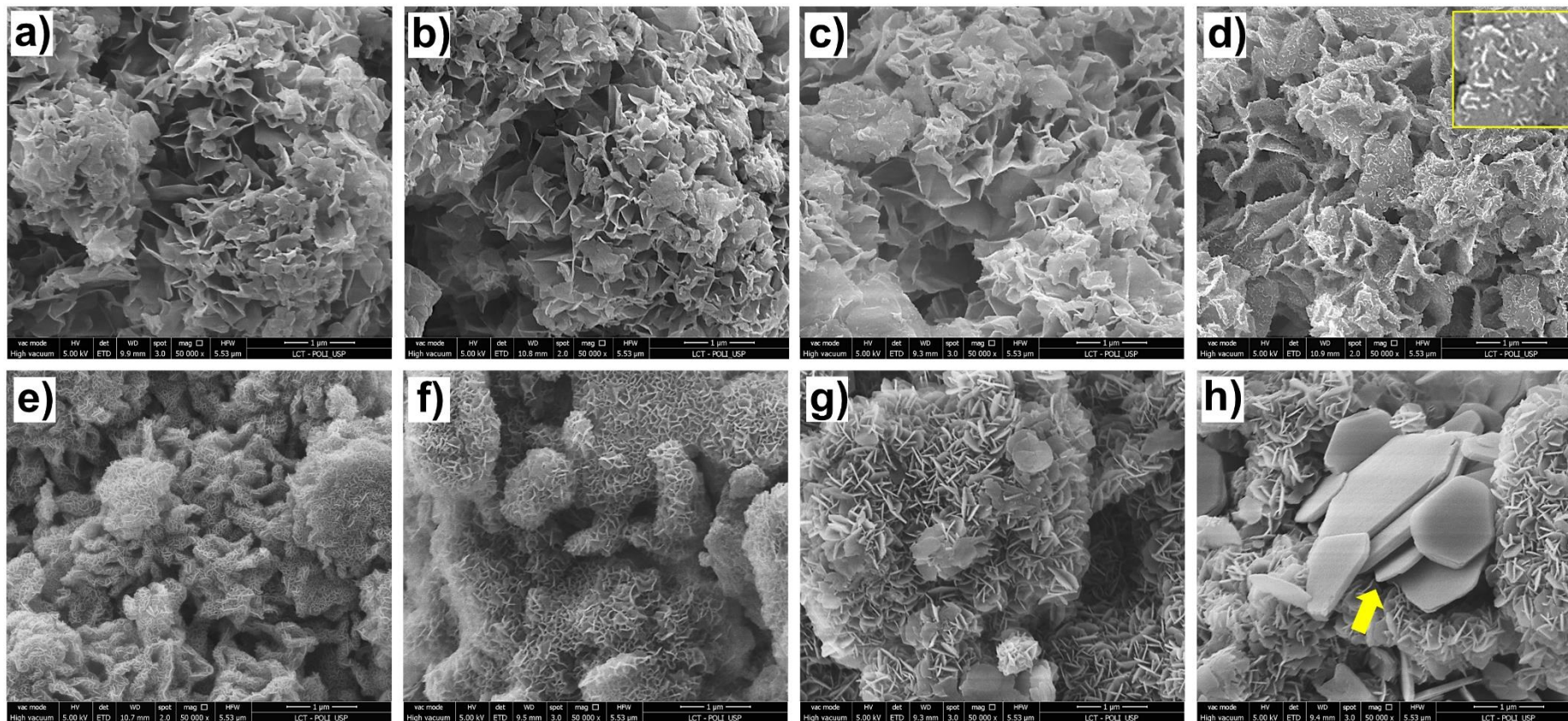


Figure 8. SEM micrographies of Mg₂Al-Fol (a) Mg₂Al-Fol-360r (b); Mg₂Al-Fol-360/0.5r (c), Mg₂Al-Fol-410r (d), Mg₂Al-Fol-450r (e), Mg₂Al-Fol-600r (f), Mg₂Al-Fol-800r (g) and Mg₂Al-Fol-1000r (h).

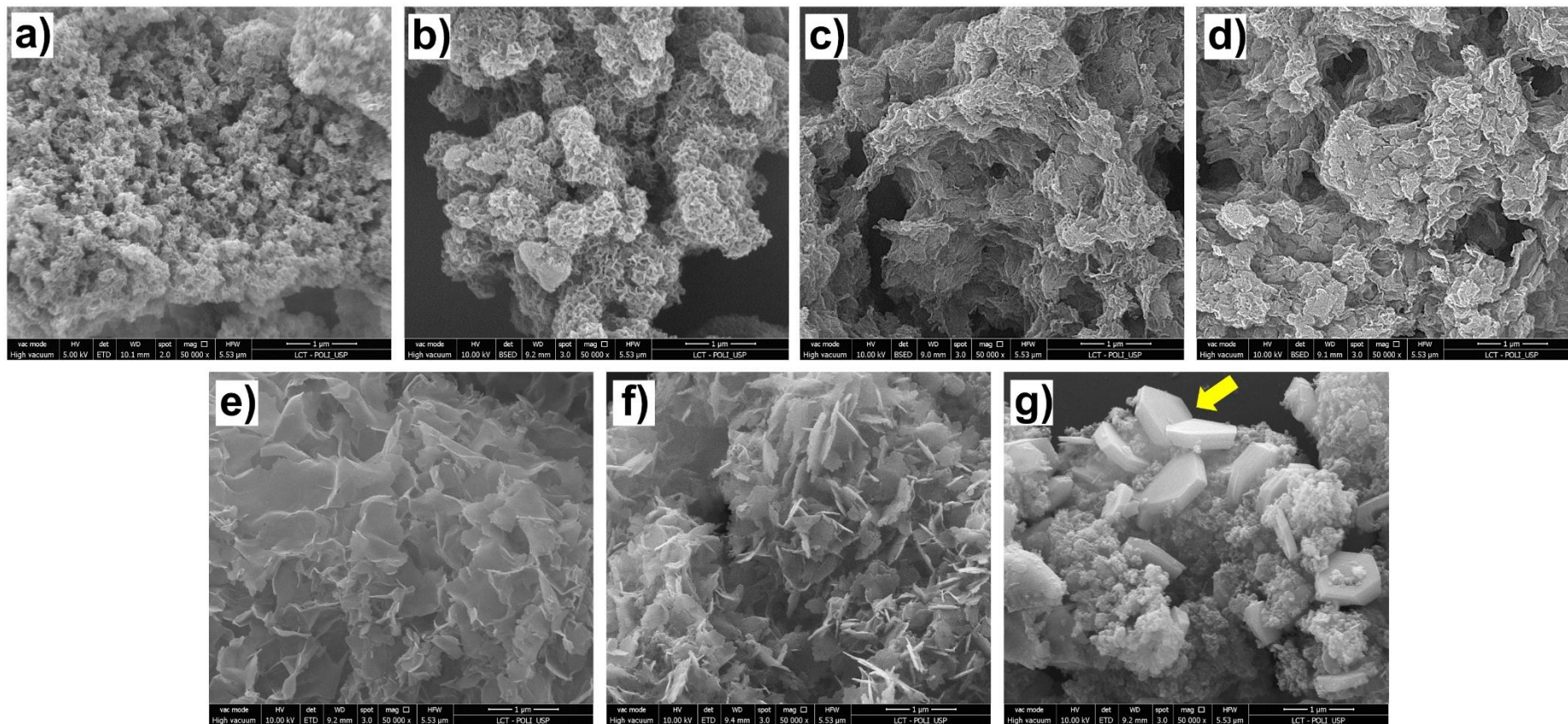


Figure 9. SEM microographies of Zn₂Al-HFol (a) Zn₂Al-HFol-360r (b); Zn₂Al-HFol-360/0.5r (c), Zn₂Al-HFol-430r (d), Zn₂Al-HFol-500r (e), Zn₂Al-HFol-600r (f) and Zn₂Al-HFol-800r (g). Magnification: 50k.

Significant changes in the morphology of materials occurred after the second step of folate anion decomposition (TGA/DSC and EGA analysis; **Figure 2b**). In Mg₂Al-Fol-450r, the structure became similar to the characteristic sand-rose habit, typically observed for reconstructed Mg/Al-LDH (Gao et al., 2018; Xu et al., 2019). Such structure was conserved up to 800°C (**Figure 8e-g**), increasing the agglomerate particle size as noticed for Mg₂Al-Fol-800r (**Figure 8g**). Otherwise, the growth of sheets and the formation of aggregates with scalelike surfaces and without a defined shape was observed in SEM images of Zn₂Al-HFol-500r (**Figure 9e**) and Zn₂Al-HFol-600r (**Figure 9e**). At higher temperatures, two different particles population were observed for Mg₂Al-Fol-1000r (**Figure 8h**) and Zn₂Al-HFol-800r (**Figure 8g**). The former presented the most ordered particles: sand rose-like structure and hexagonal structured plates (yellow arrow; **Figure 8h**). In contrast, small disformed particles and hexagonal structured plates (yellow arrow; **Figure 9g**) was observed for Zn₂Al-HFol-800R.

SEM results indicated different changes in morphology for reconstituted samples obtained from pyrolysis of Zn₂Al-HFol and Mg₂Al-Fol hybrid materials. Gao et al. (2018) reported that the mechanism of LDH reconstitution was influenced by the acid-base properties of hydroxides. For Mg₂Al-Fol, the formation of a sand rose-like structure covering the layered structure (**Figure 8d-g**) could be attributed to the classical dissolution–crystallization mechanism. In this process, Mg²⁺ and Al³⁺ are dissociated into the solution by a reaction between water molecules with the active sites onto LDO surface (Mg²⁺-O²⁻ and Al³⁺-O²⁻) and OH⁻ was generated in the process (Gao et al., 2018; Jin et al., 2022). The reactions was followed by the formation of Mg(OH)₂ and Al(OH)₄⁻ that posteriorly react with each other forming LDH structure in the presence of anions, such as CO₃²⁻ and OH⁻ (Gao et al., 2018; Jin et al., 2022). Differently, due to the lower K_{sp} value of Zn(OH)₂ in comparison with Mg(OH)₂ (K_{sp} = 3x10⁻¹⁷ and 5.61x10⁻¹², respectively; Speight, 2005), the level of Zn²⁺ dissociation was low and the Zn(OH)₂ precipitation favoured onto the surfaces of the nanoparticles (Gao et al., 2018). It

prevented further cation dissolution and hampered the total conversion of Zn(Al)O into LDH (Gao et al., 2018). Hence, the structural regeneration could be characterized by a hydration process of the surface of particles as well as, at a lower level, dissolution–crystallization mechanism with stacking of LDH over oxide nanoparticles (Gao et al., 2018). The hydration process could be characterized in some way by retro-topotactic mechanism (Jin et al., 2022): (i) the water molecules interact with the highly active sites of Zn-LDO ($\text{Zn}^{2+}\text{-O}^{2-}$ and $\text{Al}^{3+}\text{-O}^{2-}$), generating OH^- onto the surface of the material; (ii) the access of water into the interlayer space opens the structure favouring the diffusion of anions and the formation of LDH phase. Santos et al. (2017) reported that the reconstitution of the $\text{Zn}_2\text{Al-LDH}$ phase occurred by an aggregative mechanism, in which the limiting step is the dissolution of the ZnO phase, described as follows: (i) the nucleation and growth of LDH layers occurred after cation dissolution and evolved to their stacking. In our case, it is difficult to propose a mechanism of reconstitution for $\text{Zn}_2\text{Al-LDH}$ material. However, the presence of different habits, such as stacked structure and opened structure (scalelike morphology), was observed in SEM images of $\text{Zn}_2\text{Al-HFol-500r}$ (lower magnification; **Figure S12**), which can be a clue of a multi-step process.

EDS mapping of $\text{Mg}_2\text{Al-Fol-Xr}$ series indicated the uniform distribution of Mg^{2+} , Al^{3+} and carbon in the particles of nanocomposites obtained up to 800 °C. On the other hand, indicatives of well-distributed Zn^{2+} , Al^{3+} , and carbon was only observed up to 600 °C for $\text{Zn}_2\text{Al-HFol-Xr}$ series. Nonetheless, EDS confirmed phase segregation for $\text{Mg}_2\text{Al-Fol-1000r}$ and $\text{Zn}_2\text{Al-Fol-800r}$. The hexagonal-shaped particles in $\text{Mg}_2\text{Al-Fol-1000r}$ (yellow-arrow; **Figure 8h**) were identified as a Mg-rich phase (**Figure 10h5**) and, based on XRD (**Figure 6b**) and FTIR results (**Figure 7a**), they can be attributed to brucite phase. In $\text{Zn}_2\text{Al-HFol-800r}$, the Zn-rich phase (**Figure 11g5**) with hexagonal habit was tentatively attributed to ZnO, based on XRD (**Figure 6c**). **Figure S13** showed that both Mg-rich and Zn-rich phases were poor in carbon.

The carbonaceous material and LDH phase were intimately mixed in nanocomposites obtained at 600 and 800 °C for Zn₂Al-HFol and Mg₂Al-Fol, respectively. Additionally, the segregation of phases occurred in temperatures much lower for Zn₂Al-HFol in comparison with Mg₂Al-HFol, for instance, 800 and 1000 °C, respectively, in agreement with XRD analysis (**Figure 6 b,c**), as well as TGA/DSC and EGA analysis (*section 3.2*).

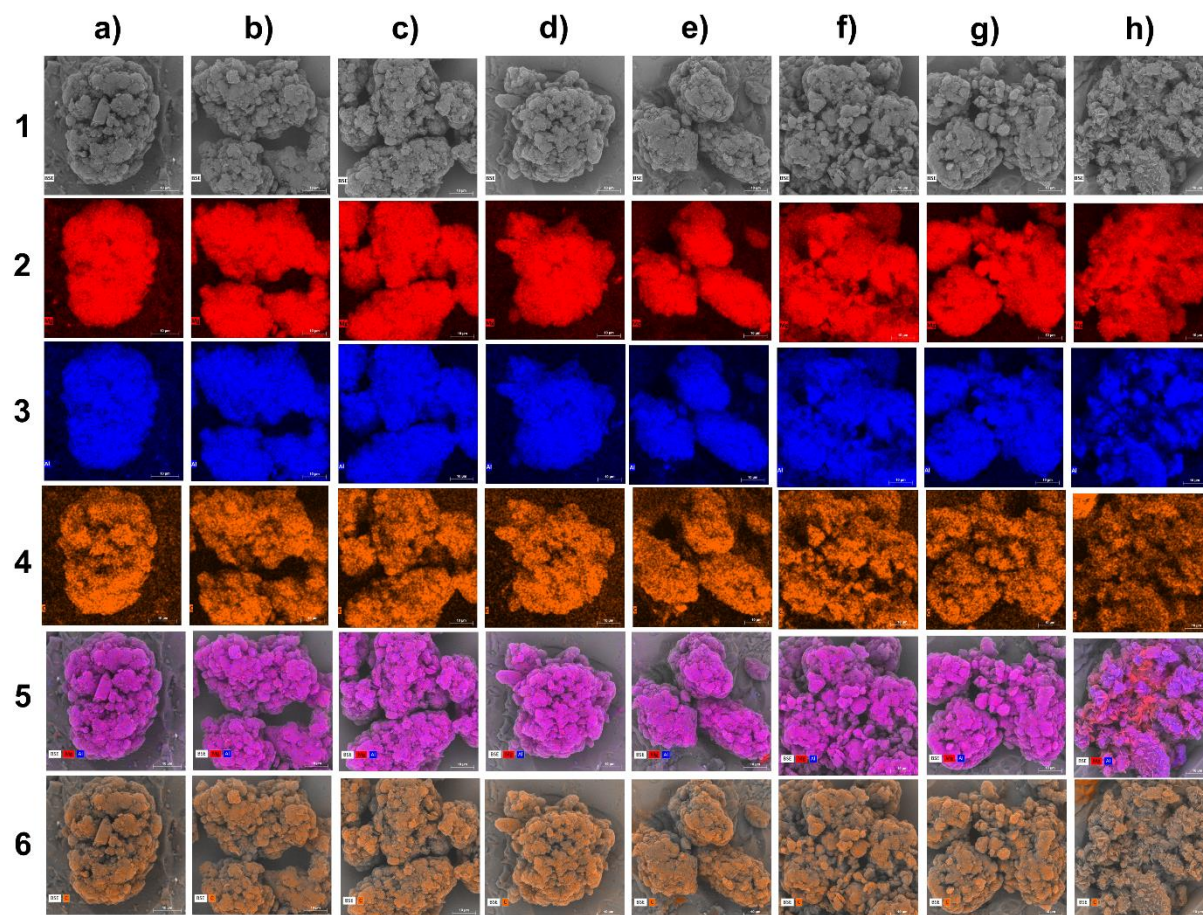


Figure 10. EDS mapping of Mg₂Al-Fol (a) Mg₂Al-Fol-360r (b); Mg₂Al-Fol-360/0.5r (c), Mg₂Al-Fol-410r (d), Mg₂Al-Fol-450r (e), Mg₂Al-Fol-600r (f), Mg₂Al-Fol-800r (g), and Mg₂Al-Fol-1000r (h). Backscattered electron (BSE) imaging (1; grey); Mg (2; red), Al (3; blue), C (4; orange), Mg/Al merge (5; pink) and C/BSE merge (6; orange-gray). Scale bar: 10 μm.

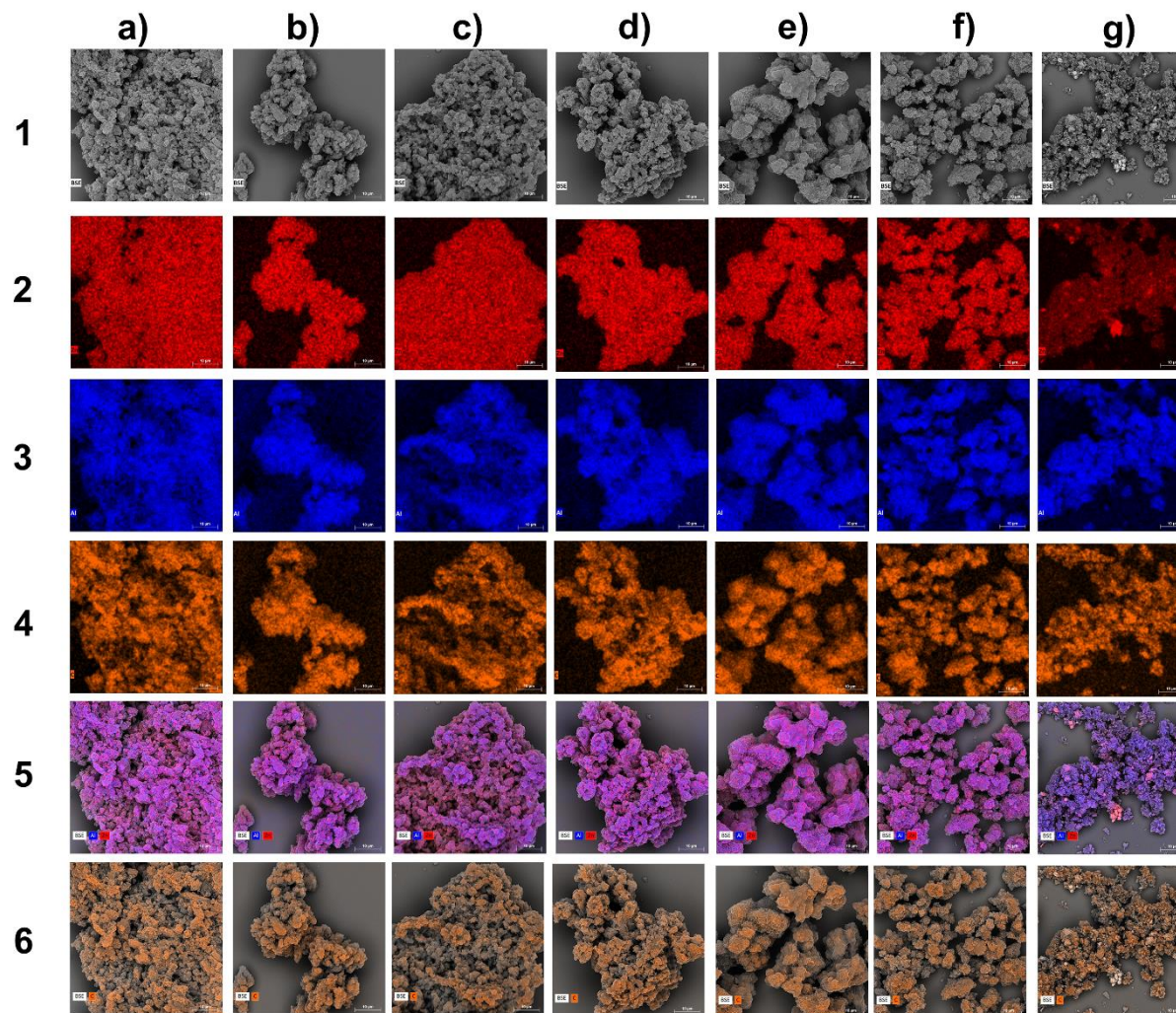


Figure 11. EDS mapping of $\text{Zn}_2\text{Al-HFol}$ (a) $\text{Zn}_2\text{Al-HFol-360r}$ (b); $\text{Zn}_2\text{Al-HFol-360/0.5r}$ (c), $\text{Zn}_2\text{Al-HFol-430r}$ (d), $\text{Zn}_2\text{Al-HFol-500r}$ (e), $\text{Zn}_2\text{Al-HFol-600r}$ (f) and $\text{Zn}_2\text{Al-HFol-800r}$ (g). Backscattered electron (BSE) imaging (1; grey); Zn (2; red), Al (3; blue), C (4; orange), Zn/Al merge (5; pink) and C/BSE merge (6; orange-gray). Scale bar: 10 μm .

Evaluation of the molar ratio by the EDS spectra for each studied condition was performed to qualify M^{2+}/Al^{3+} change in the samples during the reconstitution process. For a better analysis, samples prepared under isothermal condition at 360 °C for 0.5 h as well as the samples that presented phase segregation were excluded. Both LDH-C systems presented similar molar ratio over temperature. The molar ratio values of Mg_2Al -LDH were well described using the peak area of the EDS spectra when compared with Zn_2Al -LDH. To overcome this issue, it was applied a factor correction based on the respective M^{2+}/Al^{3+} molar ratio of precursors determined by ICP OES (**Table S4**). Although the variation of M^{2+}/Al^{3+} molar ratio was not high and is statistically constant, two temperatures zones could be proposed (**Figure 12**): (i) tendency of M^{2+} and (ii) tendency of Al^{3+} loss, in which the transition zone was at the T_p value of first degradation step of folate anions, as observed in FTIR analysis of CO_3^{2-} incorporation (Figure 7c). Further evaluation of the amount of metal release and pH values during the process is required to understand such differences better.

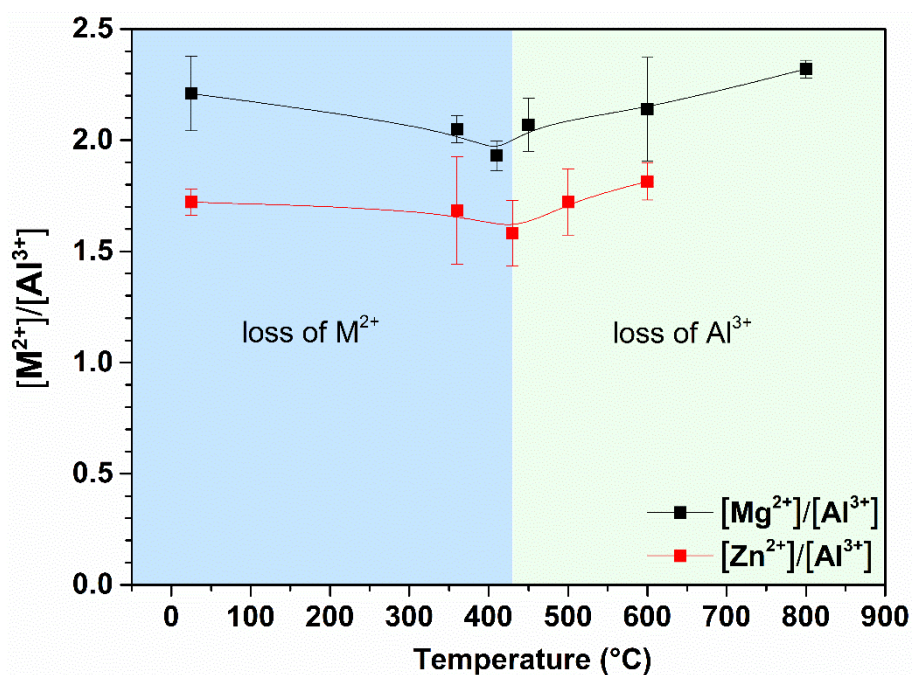


Figure 12. Variation of $[M^{2+}]/[Al^{3+}]$ molar ratio according to the temperature of pyrolysis determined by EDS analysis. Correction factors of -0.07 and 0.54, stipulated from metal analysis determined by ICP OES of precursors (**Table S4**), were applied for Mg_2Al -Fol and Zn_2Al -Fol, respectively.

TEM micrographs of LDH-C materials from Mg₂Al-Fol (**Figure 13**) presented characteristic platelet-like structures of LDH corresponding to the successful reconstitution of the hydroxide phase upon rehydration of LDO-C composites. However, increasing the pyrolysis temperature to obtain LDO-C, nanoscroll structures grow up until they reach a length of a few hundred nanometres at 800 °C (**Figure 13d-g**). Wrinkled and scrolled LDH particles were observed using organic intercalants (Rocha et al., 2016). Once the increase on nanoscrolls length seems to be associated with increasing in LDH platelets, as observed in SEM (**Figure 8**), it is hypothesized that they can correspond to the folding of LDH particles. In fact, from 800 to 1000 °C the decrease in the particles length supports the Mg(OH)₂ phase segregation, which could affect the particles size of rehydrated phases. For the system herein described, it is not discarded that carbonaceous structures can be entrapped into the scrolls assuming the role of a template during reconstitution once such structures were observed for Ni/Al-LDH synthesized *in-situ* over reduced graphene oxide sheets (Xu et al., 2014), but not for Mg₂Al-LDH reconstituted without the presence of carbon (Valente et al., 2010). Regarding the carbonaceous phase, there were not observed graphitic domains with stacking of graphene-like layers as previously reported by carbon-based nanocomposites obtained from the pyrolysis of Ni₂Al-CMC hybrid material (de Matos et al., 2020). Additionally, TEM images showed that Zn₂Al-HFol (**Figure 13i**) presented smaller particles with regard to Mg₂Al-Fol counterpart (**Figure 13a**). For comparison, Zn₂Al-HFol-600r samples present structures that do not reassemble nanoscrolls (**Figure 13j**); instead, samples presented agglomerate of particles without defined structure, in agreement with SEM analysis (**Figure 9**).

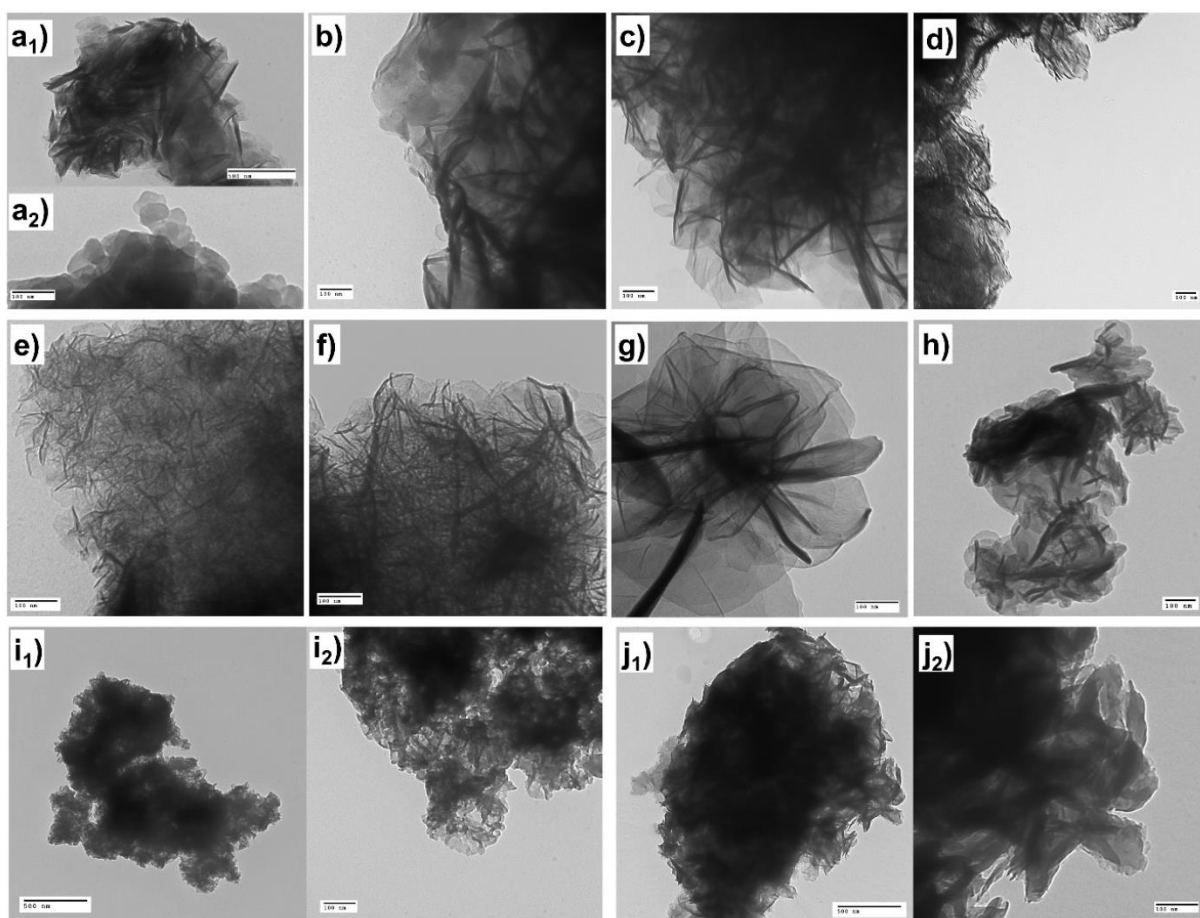


Figure 13. TEM images of $Mg_2Al-Fol$ (a) $Mg_2Al-Fol-360r$ (b); $Mg_2Al-Fol-360/0.5r$ (c), $Mg_2Al-Fol-410r$ (d), $Mg_2Al-Fol-450r$ (e), $Mg_2Al-Fol-600r$ (f), $Mg_2Al-Fol-800r$ (g) and $Mg_2Al-Fol-1000r$ (h), $Zn_2Al-HFol$ (i) and $Zn_2Al-HFol-600r$ (b). Scale bars: 500 nm (a_1 , i_1 and j_1) or 100 nm (a_2 , b-h, i_2 and j_2).

Pyrolysis of hybrid materials followed by reconstruction can be considered as an approach to intercalated organic molecules of interest (Jin et al., 2022) and/or doping the layer with active metal (e.g., Ni^{2+} , Co^{2+} , and Cu^{2+}) cations by isomorphic substitution to obtain multifunctional carbon-based nanocomposites (Takehira, 2017).

3.3. LDH/C-dots nanocomposites

The potentiality of obtaining LDH/C-dots nanocomposites was evaluated for samples pyrolyzed below 500 °C and restored by reaction with water (LDH-C). The limit temperature values for analysis were established at 500 and 600 °C for $Zn_2Al-HFol-Xr$ and $Mg_2Al-Fol-Xr$,

respectively. It was taken into account the results of FTIR and Raman spectroscopy (**Figure 4**), evaluating the presence of functional groups and the accessing of D and G bands.

Pyrolyzed materials did not present fluorescence in the solid state, in contrast which was previously reported for LDH/C-dot nanocomposites prepared from LDH-citrate (Song et al., 2015, 2016; Liu et al., 2017) and LDH-ETDA (Bai et al., 2018), for instance. Because the photoemission of C-dots can be environment-dependent (Deng et al., 2014), the optical properties (light absorption and emission) were evaluated after dispersing LDH-C in water. The results of electronic UV-VIS and fluorescence spectroscopies were presented in **Figure 14**. Folate in precursors presented electronic bands at 280-300 nm and 360 nm region (black lines in **Figure 14**) attributed to $\pi-\pi^*$ transition from *p*-ABA and PT moieties and $n-\pi^*$ transition from PT moiety of folate anions (Magri et al., 2022), respectively. As the temperature pyrolysis increased, the intensity of bands in the 360 nm decreased significantly in relation to band at 280-300 nm for Zn₂Al-HFol-Xr series (**Figure 14b**). On the other hand, the opposite was observed up to 450 °C for Mg₂Al-Fol-Xr (**Figure 14b**). Generally, the C-dots bands below and above 300 nm are attributed to $\pi-\pi^*$ and $n-\pi^*$ of sp²-carbon core and C=O/C=N groups (Mocci et al., 2022), respectively. Hence, these results are in line with FTIR analysis, which indicated the vanishing of C=O groups (**Figure 4c**) for Zn₂Al-HFol-XR, and supported the carbonization mechanism was distinct for the different LDH matrices. For Mg₂Al-Fol-XR series, the decrease of intensity of the band in the 280-300 nm could indicate the loss of *p*-ABA functional group, as shown by FTIR (**Figure 4b**), in agreement with the release of aniline accessed by EGA analysis (**Figures 2-3**). Besides, the UV-Vis spectra of Zn₂Al-HFol-500r (**Figure 14b**) and Zn₂Al-HFol-600r (**Figure S14**) presented broad absorption in the visible region (400-700 nm).

The samples presented common blue emission under 365 nm radiation from a UV lamp (inset **Figure 14**), as observed for original materials. The photoluminescence (PL) spectra under 365 nm excitation (blue line; **Figure 14**) showed emission in 440 nm with a slight shift to 420

nm with the increase of the pyrolysis temperature of the precursor LDH-C. The photoluminescence excitation (PLE) spectra for emission in 440 nm (red line; **Figure 14**) showed a profile with the maximum at 270-280 nm and 350-360 nm, already observed for precursors and assigned to PT moiety (*Chapter 4*). Hence, the materials presented a molecular fluorescence mechanism (Liu et al., 2019) coming from PT derivatives fluorophore species attached to the structure of the carbonaceous nanocomposite. A reliable proposal for the luminescence mechanism is beyond the scope of this work. The profile of PLE spectrum just changed significantly for Mg₂Al-Fol-600r (**Figure 13a**) and Zn₂Al-HFol-600r (**Figure S15**). A decrease in PLE band at 270-280 nm in relation to that one at 350-360 nm was observed, indicating the conversion of aromatic rings of folate anions into carbonaceous material.

In the series, the highest PL intensities upon 365 nm radiation excitation were observed for Zn₂Al-Fol-360r and Mg₂Al-Fol-410r (**Figure S15**). Since the proper carbonization contributes to the formation of C-dots with improved PL features in comparison with FA precursor (Zhang et al., 2019), these results could indicate that the carbonization degree was lower in Mg₂Al-LDH than in Zn₂Al-LDH matrix. For instance, the sample Mg₂Al-Fol-360/0.5r presented PL intensity comparable to Mg₂Al-Fol-410R, which demonstrated that more time or higher temperatures were necessary to increase the carbonization degree in Mg₂Al-Fol when compared to Zn₂Al-Fol (**Figure S15**). Furthermore, the decrease in PL intensity was noticed with the decreasing of functional groups (*e.g.*, COO⁻, C=O and NH), as determined by FTIR (**Figure 4b,c**) and in consequence of the increasing temperature of pyrolysis (**Figure S15**). These results are in agreement with those ones reported by Krysmann et al. (2012).

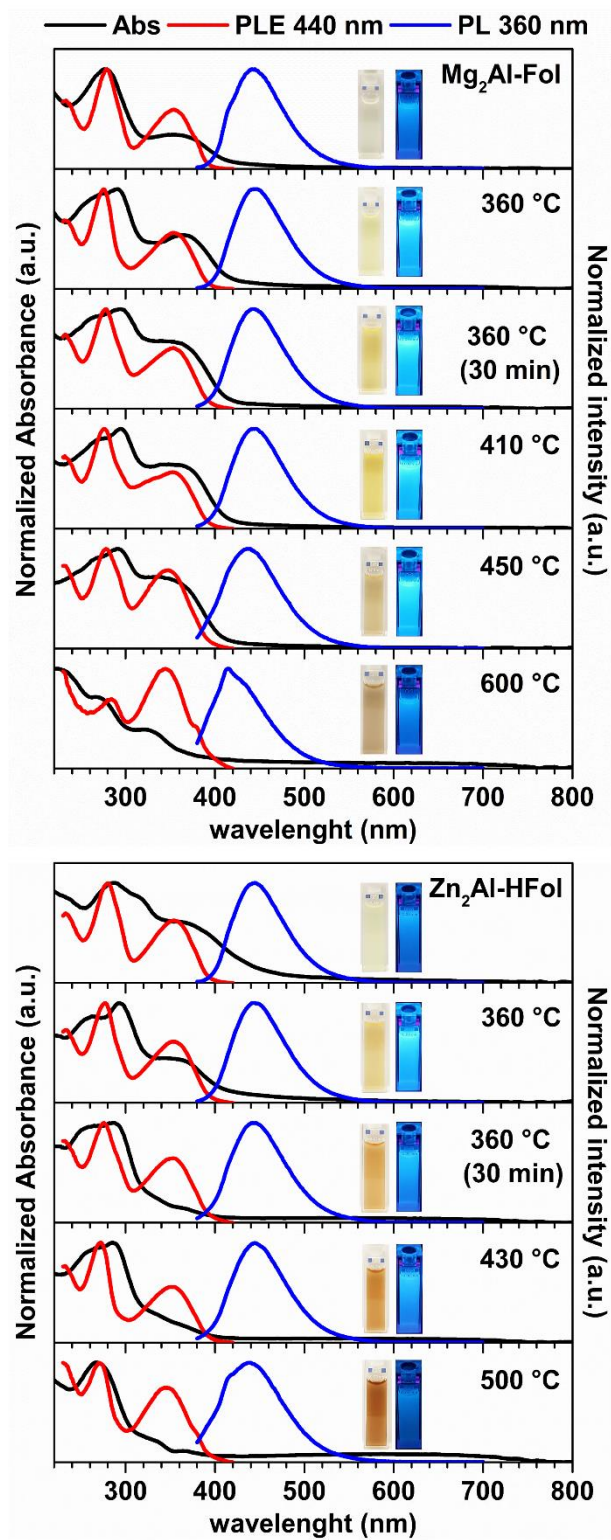


Figure 14. Optical characterization (absorption, PL and PLE spectra) of LDH-C nanocomposites obtained from pyrolysis of $\text{Mg}_2\text{Al-Fol}$ (a) and $\text{Zn}_2\text{Al-HFol}$ (b). Inset: images of the samples at daylight (left) and excited by a 365 nm UV lamp (right).

The considerable excitation-dependent PL and large Stokes shifting, characteristic of C-dots samples containing nanoparticles with distinct chemical composition and size (Gan et al., 2016), was not observed (**Figures S16-17**). The opposite was noticed for C-dots obtained from pyrolysis of pristine FA (*Chapter 4*), endorsing the controlled carbonization and homogeneity of the carbonaceous phase obtained in the confined interlayer space (Shi et al., 2017; Yao et al., 2017). According to the results obtained in this work, the temperature values for obtaining LDH-C with high PL intensity must be above the decomposition step of folate anions (determined by TGA/DSC and EGA) but below the decomposition of functional groups (FTIR).

3.5. Synthesis of LDH/C-dots by Hydrothermal Carbonization

The synthesis of LDH/C-dots was also investigated by hydrothermal carbonization of $\text{Mg}_2\text{Al-Fol}$, $\text{Zn}_2\text{Al-Fol}$ and $\text{Zn}_2\text{Al-HFol}$ hybrid materials. **Figure 15a** presents the images of the suspensions and the isolated powder after hydrothermal treatment. The samples $\text{Zn}_2\text{Al-LDH-HTX/h}$ (X is temperature and h is time) were similar in colour, changing from yellow to light brown with the increase of time at 150 °C. On the other hand, the colour of $\text{Mg}_2\text{Al-Fol}$ sample changed to yellow-grey, which was mainly observed for $\text{Mg}_2\text{Al-Fol-HT180-6h}$. In comparison, the increase of temperature to 180 °C led to the obtention of $\text{Zn}_2\text{Al-HFol}$ samples of dark brown colour. Colour changing indicated indirectly the evolution of carbonization of folate anions as far as the temperature and time increased. Additionally, under hydrothermal conditions, the carbonization was influenced more by the composition of the LDH layer and less by the charge of intercalated anion, endorsing the observations from TGA/DSC and EGA analysis (*section 3.2*).

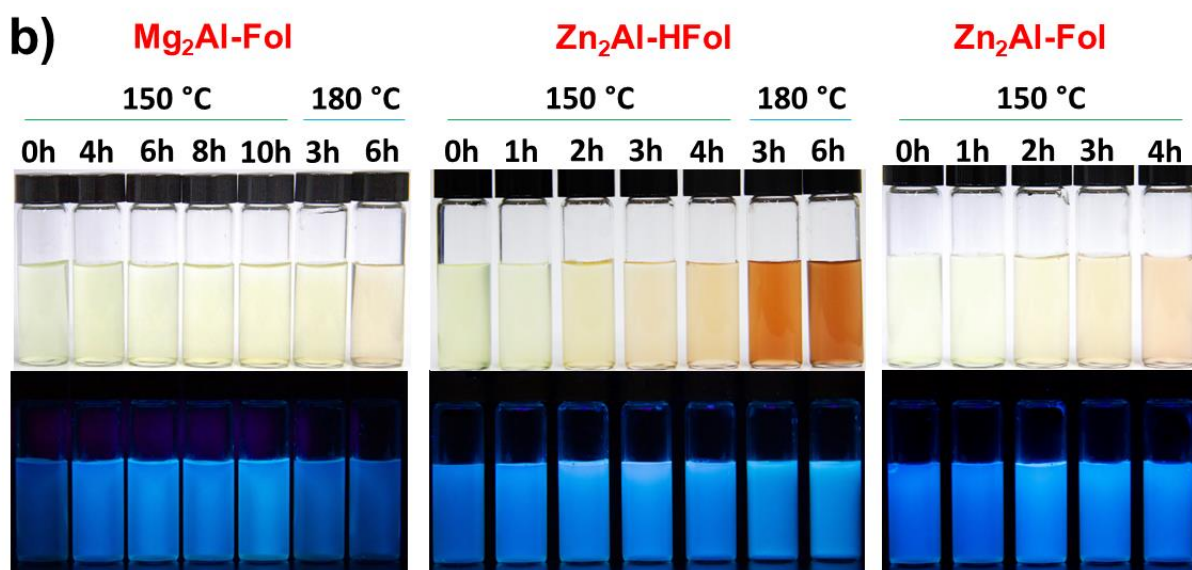
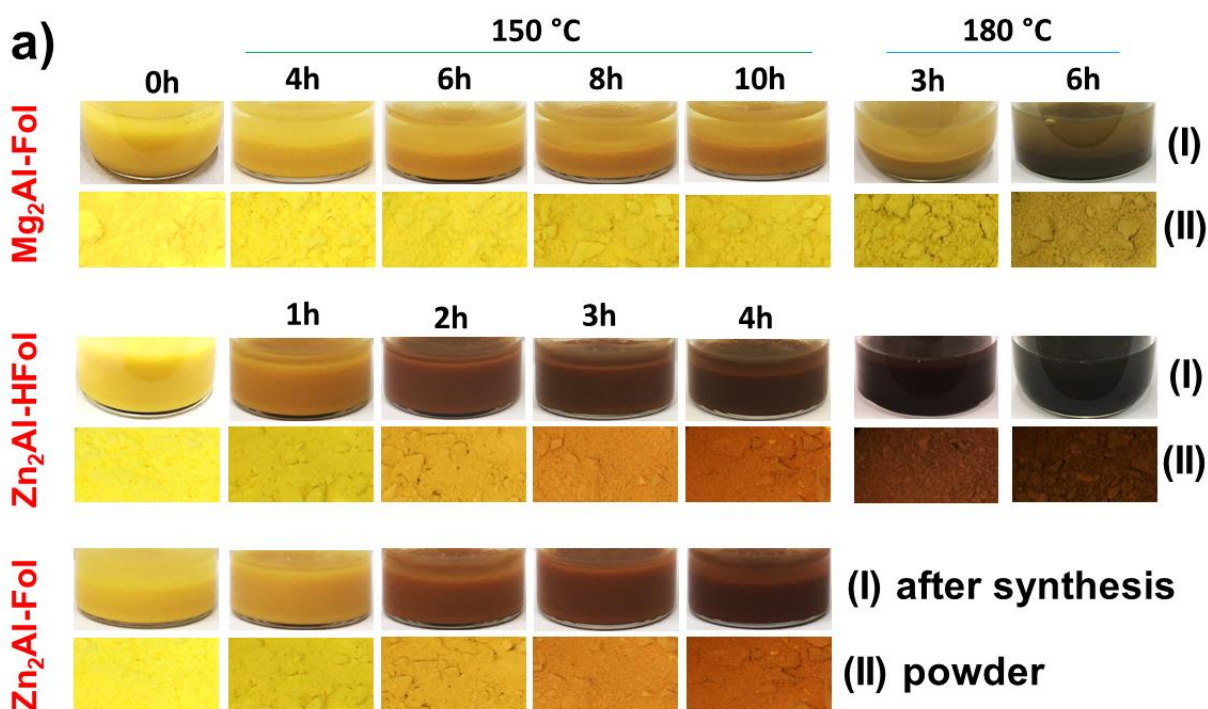


Figure 15. Representative images of samples submitted to hydrothermal carbonization (a) and respective suspensions (0.2 g L^{-1}) under daylight (up) and excited at 365 nm radiation from a UV lamp (down) (b).

$\text{Mg}_2\text{Al-Fol-HTX/h}$ materials maintained LDH structure independent of temperature and time of hydrothermal treatment (**Figure S18a**). However, as the process progressed, indications of the formation of $\text{Mg}_2\text{Al-CO}_3$ phase and traces of Al(OH)_3 was noticed in XRD patterns (**Figure 16a**) of $\text{Mg}_2\text{Al-Fol-HT180/6h}$. The formation of Al(OH)_3 was also observed for

Mg₂Al-Cl-HT150/4h (**Figure S19a**), which seems to be intrinsic to Mg₂Al-LDH materials, since it was previously observed in temperatures above 100 °C and 16 h of hydrothermal treatment (Xu et al., 2006). The FTIR spectrum confirmed the presence of carbonate in samples, as shown in **Figure 16b** and **Figure S20a**. It is proposed in this work that the CO₂ generated during the folate decomposition (GLU decomposition) was converted into CO₃²⁻ because of the basic pH of synthesis media (**Table S7**). Hence, a fraction of folate anions was exchanged by CO₃²⁻ and carbonized outside the interlayer space (**Figure 16c**). Another evidence of an anion-exchange reaction was the formation of HFol²⁻ from Fol³⁻ protonation in solution (**Figure S2**), as can be noticed by the emergence of vibrational band attributed to νC=O (1680 cm⁻¹) in FTIR of samples prepared at 150 °C (**Figure S20a**). The anion exchange process was intensified at 180 °C/6h (final pH value of about 9, **Table S7**), as can be verified in the XRD (**Figure 16a**) and FTIR (**Figure 16b**) results as well as the greyish colouring of Mg₂Al-Fol-HT180/6h sample indirectly indicated the folate anions carbonization (**Figure 15a**). The effect of pH seemed to be intrinsic to Mg₂Al-LDH materials, for which was observed a significant increase of the pH value during the hydrothermal treatment that was not observed for Zn₂Al-LDH counterparts (**Table S7**). In fact, no clearly indicative of CO₃²⁻ was noticed for samples from Zn₂Al-Fol and Zn₂Al-HFol (**Figure S20b,c**).

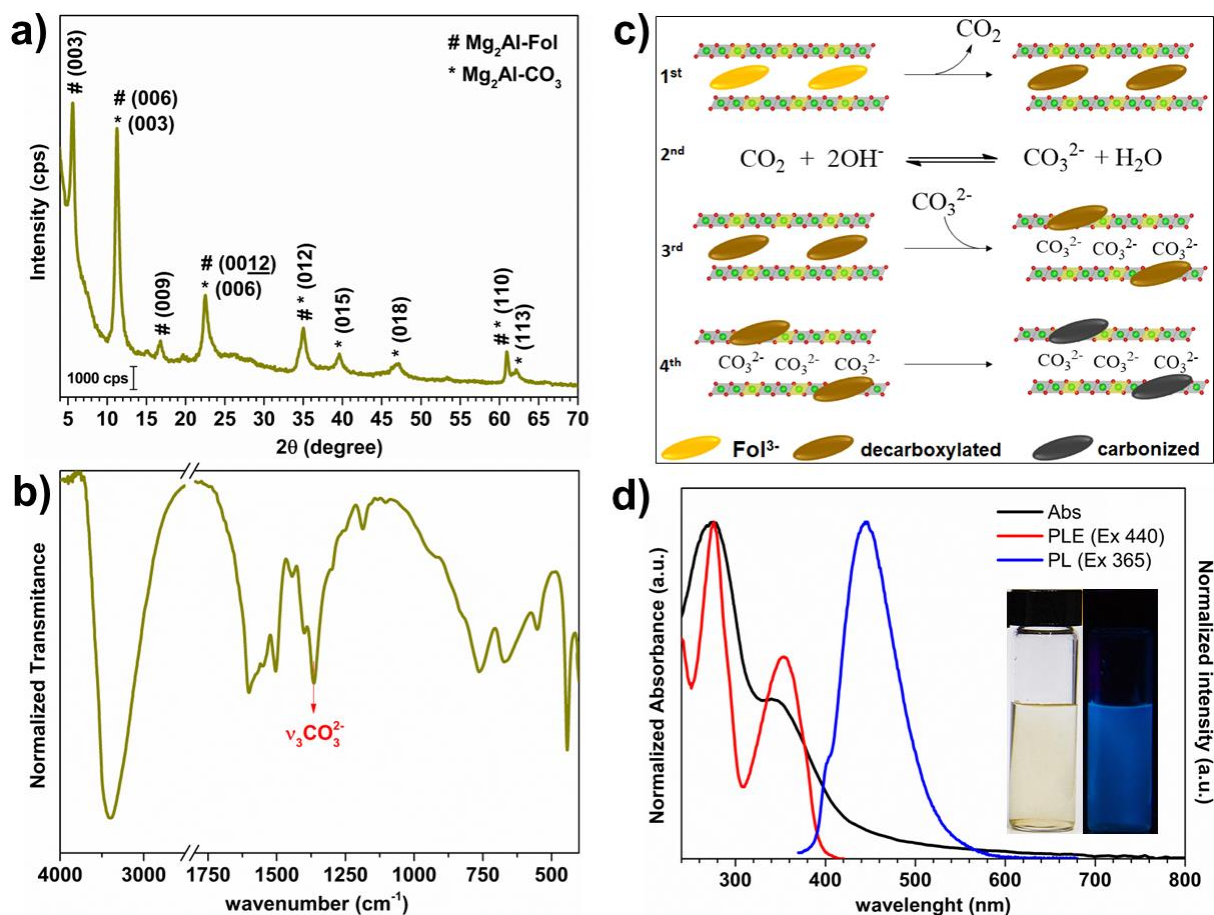


Figure 16. XRD pattern (a), FTIR spectrum (b), schematic representation of folate anions deintercalation during hydrothermal treatment (c), and Optical characterization (absorption, PL and PLE spectra) (d) of Mg₂Al-Fol-HT180/4h

The structure of Zn₂Al-HFol samples was maintained and its crystallinity was improved when hydrothermally treated at 150 °C (**Figure S18b**). Gao et al., (2021) reported the obtention of C-dot/ZnO nanocomposite from the hydrothermal treatment of a hybrid material composed of Zn₂Al-LDH/histidine at 170 °C for 8 h. In this work, the conversion of LDH structure into ZnO was observed when the temperature was increased to 180 °C (**Figure S18b**), as represented by Zn₂Al-HFol-HT180/3h nanocomposite (**Figure 17a**). The nanocomposite obtained presented mean particle size in the nanometric scale (**Figure 17b**). Nonetheless, the formation of the ZnO phase was observed at 150 °C for Zn₂Al-Fol-HT150/4h (**Figure S18c**) and Zn₂Al-Cl-HT150-4h (**Figure S19b**). In line with the data obtained for the pyrolyzed materials (*section 3.3*), the results obtained in the hydrothermal process also demonstrated the influence of

intercalated anion in the structural transformation of the LDH phase upon heating. The hindrance of ZnO formation in Zn₂Al-HFol-HT150/1-4h (**Figure S19b**) compared to Zn₂Al-Fol and Zn₂Al-Cl counterparts can be related to the higher basal spacing of the pristine precursor of Zn₂Al-HFol (**Figure S3** and **Table S1**). It was hypothesized in this work that the collapse of Zn₂Al-HFol layers, and consequently the formation of ZnO, could be precluded owing to the detachment of the layers promoted by the packing of HFol²⁻ in the interlayer spacing (parallel) in comparison with Fol³⁻ (tilted) in Zn₂Al-Fol (**Figure S3**). Hence, the formation of ZnO was only observed for Zn₂Al-HFol as far as the anions were decomposed at 180 °C. The lower hydrothermal stability observed for Zn₂Al-LDH compared with Mg₂Al-LDH at 180 °C was in agreement with the thermal analysis results (*section 3.2*) and with results from the literature (Britto et al., 2007).

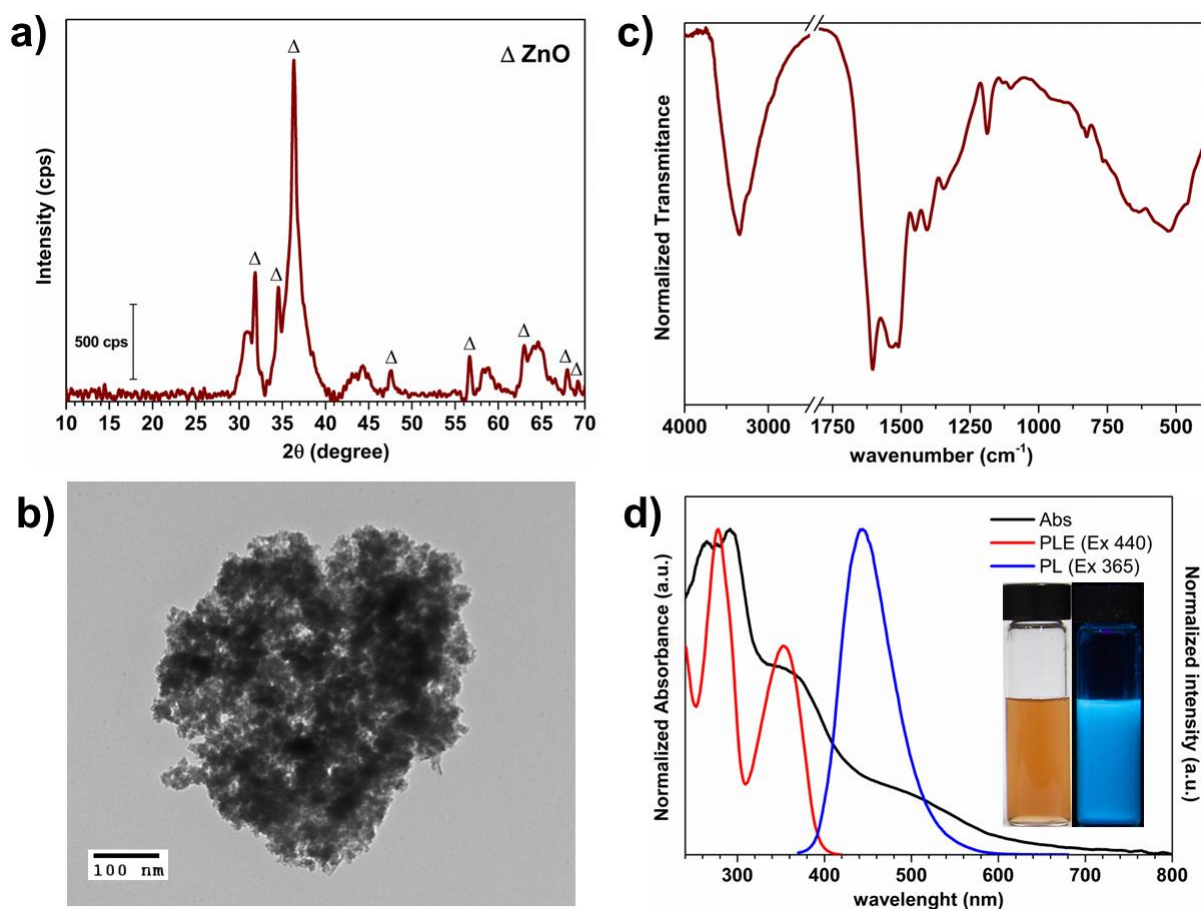


Figure 17. XRD pattern (a), TEM image (b), FTIR spectrum (c) and optical characterization (absorption, PL and PLE spectra) (d) of Zn₂Al-HFol-HT180/4h

The FTIR spectra (**Figure S20**) did not show huge changes in functional groups related to folate anions for samples prepared at 150 °C, indicating that the organic structure was almost completely preserved at this temperature. The molecular breakdown of folic acid under hydrothermal conditions (Abramova et al., 2020), as well as UV exposure (Off et al., 2005), occurs by the break of C9–N10 bond linking PT to *p*-ABA-GLU moiety; PT is posteriorly converted into 6-formil pterin (6-FPT). The breakdown of folate anions for Zn₂Al-HFol series was indicated by the decrease of the absorption band in the region of 310 nm (**Figure S21**). Concomitantly, an increase in vibrational absorption in the region of C11=O of GLU moiety (1640 cm⁻¹ region; **Figure S20**) was also noticed.

Although the band at 310 nm was in the same region of 6-FPT absorption (Off et al., 2005; Abramova et al., 2020), it was attributed to *p*-ABA-GLU moieties because it was observed from the original Zn₂Al-Fol. Besides, the molar absorptivity of 6-FPT was reported to be much lower than *p*-ABA-GLU (Off et al., 2005). The formation of 6-FPT was observed for Mg₂Al-Fol-HT150/8h and Mg₂Al-Fol-HT150/10h by the increase of absorption at 315 and 360 nm region of UV-Vis (**Figure S21a**) (Off et al., 2005; Abramova et al., 2020). The appearance of a band at 1736 cm⁻¹ in FTIR (**Figure S21a**) is attributed to νC=O of aldehyde (LARKIN, 2011). Another evidence of molecular breakdown was the increase in PL intensity. As shown in **Figure 15b**, samples presented the common blue emission under 365 nm radiation. The increase of PL intensity (**Figure S22**) was observed as far as the time increased, especially for Mg₂Al-Fol-HT150/4-6h series. According to Abramova et al. (2020), such feature could be related to molecular breakdowns of folic acid because the bonds rupture ceases the self-quenching of the excited electron transfer from PT to *p*-ABA group, improving the radiative decay.

Spectral changes in FTIR were more evident for samples hydrothermally treated at 180 °C, indicating that the carbonization of species from molecular breakdown was intensified. The

main alterations were related to PT ring (bands at 1580 cm^{-1} and 1300 cm^{-1} region), C4=O (1680 cm^{-1} region), and $-\text{COO}^-$ (1500 and 1400), as represented in **Figure 16b** and **17b**. The presence of aromatic groups originated from *p*-ABA was noticed over 6 h of treatment at 180 °C, as indicated by the band at 1600 cm^{-1} region (**Figure S20**). UV-VIS showed the intensity decrease of the band at 360 nm, strengthening the proposal of decomposition of amidic C=O groups and formation 6-FPT. A broad shoulder at 450-500 nm was observed, but it was more accentuated for $\text{Zn}_2\text{Al-HFol}$ hydrothermally treated at 180 °C, as represented in **Figure S21**. It can be attributed to the charge transfer from C-dots to ZnO semiconductor (Yu et al., 2012). Such spectral changes were also observed in UV-VIS spectrum of $\text{Zn}_2\text{Al-Fol-HT150/4h}$ (**Figure S21c**). Since the ZnO formation (**Figure S18c**) was observed for $\text{Zn}_2\text{Al-Fol-HT150/4h}$ and $\text{Zn}_2\text{Al-HFol-HT180/3-6h}$ samples, the results endorsed that the high carbonization of folate anions are driven by the stability of hydroxylated layer, as discussed before (*section 3.3*). No noticeable change in PL and PLE spectra was observed for samples prepared at 150 °C. However, a hypochromic shift from 285 to 275 nm of PLE band was observed for samples prepared at 180 °C (**Figures S21, 16b** and **17b**), indicating the partial decomposition of PT and *p*-ABA.

The hydrothermal treatment at 180 °C led to a significant decrease in PL intensity for materials obtained from $\text{Mg}_2\text{Al-Fol}$ (**Figure S22b**), probably because the deintercalation of folate anion that contributed to an uncontrolled carbonization. On the other hand, the highest PL intensity in the $\text{Zn}_2\text{Al-HFol}$ series was observed for $\text{Zn}_2\text{Al-HFol-HT180/3h}$, but it decreased again for $\text{Zn}_2\text{Al-Fol-HT180/6h}$ (**Figure S22d**).

Hydrothermal carbonization may not be the best approach to obtain LDH/C-dots nanocomposite when $\text{Mg}_2\text{Al-Fol}$ was used as a precursor. In this case, pyrolysis/reconstruction should be the method considered. However, luminescent nanocomposites based on ZnO could be achieved from the hydrothermal treatment of $\text{Zn}_2\text{Al-HFol}$ and $\text{Zn}_2\text{Al-Fol}$. Such ZnO-

nanocomposites could be potentially applied as antimicrobial agent (Gao et al., 2021) and heterogeneous photocatalyst (Yu et al., 2012).

5. Conclusion

LDH-FA materials were suitable precursors for carbon-based nanocomposites constituted of LDO or LDH. The carbonization of folate anions was controlled by their intercalation into LDH structure. The layer chemical composition was the main factor influencing the carbonization of organic species and it was observed to be more intense for Zn_2Al -LDH materials. It could be attributed to its lower temperature of dehydroxylation in comparison with Mg_2Al -LDH counterpart. Pyrolysis in isothermal condition at 360 °C presented a similar effect of pyrolysis in temperatures value of 410-430 °C and was more important for Mg_2Al -LDH due to the low rate of carbonization promoted by such material. The formation of graphitic carbon was achieved above 500-600 °C. Furthermore, the crystallization of oxides (*e.g.*, MgO and ZnO) was precluded, being initially observed at 800 °C, because of the carbonaceous material formed during the pyrolysis.

LDO-C materials were successfully restored into the LDH-C structure. A transition from the inherited-precursor structure to the LDH-CO₃ phase was observed in the peak temperature (DSC curves) values attributed to the first decomposition step of folate anions. Such a phenomenon was correlated to the decomposition of anionic groups of organic species (*e.g.*, C4-O⁻ and/or -COO⁻). Nanocomposites based on carbonaceous materials intimately mixed within the reconstructed LDH layers were obtained from precursors pyrolyzed up to 600 and 800 °C, from Zn_2Al -HFol and Mg_2Al -Fol, respectively. At higher temperatures, phase segregation was observed.

LDH-FA were also potential precursors of LDH/C-dots nanocomposites. Based on the PL intensities of the composite materials, the best temperature range was below the peak

temperature (DTG curve) of the first decomposition step of folate anion, around 410-430 °C. At higher temperatures, the decomposition of the functional organic group of folate was observed, making the PL intensity decrease. Hydrothermal carbonization was not appropriate for the production of LDH/C-dots from Mg₂Al-Fol because of the folate deintercalation during the process. However, luminescent nanosized ZnO-carbon nanocomposite was obtained through the hydrothermal treatment of Zn₂Al-HFol at 180 °C for 3 h. Further experiments should evaluate the nanostructure of carbonaceous materials formed inside the layers by acid solubilization of the LDH phase. Besides, additional characterization (*i.e.*, XPS, XANES-EXAFS and ²⁷Al-NMR) of nanocomposites must be carried out to access the degree of LDH reconstitution and the possible presence of structural defects promoted by the thermal treatment. This work will be helpful to the development of multifunctional nanocomposites based on graphite-like materials and LDH or LDO, with the potentiality to be applied in plenty of fields, from nanomedicine to environmental protection.

CRedit authorship contribution statement

Vagner R. Magri: Conceptualization, Visualization, Methodology, Investigation, Data curation, Formal analysis, Writing – original draft, Writing - review & editing. **Caroline S. de Matos:** Methodology and Writing – review & editing. **Michele A. Rocha:** Methodology and Writing – review & editing. **Rafael Macedo:** Formal analysis and Writing – review & editing. **Christine Taviot-Gueho:** Formal analysis and Writing – review & editing. **Vera R. L. Constantino:** Conceptualization, Methodology, Visualization, Formal analysis, Project administration, Funding acquisition, Writing – review & editing, Supervision.

Declaration of Competing Interest

The authors declare that they have no known competing financial interests or personal relationships that could have appeared to influence the work reported in this paper.

Acknowledgments

V.R.M. is grateful to the Coordenação de Aperfeiçoamento de Pessoal de Nível Superior (CAPES, Brazil, Finance Code 33002010191P0) for the PhD scholarship. C.S. de M. acknowledges the Fundação de Amparo à Pesquisa do Estado de São Paulo for research grant (FAPESP 12/06291-4). V.R.L.C. is thankful to the Conselho Nacional de Desenvolvimento Científico e Tecnológico (CNPq, 314034/2021-8) and Sao Paulo Research Foundation (FAPESP, INCT-INEO 2014/50869-6) for the research grants. This work was partially supported by region Auvergne-Rhone Alpes (Pack Ambition International AURA program). The authors also acknowledge the Central Analítica of Instituto de Química da Universidade de São Paulo – CA-IQUSP for elemental analysis. The authors are thankful to the Laboratório de Cristalografia (Instituto de Física - USP) for the XRD diffractograms registration, the Laboratório de Espectroscopia Molecular (LEM, Instituto de Química – USP) for the Raman and FTIR spectra recording, and to the Laboratório de Caracterização Tecnológica (LCT – USP), in especial for Ms. Liz Zanchetta for helping in SEM-EDS analysis.

Appendix A. Supplementary material

Supplementary material of this article can be found online at <https://doi.org/>

References

- Abramova, A.M., Kokorina, A.A., Sindeeva, O.A., Jolibois, F., Puech, P., Sukhorukov, G.B., Goryacheva, I.Y., Sapelkin, A. V., 2020. Molecular nature of breakdown of the folic acid under hydrothermal treatment: a combined experimental and DFT study. *Sci. Rep.* 10, 1–6. <https://doi.org/10.1038/s41598-020-76311-y>
- Acik, M., Lee, G., Mattevi, C., Pirkle, A., Wallace, R.M., Chhowalla, M., Cho, K., Chabal, Y., 2011. The role of oxygen during thermal reduction of graphene oxide studied by infrared absorption spectroscopy. *J. Phys. Chem. C* 115, 19761–19781. <https://doi.org/10.1021/jp2052618>
- Ayiania, M., Weiss-Hortala, E., Smith, M., McEwen, J.S., Garcia-Perez, M., 2020. Microstructural analysis of nitrogen-doped char by Raman spectroscopy: Raman shift analysis from first principles. *Carbon N. Y.* 167, 559–574. <https://doi.org/10.1016/j.carbon.2020.05.055>
- Bai, L., Xue, N., Zhao, Y., Wang, X., Lu, C., Shi, W., 2018. Dual-mode emission of single-layered graphene quantum dots in confined nanospace: Anti-counterfeiting and sensor applications. *Nano Res.* 11, 2034–2045. <https://doi.org/10.1007/s12274-017-1820-z>
- Bellotto, M., Rebours, B., Clause, O., Lynch, J., Bazin, D., Elkaïm, E., 1996. Hydrotalcite Decomposition Mechanism: A Clue to the Structure and Reactivity of Spinel-like Mixed Oxides. *J. Phys. Chem.* 100, 8535–8542. <https://doi.org/10.1021/jp960040i>
- Bokhoven, J.A. Van, Roelofs, J.C.A.A., Jong, K.P. De, 2001. Unique Structural Properties of the Mg - Al Hydrotalcite Solid Base Catalyst : An In Situ Study Using Mg and Al K-Edge XAFS during Calcination and Rehydration 1258–1265. [https://doi.org/10.1002/1521-3765\(20010316\)7](https://doi.org/10.1002/1521-3765(20010316)7)
- Bravo-Suárez, J.J., Páez-Mozo, E.A., Oyama, S.T., 2004. Review of the synthesis of layered double hydroxides: a thermodynamic approach. *Quim. Nova* 27, 7040–7066. <https://doi.org/10.1590/S0100-40422004000400015>
- Britto, S., Radha, A.V., Ravishankar, N., Kamath, P.V., 2007. Solution decomposition of the layered double hydroxide (LDH) of Zn with Al. *Solid State Sci.* 9, 279–286. <https://doi.org/10.1016/j.solidstatesciences.2007.01.002>
- Cao, Y., Li, G., Li, X., 2016. Graphene/layered double hydroxide nanocomposite: Properties, synthesis, and applications. *Chem. Eng. J.* 292, 207–223. <https://doi.org/10.1016/j.cej.2016.01.114>
- Carvalho, H.W.P., Pulcinelli, S.H., Santilli, C. V., Leroux, F., Meneau, F., Briois, V., 2013. XAS/WAXS time-resolved phase speciation of chlorine LDH thermal transformation: Emerging roles of isovalent metal substitution. *Chem. Mater.* 25, 2855–2867. <https://doi.org/10.1021/cm401352t>
- Cavani, F., Trifirò, F., Vaccari, A., 1991. Hydrotalcite-type anionic clays: preparation, properties and applications. *Catal. Today* 11, 173–301.
- Conterposito, E., Palin, L., Antonioli, D., Riccardi, M., Boccaleri, E., Aceto, M., Milanesio, M., Gianotti, V., 2018. On the Rehydration of Organic Layered Double Hydroxides to form Low-Ordered Carbon/LDH Nanocomposites. *Inorganics* 6, 79. <https://doi.org/10.3390/inorganics6030079>
- de Matos, C.S., Ghimbeu, C.M., Brendlé, J., Limousy, L., Constantino, V.R.L., 2020. Thermal decomposition of a layered double hydroxide as a bottom up approach for the synthesis of metallic nanoparticles embedded in carbon structures. *New J. Chem.* 44, 16721–16732. <https://doi.org/10.1039/D0NJ01938K>
- de Matos, C.S., Nóbrega, M.M., Temperini, M.L.A., Constantino, V.R.L., 2019. Hybrid Ni Al layered double hydroxide: Characterization and in situ synchrotron XRD and vibrational spectroscopic studies under high-pressure. *Appl. Clay Sci.* 174, 152–158.

- <https://doi.org/10.1016/j.clay.2019.03.031>
- Deng, Y., Chen, X., Wang, F., Zhang, X., Zhao, D., Shen, D., 2014. Environment-dependent photon emission from solid state carbon dots and its mechanism. *Nanoscale* 6, 10388–10393. <https://doi.org/10.1039/C4NR02544J>
- Ferrari, A.C., Robertson, J., 2000. Interpretation of Raman spectra of disordered and amorphous carbon. *Phys. Rev. B* 61, 14095–14107. <https://doi.org/10.1103/PhysRevB.61.14095>
- Ferrari, A.C., Rodil, S.E., Robertson, J., 2003. Interpretation of infrared and Raman spectra of amorphous carbon nitrides. *Phys. Rev. B* 67, 155306. <https://doi.org/10.1103/PhysRevB.67.155306>
- Gan, Z., Xu, H., Hao, Y., 2016. Mechanism for excitation-dependent photoluminescence from graphene quantum dots and other graphene oxide derivatives: consensus, debates and challenges. *Nanoscale* 8, 7794–7807. <https://doi.org/10.1039/C6NR00605A>
- Gao, X., Ma, X., Han, X., Wang, X., Li, S., Yao, J., Shi, W., 2021. Synthesis of carbon dot-ZnO-based nanomaterials for antibacterial application. *New J. Chem.* 45, 4496–4505. <https://doi.org/10.1039/D0NJ05741J>
- Gao, Z., Sasaki, K., Qiu, X., 2018. Structural Memory Effect of Mg–Al and Zn–Al layered Double Hydroxides in the Presence of Different Natural Humic Acids: Process and Mechanism. *Langmuir* 34, 5386–5395. <https://doi.org/10.1021/acs.langmuir.8b00059>
- Gordon, I.E., Rothman, L.S., Hargreaves, R.J., et al. The HITRAN2020 molecular spectroscopic database. *J. Quant. Spectrosc. Radiat. Transf.* 277, 107949. <https://doi.org/10.1016/j.jqsrt.2021.107949>
- Hammer, P., Lacerda, R.G., Droppa, R., Alvarez, F., 2000. Comparative study on the bonding structure of hydrogenated and hydrogen free carbon nitride films with high N content. *Diam. Relat. Mater.* 9, 577–581. [https://doi.org/10.1016/S0925-9635\(99\)00300-3](https://doi.org/10.1016/S0925-9635(99)00300-3)
- Hobbs, C., Jaskaniec, S., McCarthy, E.K., Downing, C., Opelt, K., Güth, K., Shmeliov, A., Mourad, M.C.D., Mandel, K., Nicolosi, V., 2018. Structural transformation of layered double hydroxides: an in situ TEM analysis. *npj 2D Mater. Appl.* 2, 4. <https://doi.org/10.1038/s41699-018-0048-4>
- Inagaki, M., Toyoda, M., Soneda, Y., Morishita, T., 2018. Nitrogen-doped carbon materials. *Carbon N. Y.* 132, 104–140. <https://doi.org/10.1016/j.carbon.2018.02.024>
- Jin, L., Zhou, X., Wang, F., Ning, X., Wen, Y., Song, B., Yang, C., Wu, D., Ke, X., Peng, L., 2022. Insights into memory effect mechanisms of layered double hydroxides with solid-state NMR spectroscopy. *Nat. Commun.* 13, 6093. <https://doi.org/10.1038/s41467-022-33912-7>
- Kato, T., Yamada, Y., Nishikawa, Y., Ishikawa, H., Sato, S., 2021. Carbonization mechanisms of polyimide: Methodology to analyze carbon materials with nitrogen, oxygen, pentagons, and heptagons. *Carbon N. Y.* 178, 58–80. <https://doi.org/10.1016/j.carbon.2021.02.090>
- Khorshidi, M., Asadpour, S., Sarmast, N., Dinari, M., 2022. A review of the synthesis methods, properties, and applications of layered double hydroxides/carbon nanocomposites. *J. Mol. Liq.* 348, 118399. <https://doi.org/10.1016/j.molliq.2021.118399>
- Klopprogge, J.T., Hickey, L., Frost, R.L., 2004. FT-Raman and FT-IR spectroscopic study of synthetic Mg/Zn/Al-hydrotalcites. *J. Raman Spectrosc.* 35, 967–974. <https://doi.org/10.1002/jrs.1244>
- Krysmann, M.J., Kelarakis, A., Dallas, P., Giannelis, E.P., 2012. Formation Mechanism of Carbogenic Nanoparticles with Dual Photoluminescence Emission. *J. Am. Chem. Soc.* 134, 747–750. <https://doi.org/10.1021/ja204661r>
- Larkin, P. J., 2011. *Infrared and Raman Spectroscopy Principles and Spectral Interpretation*, 1st ed. Elsevier.
- Liu, M.L., Chen, B. Bin, Li, C.M., Huang, C.Z., 2019. Carbon dots: synthesis, formation

- mechanism, fluorescence origin and sensing applications. *Green Chem.* 21, 449–471. <https://doi.org/10.1039/c8gc02736f>
- Liu, W., Xu, S., Liang, R., Wei, M., Evans, D.G., Duan, X., 2017. In situ synthesis of nitrogen-doped carbon dots in the interlayer region of a layered double hydroxide with tunable quantum yield. *J. Mater. Chem. C* 5, 3536–3541. <https://doi.org/10.1039/C6TC05463C>
- Liu, X., Li, S., Liu, L., Wang, Z., 2021. Facile pyrolysis approach of folic acid-derived high graphite N-doped porous carbon materials for the oxygen reduction reaction. *New J. Chem.* 45, 5949–5957. <https://doi.org/10.1039/D0NJ06174C>
- Liu, Y., Gao, Y., Wang, Q., Lin, W., 2018. The synergistic effect of layered double hydroxides with other flame retardant additives for polymer nanocomposites: a critical review. *Dalt. Trans.* 47, 14827–14840. <https://doi.org/10.1039/C8DT02949K>
- Magri, V.R., Duarte, A., Perotti, G.F., Constantino, V.R.L., 2019. Investigation of Thermal Behavior of Layered Double Hydroxides Intercalated with Carboxymethylcellulose Aiming Bio-Carbon Based Nanocomposites. *ChemEngineering* 3, 55. <https://doi.org/10.3390/chemengineering3020055>
- Magri, V.R., Rocha, M.A., de Matos, C.S., Petersen, P.A.D., Leroux, F., Petrilli, H.M., Constantino, V.R.L., 2022. Folic acid and sodium folate salts: Thermal behavior and spectroscopic (IR, Raman, and solid-state ^{13}C NMR) characterization. *Spectrochim. Acta Part A Mol. Biomol. Spectrosc.* 273, 120981. <https://doi.org/10.1016/j.saa.2022.120981>
- Millange, F., Walton, R.I., O'Hare, D., 2000. Time-resolved in situ X-ray diffraction study of the liquid-phase reconstruction of Mg–Al–carbonate hydrotalcite-like compounds. *J. Mater. Chem.* 10, 1713–1720. <https://doi.org/10.1039/b002827o>
- Mocci, F., de Villiers Engelbrecht, L., Olla, C., Cappai, A., Casula, M.F., Melis, C., Stagi, L., Laaksonen, A., Carbonaro, C.M., 2022. Carbon Nanodots from an In Silico Perspective. *Chem. Rev.* 122, 13709–13799. <https://doi.org/10.1021/acs.chemrev.1c00864>
- Linstrom, P.J. and Mallard W.G., Eds., NIST Chemistry WebBook, NIST Standard Reference Database Number 69, National Institute of Standards and Technology, Gaithersburg MD, 20899, <https://doi.org/10.18434/T4D303>
- Off, M.K., Steindal, A.E., Porojnicu, A.C., Juzeniene, A., Vorobey, A., Johnsson, A., Moan, J., 2005. Ultraviolet photodegradation of folic acid. *J. Photochem. Photobiol. B Biol.* 80, 47–55. <https://doi.org/10.1016/j.jphotobiol.2005.03.001>
- Prevot, V., Forano, C., Besse, J.P., Abraham, F., 1998. Syntheses and Thermal and Chemical Behaviors of Tartrate and Succinate Intercalated Zn_3Al and Zn_2Cr Layered Double Hydroxides. *Inorg. Chem.* 37, 4293–4301. <https://doi.org/10.1021/ic9801239>
- Radha, A. V., Thomas, G.S., Vishnu Kamath, P., Antonyraj, C.A., Kannan, S., 2010. Thermal decomposition of Co–Al layered double hydroxide: Identification of precursor to oxide with spinel structure. *Bull. Mater. Sci.* 33, 319–324. <https://doi.org/10.1007/s12034-010-0049-1>
- Rocha, M.A., Petersen, P.A.D., Teixeira-Neto, E., Petrilli, H.M., Leroux, F., Taviot-Gueho, C., Constantino, V.R.L., 2016. Layered double hydroxide and sulindac coiled and scrolled nanoassemblies for storage and drug release. *RSC Adv.* 6, 16419–16436. <https://doi.org/10.1039/C5RA25814F>
- Santos, R.M.M., Tronto, J., Briois, V., Santilli, C. V., 2017. Thermal decomposition and recovery properties of $\text{ZnAl}-\text{CO}_3$ layered double hydroxide for anionic dye adsorption: insight into the aggregative nucleation and growth mechanism of the LDH memory effect. *J. Mater. Chem. A* 5, 9998–10009. <https://doi.org/10.1039/C7TA00834A>
- Schroeder, P., 2002. Infrared spectroscopy in clay science. *C. Work. Lect.* 11, 181–206.
- Shi, W.Y., Wang, X.R., Lu, C., Bai, L.Q., Xue, N., 2017. Activating efficient room temperature phosphorescence of carbon dots by synergism of orderly non-noble metals and dual structural confinements. *Nanoscale* 9, 6658–6664. <https://doi.org/10.1039/c6nr09648d>

- Song, L., Shi, J., Lu, J., Lu, C., 2015. Structure observation of graphene quantum dots by single-layered formation in layered confinement space. *Chem. Sci.* 6, 4846–4850. <https://doi.org/10.1039/C5SC01416F>
- Song, L., Shi, W., Lu, C., 2016. Confinement Effect in Layered Double Hydroxide Nanoreactor: Improved Optical Sensing Selectivity. *Anal. Chem.* 88, 8188–8193. <https://doi.org/10.1021/acs.analchem.6b02000>
- Speight, J., 2005. *Lange's Handbook Of Chemistry*, Sixteenth Edition.
- Sun, J., Liu, H., Chen, X., Evans, D.G., Yang, W., Duan, X., 2012. Synthesis of graphene nanosheets with good control over the number of layers within the two-dimensional galleries of layered double hydroxides. *Chem. Commun.* 48, 8126. <https://doi.org/10.1039/c2cc33782g>
- Takehira, K., 2017. Recent development of layered double hydroxide-derived catalysts – Rehydration, reconstitution, and supporting, aiming at commercial application. *Appl. Clay Sci.* 136, 112–141. <https://doi.org/10.1016/j.clay.2016.11.012>
- Taviot-Guého, C., Prévot, V., Forano, C., Renaudin, G., Mousty, C., Leroux, F., 2018. Tailoring Hybrid Layered Double Hydroxides for the Development of Innovative Applications. *Adv. Funct. Mater.* 28, 1703868. <https://doi.org/10.1002/adfm.201703868>
- Valente, J.S., Lima, E., Toledo-Antonio, J.A., Cortes-Jacome, M.A., Lartundo-Rojas, L., Montiel, R., Prince, J., 2010. Comprehending the thermal decomposition and reconstruction process of sol-gel MgAl layered double hydroxides. *J. Phys. Chem. C* 114, 2089–2099. <https://doi.org/10.1021/jp910538r>
- Wani, A.A., Khan, A.M., Manea, Y.K., Shahadat, M., Ahammad, S.Z., Ali, S.W., 2020. Graphene-supported organic-inorganic layered double hydroxides and their environmental applications: A review. *J. Clean. Prod.* 273, 122980. <https://doi.org/10.1016/j.jclepro.2020.122980>
- Warringham, R., Mitchell, S., Murty, R., Schäublin, R., Crivelli, P., Kenvin, J., Pérez-Ramírez, J., 2017. Mapping the Birth and Evolution of Pores upon Thermal Activation of Layered Hydroxides. *Chem. Mater.* 29, 4052–4062. <https://doi.org/10.1021/acs.chemmater.7b00734>
- Xu, J., Gai, S., He, F., Niu, N., Gao, P., Chen, Y., Yang, P., 2014. A sandwich-type three-dimensional layered double hydroxide nanosheet array/graphene composite: Fabrication and high supercapacitor performance. *J. Mater. Chem. A* 2, 1022–1031. <https://doi.org/10.1039/c3ta14048b>
- Xu, S., Zhao, J., Yu, Q., Qiu, X., Sasaki, K., 2019. Effect of Natural Organic Matter Model Compounds on the Structure Memory Effect of Different Layered Double Hydroxides. *ACS Earth Sp. Chem.* 3, 2175–2189. <https://doi.org/10.1021/acsearthspacechem.9b00175>
- Xu, Z.P., Stevenson, G., Lu, C.-Q., Lu, G.Q.M., 2006. Dispersion and Size Control of Layered Double Hydroxide Nanoparticles in Aqueous Solutions. *J. Phys. Chem. B* 110, 16923–16929. <https://doi.org/10.1021/jp062281o>
- Yao, Q., Wang, S., Shi, W., Lu, C., Liu, G., 2017. Graphene Quantum Dots in Two-Dimensional Confined and Hydrophobic Space for Enhanced Adsorption of Nonionic Organic Adsorbates. *Ind. Eng. Chem. Res.* 56, 583–590. <https://doi.org/10.1021/acs.iecr.6b02389>
- Ye, H., Liu, S., Yu, D., Zhou, X., Qin, L., Lai, C., Qin, F., Zhang, M., Chen, Wenjing, Chen, Wenfang, Xiang, L., 2022. Regeneration mechanism, modification strategy, and environment application of layered double hydroxides: Insights based on memory effect. *Coord. Chem. Rev.* 450, 214253. <https://doi.org/10.1016/j.ccr.2021.214253>
- Yu, H., Zhang, H., Huang, H., Liu, Y., Li, H., Ming, H., Kang, Z., 2012. ZnO/carbon quantum dots nanocomposites: one-step fabrication and superior photocatalytic ability for toxic

- gas degradation under visible light at room temperature. *New J. Chem.* 36, 1031. <https://doi.org/10.1039/c2nj20959d>
- Zhang, Q., Deng, S., Liu, J., Zhong, X., He, J., Chen, X., Feng, B., Chen, Y., Ostrikov, K. (Ken), 2019. Cancer-Targeting Graphene Quantum Dots: Fluorescence Quantum Yields, Stability, and Cell Selectivity. *Adv. Funct. Mater.* 29, 1–11. <https://doi.org/10.1002/adfm.201805860>
- Zhao, M.Q., Zhang, Q., Huang, J.Q., Wei, F., 2012. Hierarchical nanocomposites derived from nanocarbons and layered double hydroxides - Properties, synthesis, and applications. *Adv. Funct. Mater.* 22, 675–694. <https://doi.org/10.1002/adfm.201102222>
- Zhao, X., Zhang, F., Xu, S., Evans, D.G., Duan, X., 2010. From layered double hydroxides to ZnO-based mixed metal oxides by thermal decomposition: Transformation mechanism and UV-blocking properties of the product. *Chem. Mater.* 22, 3933–3942. <https://doi.org/10.1021/cm100383d>
- Zheng, Y., Wang, F., Yang, X., Huang, Y., Liu, C., Zheng, Z., Gu, J., 2017. Study on aromatics production via the catalytic pyrolysis vapor upgrading of biomass using metal-loaded modified H-ZSM-5. *J. Anal. Appl. Pyrolysis* 126, 169–179. <https://doi.org/10.1016/j.jaap.2017.06.011>

Supporting Information material of Chapter 2

V.R. Magri, A. Duarte, G.F. Perotti, V.R.L. Constantino, Investigation of Thermal Behavior of Layered Double Hydroxides Intercalated with Carboxymethylcellulose Aiming Bio-Carbon Based Nanocomposites, **ChemEngineering**. 3 (2019) 55.
<https://doi.org/10.3390/chemengineering3020055>

Investigation of Thermal Behaviour of Layered Double Hydroxides Intercalated with Carboxymethylcellulose Aiming Bio-Carbon Based Nanocomposites

Vagner R. Magri ¹, Alfredo Duarte ¹, Gustavo F. Perotti ^{1,2}, and Vera R.L. Constantino ^{1,*}

¹ Departamento de Química Fundamental, Instituto de Química, Universidade de São Paulo (USP), Av. Prof. Lineu Prestes 748, CEP 05508-000, São Paulo, SP, Brazil; vrlconst@iq.usp.br (V.R.L.C.); vmagri@usp.br (V.R.M.); aduarte@iq.usp.br (A.D.)

² Instituto de Ciências Exatas e Tecnologia, Universidade Federal do Amazonas (UFAM), Rua Nossa Senhora do Rosário 3863, CEP 69103-128, Itacoatiara, AM, Brazil; gustavoperotti@ufam.edu.br (G.F.P.)

* Correspondence: vrlconst@iq.usp.br; Tel.: +55-11-3091-9152

Received: 31 March 2019; Accepted: 27 May 2019; Published: date

Table S1. Interplanar distances d_{hkl} and 2θ ($\text{CuK}\alpha$) values from X-ray diffraction data of LDH- CO_3 and LDH-CMC. The indexation of diffraction peaks is based on R-3m space group.

<i>hkl</i>	$\text{Zn}_2\text{Al-CO}_3$		$\text{Mg}_2\text{Al-CO}_3$		$\text{Zn}_2\text{Al-CMC}$		$\text{Mg}_2\text{Al-CMC}$	
	2θ (°)	<i>d</i> (nm)	2θ (°)	<i>d</i> (nm)	2θ (°)	<i>d</i> (nm)	2θ (°)	<i>d</i> (nm)
(003)	11.729	0.754	11.570	0.765	3.543	2.492	5.047	1.750
(006)	23.562	0.378	23.290	0.382	6.156	1.435	10.578	0.836
(009)	35.809	0.251	--	--	10.130	0.873	--	--
(101)	33.968	0.264	--	--	--	--	--	--
(012)	34.675	0.259	34.905	0.257	33.930	0.264	35.270	0.254
(104)	37.379	0.241	--	--	--	--	--	--
(015)	39.300	0.229	39.406	0.229	--	--	--	--
(107)	44.078	0.205	--	--	--	--	--	--
(018)	46.866	0.194	46.788	0.194	--	--	--	--
(0012)	48.145	0.189	--	--	--	--	--	--
(1010)	53.090	0.172	52.899	0.173	--	--	--	--
(0111)	56.491	0.163	56.242	0.164	--	--	--	--
(110)	60.306	0.153	60.853	0.152	60.547	0.153	61.208	0.151
(113)	61.663	0.150	62.161	0.149	--	--	--	--
(1013)	63.823	0.146	63.395	0.147	--	--	--	--
(116)	65.645	0.142	66.054	0.141	--	--	--	--
(0114)	67.751	0.138	--	--	--	--	--	--
d_{003} (nm)	0.754		0.765		2.492		1.750	
<i>c</i> (nm) *	2.262		2.295		7.476		5.250	
<i>a</i> and <i>b</i> (nm)	0.306		0.304		0.306		0.302	

(*) *c* parameter was calculated considering $c = 3 \times d_{003}$; (#) *a/b* parameter was calculated considering $a = 2 \times d_{110}$.

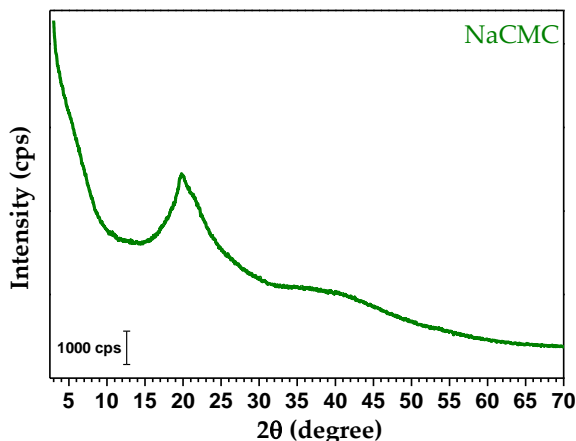


Figure S1. XRD pattern of sodium carboxymethylcellulose (NaCMC).

FTIR-ATR and Raman Spectra of LDH-CO₃ Samples

The infrared spectra of Zn₂Al-CO₃ and Mg₂Al-CO₃ are presented in Figure 4 in the main text. The broad band in the region between 3700–3100 cm⁻¹ can be attributed to the stretching vibrations of the hydroxyl groups (νOH) from inorganic layer and the water molecules hydrogen-bonded. The shoulder at 3020 cm⁻¹ region is assigned to νOH of H₂O molecules interacting with CO₃²⁻ by hydrogen bonding while the band at 1600–1635 cm⁻¹ is related to the in-plane bending vibration of H₂O [1–4]. The bands of carbonate ions are observed in the region of 1354 cm⁻¹ (antisymmetric stretching, ν₃), 860 cm⁻¹ (out of plane, ν₂) and 680 cm⁻¹ (in-plane bending, ν₄) [1,4,5]. In the region below 1000 cm⁻¹, the spectra show bands attributed to the lattice vibrations modes of the groups M-O-M and HO-M-OH (M = Zn²⁺, Mg²⁺, Al³⁺). The strong band at 760 cm⁻¹ is attributed to antisymmetric bending vibrations of HO-Al-OH groups [3,6] while the band at 674 cm⁻¹, only observed in Mg₂Al-CO₃ spectrum, can be attributed to antisymmetric bending of HO-Mg-OH groups.

FT-Raman spectra of Zn₂Al-CO₃ and Mg₂Al-CO₃ are also presented in Figure 4 in the main text. The broad band in the 3140 cm⁻¹ region is attributed to the stretching vibrations of the layer hydroxide ions (νOH) and the H₂O molecules. The band at 1060 cm⁻¹ is assigned to symmetric stretching (ν₁) of carbonate anion [1,5]. The band at 495 cm⁻¹ is attributed to the antisymmetric stretching lattice of M²⁺-O-Al [3] and shown to be dependent of M²⁺ cation, being more intense to Zn²⁺ possibly owing to its higher polarizability than Mg²⁺. A tentative attribution of the main vibrational bands is presented in Table S2.

Table S2. Vibrational data of Zn₂Al-CO₃ and Mg₂Al-CO₃ samples.

Zn ₂ Al-CO ₃		Mg ₂ Al-CO ₃		Tentative Attribution	Reference
FTIR	Raman	FTIR	Raman		
3700–3100	3143	3700–3100	3143	vOH (M-OH and H ₂ O)	[1–4]
3026 (sh)	--	3026 (sh)	--	vOH (H ₂ O---CO ₃ ²⁻)	
1400(sh)	--	1400(sh)	--	v ₃ CO ₃ ²⁻	[1,4,5]
1351	--	1358	--	v ₃ CO ₃ ²⁻	
1632	--	1600	--	δ _{ip} H ₂ O	[1–4]
1058	1060	1058	1059	v ₁ CO ₃ ²⁻	[1,4,5]
946 (sh)	--	946 (sh)	--	δAl-O-H	[6]
863 (sh)	--	863 (sh)	--	v ₂ CO ₃ ²⁻	[1,4,5]
760	--	760	--	δ _{as} (HO-Al-OH) _l	[3,6]
--	698	688 (sh)	698	v ₄ CO ₃ ²⁻	[1,4,5]
--	--	674	--	δ _{as} (HO-Mg-OH) _l	[3]
630	--	630 (sh)	--	δ _s (HO-Al-OH) _l	[3]
556	--	558	--	v _{as} (M ²⁺ -O-Al) _L	[3]
--	565	--	565	v _s (M ²⁺ -O-Al) _L	[3]
525	--	--	--	δ _{as} (HO-Zn ²⁺ -OH) _l	[4]
423	495	--	483	v _s (M ²⁺ -O-Al) _L	[3]
--	--	440 (sh)	--	δ _{as} (M ²⁺ -O-Al) _L	[3]
--	155	--	151	δ(O-M ²⁺ -O)	[7]

v = stretching; δ = bending; s: symmetric; as: antisymmetric; ip: in plane; sh: shoulder; L: lattice; l = vibrations; M²⁺ = divalent cation; v₁ = symmetric stretching; v₃ = antisymmetric stretching ; v₂ = bending out of plane; v₄ = bending in plane.

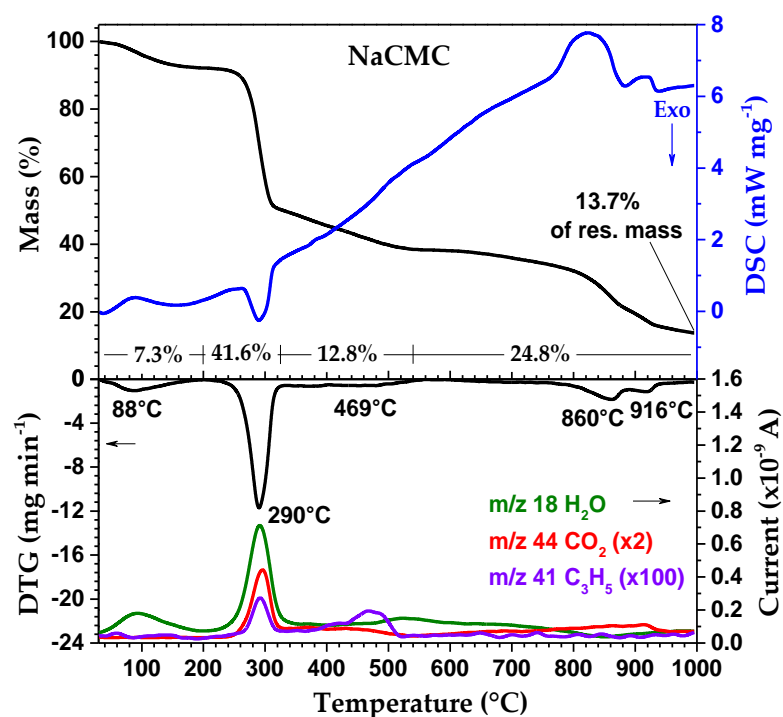
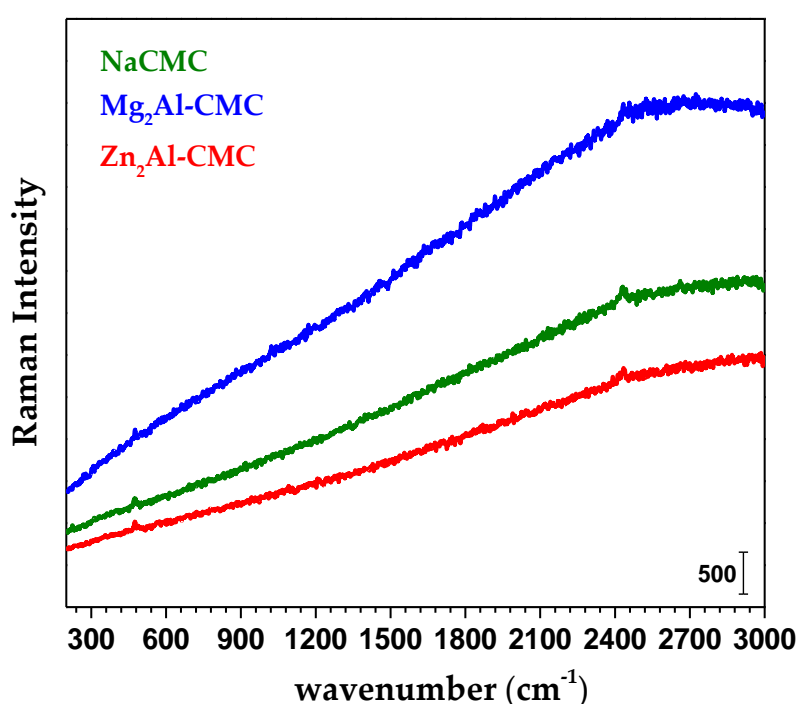


Figure S2. TG-DSC (up) and DTG-MS (down) curves of sodium carboxymethylcellulose (NaCMC) under N₂ atmosphere.

Table S3. Chemical analysis data and proposed formula for LDH-CO₃ and LDH-CMC samples.

Sample	Proposed Formula [§]	%C [†]	%H ₂ O [*]
Mg ₂ Al-CO ₃	[Mg _{2.00} Al(OH) _{6.00}](CO ₃) _{0.50} ·2.43 H ₂ O	-- (2.39)	17.40 (17.40)
Zn ₂ Al-CO ₃	[Zn _{2.14} Al(OH) _{6.28}](CO ₃) _{0.50} ·3.28 H ₂ O	-- (1.66)	16.30 (16.30)
Mg ₂ Al-CMC	[Mg _{2.18} Al(OH) _{6.36}](RU) _{1.15} (Cl) _{0.20} ·2.36 H ₂ O	20.80 (20.90)	8.80 (8.68)
Zn ₂ Al-CMC	[Zn _{1.84} Al(OH) _{5.68}](RU) _{1.43} (Na _{0.23} RU _{0.33})·2.88 H ₂ O	22.80 (22.80)	7.56 (7.56)

[§] M²⁺/Al³⁺ metal ratio was calculated from ICP OES; [†] calculated from carbon elemental analysis; ^{*} calculated from TG curves; RU: (C₆H₁₀O₅)(C₂H₂O₂)_{0.7}; () values obtained based on the proposed formula.

**Figure S3.** Raman spectra ($\lambda_{exc.} = 532$ nm) of NaCMC and LDH-CMC samples.

FTIR-ATR Spectra of LDH-CO₃ Calcined Samples

FTIR-ATR spectra of calcined samples (MMO/C nanocomposites) are shown in Figure S4. LDH-CO₃ samples submitted to the same conditions than LDH-CMC materials were analysed by this vibrational technique for comparison. Zn₂Al-CO₃ sample heated at 500 °C presents two remarkable bands at 1532 cm⁻¹ and 1388 cm⁻¹ attributed to the split of ν_3 vibrational mode of carbonate anion. These vibrational bands present $\Delta\nu$ equal to 144 cm⁻¹ and can be assigned to CO₃²⁻ ion coordinated to the layer metal cations [8]. Coordination process also activates the ν_1 mode of carbonate. The ν_3 bands are also noticed with low intensity in the spectrum of Zn₂Al-CO₃ calcined at 600 °C but are practically absent in FTIR-ATR spectra of samples calcined at 800 and 1000 °C. Hence, carbonate coordination to metal sites of LDH layers can explain the thermal profile observed above 500 °C for Zn₂Al-CO₃ sample (Figure 5 in the main text). Mg₂Al-CO₃ spectra also show bands at 1600–1350 cm⁻¹ region but with different shape that can be attributed mainly to absorption of atmospheric carbon dioxide at high basic surface of

calcined samples [9,10] (spectra were recorded in *ex situ* mode). In general, bands observed below 900 cm^{-1} are assigned to vibrational modes of M-O bonds, as presented in Table S2.

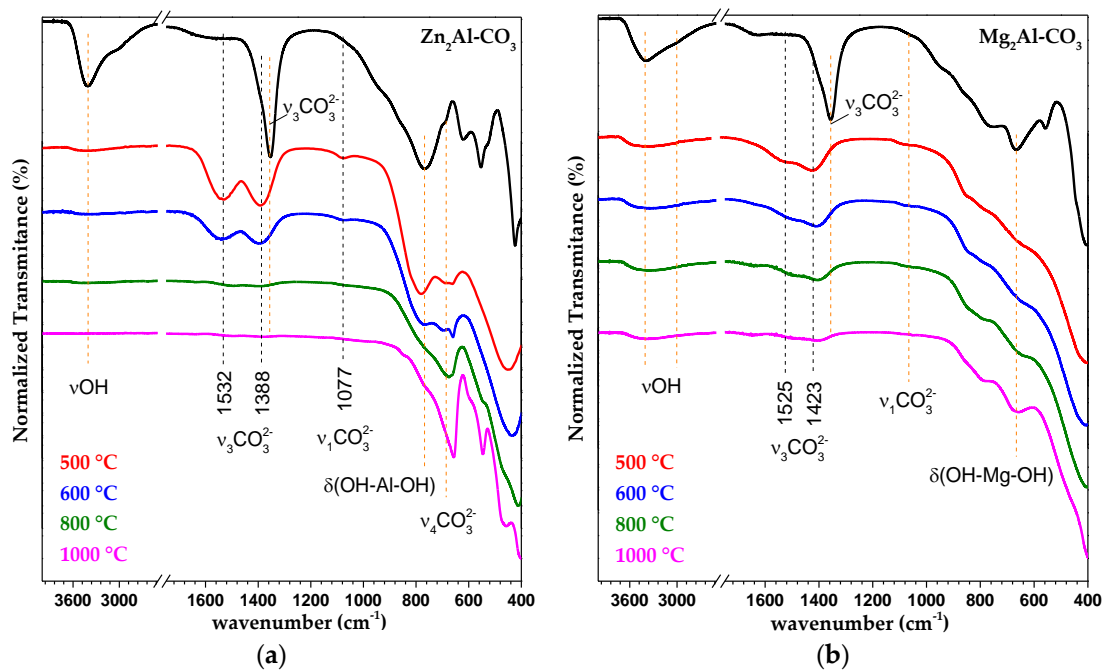


Figure S4. FTIR-ATR spectra of $\text{Zn}_2\text{Al-CO}_3$ (a) and $\text{Mg}_2\text{Al-CO}_3$ (b) samples calcined at 500, 600, 800 and 1000 °C under N_2 atmosphere.

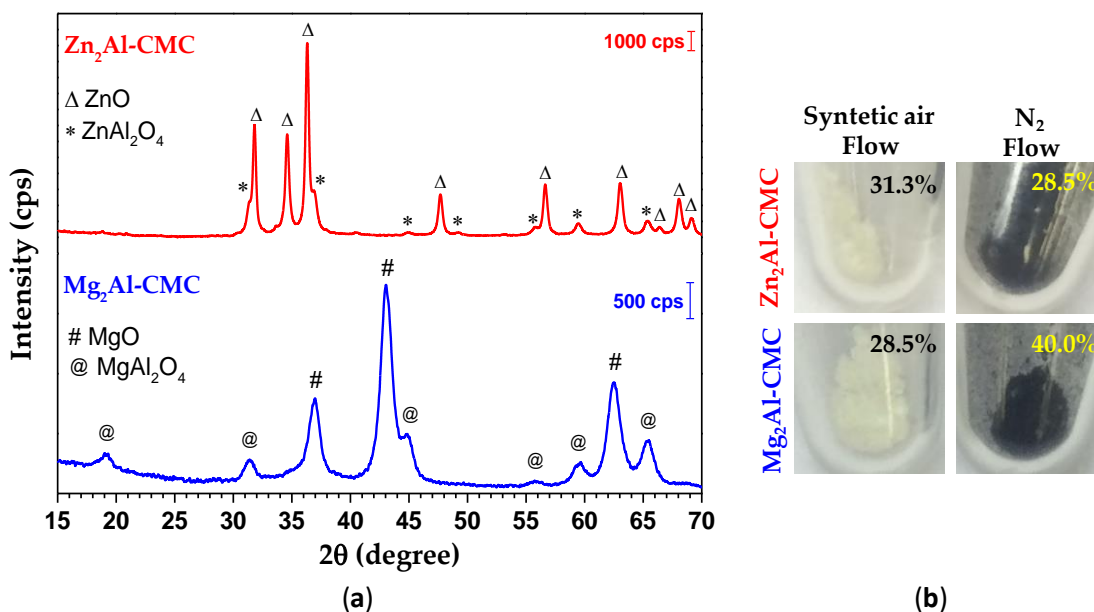


Figure S5. XRD patterns of $\text{M}_2\text{Al-CMC}$ samples calcined at 1000 °C under synthetic air (a). Pictures of $\text{M}_2\text{Al-CMC}$ samples calcined at 1000 °C under synthetic air or nitrogen atmosphere, indicating the percentage of residue after each heating process (b).

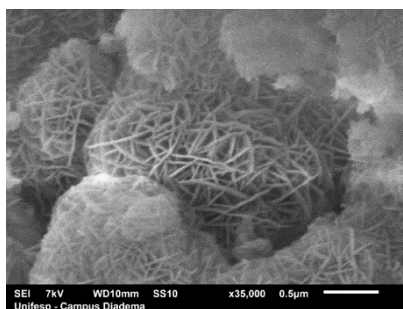


Figure S6. SEM image of Mg₂Al-CO₃ sample.

Thermodynamic Considerations about Carbothermic Reaction

Thermodynamic parameters were used to calculate the Gibbs free energy of carbothermic reaction ($\Delta_R G^\circ$) between graphite carbon and metal oxides (ZnO and MgO). The standard molar thermodynamic parameters of each substance at 25 °C are shown in Table S4 and the results are presented in Table S5.

Table S4. Standard molar thermodynamic parameters of substances at 25 °C.

Substance	State	$\Delta_f H^\circ$ kJ mol ⁻¹	S° J K ⁻¹ mol ⁻¹	$\Delta_f G^\circ$ kJ mol ⁻¹	Reference
C _(graf.)	s	0	5.74(10)	0	[11]
CO	g	-110.53(17)	197.660(4)	-137.16	[11]
ZnO	s	-348.280	43.64	-318.30	[12]
Zn ⁰	s	0	41.63(15)	0	
	g	130.40(40)	160.990(4)	95.14	[11,12]
MgO	s	-601.6	26.95	-569.3	[11,12]
Mg ⁰	s	0	32.67(10)	0	
	g	147.1(8)	148.648(3)	113.10	[11]

Table S5. Standard molar thermodynamic values for the carbothermic reaction between graphitic carbon and zinc or magnesium oxides at 25 °C. Values calculates from data presented in Table S4.

Chemical Equation of Reaction	$\Delta_R H^\circ$ kJ mol ⁻¹	$\Delta_R S^\circ$ J K ⁻¹ mol ⁻¹	$\Delta_R G^\circ$ kJ mol ⁻¹	T _{RS} (°C)	T _{exp} * (°C)
ZnO _(s) + C _(s) → Zn ⁰ _(v) + CO _(g)	368.15	309.26	276.29	917	>880
MgO _(s) + C _(s) → Mg ⁰ _(v) + CO _(g)	638.28	313.62	545.24	1762	--

T_{RS} = temperature of reaction spontaneity; * taken from the thermal analysis result (Figure 5).

Carbothermic reactions are obviously not spontaneous at 25 °C but the entropy ($\Delta_R S^\circ$) is positive and the reactions tend to become spontaneous with increasing of the temperature. The value of temperature to promote a spontaneous carbothermic reaction (T_{RS}) was estimated considering that $\Delta_R H^\circ$ and $\Delta_R S^\circ$ do not change significantly and the equilibrium conditions. The calculated T_{RS} value suggests that carbothermic reaction for ZnO reduction tends to become spontaneous above 917 °C, a value very close to that one observed in this work (880 °C). For MgO, the T_{RS} value is much higher (1762 °C) than for ZnO. The results of calculations agree with the processes experimentally observed.

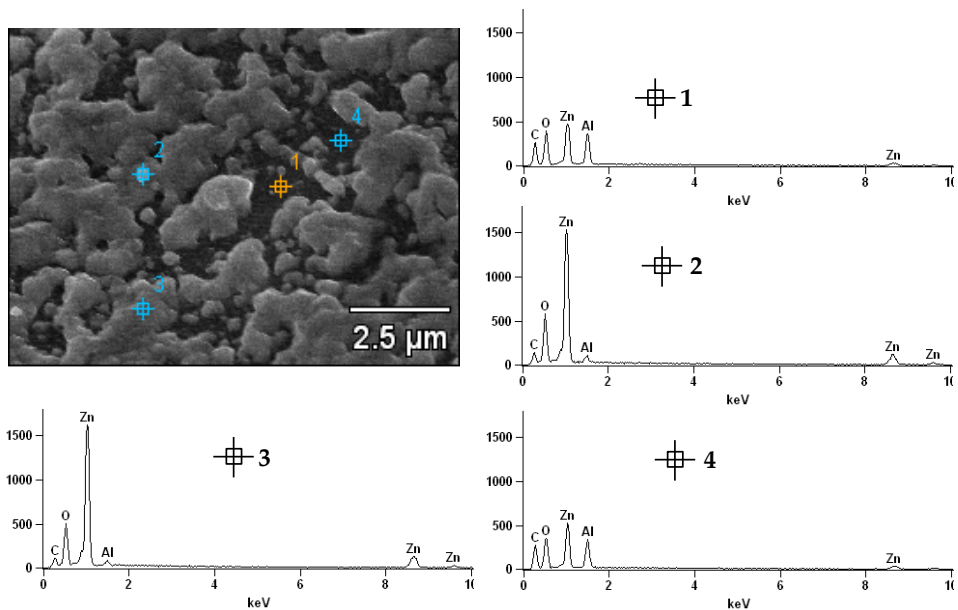


Figure S7. EDS spectra of Zn₂Al-CMC sample pyrolyzed at 800 °C.

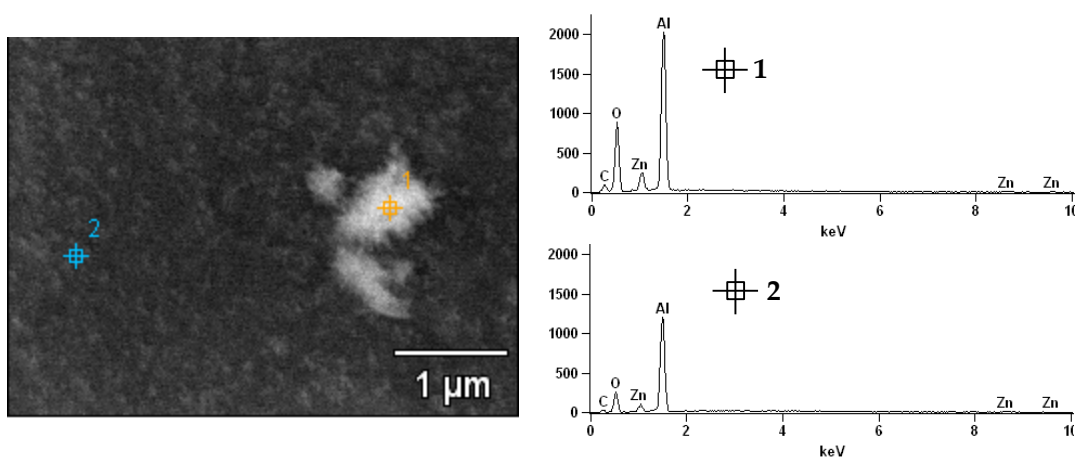


Figure S8. EDS spectra of Zn₂Al-CMC sample pyrolyzed at 1000 °C.

References

1. Labajos, F.M.; Rives, V.; Ulbarri, M.A. Effect of hydrothermal and thermal treatments on the physicochemical properties of Mg-Al hydrotalcite-like materials. *J. Mater. Sci.* **1992**, *27*, 1546–1552.
2. Kloprogge, J.T.; Frost, R.L. Fourier Transform Infrared and Raman Spectroscopic Study of the Local Structure of Mg-, Ni-, and Co-Hydrotalcites. *J. Solid State Chem.* **1999**, *146*, 506–515.
3. Kagunya, W.; Baddour-Hadjean, R.; Kooli, F.; Jones, W. Vibrational modes in layered double hydroxides and their calcined derivatives. *Chem. Phys.* **1998**, *236*, 225–234.
4. Kloprogge, J.T.; Hickey, L.; Frost, R.L. The effects of synthesis pH and hydrothermal treatment on the formation of zinc aluminum hydrotalcites. *J. Solid State Chem.* **2004**, *177*, 4047–4057.
5. Kloprogge, J.T.; Wharton, D.; Hickey, L.; Frost, R.L. Infrared and Raman study of interlayer anions CO_3^{2-} , NO_3^- , SO_4^{2-} and ClO_4^- in Mg/Al-hydrotalcite. *Am. Mineral.* **2002**, *87*, 623–629.
6. Theo Kloprogge, J.; Frost, R.L. Infrared emission spectroscopic study of the dehydroxylation of synthetic Mg/Al and Mg/Zn/Al-hydrotalcites. *Phys. Chem. Chem. Phys.* **1999**, *1*, 1641–1647.
7. Gil, O.M.; Rocha, M.A.; Constantino, V.R.L.; Koh, I.H.J.; de Faria, D.L.A. Modified drug release system based on Sulindac and layered double hydroxide: An in vivo Raman investigation. *Vib. Spectrosc.* **2016**, *87*, 60–66.
8. Greenaway, A.M.; Dasgupta, T.P.; Koshy, K.C.; Sadler, G.G. A correlation between infrared stretching mode absorptions and structural angular distortions for the carbonato ligand in a wide variety of complexes. *Spectrochim. Acta Part A Mol. Spectrosc.* **1986**, *42*, 949–954.
9. Constantino, V.R.L.; Pinnavaia, T.J. Basic Properties of $\text{Mg}^{2+}_{1-x}\text{Al}^{3+}_x$ Layered Double Hydroxides Intercalated by Carbonate, Hydroxide, Chloride, and Sulfate Anions. *Inorg. Chem.* **1995**, *34*, 883–892.
10. Prinetto, F.; Ghiotti, G.; Giuria, V.P.; Durand, R.; Tichit, D. Investigation of Acid-Base Properties of Catalysts Obtained from Layered Double Hydroxides. *J. Phys. Chem. B* **2000**, *104*, 11117–11126.
11. Speight, J. *Lange's Handbook Of Chemistry*, 16th ed.; 2005; ISBN 9780071432207.
12. Atkins, P.W.; Paula, J. *Físico-química*; vol. 1, 9th ed.; LTC: Rio de Janeiro, 2010; ISBN 978-85-216-2104-1.



© 2019 by the authors. Submitted for possible open access publication under the terms and conditions of the Creative Commons Attribution (CC BY) license (<http://creativecommons.org/licenses/by/4.0/>).

Supporting Information material of Chapter 3

V.R. Magri, M.A. Rocha, C.S. de Matos, P.A.D. Petersen, F. Leroux, H.M. Petrilli, V.R.L. Constantino, Folic acid and sodium folate salts: Thermal behavior and spectroscopic (IR, Raman, and solid-state ^{13}C NMR) characterization, **Spectrochim. Acta Part A Mol. Biomol. Spectrosc.** 273 (2022) 120981.

<https://doi.org/10.1016/j.saa.2022.120981>

Appendix A. Supplementary material

Folic Acid and Sodium Folate Salts: Thermal Behavior and Spectroscopic (IR, Raman, and Solid-state ^{13}C -NMR) Characterization

Vagner R. Magri,^a Michele A. Rocha,^a Caroline S. de Matos,^a Philippe A. D. Petersen,^b Fabrice Leroux,^{c,d} Helena M. Petrilli^b and Vera R. L. Constantino^{a*}

^aDepartamento de Química Fundamental, Instituto de Química, Universidade de São Paulo, Av. Prof. Lineu Prestes 748, CEP 05508-000, São Paulo, SP, Brazil
vrlconst@iq.usp.br

^bDepartamento de Física de Materiais e Mecânica, Instituto de Física, Universidade de São Paulo, Rua do Matão 1371, CEP 05508-090, São Paulo, SP, Brazil

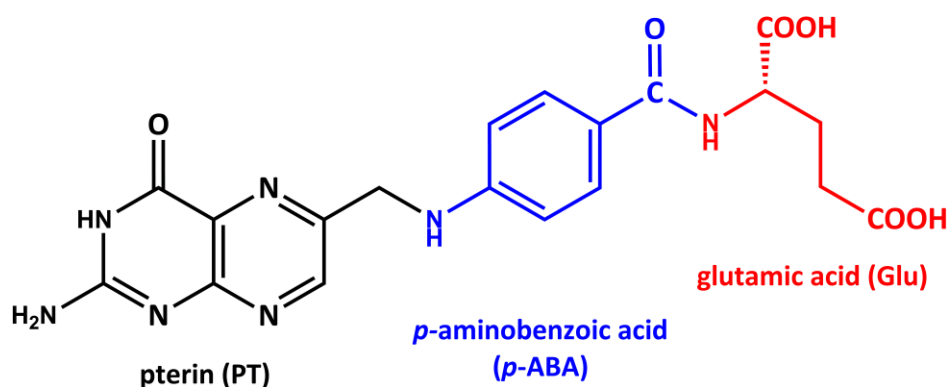
^cUniversité Clermont Auvergne, Institut de Chimie de Clermont-Ferrand, BP 10448, F-63000 Clermont-Ferrand, France

^dCNRS, UMR 6296, ICCF, F-63178 Aubiere, France.

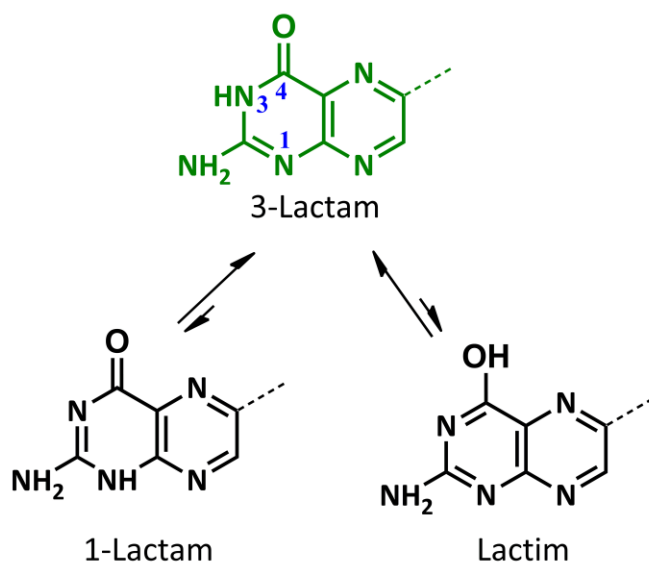
1. Reviewing pterin tautomerism and mesomerism

Pterin (PT) comprises of two fused heterocyclic 6-membered rings (pyrimidine and pyrazine). The neutral PT group (in folic acid, FA, and HFol^{2-}) can exist in different tautomeric forms while the anionic PT (in Fol^{3-}), in different mesomeric forms (**Figure A.1**).

a) Folic acid



b) Neutral PT



c) Anionic PT

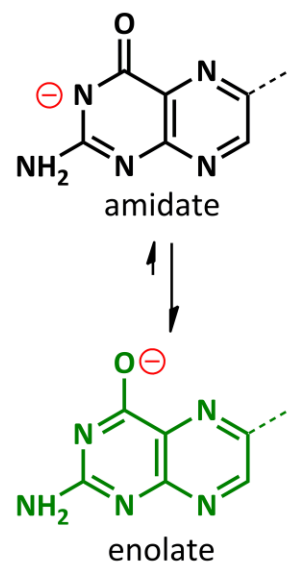


Figure A.1. a) Molecular structure of FA; b) Tautomeric equilibrium of neutral PT moiety (in FA and HFol^{2-}): lactim (enol), 1-lactam (keto) and 3-lactam (keto) tautomers; and c) mesomeric resonance structures of anionic PT (in Fol^{3-}): amidate and enolate mesomers. Highlighted in green are the most stable tautomeric and mesomeric forms of neutral and anionic PT moiety, respectively.

FA (**Figure A.1a**) are usually represented in literature both as 1- or 3-lactam (keto) [1–4] and lactim (enol) [3,5–7] tautomeric forms. As represented in **Figure A.1b**, neutral PT may exhibit a keto-enol equilibrium between C(4)=O and N(3)-H groups, and further, the keto form can present two different tautomeric species, comprising the proton bonded to N(3) or N(1) atom. To the best of our knowledge, no data were recorded for tautomeric equilibrium constants of FA or PT. However, different DFT studies of pyrimidinone derivatives (including HFol²⁻ and 6-methyl-pterin in the simulated aqueous environment) showed that the thermodynamic stability of tautomers in water follows the order: 3-Lactam > 1-Lactam > Lactim [4,8–10]. In addition, theoretical calculations of pyrimidinone derivatives, as guanine and inosine, predicted that the content of 3-Lactam tautomer in water corresponds to almost 100% of the species [9,11].

According to Gocheva et al. [4], by means of theoretical (applying DFT and PCM) and experimental ¹³C-NMR results for HFol²⁻, the 3-Lactam and 1-Lactam forms could be present in water in a dynamic equilibrium, but the former is theoretically predicted to be the predominant and the most stable tautomer species independent of the conformer. No experimental evidence of the enol form presence was observed, as also noticed in previous works about 4-pyrimidinone (vibrational IR spectral analysis) [12] and inosine (IR and Raman analysis) [11]. In the case of anionic PT moiety, DFT calculations by the water solvation model indicated that the enolate ion (**Figure A.1c**) is the most stable mesomeric form [10,13]. Furthermore, the deprotonation of PT group can lead to an increase in the pyrimidine ring aromaticity [10].

In the solid state, the tautomeric predominance of pyrimidinone derivatives is also experimentally observed to be the 3-Lactam form [8]. In fact, crystallographic data of FA dihydrate crystal establish the molecule being in the 3-Lactam form [14–16]. Furthermore, crystallographic data of anionic PT coordinated to rhenium(I) support the presence of enolate

anion species complexed to the metal [17]. Taken in account chemical concepts and the literature data [4,8,10–18], the interpretation of the results in this work considered the 3-Lactam as the most representative tautomer for FA and Na₂HFol, and the enolate anion as the mesomeric form for Na₃Fol.

2. Crystal structure of FA dihydrate

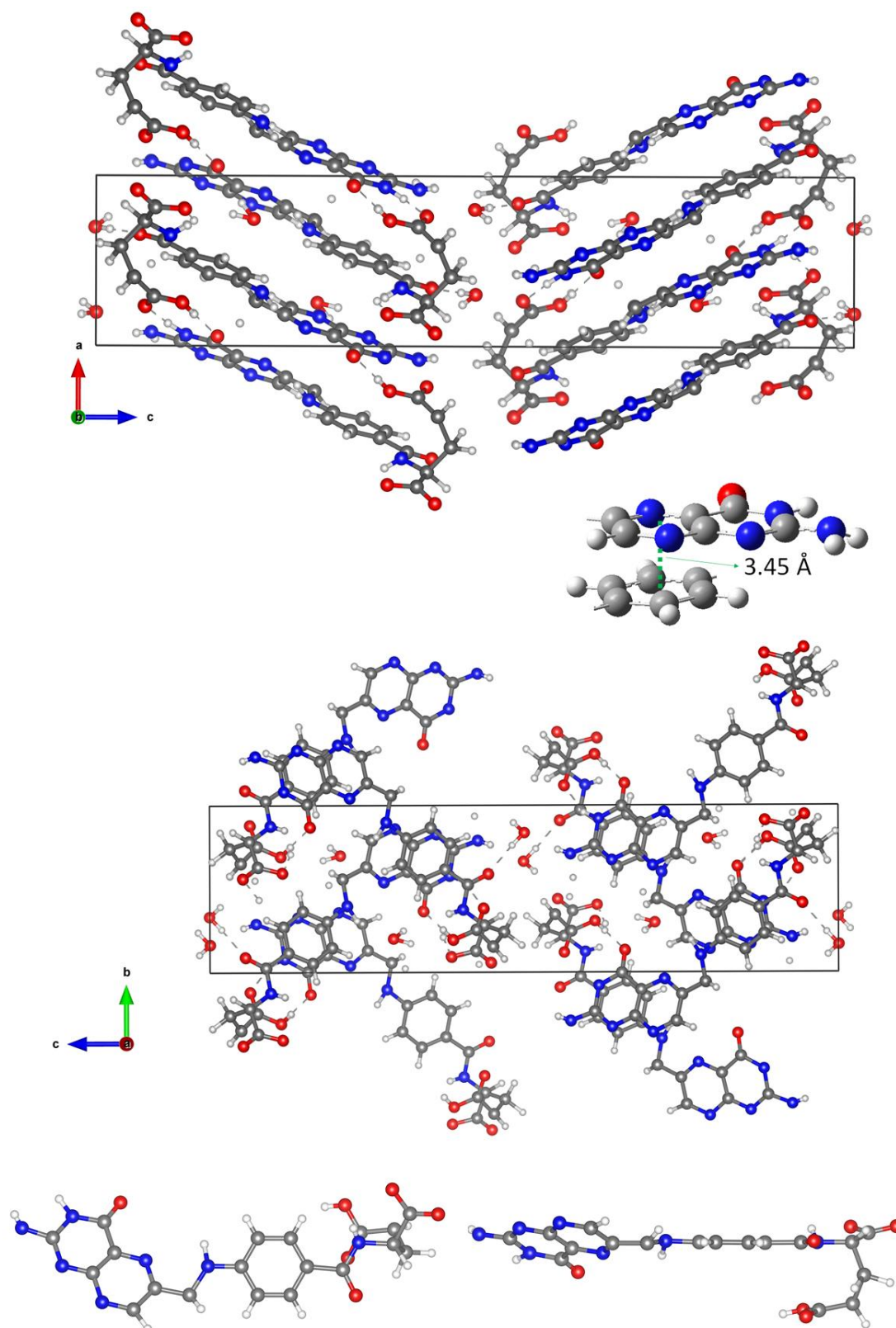


Figure A.2. Crystal structure of FA dihydrate viewed from the *b*-axis (top) and *a*-axis (middle); and its molecular conformation (down). Color of the atoms: carbon in grey; hydrogen in white; oxygen in red; and nitrogen in blue. The figure was drawn by using VESTA[19] software and the CIF obtained from the Cambridge Crystallographic Data Centre (CCDC N 1489544) provided by reference [15].

3. FA self-assembly

To the best of our knowledge, the crystal structures of Na_2HFol and Na_3Fol are not reported in the literature. On the other hand, the structure of FA and derivatives are studied in solution, and they can form supramolecular structures afforded by H-bonds and π - π interaction [20–24]. The molecular arrangement can be tuned on different structures as ribbon- and disk-like, according to the supramolecular agent concentration, the solvent, and pH value of the media [20–24]. In water, the most expected supramolecular structure for dianionic folate (HFol^{2-}) is the disk-type arrays of folate tetramers [20–22], as represented in **Figure A.3**.

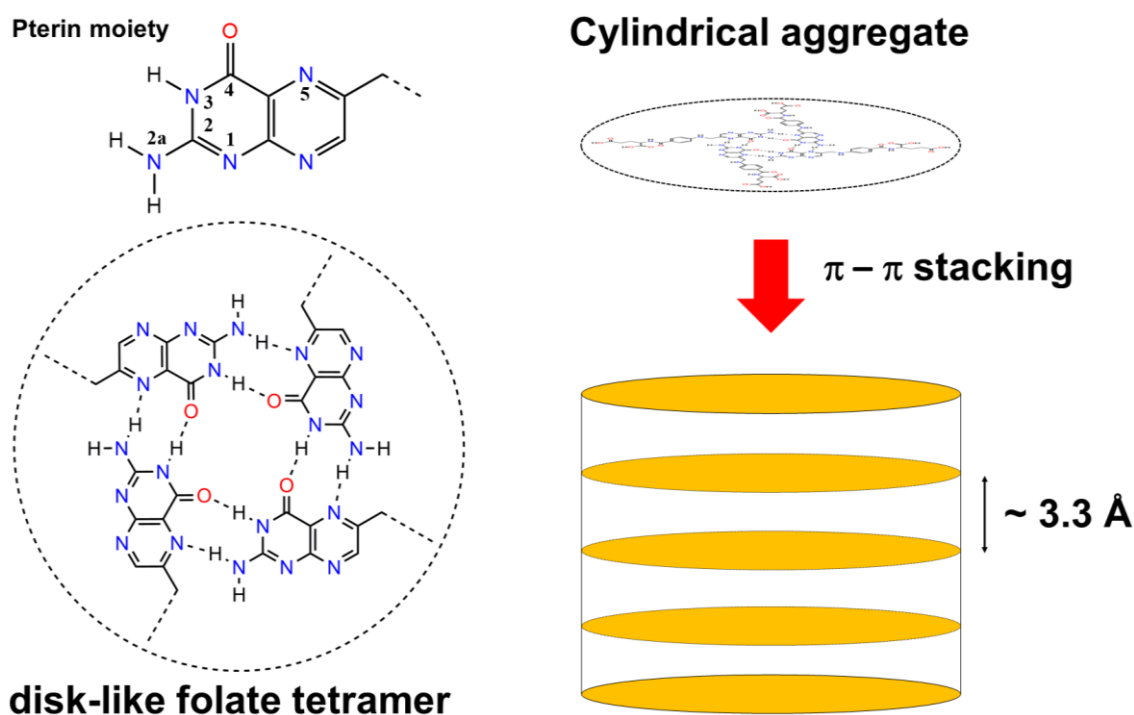


Figure A.3. Scheme of self-assembly of dianionic folate ions in water leading to the formation of disk-like tetramers (left) and π - π stacking of discotic tetramers forming columns (right). Adapted from works of Spada and co-workers [20–22].

According to Spada and co-workers [20–22], the self-assembly into disk-like tetramers occurs through intermolecular hydrogen bonds involving N(3)-H \cdots O=C(4) and N(2a)-H \cdots N(5) groups of PT moiety, and the discoid tetramers pile up by π - π stacking forming columns [20–22]. The distance between the disks in the column is in the range of 0.33-0.35 nm [20–22,25], and thus, it is reasonable to attribute the diffraction peak at 27.10° (*ca.* 0.33 nm) in the XRD of Na₂HFol sample (see the main text; **Figure 2**) to the distance between the disk-like tetramers.

4. Electronic UV-VIS spectra of FA revisited

Aiming to evaluate the electronic absorption spectra of monomeric anionic species of deprotonated FA in water, a titration in the pH values from 4.32 to 9.96 was performed, and the solution was analyzed by UV-VIS spectroscopy (**Figure A.4**).

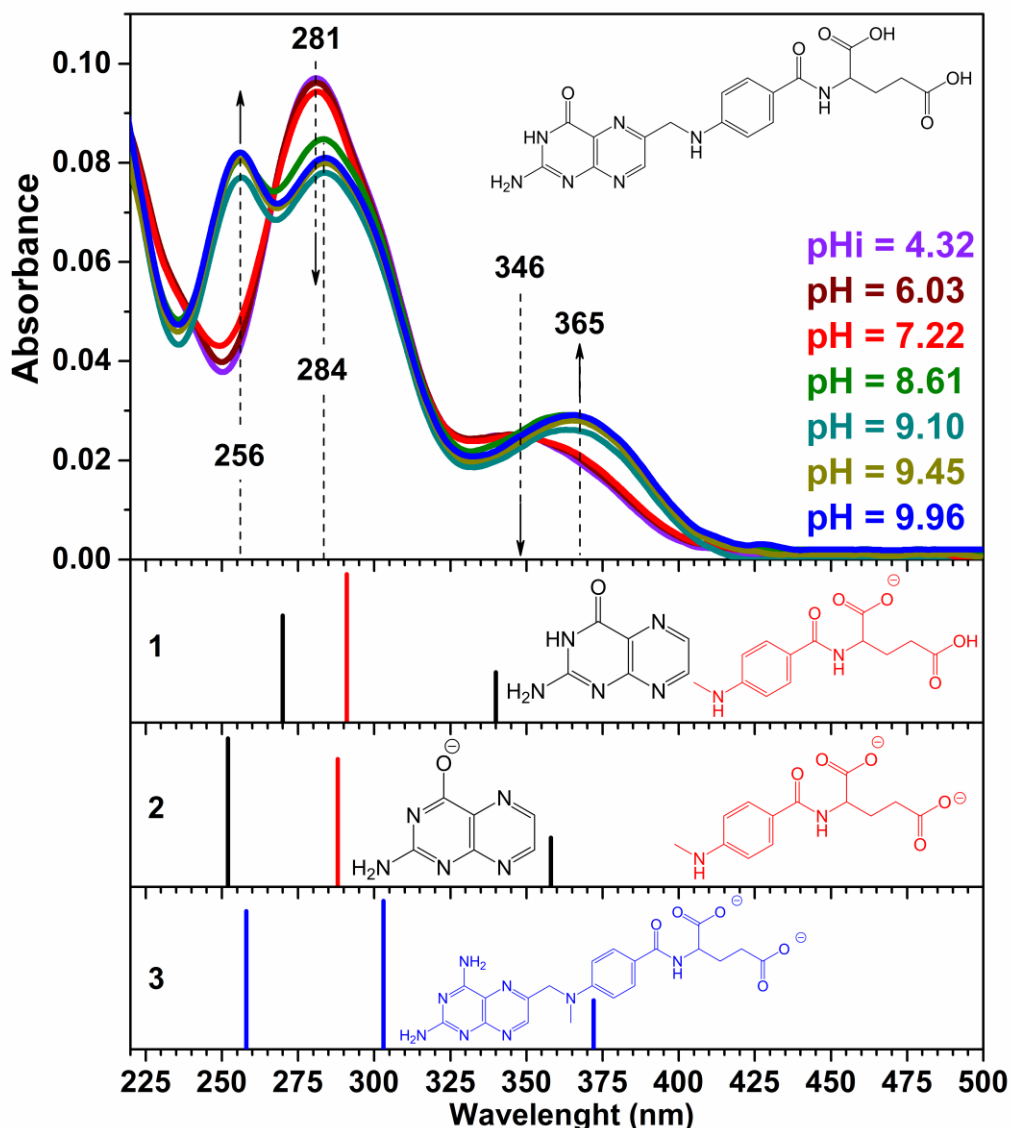


Figure A. 4. Experimental electronic UV-VIS spectra of FA titrated with sodium hydroxide (0.1 mol L^{-1}) in aqueous media. pH value was ranged from 4.32 to 9.96, and pHi indicates the initial value after the dissolution of FA. On the bottom, the titration results are compared with the wavelength of maximum absorption (λ_{abs}) of some anions of FA moieties. **1** and **2**: λ_{abs} values of neutral and anionic PT (in black) according to Wolcan [26]; and empirically estimated λ_{abs} values for monovalent and divalent *p*-methylaminobenzoyl-L-glutamic acid (in red), based on experimental results from Off et al. [27] and Szakács and Noszál [28] for *p*-ABA-Glu; **3** for comparison purposes: the λ_{abs} values of methotrexate (MTX, in blue), according to Ayyappan et al. [29].

According to FA speciation (**Figure 1** in the main text), the species varied mainly from $\text{H}_2\text{Fol}^{1-}$ (pHi = 4.32) to HFol^{2-} (pH = 6.03-7.22) and Fol^{3-} (pH = 8.61-9.96). The electronic spectra of $\text{H}_2\text{Fol}^{1-}$ and HFol^{2-} present almost the same profile with main bands centered at about 280 nm and 346 nm. Moreover, the UV-VIS spectra of such species are closely similar to that of FA in DMSO recorded in the literature [30]. Glu moiety presents no absorption in the analyzed UV-VIS region [31], and its deprotonation does not influence in the electronic absorption profile. Therefore, it is difficult to differentiate $\text{H}_2\text{Fol}^{1-}$ and HFol^{2-} species in water by ordinary UV-VIS analysis. Alternately, the electronic spectrum of Fol^{3-} presents a different profile with bands centered at 256 nm, 284 nm, and 365 nm.

The spectra of anions from FA are similar to the sum of the spectra of *p*-ABA-Glu [27,28] and PT [26] recorded in the literature (**Figure A.4**). The UV-VIS electronic spectrum of *p*-ABA-Glu presents a band in the region of 275 nm regardless if the species is neutral, monoanionic or dianionic [27,28]. Consequently, it is not expected a huge change of related electronic transition bands with the increasing of the pH values. Besides, applying empirical rules considering the $-\text{NH}(\text{CH}_3)$ group instead of $-\text{NH}_2$ in the *para* position, such band is estimated to be located in the 290 nm region [32]. On the other hand, the UV-VIS electronic spectrum of PT changes according to the pH value of the media. The neutral form presents absorption bands at 270 nm and 340 nm whereas, for the deprotonated PT, the higher-energy band is blue shifted to 252 nm and the lower-energy band is redshifted to 358 nm [26]. Considering such information, the electronic transition bands were attributed (**Figure A.4**):

- (I) **$\text{H}_2\text{Fol}^{1-}$ and HFol^{2-}** : the band at 280 nm is attributed to the $\pi-\pi^*$ electronic transition of both *p*-ABA-Glu [33–35] and PT moieties [26,36]. The band at 346 nm is assigned to $\pi-\pi^*$ and $n-\pi^*$ electronic transition of PT group [26,36].
- (II) **Fol^{3-}** : the band at 256 nm is attributed to the $\pi-\pi^*$ of deprotonated PT group in Fol^{3-} species [26,35–37]. The band at 280 nm is slightly redshifted to 284 nm and is

attributed to the $\pi-\pi^*$ electronic transition of *p*-ABA-Glu [33–35], while the band at 365 nm is attributed to $\pi-\pi^*$ and $n-\pi^*$ of PT group [26,36,37]. In addition, the UV-VIS spectrum of Fol^{3-} is similar to that of antifolate methotrexate (MTX) [29]. Such electronic behavior may be attributed to the naphthalenoid structure, which agrees with the enolate mesomer form as the most stable for Fol^{3-} (see **Figure A.1**).

5. Thermal Analysis (TG/DTG-DSC) coupled to mass spectrometry (MS) under N₂ atmosphere

According to Vora et al. [38], FA does not present an apparent temperature of melting point because the sample seems to melt and decompose in three overlapped steps around 250°C. On the other hand, the supplier indicates that the melting of FA occurs above 250 °C and the literature states that FA decomposes (darkens followed by charring) at this temperature [39,40]. The decomposition temperature of FA, Na₂HFol and Na₃Fol in N₂ atmosphere were respectively estimated at 200 °C, 270 °C and 300 °C, when considering the beginning of releasing of fragment $m/z = 44$ assigned to CO₂ (MS curve; **Figure A.5a**). The events coincide with endothermic peaks in DSC curves centered respectively at 210 °C, 296 °C and 338 °C that could indicate a phase transition. However, analyzing the samples in a melting point apparatus, instead of melt, it was only visually the darkening of samples (see pictures in **Figure A.5b**) starting around 210 °C, 280°C and 300°C, respectively. In addition, the sample becomes soaked after such change of color, which can indicate the formation of volatile products during the decomposition, in consonance with the endothermic peaks in the DSC curve (**Figure A.5b**). Based on the literature, it is proposed that some of such volatile products are 2-pyrrolidone and aniline from the decomposition of Glu [41] and *p*-ABA [42] moieties, respectively. With the temperature increasing, samples became black, indicating a charring.

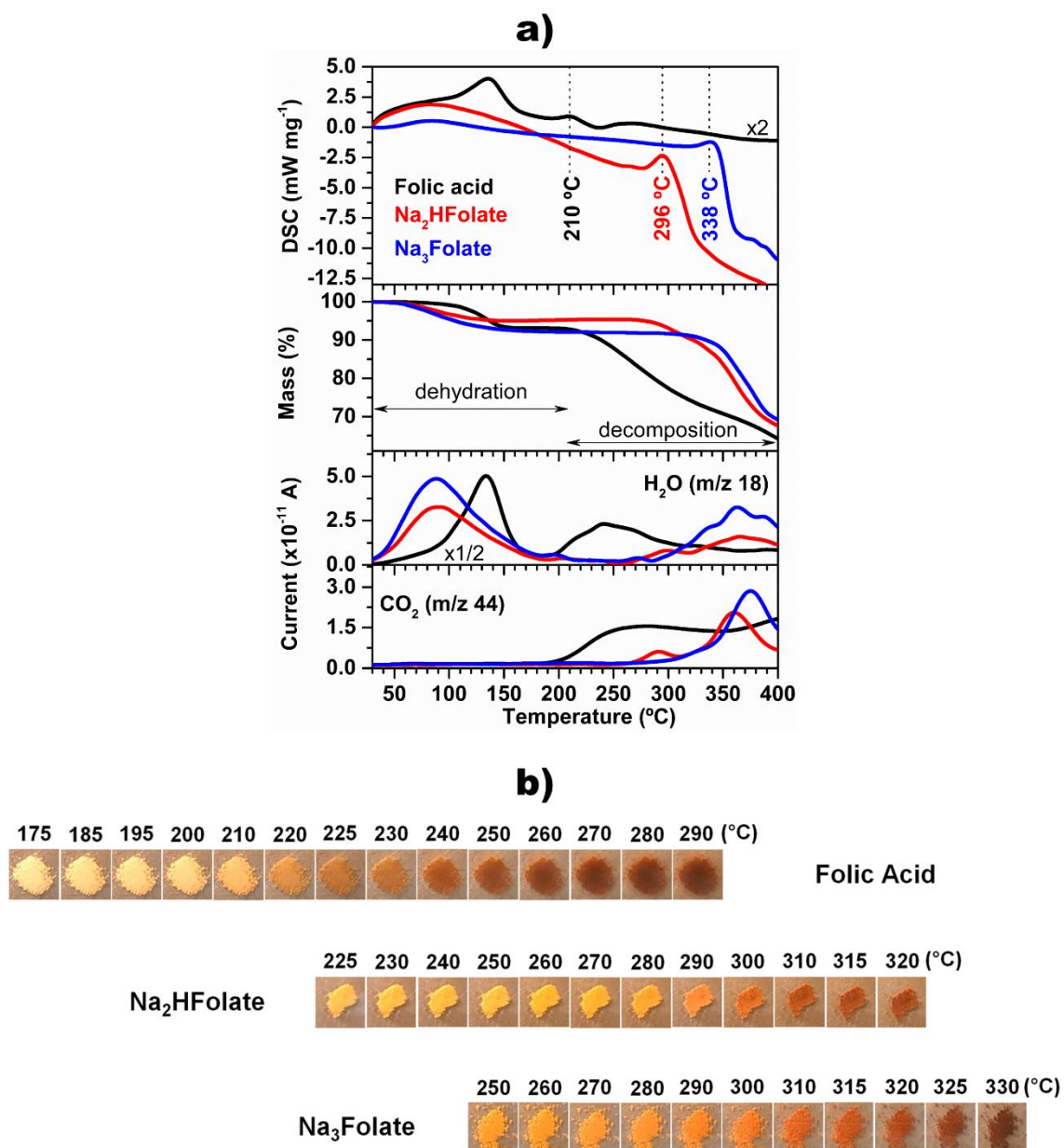
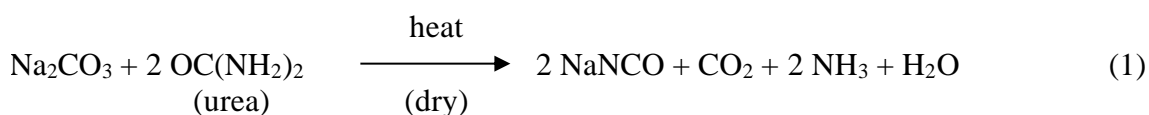


Figure A.5. a) DSC-TG-MS curves of FA and folate sodium salts in N₂ atmosphere. Dashed lines indicate the DSC temperature values; b) pictures of transformations visualized when submitting FA and its salts to heating under ambient atmosphere and pressure in the heating block of the melting point apparatus.

6. Thermal Analysis (TG/DTG-DSC) coupled to mass spectrometry (MS) under air atmosphere

Carbonized matter can be generated in the process of thermal oxidation of organic molecules and sodium salts [42,43]. The exothermic peak around 720 °C on the DSC curve of FA sample (see **Figure 4a** in the main text) can indicate the oxidation of carbonaceous residue (exp. 2.1%). The small weight loss events around 530-740 °C, observed in the analysis of salts, are associated with the release of different gaseous products (detected by MS, **Figure 4b** in the main text). For Na₂HFol, only the release of CO₂ could be observed in the event occurring in the 528-700 °C range. On the other hand, for Na₃Fol, the event around 547-740 °C releases NO, NO₂ and CO₂.

The thermal oxidation of glutamate moiety in both salts sample can initially conduct to the formation of Na₂C₂O₄ and/or Na₂CO₃, followed by the conversion of Na₂C₂O₄ to Na₂CO₃ at around 500 °C, as observed for alkali metal formates [44]. Sodium cyanate can be also generated either by a reaction between Na₂CO₃ and an amidic group (as exemplified in **Equation 1** [45]) or by the decomposition of anionic PT having sodium as the counter ion.



The proposal of NaNCO formation is supported by the presence of endothermic peak at 538 °C followed by an exothermic event around 670 °C in DSC curves (**Figure 4** of the main text) that are attributed to the melting point and decomposition of NaNCO, respectively. The interpretation was made in light of the work of Dong et al. [46]. The authors reported that for pure NaNCO, the melting process occurs at 537/563°C and the decomposition into Na₂CO₃ is observed in the range of 550-750 °C (T_{onset} on TG at 627°C) with an exothermic peak at 683°C. Residual mass at 800 °C is consistent with Na₂CO₃ (melting point 851 °C, endothermic peak in DSC curve, **Figure 4a** in the main text), which is decomposed into Na₂O above 860°C (incomplete at 1000 °C) [46].

Table A.1Thermal analysis data of FA, Na₂HFol and Na₃Fol samples under air atmosphere.

Sample ^a	event ^b	step	Temp. range (°C) ^c	Tp (°C) ^{d#}	%wt. loss ^e
C₁₉H₁₉N₇O₆·2.1H₂O	dhyd.	1 st	30-172	121	7.9 (7.5)
Folic acid	(I)	2 nd	198-292	252	12.5
	(II)	3 rd	292-391	362	15.0
	(III)	4 th ; 5 th ; 6 th	391-528	421; 466; 532(sh)	25.6
	(IV)	7 th ; 8 th ;	528-707	567; 656sh;	38.6
	(V)	9 th	707-740	704(sh); (718)	2.1
Na₂C₁₉H₁₇N₇O₆·2.3H₂O	dhyd.	1 st	30-200	85	7.6 (8.5)
Na₂HFol	(I)	2 nd	267-323	315	7.8 (7.7)
	(II)	3 rd	323-383	350	15.8
	(III)	4 th ; 5 th	383-528	402(sh); 447	43.0
	(IV)	6 th	528-700	636;(538; ~ 670)	3.5
Na₃C₁₉H₁₆N₇O₆·2.8H₂O	dhyd.	1 st	30-205	86	9.0 (9.6)
Na₃Fol	(I)	2 nd	300-394	358	20.8
	(II)	3 rd	394-547	463; (~ 538)	36.6
	(III)	4 th	547-752	651; (670)	3.2

^aFormula proposed from thermal analysis results; ^bdhyd.: dehydration step; I-IV: events regarding the organic matter decomposition; ^cValues from TG/DTG-MS data; ^dValues from DTG and DSC curves; ^eValues in parenthesis are the expected percentage of water considering the proposed formulas. [#]Tp: temperature of DTG peak; (sh): shoulder

7. Structural simulation of FA, Na₂Fol and Na₃Fol by DFT

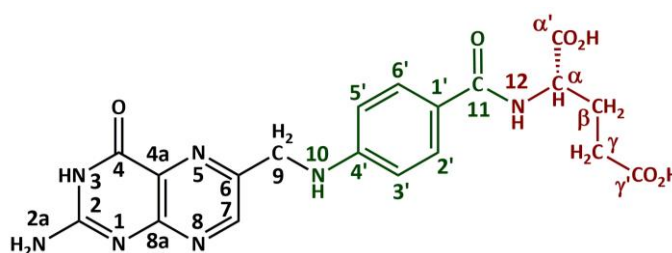


Table A.2

Bond Lengths (Å) and Bond Angles (deg) for the Most Stable Conformations of FA, Na₂HFol and Na₃Fol calculated at the B3LYP/6-311++G(d,p) Level of Theory.

Parameter*	Folic Acid		Na ₂ HFol	Na ₃ Fol	
	Calculated	Exp. ^a	Calculated	Calculated	Exp. ^b
Bond lengths (Å)					
C γ '-O γ '	1.206	1.243	1.271	1.271	
C γ '-O(H) γ '	1.358	1.346	1.270	1.270	
C γ -C γ '	1.509	1.461	1.525	1.525	
C α '-O α '	1.207	1.224	1.272	1.272	
C α '-O(H) α '	1.351	1.299	1.264	1.264	
C α -C α '	1.519	1.519	1.534	1.534	
C α -N12	1.450	1.478	1.457	1.457	
C11-N12	1.372	1.345	1.360	1.362	
C11-O11	1.229	1.229	1.230	1.231	
C1'-C11	1.490	1.526	1.501	1.499	
C4'-N10	1.373	1.419	1.381	1.377	
C9-N10	1.438	1.458	1.438	1.440	
C4-O4	1.211	1.208	1.211	1.258	1.284
C4-N3	1.408	1.391	1.409	1.367	1.327
C2-N3	1.377	1.393	1.376	1.357	1.368
C2-N2a	1.367	1.385	1.369	1.380	1.328
C4-C4a	1.475	1.459	1.475	1.465	1.436
C4a-C8a	1.414	1.412	1.414	1.418	1.404
N1-C2	1.299	1.324	1.298	1.320	1.335
N1-C8a	1.370	1.345	1.371	1.355	1.349
Na \cdots O γ '			2.203	2.202	
Na \cdots O(H) γ '			2.198	2.197	
Na \cdots O α '			2.214	2.213	
Na \cdots O(H) α '			2.209	2.207	
Na \cdots O(4)				2.187	
Na \cdots N(3)				2.305	
O(4)---Re(I)					2.162

Table A.2*Continued...*

Parameter*	Folic Acid		Na ₂ HFol	Na ₃ Fol	
	Calculated	Exp. ^a	Calculated	Calculated	Exp. ^b
Bond Angles (°)					
Oγ'-Cγ'-O(H)γ'	122.26	122.65	122.97	122.95	
Cγ-Cγ'-Oγ'	126.44	123.53	119.08	119.14	
Cγ-Cγ'-O(H)γ'	111.29	113.95	117.94	117.91	
Oα'-Cα'-O(H)α'	122.56	122.45	123.41	123.36	
Cα-Cα'-Oα'	125.15	119.16	118.40	118.48	
Cα-Cα'-O(H)α'	112.28	117.35	118.18	118.14	
Cβ-Cγ-Cγ'	112.64	112.24	114.04	114.10	
Cα-Cβ-Cγ	114.03	116.35	114.30	114.32	
Cα'-Cα-Cβ	112.06	106.24	111.41	111.46	
N12-Cα-Cβ	111.63	110.15	111.18	111.18	
N12-Cα-Cα'	107.62	115.15	108.40	108.55	
C11-N12-Cα	120.35	118.04	122.65	122.48	
O11-C11-N12	116.99	122.94	122.27	122.09	
C1'-C11-N12	120.67	115.44	116.41	116.45	
C1'-C11-O11	122.34	121.64	121.31	121.47	
C2'-C1'-C11	124.34	124.80	124.26	124.24	
C6'-C1'-C11	117.81	115.19	117.94	118.04	
C9-N10-C4'	124.21	121.74	123.20	123.70	
C6-C9-N10	110.78	111.74	110.98	110.54	
C7-C6-C9	120.98	120.54	120.87	120.93	
N5-C6-C9	118.88	117.84	119.02	118.81	
N3-C4-C4a	111.79	112.75	111.80	117.16	120.14
N3-C4-O4	120.66	121.55	120.56	119.78	
O4-C4-C4a	127.55	125.74	127.63	123.06	
C2-N3-C4	124.36	123.44	124.37	118.81	116.64
C4-C4a-C8a	119.42	119.52	119.38	117.74	118.54
C4-C4a-N5	118.34	117.28	118.34	120.07	118.74
N5-C4a-C8a	122.24	123.20	122.28	122.19	122.84
N1-C2-N3	123.81	123.74	123.82	127.97	127.44
N2a-C2-N3	116.45	114.84	116.39	115.63	115.74
N2a-C2-N1	119.71	121.54	119.75	116.37	116.94

*The hydrogen atoms in parentheses are just specifying the related oxygen atom; ^a data from reference [15]; ^b data from reference regarding to a Re(I) complex [17].

8. IR and Raman vibrational spectroscopies

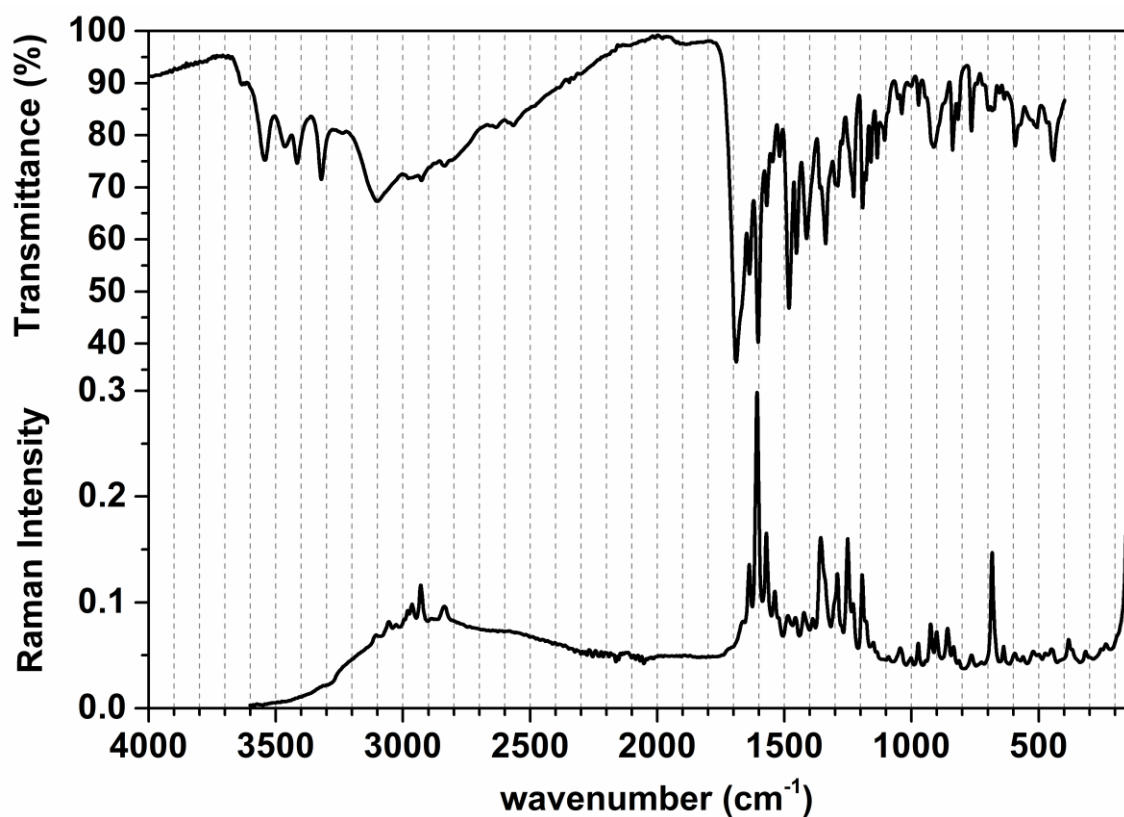


Figure A.6. Experimental infrared (top) and Raman (bottom) spectra of commercial dihydrate FA.

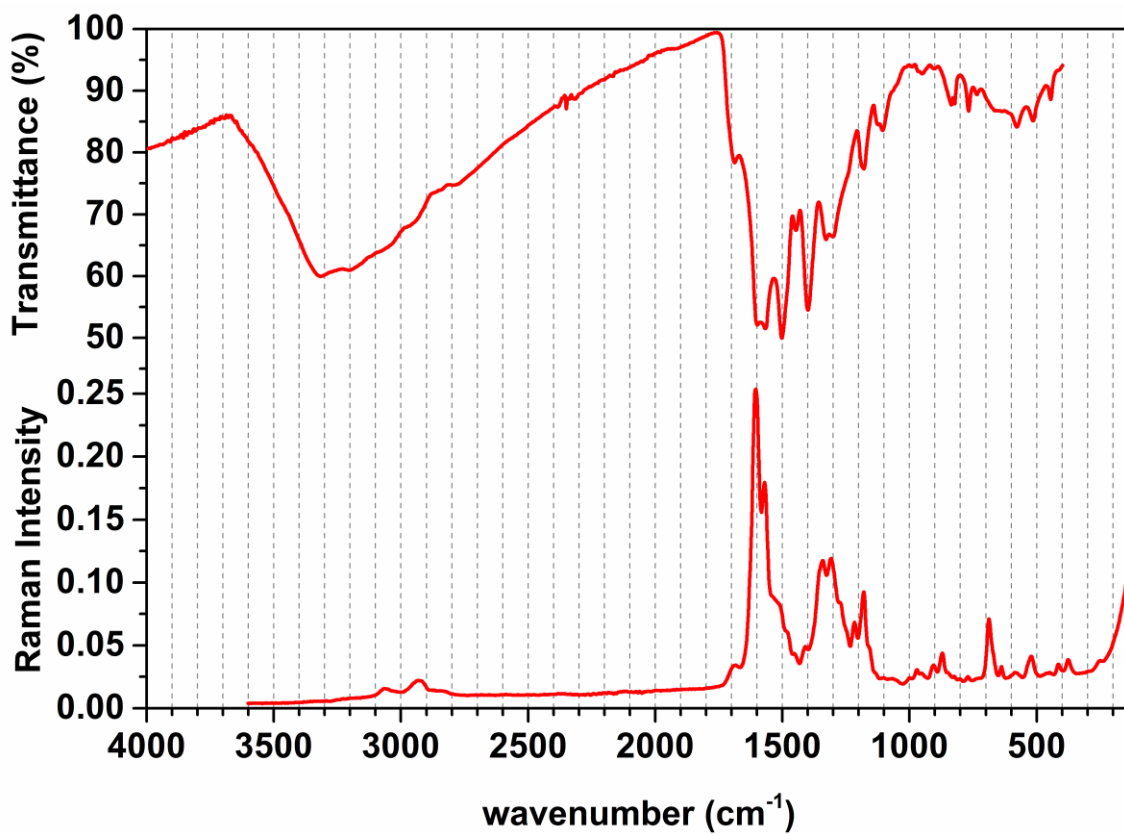


Figure A.7. Experimental infrared (top) and Raman (bottom) spectra of Na₂HFoI.

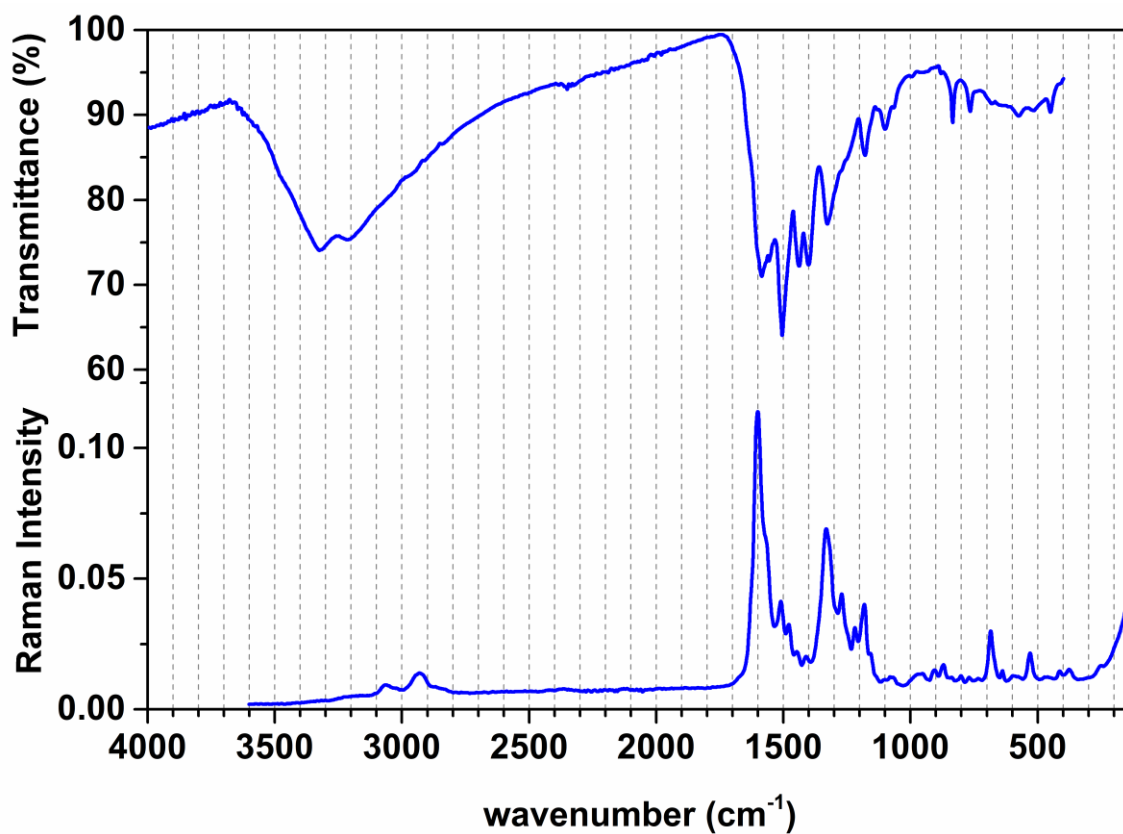


Figure A.8. Experimental infrared (top) and Raman (bottom) spectra of Na₃FoI.

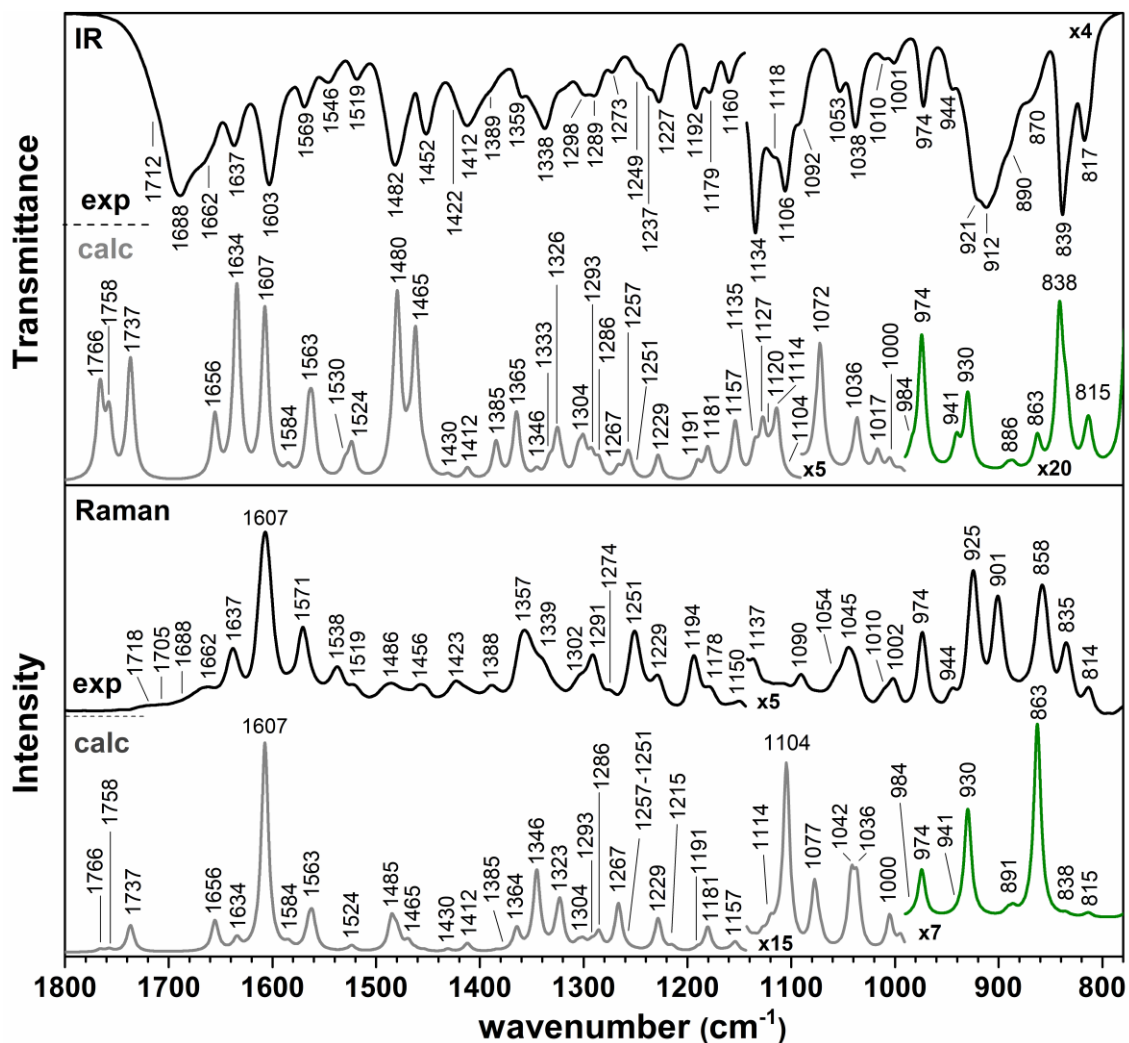


Figure A.9. Experimental (exp) and DFT calculated (calc) infrared (IR) and Raman spectra of FA. The DFT spectra are shown applying a 0.975 correction factor (in grey color) and unscaled (in green color).

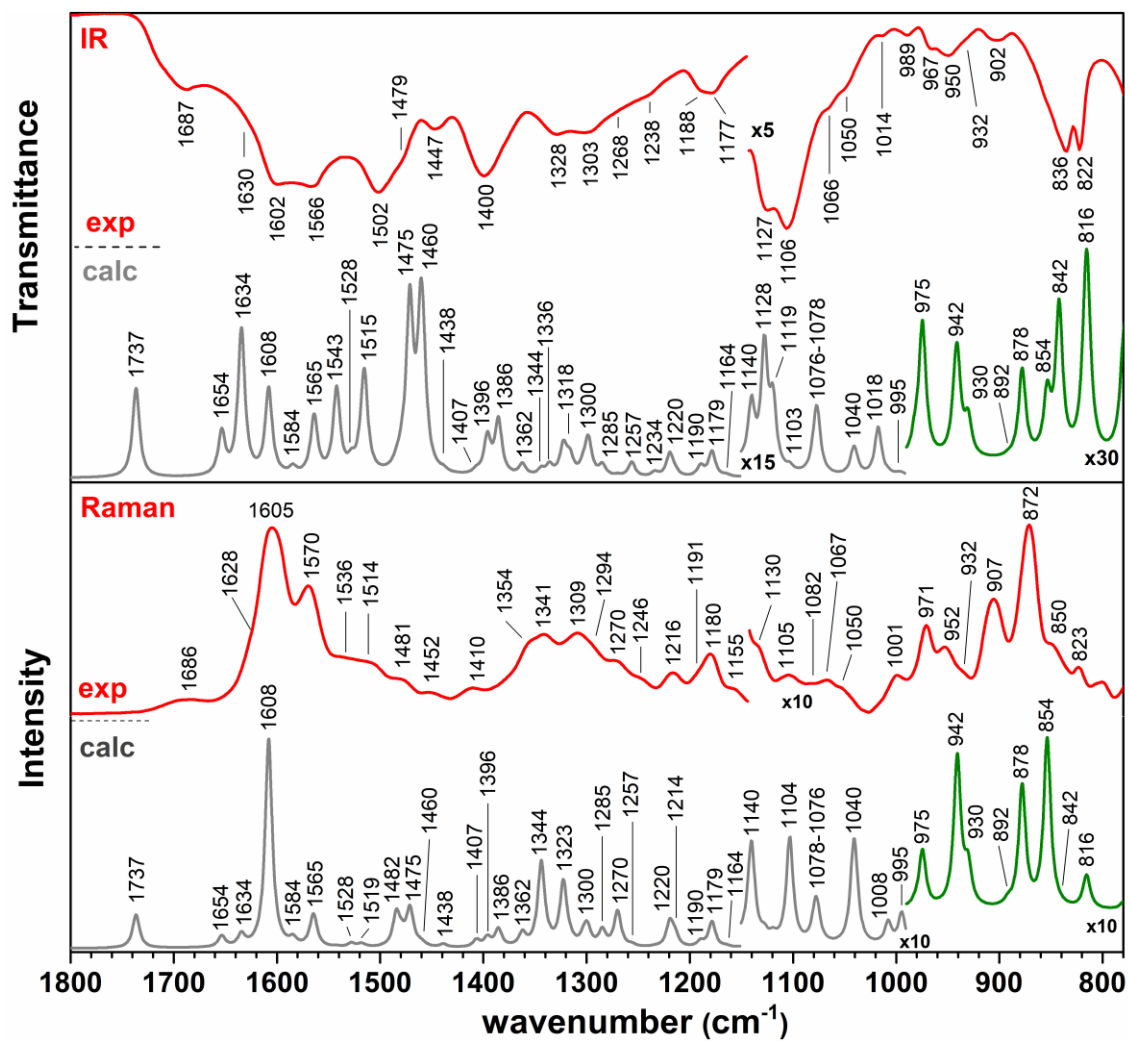


Figure A.10. Experimental (exp) and DFT calculated (calc) infrared (IR) and Raman spectra of Na_2HFol . The DFT spectra are shown applying a 0.975 correction factor (in grey color) and unscaled (in green color).

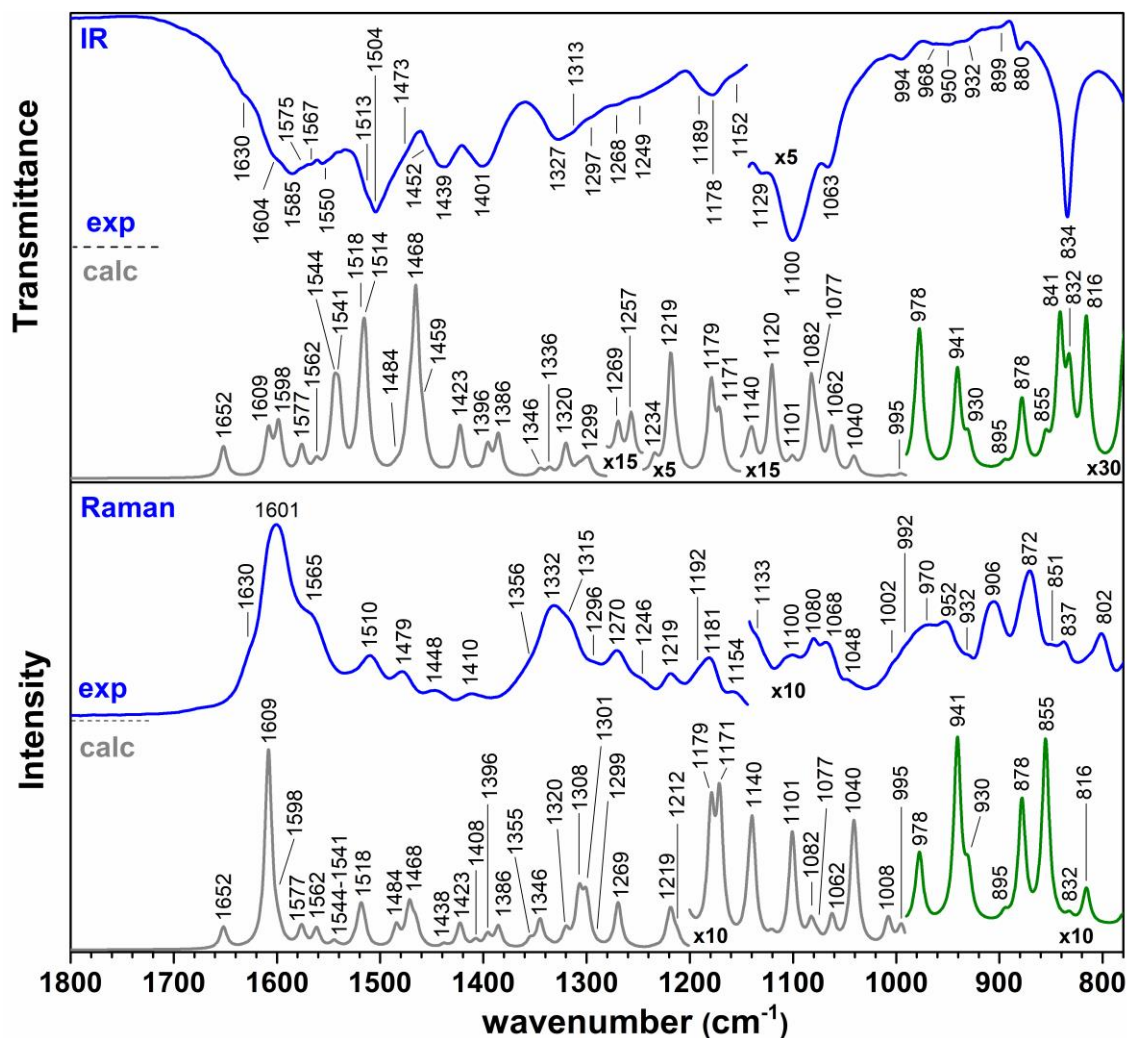


Figure A.11. Experimental (exp) and DFT calculated (calc) infrared (IR) and Raman spectra of Na_3Fol . The DFT spectra are shown applying a 0.975 correction factor (in grey color) and unscaled (in green color).

The assignments of the main bands were displayed in the main text (**Table 2**). Following, some other relevant bands are discussed by regions:

1520-1460 cm^{-1} range. The bands in the range of 1540-1510 cm^{-1} and around 1480 cm^{-1} region have the contribution of C11–N12 stretching (ν) coupled to N12–H bending (δ) (Amide II) and $\nu(\text{C4}'\text{--N10})/\delta(\text{N10--H})$. Such observations agree with literature reported for peptide bonds [47,48] and secondary amines linked to benzene ring [49], respectively. In the 1520-1510 cm^{-1} spectral range, bands are also predicted to have contribution of C-C stretching of phenylene

ring (see the main text; **Table 2**), as it was already observed for *p*-ABA alkaline salts [50] and tyrosine/tyrosinase [51]. Regarding the vibration of CH₂ groups, the DFT calculation reveals a tendency of the frequency values of C^αH₂, C^βH₂, C^γH₂ groups deformations: scissoring (*ca.* 1480-1400 cm⁻¹) > wagging (about 1400-1300 cm⁻¹) > twisting (*ca.* 1300-1050 cm⁻¹) > rocking (below 1050 cm⁻¹).

1400-1240 cm⁻¹ region. The in-plane δ(OH) vibrational modes are predicted in 1400-1340 cm⁻¹ and 1300-1230 cm⁻¹ regions. The bands assigned to C–NH₂ stretching mode are shown at about 1300 cm⁻¹ for FA and Na₂HFol (**Table 2**). The deprotonation of PT ring in the trisodium salt shifts this bands to higher energy region (about 1440-1350 cm⁻¹) even though the calculation predicts that the C–NH₂ bond is weaker (bond length gets longer) in Na₃Fol (**Table A.1**). Such vibration seems to be coupled to PT ring stretching as it is shown by the vectors related to theoretical band at 1423 cm⁻¹ (**Figure A.16**). The vibration is like the antisymmetric stretching of a guanidyl group (C linked to three N).

1270-1110 cm⁻¹ range. The C1'-C11 stretching are expected to occur in the 1270-1230 cm⁻¹ region for FA with a contribution to Amide III mode [52]. These vibrations occur at lower energy for the folates (1220-1215 cm⁻¹), in line with the calculated increasing of this length bond (weaker force) from the protonated FA to its deprotonated form. FA spectrum displays bands of medium intensity around 1230-1180 cm⁻¹ spectral region. The band at 1227 cm⁻¹ is attributed to vibration modes of glutamic acid (Glu) and *p*-ABA units related to OH, CH and CH₂ deformations, in addition to the in-phase combination of the N12H bending and the C11N12 stretching (Amide III) [52], also predicted to occur in the region of 1300 cm⁻¹ and 1270 cm⁻¹. On the other hand, the folates show low intensity bands in the 1230 cm⁻¹ region probably because the FA deprotonation. The C9–N10 stretching is observed in the 1200-1100 cm⁻¹ region. The band around 1190 cm⁻¹ region can be attributed to ν(C9–N10) coupled to C–H bending (*9a*) of phenylene, in agreement with the literature [49,51]. The band at 1179 cm⁻¹ can

be attributed to *p*-ABA and PT groups vibrations modes. According to DFT calculations for FA, bands in the region of 1140-1130 cm^{-1} are assigned to vibrations from all the three moieties of molecule, as: (i) $\nu(\text{PT rings}) + \rho(\text{NH}_2) + \delta(\text{N3H}) + \delta(\text{C7H})$, from PT moiety; (ii) $\nu(\text{C9N10}) + \phi[18\text{b}]/\text{D27} + \nu(\text{C11N12C}\alpha)$, from *p*-ABA moiety; and (iii) $\nu(\text{C-O})_{\text{OH}}$ (also predicted in 1180-1090 cm^{-1} region), from Glu moiety. From FA to salts, changes observed in above-mentioned spectral range are associated to deprotonation of carboxylic groups, and from FA to Na_3Fol , the changes are associated to PT deprotonation.

Bellow 1110 cm^{-1} range. Regarding the C-C stretching of Glu moiety, bands are predicted bellow 1100 cm^{-1} region. Specifically for the C-C stretching of all Glu chain, $\nu(\text{Glu})_{\text{ch}}$, bands are predicted in 1090-1050 cm^{-1} , 950-930 cm^{-1} and 890-830 cm^{-1} regions by DFT calculations. Vibrations related to out-of-plane $\delta(\text{COOH})$ group are envisaged in 1160-1050 cm^{-1} and 920-870 cm^{-1} spectral region. In salts, out-of-plane $\delta(\text{COO}^-)$ and $\nu(\text{C-C})$ vibrational modes are foreseen to be slightly redshifted. Bands in the region of 1090-1080 cm^{-1} are attributed to NH_2 rocking (ρ) and $\nu(\text{PT rings})$. ρNH_2 is also predicted to contribute with bands in 1140-1100 cm^{-1} , 1000-970 cm^{-1} and 870 cm^{-1} spectral regions.

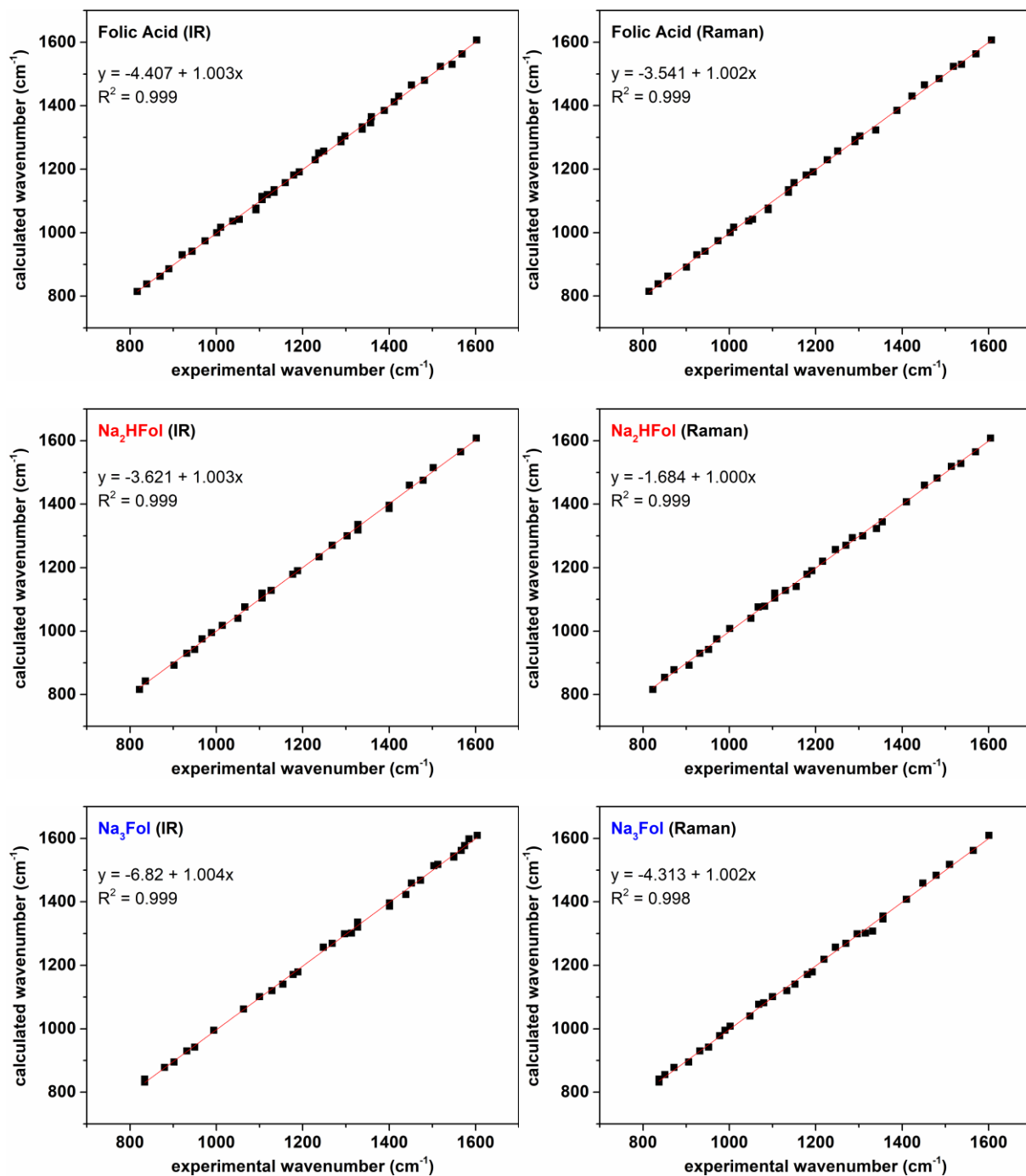


Figure A.12. Correlation between experimental and calculated (DFT method) wavenumber from IR and Raman spectra of FA, Na₂HFol and Na₃Fol, excluding the bands above 1610 cm⁻¹.

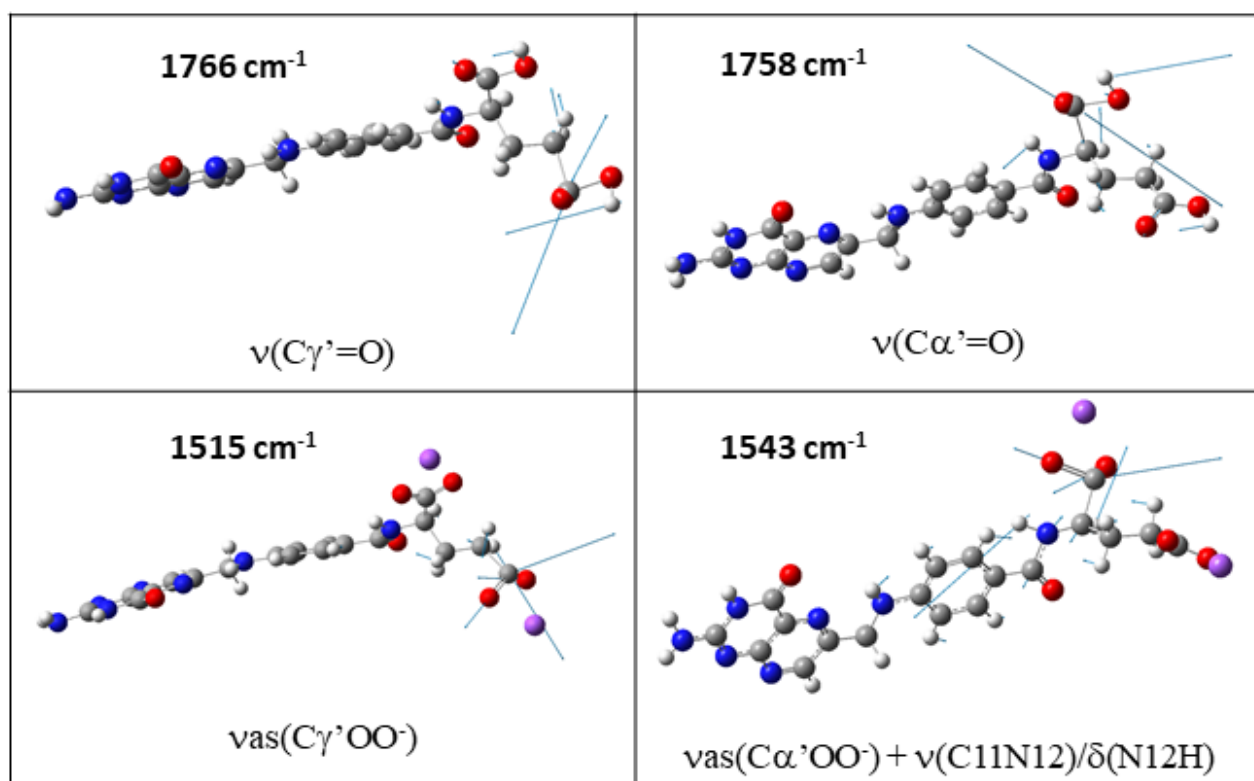


Figure A.13. Some vibrational modes for FA and Na₂HFol obtained by DFT calculations.

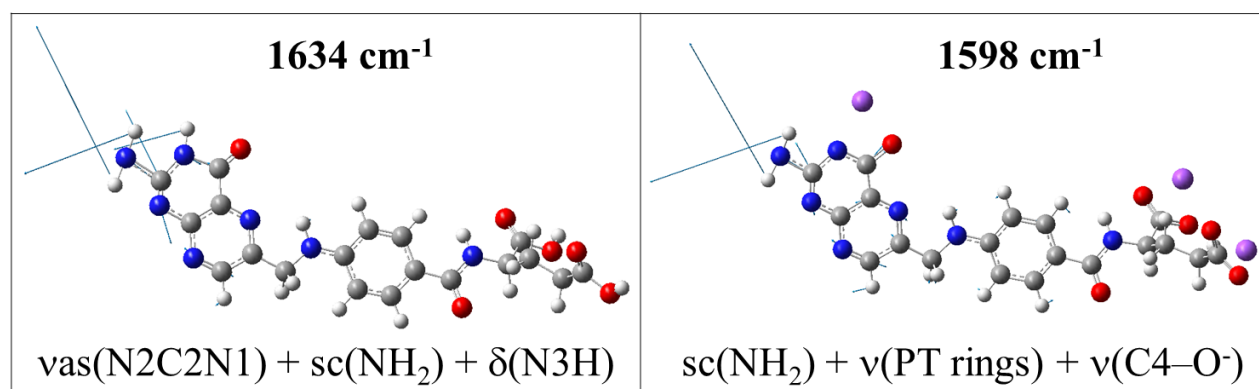


Figure A.14. Some vibrational modes for FA and Na₃Fol obtained by DFT calculations.

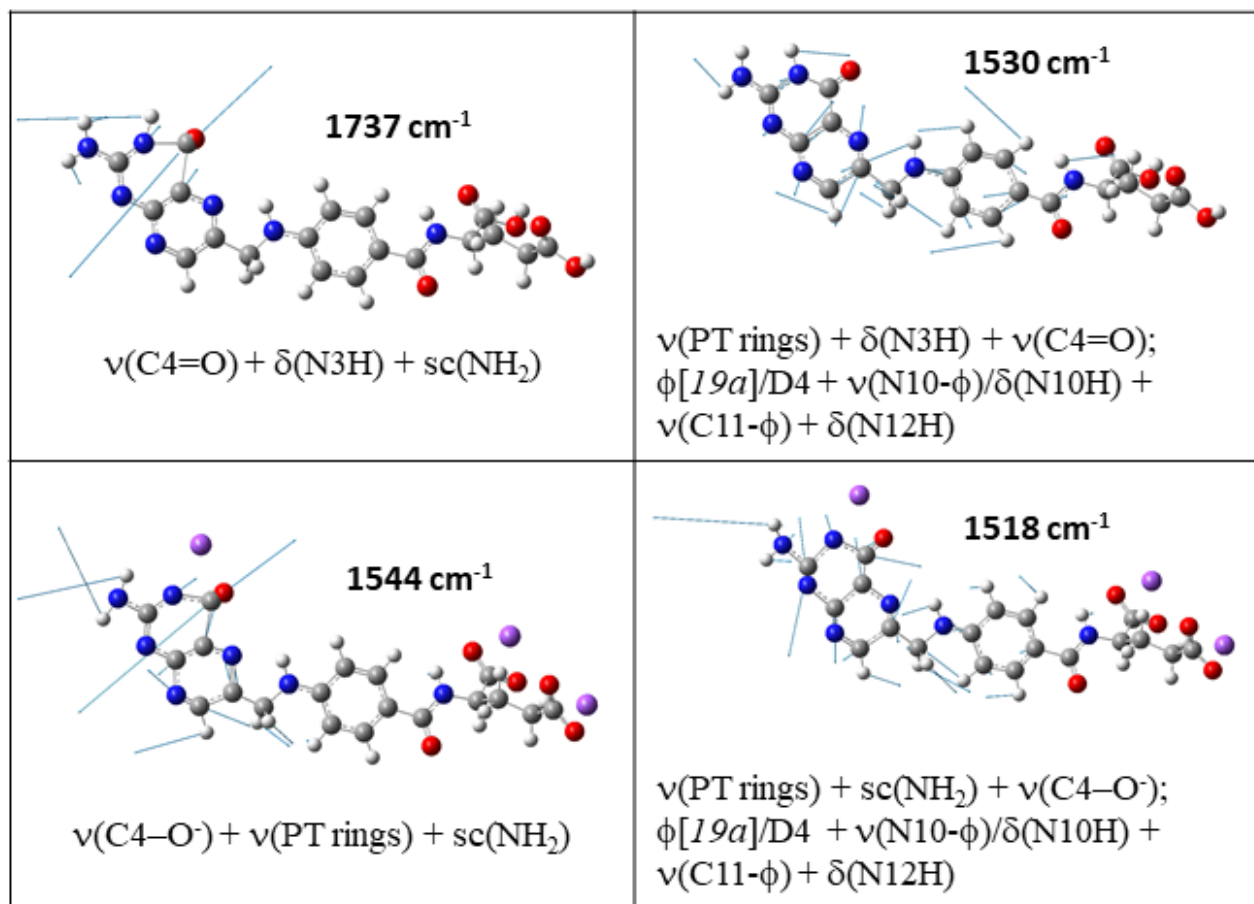


Figure A.15. Some vibrational modes for FA and Na₃Fol obtained by DFT calculations.

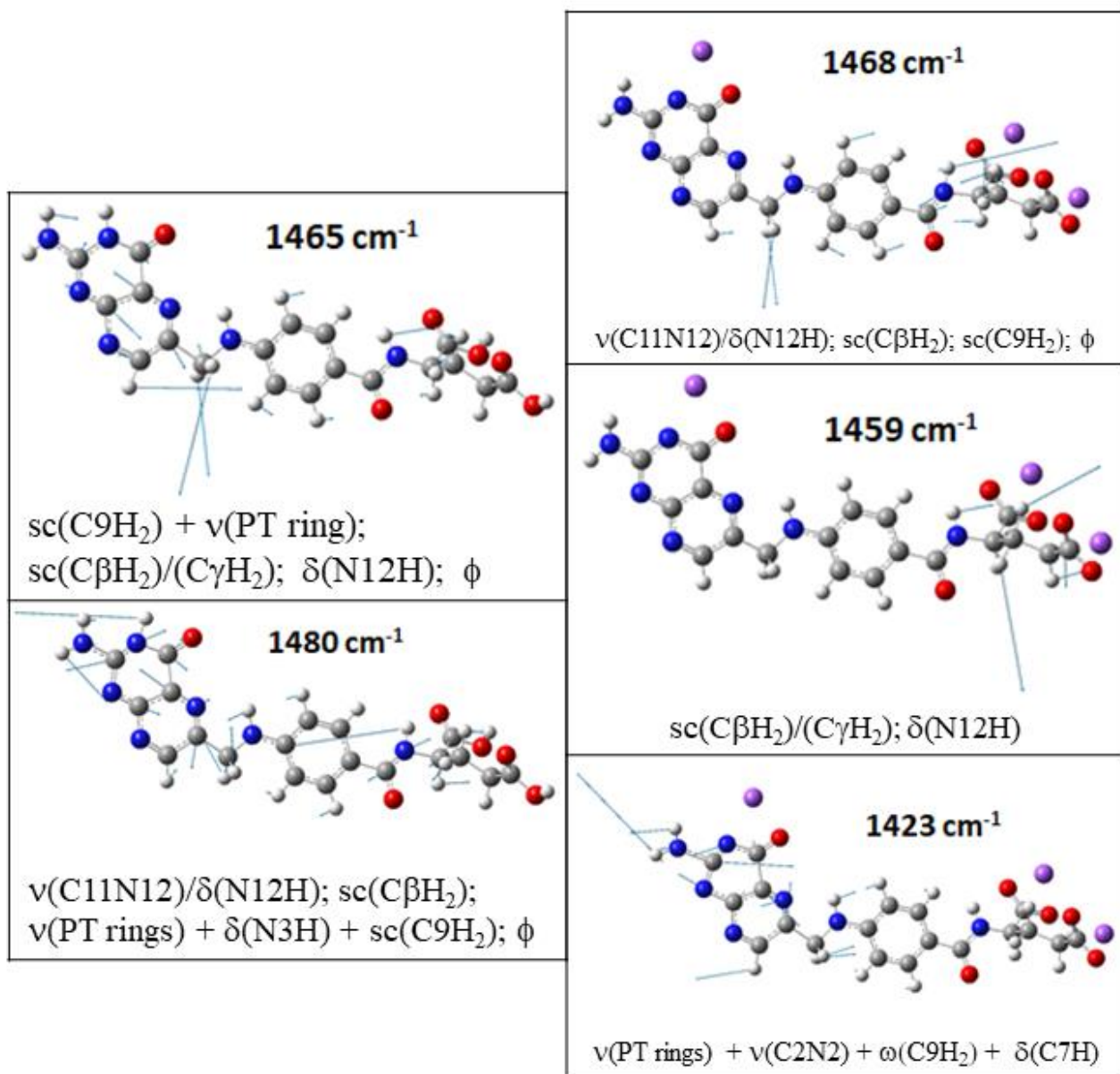


Figure A.16. Some vibrational modes for FA and Na₃Fol obtained by DFT calculations.

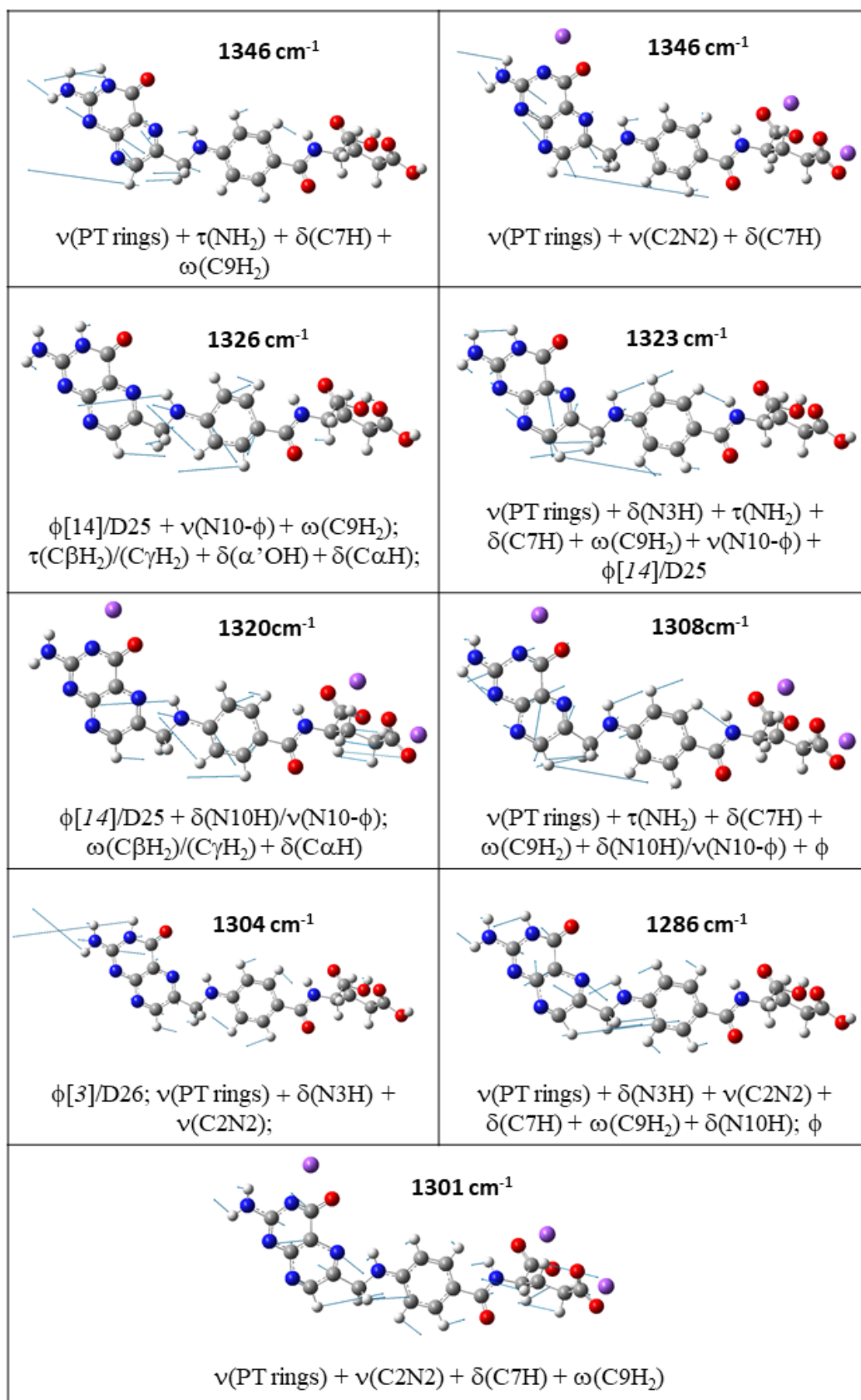


Figure A.17. Some vibrational modes for FA and Na₃Fol obtained by DFT calculations.

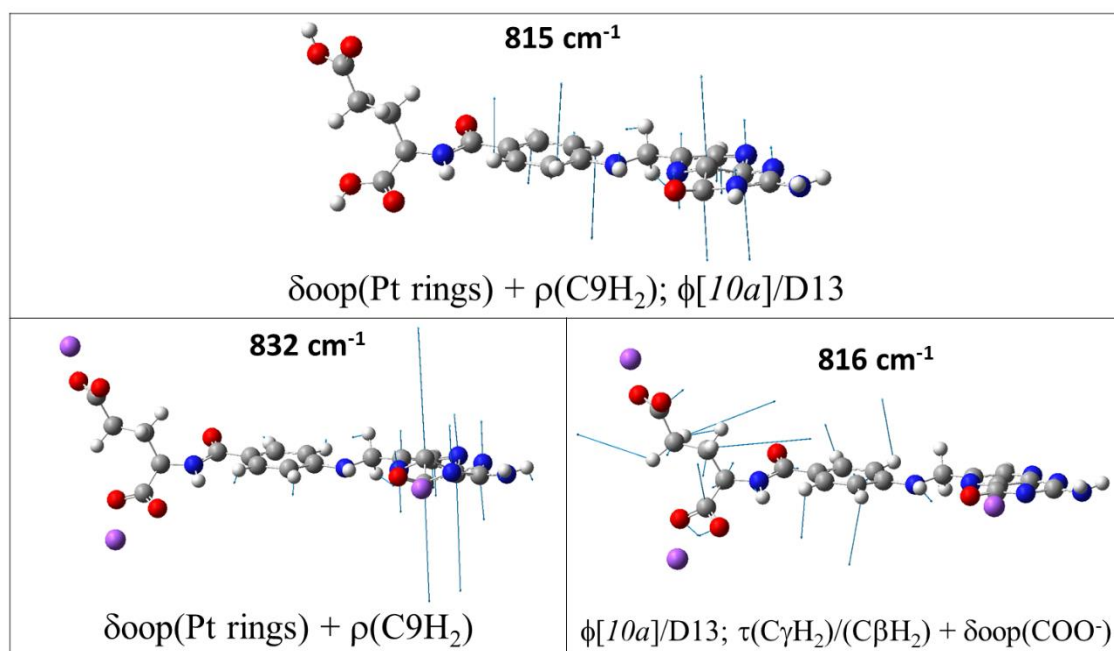


Figure A.18. Some vibrational modes for FA and Na₃Fol obtained by DFT calculations.

9. Solid state ^{13}C -NMR spectroscopy

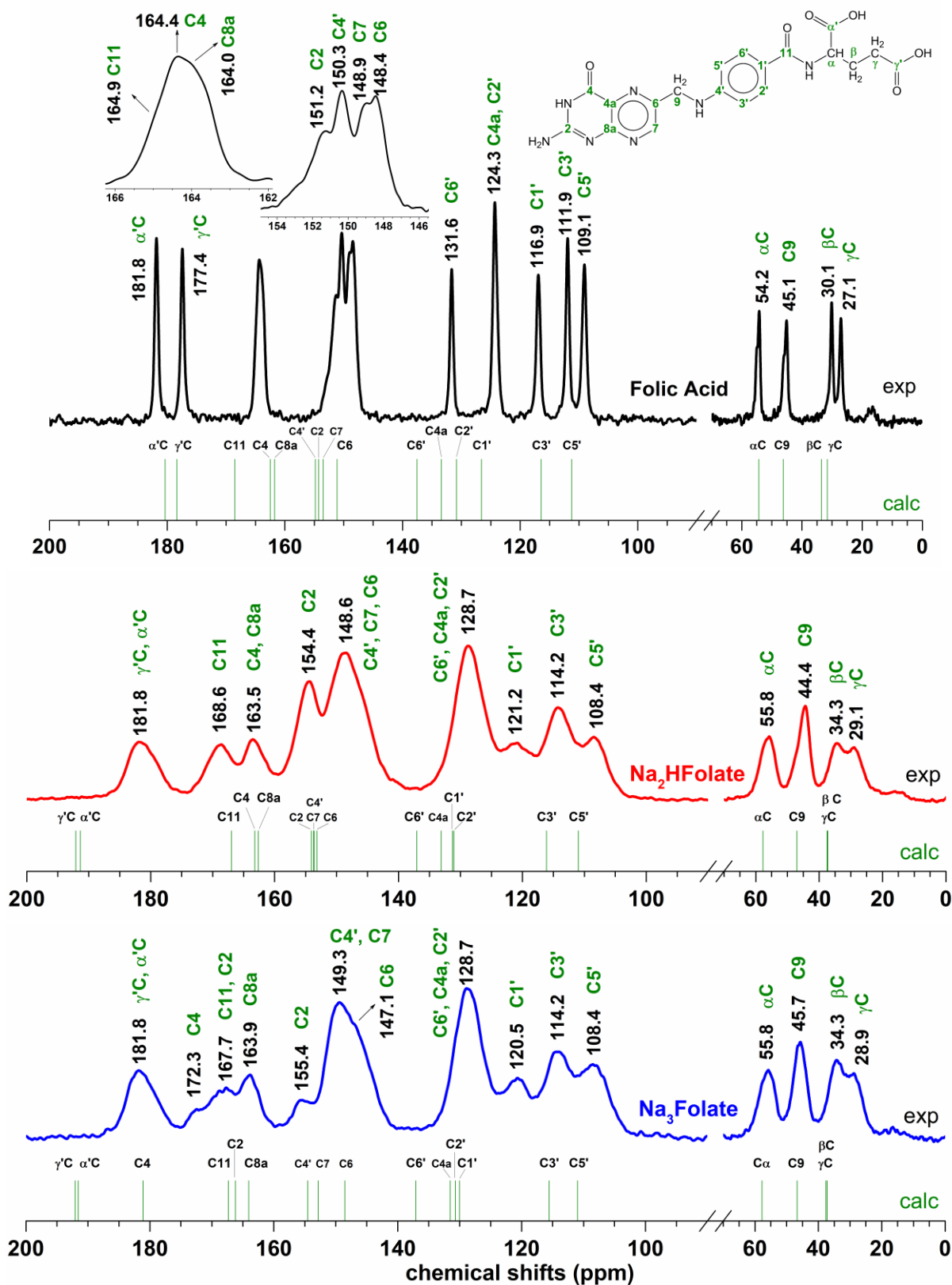


Figure A.19. Experimental and DFT calculated solid-state ^{13}C NMR spectra of FA, $\text{Na}_2\text{HFolate}$ and Na_3Folate .

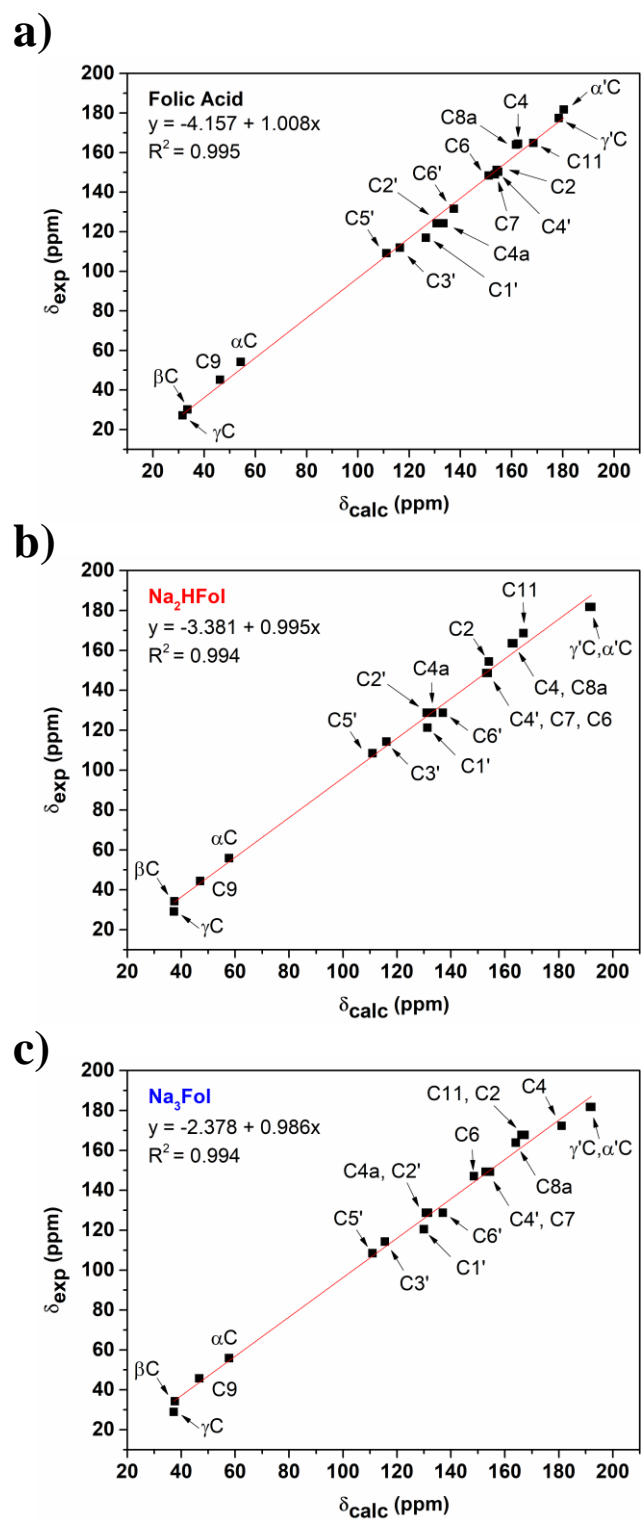


Figure A.20. Experimental *versus* calculated (DFT) ^{13}C chemical shifts for: a) FA; b) $\text{Na}_2\text{HFolate}$ and c) Na_3Folate .

References

- [1] A. Kokaislová, T. Helešicová, M. Ončák, P. Matějka, Spectroscopic studies of folic acid adsorbed on various metal substrates: does the type of substrate play an essential role in temperature dependence of spectral features?, *J. Raman Spectrosc.* 45 (2014) 750–757. <https://doi.org/10.1002/jrs.4557>.
- [2] A.M. Naglah, M.S. Refat, M.A. Al-Omar, M.A. Bhat, H.M. Alkahtani, A.S. Al-Wasidi, Synthesis of a vanadyl (IV) folate complex for the treatment of diabetes: Spectroscopic, structural, and biological characterization, *Drug Des. Devel. Ther.* 13 (2019) 1409–1420. <https://doi.org/10.2147/DDDT.S190310>.
- [3] R.A.R. Teixeira, F.R.A. Lima, P.C. Silva, L.A.S. Costa, A.C. Sant’Ana, Tracking chemical interactions of folic acid on gold surface by SERS spectroscopy, *Spectrochim. Acta Part A Mol. Biomol. Spectrosc.* 223 (2019) 117305. <https://doi.org/10.1016/j.saa.2019.117305>.
- [4] G. Gocheva, N. Petkov, A. Garcia Luri, S. Iliev, N. Ivanova, J. Petrova, Y. Mitrev, G. Madjarova, A. Ivanova, Tautomerism in folic acid: Combined molecular modelling and NMR study, *J. Mol. Liq.* 292 (2019) 111392. <https://doi.org/10.1016/j.molliq.2019.111392>.
- [5] J.J. Castillo, T. Rindzevicius, K. Wu, C.E. Rozo, M.S. Schmidt, A. Boisen, Silver-capped silicon nanopillar platforms for adsorption studies of folic acid using surface enhanced Raman spectroscopy and density functional theory, *J. Raman Spectrosc.* 46 (2015) 1087–1094. <https://doi.org/10.1002/jrs.4734>.
- [6] M. Baibarac, I. Smaranda, A. Nila, C. Serbschi, Optical properties of folic acid in phosphate buffer solutions: the influence of pH and UV irradiation on the UV-VIS absorption spectra and photoluminescence, *Sci. Rep.* 9 (2019) 14278. <https://doi.org/10.1038/s41598-019-50721-z>.
- [7] J.J. Castillo, T. Rindzevicius, C.E. Rozo, A. Boisen, Adsorption and Vibrational Study of Folic Acid on Gold Nanopillar Structures Using Surface-Enhanced Raman Scattering Spectroscopy, *Nanomater. Nanotechnol.* 5 (2015) 29. <https://doi.org/10.5772/61606>.
- [8] T. Wang, J.S. Stevens, T. Vetter, G.F.S. Whitehead, I.J. Vitorica-Yrezabal, H. Hao, A.J. Cruz-Cabeza, Salts, Cocrystals, and Ionic Cocrystals of a “Simple” Tautomeric Compound, *Cryst. Growth Des.* 18 (2018) 6973–6983. <https://doi.org/10.1021/acs.cgd.8b01159>.
- [9] Y.H. Jang, W.A. Goddard, K.T. Noyes, L.C. Sowers, S. Hwang, D.S. Chung, pKa Values of Guanine in Water: Density Functional Theory Calculations Combined with Poisson–Boltzmann Continuum–Solvation Model, *J. Phys. Chem. B.* 107 (2003) 344–357. <https://doi.org/10.1021/jp020774x>.
- [10] M. Soniat, C.B. Martin, Theoretical Study on the Relative Energies of Neutral Pterin Tautomers, *Pteridines.* 19 (2008) 13–22. <https://doi.org/10.1515/pteridines.2008.19.1.120>.
- [11] N. Markova, V. Enchev, Tautomerism of Inosine in Water: Is It Possible?, *J. Phys. Chem. B.* 123 (2019) 622–630. <https://doi.org/10.1021/acs.jpcc.8b11316>.

- [12] C.S. Peng, A. Tokmakoff, Identification of Lactam–Lactim Tautomers of Aromatic Heterocycles in Aqueous Solution Using 2D IR Spectroscopy, *J. Phys. Chem. Lett.* 3 (2012) 3302–3306. <https://doi.org/10.1021/jz301706a>.
- [13] M. Soniat, C.B. Martin, Theoretical Study on the Relative Energies of Anionic Pterin Tautomers, *Pteridines*. 20 (2009) 13–22. <https://doi.org/10.1515/pteridines.2009.20.1.124>.
- [14] D. Mastropaolo, A. Camerman, N. Camerman, Folic acid: crystal structure and implications for enzyme binding, *Science* (80). 210 (1980) 334–336. <https://doi.org/10.1126/science.7423195>.
- [15] J.A. Kaduk, C.E. Crowder, K. Zhong, Crystal structure of folic acid dihydrate, $C_{29}H_{29}N_2O_6(H_2O)_2$, *Powder Diffr.* 30 (2015) 52–56. <https://doi.org/10.1017/S0885715614000815>.
- [16] D. Braga, L. Chelazzi, F. Grepioni, L. Maschio, S. Nanna, P. Taddei, Folic Acid in the Solid State: A Synergistic Computational, Spectroscopic, and Structural Approach, *Cryst. Growth Des.* 16 (2016) 2218–2224. <https://doi.org/10.1021/acs.cgd.6b00043>.
- [17] F. Ragone, G.T. Ruiz, O.E. Piro, G.A. Echeverría, F.M. Cabrerizo, G. Petroselli, R. Erra-Balsells, K. Hiraoka, F.S. García Einschlag, E. Wolcan, Water-Soluble (Pterin)rhenium(I) Complex: Synthesis, Structural Characterization, and Two Reversible Protonation-Deprotonation Behavior in Aqueous Solutions, *Eur. J. Inorg. Chem.* 2012 (2012) 4801–4810. <https://doi.org/10.1002/ejic.201200681>.
- [18] R.A. Sayle, So you think you understand tautomerism?, *J. Comput. Aided. Mol. Des.* 24 (2010) 485–496. <https://doi.org/10.1007/s10822-010-9329-5>.
- [19] K. Momma, F. Izumi, VESTA 3 for three-dimensional visualization of crystal, volumetric and morphology data, *J. Appl. Crystallogr.* 44 (2011) 1272–1276. <https://doi.org/10.1107/S0021889811038970>.
- [20] S. Bonazzi, M.M. DeMoraes, G. Gottarelli, P. Mariani, G.P. Spada, Self-Assembly and Liquid Crystal Formation of Folic Acid Salts, *Angew. Chemie Int. Ed. English.* 32 (1993) 248–250. <https://doi.org/10.1002/anie.199302481>.
- [21] F. Ciuchi, G. Di Nicola, H. Franz, G. Gottarelli, P. Mariani, M.G. Ponzi Bossi, G.P. Spada, Self-Recognition and Self-Assembly of Folic Acid Salts: Columnar Liquid Crystalline Polymorphism and the Column Growth Process, *J. Am. Chem. Soc.* 116 (1994) 7064–7071. <https://doi.org/10.1021/ja00095a008>.
- [22] G. Gottarelli, E. Mezzina, G.P. Spada, F. Carsughi, G. Di Nicola, P. Mariani, A. Sabatucci, S. Bonazzi, The Self-Recognition and Self-Assembly of Folic Acid Salts in Isotropic Water Solution, *Helv. Chim. Acta.* 79 (1996) 220–234. <https://doi.org/10.1002/hlca.19960790123>.
- [23] P. Xing, X. Chu, M. Ma, S. Li, A. Hao, Supramolecular gel from folic acid with multiple responsiveness, rapid self-recovery and orthogonal self-assemblies, *Phys. Chem. Chem. Phys.* 16 (2014) 8346–8359. <https://doi.org/10.1039/c4cp00367e>.

- [24] X. Wang, J. Sun, T. Li, Z. Song, D. Wu, B. Zhao, K. Xiang, W. Ai, X.Z. Fu, J.L. Luo, Folic acid self-assembly synthesis of ultrathin N-doped carbon nanosheets with single-atom metal catalysts, *Energy Storage Mater.* 36 (2021) 409–416. <https://doi.org/10.1016/j.ensm.2021.01.024>.
- [25] R. Atluri, M.N. Iqbal, Z. Bacsik, N. Hedin, L.A. Villaescusa, A.E. Garcia-Bennett, Self-Assembly Mechanism of Folate-Templated Mesoporous Silica, *Langmuir*. 29 (2013) 12003–12012. <https://doi.org/10.1021/la401532j>.
- [26] E. Wolcan, On the origins of the absorption spectroscopy of pterin and $\text{Re}(\text{CO})_3(\text{pterin})(\text{H}_2\text{O})$ aqueous solutions. A combined theoretical and experimental study, *Spectrochim. Acta Part A Mol. Biomol. Spectrosc.* 129 (2014) 173–183. <https://doi.org/10.1016/j.saa.2014.03.022>.
- [27] M.K. Off, A.E. Steindal, A.C. Porojnicu, A. Juzeniene, A. Vorobey, A. Johnsson, J. Moan, Ultraviolet photodegradation of folic acid, *J. Photochem. Photobiol. B Biol.* 80 (2005) 47–55. <https://doi.org/10.1016/j.jphotobiol.2005.03.001>.
- [28] Z. Szakács, B. Noszál, Determination of dissociation constants of folic acid, methotrexate, and other photolabile pteridines by pressure-assisted capillary electrophoresis, *Electrophoresis*. 27 (2006) 3399–3409. <https://doi.org/10.1002/elps.200600128>.
- [29] S. Ayyappan, N. Sundaraganesan, V. Aroulmoji, E. Murano, S. Sebastian, Molecular structure, vibrational spectra and DFT molecular orbital calculations (TD-DFT and NMR) of the antiproliferative drug Methotrexate, *Spectrochim. Acta - Part A Mol. Biomol. Spectrosc.* 77 (2010) 264–275. <https://doi.org/10.1016/j.saa.2010.05.021>.
- [30] A.M. Butt, M.C. Iqbal, M. Amin, H. Katas, Synergistic effect of pH-responsive folate-functionalized poloxamer 407-TPGS-mixed micelles on targeted delivery of anticancer drugs, *Int. J. Nanomedicine*. 10 (2015) 1321–1334. <https://doi.org/10.2147/IJN.S78438>.
- [31] Y.Y. He, X.C. Wang, P.K. Jin, B. Zhao, X. Fan, Complexation of anthracene with folic acid studied by FTIR and UV spectroscopies, *Spectrochim. Acta Part A Mol. Biomol. Spectrosc.* 72 (2009) 876–879. <https://doi.org/10.1016/j.saa.2008.12.021>.
- [32] D.L. Pavia, G.M. Lampman, G.S. Kriz, *Introduction to Spectroscopy: A Guide for Students of Organic Chemistry*, 3rd ed., W.B. Saunders Co, Philadelphia, 1979.
- [33] H.-B. Guo, F. He, B. Gu, L. Liang, J.C. Smith, Time-Dependent Density Functional Theory Assessment of UV Absorption of Benzoic Acid Derivatives, *J. Phys. Chem. A*. 116 (2012) 11870–11879. <https://doi.org/10.1021/jp3084293>.
- [34] J.C. Baum, D.S. McClure, The ultraviolet transitions of benzoic acid. 1. Interpretation of the singlet absorption spectrum, *J. Am. Chem. Soc.* 101 (1979) 2335–2339. <https://doi.org/10.1021/ja00503a016>.

- [35] G. Li, D. Magana, R.B. Dyer, Photoinduced electron transfer in folic acid investigated by ultrafast infrared spectroscopy, *J. Phys. Chem. B.* 116 (2012) 3467–3475. <https://doi.org/10.1021/jp300392a>.
- [36] X. Chen, E. Xu, Z. Cao, Theoretical study on the singlet excited state of pterin and its deactivation pathway, *J. Phys. Chem. A.* 111 (2007) 9255–9262. <https://doi.org/10.1021/jp0727502>.
- [37] S.F. Mason, Pteridine studies. Part VI. The ultraviolet and infrared absorption spectra of the monosubstituted pteridines, *J. Chem. Soc.* (1955) 2336–2346. <https://doi.org/10.1039/jr9550002336>.
- [38] A. Vora, A. Riga, K. Alexander, Processes to Identify the Degradation Mechanism of a Solid which Appears to Undergo a Complex Reaction: Folic Acid, *Instrum. Sci. Technol.* 30 (2002) 193–203. <https://doi.org/10.1081/CI-120003899>.
- [39] P.B. Ottaway, *The Technology of Vitamins in Food*, 1st ed., Springer US, 1993. <https://doi.org/10.1007/978-1-4615-2131-0>.
- [40] D.R. Lide, *CRC Handbook of Chemistry and Physics*, 90th ed., CRC Press (Taylor & Francis Group), 2009-2010. ISBN 978-1-4200-9084-0
- [41] I.M. Weiss, C. Muth, R. Drumm, H.O.K. Kirchner, Thermal decomposition of the amino acids glycine, cysteine, aspartic acid, asparagine, glutamic acid, glutamine, arginine and histidine, *BioRxiv.* (2017) 1–15. <https://doi.org/10.1101/119123>.
- [42] J.A. Teixeira, W.D.G. Nunes, T.A.D. Colman, A.L.C. do Nascimento, F.J. Caires, F.X. Campos, D.A. Gálico, M. Ionashiro, Thermal and spectroscopic study to investigate p-aminobenzoic acid, sodium p-aminobenzoate and its compounds with some lighter trivalent lanthanides, *Thermochim. Acta.* 624 (2016) 59–68. <https://doi.org/10.1016/j.tca.2015.11.023>.
- [43] J.P. Soares, J.E. Santos, G.O. Chierice, E.T.G. Cavalheiro, Thermal behavior of alginic acid and its sodium salt, *Eclética Química.* 29 (2004) 57–64. <https://doi.org/10.1590/S0100-46702004000200009>.
- [44] T. Meisel, Z. Halmos, K. Seybold, E. Pungor, The thermal decomposition of alkali metal formates, *J. Therm. Anal.* 7 (1975) 73–80. <https://doi.org/10.1007/BF01911627>.
- [45] N.N. Greenwood, A. Earnshaw, *Chemistry of the Elements*, 2nd ed., Elsevier, 1998.
- [46] K. Dong, F. Xie, Y. Chang, C. Chen, W. Wang, D. Lu, X. Gu, A novel strategy for the efficient decomposition of toxic sodium cyanate by hematite, *Chemosphere.* 256 (2020) 127047. <https://doi.org/10.1016/j.chemosphere.2020.127047>.
- [47] B. Hernández, Y.-M. Coïc, F. Pflüger, S.G. Kruglik, M. Ghomi, All characteristic Raman markers of tyrosine and tyrosinate originate from phenol ring fundamental vibrations, *J. Raman Spectrosc.* 47 (2016) 210–220. <https://doi.org/10.1002/jrs.4776>.

- [48] B. Sjöberg, S. Foley, B. Cardey, M. Enescu, An experimental and theoretical study of the amino acid side chain Raman bands in proteins, *Spectrochim. Acta - Part A Mol. Biomol. Spectrosc.* 128 (2014) 300–311. <https://doi.org/10.1016/j.saa.2014.02.080>.
- [49] N.B. Colthup, L.H. Daly, S.E. Wiberley, *Introduction to Infrared and Raman Spectroscopy*, 3rd ed., Academic Press, 1990.
- [50] R. Świsłocka, M. Samsonowicz, E. Regulska, W. Lewandowski, Molecular structure of 4-aminobenzoic acid salts with alkali metals, *J. Mol. Struct.* 792–793 (2006) 227–238. <https://doi.org/10.1016/j.molstruc.2005.10.060>.
- [51] B. Profantová, V. Profant, V. Zíma, V. Kopecký, L. Bednářová, C. Zentz, V. Baumruk, P.Y. Turpin, J. Štěpánek, Protonation effect of tyrosine in a segment of the SRF transcription factor: A combined optical spectroscopy, molecular dynamics, and density functional theory calculation study, *J. Phys. Chem. B.* 117 (2013) 16086–16095. <https://doi.org/10.1021/jp4099864>.
- [52] A. Barth, Infrared spectroscopy of proteins, *Biochim. Biophys. Acta - Bioenerg.* 1767 (2007) 1073–1101. <https://doi.org/10.1016/j.bbabbio.2007.06.004>.

Supporting Information material of Chapter 4

Supplementary Material

Pyrolysis mechanism of Folic Acid: identification of gaseous products and characterization of N-doped carbon materials

Vagner R. Magri^a, Caroline S. de Matos^a, Michele A. Rocha^a, Christine Taviot-Gueho^{bc} and Vera R.L. Constantino^{*a}

^a*Departamento de Química Fundamental, Instituto de Química, Universidade de São Paulo, Av. Lineu Prestes 748, CEP 05508-000, São Paulo, SP, Brazil.*

^b*Université Clermont Auvergne, Université Blaise Pascal, Institut de Chimie de Clermont-Ferrand, BP 10448, F-63000 Clermont-Ferrand, France*

^c*CNRS, UMR 6296, ICCF, F-63178 Aubiere, France*

* *Corresponding author.*

E-mail address: vrlconst@iq.usp.br (V.R.L. Constantino)

Content

1. *Supplementary experimental*
 - 1.1. *Chemicals*
 - 1.2. *Patterns used for the interpretation of TGA-FTIR data (Fig. S1)*
 - 1.3. *Purification of C-dots extracted in NaOH aqueous solution (Fig. S2)*
2. *Supplementary Results*
 - 2.1. *TGA-FTIR and TGA-MS data of FA and folate salts (Table S1 and Figs. S3-S5)*
 - 2.2. *XRD, SEM, FTIR, Raman and XPS data of chars*
 - 2.2.1. *In-situ XRD of FA (Figs. S6-S8)*
 - 2.2.2. *SEM data of pyrolyzed FA (Fig. S9)*
 - 2.2.3. *In-situ and ex-situ XRD of sodium folate salts (Figs. S10-S12)*
 - 2.2.4. *FTIR data of pyrolyzed sodium folate salts (Figs. S13-S14)*
 - 2.2.5. *Raman spectroscopic data of pyrolyzed FA and sodium folate salts (Figs. S15-S16; Table S2)*
 - 2.2.6. *XPS data of pyrolyzed FA (Table S3 and Fig. S17)*
 - 2.3. *FA pyrolytic mechanism (Table S4 and Schemes S1-S2)*
 - 2.4. *Sodium folate salts pyrolytic mechanism*
 - 2.5. *Analysis of C-dots extracted from pyrolyzed FA and folate sodium salts (Figs. S18-S23)*
3. *References*

1. Supplementary experimental

1.1. Chemicals

Folic acid di-hydrated ($C_{19}H_{19}N_7O_6 \cdot 2H_2O$; $\geq 97\%$) was purchased from Sigma-Aldrich and used as received. The folate sodium salts $Na_2C_{19}H_{17}N_7O_6 \cdot 2.5H_2O$ (Na_2HFol) and $Na_3C_{19}H_{16}N_7O_6 \cdot 3.0H_2O$ (Na_3Fol) were prepared by the stoichiometric reaction between FA and NaOH aqueous solution, and the chemical formula was determined by simultaneous thermogravimetric analysis and differential scanning calorimetry coupled to mass spectrometry (TGA/DSC-MS) in air atmosphere, as reported in previous work [1]. Dimethyl sulfoxide (DMSO) was also supplied by Sigma-Aldrich.

1.2. Patterns used for the interpretation of TGA-FTIR data

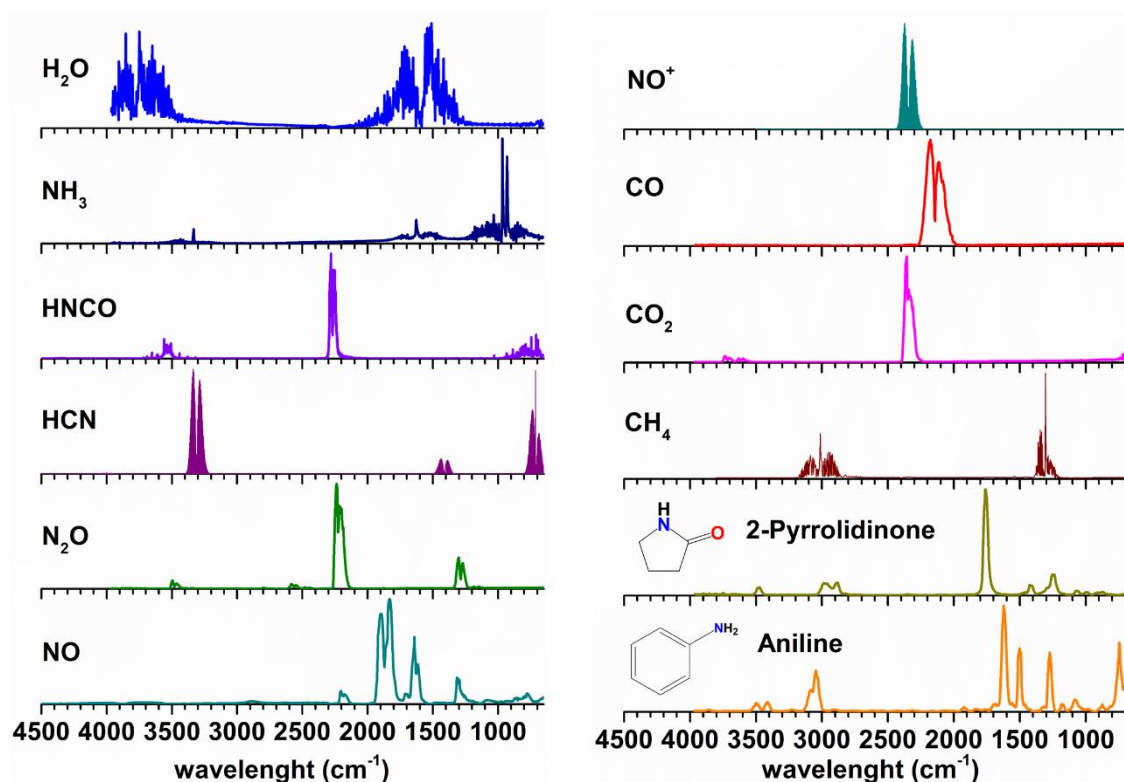


Figure S1. Infrared spectra of gaseous molecules taken from NIST [2] and HITRAN [3] database and compared with the spectra of gaseous/volatile products released during the pyrolysis of samples.

1.3. Purification of C-dots extracted in NaOH aqueous solution

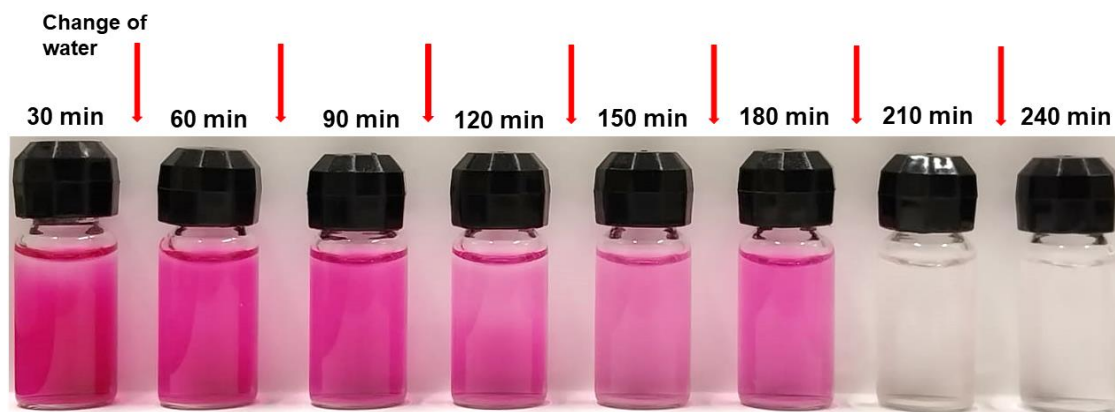


Figure S2. Water samples from dialyzes (purification step) of the C-dots obtained from FA pyrolyzed at 350 °C and extracted with aqueous NaOH solution (0.1 mol L⁻¹).

2. Supplementary Results

2.1. TGA-FTIR and TGA-MS data of FA and folate salts

Table S1. Data from TGA-MS and TGA-FTIR curves for folic acid and sodium folate salts samples.

Folic Acid (C₁₉H₁₉N₇O₆·2H₂O)			
event[#]	Temp. (°C)	%Mass	EGA (TG-MS and TG-FTIR)
dehy	30-175	6.9	H ₂ O
I	200-350	22.4	H ₂ O, CO ₂ , NH ₃ ; aniline; 2-pyrrolidone
II	350-570	25.9	H ₂ O, CO ₂ , NH ₃ ; CO; NO; N ₂ O; HCN; HNCO; aniline; 2-pyrrolidone; C ₃ H ₅ (<i>m/z</i> 41)
III	570-800	14.5	H ₂ O, CO ₂ , NH ₃ ; CO; NO; N ₂ O; HCN; HNCO
IV	800-1000	6.3	CO ₂ , CO; NO; HCN; HNCO
Na₂HFol (Na₂C₁₉H₁₇N₇O₆·2.5H₂O)			
event[#]	Temp. (°C)	%Mass	EGA (TG-MS and TG-FTIR)
dehy	30-190	4.9	H ₂ O
I	260-320	5.1	H ₂ O, CO ₂ , NH ₃ ; aniline; HNCO
II	320-430	26.0	H ₂ O, CO ₂ , NH ₃ ; CO; NO; N ₂ O; HNCO; aniline; 2-pyrrolidone; C ₃ H ₅ (<i>m/z</i> 41)
III	430-570	8.8	H ₂ O, CO ₂ , NH ₃ ; CO; NO; N ₂ O; HCN; HNCO; aniline; C ₃ H ₅ (<i>m/z</i> 41)
IV	570-725	12.3	H ₂ O, CO ₂ , NH ₃ ; CO; NO; N ₂ O; HCN; HNCO
V	725-1000	38.1	H ₂ O, CO ₂ , NH ₃ ; CO; NO; HCN; HNCO
Na₃Fol (Na₃C₁₉H₁₆N₇O₆·3.0H₂O)			
event[#]	Temp. (°C)	%Mass	EGA (TG-MS and TG-FTIR)
dehy	30-220	7.9	H ₂ O
I	300-430	25.0	H ₂ O, CO ₂ , NH ₃ ; CO; NO; N ₂ O; HNCO; aniline; 2-pyrrolidone; C ₃ H ₅ (<i>m/z</i> 41)
II	430-600	16.6	H ₂ O, CO ₂ , NO; CO; NH ₃ ; HNCO
III	600-800	18.6	H ₂ O, CO ₂ , NO; CO; NH ₃ ; HNCO
IV	800-1000	24.0	H ₂ O, CO ₂ , NO; NO ⁺

[#]dehy: dehydration; Roman numbers indicates the degradation steps; *EGA: Evolved gas analysis carried out by TG-MS and TG-FTIR.

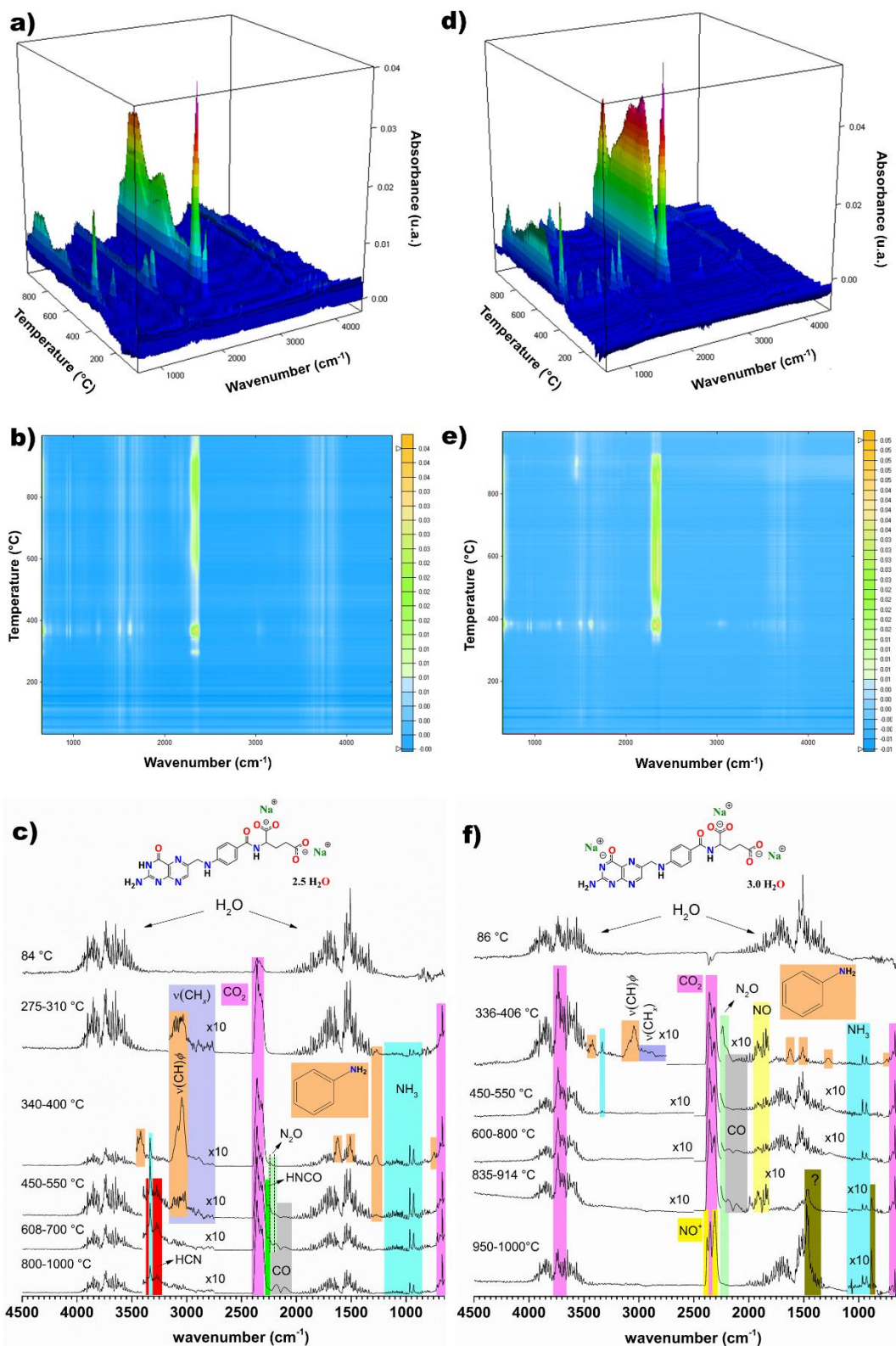


Figure S3. (a,d) 3D plot of TGA-FTIR data, (b,e) contour map (yellow and blue colours are defined as intensity increasing and decreasing, respectively), and (c,f) FTIR spectra of gases/volatiles identified (at selected temperature ranges) for (a-c) Na₂HFol and (d-f) Na₃Fol samples.

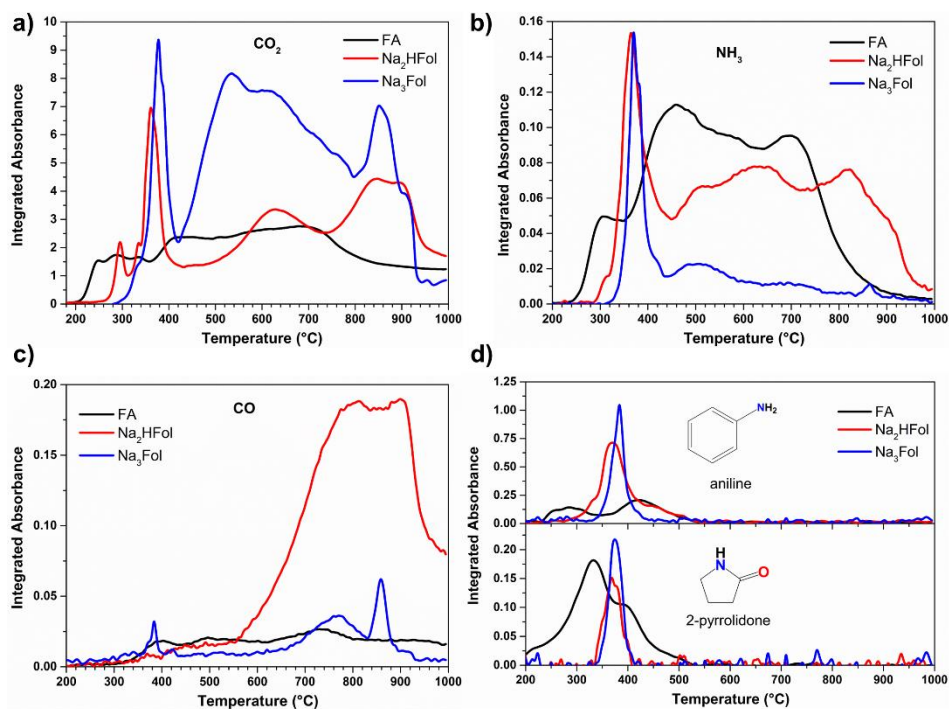


Figure S4. Integrated absorbance of TGA-FTIR curves for FA, Na₂HFol and Na₃Fol: (a) CO₂ (2360 cm⁻¹), (b) NH₃ (966 cm⁻¹), (c) CO (2114 cm⁻¹), and (d) 2-pyrrolidone (1760 cm⁻¹) and aniline (1622 cm⁻¹). The intensities were normalized taking into account the mols number of FA and salts used in TGA/DSC analysis.

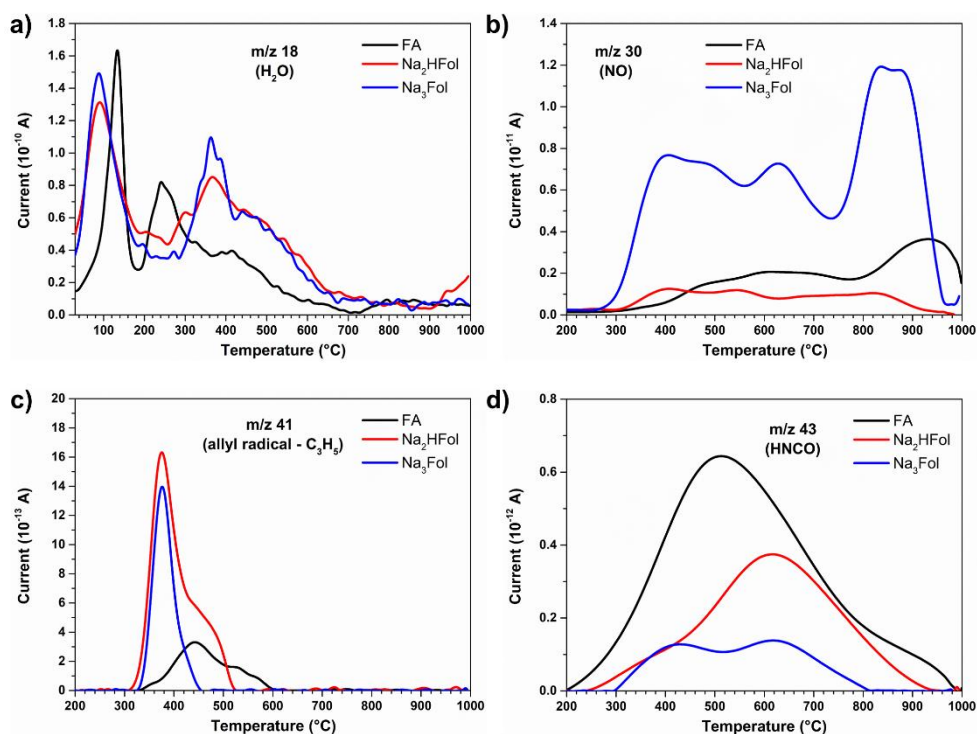


Figure S5. TGA-MS curves of FA, Na₂HFol and Na₃Fol: (a) $m/z = 18$ (H₂O), (b) $m/z = 30$ (NO), (c) $m/z = 41$ (allyl radical - C₃H₅), and (d) $m/z = 43$ (HNCO). The intensities were normalized taking into account the mols number of FA and salts used in TGA/DSC analysis.

FA presented a higher dehydration temperature in comparison to its sodium salts, as observed in **Fig. 2** (main text) and **Fig. S5a**, possibly due to entrapment of water into crystalline lattice. In folic acid dihydrate, the water molecules are hydrogen bonded to oxygen and nitrogen atoms of FA molecule and belong to the structure. Therefore, it is crystalline water, and its release is observed at a fixed temperature often slightly higher than 100°C while the release of physisorbed water starts at 50°C.

2.2. XRD, SEM, FTIR, Raman and XPS data of chars

2.2.1. In-situ XRD of FA

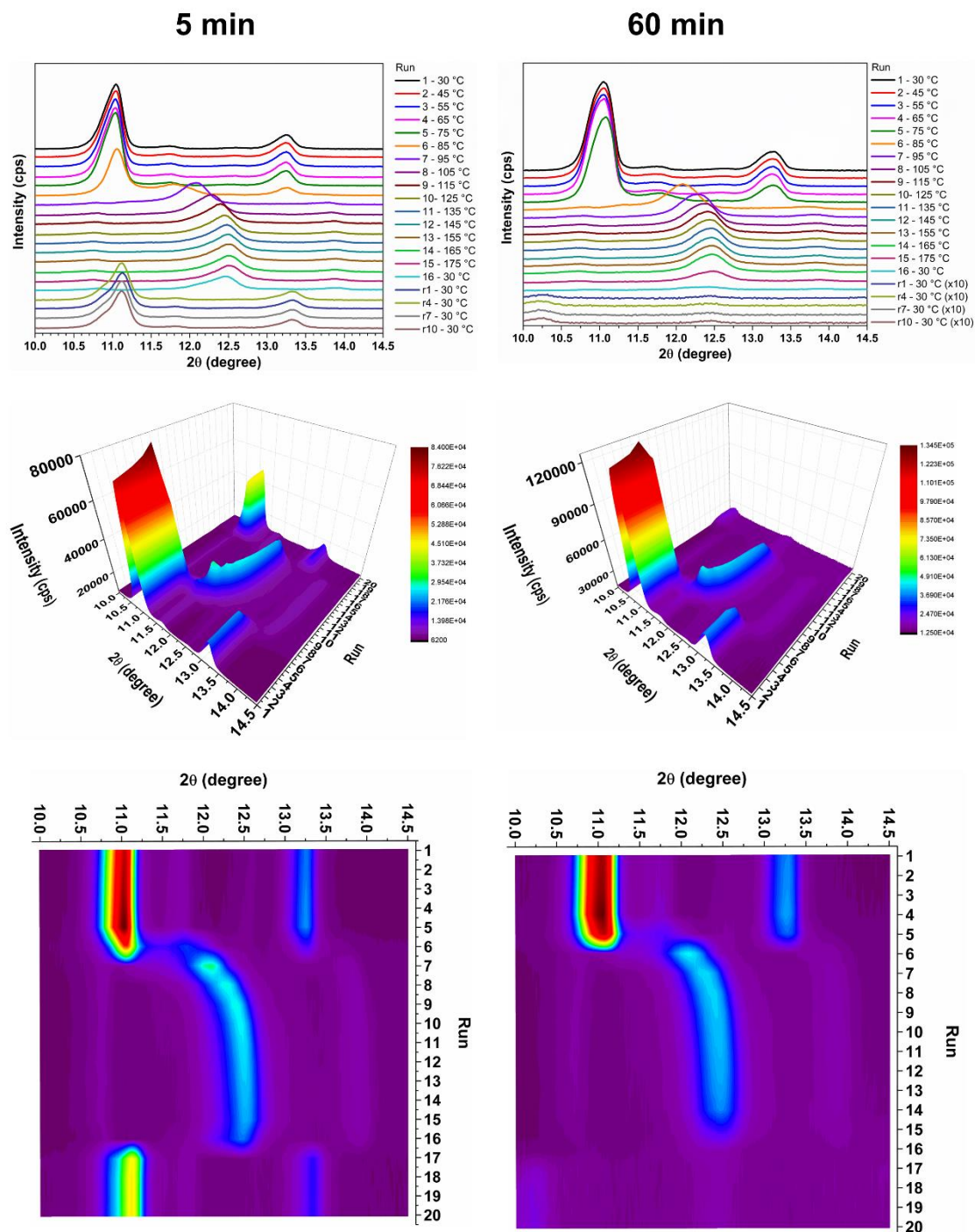


Figure S6. In-situ XRD of FA during heating in the range from 30 to 175 °C (runs 1-15) and after colling and chamber opening (runs 16-20; rehydration) with analysis after 5 minutes (right column) and 60 minutes (left column). The structural change caused by dehydration starts to occur above 85 °C.

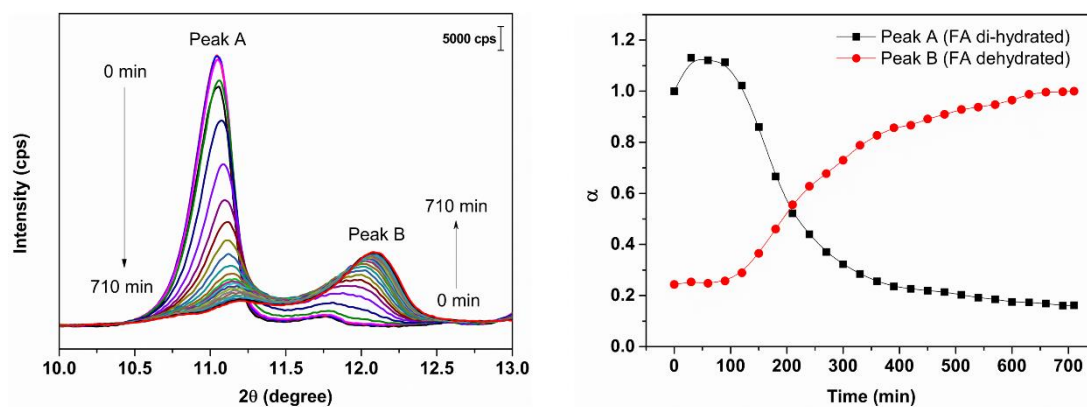


Figure S7. Dehydration kinetic assay of FA heated at 85 °C. Peak A is attributed to di-hydrated FA (orthorhombic crystal system and $P2_12_12_1$ space group) and Peak B is assigned to dehydrated sample (monoclinic crystal system and $P2_1$ space group), according to Braga et al. [4].

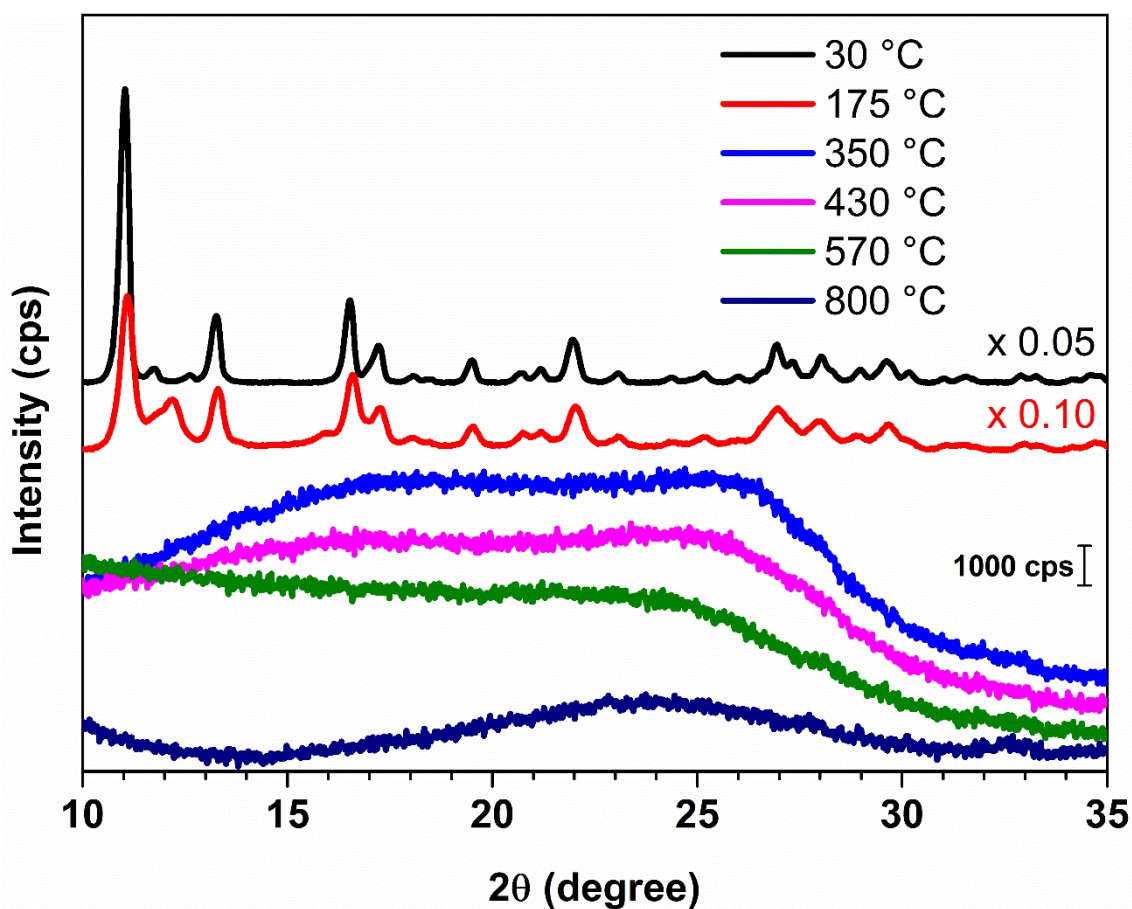


Figure S8. *In-situ* XRD analysis collected during FA pyrolysis up to 800 °C after cycles of heating and cooling.

2.2.2. SEM data of pyrolyzed FA

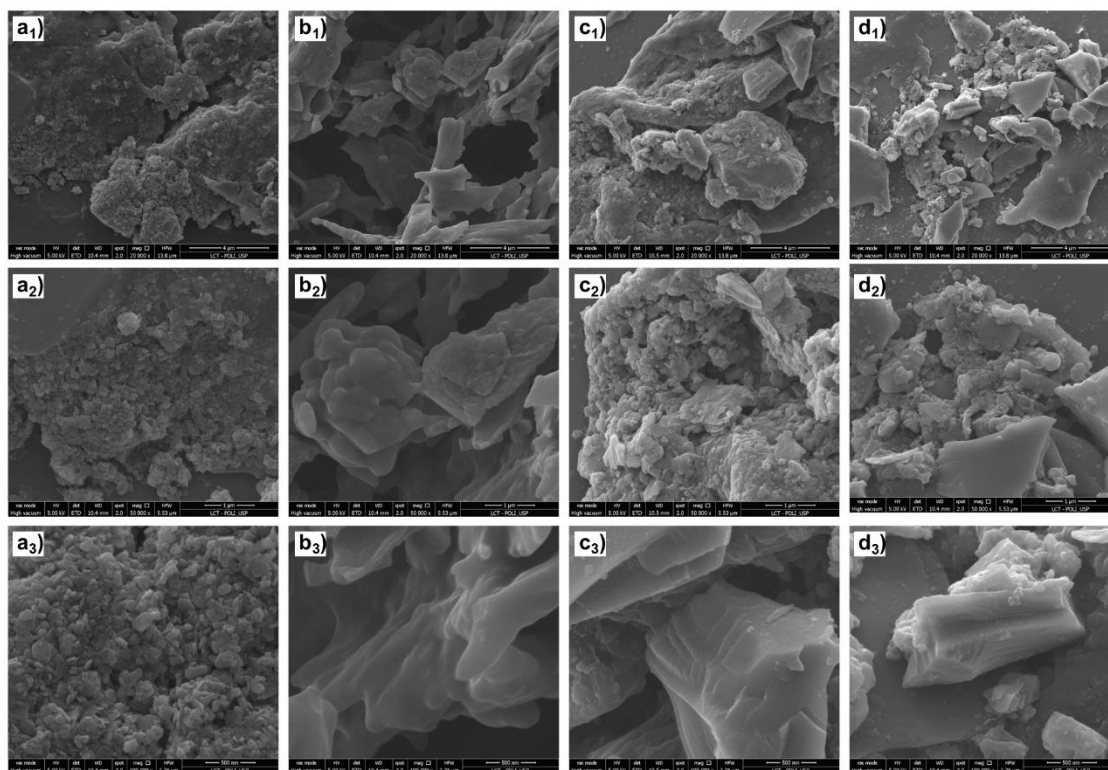


Figure S9. SEM micrographs of FA pyrolyzed at (a) 350 °C, (b) 570 °C, (c) 800 °C, and (d) 1000 °C. First line: scale bar = 4 μm ; second line: scale bar = 1 μm ; and third line: scale bar = 500 nm.

2.2.3. In-situ and ex-situ XRD of sodium folate salts

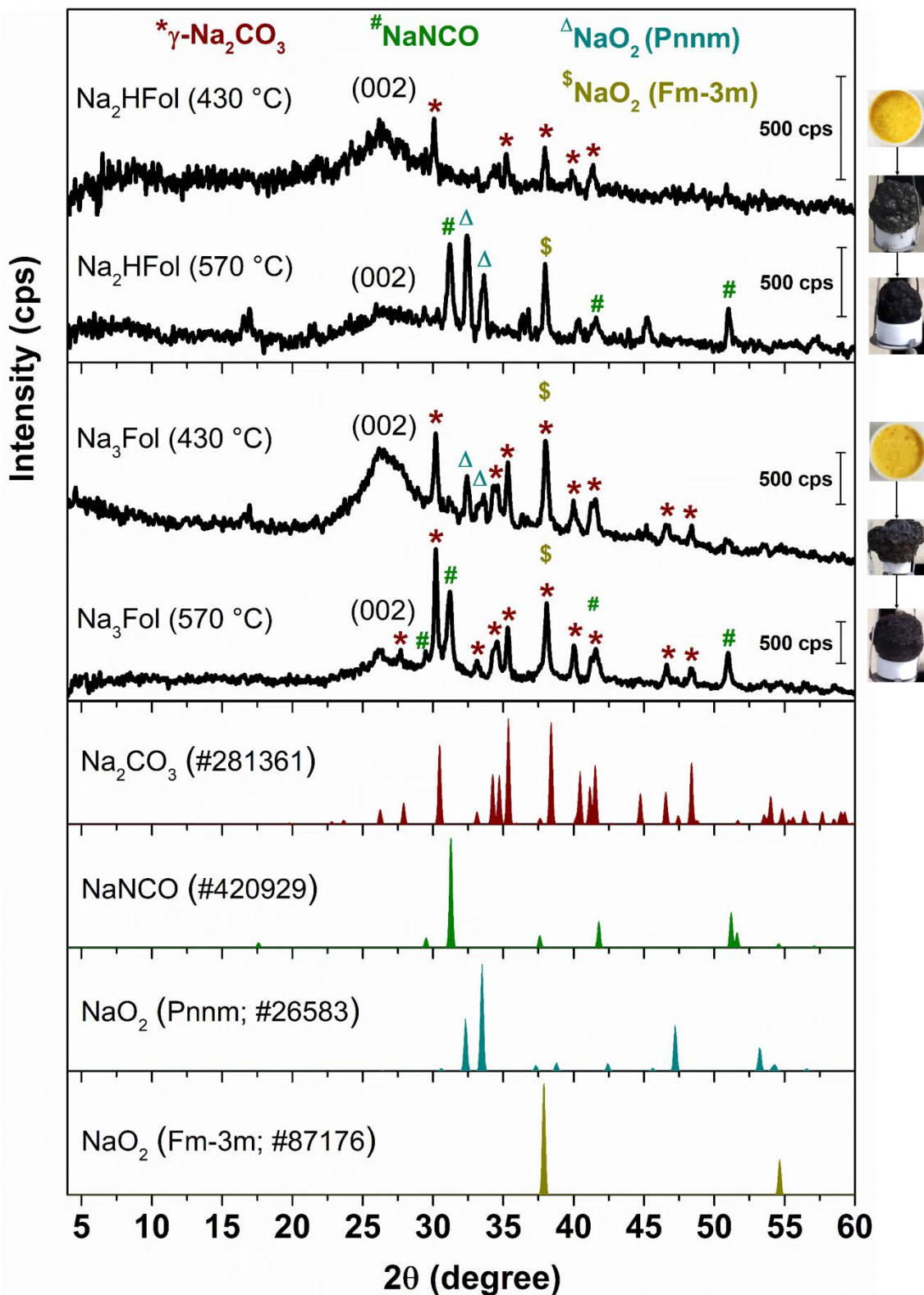


Figure S10. Ex-situ XRD pattern of char samples of Na₂HFol and Na₃Fol pyrolyzed at 430 and 570 °C. Insets show the photos of samples before (yellow-orange powders) and after (black foam-like materials) the pyrolysis process.

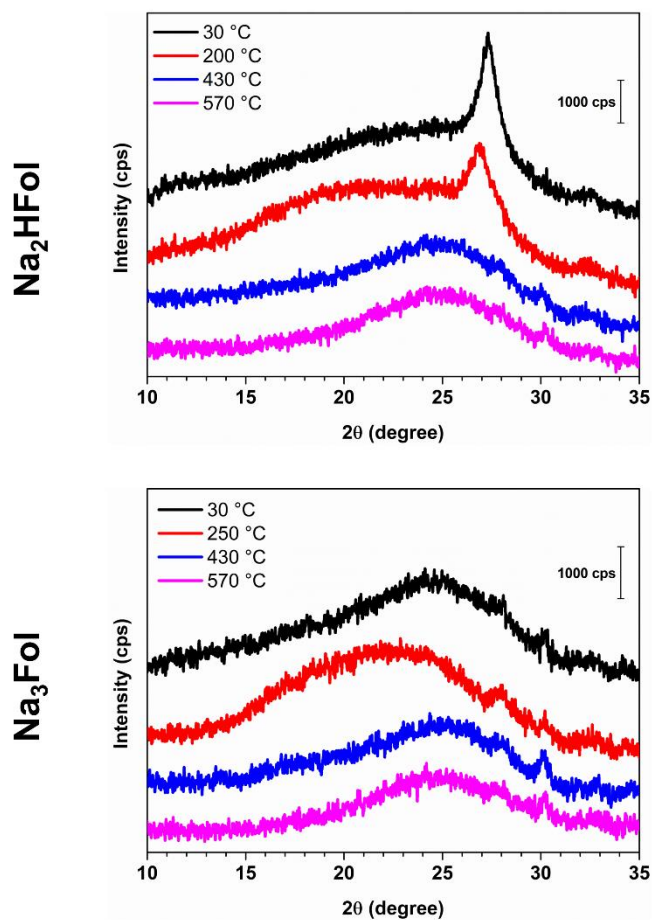


Figure S11. *In-situ* XRD analysis during pyrolysis of Na₂HFol and Na₃Fol up to 570 °C registered after cycles of heating and cooling. Na₂HFol and Na₃Fol precursors are amorphous compounds as it was previously reported [1]. However, Na₂HFol presents a supramolecular structure composed by π -stacked tetramers [1], as indicated by diffraction peak near 27° (2θ).

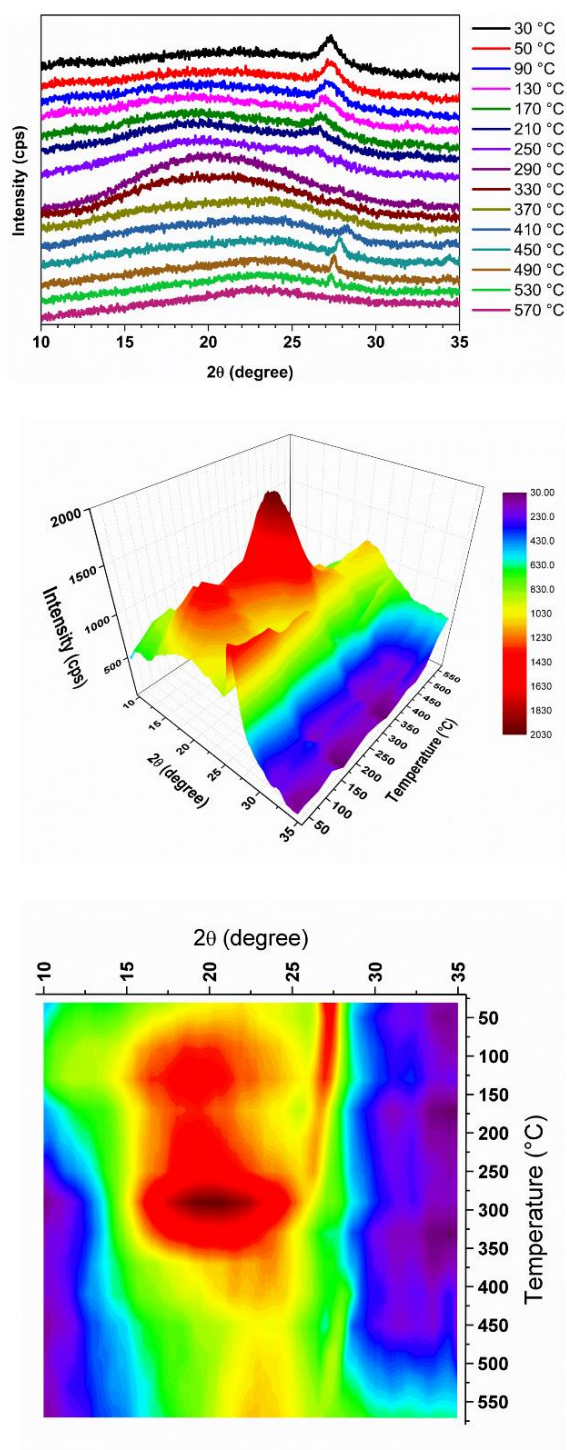


Figure S12. *In-situ* XRD collected during the heating of Na₂HFol in the range from 30 to 570 °C. The peak attributed to π -stacked structure near 27°(2 θ) are maintained after dehydration temperature (210 °C) and its still observed up to 250 °C, before the beginning of decomposition (above 270 °C).

2.2.4. FTIR data of pyrolyzed sodium folate salts

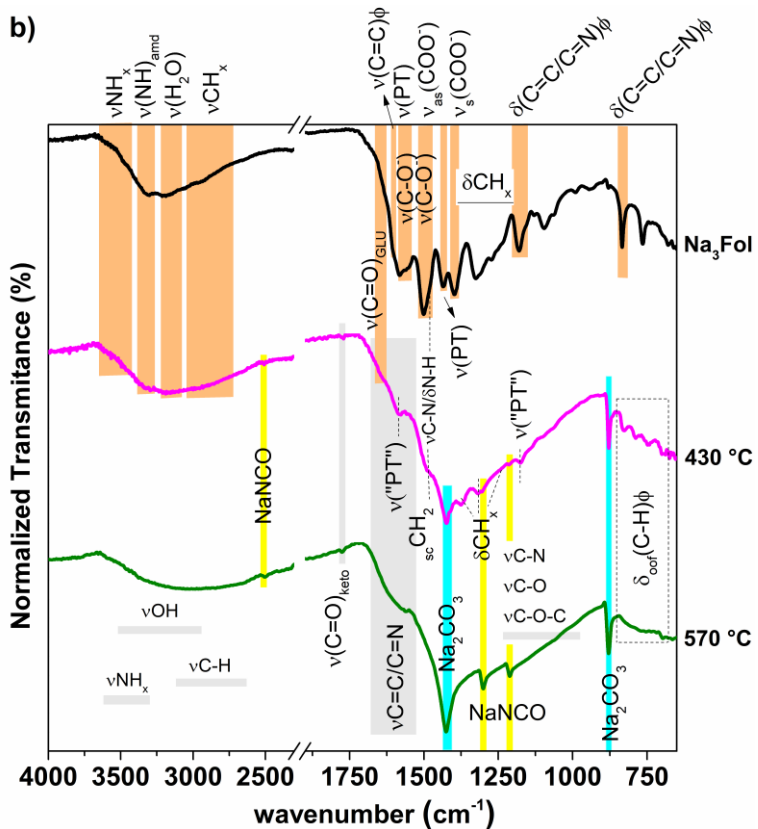
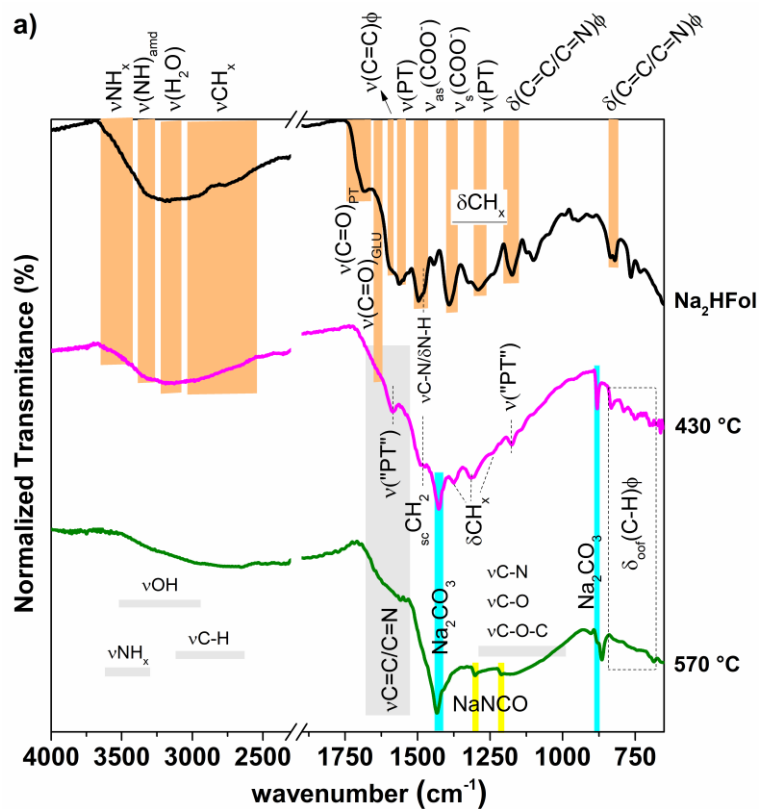


Figure S13. FTIR-ATR spectra of (a) Na₂HFol and (b) Na₃Fol and its pyrolyzed samples; ν = stretching, δ = bending, ϕ = aromatic ring, PT = pterin ring.

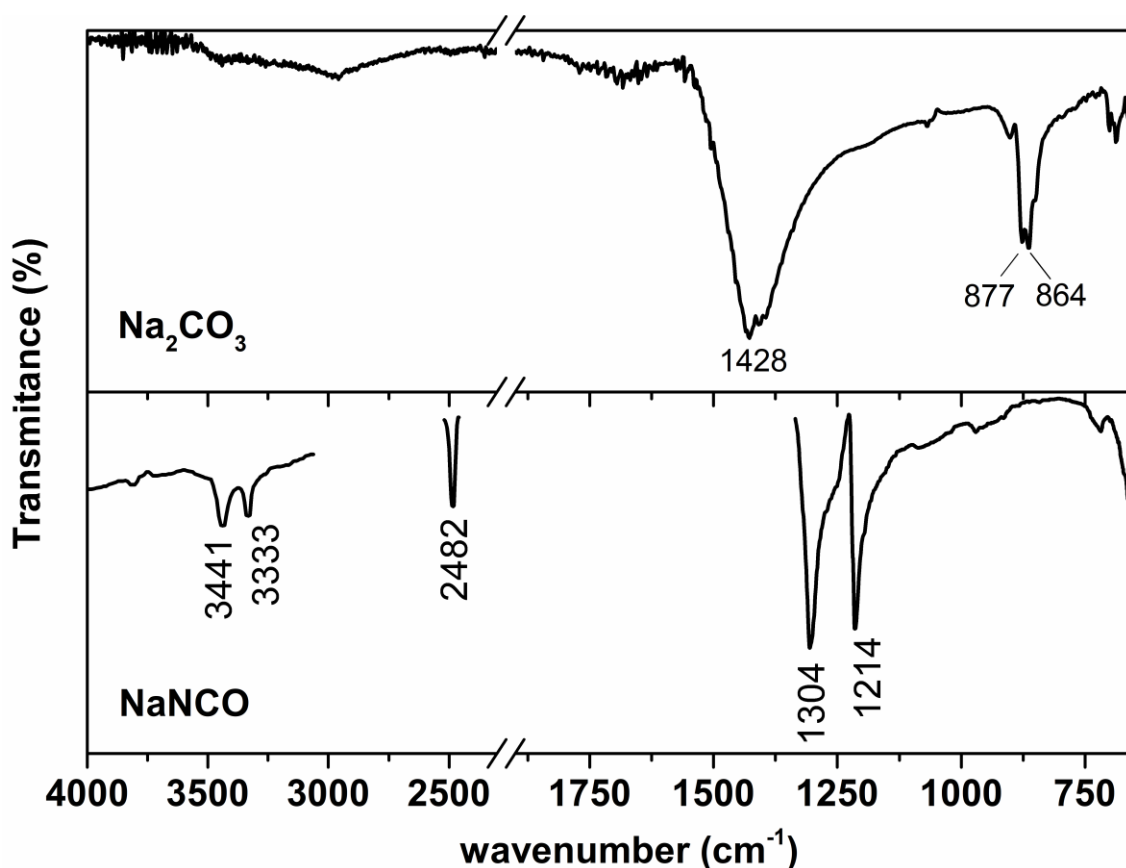


Figure S14. FTIR spectra of Na₂CO₃ and NaNCO inorganic salts. The NaNCO spectra was found on NIST database [2].

Fig. S13 presents the FTIR-ATR spectra of folate sodium salts and their pyrolyzed samples. At 430 °C, in the end of the first pyrolysis stage, the results suggested the consumption of functional groups such as benzene ring of *p*-ABA moiety (1600 cm⁻¹ region; ν C=C ϕ) and carboxylate groups of glutamate moiety (1500 cm⁻¹ and 1400 cm⁻¹; respectively ν_{as} COO⁻ and ν_s COO⁻). The bands attributed to amide groups at 3300 cm⁻¹ region (ν N-H), 1680-1630 cm⁻¹ (ν C=O) and 1480/1310/1240 cm⁻¹ (ν C-N/ δ N-H coupled to δ C-H) [1,5,6] were also observed to

decrease significantly. Such results are in line with the release of gaseous/volatiles species determined by EGA experiments (**Figs. S3-5**). The presence of hydroxyl groups and physisorbed H₂O is indicated by the broad bands in the 3500-3000 cm⁻¹ (νOH) [5,7-9] and 1650 cm⁻¹ (H₂O bending) regions [10]. Vibrational bands of sp³ C-H_{2,3} stretching at 3100-2700 cm⁻¹ and bending at 1480, 1370, 1310 and 1240 cm⁻¹ were observed [6,7,11]. The sharp bands at 1580 and 1180 cm⁻¹ suggest the presence of N-heteroaromatic rings derived from PT groups [12,13], indicated as ν("PT") in **Figure S13**. The bands at 900-650 cm⁻¹ can be attributed to out-of-plane bending of aromatic C-H [6,7,11]. At 570 °C, the intensity of IR bands increased in the region related to the stretching modes of C-N (1300-1000 cm⁻¹) [10,14] and C-O/C-O-C (1200-1000 cm⁻¹) [6,8,9]. However, such modifications occurred in a minor extension for Na₃Fol, which corroborate with the high release of CO₂ and NO gases during the pyrolysis (**Figs. S3-S5**). In addition, the presence of bands attributed to Na₂CO₃ and NaNCO inorganic compounds (**Fig. S13-14**) were noticed for both salts, confirming the XRD results (see **Fig. S10**).

2.2.5. Raman spectroscopic data of pyrolyzed FA and sodium folate salts

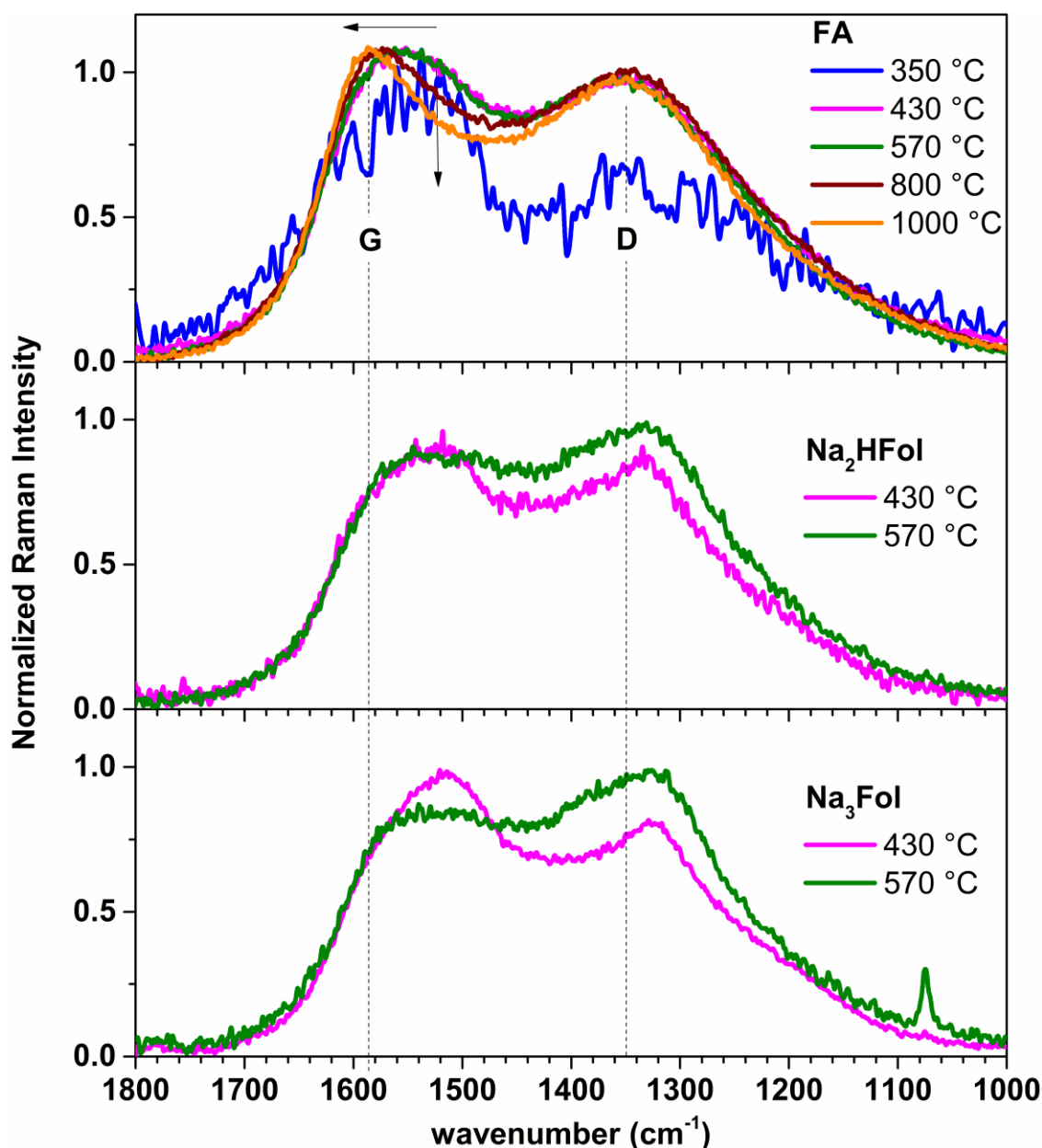


Figure S15. Normalized and baseline corrected Raman of FA pyrolyzed from 430 to 1000°C. The G band is attributed to in-plane bond-stretching motion (E_{2g} symmetry) of C=C groups, both in aromatic rings and chains [6,14–21]. The D band is attributed to the aromatic ring breathing mode (A_{1g} symmetry) and, differently of G band, its intensity raise is dependent of the presence of clusters containing at least sixfold fused rings [6,14–21]. It is also related with defects and disorder in carbonic structure, such as turbostratic stacking, edges in micro/nanocrystalline domains, doping and vacancies in the layer [6,14–21].

Table S2. Values of D and G band position and FWHM (cm^{-1}), $I(\text{D})/I(\text{G})$ and $A(\text{D})/A(\text{G})$ ratios taken from Raman analysis of pyrolyzed materials.

Sample	Pyrolysis temperature ($^{\circ}\text{C}$)	G band		D band		$I(\text{D})/I(\text{G})$	$A(\text{D})/A(\text{G})$
		ν (cm^{-1})	FWHM (cm^{-1})	ν (cm^{-1})	FWHM (cm^{-1})		
FA	350	1558	166	1318	242	0.64	0.91
	430	1568	137	1360	296	1.14	2.48
	570	1570	135	1364	292	1.14	2.46
	800	1579	123	1364	308	1.19	3.00
	100	1584	111	1369	301	1.13	3.09
Na ₂ HFol	430	1551	144	1352	241	1.03	1.72
	570	1555	142	1355	260	1.37	2.53
Na ₃ Fol	430	1538	144	1341	244	0.88	1.48
	570	1532	138	1352	246	1.38	2.48

FWHM = *full width at half maximum*; I = band intensity; A = band area

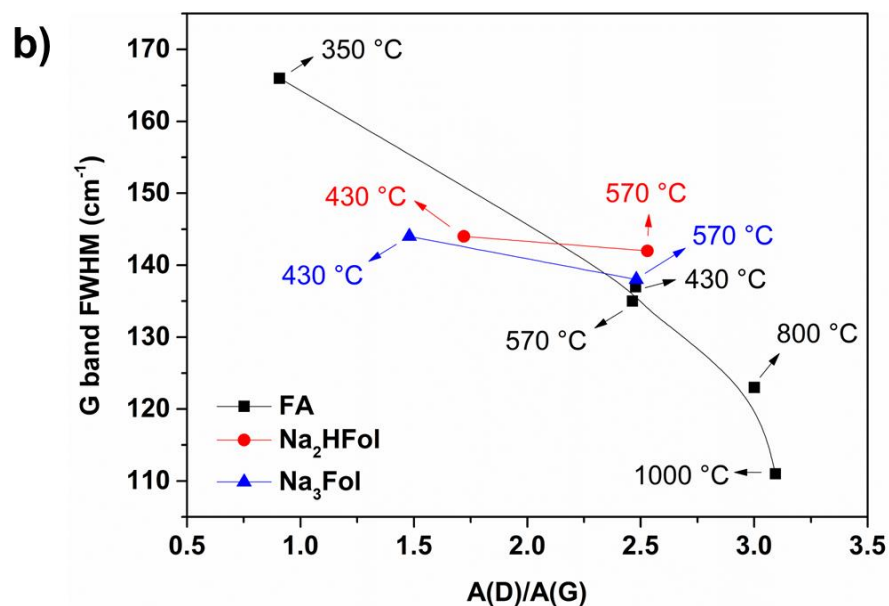
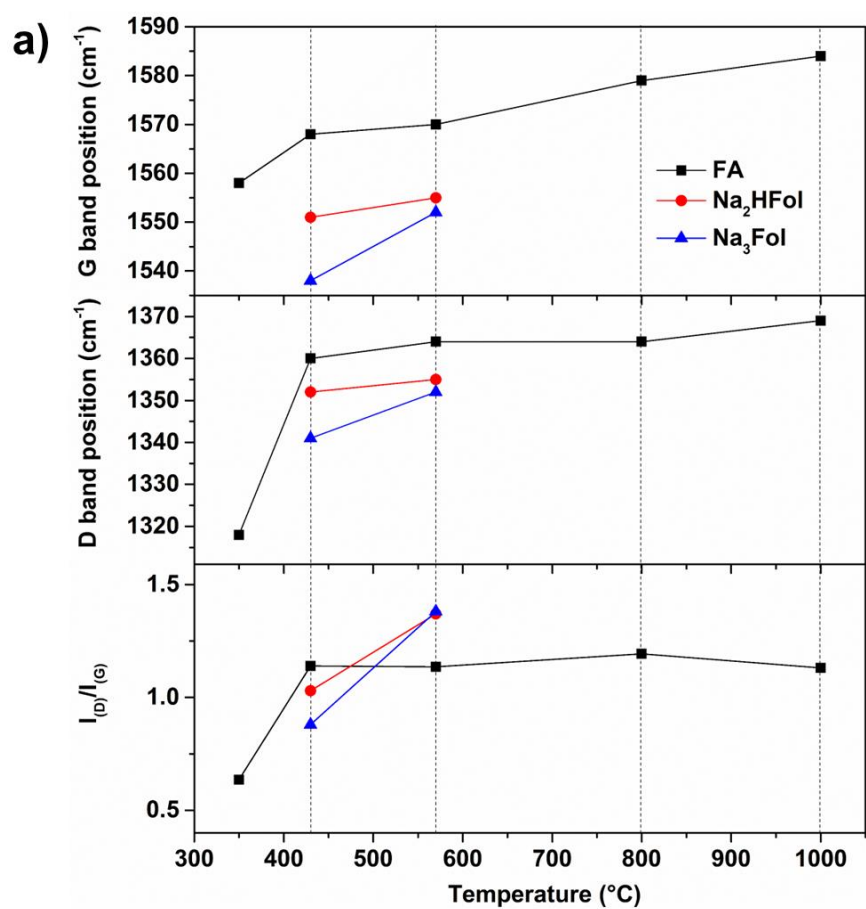


Figure S16. (a) Variation of G and D band position and I(D)/I(G) ratio with the temperature of pyrolysis and (b) FWHM of G band as a function of A(D)/A(G) ratio.

2.2.6. XPS data of pyrolyzed FA

Follow a discussion about XPS spectra shown in **Fig. 8** (main text). In the C1s spectra of FA pyrolyzed samples were identified peaks attributed to groups of C–C(five membered rings)/C–H (283.3-284.0 eV), C=C/C≡N (284.3-284.7 eV), C–C(rings with more than 7 atoms)/C=N(pyridinic)/C–N(Pyrrolic) (285.1-285.5 eV), C–O/Csp³–N/C–N=O (285.9-286.4 eV), C=O (286.9-287.5 eV), COO/CN₃/CON₂ (288.4-288.9 eV) and satellite π – π^* (about 291.0 eV) [6,22]. The presence of oxygenated and hydrogenated groups challenge the accurate interpretation of N1s XPS spectra [23]. Hence, the peak deconvolution/attribution was made in a simplified manner as follow: -C≡N (about 397.6 eV), N-pyridine (397.8-398.8 eV), NH/NH₂ (398.7-399.9 eV), N-amide/NR₃ (399.6-399.9 eV), N-pyrrole (399.9-400.7 eV), N-graphitic (400.8-401.8 eV) and N-oxide (> 402.2 eV) [6,22]. O1s peaks were attributed as C=O (530.7-531.6 eV), C–O (ether or C–OH bonded to aliphatic group/C–O linked to C–N in hexagonal ring; 532.0-532.9 eV), C–O (ether or C–OH bonded to aromatic group/in penta and hexa rings; 532.9-533.4 eV), N-oxide (534.0-534.8 eV) and physisorbed H₂O (534.8-535.2 eV) [6,22,24].

Table S3. Peak positions (eV), full width half maximum (FWHM) and peak composition (integrated area in percentage) after XPS data deconvolution of pyrolyzed FA samples from 350 °C to 1000 °C.

Assignment*	350 °C			570 °C			800 °C			1000 °C		
	Peak centre	FWHM	Area (%)	Peak centre	FWHM	Area (%)	Peak centre	FWHM	Area (%)	Peak centre	FWHM	Area (%)
C1s												
C-C _{low} /C-H	283.8	1.5	11.4	283.3	1.7	6.4	283.3	1.6	18.0	283.3	1.6	4.0
C=C/Nitrile	284.6	1.4	34.4	284.7	1.3	44.6	284.5	1.7	52.9	284.7	1.3	59.2
C-C _{high} /C=N/C-N	285.5	1.5	27.7	285.5	1.2	21.7	285.6	1.3	9.8	285.7	1.3	10.9
C-O/C-N=O/Csp ³ -N	286.6	1.3	9.4	286.4	1.3	12.8	286.4	1.5	8.9	286.3	1.5	12.3
C=O	287.8	1.5	7.5	287.4	1.6	6.9	287.4	1.6	5.7	287.5	1.5	5.7
COO	288.9	1.6	8.4	288.8	1.6	5.3	288.8	1.5	3.1	288.8	1.6	4.7
π - π *	290.7	1.7	1.1	291.0	2.5	2.4	290.7	2.5	1.6	291.1	3.0	3.2
N1s												
Nitrile	397.5	1.4	5.5	397.6	1.2	4.1	397.5	1.6	17.1	397.6	1.2	5.7
Pyridinic	398.5	1.6	40.7	398.4	1.4	31.0	398.4	1.4	29.4	398.3	1.3	23.6
Amidic/NR ₃	399.3	1.4	14.3	399.1	1.2	13.4	399.2	1.2	12.5	399.1	1.2	8.9
NH/NH ₂	399.8	1.4	23.7	399.7	1.3	2.5	399.8	1.4	5.2	399.7	1.2	5.1
Pyrrolic	400.4	1.3	8.8	400.4	1.4	13.0	400.1	1.4	13.5	400.3	1.2	6.9
Graphitic	400.9	1.3	5.7	401.2	1.6	26.2	400.9	1.7	16.6	401.1	1.5	37.9
N-oxide	402.2	1.8	1.3	403.1	1.8	4.9	402.7	1.7	4.2	402.7	1.4	9.1
	--	--	--	404.9	1.4	4.9	404.4	1.7	1.6	404.1	1.3	2.8
O1s												
C=O	531.5	2.2	35.7	530.9	2.2	25.6	530.8	2.0	32.3	531.2	2.3	34.0
C-O (aromatic)	532.2	2.0	29.9	532.0	1.3	38.1	532.0	1.6	39.6	532.1	1.2	29.3
C-O (aliphatic)	533.5	1.9	32.4	532.9	1.4	25.6	532.9	1.6	19.2	533.1	1.6	28.9
N-oxide	534.4	1.2	0.7	534.0	1.2	9.3	534.0	1.7	8.9	534.0	1.6	7.9
H ₂ O	535.2	1.3	1.3	535.2	1.2	1.5	--	--	--	--	--	--

*According to references [6,22,24]; C-C_{low}: five membered rings; C-C_{high}: seven or more membered ring.

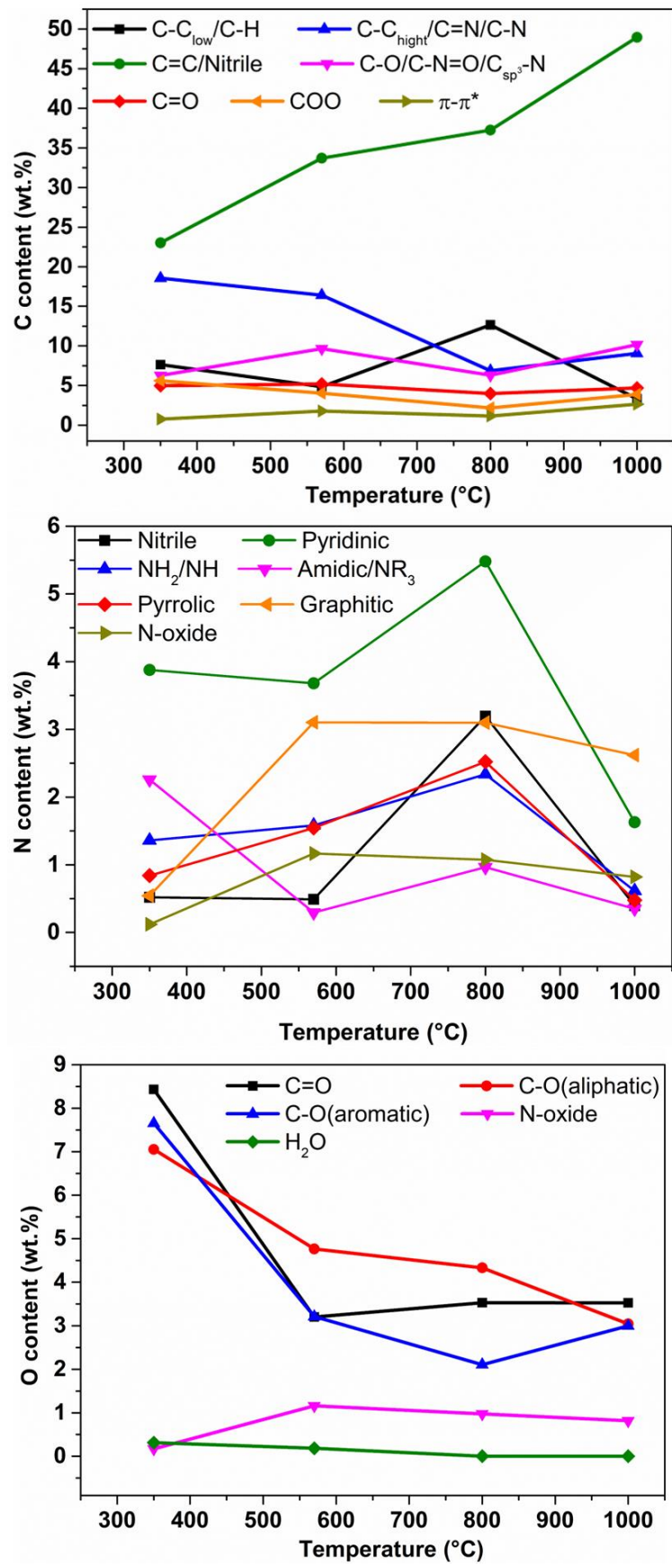
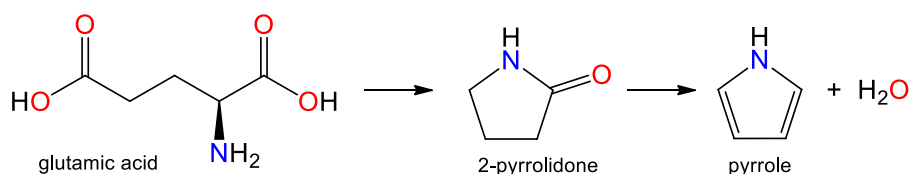


Figure S17. Relative amount of C-, N- and O-containing groups in relation to FA pyrolysis temperature according to XPS data.

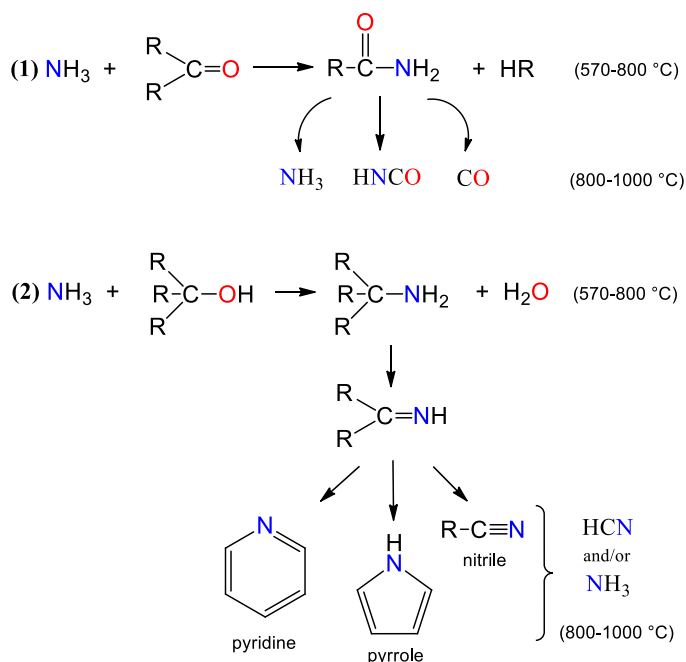
2.3. FA pyrolytic mechanism

Table S4. Common gaseous product released during pyrolysis of organic species and mainly functional group or molecule of origin.

Gaseous Product	Related functional group or molecule	Ref.
H ₂ O	H ₂ O (hydration); C–OH; COOH; R–O; R–H	[25]
CO	C=O; C–O–C	[25]
CO ₂	C=O; COOH/COO ⁻ ; C–O–C; C–O–C=O	[25]
C _x H _y	Alkyl structures	[25]
NO	HNCO	[25]
NH ₃	–NH ₂ ; pyridinic–N	[25]
HCN	pyridinic–N; –C≡N	[25,26]
HNCO	H–N–C=O (amide group)	[25]
2-pyrrolidone	Glutamic acid	[27,28]
aniline	<i>p</i> -aminobenzoic acid	[29]



Scheme S1. Simplified representation of the mechanism related to the formation of pyrrole from 2-pyrrolidone, based on Kibet et al. [27]. Only the main products are indicated.



Scheme S2. Simplified representation of the mechanism related to the reforming of NH₃ and possible species formed with the temperature increase, based on the works of Chen et al. [30] and Tian et al. [31]. Only the main products are indicated.

2.4. Sodium folate salts pyrolytic mechanism

Thermal analysis coupled to FTIR and MS as well as the char analysis (FTIR and Raman) showed that the pyrolysis mechanism of sodium folate salts (Na_2HFol and Na_3Fol) was significantly modified in relation to FA counterpart, implying that the level of protonation of folate and the presence of a metal cation exert an important role during carbonization process. According to literature [32–37], alkaline-metal ions can catalyse the ring-opening and depolymerization reactions, favouring the production of low-weight volatile molecules. Alkali-metal seems to promote dehydration, deoxygenation and denitrogenating reactions [32–37]. Theoretical calculations suggest that Na^+ can weakened the strength of the C-O, C-C and C-N bonds by direct or indirect interaction (adjacent bond interaction) with them, what can enhance the reactivity of such groups and/ or the cracking of char [32,35,38]. In comparison with FA, it was observed the increase in the release of H_2O , aniline, 2-pyrrolidone and aliphatic molecules up to 430 °C (**Figs. S4-S5**) and in the hindrance of organized graphitic-like structure formation (Raman and FTIR results). In addition, the enhancement of deoxygenation/dehydrogenation reaction using Na_2HFol as precursor occurred mainly by the release of CO and NH_3 whereas Na_3Fol pyrolysis favoured CO_2 and NO production. Such results imply that either the level of the organic anion protonation and/or the Na^+ amount can change the reaction pathway.

The residual mass of folate sodium salts at 1000 °C was much lower (**Fig. 2**) than what one expected considering the sodium percentage in Na_2HFol (8.67 wt.%) and Na_3Fol (12.29 wt.%). Besides, the residual mass is much lower than FA residue even though the XRD results showed that during the pyrolysis of folate sodium salts occurred the formation of inorganic compounds, such as Na_2CO_3 and NaNCO , for instance. Thus, elemental sodium as well as carbonaceous material can be lost during the pyrolysis of folate sodium salts. Three possibilities of mass loss can be proposed: (i) Na^+ can be volatilized attached to oxygenated groups (*i.e.*; $-\text{COO}^-\text{Na}^+$), as reported by Quyn et al. [39]; (ii) redox reaction converting graphitic carbon in

gaseous CO (spontaneous reaction according to the Ellingham diagram [40] above 800 °C), as represented in equation 1 [41,42], or (ii) carbothermic reaction (above 850 °C) leading to the volatilization of metallic sodium, as represented in equations 2-4 [41,42].



2.5 Analysis of C-dots extracted from pyrolyzed FA and folate sodium salts

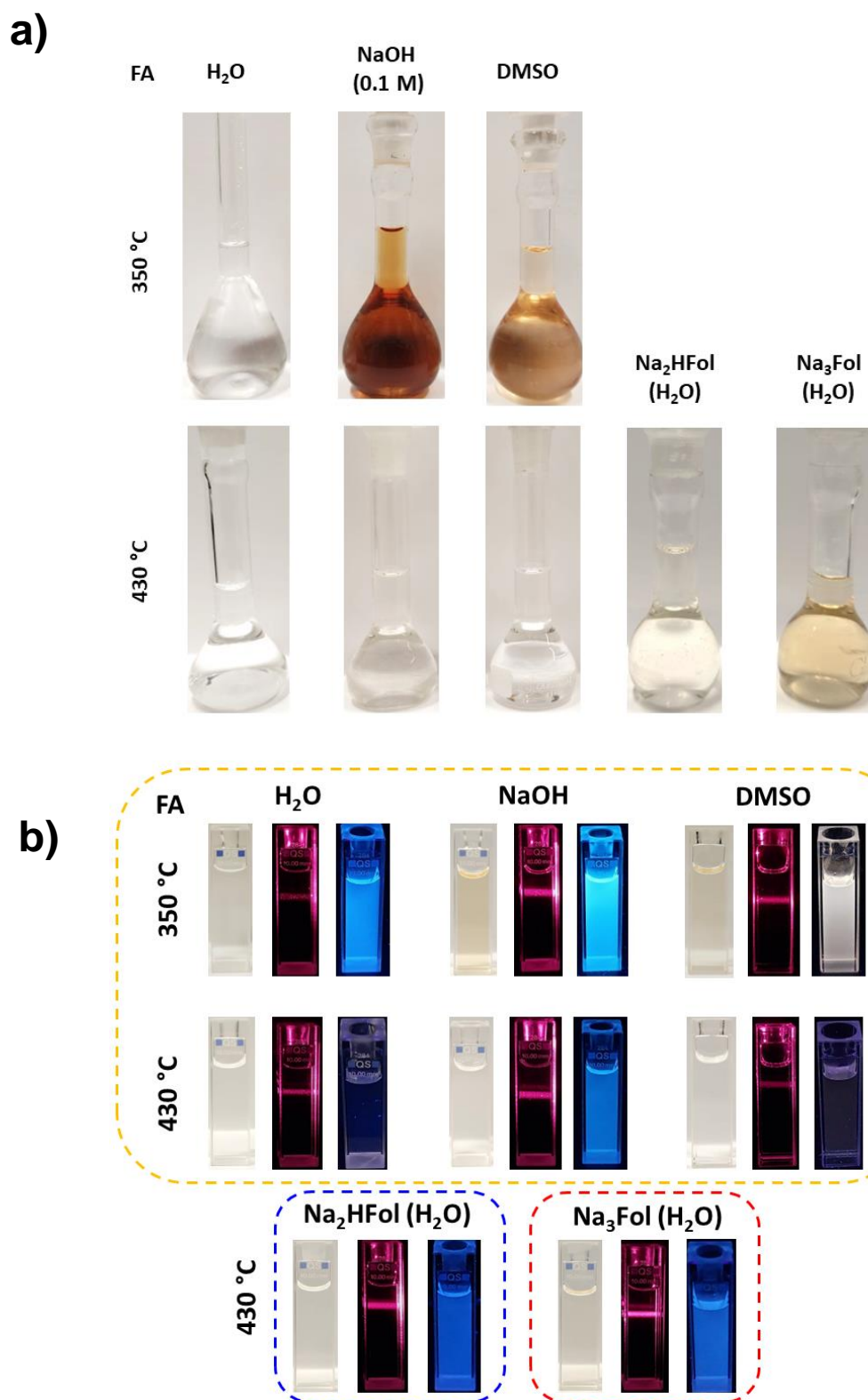


Figure S18. Photographs of (a) C-dots suspension after extraction and (b) diluted suspensions under daylight (right), Tyndall effect (middle) and under 365 nm UV lamp (left) obtained from pyrolysis of FA and its sodium salts at 350°C and 430°C.

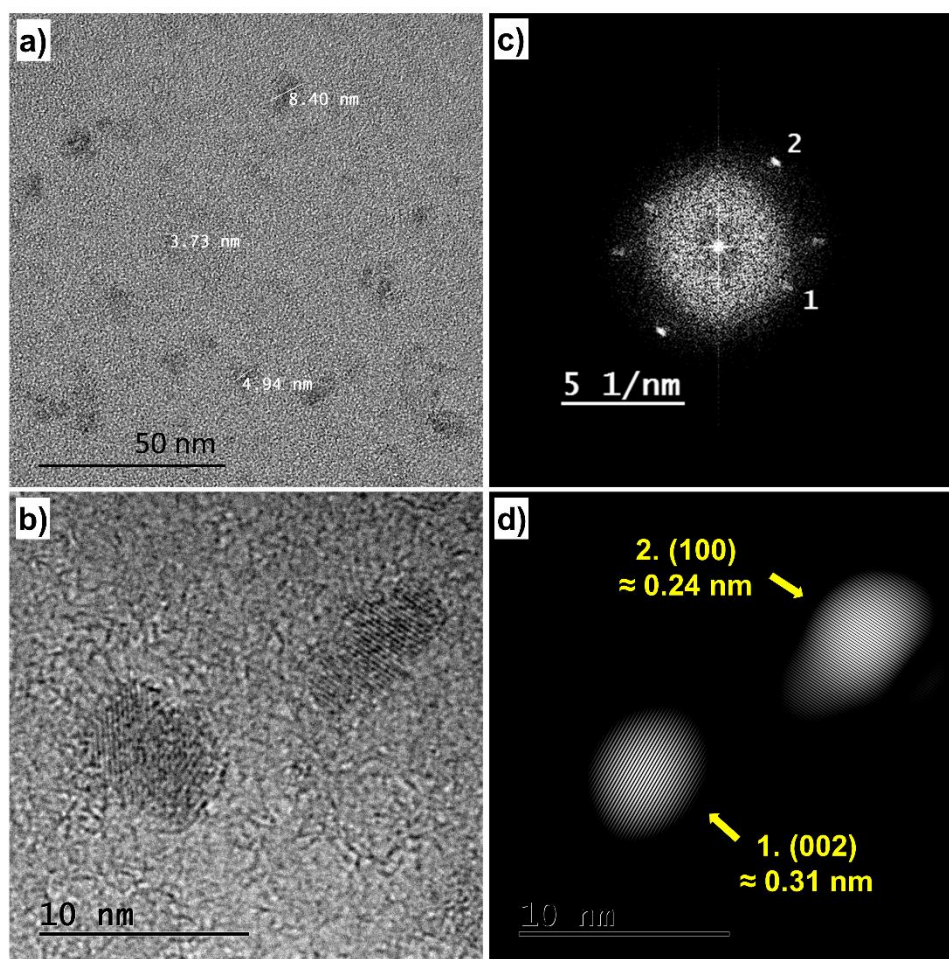


Figure S19. (a,b) TEM image of C-dots obtained from FA (350 °C) and extracted in DMSO; (c) fast-Fourier-transform (FFT) pattern of corresponding C-dots depicted in (b) showing the spots related to (002) and (100) planes; (d) Inverse FFT filtering from (002) and (100) reflections producing their correspondent false dark field images.

Table S5. Zeta Potential vales of C-dots particles extracted with H₂O.

Precursor	Pyrolysis temperature (°C)	Zeta potential (mV)
FA	350	-20±4
FA	430	-15±7
Na ₂ HFol	430	-20±1
Na ₃ Fol	430	-30±2

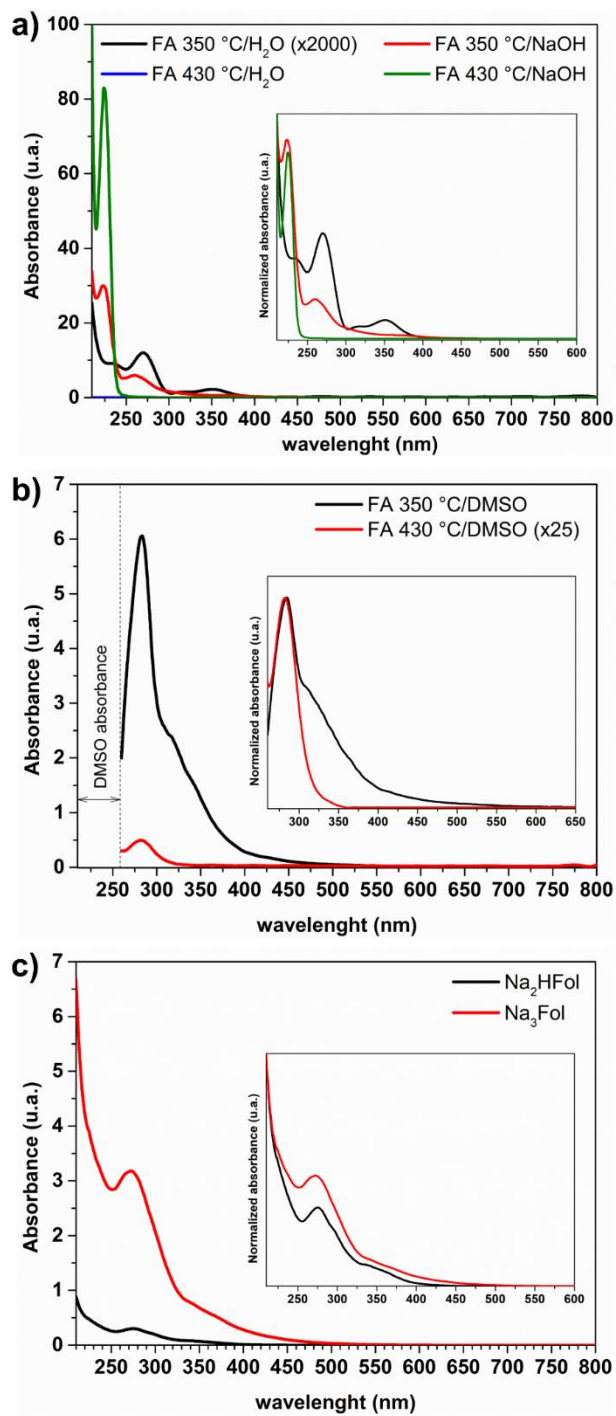


Figure S20. Electronic UV-VIS spectra of C-dots particles extracted with water, NaOH solution or DMSO as indicated.

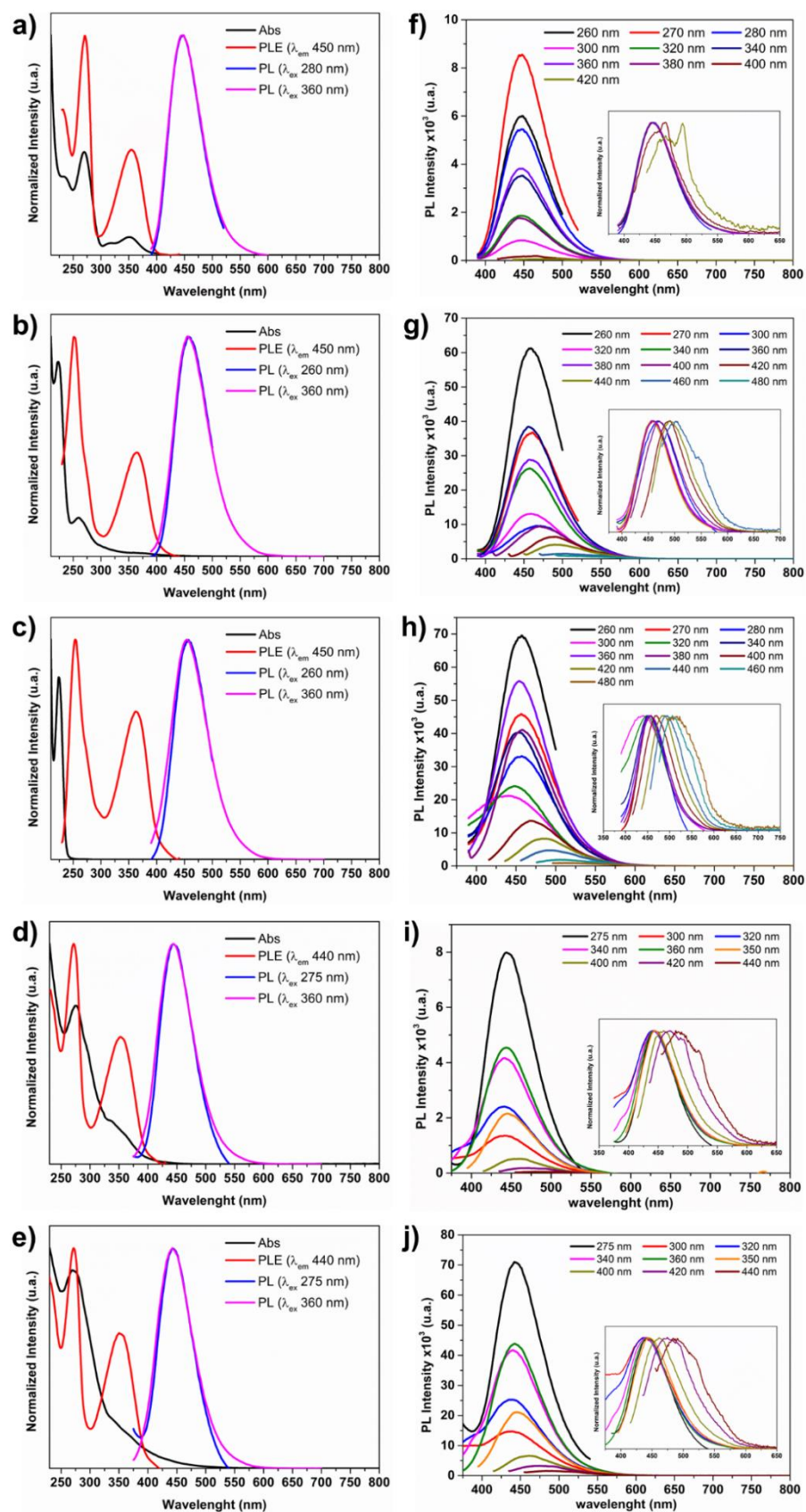


Figure S21. (a-e) Electronic UV-VIS, PL excitation (PL) and PL emission (PLE) spectra; (f-j) PL emission spectra of C-dots dispersions varying the excitation wavelength: (a,f) FA (350 °C)/H₂O; (b,g) FA (350 °C)/NaOH; (c,h) FA (430 °C)/NaOH; (d,i) Na₂HFol (430 °C)/H₂O; and (e,j) Na₃Fol (430 °C)/H₂O.

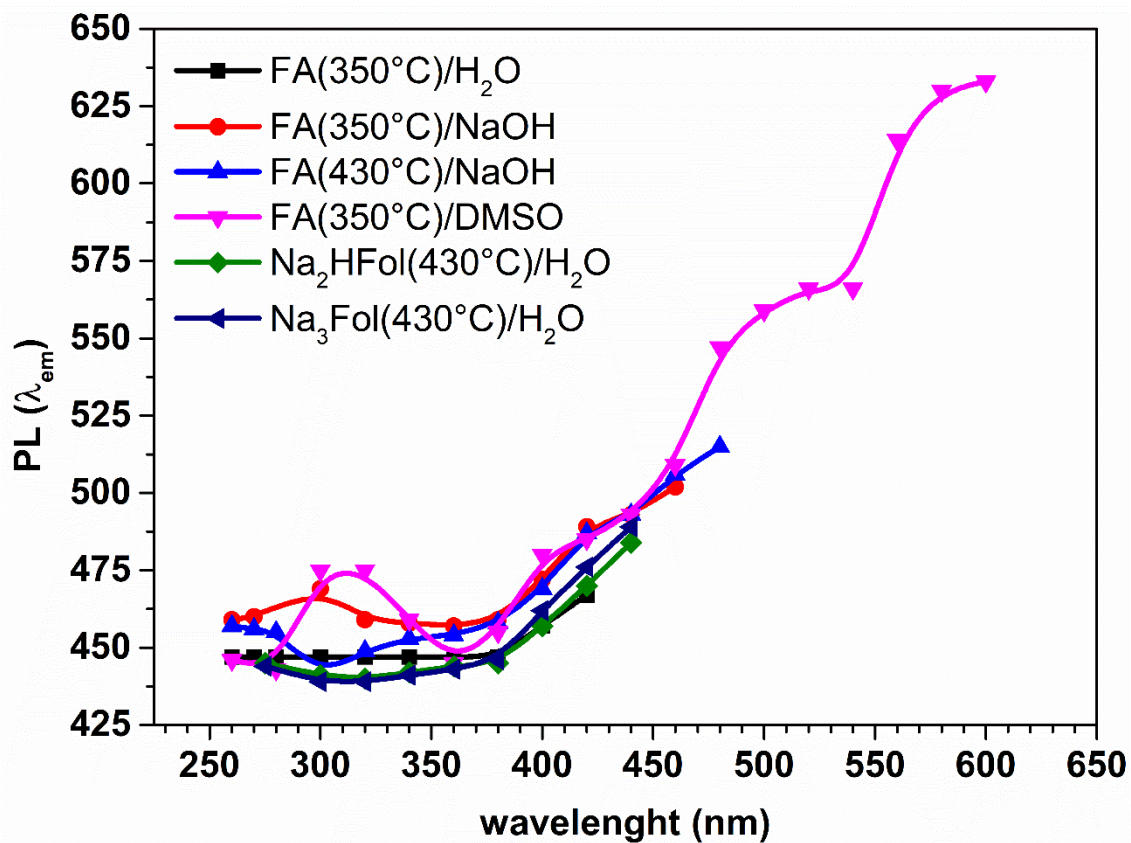


Figure S22. Wavelength dependence of the maximum of PL emission as a function of the excitation wavelength.

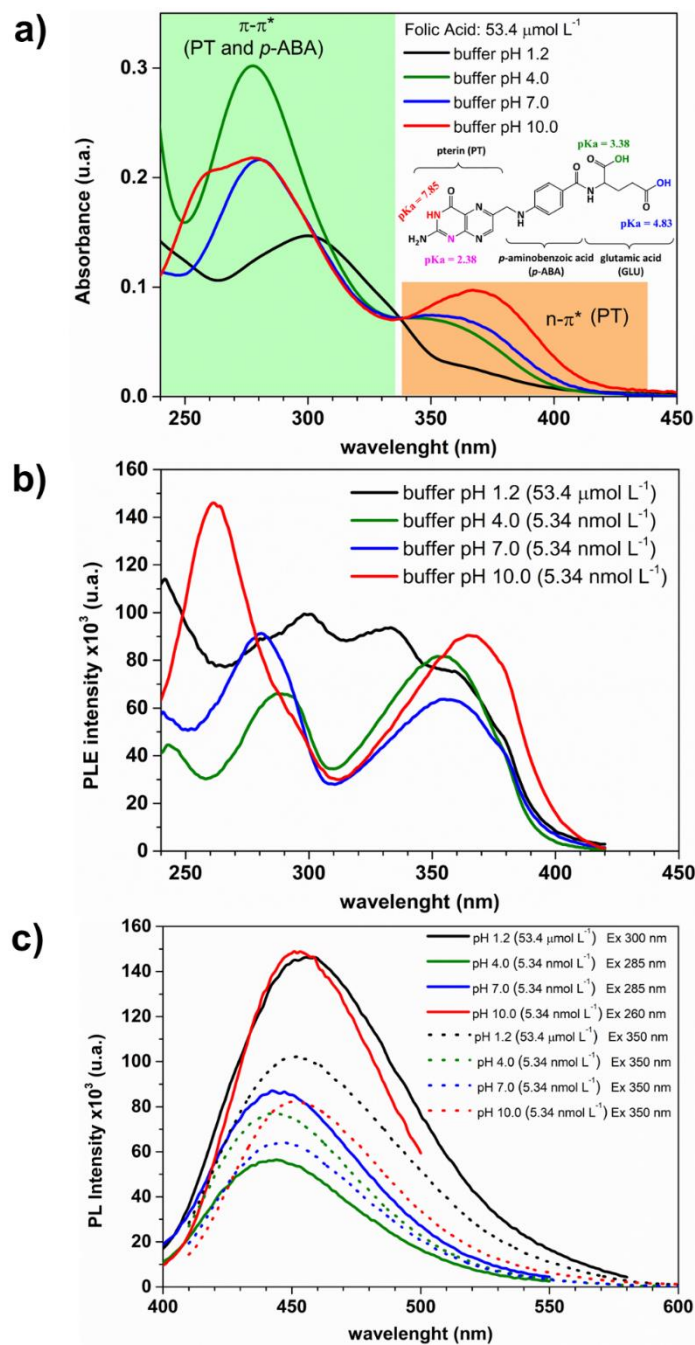


Figure S23. (a) UV-VIS absorption, (b) Photoluminescence excitation (PLE) and (c) Photoluminescence emission spectra of FA in buffer solutions with different pH values. The FA saturated solution of $0.1068 \text{ mmol L}^{-1}$ was diluted ($53.4 \mu\text{mol L}^{-1}$ or 5.34 nmol L^{-1}) in buffer solutions with pH values of 1.2, 4.0, 7.0 and 10.0. The optical properties of FA change with the variation of pH value of solution that leads to PT moiety protonation (cationic in buffer solution of pH 1.2 and neutral in pH 4.0 and 7.0) or deprotonation (anionic in buffer solution of pH 10.0). The Fluorescence intensity is increased around 10.000 times (in FA concentration) changing pH value from 1.2 to 10.0.

3. References

- [1] V.R. Magri, M.A. Rocha, C.S. de Matos, P.A.D. Petersen, F. Leroux, H.M. Petrilli, V.R.L. Constantino, Folic acid and sodium folate salts: Thermal behavior and spectroscopic (IR, Raman, and solid-state ^{13}C NMR) characterization, *Spectrochim. Acta Part A Mol. Biomol. Spectrosc.* 273 (2022) 120981. <https://doi.org/10.1016/j.saa.2022.120981>.
- [2] P.J. Linstrom and W.G. Mallard, Eds., NIST Chemistry WebBook, NIST Standard Reference Database Number 69, National Institute of Standards and Technology, Gaithersburg MD, 20899, <https://doi.org/10.18434/T4D303>
- [3] I.E. Gordon, L.S. Rothman, R.J. Hargreaves, R. Hashemi, et al., The HITRAN2020 molecular spectroscopic database, *J. Quant. Spectrosc. Radiat. Transf.* 277 (2022) 107949. <https://doi.org/10.1016/j.jqsrt.2021.107949>.
- [4] D. Braga, L. Chelazzi, F. Grepioni, L. Maschio, S. Nanna, P. Taddei, Folic Acid in the Solid State: A Synergistic Computational, Spectroscopic, and Structural Approach, *Cryst. Growth Des.* 16 (2016) 2218–2224. <https://doi.org/10.1021/acs.cgd.6b00043>.
- [5] N.B. Colthup, L.H. Daly, S.E. Wiberley, *Introduction to Infrared and Raman Spectroscopy*, 3rd ed., Academic Press, 1990. <https://doi.org/10.1016/C2009-0-21628-X>.
- [6] T. Kato, Y. Yamada, Y. Nishikawa, H. Ishikawa, S. Sato, Carbonization mechanisms of polyimide: Methodology to analyze carbon materials with nitrogen, oxygen, pentagons, and heptagons, *Carbon N. Y.* 178 (2021) 58–80. <https://doi.org/10.1016/j.carbon.2021.02.090>.
- [7] X. Cui, H. Yan, P. Zhao, Y. Yang, Y. Xie, Modeling of molecular and properties of anthracite base on structural accuracy identification methods, *J. Mol. Struct.* 1183 (2019) 313–323. <https://doi.org/10.1016/j.molstruc.2019.01.092>.
- [8] M. Acik, G. Lee, C. Mattevi, M. Chhowalla, K. Cho, Y.J. Chabal, Unusual infrared-absorption mechanism in thermally reduced graphene oxide, *Nat. Mater.* 9 (2010) 840–845. <https://doi.org/10.1038/nmat2858>.
- [9] E. Fuente, J.A. Menéndez, M.A. Díez, D. Suárez, M.A. Montes-Morán, Infrared spectroscopy of carbon materials: A quantum chemical study of model compounds, *J. Phys. Chem. B.* 107 (2003) 6350–6359. <https://doi.org/10.1021/jp027482g>.
- [10] S.E. Rodil, Infrared spectra of amorphous carbon based materials, *Diam. Relat. Mater.* 14 (2005) 1262–1269. <https://doi.org/10.1016/j.diamond.2005.01.044>.
- [11] S. Kanazawa, Y. Yamada, S. Sato, Infrared spectroscopy of graphene nanoribbons and aromatic compounds with $\text{sp}^3\text{C-H}$ (methyl or methylene groups), *J. Mater. Sci.* 56 (2021) 12285–12314. <https://doi.org/10.1007/s10853-021-06001-1>.
- [12] S. Breda, I.D. Reva, L. Lapinski, M.J. Nowak, R. Fausto, Infrared spectra of pyrazine, pyrimidine and pyridazine in solid argon, *J. Mol. Struct.* 786 (2006) 193–206. <https://doi.org/10.1016/j.molstruc.2005.09.010>.
- [13] H. Schmiers, J. Friebel, P. Streubel, R. Hesse, R. Köpsel, Change of chemical bonding of nitrogen of polymeric N-heterocyclic compounds during pyrolysis, *Carbon N. Y.* 37 (1999) 1965–1978. [https://doi.org/10.1016/S0008-6223\(99\)00071-8](https://doi.org/10.1016/S0008-6223(99)00071-8).

- [14] A.C. Ferrari, S.E. Rodil, J. Robertson, Interpretation of infrared and Raman spectra of amorphous carbon nitrides, *Phys. Rev. B.* 67 (2003) 155306. <https://doi.org/10.1103/PhysRevB.67.155306>.
- [15] A.C. Ferrari, J. Robertson, Interpretation of Raman spectra of disordered and amorphous carbon, *Phys. Rev. B.* 61 (2000) 14095–14107. <https://doi.org/10.1103/PhysRevB.61.14095>.
- [16] A.C. Ferrari, D.M. Basko, Raman spectroscopy as a versatile tool for studying the properties of graphene, *Nat. Nanotechnol.* 8 (2013) 235–246. <https://doi.org/10.1038/nnano.2013.46>.
- [17] M.W. Smith, I. Dallmeyer, T.J. Johnson, C.S. Brauer, J.-S. McEwen, J.F. Espinal, M. Garcia-Perez, Structural analysis of char by Raman spectroscopy: Improving band assignments through computational calculations from first principles, *Carbon N. Y.* 100 (2016) 678–692. <https://doi.org/10.1016/j.carbon.2016.01.031>.
- [18] M. Ayiania, E. Weiss-Hortala, M. Smith, J.S. McEwen, M. Garcia-Perez, Microstructural analysis of nitrogen-doped char by Raman spectroscopy: Raman shift analysis from first principles, *Carbon N. Y.* 167 (2020) 559–574. <https://doi.org/10.1016/j.carbon.2020.05.055>.
- [19] P.K. Chu, L. Li, Characterization of amorphous and nanocrystalline carbon films, *Mater. Chem. Phys.* 96 (2006) 253–277. <https://doi.org/10.1016/j.matchemphys.2005.07.048>.
- [20] A.C. Ferrari, J. Robertson, Raman spectroscopy of amorphous, nanostructured, diamond-like carbon, and nanodiamond, *Philos. Trans. R. Soc. London. Ser. A Math. Phys. Eng. Sci.* 362 (2004) 2477–2512. <https://doi.org/10.1098/rsta.2004.1452>.
- [21] C. Casiraghi, A.C. Ferrari, J. Robertson, Raman spectroscopy of hydrogenated amorphous carbons, *Phys. Rev. B.* 72 (2005) 085401. <https://doi.org/10.1103/PhysRevB.72.085401>.
- [22] M. Ayiania, M. Smith, A.J.R. Hensley, L. Scudiero, J.-S. McEwen, M. Garcia-Perez, Deconvoluting the XPS spectra for nitrogen-doped chars: An analysis from first principles, *Carbon N. Y.* 162 (2020) 528–544. <https://doi.org/10.1016/j.carbon.2020.02.065>.
- [23] T. Kato, Y. Yamada, Y. Nishikawa, T. Otomo, H. Sato, S. Sato, Origins of peaks of graphitic and pyrrolic nitrogen in N1s X-ray photoelectron spectra of carbon materials: quaternary nitrogen, tertiary amine, or secondary amine?, *J. Mater. Sci.* 56 (2021) 15798–15811. <https://doi.org/10.1007/s10853-021-06283-5>.
- [24] M. Smith, L. Scudiero, J. Espinal, J.-S. McEwen, M. Garcia-Perez, Improving the deconvolution and interpretation of XPS spectra from chars by ab initio calculations, *Carbon N. Y.* 110 (2016) 155–171. <https://doi.org/10.1016/j.carbon.2016.09.012>.
- [25] G.S. Ghodake, S.K. Shinde, A.A. Kadam, R.G. Saratale, G.D. Saratale, M. Kumar, R.R. Palem, H.A. AL-Shwaiman, A.M. Elgorban, A. Syed, D.-Y. Kim, Review on biomass feedstocks, pyrolysis mechanism and physicochemical properties of biochar: State-of-the-art framework to speed up vision of circular bioeconomy, *J. Clean. Prod.* 297 (2021) 126645. <https://doi.org/10.1016/j.jclepro.2021.126645>.
- [26] L. Leng, S. Xu, R. Liu, T. Yu, X. Zhuo, S. Leng, Q. Xiong, H. Huang, Nitrogen containing functional groups of biochar: An overview, *Bioresour. Technol.* 298 (2019) 122286. <https://doi.org/10.1016/j.biortech.2019.122286>.

- [27] J.K. Kibet, L. Khachatryan, B. Dellinger, Molecular products from the thermal degradation of glutamic acid, *J. Agric. Food Chem.* 61 (2013) 7696–7704. <https://doi.org/10.1021/jf401846t>.
- [28] H. Chen, Y. Xie, W. Chen, M. Xia, K. Li, Z. Chen, Y. Chen, H. Yang, Investigation on co-pyrolysis of lignocellulosic biomass and amino acids using TG-FTIR and Py-GC/MS, *Energy Convers. Manag.* 196 (2019) 320–329. <https://doi.org/10.1016/j.enconman.2019.06.010>.
- [29] J.A. Teixeira, W.D.G. Nunes, A.L.C.S. do Nascimento, T.A.D. Colman, F.J. Caires, D.A. Gálico, M. Ionashiro, Synthesis, thermoanalytical, spectroscopic study and pyrolysis of solid rare earth complexes (Eu, Gd, Tb and Dy) with p-aminobenzoic acid, *J. Anal. Appl. Pyrolysis.* 121 (2016) 267–274. <https://doi.org/10.1016/j.jaap.2016.08.006>.
- [30] W. Chen, K. Li, M. Xia, Y. Chen, H. Yang, Z. Chen, X. Chen, H. Chen, Influence of NH₃ concentration on biomass nitrogen-enriched pyrolysis, *Bioresour. Technol.* 263 (2018) 350–357. <https://doi.org/10.1016/j.biortech.2018.05.025>.
- [31] Y. Tian, J. Zhang, W. Zuo, L. Chen, Y. Cui, T. Tan, Nitrogen Conversion in Relation to NH₃ and HCN during Microwave Pyrolysis of Sewage Sludge, *Environ. Sci. Technol.* 47 (2013) 3498–3505. <https://doi.org/10.1021/es304248j>.
- [32] X. Zhou, H.B. Mayes, L.J. Broadbelt, M.W. Nolte, B.H. Shanks, Fast pyrolysis of glucose-based carbohydrates with added NaCl part 1: Experiments and development of a mechanistic model, *AIChE J.* 62 (2016) 766–777. <https://doi.org/10.1002/aic.15106>.
- [33] S. Wang, G. Dai, H. Yang, Z. Luo, Lignocellulosic biomass pyrolysis mechanism: A state-of-the-art review, *Prog. Energy Combust. Sci.* 62 (2017) 33–86. <https://doi.org/10.1016/j.pecs.2017.05.004>.
- [34] E. Leng, Y. Guo, Y. Yin, Y. Yu, X. Gong, J. Chen, Y. Xue, J. E, In situ evolution of functional groups in char during cellulose pyrolysis under the catalysis of KCl and CaCl₂, *Fuel.* 309 (2022) 122227. <https://doi.org/10.1016/j.fuel.2021.122227>.
- [35] A. Saddawi, J.M. Jones, A. Williams, Influence of alkali metals on the kinetics of the thermal decomposition of biomass, *Fuel Process. Technol.* 104 (2012) 189–197. <https://doi.org/10.1016/j.fuproc.2012.05.014>.
- [36] S.G. Wabo, O. Klepel, Nitrogen release and pore formation through KOH activation of nitrogen-doped carbon materials: an evaluation of the literature, *Carbon Lett.* 31 (2021) 581–592. <https://doi.org/10.1007/s42823-021-00252-3>.
- [37] X. Guo, W. Zhang, L. Wang, J. Hao, Comparative study of nitrogen migration among the products from catalytic pyrolysis and gasification of waste rigid polyurethane foam, *J. Anal. Appl. Pyrolysis.* 120 (2016) 144–153. <https://doi.org/10.1016/j.jaap.2016.04.018>.
- [38] M. Dong, H. Wang, L. Xu, Y. Zou, B. Shen, X. Wang, J. Yang, DFT Study on the Effect of Na on NO Reduction with Nitrogen-Containing Char from Zhundong Coal, *J. Phys. Chem. A.* 126 (2022) 6148–6159. <https://doi.org/10.1021/acs.jpca.2c04565>.
- [39] D.M. Quyn, H. Wu, S.P. Bhattacharya, C.-Z. Li, Volatilisation and catalytic effects of alkali and alkaline earth metallic species during the pyrolysis and gasification of Victorian

brown coal. Part II. Effects of chemical form and valence, *Fuel*. 81 (2002) 151–158. [https://doi.org/10.1016/S0016-2361\(01\)00128-4](https://doi.org/10.1016/S0016-2361(01)00128-4).

[40] University of Cambridge, The interactive Ellingham diagram, https://www.doitpoms.ac.uk/tlplib/ellingham_diagrams/interactive.php, accessed 13 November 2022.

[41] J.-W. Kim, H.-G. Lee, Thermal and carbothermic decomposition of Na_2CO_3 and Li_2CO_3 , *Metall. Mater. Trans. B*. 32 (2001) 17–24. <https://doi.org/10.1007/s11663-001-0003-0>.

[42] G.B. Dunks, D. Stelman, S.J. Yosim, Graphite oxidation in molten sodium carbonate, *Carbon* N. Y. 18 (1980) 365–370. [https://doi.org/10.1016/0008-6223\(80\)90008-1](https://doi.org/10.1016/0008-6223(80)90008-1).

Supporting Information material of Chapter 5

Supporting Information for Applied Clay Science

Hybrid nanomaterials based on Folic Acid intercalated into M^{2+}/Al^{3+} ($M^{2+} = Mg^{2+}$ and Zn^{2+}) Layered Double Hydroxides as precursors of Carbon-based nanocomposites

Vagner R. Magri,^a Caroline S. de Matos^a, Michele A. Rocha^a, Rafael Macedo^b, Christine Taviot-Gueho^{cd} and Vera R.L. Constantino^{*a}

^aDepartamento de Química Fundamental, Instituto de Química, Universidade de São Paulo, CEP 05513-970, São Paulo, SP, Brazil. E-mail: vrlconst@iq.usp.br

^b Escola Politécnica da Universidade de São Paulo - Departamento de Engenharia de Minas e de Petróleo, Laboratório de Caracterização Tecnológica, CEP 05508-030, São Paulo, SP, Brazil

^cUniversité Clermont Auvergne, Université Blaise Pascal, Institut de Chimie de Clermont-Ferrand, BP 10448, F-63000 Clermont-Ferrand, France

^dCNRS, UMR 6296, ICCF, F-63178 Aubiere, France

1. Experimental

1.1. Chemicals

Magnesium chloride hexahydrate ($\text{MgCl}_2 \cdot 6\text{H}_2\text{O}$; 99%) was purchase from Merck. Folic acid di-hydrated (FA; $\text{C}_{19}\text{H}_{19}\text{N}_7\text{O}_6 \cdot 2\text{H}_2\text{O}$; $\geq 97\%$), zinc chloride anhydrous (ZnCl_2 ; $\geq 98\%$), aluminium chloride hexahydrate ($\text{AlCl}_3 \cdot 6\text{H}_2\text{O}$; 99%) and sodium hydroxide (NaOH ; $\geq 98\%$) were acquired from Sigma-Aldrich. The reagents were used without any further purification and deionized water (18 M Ω Milli-Q[®], Millipore system) was used in all experiments.

1.2. Synthesis of the layered double hydroxide (LDH)

The synthesis of LDH hybrid materials were performed based on previously work (Cunha et al., 2012, 2020; Rocha et al., 2016), with some modifications. The intercalation of divalent folate anion (HFol^{2-}) into Zn/Al-LDH was performed at constant pH value in a sealed system under N_2 atmosphere. In detail, an aqueous solution containing 16.67 mmol of ZnCl_2 and 8.33 mmol of $\text{AlCl}_3 \cdot 6\text{H}_2\text{O}$ (*ca.* 0.1 mol L^{-1}) were dropwise in an aqueous solution containing 8.33 mmol of FA at pH value previously adjusted to 7.5 by the addition of NaOH aqueous solution (*ca.* 0.2 mol $\cdot \text{L}^{-1}$). The addition was carried out in a flow of nitrogen 0.5-0.6 mL $\cdot \text{min}^{-1}$ under vigorous mechanical stirring and at 60 ± 5 °C. The pH value of the medium was maintained constant by the concomitant addition of NaOH solution. After the complete addition of the metal cation solution, the system was kept at the same conditions (*i.e.*, 60 °C, mechanical stirring and N_2 atmosphere) for 24 h. The yellow solid precipitated was isolated and rinsed with deionized water by centrifugation (17 000 rpm during 5 min at 25 °C) until a negative chloride ion test (monitored by AgNO_3). The slurry was than dispersed in water, frozen under immersion in liquid nitrogen (-196 ° C) and dried by lyophilisation process for three days in a Thermo

Savant ModulyoD equipment (200 mPa and -50 °C). The intercalation of trivalent folate anion (Fol^{3-}) into Mg/Al-LDH was carried out by the same synthetic method reported above, but at pH value of 9.5 and using solutions containing 20.0 mmol of $\text{MgCl}_2 \cdot 6\text{H}_2\text{O}$ and 10.0 mmol of $\text{AlCl}_3 \cdot 6\text{H}_2\text{O}$ (ca. 0.1 mol L^{-1}) and 10.0 mmol of FA. For comparison purpose, a small scale synthesis was performed at pH value of 9.0, using 3.33 mmol of ZnCl_2 plus 1.67 mmol of $\text{AlCl}_3 \cdot 6\text{H}_2\text{O}$ (ca. 0.1 mol L^{-1}) and 1.67 mmol of FA.

Reference materials intercalated with chloride anion (Cl^-) were also synthesized. The Zn/Al-LDH was synthesized by the addition of a solution containing 17.3 mmol of ZnCl_2 and 8.67 mmol of $\text{AlCl}_3 \cdot 6\text{H}_2\text{O}$ (ca. 0.1 mol L^{-1} and Zn/Al molar ratio equal to 2) to 250 mL of deionized water with pH value previously adjusted to 7.5. The Mg/Al-LDH were synthesized using a solution containing 21.0 mmol of $\text{MgCl}_2 \cdot 6\text{H}_2\text{O}$ plus 10.5 mmol of $\text{AlCl}_3 \cdot 6\text{H}_2\text{O}$ (ca. 0.1 mol L^{-1}) added to 315 mL of deionized water which had its pH value previously adjusted to 9.5. Both syntheses were performed in a sealed system under N_2 atmosphere.

The isolated materials were abbreviated as LDH-FA, LDH-Cl or $\text{M}_R^{2+}\text{Al-A}$, where M^{2+} is the divalent cation (Mg or Zn), R represent the $\text{M}^{2+}/\text{Al}^{3+}$ nominal molar ratio, and A is the anion.

1.3. Characterization of LDH

1.3.1. Elemental Analysis

C, H and N elemental analyses were performed in a Perkin-Elmer model 2400 analyser and magnesium, zinc and aluminium metal contents were determined by inductively coupled plasma optical emission spectroscopy (ICP OES) on a Spectro Arcos spectrometer. Both analyses were carried out in triplicate at the Central Analítica of Instituto de Química da Universidade de São Paulo (CA-IQUSP).

The percentage of hydration water and residual mass was determined by thermal analysis in a compressed air atmosphere in a Netzsch thermoanalyzer, model STA 409 PC Luxx, coupled to a QMS 403C Aëolos MSD mass spectrometer, using the same parameters as indicated in the main text.

1.3.2. Vibrational spectroscopy

The charge of intercalated folate anion (*i.e.*, HFol²⁻ or Fol³⁻) was also evaluated by vibrational spectroscopy, based on previously described article (Magri et al., 2022). The FTIR-ATR analysis was carried out as described in the main text and Fourier transform Raman (FT-Raman) spectra were recorded on Bruker instrument, MultiRam model, equipped with Ge detector (cooled by liquid nitrogen) using excitation radiation of 1064 nm (Nd³⁺/YAG laser) and 100-200 mW of power on the sample, in the 3500–150 cm⁻¹ spectral range, with 4 cm⁻¹ of resolution and accumulating 1024 (or 2048) scans.

1.3.3. XRD analysis

X-ray diffraction (XRD) patterns of powdered samples were recorded in a Bruker D8 DISCOVER diffractometer (40 kV and 30 mA) with CuK α radiation ($\lambda = 0.15418$ nm) source and collected in the 3–70° (2 θ) range, with steps of 0.05°/2 θ and scan speed of 0.05°/3s.

1.4. Hydrothermal Carbonization

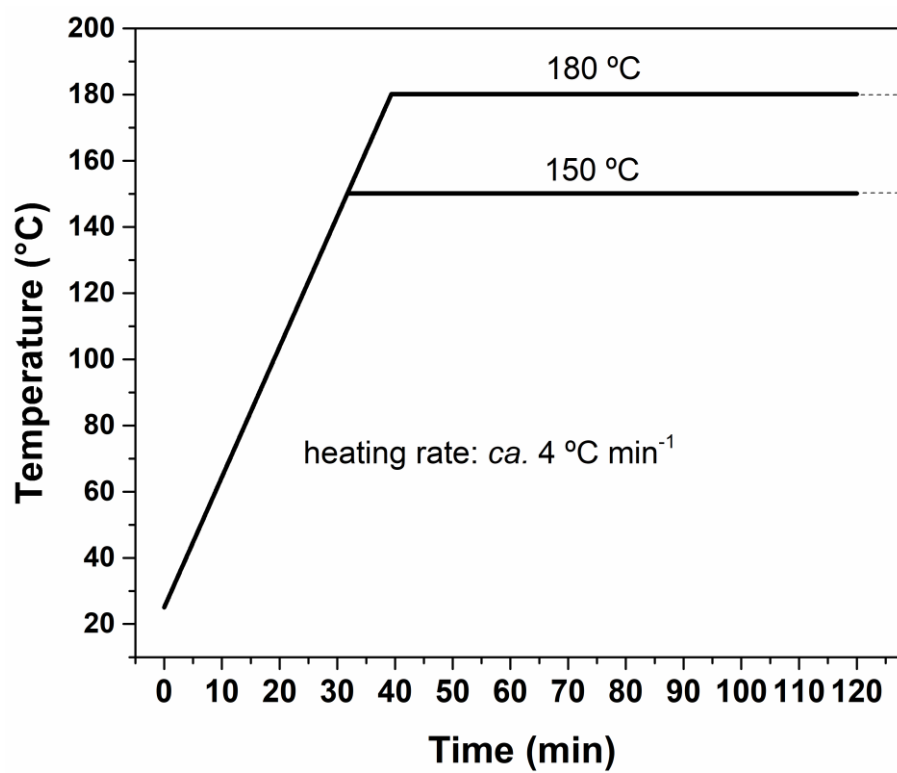


Figure S1. Heating ramp utilized to set up the oven in the hydrothermal carbonization experiments.

2. Results and discussion

2.1. Characterization of LDH-FA hybrid materials

For the interpretation of the results of hybrid materials characterization, it was considered that FA molecule has two carboxylic acid and one amidic group, tagged in **Figure 1b** of the main text as $C\alpha'OOH$ ($pK_{a2} = 3.38$), $C\gamma'OOH$ ($pK_{a2} = 4.83$) and $N3-H$ ($pK_{a3} = 7.85$), which could be deprotonated in the basic media of the syntheses (Szakács and Noszál, 2006). Accordingly, the anionic predominant species at pH value of synthesis of $Zn_2Al-HFol$ (pH 7.5) was $HFol^{2-}$, while for $Zn_2Al-Fol$ (pH 9.0) and $Mg_2Al-Fol$ (pH 9.5), the predominant specie was Fol^{3-} (**Figure S2**).

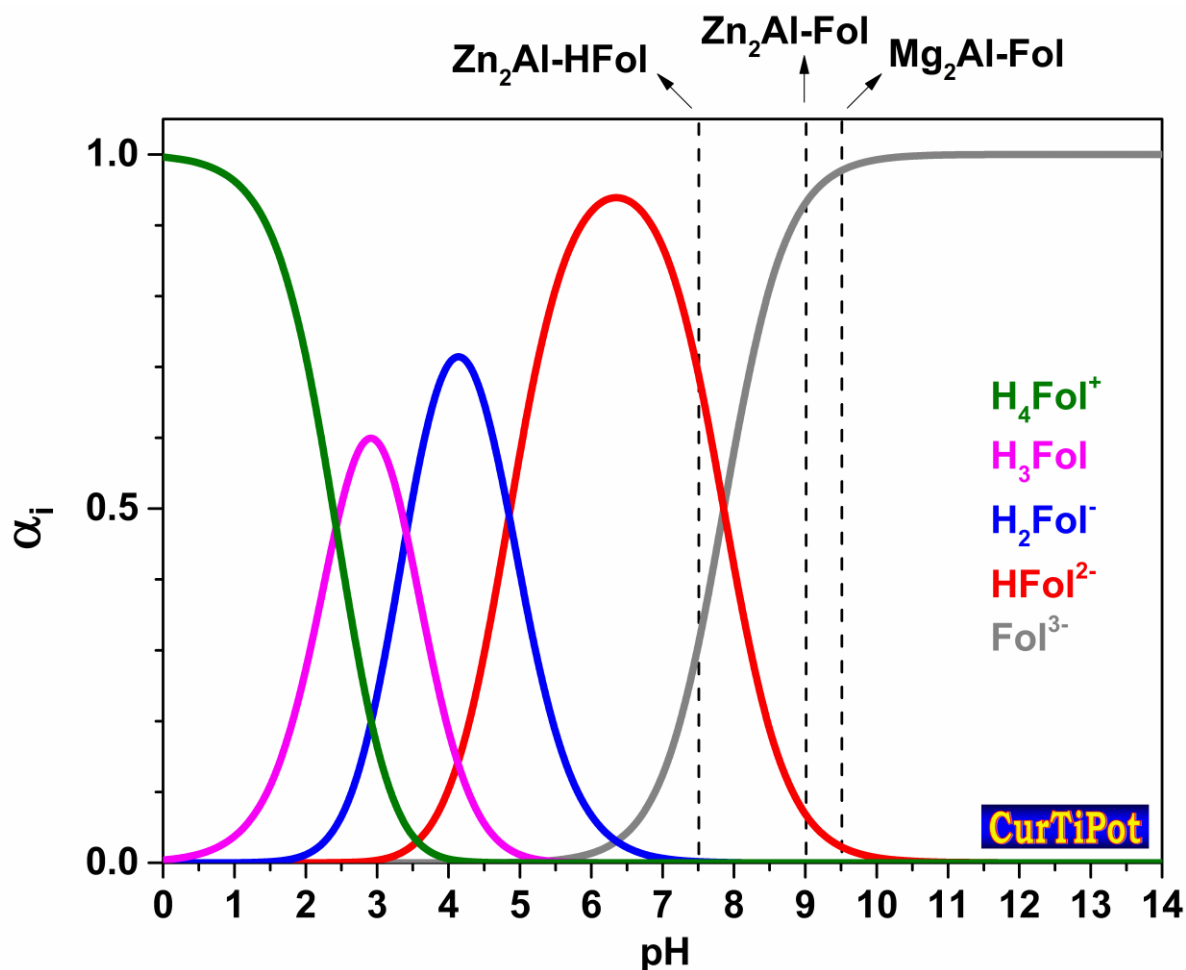


Figure S2. Folic acid speciation curves according to the apparent pKa values reported by (Szakács and Noszál, 2006).

2.1.1. XRD data

The XRD patterns of hybrid LDH-FA samples were typical of materials with LDH structure (**Figure S3a**). The diffraction peaks were indexed considering a hexagonal cell of rhombohedral symmetry (3R polytype) in R-3m space group. The interplanar spacings and lattice parameters calculated from XRD data are summarised in **Table S1**. The intercalation of folate anions in the interlayer space of LDH was confirmed by the displacement of the peaks attributed to the family of $00l$ planes (related to the basal spacing – d_{00l} ; **Figure S3a**) to lower 2θ values, in comparison with LDH-Cl counterpart (**Figure S3b** and **Table S2**).

The d_{00l} was increased from around 0.77 nm (for LDH-Cl) to around 2.56 nm, 1.66 nm and 1.61 nm for Zn_2Al -HFol (pH 7.5), Zn_2Al -Fol (pH 9.0) and Mg_2Al -Fol (pH 9.5), respectively. The d_{00l} value were tuneable according to the pH value of synthesis. Accordingly, $HFol^{2-}$ and Fol^{3-} were intercalated with different arrangements in the interlayer space of LDH matrices due to the speciation of FA in water (**Figure S2**). The crystallinity of materials was improved when increasing the pH from 7.5 to 9.0, as can be noticed from the better resolution of $00l$ diffraction lines observed in the diffractogram of Zn_2Al -Fol (**Figure S3**). Results from literature reported d_{00l} values varying around 1.60 nm and 1.82 nm for Mg_2Al -LDH materials synthesized by co-precipitation method at pH 10, in which Fol^{3-} is the dominant specie (**Figure 1**), and $R = 2$ (Qin et al., 2008; Mallakpour and Hatami, 2019). In this work, the result was in agreement with the 1.60 nm value previously reported by Qin et al. (2008). The works previously reported concerning Zn/Al-LDH synthesis (Arízaga et al., 2016; Arratia-Quijada et al., 2016) used ion-exchange method at pH 7-8 and $R = 2$ -2.5; the d_{00l} value noticed were around 1.60 nm, a value much lower than that one observed in this work for Zn_2Al -HFol (**Figure S3** and **Table S1**). Therefore, the synthesis method can also influence the arrangement of folate anions inside the interlayer space because the level of ion exchanged anions can be low, generating materials with co-intercalated anions (Figueiredo et al., 2022). In these cases, the

organic species (usually bigger than the anions in the precursor LDH) can take a tilted orientation in relation to the layers, decreasing the basal spacing (Figueiredo et al., 2022). In fact, higher amount of folate was reported to be intercalated by co-precipitation than by ion-exchange method (Qin et al., 2008; Mallakpour and Hatami, 2019).

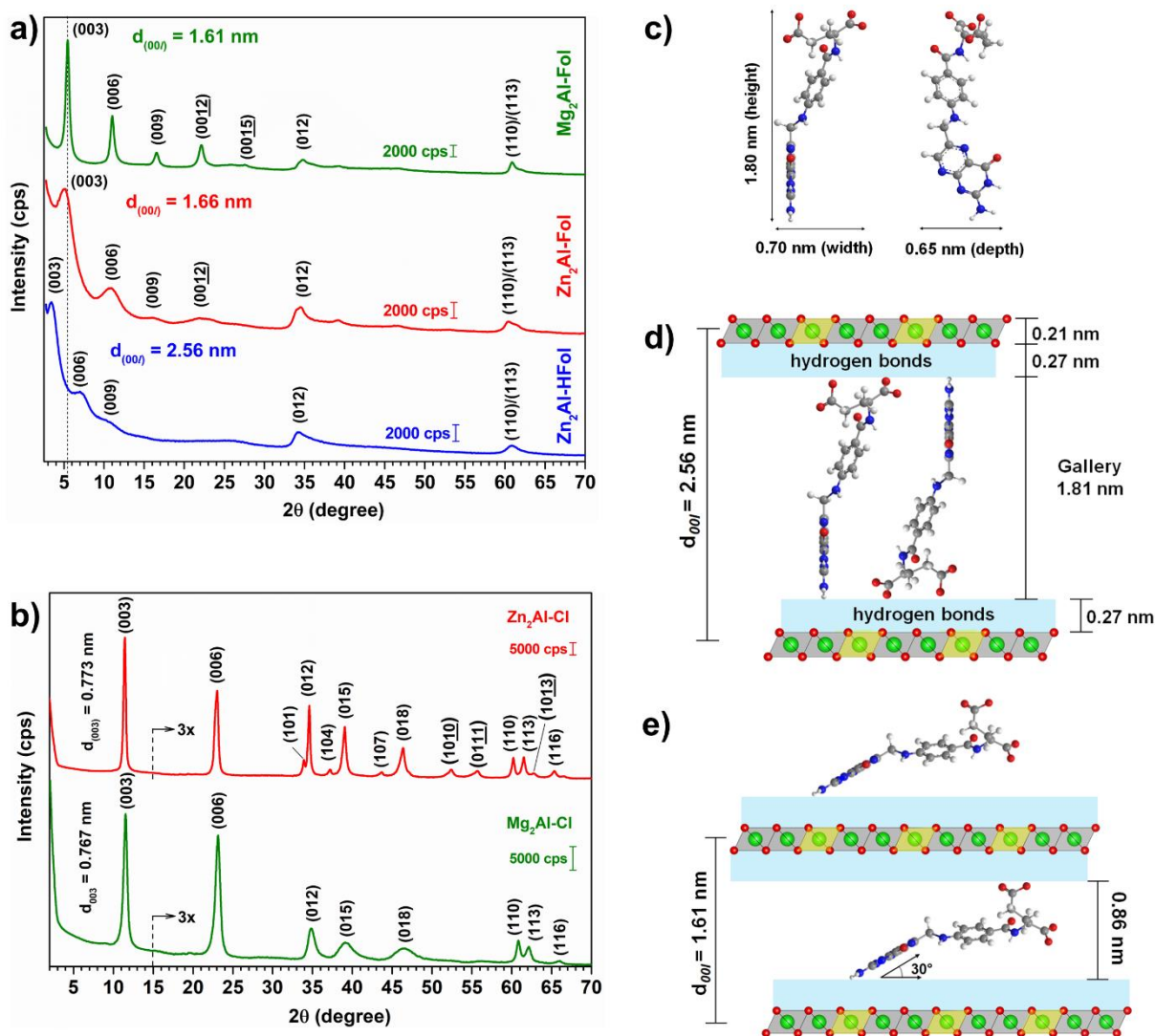


Figure S3. XRD patterns of powdered LDH-FA (a) compared to LDH-Cl (b) and schematic representation of three-dimensional structure of HFol²⁻ anion (based on the molecular array of di-hydrated folic acid in crystal (Kaduk et al., 2015); Dimensions were estimated by Chem Drown software) (c) and the arrangement of HFol²⁻ and Folate intercalated into Zn₂Al-HFol (d) and Mg₂Al-Fol (e), respectively.

Table S1. Interplanar distances (d_{hkl}), 2θ ($\text{CuK}\alpha$) and lattice parameters values calculated from XRD data of LDH–Folⁿ⁻ samples.

<i>hkl</i> and lattice parameters	Zn₂Al-HFol (pH 7.5)		Zn₂Al-Fol (pH 9)		Mg₂Al-Fol (pH 9.5)	
	2θ (°)	<i>d</i> (nm)	2θ (°)	<i>d</i> (nm)	2θ (°)	<i>d</i> (nm)
(003)	3.42	2.58	5.06	1.75	5.46	1.62
(006)	6.98	1.27	10.8	0.817	11.0	0.803
(009)	--	--	16.2	0.545	16.5	0.536
(0012)	--	--	21.8	--	22.1	0.402
(0015)	--	--	--	--	27.6	0.323
(012)	34.3	0.262	34.5	0.260	34.7	0.258
(110)	60.9	0.152	60.4	0.153	60.9	0.152
d_{00l} (nm)*	2.56		1.66		1.61	
<i>c</i> (nm) [#]	7.67		4.98		4.83	
<i>a</i> (nm) [‡]	0.304		0.306		0.304	

* $d_{00l} = [d_{003} + (2 \times d_{006}) + \dots + ((n/3) \times d_{00nl})]/(n/3)$; [#] $c = 3 \times d_{00l}$; [‡] $a = 2 \times d_{110}$.

Table S2. Interplanar distances (d_{hkl}), 2θ ($\text{CuK}\alpha$) and lattice parameters values calculated from XRD data of LDH–Cl samples. The peaks were indexed considering the R-3m space group.

<i>hkl</i> and lattice parameters	Zn₂Al-Cl (pH 7.5)		Mg₂Al-Cl (pH 9.5)	
	2θ (°)	<i>d</i> (nm)	2θ (°)	<i>d</i> (nm)
(003)	11.4	0.773	11.5	0.767
(006)	23.0	0.386	23.1	0.384
(012)	34.6	0.259	34.8	0.258
(110)	60.2	0.154	60.8	0.152
(113)	61.5	0.151	62.1	0.149
d_{basal} (nm)	0.773		0.768	
<i>c</i> (nm) [#]	2.32		2.30	
<i>a</i> (nm) [‡]	0.308		0.304	

The *a*-axis value (**Table S1**) is related to the interatomic distance of metals in the LDH layer and varies according to the $\text{M}^{2+}/\text{M}^{3+}$ molar ratio as well as the ionic radii of metal cation (Evans and Slade, 2006). For Zn₂Al-HFol, Zn₂Al-Fol and Mg₂Al-Fol were calculated to 0.304, 0.306 and 0.304 nm, respectively. The results for Zn₂Al-Fol and Mg₂Al-Fol are consistent with literature data (Rocha et al., 2016; Cunha et al., 2020) for related hybrid materials with $\text{M}^{2+}/\text{Al}^{3+}$ ratio around 2.0 (R nominal value). However, the low value for Zn₂Al-HFol (synthesized at pH 7.5), compared with Zn₂Al-Fol (synthesized at pH 9.0) and data from literature (Rocha et al.,

2016; Cunha et al., 2020) indicated a Zn^{2+}/Al^{3+} ratio lower than the nominal, as also observed by metal analysis (discussed later).

Considering the LDH layer thickness (0.21 nm) and the hydrogen-bond distances between LDH and intercalated anions (2×0.27 nm), the interlayer distances occupied by the guest anion were about 1.81 nm and 0.86 nm, for Zn_2Al -HFol and Mg_2Al -Fol, respectively. The proposal of an arrangement for folate anions inside the interlayer space is not straightforward because the FA molecule present a high degree of structural freedom making many folded conformations possible (Gocheva et al., 2019). Although, organic anions can be intercalated in LDH maintaining a similar conformation as its acid form in solid crystal (Cunha et al., 2016; Rocha et al., 2016). In the molecular array of di-hydrated Folic Acid in crystal, the Glu groups are bent in relation to the *p*-ABA and PT moiety, that in turn are tilted in relation each other (Kaduk et al., 2015), as represented in **Figure S3c**. The unit cell *c*-axis of di-hydrated Folic Acid is 3.24 nm and the d_{002} value (related to the height dimension of one molecule) is *ca.* 1.60 nm (Kaduk et al., 2015). Considering the FA structure in crystal and a rectangular parallelepiped, the dimensions of $HFol^{2-}$ in this work are estimated as $1.80 \times 0.70 \times 0.65$ nm (**Figure S3c**). The difference in relation to FA (1.60 nm) and $HFol^{2-}$ (1.80 nm) dimensions can rely on the Glu moiety that is not as folded as in FA crystal.

The match between the estimated height dimension of the $HFol^{2-}$ (1.80 nm) and the room available in the interlayer space of Zn_2Al -HFol (1.81 nm) suggested that the anion is intercalated in a monolayer arrangement with species interdigitated, like the FA in the crystal (CCDC N 1489544). The deprotonated Glu groups can be pointed out to the LDH layer, while PT moiety is perpendicular to the opposite layer (**Figure S3d**). For materials synthesized in pH value above 9.0, considering the gallery room available (0.86 nm), it is proposed that Fol^{1-} anions are intercalated in a monolayer array with molecules tilted along crystallographic *c*-axis in an estimated angle of around 30° , in which PT moiety is tilted to the layer (**Figure S3e**).

Some reported works also proposed that the Fol^{3-} is tilted along the c-axis, but the tilt angle estimated by them varied around 60 and 70°, though the unfolded anion structure was considered and hydrogen-bonds between guest and host was disregarded (Qin et al., 2008, 2014; Xiao et al., 2011; Kim and Oh, 2016). Such changes in anion array according to the pH of synthesis can be attributed to the fact that Fol^{3-} also has a charge located in the pterin group, and so, the anion tends to be arranged in a tilted form in order to maximize the interactions between the anion and the opposite charged layer (Cunha et al., 2016).

Taking into account an ideal Al^{3+} distribution, the surface area occupied by one electric charge in LDH structure is around $0.25 \text{ nm}^2/q^+$ or $0.50 \text{ nm}^2/q^+$ considering both sides of the layer (Rocha et al., 2016). Regarding the arrangement proposed above and HFol^{2-} as a parallelepiped with charges located only on one side (GLU moiety side; **Figure S3c**), the area occupied by the two charges is 0.46 nm^2 ($0.70 \times 0.65 \text{ nm}$), corresponding to a charge density of $0.23 \text{ nm}^2/q^-$. This value is just slightly lower than the charge density of LDH (considering one side) and is consistent with the close packing of anions proposed in **Figure S3d**. In addition, the co-intercalation of small ions such as chloride is not necessary to reach the electroneutrality of the material, as it was previously observed for large anions with small electric charge such as sulindac (Rocha et al., 2016), pravastatin (Cunha et al., 2012) or mefenamate (Cunha et al., 2016), for instance. Differently, if an inclination is considered for intercalated Fol^{3-} species (in $\text{Mg}_2\text{Al-LDH}$ or $\text{Zn}_2\text{Al-LDH}$ synthesized at pH 9-9.5), the projected area of anion to the layer is estimated as 1.00 nm^2 ($1.60 \text{ nm} \times 0.65 \text{ nm}$), or 2.00 nm^2 if both sides are considered, corresponding to a charge density of $0.33 \text{ nm}^2/q^-$ or $0.66 \text{ nm}^2/q^-$, respectively. Hence, the area corresponding to ten positive charges (2.5 nm^2) can be occupied by three Fol^{3-} (2.97 nm^2 per $9q^-$), but as this value is higher than the LDH density charge, it is expected that the molecules are arranged away from each other and the co-intercalation of chloride anion is required to reach the neutrality (Cunha et al., 2012, 2016).

2.1.2. Vibrational spectroscopy data

The FTIR-ATR and FT-Raman spectra of LDH-FA samples are displayed in **Figure S4a**. The main vibrational bands from the organic anions are tentatively attributed in **Table S3**. In our previous work (Magri et al., 2022), it was shown that main spectroscopical differences among FA and its sodium salts (Na_2HFol and Na_3Fol) in the IR spectral region were the presence of bands at $1550\text{-}1500\text{ cm}^{-1}$ and 1400 cm^{-1} regions attributed to antisymmetric (ν_{as}) and symmetric stretching (ν_{s}) vibration of carboxylate groups (COO^-), respectively. Further, from Na_2HFol to Na_3Fol , the main difference is related to bands associated to vibrations from PT moiety due to the increase of its aromaticity induced by the deprotonation of N3-H group. Accordingly, in the IR spectra, the band at 1500 cm^{-1} region (PT stretching, $\nu_{\text{C}(4)\text{-O}^-}$ and $\nu_{\text{asC}\alpha'\text{OO}^-}$) that is more intense than the band at 1600 cm^{-1} (benzene stretching) is characteristic of Fol^{3-} species. Besides, while Raman spectrum of Na_2HFol presented splitted bands at 1330 and 1300 cm^{-1} region (also in IR spectra), Na_3Fol presented overlapped bands around 1340 cm^{-1} , which is attributed to deprotonated PT moiety. Taking the sodium folate salts as reference of di- and trivalent anions, the same tendence was observed for $\text{Zn}_2\text{Al-HFol}$ and $\text{Mg}_2\text{Al-Fol}$ spectra (**Figure S4a**), confirming that HFol^{2-} and Fol^{3-} were intercalated in the materials, respectively. Such difference can be attributed to the distinct pH used in their synthesis (**Figure S2**). Although $\text{Zn}_2\text{Al-Fol}$ presented a vibrational profile like that of $\text{Zn}_2\text{Al-HFol}$, the sample also showed bands identified with Fol^{3-} , such as the intense bands at around 1335 cm^{-1} in Raman and IR spectra. These results suggest the intercalation of both $\text{HFol}^{2-}/\text{Fol}^{3-}$, in agreement with elemental analysis discussed below. The bands position of LDH-FA regarding the carboxylate and PT groups presented values close to sodium salts (**Table S3**) which indicates a coulombic interaction between guest and host (Nara et al., 1996). In addition, vibrational spectroscopy results also indicated that the organic anions were not decomposed during the synthesis, keeping their chemical identities.

The strong broad band at 2800-3600 cm^{-1} region in IR spectra can be attributed to O–H stretching from M-OH groups of LDH layers (Kloprogge et al., 2004) and H_2O (hydration water). Also, signal around 1650 cm^{-1} has contribution of bending vibration of hydration water (Kloprogge et al., 2004). The bands bellow 1000 cm^{-1} have contribution of M–OH and M–O vibrations. Compared to LDH-Cl (**Figure S4b**), such bands are not resolved in the Raman spectra of LDH-FA because of the cross section of LDH layer is not as higher as those of the organic anion (Gil et al., 2016).

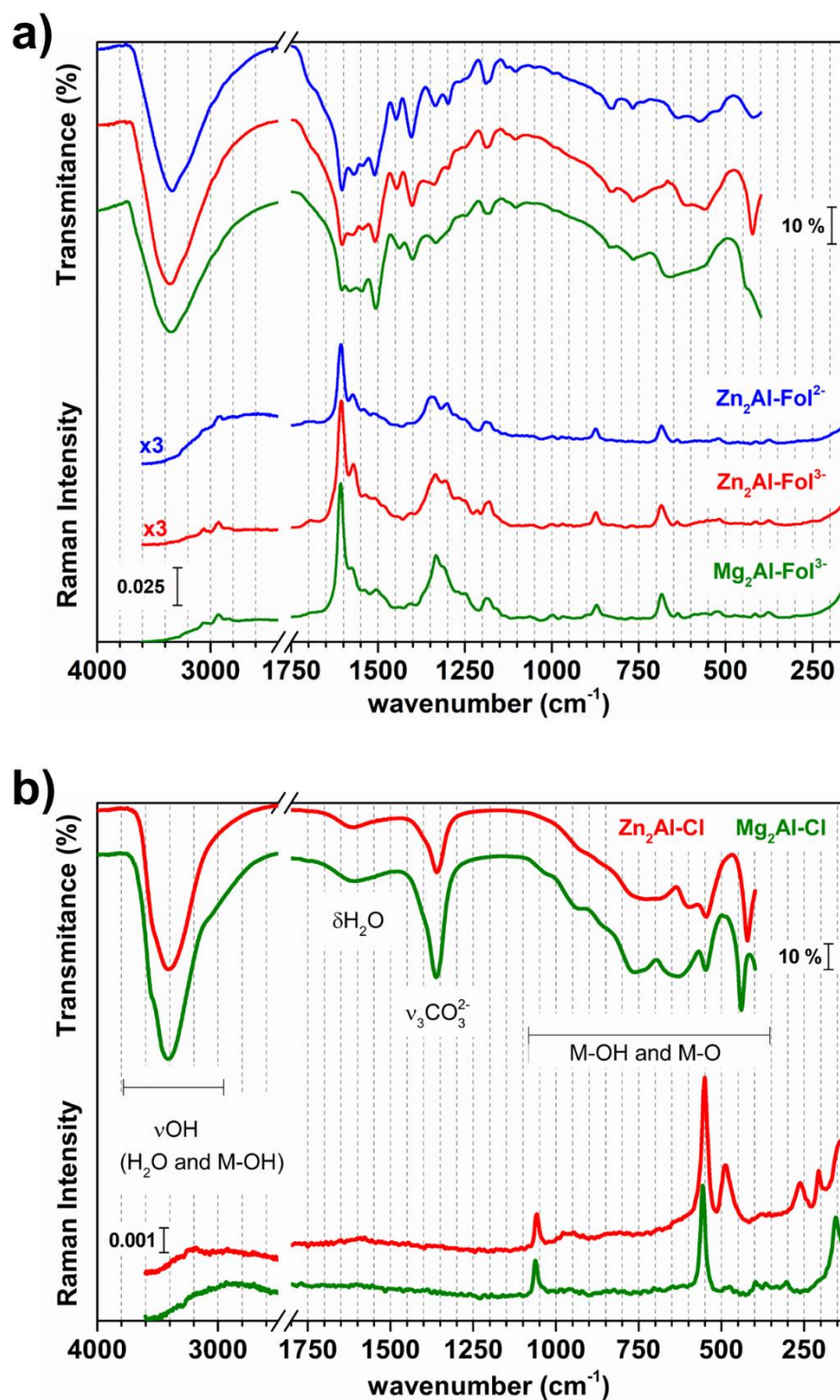


Figure S4. Experimental FTIR-ATR (top) and FT-Raman (bottom) spectra of LDH-FA (a) and LDH-Cl (b) samples. The attribution of vibrational bands of LDH-Cl spectra were made according to (Kloprogge et al., 2004).

Table S3. Experimental IR and Raman wavenumber values (cm⁻¹) for Zn₂Al-HFol and Mg₂Al-Fol samples.

Na ₂ HFol ^(a,b)		Zn ₂ Al-HFol ^(b)		Na ₃ Fol ^(a,b)		Mg ₂ Al-Fol ^(b)		Tentative of Attribution of main vibrations ^(a-e)
IR	Raman	IR	Raman	IR	Raman	IR	Raman	
1687w	1686w	1695m	1695w					v(C4=O) + δ(N3-H) + sc(NH ₂)
1630sh	1628sh	1640sh	#	1630sh	1630sh	1665sh	#	v(C11=O) + δ(N12-H)
1602s	1605s	1604s	1607s	1604sh	1601	1605s	1608s	v(C=C)φ
				1575sh	#	1580s	1577s	v(PT rings) + sc(NH ₂) + v(C4-O ⁻); v(C=C)φ
1566s;br	1570s;br	1570s;br	1573s					v(PT rings) + sc(NH ₂) + δ(N3-H); v(C=C)φ
				1550br	#	1547s		v(C4-O ⁻) + v(PT rings) + sc(NH ₂)
#	#	1545s	1542m				1540m	v _{as} (Cα'OO ⁻) + v(C11-N12)/δ(N12-H)
#	1536sh	1536sh	#					v(PT rings) + δ(N3-H) + v(C4=O);
#	1514sh		1515m					v(C=C)φ; v(PT rings)
1502br	#	1510s	1505sh	1513sh	1510m	1504br;s	1506m	v _{as} (Cγ'OO ⁻)
				1504br				v(PT rings) + v(C4-O ⁻)
1447m	1452w	1448m	1448vw	1439m;br	#	1439s	1439vw	v(PT rings); sc(CH ₂);v(C11-N12)/δ(N12-H)
1400br	#	1404s	1403vw	1401br		1401s	1407br;w	v _s (COO ⁻)/v(C-C) + ω(Cβ,γH ₂); GLU
1328br	#	1336m	1336m	1327br	#	1334s	1333s	δ(C-H)φ; ω(Cβ,γH ₂) + δ(Cα-H) + v _{as} (Cα'OO ⁻); GLU
				#	1332			v(PT rings) + τ(NH ₂) + δ(C7-H) + ω(C9H ₂)
				1313sh	1315sh	1312sh	1313sh	v(PT rings) + v(C2-N2)
								v(PT rings) + v(C2-N2) + δ(N3-H)
1303m;br	1309s;br	1300m	1302s					δ(C-H)φ + v(C11-N12)/δ(N12-H) + δ(Cα-H) +
				1297sh	1296sh	1296sh	#	τ(Cβ,γH ₂); GLU

^(a)from (Magri et al., 2022); ^(b)s = strong, m = medium, br = broad, sh = should, w = weak, vw = very weak and # = very weak and/or not resolved band; ^(c)v_s = symmetric stretching, v_{as} = antisymmetric stretching, δ = bending (in plane; ip); sc = scissoring (ip bending), ω = wagging (oop bending), τ = twisting (oop bending), v(PT rings) = (C=C) and (C=N) stretching of pterin moiety and GLU = glutamate moiety; ^(d)phenylene ring (φ); ^(e)The numbers and letters are related to the carbon indexation in folic acid structure shown in Figure 1b;

2.1.3. Chemical elemental Analysis

The chemical elemental analysis data is presented in **Table S4**. The results indicated that Mg₂Al-Fol and Zn₂Al-Fol layers had an experimental M²⁺/Al³⁺ molar ratio close to the nominal value (*i.e.*, 2), but for Zn₂Al-HFol this value was lower than the expected one. It can be related to the good complexing/chelating character of folic acid (folate) towards transition metals (Dametto et al., 2014); rarely an experimental M²⁺/Al³⁺ molar ratio is different from the nominal value for LDH-Cl materials, as can be observed in **Table S4**. One can consider that during the synthesis of LDH-FA, both precipitation and complexation reactions take place concomitantly, but the former is favoured when the pH is increased (Tronto et al., 2001), as can be noticed comparing the metals ratio of Zn₂Al-HFol (obtained by coprecipitation at pH 7.5) and Zn₂Al-Fol (obtained at pH 9). The complexation reaction can also be precluded by lowering the [FA]/[Al³⁺] ratio, what could minimize the solubilization of Zn²⁺ by complexation reaction.

The pH value of synthesis also affected the level of protonation of intercalated folate as suggested the mixture of HFol²⁻/Fol³⁻ species confined in Zn₂Al-Fol samples. According to the FA speciation curves (**Figure S2**), at pH 7.5 the molar fractions of divalent (HFol²⁻) and trivalent (Fol³⁻) folate anions in solution are expected to be 0.75 and 0.25, respectively. However, chemical elemental analysis data indicates that the intercalated HFol²⁻ corresponds to a molar fraction around 0.96. Besides, at pH 9.0, the HFol²⁻ molar fraction is around 0.07, but 0.17 is intercalated, which could indicate the preferential intercalation of HFol²⁻ against Fol³⁻ despite the lower charge. On the other hand, for Mg₂Al-Fol synthesized at pH 9.5, there was only indicative of intercalated Fol³⁻ ions. Additionally, it is worth to highlight that the elemental analysis results also pointed a low amount of co-intercalated Cl⁻ ([Fol³⁻]/[Cl⁻] molar ratio of 3:1; **Table S4**), as predicted from XRD analysis. The chemical elemental analysis results are in a good agreement with thermal analysis (**Table S4**), XRD and spectroscopic (IR and Raman)

data. The loading capacity of LDH-FA materials synthesized in this work were higher or as higher as those reported in the literature (**Table S5**).

Table S4. Chemical composition and proposed formula for LDH-FA materials and LDH-Cl counterparts.

Proposed Formula	M^{2+}/Al^{3+}	wt. % H₂O*	wt. % C[†]	wt. % N[†]	wt. % Rm^{‡*}
Zn₂Al-Fol²⁻ [Zn _{1.74} Al(OH) _{5.48}](C ₁₉ H ₁₇ O ₆ N ₇ ²⁻) _{0.47} (C ₁₉ H ₁₆ O ₆ N ₇ ³⁻) _{0.02} ·2.47 H ₂ O	1.72±0.02 (1.74)	9.49 (9.00)	22.8±0.04 (22.7)	9.62±0.10 (9.73)	39.3 (39.0)
Zn₂Al-Fol³⁻ [Zn _{1.90} Al(OH) _{5.80}](C ₁₉ H ₁₆ O ₆ N ₇ ³⁻) _{0.27} (C ₁₉ H ₁₇ O ₆ N ₇ ²⁻) _{0.05} Cl ⁻ _{0.09} ·2.32H ₂ O	1.90±0.02 (1.90)	9.65 (9.60)	16.7±0.09 (16.8)	7.21±0.01 (7.21)	47.9 (47.3)
Mg₂Al-Fol³⁻ [Mg _{2.21} Al(OH) _{6.42}](C ₁₉ H ₁₆ O ₆ N ₇ ³⁻) _{0.30} Cl ⁻ _{0.10} ·2.70H ₂ O	2.21±0.07 (2.21)	13.2 (13.0)	18.8±0.12 (18.3)	7.81±0.04 (7.88)	37.0 (37.5)
Mg₂Al-Cl [Mg _{2.14} Al(OH) _{6.28}]Cl·1.50H ₂ O	2.14±0.10 (2.14)	11.10 (10.90)	--	--	--
Zn₂Al-Cl [Zn _{2.11} Al(OH) _{6.22}]Cl·1.96H ₂ O	2.11±0.02 (2.11)	10.35 (10.35)	--	--	--

[§]measured by IC POES (M²⁺: Mg²⁺ or Zn²⁺); *measured by thermal analysis under air atmosphere; [†]measured by CHN analysis. [‡]Rm refers to residual mass from thermal analysis results. () indicates theoretical results calculated from proposed formulas.

Table S5. A comparative of synthesis method and percentage of intercalated folate anions reported in the literature and in this work.

Nominal Formula ^a	Synthesis method	pH value of synthesis ^{b,c}	%LC ^{e,d,e,f}	Reference
Mg ₂ Al-LDH	co-precipitation	10.0 (Fol ³⁻)	19.3	(Qin et al., 2008)
Mg ₂ Al-LDH	ion-exchange	n. i.	17.9	
Mg _{1.5} Zn _{1.5} Al-LDH	co-precipitation	n. i.	45.2	(Xiao et al., 2011)
Mg ₃ Al-LDH	co-precipitation	n. i.	32.4	(Qin et al., 2014)
Ca ₂ Al-LDH	co-precipitation	11.5 (Fol ³⁻)	42.8	(Kim and Oh, 2016)
Ca ₂ Fe-LDH	co-precipitation	13.5 (Fol ³⁻)	n. i.	
Zn _{2.5} Al-LDH	ion-exchange	7.0 (HFol ²⁻)	n. i.	(Arratia-Quijada et al., 2016)
Zn _{2.5} Al _{0.95} Dy _{0.05} -LDH	ion-exchange	7.0 (HFol ²⁻)	n. i.	(Arízaga et al., 2016)
Zn _{2.5} Al-LDH	ion-exchange	7.0 (HFol ²⁻)	n. i.	(Arízaga et al., 2016)
Mg ₂ Al-LDH	co-precipitation	10.0 (Fol ³⁻)	33.4	(Mallakpour and Hatami, 2019)
Mg ₂ Al-LDH	ion-exchange	10.0 (Fol ³⁻)	15.6	
Mg ₂ Al-LDH	ion-exchange	8.0 (HFol ²⁻ /Fol ³⁻)	36.6	(Pagano et al., 2019)
Zn ₂ Al-LDH	ion-exchange	8.0 (HFol ²⁻ /Fol ³⁻)	28.3	
Zn ₂ Al-LDH	co-precipitation	7.5 (HFol ²⁻)	43.6	This work
Zn ₂ Al-LDH	co-precipitation	9.0 (Fol ³⁻)	32.2	This work
Mg ₂ Al-LDH	co-precipitation	9.5 (Fol ³⁻)	35.2	This work

^ametals molar ratio in the synthesis; ^bbased on the folic acid speciation (Figure S2), the mainly anion available in the pH value of synthesis is pointed between parentheses; ^cn. i. (not indicated); ^dLC is the loading capacity calculated by the formula: %LC = [intercalated A/LDH-A weight] * 100; ^eKim and Oh (2016) also employed other synthesis methods as ion-exchange, solid phase reaction and exfoliation-reassembly handling the monovalent folate salt (NaH₂Fol), and the authors claimed a %LC between 38.95 to 72.20;

2.1.4. Thermal Analysis data

Table S6. Results of thermal analysis (in N₂ atmosphere) and evolved gas analysis (TG-MS and TG-FTIR) of LDH-FA hybrid materials.

Mg₂Al-Fol				
event [#]	Temp. (°C)	T _p (°C) [‡]	%Mass	EGA*
dehy	30-213	100 181	10.5	H ₂ O
I(D)	250-450	406	21.5	H ₂ O; CO ₂ ; CO; NH ₃ ; N ₂ O; aniline; CH ₄ ; C ₃ H ₅ (m/z 41)
II	450-600	490	10.04	CO ₂ ; CO; NH ₃ ; aniline; CH ₄ ; C ₃ H ₅ (m/z 41); N ₂ O; HCN; H ₂ O
III	600-800	und.	6.36	CO ₂ ; CO; NH ₃ ; N ₂ O; HCN; HNCO; C ₃ H ₅ (m/z 41)
IV	800-1000	und.	6.42	CO ₂ ; CO; NH ₃ ; HCN
Zn₂Al-Fol				
event [#]	Temp. (°C)	T _p (°C)	%Mass	EGA
dehy	30-170	96 157	10.1	H ₂ O
I(D)	170-272	213	10.3	H ₂ O
II	272-514	430	12.6	CO ₂ ; CO; NH ₃ ; HCN; aniline; CH ₄ ; C ₃ H ₅ (m/z 41); H ₂ O
III	514-800	und.	20.9	CO ₂ ; CO; NH ₃ ; HCN; CH ₄ ; H ₂ O
Zn₂Al-HFol				
event [#]	Temp. (°C)	T _p (°C)	%Mass	EGA
dehy	30-156	94	10.4	H ₂ O
I(D)	156-272	195	8.00	H ₂ O
II	272-516	426	17.3	CO ₂ ; CO; NH ₃ ; aniline; CH ₄ ; C ₃ H ₅ (m/z 41); N ₂ O; H ₂ O
III	516-800	und.	24.0	CO ₂ ; CO; NH ₃ ; HCN; N ₂ O

[#]dehy.: dehydration; D: dehydroxylation of LDH layer; Roman numbers indicate the degradation steps; [‡]und.: undefined; T_p: peak temperature of the mass loss event, according to DTG. *EGA: Evolved gas analysis carried out by infrared spectroscopy (IR) and mass spectrometry (MS).

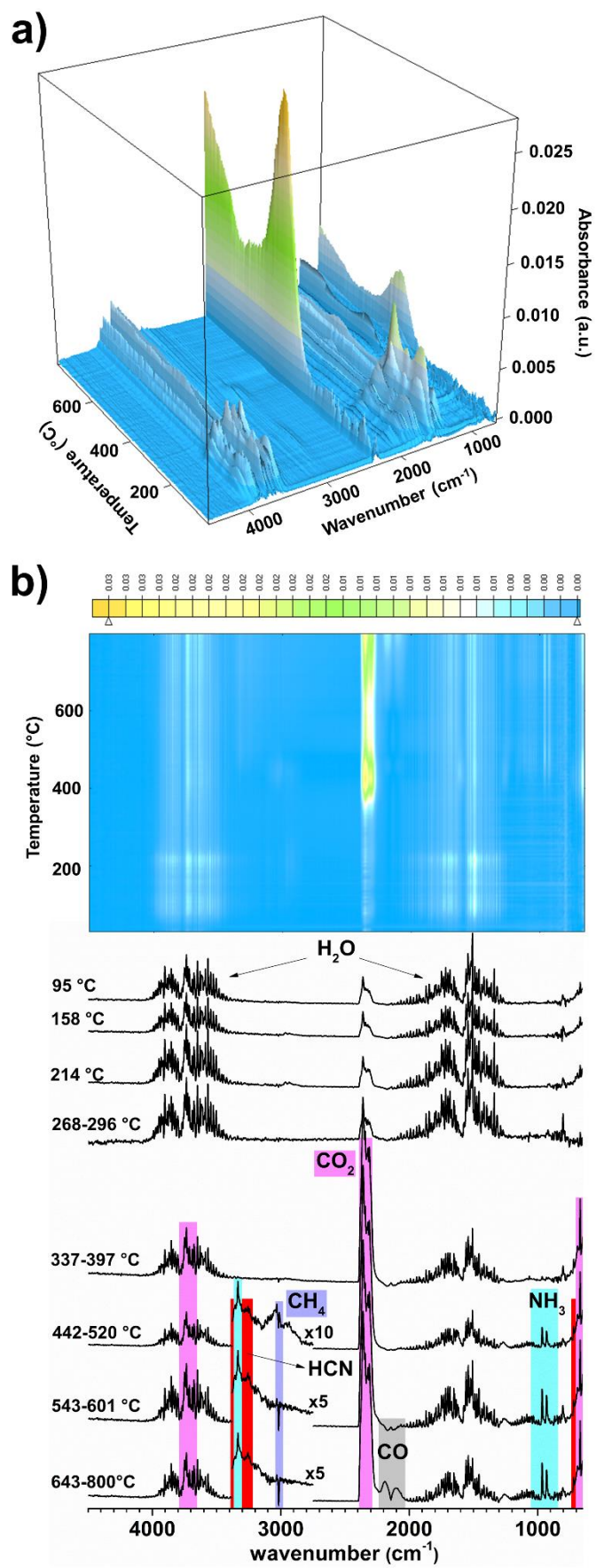


Figure S5. 3D FTIR (a) and contour map along with temperature selected FTIR spectra (b) for Zn₂Al-Fol.

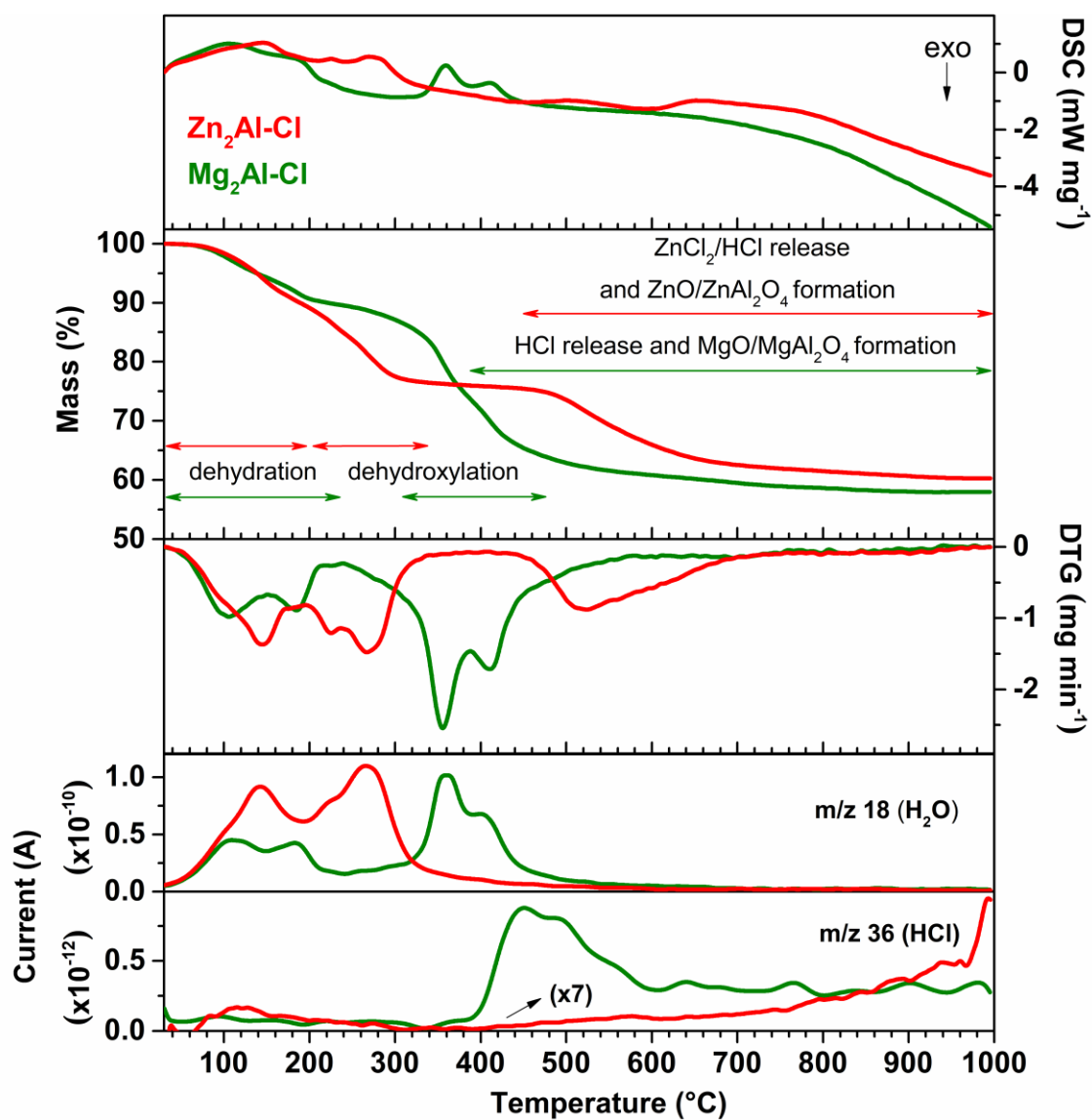
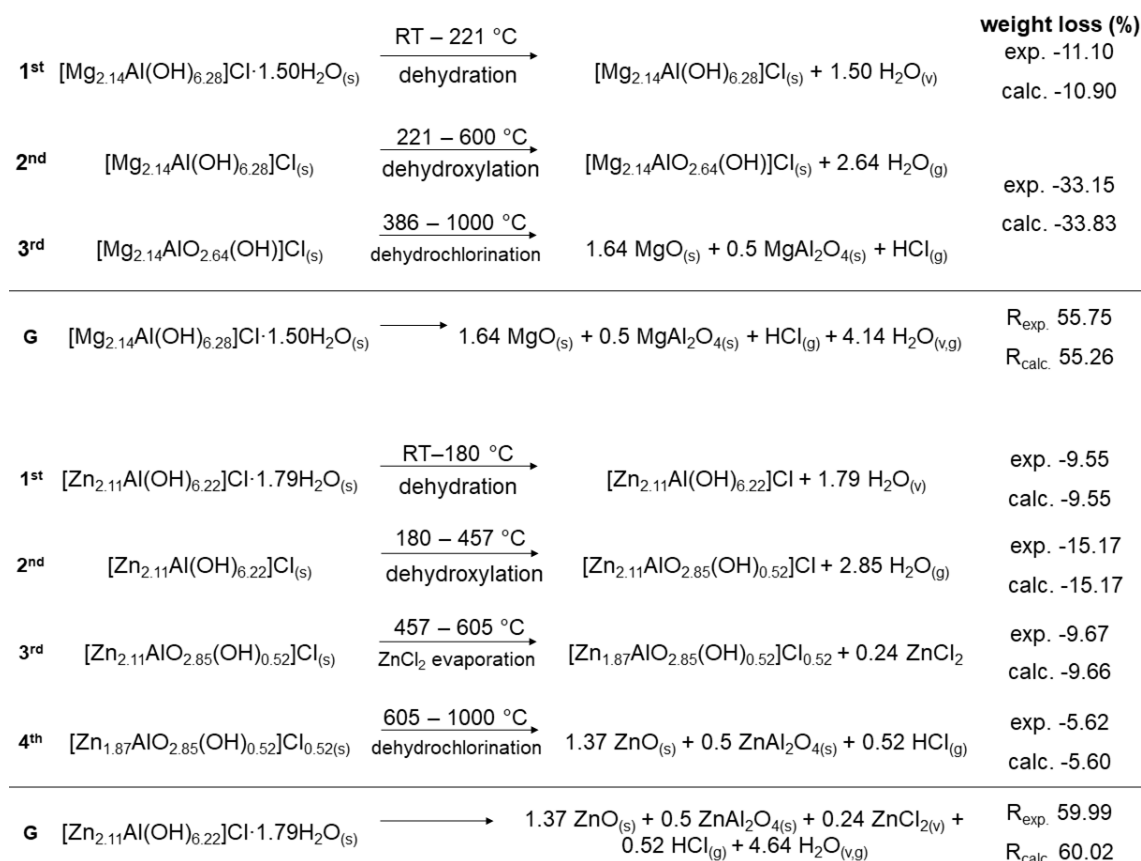


Figure S6. Thermal Analysis data (TGA/DTG/DSC-MS curves) of LDH-Cl materials under N_2 atmosphere.



Scheme S1. Proposed chemical equations for the decomposition steps of LDH-Cl materials under N₂ atmosphere. R is the percentage of residual mass at 1000 °C and G is the global chemical equation of material decomposition.

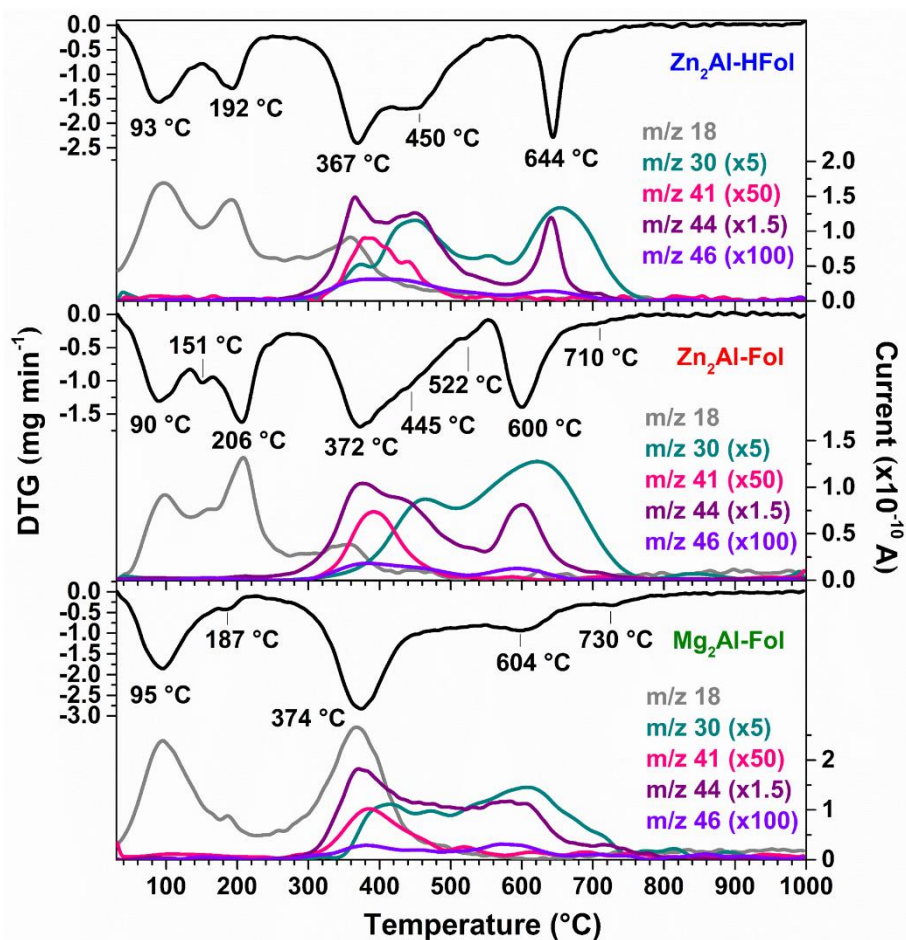
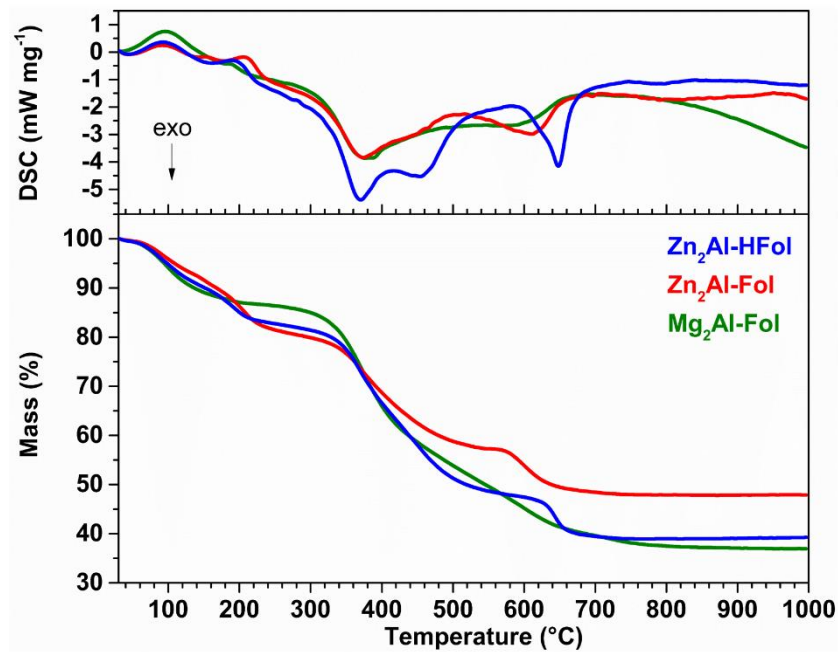


Figure S7. Thermal Analysis data (TGA/DTG/DSC-MS) of LDH-FA materials under air atmosphere.

2.1.5. Carbothermic reaction

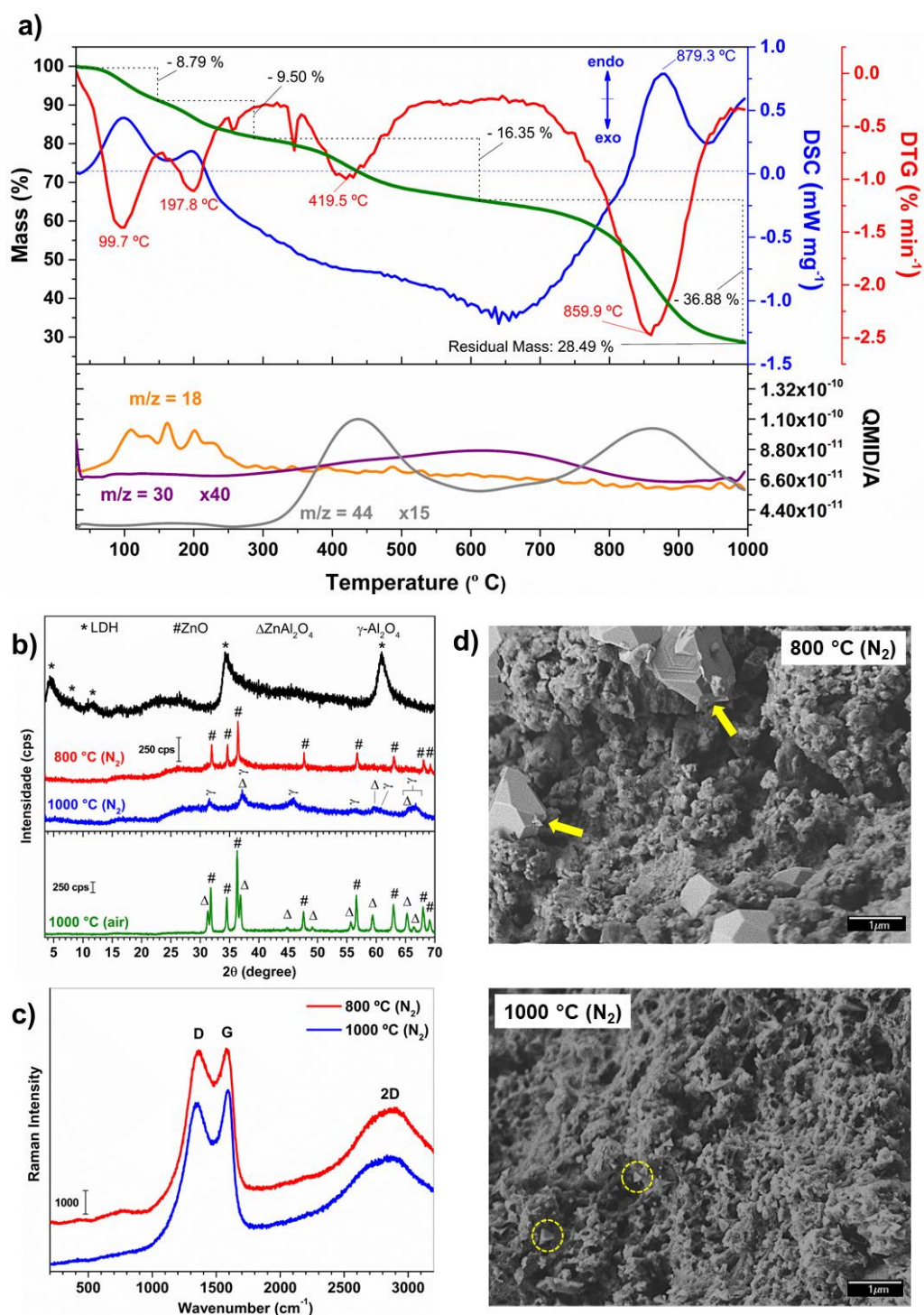


Figure S8. Carbothermic reaction assay of Zn₂Al-HFol, [Zn_{2.29}Al(OH)_{6.58}](C₁₉H₁₇N₇O₆)_{0.47}(C₁₉H₁₆N₇O₆)_{0.02}·2.8H₂O. TGA/DTG/DSC curves under N₂ atmosphere (a), XRD analysis of precursor (black line), samples pyrolyzed (800 °C, red line; and 1000 °C; blue line) and sample calcined at 1000 °C (green line) (b). Raman (excitation 532 nm) spectra (c) and SEM micrography (d) of samples pyrolyzed at 800 and 1000 °C. Yellow arrows indicated ZnO particles and dashed yellow circles, γ-Al₂O₃.

In TGA/DSC curves (**Figure S8a**), the event of mass loss with endothermic peak at 879 °C indicated the carbothermic reaction: $\text{ZnO}_{(s)} + \text{C}_{(gr)} \rightarrow \text{Zn}_{(v)} + \text{CO}_{(g)}$, as reported in a previous work (Magri et al., 2019). The formation of ZnO at 800 °C was confirmed by XRD (red line; **Figure S8b**) and SEM (yellow arrow, **Figure S8d**). The D, G and 2D bands in Raman spectra indicated the formation of graphitic carbon (**Figure S8c**). The loss of Zn (vapour) above 800 °C was inferred considering the endothermic event peak at 879 °C in TGA/DSC results as well as the disappearing of the diffraction peaks attributed to ZnO in XRD (**Figure S8b**) and the loss of the structures attributed to ZnO in SEM (**Figure S8d**), as the temperature increased from 800 to 1000 °C. The process led to the generation of $\gamma\text{-Al}_2\text{O}_3$ (ICSD 249140), as indicated in XRD pattern (blue line; **Figure S8b**) and SEM images (yellow dashed circles; **Figure S8d**).

2.1.6. In-situ HT-XRD data

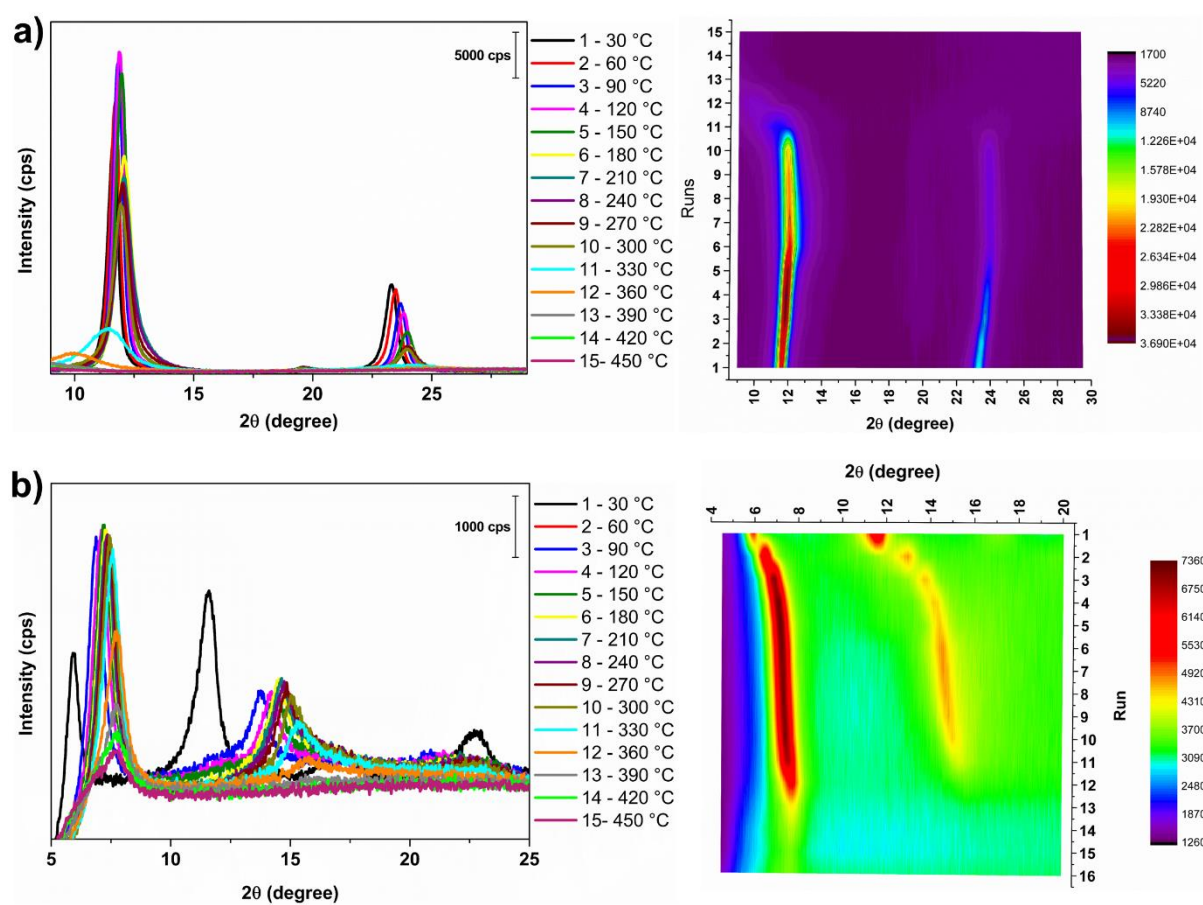


Figure S9. In-situ HT-XRD patterns (left) and respective contour maps (right) of Mg₂Al-Cl (a) and Mg₂Al-Fol (b) under a N₂ atmosphere.

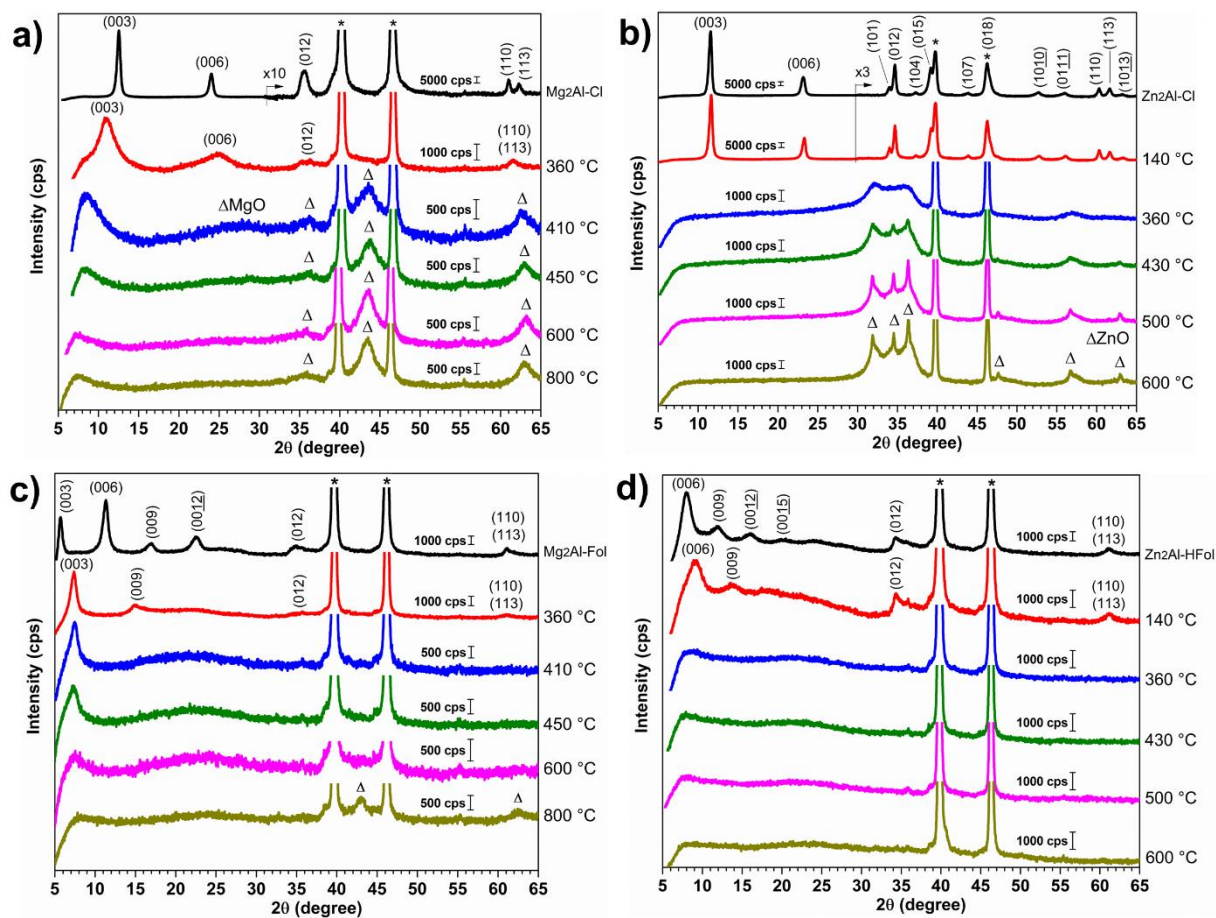


Figure S10. *In-situ* HT-XRD patterns of Mg₂Al-Cl (a), Zn₂Al-Cl (b), Mg₂Al-Fol (c) and Zn₂Al-HFol-HT150/1h (d). The experiment was carried out for Zn₂Al-HFol-HT150/1h due to its higher crystallinity than the pristine Zn₂Al-HFol and the (003) could not be probed because of its low angle region (equipment limitation). *sample holder.

2.1.7. SEM-EDS data

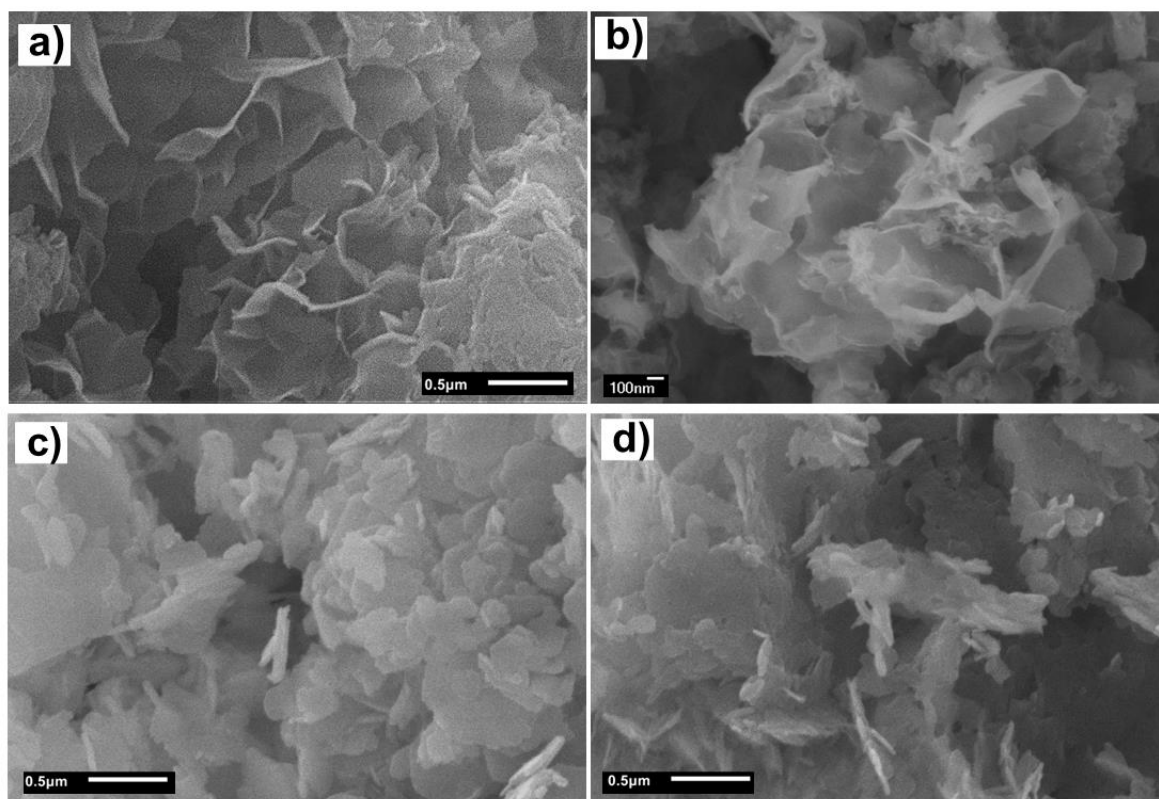


Figure S11. SEM micrographies of Mg₂Al-Fol (a) Zn₂Al-Fol (b), Zn₂Al-Cl (c) and Mg₂Al-Cl (d) materials at (x35k of magnification).

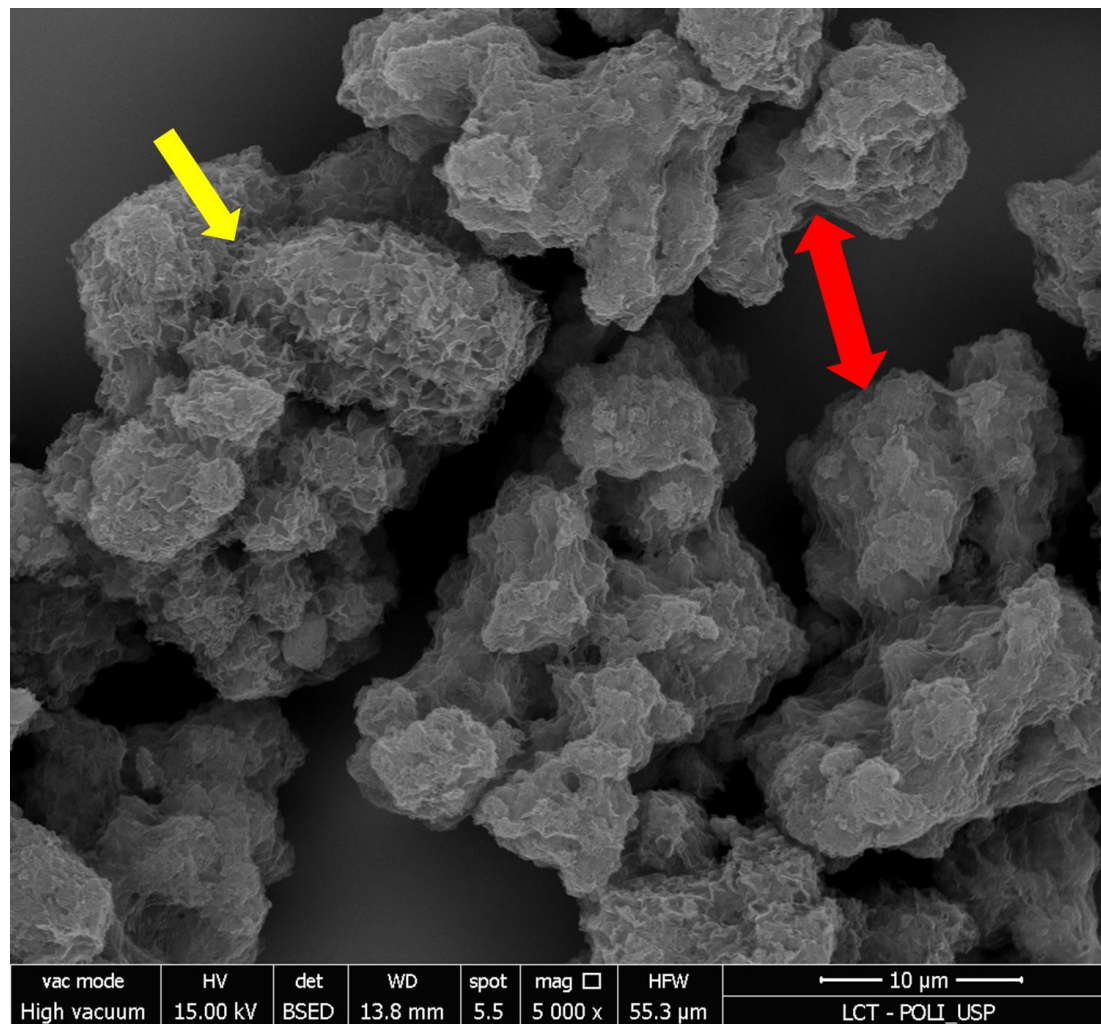


Figure S12. SEM micrographies of Zn₂Al-HFol-500r (a) and Zn₂Al-HFol-600r (b). The arrows indicates: opened structure (yellow) and stacked structure (red).

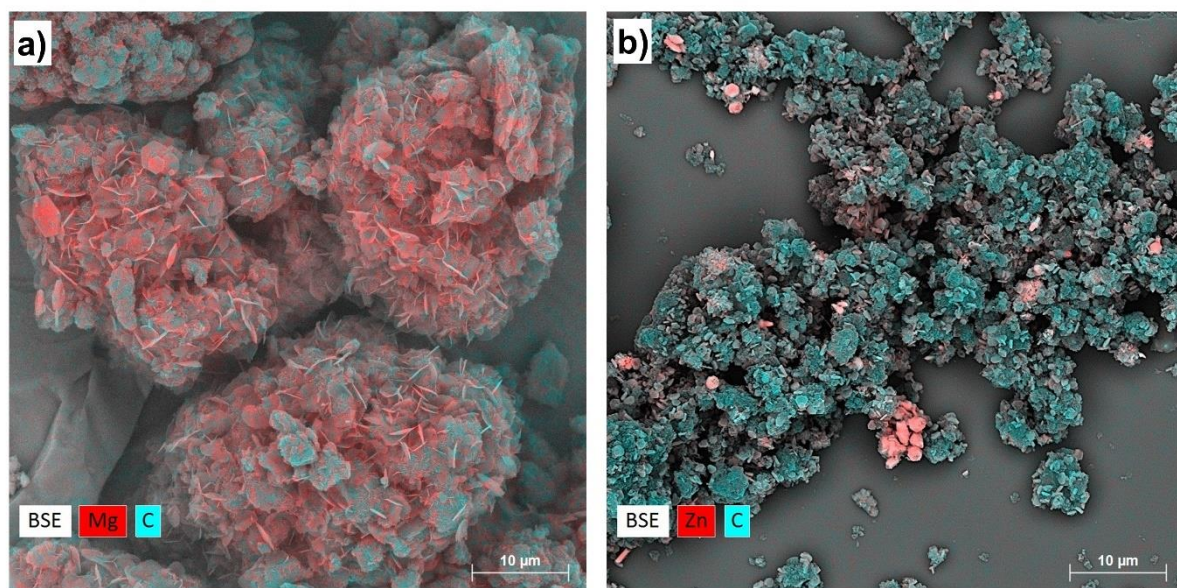


Figure S13. EDS mapping merge of carbon and Mg (a) or Zn (b) for $\text{Mg}_2\text{Al-Fol-1000r}$ and $\text{Zn}_2\text{Al-HFol-800r}$ samples, respectively.

2.1.8. UV-VIS and Photoluminescence spectroscopic data of LDH/C-dots (pyrolysis)

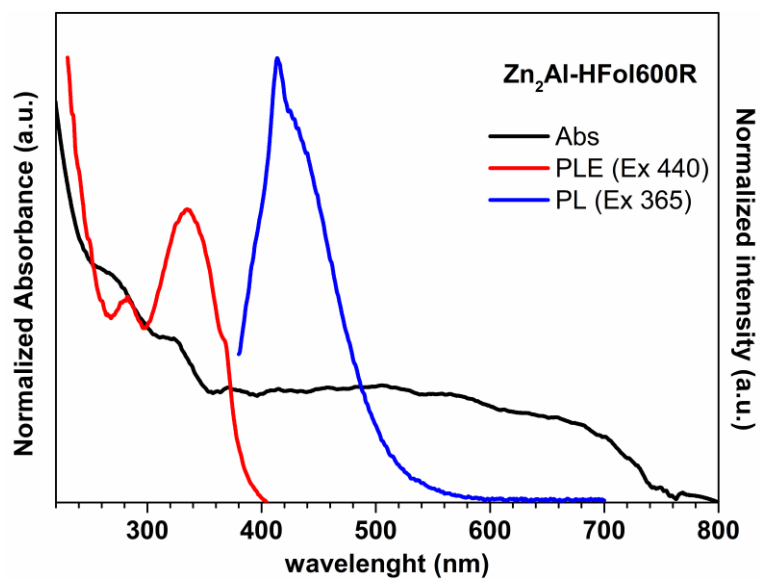


Figure S14. Optical characterization (absorption, PL and PLE spectra) of Zn₂Al-HFol-600r sample.

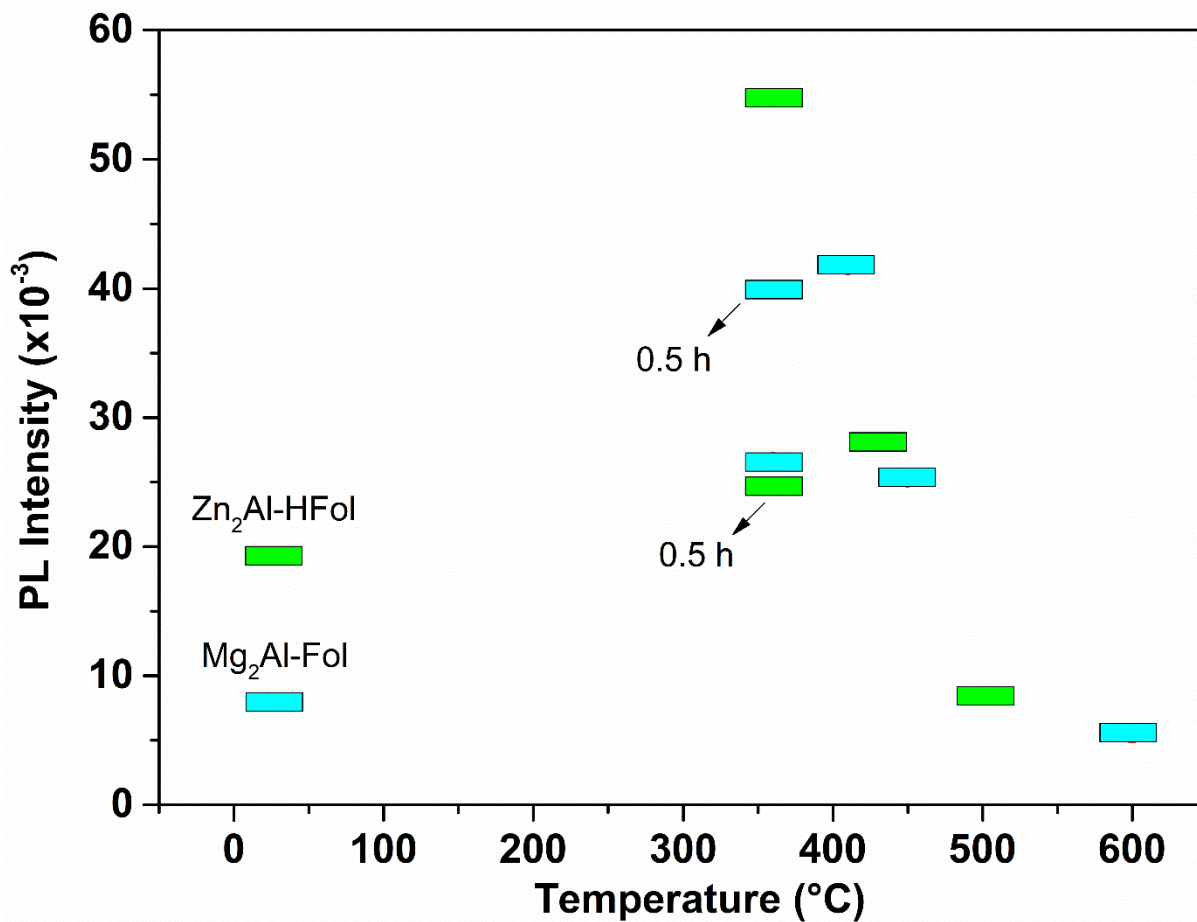


Figure S15. PL intensity in aqueous suspension (0.5 mg L^{-1}) under 365 nm excitation radiation of LDH-Fol samples after pyrolysis/reconstitution. 0.5 h indicated isothermal conduction at 360 °C for 0.5 h.

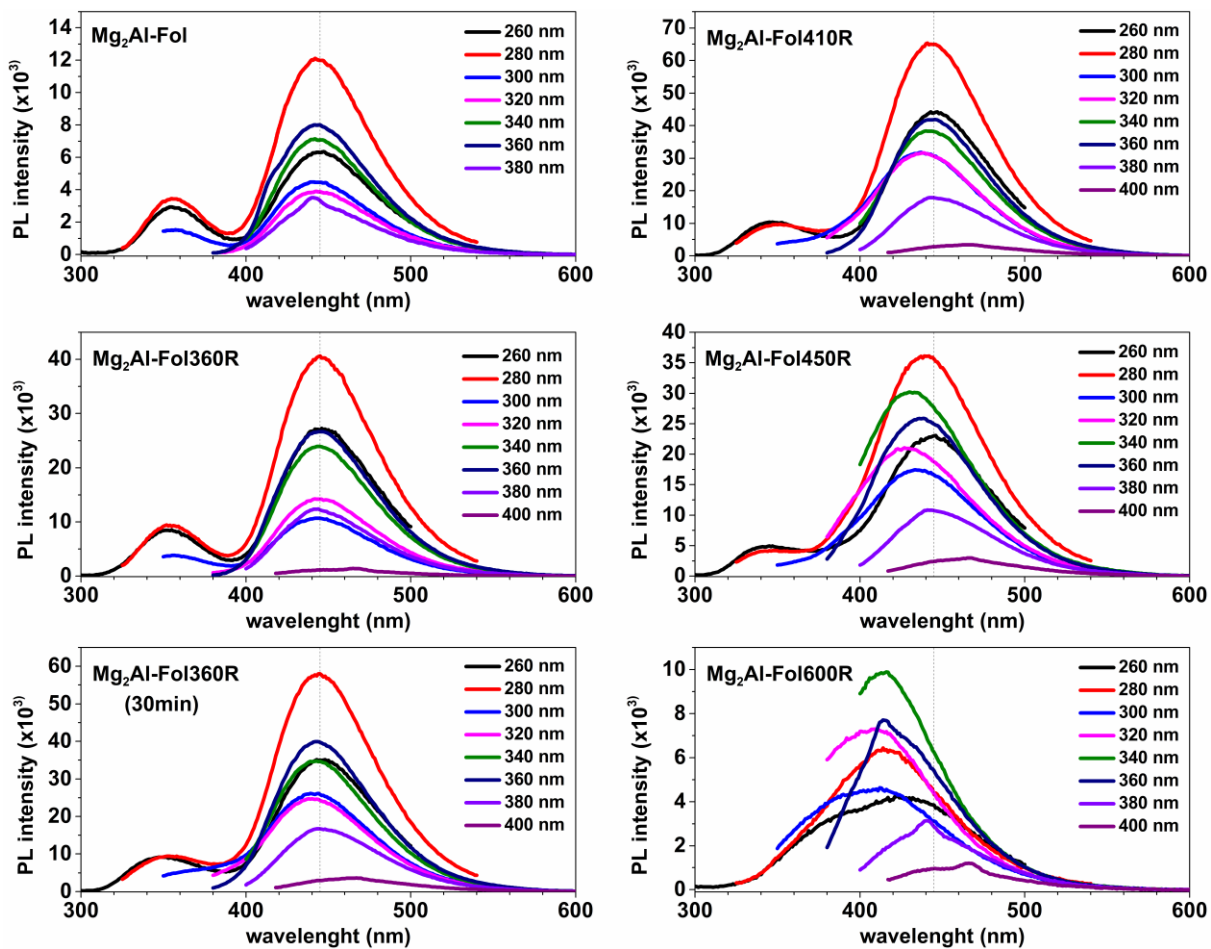


Figure S16. PL spectra in aqueous suspension (0.5 mg L^{-1}) under different excitation radiation of Mg₂Al-Fol samples after pyrolysis/reconstitution.

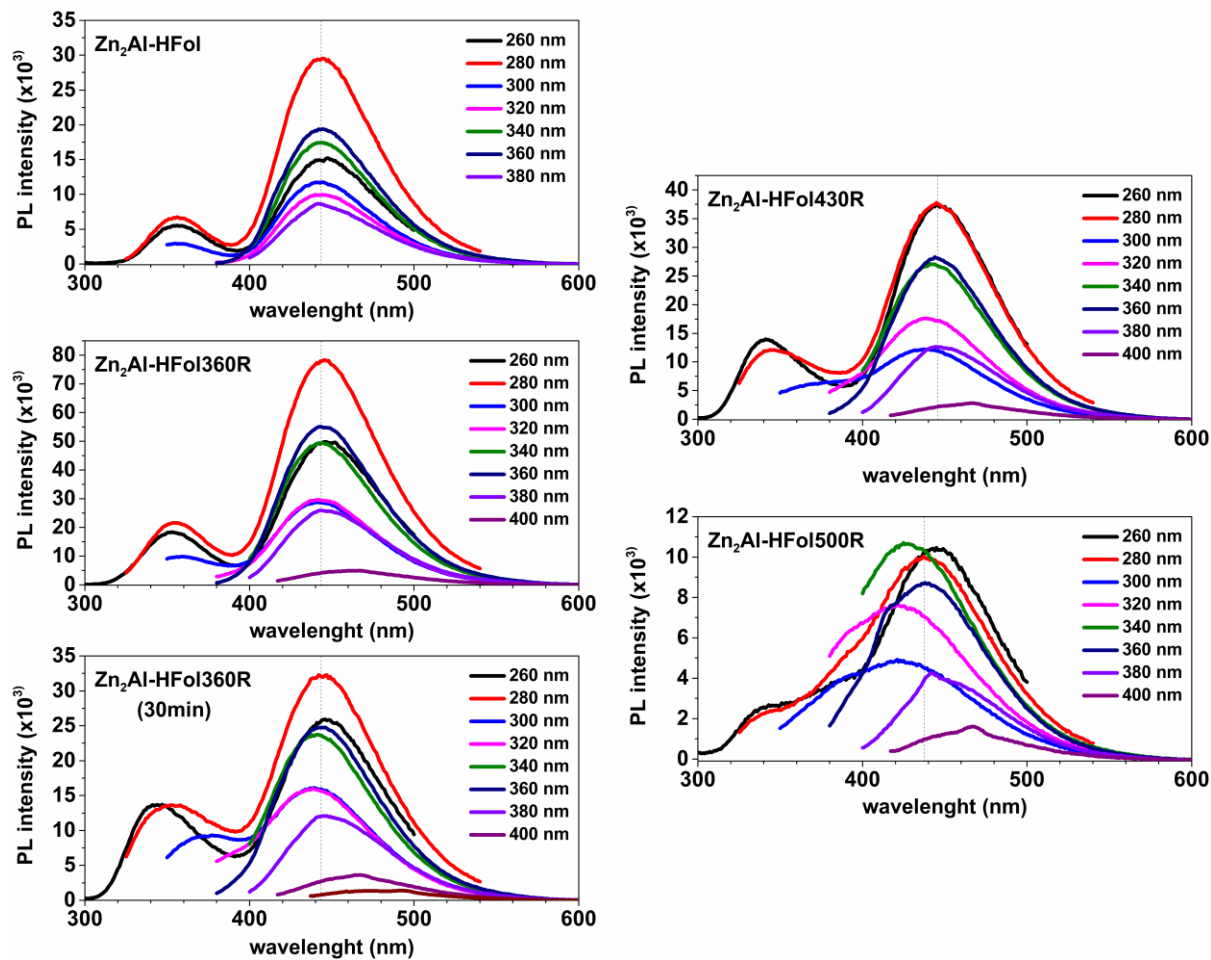


Figure S17. PL spectra in aqueous suspension (0.5 mg L^{-1}) under different excitation radiation of $\text{Zn}_2\text{Al-HFol}$ samples after pyrolysis/reconstitution.

2.1.9. LDH/C-dots obtained by Hydrothermal Carbonization

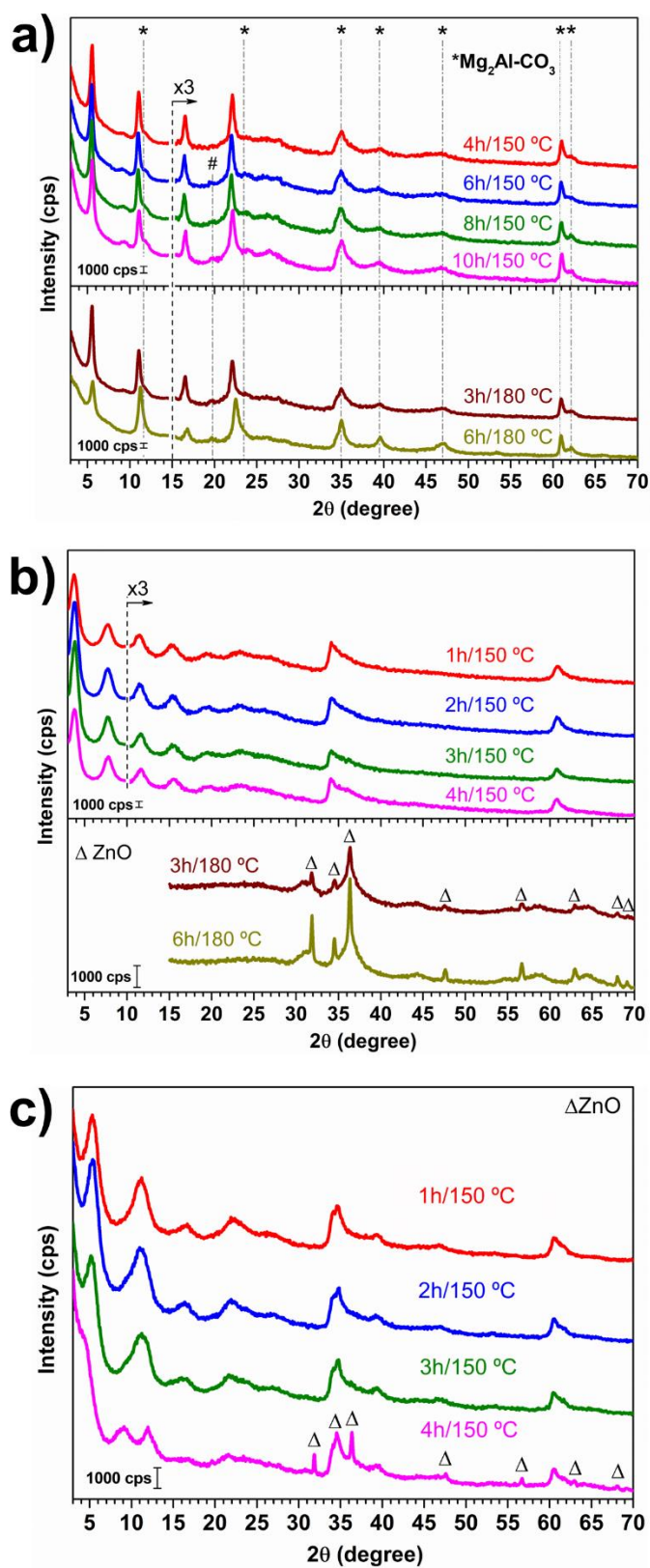


Figure S18. XRD patterns of Mg₂Al-Fol (a), Zn₂Al-HFol (b) and Zn₂Al-Fol (c) hydrothermally treated.

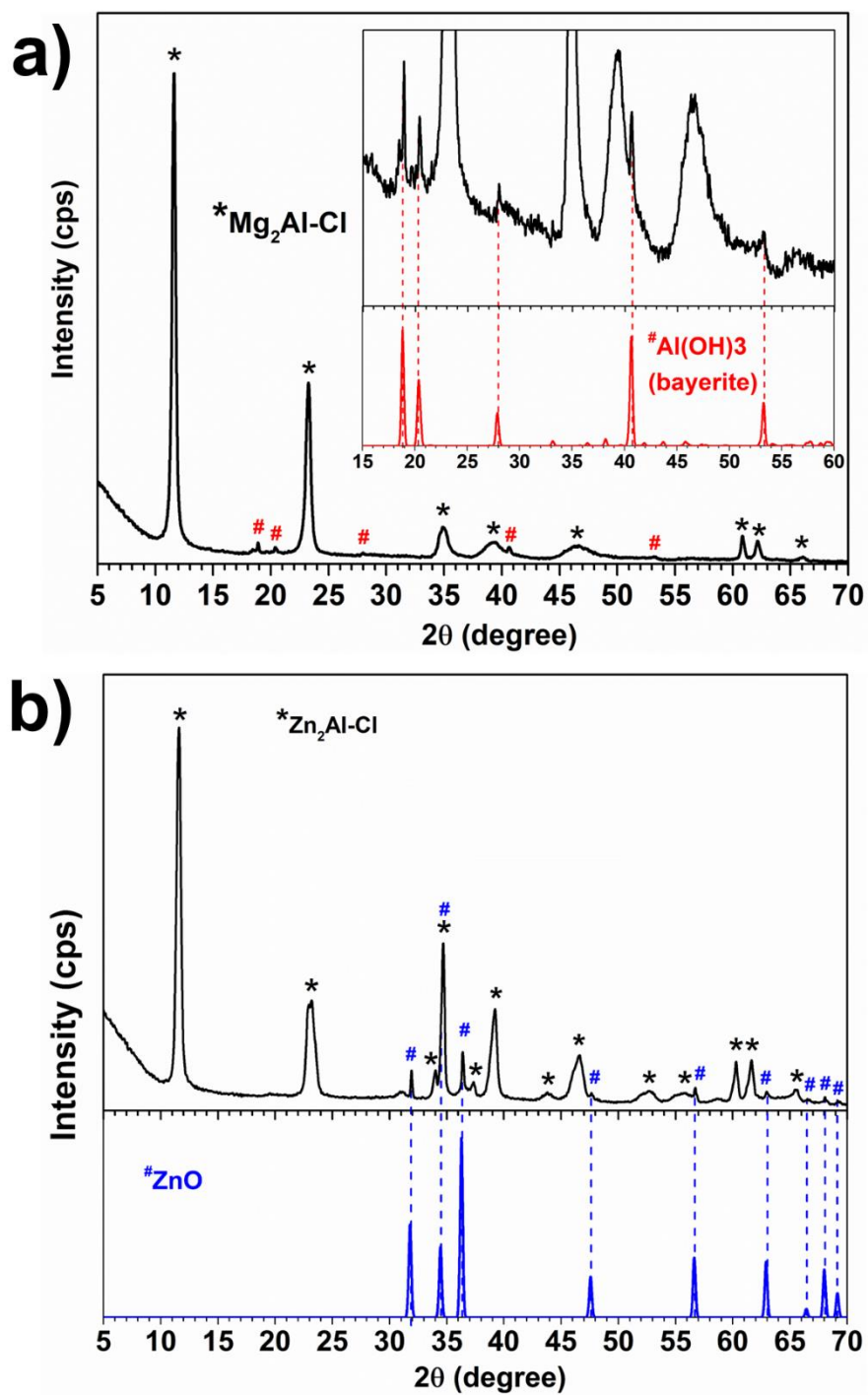


Figure S19. XRD patterns of $\text{Mg}_2\text{Al-Cl}$ (a) and $\text{Zn}_2\text{Al-Cl}$ (b) hydrothermally treated at 150°C for 4 h. Inset: Al(OH)_3 (bayerite, ICSD 26830) (a) and ZnO (wurtzite; ICSD 26170).

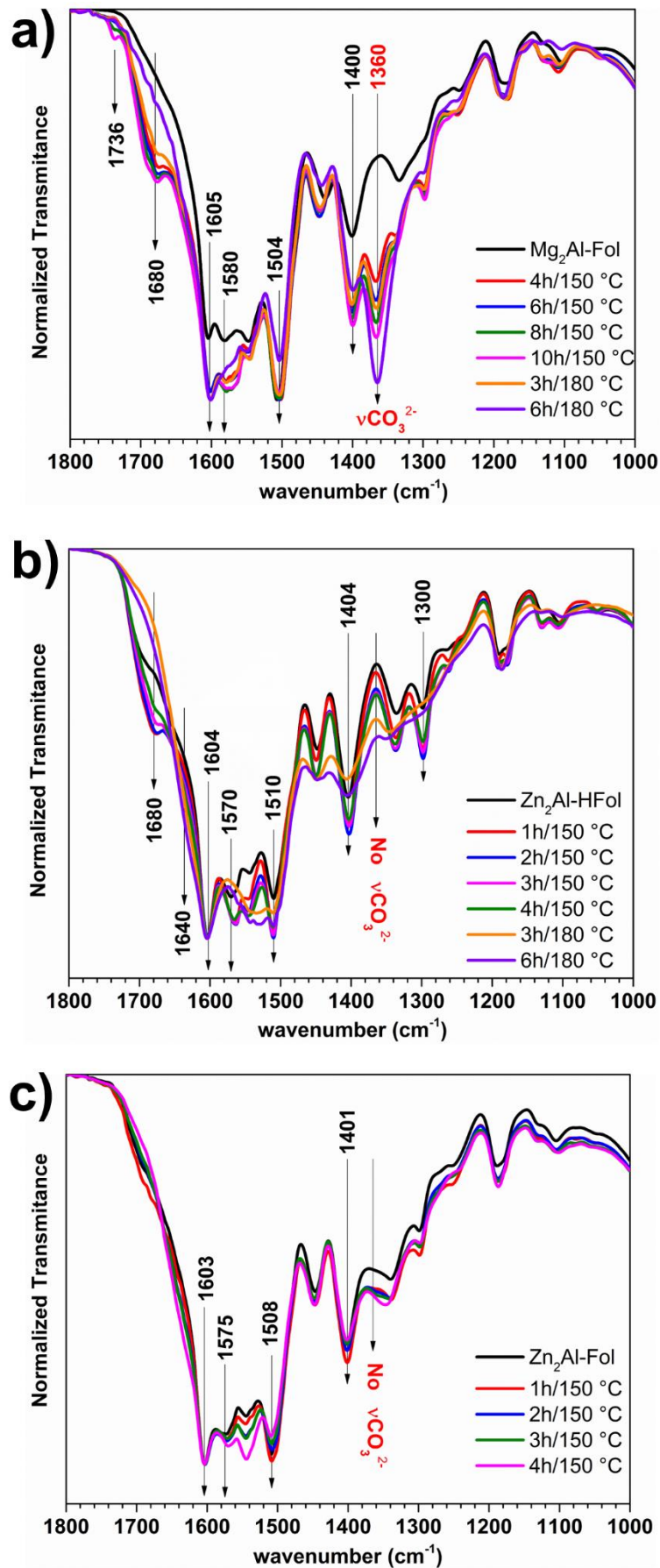


Figure S20. FTIR spectra of $\text{Mg}_2\text{Al-Fol}$ (a), $\text{Zn}_2\text{Al-HFol}$ (b) and $\text{Zn}_2\text{Al-Fol}$ (c) materials hydrothermally treated.

Table S7. Initial and final pH values of synthesis media and identified phases by XRD.

Sample	pH_i	pH_f	ΔpH	Identified phases
Mg₂Al-Cl	8.26			LDH
4h/150 °C	--	8.52	0.26	LDH and Al(OH) ₃ (bayerite)
Zn₂Al-Cl	6.14			LDH
4h/150 °C	--	6.19	0.05	LDH and ZnO (wurtzite)
Mg₂Al-Fol³⁻	8.03			LDH
4h/150 °C	--	8.45	0.42	LDH
6h/150 °C	--	8.55	0.52	LDH
8h/150 °C	--	8.51	0.48	LDH
10h/150 °C	--	8.56	0.53	LDH
3h/180 °C	--	9.46	1.43	LDH
6h/180 °C	--	9.03	1.00	LDH
Zn₂Al-Fol²⁻	7.18			LDH
1h/150 °C	--	6.95	-0.23	LDH
2h/150 °C	--	6.77	-0.41	LDH
3h/150 °C	--	6.5	-0.68	LDH
4h/150 °C	--	6.64	-0.54	LDH
3h/180 °C	--	6.66	-0.52	ZnO
6h/180 °C	--	6.81	-0.37	ZnO
Zn₂Al-Fol³⁻	7.10			LDH
1h/150 °C	--	7.01	-0.09	LDH
2h/150 °C	--	7.11	0.01	LDH
3h/150 °C	--	6.65	-0.45	LDH
4h/150 °C	--	7.07	-0.03	LDH and ZnO

pH_i = initial pH value; pH_f = final pH value;

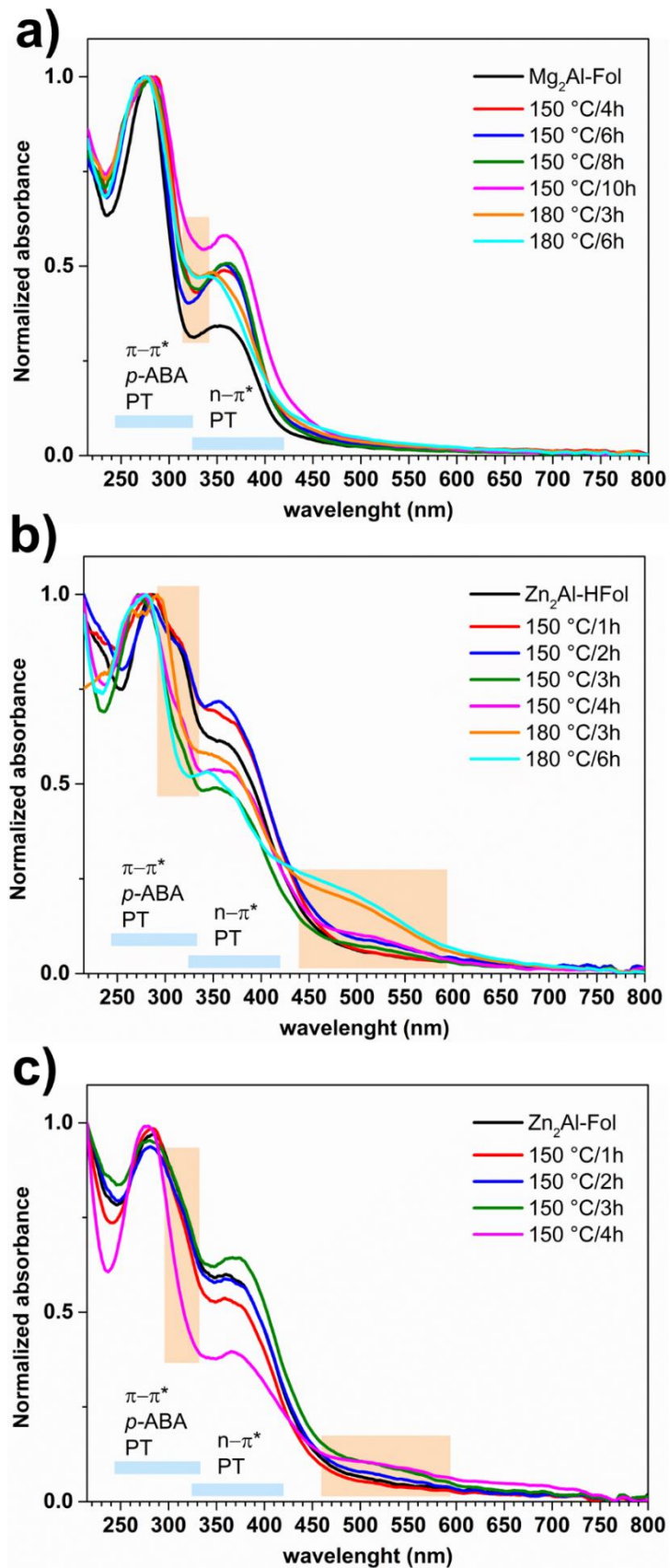


Figure S21. Electronic UV-VIS spectra of $Mg_2Al-Fol$ (a), $Zn_2Al-HFol$ (b) and $Zn_2Al-Fol$ (c) materials hydrothermally treated.

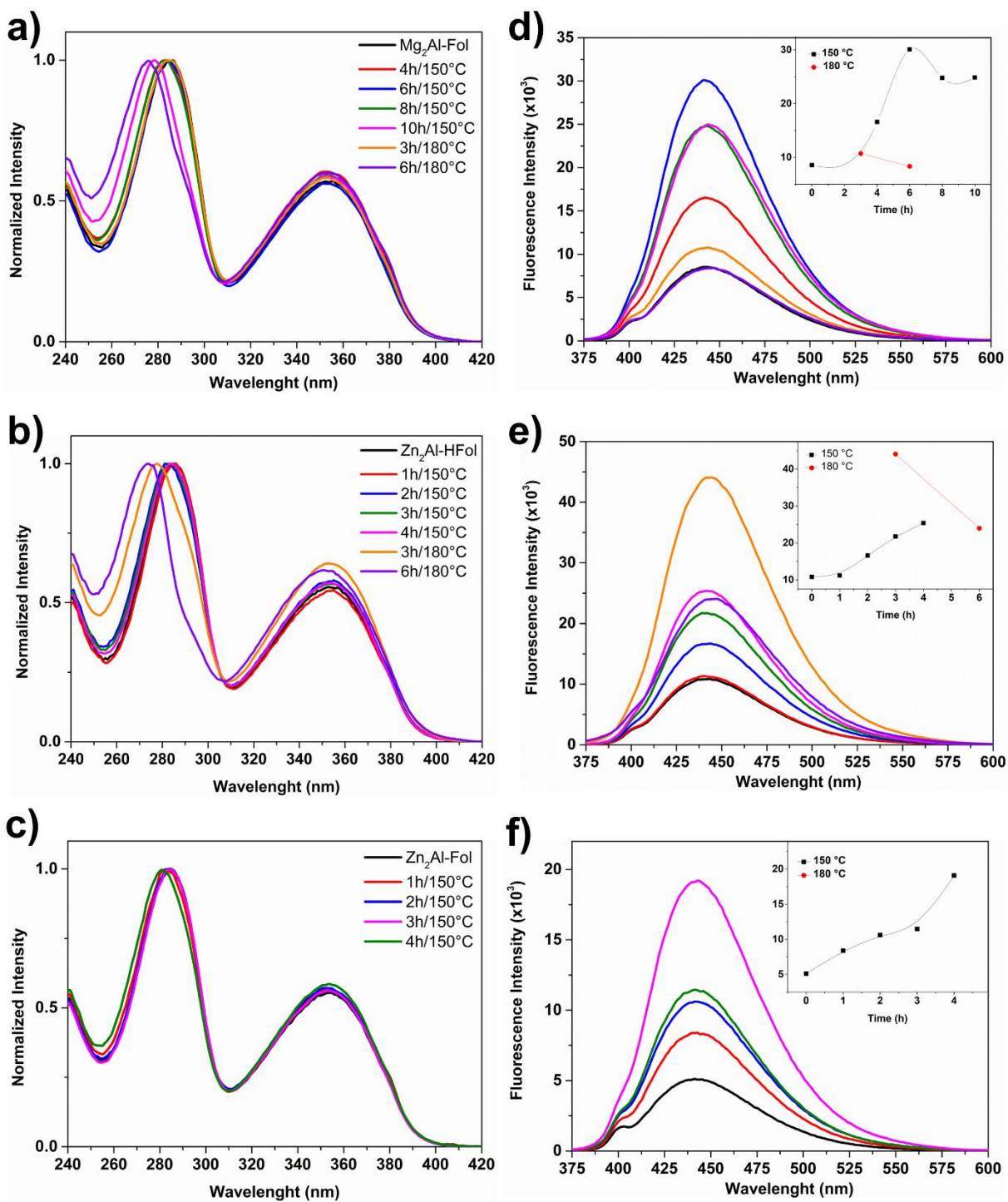


Figure S22. PLE (a-c) and PL(d-f) spectra of Mg₂Al-Fol (a,d), Zn₂Al-HFol (b,e) and Zn₂Al-Fol (c,f) materials hydrothermally treated.

References

- Arízaga, G.G.C., Jiménez, C.S., Saavedra, K.J.P., Lamas, A.M.M., Pérez, A.M.P., 2016. Folate-intercalated layered double hydroxide as a vehicle for cyclophosphamide, a non-ionic anti-cancer drug. *Micro Nano Lett.* 11, 360–362. <https://doi.org/10.1049/mnl.2016.0106>
- Arratia-Quijada, J., Sánchez Jiménez, C., Gurinov, A., Pérez Centeno, A., Ceja Andrade, I., Carbajal Arízaga, G.G., 2016. Dysprosium-containing layered double hydroxides nanoparticles intercalated with biologically active species as an approach for theranostic systems. *Mater. Sci. Eng. B Solid-State Mater. Adv. Technol.* 203, 7–12. <https://doi.org/10.1016/j.mseb.2015.10.004>
- Cunha, V.R.R., Guilherme, V.A., de Paula, E., de Araujo, D.R., Silva, R.O., Medeiros, J.V.R., Leite, J.R.S.A., Petersen, P.A.D., Foldvari, M., Petrilli, H.M., Constantino, V.R.L., 2016. Delivery system for mefenamic acid based on the nanocarrier layered double hydroxide: Physicochemical characterization and evaluation of anti-inflammatory and antinociceptive potential. *Mater. Sci. Eng. C* 58, 629–638. <https://doi.org/10.1016/j.msec.2015.08.037>
- Cunha, V.R.R., Petersen, P.A.D., Gonçalves, M.B., Petrilli, H.M., Taviot-Gueho, C., Leroux, F., Temperini, M.L.A., Constantino, V.R.L., 2012. Structural, spectroscopic (NMR, IR, and Raman), and DFT investigation of the self-assembled nanostructure of pravastatin-LDH (layered double hydroxides) systems. *Chem. Mater.* 24, 1415–1425. <https://doi.org/10.1021/cm202953y>
- Cunha, V.R.R., Petersen, P.A.D., Souza, R.B., Martins, A.M.C.R.P.F., Leroux, F., Taviot-Gueho, C., Petrilli, H.M., Koh, I.H.J., Constantino, V.R.L., 2020. Phytochemical species intercalated into layered double hydroxides: structural investigation and biocompatibility assays. *New J. Chem.* 44, 10011–10021. <https://doi.org/10.1039/D0NJ00238K>
- Dametto, P.R., Ambrozini, B., Caires, F.J., Franzini, V.P., Ionashiro, M., 2014. Synthesis, characterization and thermal behaviour of solid-state compounds of folates with some bivalent transition metals ions. *J. Therm. Anal. Calorim.* 115, 161–166. <https://doi.org/10.1007/s10973-013-3276-z>
- Evans, D.G., Slade, R.C.T., 2006. Structural Aspects of Layered Double Hydroxides, in: *Structure & Bonding*. Springer-Verlag, Berlin/Heidelberg, pp. 1–87. https://doi.org/10.1007/430_005
- Figueiredo, M.P., Cunha, V.R.R., Cellier, J., Taviot-Gueho, C., Constantino, V.R.L., 2022. Fe(III)-Based Layered Double Hydroxides Carrying Model Naproxenate Anions: Compositional and Structural Aspects. *ChemistrySelect* 7. <https://doi.org/10.1002/slct.202103880>
- Gil, O.M., Rocha, M.A., Constantino, V.R.L., Koh, I.H.J., de Faria, D.L.A., 2016. Modified drug release system based on Sulindac and layered double hydroxide: An in vivo Raman investigation. *Vib. Spectrosc.* 87, 60–66. <https://doi.org/10.1016/j.vibspec.2016.09.010>
- Gocheva, G., Petkov, N., Garcia Luri, A., Iliev, S., Ivanova, N., Petrova, J., Mitrev, Y., Madjarova, G., Ivanova, A., 2019. Tautomerism in folic acid: Combined molecular modelling and NMR study. *J. Mol. Liq.* 292, 111392. <https://doi.org/10.1016/j.molliq.2019.111392>
- Kaduk, J.A., Crowder, C.E., Zhong, K., 2015. Crystal structure of folic acid dihydrate, C₂₉H₂₉N₂O₆ (H₂O)₂. *Powder Diffr.* 30, 52–56. <https://doi.org/10.1017/S0885715614000815>

- Kim, T.H., Oh, J.M., 2016. Dual nutraceutical nanohybrids of folic acid and calcium containing layered double hydroxides. *J. Solid State Chem.* 233, 125–132. <https://doi.org/10.1016/j.jssc.2015.10.019>
- Kloprogge, J.T., Hickey, L., Frost, R.L., 2004. FT-Raman and FT-IR spectroscopic study of synthetic Mg/Zn/Al-hydrotalcites. *J. Raman Spectrosc.* 35, 967–974. <https://doi.org/10.1002/jrs.1244>
- Magri, V.R., Duarte, A., Perotti, G.F., Constantino, V.R.L., 2019. Investigation of Thermal Behavior of Layered Double Hydroxides Intercalated with Carboxymethylcellulose Aiming Bio-Carbon Based Nanocomposites. *ChemEngineering* 3, 55. <https://doi.org/10.3390/chemengineering3020055>
- Magri, V.R., Rocha, M.A., de Matos, C.S., Petersen, P.A.D., Leroux, F., Petrilli, H.M., Constantino, V.R.L., 2022. Folic acid and sodium folate salts: Thermal behavior and spectroscopic (IR, Raman, and solid-state ^{13}C NMR) characterization. *Spectrochim. Acta Part A Mol. Biomol. Spectrosc.* 273, 120981. <https://doi.org/10.1016/j.saa.2022.120981>
- Mallakpour, S., Hatami, M., 2019. Fabrication and characterization of pH-sensitive bio-nanocomposite beads having folic acid intercalated LDH and chitosan: Drug release and mechanism evaluation. *Int. J. Biol. Macromol.* 122, 157–167. <https://doi.org/10.1016/j.ijbiomac.2018.10.166>
- Nara, M., Torii, H., Tasumi, M., 1996. Correlation between the Vibrational Frequencies of the Carboxylate Group and the Types of Its Coordination to a Metal Ion: An ab Initio Molecular Orbital Study. *J. Phys. Chem.* 100, 19812–19817. <https://doi.org/10.1021/jp9615924>
- Pagano, C., Perioli, L., Latterini, L., Nocchetti, M., Ceccarini, M.R., Marani, M., Ramella, D., Ricci, M., 2019. Folic acid-layered double hydroxides hybrids in skin formulations: Technological, photochemical and in vitro cytotoxicity on human keratinocytes and fibroblasts. *Appl. Clay Sci.* 168, 382–395. <https://doi.org/10.1016/j.clay.2018.12.009>
- Qin, L., Wang, S., Zhang, R., Zhu, R., Sun, X., Yao, S., 2008. Two different approaches to synthesizing Mg–Al-layered double hydroxides as folic acid carriers. *J. Phys. Chem. Solids* 69, 2779–2784. <https://doi.org/10.1016/j.jpcs.2008.06.144>
- Qin, L., Wang, W., You, S., Dong, J., Zhou, Y., Wang, J., 2014. In vitro antioxidant activity and in vivo antifatigue effect of layered double hydroxide nanoparticles as delivery vehicles for folic acid. *Int. J. Nanomedicine* 9, 5701. <https://doi.org/10.2147/IJN.S74306>
- Rocha, M.A., Petersen, P.A.D., Teixeira-Neto, E., Petrilli, H.M., Leroux, F., Taviot-Gueho, C., Constantino, V.R.L., 2016. Layered double hydroxide and sulindac coiled and scrolled nanoassemblies for storage and drug release. *RSC Adv.* 6, 16419–16436. <https://doi.org/10.1039/C5RA25814F>
- Szakács, Z., Noszál, B., 2006. Determination of dissociation constants of folic acid, methotrexate, and other photolabile pteridines by pressure-assisted capillary electrophoresis. *Electrophoresis* 27, 3399–3409. <https://doi.org/10.1002/elps.200600128>
- Tronto, J., Crepaldi, E.L., Pavan, P.C., Cipriano De Paula, C., Valim, J.B., 2001. Organic Anions of Pharmaceutical Interest Intercalated in Magnesium Aluminum LDHs by Two Different Methods. *Mol. Cryst. Liq. Cryst. Sci. Technol. Sect. A. Mol. Cryst. Liq. Cryst.* 356, 227–237. <https://doi.org/10.1080/10587250108023703>

Xiao, R., Wang, W., Pan, L., Zhu, R., Yu, Y., Li, H., Liu, H., Wang, S.L., 2011. A sustained folic acid release system based on ternary magnesium/zinc/ aluminum layered double hydroxides. *J. Mater. Sci.* 46, 2635–2643. <https://doi.org/10.1007/s10853-010-5118-8>

SÚMULA CURRICULAR

I. DADOS PESSOAIS

Nome: Vagner Roberto Magri

Local e data de nascimento: Palestina-SP, Brasil, 26 de junho de 1990

<http://lattes.cnpq.br/6952807557369194>

<https://orcid.org/0000-0001-9746-3797>

II. EDUCAÇÃO

II. I. Colégio: Centro Estadual de Educação Tecnológica Paula Souza – CEETEPS, Monte Aprazível-SP, 2007.

II. II. Graduação: Licenciatura Plena em Química, Centro Universitário de Votuporanga (UNIFEV), Bolsa PROUNI integral, Votuporanga-SP, 2011

II. III. Pós-graduação: Mestrado em Química, Instituto de Biociências, Letras e Ciências Exatas da Universidade Estadual Paulista "Júlio de Mesquita Filho" – IBILCE/UNESP, São José do Rio Preto-SP, 2015

Título: Adsorção-fotodegradação do herbicida paraquate em água pela argila Na-Bentonita e por novos materiais TiO₂-Bentonita, TiO₂/ZnO-Bentonita, Al/Fe-Bentonita e Al/Fe.Cu-Bentonita

III. FORMAÇÃO COMPLEMENTAR

III. I. Cursos Técnicos: em Agricultura, Pecuária e Meio Ambiente, Centro Estadual de Educação Tecnológica Paula Souza – CEETEPS, Monte Aprazível-SP, 2007

III. II. Cursos de curta duração (período do doutoramento):

“Aplicação de espectroscopia EPR na caracterização e estudos de argilas”, Universidade de Franca (UNIFRAN), Brasil, 2019, 6h

“Microscopia Eletrônica de Varredura para Argilas” - Universidade Federal do Piauí (UFPI) – 2018, 8h

“Workshop de Análise Térmica”, Instituto de Biociências, Letras e Ciências Exatas da Universidade Estadual Paulista “Júlio de Mesquita Filho” – IBILCE/UNESP, 2017, 8h

.

IV. OCUPAÇÃO

Bolsista de Doutorado, Coordenação de Aperfeiçoamento de Pessoal de Nível Superior (CAPES), bolsa 33002010191P0 – Química, 03/2016 a 03/2020

V. EXPERIENCIA INTERNACIONAL

Estagio no *Institut de Chimie de Clermont-Ferrand (ICCF)* da *Université Clermont Auvergne (UCA)* – 24/01/022 a 22/04/2022

O trabalho intitulado “*Layered Double Hydroxide (LDH) intercalated with organic species for “adsolubilization” of molecules of interest*” foi realizado sob a supervisão da Profa. Dra. Christine Taviot-Gueho da equipe de *Matériaux Inorganiques* daquele instituto. O estágio foi financiado pelo *Centre National de la Recherche Scientifique (CNRS)* por meio do projeto Pack Ambition International 2019 E LS 200788

VI. ATIVIDADES COMPLEMENTARES

VI. I. Estagio supervisionado (durante o período de doutoramento): Instituto de Química da Universidade de São Paulo (IQ-USP), atuando nas seguintes disciplinas:

Química Inorgânica – 2016

Química Geral – 2017 (Bolsa do Programa de Aperfeiçoamento de Ensino – PAE)

VI. II. Participação em Comissão Organizadora de eventos (durante o período de doutoramento):

“III Reunião Anual de Argilas”, IQ-USP, São Paulo-SP, Brasil, 2017

“X Congraço Brasileiro/IV Congresso Panamericano de Analise Térmica e Calorimetria (CBRATEC/CPANATEC)”, São Paulo-SP, Brasil, 2016

VII. PUBLICAÇÕES

VII. I. Artigos Completos:

Magri, V. R., Rocha, M. A., de Matos, C. S., Petersen, P. A. D., Leroux, F., Petrilli, H. M., Constantino, V. R. L. Folic acid and sodium folate salts: Thermal behavior and spectroscopic (IR, Raman, and solid-state ¹³C NMR) characterization. **Spectrochim. Acta Part A Mol. Biomol. Spectrosc.** 273, 120981, 2022. <https://doi.org/10.1016/j.saa.2022.120981>

Vagner R. Magri, Alfredo Duarte, A. Gustavo F. Perotti and Vera R. L. Constantino. Investigation of Thermal Behavior of Layered Double Hydroxides Intercalated with Carboxymethylcellulose Aiming Bio-Carbon Based Nanocomposites. **ChemEngineering**, v. 3, p. 55, 2019. <https://doi.org/10.3390/chemengineering3020055>

Vera Regina Leopoldo Constantino, Mariana Pires Figueiredo, Vagner Roberto Magri, Denise Eulálio, Vanessa Roberta Rodrigues Cunha, Ana Clecia Santos Alcântara and Gustavo Frigi Perotti. Biomaterials Based on Organic Polymers and Layered Double Hydroxides Nanocomposites: Drug Delivery and Tissue Engineering. **Pharmaceutics**, 15(2), 413, 2023. <https://doi.org/10.3390/pharmaceutics15020413>

VII. II. Capítulo de Livro

Vera R. L. Constantino, Vanessa R. R. Cunha, Michele A. Rocha, Mariana P. Figueiredo, Vagner R. Magri, Denise Eulálio, Gustavo F. Perotti, Marcos A. Bizeto, Willian F. Zambuzzi e Ivan H.J. Koh. **Layered Double Hydroxides: characterization, biocompatibility and therapeutic purposes in Progress in Layered Double Hydroxides from synthesis to new applications** (*Series on Chemistry, Energy and the Environment: Volume 8*). Ed.: Morena Nocchetti and Umberto Costantino, 528 p., 2022. https://doi.org/10.1142/9789811240614_0006

VII. III. Resumos em Congressos (durante o período de doutoramento):

Magri, V. R.; Loureiro, P. A. C.; Constantino, V. R. L. Comparative Characterization of M^{2+}/M^{3+} ($M^{2+} = Mg^{2+}$ or Zn^{2+} and $M^{3+} = Al^{3+}$ or Ga^{3+}) Carbonate-Intercalated Layered Double Hydroxides, 20th International Symposium on Intercalation Compounds (ISIC), Campinas-SP, Brazil, **2019**.

Magri, V.R.; Duarte, A.; Perotti, G. F.; Constantino, V. R. L. Layered Double Hydroxides Intercalated with Carboxymethylcellulose as Precursor of Carbon-Based Nanocomposites, V Reunião sobre Argilas Aplicadas, Franca-SP, Brasil, **2019**.

Magri, V. R.; Constantino, V. R. L. Hidróxido duplo lamelar de Mg^{2+}/Al^{3+} intercalado com carboximetilcelulose: potencial precursor de nanocompósitos constituídos por material carbonáceo, IV Reunião sobre Argilas Aplicadas e I Ciclo de Minicursos em Materiais, Teresina-PI, Brazil, **2018**.
Trabalho premiado em segundo lugar na modalidade pôster

Magri, V. R.; De Matos, C. S.; Rocha, M. A.; Constantino, V. R. L. Thermal Behavior of Zn/Al Layered Double Hydroxide Intercalated with Folate: Relevance for Production of Carbon Nanocomposites, 46th World Chemistry Congress, 40th Annual Meeting of The Brazilian Chemical Society and Iupac 49th General Assembly, São Paulo-Sp, Brazil, **2017**.

Dadamos, T. R. L.; Franzin, B. T.; Guizellini, F. C.; Magri, V. R.; Da Silva, R. J. N. B.; Pastre, I. A.; Fertoni, F. L. Caracterização Térmica E Microestrutural de Sensor Fluorimétrico para Detecção do Herbicida Paraquate em Águas, XI Congresso Brasileiro de Análise Térmica e Calorimetria (XI CEBRATEC), Rio De Janeiro-RJ, Brasil, **2018**.

Dadamos, T. R. L.; Magri, V. R.; Franzin, B. T.; Ribeiro, W. S. C.; Abra, L. M.; Fertoni, F. L.; Pastre, I. A. Interação Argilas-Herbicida Paraquate, III Reunião sobre Argilas, São Paulo-SP, Brasil, **2017**.

De Matos, C.S.; Rocha, M. A.; Magri, V. R.; T.-Gueho, C.; Leroux, F.; Araki, K.; Constantino, V.R.L. Effect of Layer Composition on Pyrolysis of M_2Al -Folate ($M = Ni, Zn$ or Mg) Layered Double Hydroxides, 19th International Symposium on Intercalation Compounds, Assisi, Italy, **2017**.

VIII. OUTRAS ATIVIDADES:

VIII. I. Minicurso de curta duração ministrado:

Magri, V.R.; Figueiredo, M. P. *Materiais Lamelares: Estrutura e Propriedades*. 2020.

VIII. II. Representação discente:

Membro titular na Comissão de Ética e Direitos Humanos (CEDH) do IQ-USP, 2016-2018

Membro titular na Congregação do IQ-USP, 2016-2017

Membro suplente na Congregação do IQ-USP, 2017-2018

Membro suplente na Comissão Coordenadora de Programa (CCP) Química do IQ-USP, 2016-2017

VIII. II. Participação em bancas de trabalhos de conclusão:

Pastre, I. A.; Lima, M. F.; Magri, V. R. Participação em Banca de Walter Dos Santos Cardozo Ribeiro. Adsorção e Fotodegradação do Herbicida Paraquat por Bentonita Sódica e Al/Fe-Bentonita Pilarizada. **2017**. Trabalho de Conclusão de Curso (Graduação Em Química). Instituto de Biociências, Letras e Ciências Exatas da Universidade Estadual Paulista "Júlio de Mesquita Filho" – IBILCE/UNESP, São José do Rio Preto–SP.